

Ivan Zelinka
Vo Hoang Duy
Jaesang Cha *Editors*

AETA 2013: Recent Advances in Electrical Engineering and Related Sciences

Lecture Notes in Electrical Engineering

Volume 282

For further volumes:
<http://www.springer.com/series/7818>

About this Series

“Lecture Notes in Electrical Engineering (LNEE)” is a book series which reports the latest research and developments in Electrical Engineering, namely:

- Communication, Networks, and Information Theory
- Computer Engineering
- Signal, Image, Speech and Information Processing
- Circuits and Systems
- Bioengineering

LNEE publishes authored monographs and contributed volumes which present cutting edge research information as well as new perspectives on classical fields, while maintaining Springer’s high standards of academic excellence. Also considered for publication are lecture materials, proceedings, and other related materials of exceptionally high quality and interest. The subject matter should be original and timely, reporting the latest research and developments in all areas of electrical engineering.

The audience for the books in LNEE consists of advanced level students, researchers, and industry professionals working at the forefront of their fields. Much like Springer’s other Lecture Notes series, LNEE will be distributed through Springer’s print and electronic publishing channels.

Ivan Zelinka · Vo Hoang Duy
Jaesang Cha
Editors

AETA 2013: Recent Advances in Electrical Engineering and Related Sciences

Editors

Ivan Zelinka

Department of Computer Science
Faculty of Electrical Engineering and
Computer Science
VŠB-Technical University of Ostrava
Ostrava-Poruba
Czech Republic

Jaesang Cha

Seoul National University of Science and
Technology
Dept. of Electronice and IT
Media Engineering
Seoul
Korea, Republic of (South Korea)

Vo Hoang Duy

Department of Automatic Control
Faculty of Electrical - Electronics
Engineering
Ton Duc Thang University
Ho Chi Minh City
Vietnam

ISSN 1876-1100

ISBN 978-3-642-41967-6

DOI 10.1007/978-3-642-41968-3

Springer Heidelberg New York Dordrecht London

ISSN 1876-1119 (electronic)

ISBN 978-3-642-41968-3 (eBook)

Library of Congress Control Number: 2013951888

© Springer-Verlag Berlin Heidelberg 2014

This work is subject to copyright. All rights are reserved by the Publisher, whether the whole or part of the material is concerned, specifically the rights of translation, reprinting, reuse of illustrations, recitation, broadcasting, reproduction on microfilms or in any other physical way, and transmission or information storage and retrieval, electronic adaptation, computer software, or by similar or dissimilar methodology now known or hereafter developed. Exempted from this legal reservation are brief excerpts in connection with reviews or scholarly analysis or material supplied specifically for the purpose of being entered and executed on a computer system, for exclusive use by the purchaser of the work. Duplication of this publication or parts thereof is permitted only under the provisions of the Copyright Law of the Publisher's location, in its current version, and permission for use must always be obtained from Springer. Permissions for use may be obtained through RightsLink at the Copyright Clearance Center. Violations are liable to prosecution under the respective Copyright Law.

The use of general descriptive names, registered names, trademarks, service marks, etc. in this publication does not imply, even in the absence of a specific statement, that such names are exempt from the relevant protective laws and regulations and therefore free for general use.

While the advice and information in this book are believed to be true and accurate at the date of publication, neither the authors nor the editors nor the publisher can accept any legal responsibility for any errors or omissions that may be made. The publisher makes no warranty, express or implied, with respect to the material contained herein.

Printed on acid-free paper

Springer is part of Springer Science+Business Media (www.springer.com)

Foreword

Modern world is based on vitally important technologies that merge e.g. electronics, cybernetics, computer science, telecommunication, and physics together. Since the beginning of our technologies, we have been confronted with numerous technological challenges such as finding the optimal solution of various problems including controlling technologies, power sources construction, robotics, etc. Technology development of those and related areas has had and continues to have profound impact on our civilization and our future life style.

Therefore, this proceeding book containing articles of international conference AETA 2013, edited by Ivan Zelinka (Czech Republic), Vo Hoang Duy (Vietnam) and Jaesang Cha (Korea), is a timely volume to be welcome by the community focused on telecommunication, power control and optimization as well as computational science community and beyond.

This proceeding book consists of 12 topic areas of selected papers like: telecommunication, power systems, digital signal processing, robotics, control system, renewable energy, power electronics, soft-computing and more. Readers can find interesting papers about multi-receive antennas, EEG data similarity using Lempel-Ziv complexity, study on design for a new underwater disk Robo, adaptive network-based fuzzy inference system controller for an active magnetic bearing system with unbalance mass or evolutionary control of chaotic Lozi map by means of chaos driven differential evolution. All selected papers represent interesting ideas and state of art overview.

Participations were carefully selected and reviewed, hence, this proceeding book certainly is one of the few discussing the benefit from intersection of those modern and fruitful scientific fields of research. We hope that the proceeding book will be an instructional material for senior undergraduate and entry-level graduate students working in the area of electronic, power technologies, energy distribution, control and robotics, etc. The proceeding book will also be resource and material for practitioners who want to apply discussed topics to solve real-life problems in their challenging applications. The important part of proceeding book is participations of three keynote speakers from the Czech Republic and France.

The decision to organize AETA conference and to create this proceeding book was based on facts that technologies mentioned above, their use and impact on life is an interesting area, which is under intensive research from many other branches of science today. This proceeding book is written to contain simplified versions of experiments with the aim to show how, in principle, problems about power systems can be solved.

It is obvious that this proceeding book does not encompass all aspects of discussed topics due to limited space and time of conference. Only the main ideas and results of selected papers are reported here. The authors and editors hope that the readers will be inspired to do their own experiments and simulations, based on information reported in this proceeding book, thereby moving beyond the scope of it.

This proceeding book is devoted to the studies of common and related subjects in intensive research fields of modern electric, electronic and related technologies. For these reasons, we believe that this proceeding book will be useful for scientists and engineers working in the above-mentioned fields of research and applications.

At the end we would like to thank to Ton Duc Thang University (Ho Chi Minh City, Vietnam), VŠB-Technical University (Ostrava, Czech Republic) for interest and strong support in AETA conference organization. Also many thanks belong to Springer publishing company for its highly professional, precise and quick production process. Without all of this would be impossible to organize successful conference joining European and Asian participants.

September 2013

Ivan Zelinka, Czech Republic

Vo Hoang Duy, Vietnam

Jaesang Cha, Korea

This conference was supported by the Ton Duc Thang University (Ho Chi Minh City, Vietnam) and VŠB - Technical University (Ostrava, Czech Republic) and by the Development of human resources in research project, reg. no. CZ.1.07/2.3.00/20.0072 funded by Operational Programme Education for Competitiveness, co-financed by ESF and state budget of the Czech Republic.



INVESTMENTS IN EDUCATION DEVELOPMENT

Contents

Keynotes

Recent Advances in Speech Quality Assessment and Their Implementation	1
<i>Miroslav Voznak</i>	
On Evolutionary Design of Complex Structures and Electronic Circuits	15
<i>Ivan Zelinka</i>	
Fault Diagnosis and Fault Tolerant Control for Fuzzy Systems: Application to Vehicle Dynamic	25
<i>M. Chadli</i>	

Power System

Analysis of Electron Transport Coefficients in $\text{CF}_3\text{I-N}_2$ Mixture Gas Using an Electron Swarm Study	29
<i>Do Anh Tuan, Chu Dinh Hanh</i>	
Analysis of the Electromagnetic Force in an Magnetohydrodynamic Flowmeter	39
<i>Le Chi Kien</i>	
Enhancing Total Transfer Capability via Optimal Location of TCSC in Deregulated Electricity Market	47
<i>ThanhLong Duong, Yao JianGang, LeAnhTu Nguyen, Guo ZhenWei</i>	
Augmented Lagrange Hopfield Network Based Method for Multi-objective Hydrothermal Scheduling	57
<i>Nguyen Trung Thang, Vo Ngoc Dieu</i>	

Technical Efficiency for Selection and Estimation Quality of Distance Relay Protection Setting	67
<i>Tran Hoang Quang Minh</i>	
Optimal Load Shedding Based on Frequency, Voltage Sensitivities and AHP Algorithm	75
<i>Huy Anh Quyen, Quang Anh Bui, Trong Nghia Le, Tan Thanh Tung Le</i>	
Renewable Energy	
Modeling a Wind Turbine System Using DFIG and Realization of Current Control on the Model with Fuzzy Logic Controller	85
<i>Ho-Ling Fu, Huynh Thanh Thien</i>	
Combining the Daylight and Artificial Light Based on Fuzzy Logic	93
<i>Huy Anh Quyen, Tan Thanh Tung Le, Trong Nghia Le, Thi Minh Thuy Pham</i>	
Improved Pitch Angle Control for Variable-Speed Wind Turbine System.....	103
<i>Tan Luong Van, Buu Pham Nhat Tan Nguyen, Trung Hieu Truong, Tran Thanh Trang</i>	
Nonlinear Control of PMSG Wind Turbine Systems	113
<i>Tan Luong Van, Trung Hieu Truong, Buu Pham Nhat Tan Nguyen, Tran Thanh Trang</i>	
Optimization of Water Cooling for a Converter	125
<i>Roman Sprlak, Petr Chlebis</i>	
Power Electronics	
Approximate 2DOF Digital Controller for Interleaved PFC Boost Converter	135
<i>Yuto Adachi, Yohei Mochizuki, Kohji Higuchi, Kosin Chamnongthai</i>	
A Study of Virtual Model of Power Supply Laboratory	145
<i>Pham Thanh Nhan, Nguyen Thanh Nghia, Huynh Xuan Dung, Quyen Huy Anh, Bui Huu Phu, Tran Thanh Trang</i>	
Neutral Point Voltage Balancing Method and the Influence of Some Parameters on Capacitor Voltage in Three-Level NPC Converter	159
<i>Vo Xuan Nam, Le Van Manh Giau, Nguyen Van Nho, Tran Thanh Trang</i>	

Telecommunications

TLSR: A Tree Link State Routing for Infrastructure-Based Mobile Ad Hoc Networks	169
<i>Chi Trung Ngo, Hoon Oh</i>	
Selection Combining Technique and Its Real-Time FPGA Implementation for Spectrum Sensing Efficiency Improvement in Cognitive Radio	181
<i>Tu T. Nguyen, Tri M. Nguyen, Khoa L. Dang, Phuong H. Nguyen</i>	
Performance Analysis of the IEEE 802.11p under Finite Traffic Conditions	191
<i>Duc Ngoc Minh Dang, Hanh Ngoc Dang, The Cuong Do, Choong Seon Hong</i>	
Wireless Digital Signage for Intelligent Traffic Management System	201
<i>Mukti Winanda, Nila Gita Cahyani, Whilda Chaq</i>	
Text Similarity Based on Data Compression in Arabic	211
<i>Hussein Soori, Michal Prilepok, Jan Platos, Eshetie Berhan, Vaclav Snasel</i>	
Peak-to-Average Power Ratio Reduction in Long Haul Coherent Optical OFDM Systems	221
<i>Dang Le Khoa, Nguyen Thanh Tu, Nguyen Thi Hong Thu, Nguyen Huu Phuong</i>	
A Novel Wideband VHF Antenna for Impulse Ground Penetrating Radar Systems	229
<i>Dong Tan Phuoc, Pham Minh Quang, Bui Huu Phu, Lai Nguyen Duy</i>	
TOA Estimation Algorithm Based on Shift-Invariant Technique for Multi-band Signals	241
<i>Ying-chun Li, Seungryeol Go, Hyung-ryeol Yoo, Sang-deok Kim, Jong-Wha Chong</i>	
PWM Noise Reduction in OFDM-Based Power Supply Overlaid Communication System for Industrial Machine Control	247
<i>Hidetsugu Koga, Masayuki Kurosaki, Hiroshi Ochi</i>	
Digital Signal Processing	
Measuring and Control Central Based on Digital Signal Controller	259
<i>Josef Oplustil, Roman Sprlak, Daniel Kalvar, Miroslav Uchoc, Petr Palacky, Vaclav Sladeczek</i>	

Autocorrelation Properties of Walsh Function for Logic Synthesis FPGA	269
<i>Nguyen Huu Khanh Nhan</i>	
Application of Street Tracking Algorithm in a Feedback Configuration for an Integrated INS/GPS Navigation System...	279
<i>Nguyen Van Thang, Chu Duc Trinh, Tran Duc Tan</i>	
EEG Data Similarity Using Lempel-Ziv Complexity	289
<i>Ibrahim Salem Jahan, Michal Prilepok, Vaclav Snasel</i>	
An Energy-Aware Routing Protocol for Wireless Sensor Networks Based on K-Means Clustering	297
<i>Thai T. Vu, Viet D. Nguyen, Hien M. Nguyen</i>	
Image Processing	
Neighboring Pixels Based on a Log-linearized Gaussian Mixture Model for Image Segmentation	307
<i>Khoa Anh Tran, Gueesang Lee</i>	
Uncertainty Analysis of LIDAR and Panoramic Camera Calibration	317
<i>Angel-Iván García-Moreno, José-Joel Gonzalez-Barbosa, Francisco-Javier Ornelas-Rodriguez, Juan B. Hurtado-Ramos</i>	
An Implementation of High Speed DCT and Hadamard Transform for H.264	329
<i>Bui An Dong, Huynh Quoc Thinh</i>	
Computer Science	
Dynamic Identity-Based Authentication Scheme with Perfect Forward Secrecy Session Key	339
<i>Toan-Thinh Truong, Minh-Triet Tran, Anh-Duc Duong</i>	
Automated Face Comparison with Facebook Friend's Faces and Flickr Photos.....	349
<i>Petr Šaloun, Jakub Stonawski, Ivan Zelinka</i>	
Soft Computing	
A Hybrid Genetic Algorithm – Sequential Quadratic Programing Approach for Canting Keel Optimization in Transverse Stability of Small Boat Design	363
<i>Tat-Hien Le, Vo Hoang Duy, Pham Nhat Phuong, Jong-Ho Nam</i>	

Evolutionary Control of Chaotic Lozi Map by Means of Chaos Driven Differential Evolution	371
<i>Roman Senkerik, Michal Pluhacek, Ivan Zelinka, Donald Davendra, Zuzana Kominkova Oplatkova, Roman Jasek</i>	
Arnold Cat Map and Sinai as Chaotic Numbers Generators in Evolutionary Algorithms	381
<i>Lenka Skanderova, Ivan Zelinka</i>	
Optimizing Transportation Sequence in Warehouse with Genetic Algorithms	391
<i>Xuan-Thuong Tran, Thanh-Do Tran, Hwan-Seong Kim</i>	
Control System	
Decentralized Output Feedback Control for Mismatched Uncertain Large Scale Systems: An LMI Approach	403
<i>Yao-Wen Tsai, Huynh Van Van, Lee Cua Ting, Kuo-Kai Shyu</i>	
A Simulation Study of Power Management for a Series Hydraulic Hybrid Vehicle	413
<i>Chih-Keng Chen, Tri-Vien Vu, Chih-Wei Hung</i>	
Fuzzy Model Predictive Control of DC-DC Converters	423
<i>O. Hazil, S. Bououeden, M. Chadli, S. Filali</i>	
Adaptive Network-Based Fuzzy Inference System (ANFIS) Controller for an Active Magnetic Bearing System with Unbalance Mass	433
<i>Seng-Chi Chen, Dinh-Kha Le, Van-Sum Nguyen</i>	
Stabilization of the Rotational Inverted Pendulum Using Mixed H_2/H_∞ PID Controller	445
<i>Vo Hoang Duy, Dong Si Thien Chau, Vo Huu Hau, Phan Thai Hoa, Tran Trong Dao</i>	
Study on Control of Quarter Car Suspension Using Simple Force Actuator for Education Purpose	457
<i>Duy Anh Nguyen, Hwan Seong Kim, Sang Bong Kim, Tan Tien Nguyen</i>	
Remote Mouse Control Using Fingertip Tracking Technique	467
<i>Phuong Dat Le, Vinh Hao Nguyen</i>	

Motor Control

- Rotor Speed Estimation Based on Extended Kalman Filter for Sensorless Vector Control of Induction Motor** 477
Phuc Thinh Doan, Thanh Luan Bui, Hak Kyeong Kim, Gi Sig Byun, Sang Bong Kim

- Application of Stepper Motors in Medical Electronics** 487
Vaclav Sladecek, Petr Palacky, Josef Oplustil, Miroslav Uchoc, Karel Frydrysek, Leopold Pleva, Lubos Zilka

- Optimization of Electric Energy in Three-Phase Induction Motor by Balancing of Torque and Flux Dependent Losses** 497
Nguyen Thanh Hung, Nguyen Chi Thien, Thanh Phuong Nguyen, Viet So Le, Doan Anh Tuan

Robotics

- Adaptive Motion Controller Design for an Omnidirectional AGV Based on Laser Sensor** 509
Thanh Luan Bui, Phuc Thinh Doan, Hak Kyeong Kim, Van Giap Nguyen, Sang Bong Kim

- Position Control of a Small Scale Quadrotor Using Block Feedback Linearization Control** 525
Van Tu Duong, Hak Kyeong Kim, Tan Tien Nguyen, Sea June Oh, Sang Bong Kim

- Trajectory Tracking Algorithm for Automatic Guided Vehicle Based on Adaptive Backstepping Control Method** 535
Pandu Sandi Pratama, Bui Thanh Luan, Thien Phuc Tran, Hak Kyeong Kim, Sang Bong Kim

- A Study on Controllers Design Based on Centroid Displacements for Depth Motion of a 3-Joint Carangiform Fish Robot** 545
Khac Anh Hoang, Tuong Quan Vo

- Experimental Comparison of A* and D* Lite Path Planning Algorithms for Differential Drive Automated Guided Vehicle** 555
Yuhanes Dedy Setiawan, Pandu Sandi Pratama, Sang Kwon Jeong, Vo Hoang Duy, Sang Bong Kim

- Study on Design for a New Underwater Disk Robot** 565
Ngoc-Huy Tran, Hyeung-Sik Choi, Sang-Seob Lee, Jeong-min Seo

- Tracking Control of an Unmanned Surface Vehicle** 575
Ngoc-Huy Tran, Hyeung-Sik Choi, Se-Hoon Baek, Hee-Young Shin

Integral Sliding Mode Control of Two-Wheeled Welding Mobile Robot for Tracking Desired Welding Path.....	585
<i>Nguyen Hung, Pham Hung Kim Khanh, Than Van The</i>	
A Study on Locomotions of Quadruped Robot	595
<i>Than Trong Khanh Dat, Tran Thien Phuc</i>	
Adaptive Line Trajectory Identification of Industrial 5-DOF Robot Arm Using Neural MIMO NARX Model	605
<i>Ho Pham Huy Anh, Nguyen Thanh Nam</i>	
An Alternative Method to Approximate the Inverse Kinematics of Unknown Geometry Manipulators Using an RBFN with Regularly-Spaced Position Centres	617
<i>Bach H. Dinh, Thang T. Nguyen, Bao Q. Nguyen</i>	
Mechanical	
Study on Plasma Nitriding Technology Imposed to Several Machine Parts Made of 40CrMo Steel	627
<i>Luc Van Thuong, Dao Duy Trung, Hoang Van Chau, Hoang Minh Thuan, Dao Quang Ke</i>	
Characteristic of Corrosion Resistance under Different Heat Treatment Conditions of Coated Zinc Coating Steel with Cr-free Solution	635
<i>Ki-Woo Nam, Dae-Woong Kim, Nam-Suk Kim, Ki-Yong Seong</i>	
Author Index	645

Recent Advances in Speech Quality Assessment and Their Implementation

Miroslav Voznak

Dept. of Telecommunications, VSB-Technical University of Ostrava,
17. listopadu 15/2172, 708 33 Ostrava, Czech Republic
miroslav.voznak@vsb.cz

Abstract. This paper deals with a speech quality assessment, especially with non-intrusive methods which are suitable for speech quality evaluation in real-time communication. The first part contains introduction to models of objective speech quality assessment based on evaluation of signals in time-frequency domain and afterwards a non-intrusive approach, which is known as E-model, is explained. The main contribution of this paper lies in proposal of a simplified E-model and its practical implementation into the Monitoring module in BESIP project. Next part deals with an impact of atmospheric conditions on the speech quality in the GSM using PESQ approach. Results from the MOS assessments based on long term measurements are reported, and an analysis of the obtained data is presented with outcomes from experiments which were performed in VSB-Technical University of Ostrava.

Keywords: E-model, MOS, R-factor, PESQ, Speech quality, BESIP.

1 Introduction

Methodologies evaluating speech quality can be sub-divided into two groups according to the approach applied - conversational and listening. Conversational tests are based on mutual interactive communication between two subjects through the whole transmission chain of the tested communication system. Listening tests do not provide such plausibility as conversational tests but they are recommended more frequently [1]. According to the method of assessment, speech quality evaluation methodologies can be subdivided into subjective methods and objective methods. To evaluate speech quality, MOS (Mean Opinion Score) scale as defined by the ITU-T recommendation P.800 is applied [2]. The basic scale of assessment as prescribed by the recommendation is depicted on Fig. 1. In order to avoid misunderstanding and incorrect interpretation of MOS values, ITU-T published recommendation P.800.1 in 2003 [3]. This recommendation defines scales both for subjective and objective methods as well as for individual conversational and listening tests [1].



Fig. 1. MOS Scale

2 Methods of Assessment

Subjective methods are based on evaluation by human beings (listeners), i.e. subjects. During the testing, samples are played to a sufficient number of subjects, and their results are subsequently analysed statistically. Subjects can evaluate speech quality on a five-degree scale in accordance with the MOS model as defined by ITU-T [2]. The best known representatives of these measurements include methods such as ACR (Absolute Category Rating) or DCR (Degradation Category Rating). Major disadvantages of these methods are high requirements on time, the fact that final evaluation is influenced by listener's subjective opinion and most of all impossibility to use them for testing in real time.

Objective methods substitute the necessity to involve humans in the testing by mathematical computational models or algorithms. Their output is again a MOS value or, depending on the algorithm applied, a different value which can be converted into a MOS value using a suitable mapping function. The aim of objective methods is to estimate, as precisely as possible, the MOS value which would be obtained by a subjective evaluation involving a sufficient number of evaluating subjects. Objective testing's exactness and efficiency is therefore a correlation of results from both subjective and objective measurements [4]. Objective methods can be sub-divided into two groups, Intrusive and Non-intrusive.

2.1 Intrusive Approach

The core of intrusive (also referred to as input-to-output) measurements is the comparison of the original sample and the degraded sample affected by a transmission chain [4], [5]. The intrusive methods use the original voice sample as it has entered the communication system and compare it with the degraded one as it has been outputted by this transmission chain. The following list contains the most important intrusive algorithms:

- Perceptual Speech Quality Measurement PSQM,
- Perceptual Analysis Measurement System PAMS,
- Perceptual Evaluation of Speech Quality PESQ,
- Perceptual Objective Listening Quality Assessment P.OLQA.

Among these, PESQ is currently the most commonly applied algorithm [6]. It combines the advantages of PAMS (robust temporal alignment techniques) and PSQM (exact sensual perception model) and is described in ITU-T's recommendation P.862. The last algorithm mentioned, P.OLQA, also known as ITU-T P.863, is intended to be a successor of the PESQ. It strives to avoid the weaknesses of the PESQ's model and to incorporate a better wideband codec analysis in comparison with PESQ. The basic philosophy of the PESQ approach is depicted on Fig.2. As stated above, the principle of this intrusive test is the comparison of original and degraded signals, their mathematical analysis and interpretation in the cognitive model.

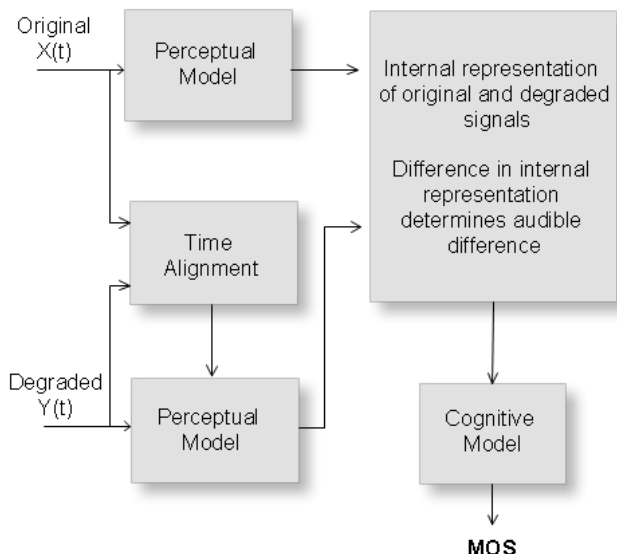


Fig. 2. The basic philosophy used in PESQ

The model begins by level aligning both signals to a standard listening level. They are filtered (using an FFT) with an input filter to model a standard telephone handset. The signals are aligned in time and then processed through an auditory transform similar to that of PSQM. The transformation also involves equalising for linear filtering in the system and for gain variation. Two distortion parameters are extracted from the disturbance (the difference between the transforms of the signals) and are aggregated in frequency and time and mapped to a prediction of subjective mean opinion score (MOS) [5], [6].

2.2 Non-intrusive Approach

Contrary to intrusive methods which require both the output (degraded) sample and the original sample, non-intrusive methods do not require the original sample. This is why they are more suitable to be applied in real time. Yet, since the original sample is

not included, these methods frequently contain far more complex computation models. Intrusive methods are very precise but their application in real-time measurement is unsuitable because they require sending a calibrated sample and both endpoints of the examined communication. Nevertheless, we usually need to assess the speech quality in real traffic and be able to record its changes, especially degradation. Non-intrusive approaches investigate the receiving signal. Two basic principles exist: a source-based approach and a priori-based. The former, the source-based approach, is based on knowledge of various types of impairments, i.e. a set of all impairments gained by comparison of original and degraded signal characteristics. The PLP (Perceptual-linear Prediction) model is a representative of this approach. PLP compares the perceptual vectors extracted from examined samples with the untainted vectors gained from original samples. As I have mentioned, it requires a database with the set of impairments and high computational complexity. Later the PLP model was modified and the computation was accelerated, nevertheless this model is not suitable for implementation in practice as its accuracy strongly depends on the quality of the database with patterns. As for the latter approach, I would like to mention the pioneer work of Zoran and Plakal [7]. They applied artificial neural networks (ANN) to determine statistical ties between a subjective opinion and a characteristic deformation in the received sample. They also investigated spectrograms (a spectrogram is defined as a two-dimensional graphical representation of a spectrum varying in time) and they were able to establish typical uniform aspects of speech in spectrograms. The important method was standardized in recommendation ITU-T P.562 (INMD) and in ITU-T G.107, so-called E-model [8]. INMD measurement (In-service Non-intrusive Measurement Devices) is applied primarily to measure voice-grade parameters such as speech, noise and echo. The output from the model is a prediction of customer opinion Y_C^B (1).

$$Y_C^B = 1 + (E^B \cdot Y_{C_{pre-echo}}^B) \quad (1)$$

E^B is an echo and a delay multiplier, its value is between zero and one, to modify the pre-echo opinion score to take account of echo and delay impairments. $Y_{C_{pre-echo}}^B$ is the calculated pre-echo opinion score, on a zero-to-four scale, which takes into account effects of noise and loss. The addition of one converts Y_C^B to a one-to-five scale. All intermediate opinion score values are based on a zero-to-four scale for ease of calculation. It is possible to generate a rating R (2) using INMD measurements for a connection which is translated into a customer opinion of E-model [8], [9]. The E-model is one of the most modern non-intrusive methods and will be described in the chapter.

$$R = R_0 - I_{OLR} - I_{DD} - I_{e-eff} - I_{DTE} \quad (2)$$

R_0 is the signal-to-noise ratio at a 0 dB reference point. In the equations provided (2), the 0 dB reference point is at the 2-wire input to the telephone receiving system at the near end of the connection. I_{OLR} represents the impairment term for the overall loudness rating, I_{DD} the impairment term for the absolute one-way delay and I_{e-eff} is

the impairment term for the low bit-rate coding under random packet loss conditions. Last parameter I_{DTE} represents the impairment term for the delayed talker echo.

3 E-Model

The complexity of modern networks requires that individual transmission path parameters are not assessed separately but rather that all their possible combinations and their interaction are considered [9]. Partially, this can be achieved by an expert estimate based on the parameters of the transmission path, yet using a computation model is a more systemic approach. The E-model is a computation model which takes into account all the links between transmission parameters. Its output is a scalar labelled R which is a function of total expected call quality. The E-model is based on the “equipment impairment factor” method. The original structure of this model was developed by Swedish expert Nils-Olof Johannesson, member of the Voice Transmission Quality from Mouth to Ear group under ETSI. This model was further developed by the SG12 group under ITU-T and it was published in ITU-T recommendation G.107 as the E-model [8]. The computational model consists of various mathematical operations over all parameters of the transmission system. The computation itself can be split into several elements and is expressed by the following equation (3):

$$R = R_o - I_s - I_d - I_{e-eff} + A \quad (3)$$

R_o represents the signal-to-noise ratio and includes all types of noise, such noises caused by the device’s electrical circuit and noises arisen on the wiring. I_s comprises all possible impairments combinations that appear more or less simultaneously with a useful voice signal. Factor I_d represents all impairments which are caused by different combinations of delays [8]. This impairment factor is expressed by the relation (4) where it is subdivided into the three factors.

$$I_d = I_{dte} + I_{dle} + I_{dd} \quad (4)$$

The factor $Idte$ gives an estimate for the impairments due to talker echo and the factor $Idle$ represents impairments due to listener echo. Echo-cancellation is solved in recommendation ITU-T G.168 and can be effectively suppressed. Factor Idd represents the impairment caused by too-long absolute delay Ta which occurs even with perfect echo cancelling [8]. For $Ta \leq 100$ ms we can assume $Idd = 0$ because a negligible influence appears in the R-factor but with the delay increasing the overall R-factor is affected.

I_{e-eff} comprises impairments caused by using a particular voice codec, occurrence of packet loss and its resistance against losses. Specific impairment factor values for codec operation under random packet-loss have formerly been treated using tabulated, packet-loss dependent Ie values. Now, the packet-loss robustness Factor Bpl is defined as a codec-specific value. The packet-loss dependent effective equipment impairment factor $Ie-eff$ is derived using the codec-specific value for the equipment

impairment factor at zero packet-loss I_e and the packet-loss robustness factor Bpl , both listed in Appendix I of ITU-T G.113 for several codecs [10]. With the packet-loss probability Ppl , I_{e-eff} is calculated using the equation (5).

$$I_{e-eff} = I_e + (95 - I_e) \cdot \frac{P_{pl}}{\frac{P_{pl}}{BurstR} + B_{pl}} \quad (5)$$

$BurstR$ is the so-called burst ratio, defined as ratio between “Average length of observed bursts in an arrival sequence“ and “Average length of bursts expected for the network under random loss“. Where the packet loss is random, $BurstR=1$ and in case of packet loss burstiness, $BurstR>1$.

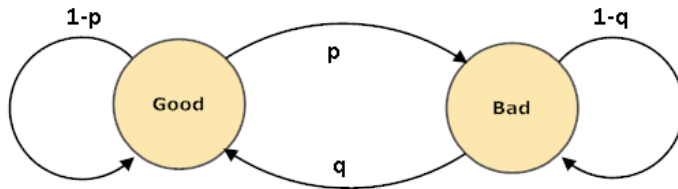


Fig. 3. Gilbert-Elliott model

As packet loss distributions correspond to the Gilbert-Elliott model with transition probabilities p between the found and a loss state, and q between the loss and the found state, the burst ratio can be calculated as $p/(p+q)$ [10]. Figure 3 illustrates such a situation. The packet loss Ppl is expressed by relation (6) and $BurstR$ can be calculated as follows (7):

$$P_{pl} = 100 \cdot \frac{p}{p+q} \quad (6)$$

$$BurstR = \frac{1-P_{pl}}{q} \cdot 100 \quad (7)$$

As can be seen from equation (5), the effective equipment impairment factor in case of $Ppl = 0$ (no packet-loss) equals I_e value defined in Appendix I of ITU-T G.113 [10]. Finally, parameter A slightly adjusts the final quality depending on user's concentration. The value of conventional (wire-bound) communication system is A=0, mobility by cellular networks in a building A=5, mobility in a geographical area or moving in a vehicle A=10 and access to hard-to-reach locations, e.g. via multi-hop satellite connections A=20. It should be noted that the above values are only provisional. The use of factor A and its selected value in a specific application is up to the planner's decision. Additional background information on the advantages of factor A can be found in Appendix II to ITU-T G.113. For all input parameters used in the E-model's algorithm, the default values are listed in recommendation ITU-T G.107. While planning the calculation, it is strongly recommended to use these default values

for all parameters which do not vary . If all parameters are set to the default values, the calculation results in a very high quality with a rating factor of $R = 93.2$.

4 Simplified E-Model and Voice Quality Monitoring

This chapter deals with the application of the computational E-model, simplified for the purpose of implementation. First, the simplified E-model itself is explained. The proposed approach was implemented in the BESIP (Bright Embedded Solution for IP telephony) project, developed by the department of telecommunications in Ostrava as an open source application [11]. The simplified E-model takes into account only effects from codec, packet loss (random packet loss) and end-to-end delay. Figure 4 illustrates the situation which corresponds to relation (9). As for the codec, it is simply identified at the receiving side. The same applies to the delay. I applied a linear regression to results gained in AT&T laboratories [12] and derived relation (8) which provides accurate results, with regression quality $r=0.99$ ranging from 0 to 400 ms.

$$I_d = \begin{cases} 0.0267 \cdot T & T < 175\text{ms} \\ 0.1194 \cdot T - 15.876 & 175\text{ms} \leq T \leq 400\text{ms} \end{cases} \quad (8)$$

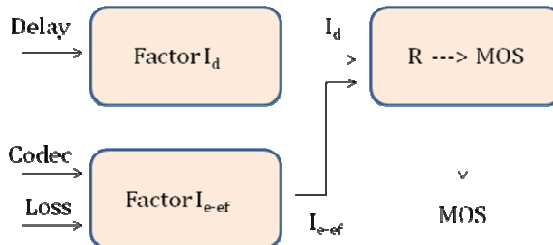


Fig. 4. E-model in simplified version

Parameters R_0 , I_s and A are replaced by constants, with their values stated in recommendation ITU-T G.107. The original relation (3) has been modified as follows (9):

$$R = 94.7688 - 1.4136 - I_d - I_{e-eff} + 0 \quad (9)$$

Parameter I_{e-eff} is computed in relation (5). Where the packet loss distribution is unknown, the value of the packet loss is assumed as random and $BurstR = 1$ and it results in the following simplification. Parameter I_e is fully taken over from recommendation ITU-T G.113 where its values for the most used codecs are listed. Finally, the computed R-factor is converted to MOS value. For this purpose, relation (10) was adopted [8]. MOS values > 100 can be achieved only provided a wide-band codec is used.

$$\begin{aligned}
 MOS &= 1 && \text{for } R < 6.5 \\
 MOS &= 1 + 0.035 \cdot R + R \cdot (R - 60) \cdot (100 - R) \cdot 7 \cdot 10^{-6} && \text{for } 6.5 \leq R \leq 100 \\
 MOS &= 4.5 && \text{for } R > 100
 \end{aligned} \tag{10}$$

4.1 BESIP

The BESIP (Bright Embedded Solution for IP Telephony) is a multiplatform embedded SIP communication server with a unified configuration interface [11]. The SIP server is based on OpenWRT project core and there are Asterisk and Kamailio inside as SIP engines. The final distribution consists of four modules Core, Security, Monitoring and PBX (Private Branche Exchange) as is depicted in Fig. 5. The entire BESIP management and development is available at the project's homepage [13]. The project has been developed as an open source under GNU/GPL license, the binary images from nightly autobuild are freely downloadable. The approach of speech quality assessment described above was implemented into the Monitoring module which forms an integral part of the official BESIP distribution.

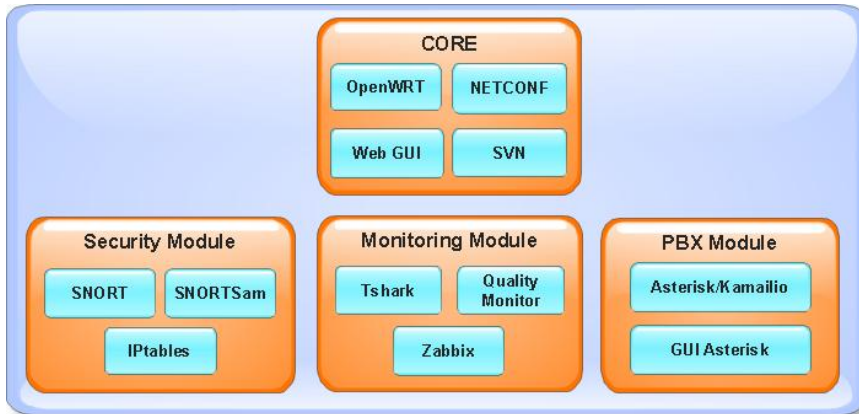


Fig. 5. BESIP modules

4.2 Voice Quality Monitoring Implementation

The overall solution of the monitoring system consists of several different open source components and also of the part that was developed solely for this purpose to meet the defined requirements. The system structure is shown in Fig. 6. The system itself consists of three logical components: being a web interface that serves the administrators (Web GUI), part of the script (Scripts) that controls obtaining information necessary to compute the speech quality in the simplified E-model and the Quality Monitor, which contains the logic for the calculation itself and processes data obtained through scripts. Results are stored in a SQLite3 database. The structure

of the application is depicted in Fig. 6. The developed application offers the comfort of management in a web application while the developed interface aggregates required functions. The monitoring tool is turned off in the default configuration and can be enabled any time using the BESIP's intuitive main interface. This part of the monitoring tool is also used as a means to display the measured and computed results. The structure of the presented data is as follows: Time, Source IP, Destination IP, MOS, R-factor and Codec. The developed module contains several scripts in PHP and necessary data are collected from application *tshark* (a small terminal-based network analyser). Scripts are launched through the web interface of the monitoring tool enabling the monitoring itself. In practice, this means starting the network traffic capture with the *tshark* tool with the RTP filter activated. The usage of the RTP filter makes working with RTP streams much easier as these streams contain some important statistical data (packet loss, jitter) and other important information (source/destination IP, codec) necessary to calculate the speech quality in the E-model.

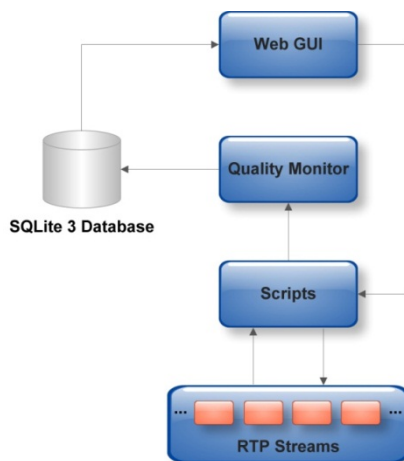


Fig. 6. Overview of VQM logical structure

Unfortunately, the collected data are stored in a text form without a compression only after *tshark* finishes. In order to reduce the storage allocation, speech quality assessments are performed in short intervals. The period of 15 minutes (duration: 900 sec.) was chosen as a suitable one. Once the traffic data have been collected and are available, the script can start the calculation of the speech quality. After processing the obtained data are erased from the storage. All data are stored in a SQLite3 database. The open source tool Java API SQLiteJDBC was selected to enable communication with the database. Speech quality monitoring is controlled through a web interface that is accessible from the main crossroads management interface. Figure 7 shows an example of the user. The status indicator is located at the top of the GUI and indicates whether the monitoring is activated in BESIP (Monitoring is running...) or is currently turned off.

Monitoring is running...					
Date	From	To	MOS	Codec	
23.04.2012 05:46	192.168.21.50	192.168.21.55	2.79	G.711	
23.04.2012 05:55	192.168.21.50	192.168.21.55	3.38	G.711	
23.04.2012 05:59	192.168.21.50	192.168.21.55	3.01	G.711	

Fig. 7. Sample of web GUI of monitoring speech quality

5 Application of Intrusive Approach in Finding Correlations between Atmospheric Conditions and Speech Quality in GSM

This chapter deals with finding the possible correlation between one or multiple weather attributes and the obtained MOS value in GSM network. Data related to weather were acquired by meteorological service of VSB-Technical University of Ostrava. These data were measured during two years 2011-2012 with the measurement period of five minutes. Intention was to find correlation between speech quality in GSM and weather. Data related to GSM were measured in real GSM network, for measuring, an application was developed which both synchronously and automatically saves current speech quality in GSM and weather data.

5.1 Using PESQ Measurement Platform

The measurement apparatus was based on an intrusive approach using a Linux system, moreover the whole platform was highly cost-effective. On the Linux machine, PBX Asterisk [14] generated one call every five minutes and these calls were routed to a SIP peer, which represented a SIP/GSM+UMTS gateway with two separate SIM cards. Each call was routed from the SIM card in module one, to the SIM in module two, thus allowing to use single BTS station in the building nearby and consequently minimize the interference caused by the BTS switching or long signal routes to best possible minimum since the measured is being performed on the closest BTS. The GSM gateway then routed the incoming calls back to Asterisk PBX, which recorded the voice data to a separate WAV file. This way the loop was created allowing the Linux system with Asterisk PBX to have access to both original WAV file and the degraded one, which was necessary for successful implementation of PESQ algorithm. The hardware requirements were a low-end HW server with Ethernet interface and SIP/GSM+UMTS gateway with two separate modules working on 1800MHz (DCM-1800). As the speech files we used the samples of calibrated voices specifically designed for the use with PESQ algorithm. The cooperation between Asterisk PBX and PESQ algorithm was achieved via the “System” command in Asterisk dialplan [14] and the python script fetching the current meteorological

data, performing the PESQ evaluation and storing the data into the database. The meteorological data were obtained from the local meteorological station working in the university campus about 300 meters far from the BTS station. The actual data transmission was implemented by HTTP communication, where python script asked meteorological station for current conditions in text format, which then was parsed and data were stored. Storing data into SQLite database is useful from the data analysis point of view, because the values of measured MOS can be displayed in almost real time with the use of the conditional database lookup for any month, day or even hour or minute thanks to the used timestamp. Moreover the aggregate functions allow quick data analysis even on the huge number of stored values. The testing platform scheme is depicted on the Fig. 8.

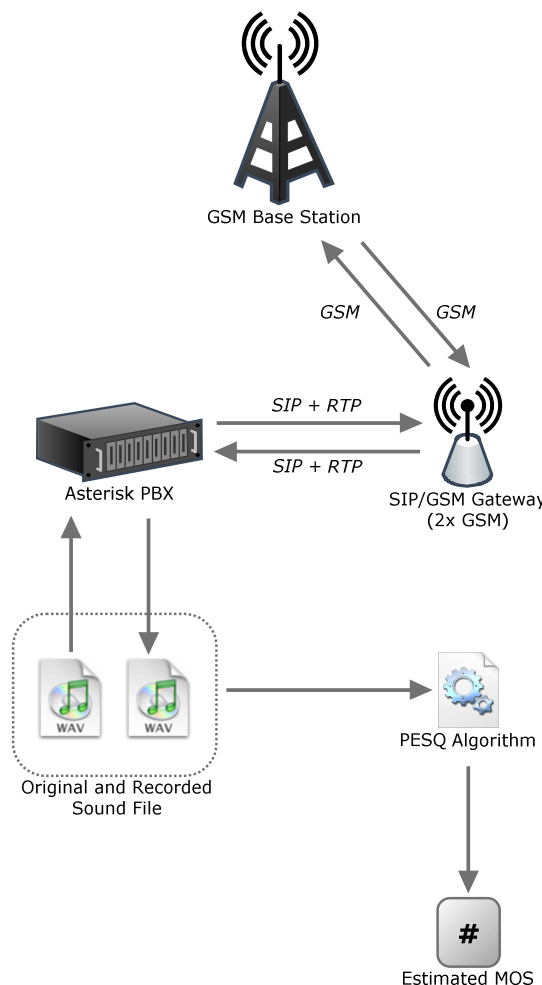


Fig. 8. Scheme of testing platform with the detail on MOS computation

5.2 Method of Evaluation

On cleaned and normalized data were used several methods such as Bayes classifier, Logistic regression, EM and K-Means, from which was chosen K-Means method achieving the best results in the distribution of data into clusters. The simplest definition of clustering is shared among all and includes one fundamental concept: the grouping together of similar data items into clusters [15]. These clusters should reflect some mechanism at work in the domain from which samples or data points are drawn, a mechanism that causes some samples to bear a stronger resemblance to one another than they do to the remaining array. Choosing k is often an ad hoc decision based on prior knowledge, assumptions, and practical experience.. Let $X \in R^m \times n$ a set of data items representing a set of m points x_i in R^n . The goal is to partition X into K groups C_k such every data that belong to the same group are more “alike” than data in different groups. Each of the K groups is called a cluster. The result of the algorithm is an injective mapping $X \rightarrow C$ of data items X_i to clusters C_k dimensional vector x . K-means algorithm is one of the most well-known and widely used partitioning methods for clustering. It works in the following steps. First, it selects k objects from the dataset, each of which initially represents a cluster center. Each object is assigned to the cluster to which it is most similar, based on the distance between the object and the cluster center. Then the means of clusters are computed as the new cluster centers. The process iterates until the criterion function converges. A typical criterion function is the squared-error criterion. For detailed description of k-means clustering, please refer to [15]. Let $S = \{X_1, X_2, \dots, X_n\}$ be a dataset with n observations, each of which is p-dimensional. The objective in K-means clustering is to group these observations into categories C_1, C_2, \dots, C_K for given K, such that the objective function (11)

$$O_K = \sum_{i=1}^n \sum_{k=1}^K I(X_i \in C_k) (X_i - \mu_k)' (X_i - \mu_k) \quad (11)$$

is minimized. Here μ_k represents the mean vector of observations from C_k , $\mu_k = \frac{1}{n_k} \sum_{i \in C_k} X_i$ where $n_k = |C_k|$ is the number of observations in C_k and $I(X \in C_k)$ is an indicator function specifying whether observation X belongs to the k th group. Further, note that the following $\|x\| = \sqrt{x'x}$ denotes the Euclidian norm of p-dimensional vector x.

5.3 Achieved Results

Analysis of all available possible influencer of MOS value in GSM/UMTS environment was performed using the mentioned K-means clustering method. To be more specific, there was explored the influence of the Current Temperature, Humidity, Rain, Dew Point, Wind Speed and Atmospheric Pressure. There was proven no statistically significant relation between MOS and atmospheric conditions with exception of rain where a measurable significance was found. The Tab. 1 shows the actual probability of MOS value depending on the current rain density. Second row in the table can be seen as the most important and tells us the following: if the

Table 1. The influence of current rain density on MOS

Column	Value	Favours	Relative Impact
RainRate [mm/h]	≥ 33.899	< 2.61	100
RainRate [mm/h]	28.502 - 33.899	< 2.61	64
RainRate [mm/h]	15.133 - 28.502	$2.61 - 2.919$	100
RainRate [mm/h]	4.883 - 15.133	$2.919 - 3.292$	100
RainRate [mm/h]	< 4.883	≥ 3.292	100

current rain density is between 28.5 and 33.9 mm/h we can expect MOS to be lower than 2.61 with the probability of 64%. Other rows can be read similarly.

These results in the following, with the increasing rain activity, the MOS value drops significantly. The last row says that if the rain density is below 4.9 mm/h then the MOS is with 100% probability greater than 3.292.

6 Conclusion

The E-model brings a modern approach to the computation of estimated quality, allowing for easy implementation. One of its advantages is that it can be applied in real time. The method is based on a mathematical computation model and can be applied as early as the planning stage a new communication system. The E-model is classified as objective non-intrusive method and is applied primarily in the Voice over IP technology. The latest version of ITU-T recommendation G.107 was released in December 2011 but the development of the E-model is not finished yet.

The proposed simplified E-model was implemented into Monitoring module in BESIP project and enables assessing the speech quality in real-time. Further possible improvements lie in the support of more codecs, acceleration and optimization of the implemented algorithm and especially in the notification of speech quality impairment. The notification of particular events is an inherent part of monitoring systems such as Zabbix or Nagios. Consequently, a log agent for the selected system could be developed in the near future.

The second contribution of this paper is the outcome of long term speech quality measurement in GSM network and the observed impact of weather conditions on speech quality in PESQ model.

Acknowledgments. This work was supported by the European Regional Development Fund in the IT4 Innovations Centre of Excellence project (CZ.1.05/1.1.00/02.0070) and by the Development of human resources in research and development of latest soft computing methods and their application in practice project (CZ.1.07/2.3.00/20.0072) funded by Operational Programme Education for Competitiveness, co-financed by ESF and state budget of the Czech Republic.

References

1. Mahdi, A.E., Picovici, D.: Advances in voice quality measurement in modern telecommunications. *Digital Signal Processing* 19(1), 79–103 (2009)
2. Methods for subjective determination of transmission quality, ITU-T Recommendation, p. 800, Geneva (August 1996)
3. Mean Opinion Score (MOS) terminology, ITU-T Recommendation, p. 800.1, Geneva (July 2006)
4. Kouril, J., Atassi, H.: Objective Speech Quality Evaluation. A primarily Experiments on a Various Age and Gender Speakers Corpus. In: Proc. 8th WSEAS International Conference on Circuits, Systems, Electronics, Control & Signal Processing, Puerto de la Cruz, pp. 333–336 (2009)
5. Rix, A., Hollier, M., Hekstra, A., Beerends, J.: Perceptual evaluation of speech quality (PESQ): The new ITU standard for end-to-end speech quality assessment. *AES: Journal of the Audio Engineering Society* 50(10), 755–764 (2002)
6. Perceptual evaluation of speech quality (PESQ): An objective method for end-to-end speech quality assessment of narrow-band telephone networks and speech codecs, ITU-T Recommendation, p. 862, Geneva (February 2001)
7. Palakal, J., Zoran, M.: Feature extraction form speech spectrograms using multi-layered network models. In: Proc. IEEE International Workshop on Tools for Artificial Intelligence, Architectures, Languages and Algorithms, pp. 224–230 (1989)
8. The E-model: A computational model for use in transmission planning, ITU-T Recommendation G.107, Geneva (April 2009)
9. Voznak, M.: E-model modification for case of cascade codecs arrangement. *International Journal of Mathematical Models and Methods in Applied Sciences* 5(8), 1439–1447 (2011)
10. Transmission impairments due to speech processing, ITU-T Recommendation G.113, Geneva (November 2007)
11. Macura, L., Voznak, M., Tomala, K., Slachta, J.: Embedded Multiplatform SIP Server Solution. In: Proc. 35th International Conference on Telecommunication and Signal Processing, Prague, pp. 263–266 (2012)
12. Cole, G., Rosenbluth, H.: Voice over IP performance monitoring. In: ACM SIGCOMM Computer Communication, New York (2001)
13. Management of BESIP, <https://homeproj.cesnet.cz/projects/besip>
14. Voznak, M., Kapicak, L., Zdralek, J., Nevlud, P., Plucar, J.: Multimedia services in Asterisk based on VoiceXML. *International Journal of Mathematics Models and Methods in Applied Science* 5(5), 857–865 (2011)
15. Zhao, Y., Zhang, C., Zhang, S., Zhao, L.-W.: Adapting K-Means Algorithm for Discovering Clusters in Subspaces. In: Zhou, X., Li, J., Shen, H.T., Kitsuregawa, M., Zhang, Y. (eds.) APWeb 2006. LNCS, vol. 3841, pp. 53–62. Springer, Heidelberg (2006)

On Evolutionary Design of Complex Structures and Electronic Circuits

Ivan Zelinka

VSB-TUO, Faculty of Electrical Engineering and Computer Science, 17. listopadu 15,
708 33 Ostrava-Poruba, Czech Republic
zelinka@fai.utb.cz

Abstract. This chapter focuses on motivating an application of evolutionary computation to complex problems especially with respect to chaotic systems. In this chapter, general evolutionary techniques are first reviewed, including the so-called evolvable hardware, with some selected examples of their applications. Then, motivation of studying chaotic systems as an interesting application domain for evolutionary algorithms is provided with brief discussions.

1 Introduction

This keynote speech, based on our long term research summarized in [20] discusses an alternative approach (in more details discussed in [20]) for symbolic structures and solutions synthesis and demonstrates a comparison with other methods, for example Genetic Programming (GP) or Grammatical Evolution (GE). Generally, there are two well known methods, which can be used for symbolic structures synthesis by means of computers. The first one is called GP and the other is GE. Another interesting research was carried out by Artificial Immune Systems (AIS) or/and systems, which do not use tree structures like linear GP and other similar algorithm like Multi Expression Programming (MEP), etc. In this chapter, a different method called Analytic Programming (AP), is presented. AP is a grammar free algorithmic superstructure, which can be used by any programming language and also by any arbitrary Evolutionary Algorithm (EA) or another class of numerical optimization method. In this keynote we describe not only theoretical principles of AP, but also its comparative study with selected well known case examples from GP as well as applications on synthesis of different structures like: controller, systems of deterministic chaos, electronics circuits, etc.

Because all above mentioned methods are different in its internal structure, we use more general term *symbolic regression* that represents a process during which measured data sets are fitted, thereby a corresponding mathematical formula is obtained in an analytical way. An output of the symbolic expression could be, for example, $\sqrt[N]{x^2 + \frac{y^3}{k}}$, and the like.

The initial idea of symbolic regression by means of a computer program was proposed in GP [1], [2]. The other approach of GE was developed in [3] and AP in [4]. Another interesting investigation using symbolic regression were carried out in [5] on AIS and Probabilistic Incremental Program Evolution (PIPE), which generates functional programs from an adaptive probability distribution over all possible programs.

Yet another new technique is the so called *Transplant Evolution*, see [6], [7] and [8] which is closely associated with the conceptual paradigm of AP, and modified for GE. GE was also extended to include DE by [9]. Generally speaking, it is a process which combines, evaluates and creates more complex structures based on some elementary and noncomplex objects, in an evolutionary way. Such elementary objects are usually simple mathematical operators ($+, -, \times, \dots$), simple functions ($\sin, \cos, \text{And}, \text{Not}, \dots$), user-defined functions (simple commands for robots – MoveLeft, TurnRight, ...), etc. An output of symbolic regression is a more complex “object” (formula, function, command,...), solving a given problem like data fitting of the so-called Sextic and Quintic problem described by Equation (1) [10], [11], randomly synthesized function by Equation (2) [11], Boolean problems of parity and symmetry solution (basically logical circuits synthesis) by Equation (3) [12], [4], or synthesis of quite complex robot control command by Equation (4) [2], [13]. Equations (1)–(4) mentioned here are just a few samples from numerous repeated experiments done by AP, which are used to demonstrate how complex structures can be produced by symbolic regression in general for different problems.

$$x \left(K_1 + \frac{(x^2 K_3)}{K_4 (K_5 + K_6)} \right) * (-1 + K_2 + 2x(-x - K_7)) \quad (1)$$

$$\sqrt{t} \left(\frac{1}{\log(t)} \right)^{\sec^{-1}(1.28)} \log^{\sec^{-1}(1.28)} (\sinh(\sec(\cos(1)))) \quad (2)$$

$$\begin{aligned} & \text{Nor}[(\text{Nand}[\text{Nand}[B||B, B\&\&A], B])\&\&C\&\&A\&\&B, \\ & \text{Nor}[(!C\&\&B\&\&A||!A\&\&C\&\&B)||!C\&\&!B\&\&!A)\&\& \\ & (!C\&\&B\&\&A||!A\&\&C\&\&B)||!C\&\&!B\&\&!A)|| \\ & A\&\&(!C\&\&B\&\&A||!A\&\&C\&\&B)||!C\&\&!B\&\&!A), \\ & (C||!C\&\&B\&\&A||!A\&\&C\&\&B)||!C\&\&!B\&\&!A)\&\&A]] \end{aligned} \quad (3)$$

$$\begin{aligned} & \text{Prog2}[\text{Prog3}[\text{Move, Right, IfFoodAhead[Left, Right]}], \\ & \text{IfFoodAhead}[\text{IfFoodAhead[Left, Right]}, \text{Prog2}[\text{IfFoodAhead} \\ & \text{IfFoodAhead}[\text{IfFoodAhead[Left, Right]}, \text{Right}], \text{Right}], \\ & \text{IfFoodAhead}[\text{Prog2}[\text{Move, Move}], \text{Right}]]]] \end{aligned} \quad (4)$$

2 Selected Methods

2.1 Genetic Programming

GP was the first tool for symbolic regression carried out by means of computers instead of humans. The main idea comes from GA, which was used in GP [1], [2]. Its ability to solve very difficult problems is well proven; for example, GP performs so well that it can be applied to synthesize highly sophisticated electronic circuits [12].

The main principle of GP is based on GA, which is working with populations of individuals represented in the LISP programming language. Individuals in a canonical form of GP are not binary strings, different from GA, but consist of LISP symbolic objects (commands, functions, ...), etc. These objects come from LISP, or they are simply

user-defined functions. Symbolic objects are usually divided into two classes: functions and terminals. Functions were previously explained and terminals represent a set of independent variables like x , y , and constants like π , 3.56, etc.

The main principle of GP is usually demonstrated by means of the so-called trees (basically graphs with nodes and edges, representing individuals in LISP symbolic syntax). Individuals in the shape of a tree, or formula like $0.234Z + X - 0.789$, are called programs. Because GP is based on GA, evolutionary steps (mutation, crossover, ...) in GP are in principle the same as GA. As an example, GP can serve two artificial parents – trees, representing programs $0.234Z + X - 0.789$ and $ZY(Y + 0.314Z)$. When crossover is applied, for example, subsets of trees are exchanged.

Subsequently, the offspring fitness is calculated, such that the behavior of the just-synthesized and evaluated individual-tree should be as similar as possible to the desired behavior. The desired behavior can be regarded as a measured data set from some process (a program that should fit them as well as possible) or like an optimal robot trajectory, i.e., when the program is evaluating a sequence of robot commands (TurnLeft, Stop, MoveForward,...) leading as close as possible to the final position. This is basically the same for GE. For more details about GP see <http://www.genetic-programming.org/>.

2.2 Grammatical Evolution

GE is another program developed in [14], which performs a similar task to that of GP. GE has one advantage over GP, and this is the ability to use any arbitrary programming language, not only LISP as in the case of the canonical version of GP. In contrast to other EA's, GE was used only with a few search strategies, and with a binary representation of the populations [14]. The last successful experiment with DE applied on GE was reported in [9]. GE in its canonical form is based on GA, thanks to a few important changes it has in comparison with GP. The main difference is in the individual coding.

While GP manipulates in LISP symbolic expressions, GE uses individuals based on binary strings. These are transformed into integer sequences and then mapped into a final program in the Backus-Naur Form (BNF) [14], as explained by the following artificial example. Let $T = \{+, -, \times, /, x, y\}$ be a set of operators and terminals and let $F = \{\text{epr}, \text{op}, \text{var}\}$ be the so-called nonterminals. In this case, the special grammar used for final program synthesis. The rule used for individuals transforming into a program is based on Equation (5) below. GE is based on binary chromosome with a variable length, divided into the so-called codons (range of integer values, 0-255), which is then transformed into an integer domain.

$$\begin{aligned} \text{unfolding} &= \text{codon mod rules} \\ \text{where rules} &\text{ is number of rules for given nonterminal} \end{aligned} \tag{5}$$

If the program is closed before the end of the chromosome is reached, then the remaining codons are ignored; otherwise, it continues again from the beginning of the chromosome. For a fully detailed description of GE principles, see [14] or consult [<http://www.grammaticalevolution.org/>].

2.3 Analytic Programming

The final method described here and used for experiments in this chapter is called AP, which has been compared to GP with very good results (see, for example, [11], [19], [4], [13], [15] and [20]) or visit the online university website www.ivanzelinka.eu.

The basic principles of AP were developed in 2001 and first published in [17] and [18]. AP is also based on the set of functions, operators and terminals, which are usually constants or independent variables alike, for example:

- **functions:** *sin, tan, tanh, And, Or,...*
- **operators:** *+, -, ×, /, dt,...*
- **terminals:** *2.73, 3.14, t,...*

All these objects create a set, from which AP tries to synthesize an appropriate solution. Because of the variability of the content of this set, it is called a general functional set (GFS). The structure of GFS is nested, i.e., it is created by subsets of functions according to the number of their arguments [20]. The content of GFS is dependent only on the user. Various functions and terminals can be mixed together. For example, GFS_{all} is a set of all functions, operators and terminals, GFS_{3arg} is a subset containing functions with maximally three arguments, GFS_{0arg} represents only terminals, etc. [20]).

AP, as further described later, is a mapping from a set of individuals into a set of possible programs. Individuals in population and used by AP consist of non-numerical expressions (operators, functions,...), as described above, which are in the evolutionary process represented by their integer position indexes [20]. This index then serves as a pointer into the set of expressions and AP uses it to synthesize the resulting function-program for cost function evaluation.

To avoid synthesis of pathological functions, a few security *tricks* are used in AP. The first one is that GFS consists of subsets containing functions with the same or a smaller number of arguments. The nested structure is used in the special security subroutine, which measures how far the end of an individual is and, according to this, mathematical elements from different subsets are selected to avoid pathological functions synthesis. More precisely, if more arguments are desired then a possible function (the end of the individual is near) will be replaced by another function with the same index pointer from the subset with a smaller number of arguments, for details see [20].

GFS need not be constructed only from clear mathematical functions as demonstrated above, but may also be constructed from other user-defined functions, e.g., logical functions, functions which represent elements of electrical circuits or robot movement commands, linguistic terms, etc.

3 Selected Applications

This section briefly describes some selected applications of AP, which has been conducted during the past few years and cover a comparative study with GP techniques published by J. R. Koza as well as other different applications. In each subsection, the main idea of the AP application is described, results alongside references to publications, cumulating in the full report of proposed application.

3.1 Comparison with Selected GP Examples

To verify more properly the functionality of AP, a set of comparative simulations based on selected examples from Koza's GP, have been done. Two algorithms were used for comparison of AP with GP - DE and SOMA. Simulations were focused on selected examples from [2] and [10], especially:

- Boolean even-k-parity problem - synthesis of logical function in a few versions containing 3, 4, 5 and 6 input variables
- Boolean symmetry problem - synthesis of logical function in a few versions containing 3, 4, 5 and 6 input variables

Based on the studies in [2] and[10], the above mentioned problems have been selected for comparative study. The first two are focused on data fitting. Data are generated by means of polynomials $x^6 - x^4 + x^2$ and $x^5 - 2x^3 + x$. Equations (6) - (9) are typical example of synthesized solutions, especially Equations (6) and 8 are solutions with general constants K and Equations (7) and (9) are their fitted versions. Another study - Booleans even-3-parity and symmetry problems were selected for comparative study and are fully reported in [21] and [22]. In general, Boolean even-k-parity problems means that if the number of logical inputs of value True is even, then the output is True. If number of logical inputs of value True is not even, then the output is False. Number of all possible inputs (combinations) from $2^3 = 8$ for 3-parity problem to $2^6 = 64$ for a 6-parity problem. Truth table for 3-parity problem is given in Table 1. Symmetry problem has been investigated in the same way. Output of this logical function is True whenever True and False values are symmetrically distributed on inputs, see [2] and[10]. The full report of this comparative study is in [21], [22] and [20].

Table 1. Truth table for Boolean even-3-parity problem according to [2]

Input 1	Input 2	Input 3	Output
True	True	True	False
True	True	False	True
True	False	True	True
False	True	True	True
True	False	False	False
False	True	False	False
False	False	True	False
False	False	False	True

$$\frac{xK[[5]]K[[6]](x(-K[[18]])-K[[19]]+2x)}{K[[23]](K[[24]]+x)+\frac{x(x-K[[20]])}{K[[21]]+K[[22]]}} + \left(\frac{K[[9]](xK[[10]]+x)(K[[25]]+x)}{K[[7]]K[[8]]} + K[[2]] - x \right) \\ (xK[[11]] - K[[12]] + x) - \frac{xK[[4]](-K[[13]]+K[[14]]+K[[17]]+\frac{K[[15]]}{K[[16]]}-x)}{-K[[3]]-x} - K[[1]] \quad (6)$$

$$\begin{aligned}
& \frac{0.00621529x(0.793939 - 1.x)}{-1.x - 0.934705} + (0.465773(x + 2.82445)x - 1.x - 7.45208)(0.181218 - 0.749217x) + \\
& \frac{2.9596(0.432881x - 3.70673)x}{\frac{0.21213(x+13.054)}{x^2} + 0.456758(x - 0.562963)x} + 1.27265
\end{aligned} \tag{7}$$

$$x(x^2(x(K[[7]] + x) - K[[2]]) + x(K[[4]] - K[[5]]) + xK[[6]] + K[[1]] - K[[3]] - 1)) \tag{8}$$

$$x(1. - 2.193908007555499^{-16}x + x^2(-2. + x(4.66960974116765^{-16} + x))) \tag{9}$$

3.2 Examples

In the diploma thesis of [23], three electronic circuits were experimentally synthesized by AP. The main point of this AP application was to confirm, that EA's with AP are possible to successfully design electronics circuits. In the first part of [23] the general theory (GP, GE and AP) is outlined, while in the experimental part the synthesis of three electronic circuits (traffic light control, heat control and train station control) is described. All three control systems has been successfully designed by AP. Each winning solution was visualized as a circuit and hardware implementation (see for example Figure 2). In all three experiments (50 times repeated) AP had been observed to be capable of electronic circuit synthesis.

Another application of AP [20] is focused on the synthesis of control law for discrete chaotic system. The interest in the control of chaotic systems has been an active area of research during the past decade. One of the first and important initial studies, of EA for control use was reported in [20], where the control law was based on the Pyragas method: Extended delay feedback control - ETDAS [15], [16]. Those papers were focused on the tuning of several parameters inside the control technique for a chaotic system. Compared to that, a presented paper [20] shows a possibility as to how to generate the whole control law (not only to optimize several parameters) for the purpose of stabilization of a chaotic system. The synthesis of control is inspired by the Pyragass delayed feedback control technique. Unlike the original OGY control method, it can be simply considered as a targeting and stabilizing algorithm together in one package. Another big advantage of the Pyragas method is the amount of accessible control parameters. Instead of EA utilization, AP was used. Control law from the proposed system can be viewed as a symbolic structure, which can be created according the requirements for the stabilization of chaotic system. The advantage is that it is not necessary to have some "preliminary" control law and only to estimate its parameters. This system will generate the structure of the law also with suitable parameter values, see [20].

Synthesis, identification and control of complex dynamical systems are usually extremely complicated. When classics methods are used, some simplifications are required, which tends to lead to idealized solutions that are far from reality. In contrast, the class of methods based on evolutionary principles is successfully used to solve this kind

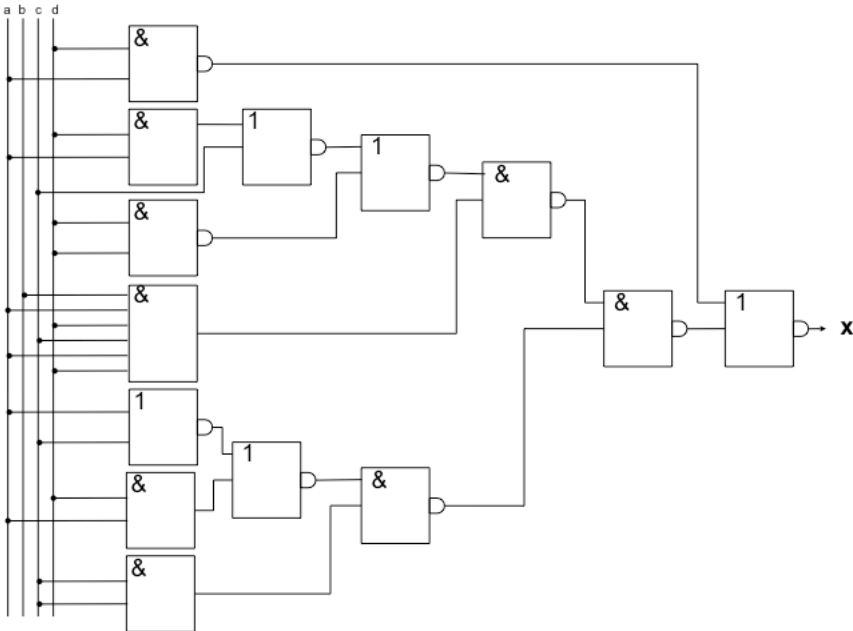


Fig. 1. Logical circuit designed by AP...

of problems with a high level of precision. In this section, an alternative method of EA's, which has been successfully proven in many experiments like chaotic systems synthesis, neural network synthesis or electrical circuit synthesis. [16] and [15] discusses the possibility of using EA's for the identification of chaotic systems. The main aim of this work is to show that EA's are capable of the identification of chaotic systems without any partial knowledge of it's internal structure, i.e. based only on measured data. A few different EA's are presented and tested in a total of 10 versions. Systems selected for numerical experiments is the well-known logistic equation. Typical example of evolutionary identification is in Equation (10), (11) and visualization in Figure 3. According to obtained results, it can be stated that evolutionary identification is an alternative and promising way as to how to identify chaotic systems. Extended case study is also reported in [16].

$$x \left(A + \frac{(-1 - A + x - Ax + x^2 - \frac{-A+x}{A}) (A + A(x + Ax))}{2A^2} \right) \quad (10)$$

$$(1 - x)x^2(3A + x - 3Ax + Ax^2) \quad (11)$$

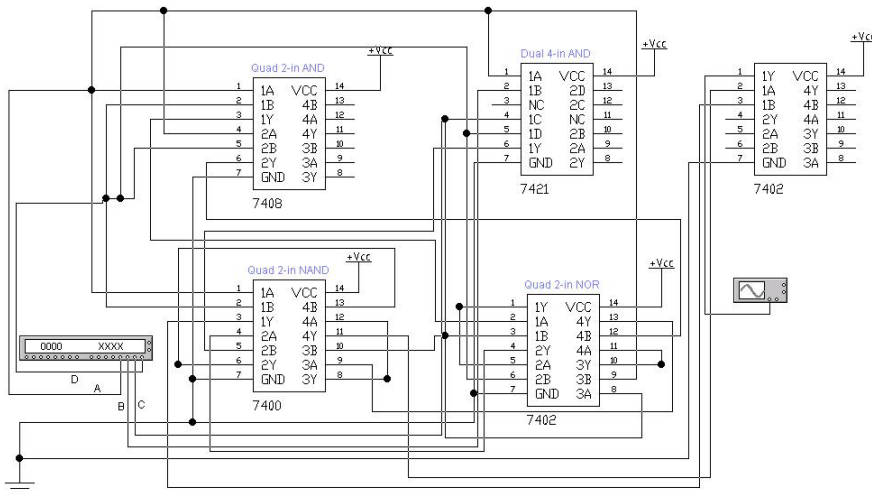


Fig. 2. ... and its scheme

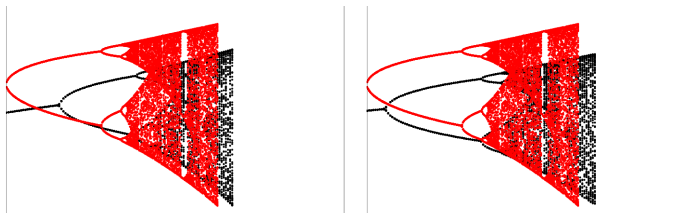


Fig. 3. Original (black fat points) and identified (red thin points) behavior

4 Conclusion

Based on various applications of methods of symbolic regression, it can be stated that symbolic regression seems to be powerful algorithmic method to design and solve complex problems like electronic circuits etc. All mentioned methods of symbolic regression and especially AP has been carefully tested during the last years on various examples including selected examples for comparative studies with very good results.

Acknowledgement. The following grants are acknowledged for the financial support provided for this research: Grant Agency of the Czech Republic - GACR P103/13/08195S, by the Development of human resources in research and development of latest soft computing methods and their application in practice project, reg. no. CZ.1.07/2.3.00/20.0072 funded by Operational Programme Education for Competitiveness, co-financed by ESF and state budget of the Czech Republic, and by Grant of SGS No. SP2013/114, VB - Technical University of Ostrava, Czech Republic.

References

1. Koza, J.: Genetic Programming: A paradigm for genetically breeding populations of computer programs to solve problems, Stanford University, Computer Science Department. Technical Report, STAN-CS-90-1314 (1990)
2. Koza, J.: Genetic Programming. MIT Press (1998)
3. Ryan, C., Collins, J.J., Neill, M.O.: Grammatical Evolution: Evolving Programs for an Arbitrary Language. In: Banzhaf, W., Poli, R., Schoenauer, M., Fogarty, T.C. (eds.) EuroGP 1998. LNCS, vol. 1391, pp. 83–96. Springer, Heidelberg (1998)
4. Zelinka, I., Oplatkova, Z., Nolle, L.: Analytic programming – Symbolic regression by means of arbitrary evolutionary algorithms. Int. J. of Simulation, Systems, Science and Technology 6(9), 44–56 (2005)
5. Johnson, C.: Artificial immune systems programming for symbolic regression. In: Ryan, C., Soule, T., Keijzer, M., Tsang, E.P.K., Poli, R., Costa, E. (eds.) EuroGP 2003. LNCS, vol. 2610, Springer, Heidelberg (2003)
6. Weisser, R., Osmera, P.: Two-Level Transplant Evolution for Optimization of General Controllers. In: New Trends in Technologies, Sciyo (2010)
7. Weisser, R., Osmera, P.: Two-level Transplant Evolution. In: 17th Zittau Fuzzy Colloquium, Zittau, Germany (2010)
8. Weisser, R., Osmera, P., Matousek, R.: Transplant Evolution with Modified Schema of Differential Evolution: Optimization Structure of Controllers. In: International Conference on Soft Computing MENDEL, Brno, Czech Republic (2010)
9. O'Neill, M., Brabazon, A.: Grammatical Differential Evolution. In: Proceedings of International Conference on Artificial Intelligence, pp. 231–236. CSEA Press (2006)
10. Koza, J., Bennet, F., Andre, D., Keane, M.: Genetic Programming III. Morgan Kaufmann, New York (1999)
11. Zelinka, I., Oplatkova, Z.: Analytic programming – Comparative study. In: Proceedings of Second International Conference on Computational Intelligence, Robotics, and Autonomous Systems, Singapore (2003)
12. Koza, J., Keane, M., Streeter, M.: Evolving inventions. Scientific American, 40–47 (2003)
13. Oplatkova, Z., Zelinka, I.: Investigation on artificial ant using analytic programming. In: Proceedings of Genetic and Evolutionary Computation Conference, Seattle, WA, pp. 949–950 (2006)
14. O'Neill, M., Ryan, C.: Grammatical Evolution, Evolutionary Automatic Programming in an Arbitrary Language. Springer, New York (2003)
15. Zelinka, I., Chen, G., Celikovsky, S.: Chaos Synthesis by Means of Evolutionary algorithms. International Journal of Bifurcation and Chaos 18(4), 911–942 (2008) ISSN 0218-1274
16. Zelinka, I., Chen, G., Celikovsky, S.: Evolutionary Algorithms and Chaotic Systems. Springer, Germany (2010)
17. Zelinka, I.: Analytic programming by Means of new evolutionary algorithms. In: Proceedings of 1st International Conference on New Trends in Physics 2001, Brno, Czech Republic, pp. 210–214 (2001)
18. Zelinka, I.: Analytic programming by means of SOMA algorithm. In: Proceedings of First International Conference on Intelligent Computing and Information Systems, Cairo, Egypt, pp. 148–154 (2002)
19. Oplatkova, Z.: Optimal trajectory of robots using symbolic regression. In: Proceedings of 56th International Astronautics Congress, Fukuoka, Japan (2005)

20. Zelinka, I., Davendra, D., Senkerik, R., Jasek, R., Oplatkova, Z.: Analytical Programming - a Novel Approach for Evolutionary Synthesis of Symbolic Structures. In: Kita, E. (ed.) Evolutionary Algorithms. InTech (2011),
<http://www.intechopen.com/books/evolutionary-algorithms/analytical-programming-a-novel-approach-for-evolutionary-synthesis-of-symbolic-structures>,
doi:10.5772/16166, ISBN: 978-953-307-171-8
21. Zelinka, I., Oplatkova, Z., Nolle, L.: Boolean Symmetry Function Synthesis by Means of Arbitrary Evolutionary Algorithms - Comparative Study. In: 18th European Simulation Multi-conference, ESM 2004, Magdeburg, Germany, Gruner Druck, GmbH (2004)
22. Zelinka, I., Oplatkova, Z.: Boolean Parity Function Synthesis by Means of Arbitrary Evolutionary Algorithms - Comparative Study. In: 8th World Multiconference on Systemics, Cybernetics and Informatics, SCI 2004, Orlando, USA (2004)
23. Strakos, R.: Design electronics circuits by means of evolution method, UTB Zlin. Diploma thesis, Czech Republic (2005)

Fault Diagnosis and Fault Tolerant Control for Fuzzy Systems: Application to Vehicle Dynamic

M. Chadli

University of Picardie Jules Verne, MIS (E.A.4290),
33 rue Saint-Leu, 80039 Amiens, France
mchadli@u-picardie.fr

Over the past decades, fault diagnosis (FDI) and fault tolerant control strategies (FTC) have been proposed based on different techniques for linear and nonlinear systems. Indeed a considerable attention is deployed in order to cope with diverse damages resulting in faults occurrence. In the literature, model-based fault diagnosis techniques have shown their interest in the industrial domain and many results on fault detection observer have been reported for linear systems and nonlinear ones. In recent years, Takagi–Sugeno (T–S) fuzzy approach has attracted a growing interest due to its universal approximation of any smooth nonlinear function by a “blending” of some local linear system models. This representation allows greatly facilitates observers/controllers design using numerical tools (LMI formulation). Many results on fault detection observer design for T–S fuzzy systems have been reported in the literature. These works generally considered that the weighting functions depend on measurable premise variables. In the field of diagnosis, this assumption forces to design observers with weighting functions depending on the input $u(t)$ for the detection of the sensors faults, and on the output $y(t)$ for the detection of actuator faults. For this reason, it is interesting to consider general case of unmeasurable variables.

On the other hand, two classes of the existing FTC strategies have been distinguished; passive FTC and active FTC. The last methods require the knowledge of the faults to reconfigure controller laws to maintain system stability. Based on control theory, relaxation schemes have been proposed for fault diagnosis and fault tolerant control. Thus, using LMI formulation and Lyapunov approach, observers and controllers design for T–S systems has been studied using a quadratic Lyapunov functions and non-quadratic approaches to reduce conservatism. Several techniques have been proposed for FDI and FTC design for T–S systems with sensor and actuators failures. For example with the aid of the descriptor approach, in which an augmented fault observer is designed to yield faults and states estimation simultaneously, observer-based output feedback fault tolerant controllers are proposed. The mixed performances are also considered for more sensitivity to faults and robustness against perturbations.

These results are successfully applied for various industrial applications such as vehicle dynamics. Indeed, in the last decades, lots of efforts have been devoted in

developing vehicles intelligent systems such that active safety systems to improve vehicle-handling characteristics like stability and comfort. Thus, majority of cars are nowadays equipped with various assistance systems such that Traction Control System (TCS), Anti-lock Braking System (ABS) and many variants of Electronic Stability Program (ESP). Various works have been also carried on collision warning, collision avoidance, automated lane-keeping systems. In this context, T-S observers design (Unknown input observer, sliding mode observer,...) is applied for lane departure detection and rollover detection.

Keywords: Takagi-Sugeno fuzzy models, unknown inputs, faults, observers, controller, FDI, FTC, LMI, vehicles dynamics.

References

- Gao, Z., Shi, P., Ding, S.X.: Fuzzy state-disturbance observer design for T-S fuzzy systems with application to sensor fault estimation. *IEEE Trans. on Systems Men and Cybernetics—Part B* 38(3), 875–880 (2008)
- Liang, W.J., Yang, G.-H., Liu, J.: An LMI approach to H_2 - index and mixed H_2/H_∞ fault detection observer design. *Automatica* 43, 1656–1665 (2007)
- Gao, Z., Ding, S.: Actuator fault robust estimation and fault tolerant control for a class of nonlinear descriptor systems. *Automatica* 43, 912–920 (2007)
- Noura, H., Jean, D.T., Ponsart, C., Chamseddine, A.: *Fault Tolerant Control Systems—Design and Practical Applications*. Springer, London (2009)
- Patton, R.: Fault tolerant control. In: Proc. of the IFAC Symposium—SAFEPROCESS 1997, Kingston-upon-Hull, UK, pp. 1035–1055 (1997)
- Blanke, M., Kinnaert, M., Lunze, J., Staroswiecki, M.: *Diagnosis and Fault Tolerant Control*. Springer, London (2006)
- Tanaka, K., Ohtake, H., Wang, H.: A descriptor system approach to fuzzy control system design via fuzzy Lyapunov functions. *IEEE Transactions Fuzzy Systems* 15(3), 333–341 (2007)
- Yoneyama, J.H.: Filtering for fuzzy systems with immeasurable premise variables: an uncertain system approach. *Fuzzy Sets and Systems* 160(12), 1738–1748 (2009)
- Chadli, M., Abdo, A., Ding, S.X.: H_2/H_∞ Fault Detection Filter Design for Discrete-time Takagi-Sugeno Fuzzy System. *Automatica* (2013), doi:10.1016/j.automatica.2013.03.014
- Chadli, M., Darouach, M.: Further Enhancement on Robust H_∞ Control Design for Discrete-Time Singular Systems. *IEEE Trans. on Automatic Control* (2013), doi:10.1109/TAC.2013.2273266
- Dahmani, H., Chadli, M., Rabhi, A., El Hajjaji, A.: Road curvature estimation for vehicle lane departure detection using a robust Takagi-Sugeno fuzzy observer. *Vehicle System Dynamics* 51(5) (2013)
- Chadli, M., Karimi, H.R.: Robust Observer Design for Unknown Inputs Takagi-Sugeno Models. *IEEE Trans. on Fuzzy Systems* 21(1), 158–164 (2013)
- Aouaouda, S., Chadli, M., Cocquempot, V., Khadir, M.T.: Multi-objective H_2/H_∞ faults detection observer design for Takagi-Sugeno fuzzy systems with unmeasurable premise variables: descriptor approach. *Int. Journal of Adaptive Control and Signal Processing* (2013), doi:10.1002/acs.2374

- Chadli, M., Guerra, T.-M.: LMI Solution for Robust Static Output Feedback Control of Takagi-Sugeno Fuzzy Models. *IEEE Trans. on Fuzzy Systems* 20(6), 1160–1165 (2012)
- Chadli, M., Darouach, M.: Novel bounded real lemma for discrete-time descriptor systems. Application to H_∞ control design. *Automatica* 48(2), 449–453 (2012)
- Chadli, M., Aouaouda, S., Karimi, H.R., Shi, P.: Robust Fault Tolerant Tracking Controller Design for a VTOL aircraft. *Journal of the Franklin Institute* (2012), doi:10.1016/j.jfranklin.2012.09.010
- Aouaouda, S., Chadli, M., Khadir, T.: Robust fault tolerant tracking controller design for unknown inputs T-S models with unmeasurable premise variables. *Journal of Process Control* 22(5), 861–872 (2012)
- Saifia, D., Chadli, M., Labiod, S., Guerra, T.M.: Robust H_∞ static output feedback stabilization of T-S fuzzy systems subject to actuator saturation. *International Journal of Control, Automation and Systems* 10(3), 613–622 (2012)
- Chadli, M., Darouach, M.: Further Enhancement on Robust H_∞ Control Design for Discrete-Time Singular Systems. *IEEE Trans. Automatic Control* (2013), doi:10.1109/TAC.2013.2273266
- Saifia, D., Chadli, M., Labiod, S., Karimi, H.R.: Fuzzy Control of DC-DC Converters with Input Constraint. *Mathematical Problems in Engineering* (2012), doi:10.1155/2012/973082
- Bououden, S., Chadli, M., Filali, S., El Hajjaji, A.: Fuzzy Model Based Multivariable Predictive Control of a Variable Speed Wind Turbine: LMI approach. *International Journal of Renewable Energy* 37, 434–439 (2012)
- Chadli, M., Darouach, M.: Robust admissibility of uncertain switched singular systems. *International Journal of Control* 84(10), 1587–1600 (2011)
- Chadli, M.: An LMI approach to Design Observer for Unknown Inputs Takagi-Sugeno Fuzzy models. *Asian Journal of Control* 12(4) (2010)
- Chadli, M., Borne, P.: Multiple models Approach in Automation: Takagi-Sugeno Fuzzy Systems. Hardcover, 208 pages. Wiley-ISTE (2013) ISBN: 978-1-84821-412-5
- Chadli, M., Zelinka, I., Youssef, T.: Unknown inputs observer design for fuzzy systems with application to chaotic system reconstruction. *Computers & Mathematics with Applications* 66(2), 147–154 (2013)

Analysis of Electron Transport Coefficients in $\text{CF}_3\text{I-N}_2$ Mixture Gas Using an Electron Swarm Study

Do Anh Tuan¹ and Chu Dinh Hanh²

¹ Faculty of Electronics and Electrical Engineering,
Hung Yen University of Technology and Education, Hung Yen City, Vietnam
tuandoanh.vn@gmail.com

² Hanoi College of Technology and Trading, Hanoi, Vietnam

Abstract. The consistent electron transport coefficients, for not only pure atoms and molecules but also binary gas mixtures, are necessary to quantitatively understand plasma phenomena and ionized gases. Electron transport coefficients in $\text{CF}_3\text{I-N}_2$ mixture gas, therefore, were calculated and analyzed using a two-term approximation of the Boltzmann equation in the E/N range (ratio of the electric field E to the neutral number density N) of 10 - 1000 Td (1 Td = 10^{-17} V.cm²) for the first time. These coefficients include electron drift velocity, density-normalized longitudinal diffusion and density-normalized effective ionization coefficients. The present results were in good agreement with the available experimental data over a wide range of E/N. The limiting field strength value of E/N for 70% $\text{CF}_3\text{I-N}_2$ mixture was derived and greater than that of the pure SF_6 gas. Gas mixtures of 65 – 75% $\text{CF}_3\text{I-N}_2$ could be considered to use in high voltage and many industries.

Keywords: Trifluoroiodomethane, Boltzmann equation analysis, electron transport coefficients, mixture gas.

1 Introduction

Sulfur hexafluoride (SF_6) has been widely used as an isolated gas in high voltage equipment. The Kyoto Protocol, however, has listed the greenhouse gases as CO_2 , CH_4 , N_2O , hydrofluorocarbons (HFCs), perfluorocarbons (PFCs) and SF_6 , and we need to regulate the emissions and utilizations of those gases in the many industries [1]. Recently, much research has been concentrated on trifluoroiodomethane (CF_3I) gas because of its low global warming potential, very short atmospheric lifetime and relatively low toxicity gas [2]-[4]. It is a gas that is a substitution candidate for the SF_6 gas and as a candidate to the replacement of potent greenhouse affects. This gas has also been considered to be a candidate replacement for bromotrifluoromethane (CF_3Br), which is used in aircraft for fuel inerting and for fire-fighting [2]. The boiling point of CF_3I gas is higher than that of the SF_6 gas. At an absolute pressure of 0.5 MPa, CF_3I becomes liquids at about 26 °C, whereas the SF_6 gas becomes liquids at about -30 °C. On the other hand, the SF_6 gas is used in gas circuit breakers at 0.5 to

0.6 MPa. Therefore, it is impossible to use CF_3I gas, if this gas is used at this pressure level [3]. However, in order to reduce the liquefaction temperature of CF_3I gas, Taki *et al.* [3] decreased partial pressure by mixing it with other gases such as N_2 and CO_2 . For example, the boiling point can be reduced from about 26 °C (pure CF_3I) to about -12 °C at 0.5 MPa by using a 30% CF_3I - CO_2 mixture [4]. Therefore, it is necessary to mix the CF_3I gas with different buffer gases.

Recently, the electron transport coefficients in CF_3I - N_2 [5], [6] mixtures were measured and calculated for the entire concentration range of CF_3I percentages and in the E/N ranges (ratio of the electric field E to the neutral number density N) of about 100 - 600 Td (1 Td = 10^{-17} V.cm²). In general, the electron transport coefficients for molecules and binary mixture gases are necessary for quantitative understanding of plasma phenomena. Moreover, the collision processes and electron transport coefficients of the binary mixtures of CF_3I gas with other gases such as Xe, Ne, He, N_2 , CO_2 , and O_2 have been scarce so far.

In the present study, in order to gain more insight into the electron transport coefficients, the electron drift velocity, density-normalized longitudinal diffusion coefficient, and density-normalized effective ionization coefficient in the E/N range of 10 - 1000 Td and the limiting field strength of E/N, $(E/N)_{\lim}$, for CF_3I - N_2 mixtures were calculated using a two-term approximation of the Boltzmann equation for the energy. The calculated electron transport coefficients in the CF_3I - N_2 mixtures with CF_3I concentrations between 5% and 70% were compared with the recent experimental results [5]. The negative differential conductivity (NDC) phenomena, that is, decreasing electron drift velocity with increasing electric field strength, in these binary gas mixtures were suggested. The present electron transport coefficients calculated were also compared with those of pure SF_6 gas in the experiments. The binary mixtures CF_3I - N_2 with CF_3I concentration equal to about 65 - 75% are considered to use in high voltage and many industries.

2 Analysis

In the present study, to the best of our knowledge, CF_3I molecule has the inelastic cross sections, which are comparable to and less than the elastic momentum transfer cross section at low energies and also at high energies [7]. We, therefore, chose a two-term approximation of the Boltzmann equation for calculating the electron transport coefficients in CF_3I - N_2 mixture gas. The electron transport coefficients were calculated using a two-term approximation of the Boltzmann equation for the energy given by Tagashira *et al.* [8] and gaseous electron collision cross section sets. The present two-term approximation of the Boltzmann equation was previously used for the Cl_2 [9] and TEOS [10] molecules. The briefly description for calculating the electron transport coefficients was also following represented. The electron drift velocity calculated from the solution of electron energy distribution function, $f(\epsilon, E/N)$, of the Boltzmann equation is defined as [11]

$$W = -\frac{1}{3} \left(\frac{2}{m} \right)^{1/2} \frac{eE}{N} \int_0^{\infty} \frac{\epsilon}{q_m(\epsilon)} \frac{df(\epsilon, E/N)}{d\epsilon} d\epsilon. \quad (1)$$

where ε is the electron energy, m is the electron mass, e is the elementary charge, and $q_m(\varepsilon)$ is the momentum-transfer cross section.

The density-normalized longitudinal diffusion coefficient is defined as [12]

$$ND_L = \frac{V_1}{3N} \left(E \int_0^\infty \frac{\varepsilon}{q_T} \frac{\partial}{\partial \varepsilon} (F_i \varepsilon^{-1/2}) d\varepsilon + \int_0^\infty \frac{\varepsilon^{1/2}}{q_T} F_0 d\varepsilon \right) - (\varpi_0 A_2 - \varpi_1 A_1 - \varpi_{02}). \quad (2)$$

where V_1 is the speed of electron, q_T is the total cross section, here F_n and ϖ_n ($n = 0, 1, 2$) are respectively the electron energy distributions of various orders and their eigenvalues. V_1 , ϖ_n , ϖ_{0n} , and A_n are given by

$$V_1 = \left(\frac{2e}{m} \right)^{1/2}; \quad \varpi_0 = V_1 N \int_0^\infty \varepsilon^{1/2} q_i F_0 d\varepsilon; \quad \varpi_1 = -\frac{V_1 E}{3N} \int_0^\infty \frac{\varepsilon}{q_T} \frac{\partial}{\partial \varepsilon} (F_0 \varepsilon^{-1/2}) d\varepsilon + (\varpi_0 A_1 - \varpi_{01}); \\ \varpi_{0n} = V_1 N \int_0^\infty \varepsilon^{1/2} q_i F_n d\varepsilon; \quad A_n = \int_0^\infty F_n d\varepsilon.$$

where q_i is the ionization cross section.

The Townsend first ionization coefficient is defined as [13]

$$\alpha/N = \frac{1}{W} \left(\frac{2}{m} \right)^{1/2} \int_1^\infty f(\varepsilon, E/N) \varepsilon^{1/2} q_i(\varepsilon) d\varepsilon. \quad (3)$$

where I is the ionization onset energy and $q_i(\varepsilon)$ is the ionization cross section.

The electron attachment coefficient is defined as [13]

$$\eta/N = \frac{1}{W} \left(\frac{2}{m} \right)^{1/2} \int_0^\infty f(\varepsilon, E/N) \varepsilon^{1/2} q_a(\varepsilon) d\varepsilon. \quad (4)$$

where $q_a(\varepsilon)$ is the attachment cross section. The electron collision cross sections for CF₃I determined by Kimura and Nakamura [7], [14] and N₂ determined by Nakamura [14] were used throughout the present study. The accuracy of the electron collision cross section set for each gas was confirmed to be consistent with all electron transport coefficients in each pure gas. A brief summary of several reaction processes of these gases for plasma modeling is given by some published reports and is listed in Table 1.

3 Results and Discussions

3.1 Electron Drift Velocities

The results for the electron drift velocities, W , as functions of E/N for the CF₃I-N₂ mixture gas calculated in the E/N range $10 < E/N < 1000$ Td using a two-term approximation of the Boltzmann equation are shown in Fig. 1. The good agreements between the present results and those measured by Urquijo *et al.* [5] in Fig. 1(b) are satisfactory over the entire E/N range. Slight regions of the NDC phenomena in these gas mixtures are observed in the E/N range $15 < E/N < 170$ Td. The NDC is relatively

shallow for all mixtures. The occurrences of these phenomena are due to the Ramsauer-Townsend minimum (RTM) of the elastic momentum transfer cross sections of the CF_3I molecule. The values of W are suggested to be between those of the pure gases over $E/N > 100 \text{ Td}$ and these values grow linearly over $E/N > 200 \text{ Td}$. For the sake of comparison, the electron drift velocity obtained by Aschwanden [15] for the pure SF_6 gas is shown in Fig. 1(a). The calculated electron drift velocity in 70% $\text{CF}_3\text{I-N}_2$ in the E/N range of $E/N < 400 \text{ Td}$ is very close to that of the pure SF_6 gas.

Table 1. Reaction processes with threshold energy for plasma modeling in gases

Types of Collision	Reactions	Threshold Energies (eV)	References
<i>* in CF_3I molecule</i>			
Momentum transfer	$\text{CF}_3\text{I} + e \rightarrow \text{CF}_3\text{I} + e$	0	[7]
Vibrational excitation (3)	$\text{CF}_3\text{I} + e \rightarrow \text{CF}_3\text{I}(v=1, 2, 3) + e$	0.032 ($v=1$), 0.067 ($v=2$), 0.134 ($v=3$)	[7]
Electronic excitation	$\text{CF}_3\text{I} + e \rightarrow \text{CF}_3 + \text{I} + e$	4.7	[7]
Electronic excitation	$\text{CF}_3\text{I} + e \rightarrow \text{CF}_3 + \text{I}^* + e$	7.2	[7]
Electronic excitation	$\text{CF}_3\text{I} + e \rightarrow \text{CF}_2\text{I} + \text{F} + e$	7.9	[7]
Electronic excitation (2)	$\text{CF}_3\text{I} + e \rightarrow \text{CF}_2 + \text{IF} + e$	8.8, 9.6	[7]
Ionization	$\text{CF}_3\text{I} + e \rightarrow \text{CF}_3\text{I}^+ + 2e$	10.2	[7]
Dissociative attachment			[7]
+ zero-energy process	$\text{CF}_3\text{I} + e \rightarrow \text{I} + \text{CF}_3$		
+ 3.8 eV process	$\text{CF}_3\text{I} + e \rightarrow \text{CF}_2\text{I} + \text{F}^-$ $\text{CF}_3\text{I} + e \rightarrow \text{CF}_3^- + \text{I}$		
<i>* in N_2 molecule</i>			
Momentum transfer	$\text{N}_2 + e \rightarrow \text{N}_2 + e$	0	[14]
Vibrational excitation (7)	$\text{N}_2 + e \rightarrow \text{N}_2(v=1, 2, 3, 4, 5, 6, 7) + e$	0.288 ($v=1$), 1.76 ($v=2$), 1.91 ($v=3$), 2.07 ($v=4$), 2.09 ($v=5$), 2.17 ($v=6$), 2.18 ($v=7$)	[14]
Electronic excitation	$\text{N}_2 + e \rightarrow \text{N}_2^*(\text{A}^3\Sigma_u^+) + e$	6.169	[14]
Electronic excitation	$\text{N}_2 + e \rightarrow \text{N}_2^*(\text{B}^3\Pi_g) + e$	7.353	[14]
Electronic excitation	$\text{N}_2 + e \rightarrow \text{N}_2^*(\text{B}^3\Sigma_u^-) + e$	8.165	[14]
Electronic excitation	$\text{N}_2 + e \rightarrow \text{N}_2^*(\text{a}^1\Pi_g) + e$	8.549	[14]
Electronic excitation	$\text{N}_2 + e \rightarrow \text{N}_2^* + e$	9.756	[14]
Electronic excitation	$\text{N}_2 + e \rightarrow \text{N}_2^*(\text{C}^3\Pi_u) + e$	11.032	[14]
Electronic excitation	$\text{N}_2 + e \rightarrow \text{N}_2^* + e$	12.579	[14]
Ionization	$\text{N}_2 + e \rightarrow \text{N}_2^+ + 2e$	15.5	[14]

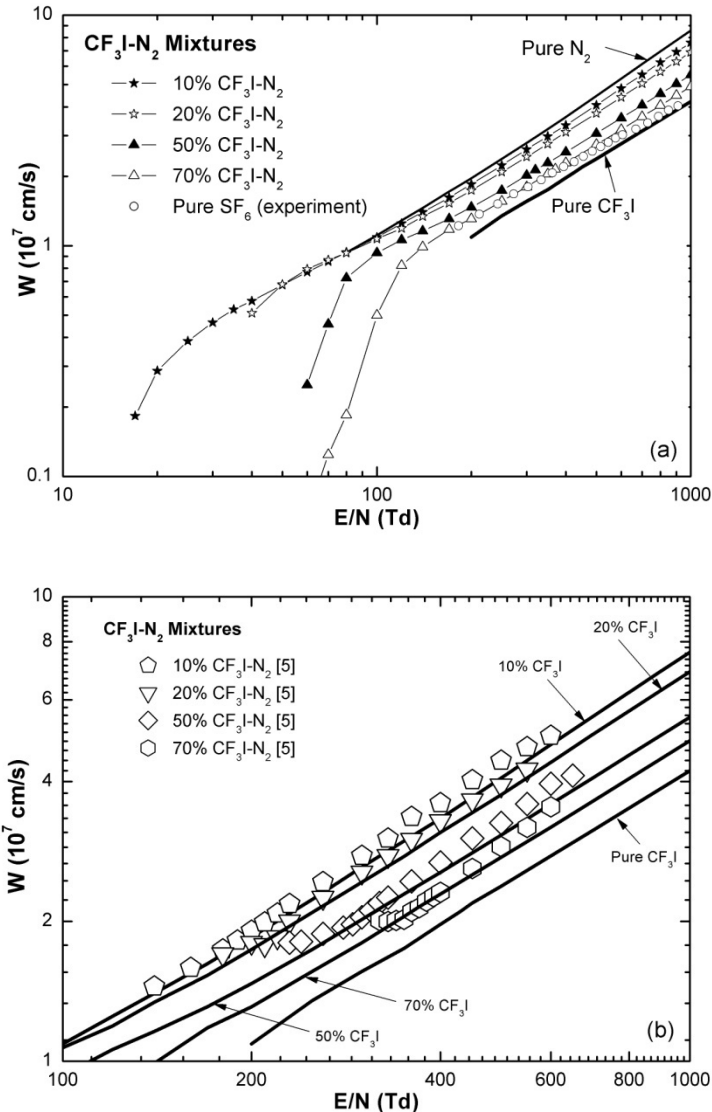


Fig. 1. Electron drift velocity, W , as functions of E/N for the $\text{CF}_3\text{I-N}_2$ mixtures with 10%, 20%, 50%, and 70% CF_3I . (a) The solid line and symbols show present W values calculated using a two-term approximation of the Boltzmann equation for the $\text{CF}_3\text{I-N}_2$ mixtures. The solid curves show present W values calculated for the pure CF_3I and N_2 molecules. The open circle symbol shows the measurement value of the pure SF_6 [15]. (b) The figure shows comparisons between the results calculated and experiments [5] for the $\text{CF}_3\text{I-N}_2$ mixtures with 10%, 20%, 50%, and 70% CF_3I , respectively. The symbols show the experiment results of the $\text{CF}_3\text{I-N}_2$ mixtures [5]. The solid curves show the present W values calculated using a two-term approximation of the Boltzmann equation for the pure CF_3I and $\text{CF}_3\text{I-N}_2$ mixtures.

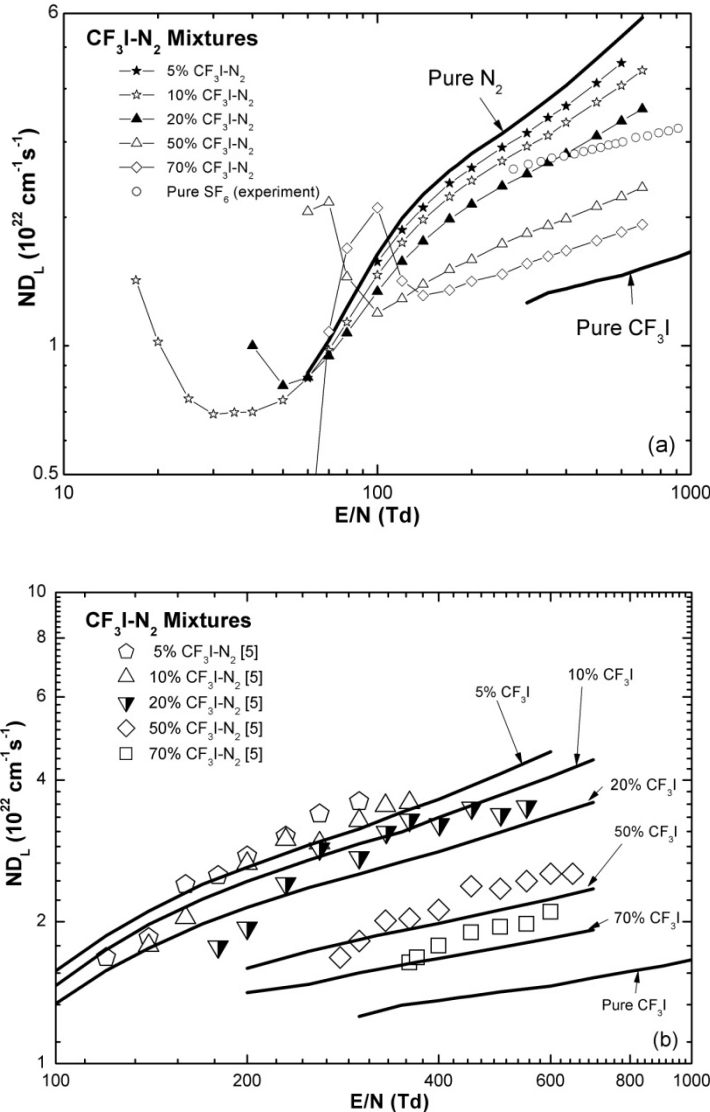


Fig. 2. Density-normalized longitudinal coefficient, ND_L , as functions of E/N for the CF_3I-N_2 mixtures with 5%, 10%, 20%, 50%, and 70% CF_3I . (a) The solid line and symbols show present ND_L values calculated using a two-term approximation of the Boltzmann equation for the CF_3I-N_2 mixtures. The solid curves show present ND_L values calculated for the pure CF_3I and N_2 molecules. The open circle symbol shows the measurement value of the pure SF_6 [15]. (b) The figure shows comparisons between the results calculated and experiments [5] of the CF_3I-N_2 mixtures with 5%, 10%, 20%, 50%, and 70% CF_3I , respectively. The symbols show the experiment results of the CF_3I-N_2 mixtures [5]. The solid curves show the present W values calculated using a two-term approximation of the Boltzmann equation for the pure CF_3I , pure N_2 , and CF_3I-N_2 mixtures.

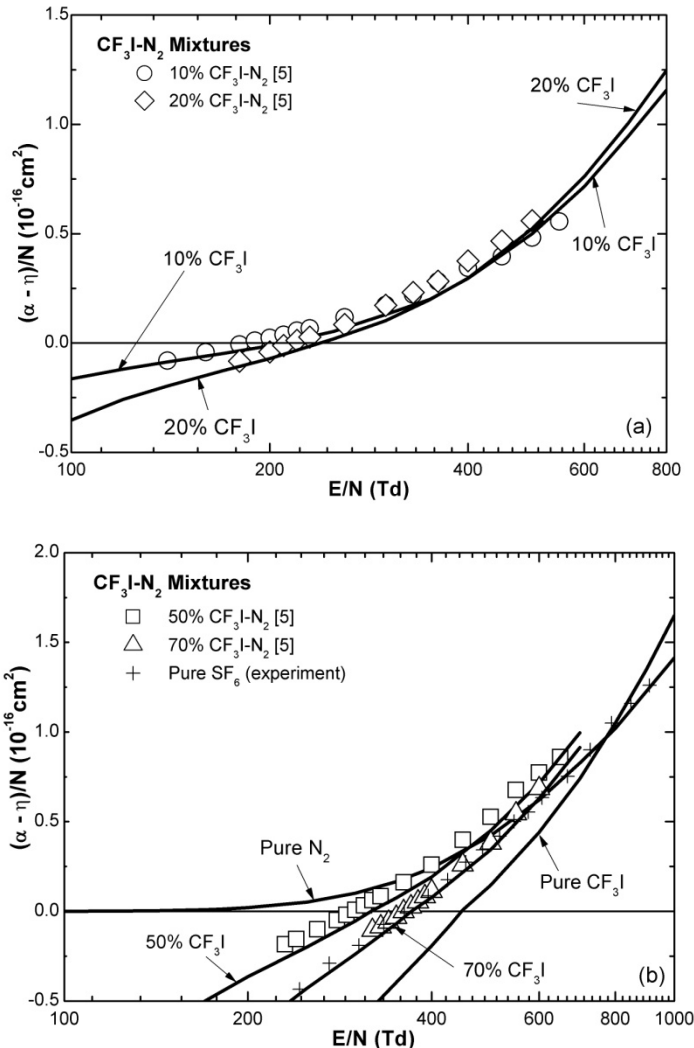


Fig. 3. (a), (b) Density normalized effective ionization coefficient, $(\alpha - \eta)/N$, as functions of E/N for the $\text{CF}_3\text{I-N}_2$ mixtures with 10%, 20%, 50%, and 70% CF_3I . The solid curves show present $(\alpha - \eta)/N$ values calculated using a two-term approximation of the Boltzmann equation for the pure CF_3I , pure N_2 molecules, and $\text{CF}_3\text{I-N}_2$ mixtures. The cross symbol shows the measurement value of the pure SF_6 [15]. The symbols show the experiment results of the $\text{CF}_3\text{I-N}_2$ mixtures [5].

3.2 Density-Normalized Longitudinal Diffusion Coefficients

The results for the density-normalized longitudinal diffusion coefficients, ND_L , as functions of E/N for the $\text{CF}_3\text{I-N}_2$ mixture gas calculated in the E/N range $10 < E/N < 1000$ Td using a two-term approximation of the Boltzmann equation are shown in

Fig. 2. In these binary mixtures, the values of ND_L are suggested to be between those of the pure gases over $E/N > 200$ Td. The agreements between the results calculated and those measured by Urquijo *et al.* [5] are satisfactory over the entire E/N range for the CF_3I-N_2 mixtures in Fig. 2(b). The density-normalized longitudinal diffusion coefficient for the pure SF_6 obtained by Aschwanden [15] is also shown in Fig. 2(a) for the aim of comparison. The ND_L values of the pure SF_6 are greater than those of these binary mixtures. The increased trends of values calculated for 50% and 70% CF_3I-N_2 mixtures are the same as those of the pure SF_6 gas with increasing electric field strength.

3.3 Density-Normalized Effective Ionization Coefficients

The results for the density-normalized effective ionization coefficients, $(\alpha - \eta)/N$, as functions of E/N for the CF_3I-N_2 mixture gas calculated using a two-term approximation of the Boltzmann equation are shown in Fig. 3. In these binary mixtures, the values of $(\alpha - \eta)/N$ are also suggested to be between those of the pure gases. The best agreements between the present results and those measured by Urquijo *et al.* [5] in Fig. 3(b) are satisfactory over the entire E/N range. For the sake of comparison, the density-normalized effective ionization coefficient obtained by Aschwanden [15] for the pure SF_6 gas is also shown in Fig. 3(b). The $(\alpha - \eta)/N$ values for 70% CF_3I-N_2 mixture are very close to those of the pure SF_6 gas over $E/N < 550$ Td.

Because of the accuracy of the electron collision cross sections for the present gases and the validity of the Boltzmann equation, the present results calculated are reliable over the $E/N < 100$ Td and the results have been also calculated for the first time. More experiments of the electron transport coefficients for the binary mixtures of the CF_3I gas with these buffer gases need to be performed over the wide range of E/N in the future. In general, when the percentage ratio of the CF_3I gas in binary mixtures increases, the values of the electron transport coefficients increase progressively to those of the pure CF_3I .

3.4 Limiting Field Strength Values of E/N

The limiting field strength values of E/N , $(E/N)_{lim}$, at which $\alpha = \eta$ for the CF_3I-N_2 mixture gas are derived at 133.322 Pa as shown in Fig. 4. The present $(E/N)_{lim}$ values calculated for the CF_3I-N_2 mixtures were in good agreement with those derived from measurement of Urquijo *et al.* [5] as shown in Fig. 4. These values are also compared with those of the SF_6-N_2 mixture gas [16] as shown in Fig. 4. The $(E/N)_{lim}$ values of the CF_3I-N_2 mixture are greater than that of the binary mixtures of CF_3I gas with the other gases over the entire CF_3I concentration. The $(E/N)_{lim}$ values of the SF_6-N_2 mixtures are the greatest when the SF_6 concentration increases to 50% in the binary mixtures. However, the $(E/N)_{lim}$ values of the CF_3I-N_2 mixtures are the greatest when the CF_3I concentration is greater than about 50% in the binary mixtures. It may be considered as a prospective substitute for the SF_6 gas. In Fig. 4, the 65 - 75% CF_3I-N_2 mixture gases are considered to use in high voltage and many industries if other chemical, physical, electrical, thermal, and economical studies are considered thoroughly.

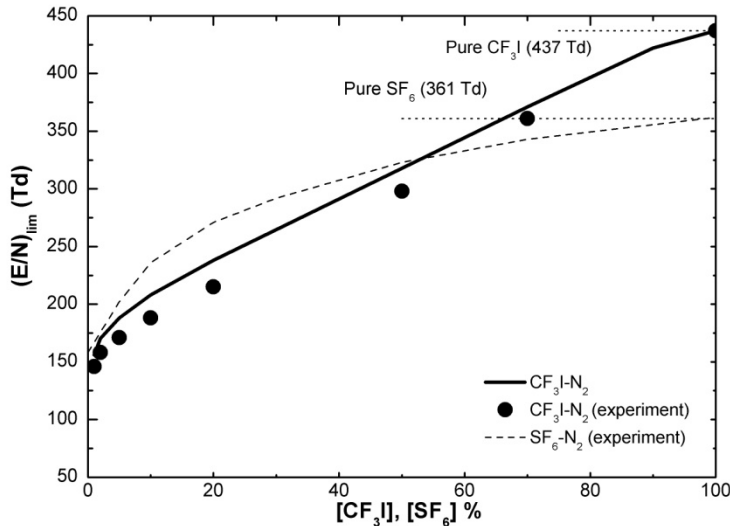


Fig. 4. Limiting field strength of E/N , $(E/N)_{\text{lim}}$, as a function of the percentage of CF_3I gas for the $\text{CF}_3\text{I-N}_2$ mixture. The solid line shows present $(E/N)_{\text{lim}}$ values for the $\text{CF}_3\text{I-N}_2$ mixture calculated using a two-term approximation of the Boltzmann equation. The solid symbols and dashed curve respectively show experimental $(E/N)_{\text{lim}}$ values for the $\text{CF}_3\text{I-N}_2$ [5] and $\text{SF}_6\text{-N}_2$ [16] mixtures.

4 Conclusion

The electron drift velocity, density-normalized longitudinal diffusion coefficient, and density-normalized effective ionization coefficient in the $\text{CF}_3\text{I-N}_2$ mixture gases are calculated using a two-term approximation of the Boltzmann equation for the energy in the E/N range of 10 - 1000 Td. The calculated electron transport coefficients in the $\text{CF}_3\text{I-N}_2$ mixtures are in good agreement with the experiments. The present results have been also calculated for the first time in the E/N range of 10 – 100 Td. The NDC phenomena in these binary gas mixtures are suggested. The electron transport coefficients calculated are also compared with those of the pure SF_6 gas in experiments. Moreover, the limiting field strength values of E/N for the 70% $\text{CF}_3\text{I-N}_2$ mixture gas are determined and essentially greater than those of the pure SF_6 gas. The binary mixtures of 65 - 75% $\text{CF}_3\text{I-N}_2$ are considered to use in high voltage and many industries. For the purposes of justification of the accuracy of our results, more experimental data for electron transport coefficients for the binary mixtures of CF_3I with these gases need to be performed over a wide range of E/N .

References

1. Conference of the Parties, Kyoto Protocol to the United Nations Framework Convention on Climate Change, Third Session Kyoto, Kyoto, Japan (1997)
2. Li, Y., Patten, O., Youn, D., Wuebbles, D.J.: Potential impacts of CF_3I on ozone as a replacement for CF_3Br in aircraft applications. *Atmos. Chem. Phys.* 6(12), 4559–4568 (2006)
3. Taki, M., Maekawa, D., Odaka, H., Mizoguchi, H., Yanabu, S.: Interruption capability of CF_3I gas as a Substitution candidate for SF_6 gas. *IEEE Trans. Dielectrics and Elec. Insulation* 14(2), 341–346 (2007)
4. Takagari, H., Kasuya, H., Mizoguchi, H., Yanabu, S.: Investigation of the performance of CF_3I gas as a possible substitute for SF_6 . *IEEE Trans. Dielectrics and Elec. Insulation* 15(5), 1424–1429 (2008)
5. de Urquijo, J., Juárez, A.M., Basurto, E., Hernández-Ávila, J.L.: Electron impact ionization and attachment drift velocities and longitudinal diffusion in CF_3I and $\text{CF}_3\text{I-N}_2$ mixtures. *J. Phys. D: Appl. Phys.* 40(7), 2205–2209 (2007)
6. Deng, Y.K., Xiao, D.M.: The effective ionization coefficients and electron drift velocities in gas mixtures of CF_3I with N_2 and CO_2 obtained from Boltzmann equation analysis. *Chin. Phys. B* 22(3), 035101-1–6 (2013)
7. Kimura, M., Nakamura, Y.: Electron swarm parameters in CF_3I and a set of electron collision cross sections for the CF_3I molecule. *J. Phys. D: Appl. Phys.* 43(14), 145202-1–6 (2010)
8. Tagashira, H., Sakai, Y., Sakamoto, S.: The development of electron avalanches in argon at high E/N values. II. Boltzmann equation analysis. *J. Phys. D: Appl. Phys.* 10(7), 1051–1063 (1977)
9. Tuan, D.A., Jeon, B.H.: Electron collision cross sections for the Cl_2 molecule from electron transport coefficients. *J. Phys. Soc. Jpn.* 80(8), 084301-1–5 (2011)
10. Tuan, D.A., Jeon, B.-H.: Electron Collision Cross Sections for the Tetraethoxysilane Molecule and Electron Transport Coefficients in Tetraethoxysilane- O_2 and Tetraethoxysilane-Ar Mixtures. *Journal of the Physical Society of Japan* 81(6), 064301-1–8 (2012)
11. Huxley, L.G.H., Crompton, R.W.: The Diffusion and Drift of Electrons in Gases, ch. 6 and ch. 13. John Wiley & Sons, New York (1974)
12. Jeon, B.H.: Determination of electron collision cross-sections for the oxygen molecule by using an electron swarm study. *J. Korean Phys. Soc.* 43(4), 513–525 (2003)
13. Christophorou, L.G., Hunter, S.R.: From basic research to application. In: Christophorou, L.G. (ed.) *Electron-Molecule Interations and Their Applications*, vol. 2, pp. 318–412. Academic Press, Florida (1984)
14. Nakamura, Y.: private communication. Tokyo Denki Univ., Tokyo (November 2010)
15. Aschwanden, T.: Die ermittlung physikalischer entladungsparameter in isoliergasen und isolergasgemischen mit einer verbesserten swarm-methode. Ph.D. dissertation, Eidgenössische Technische Hochschule Zürich, Zurich, Germany, from (8) (1985) (in German)
16. Christophorou, L.G., Van Brunt, R.J.: SF_6/N_2 mixtures: basic and HV insulation properties. *IEEE Trans. Dielectrics and Elec. Insulation* 2(5), 952–1003 (1995)

Analysis of the Electromagnetic Force in an Magnetohydrodynamic Flowmeter

Le Chi Kien

Faculty of Electrical and Electronics Engineering,
Ho Chi Minh City – University of Technical Education,
Ho Chi Minh City, Vietnam
kienlc@hcmute.edu.vn

Abstract. There are many non-contact ways for determination of flowrates in the metallurgy industry and one of those methods is Magnetohydrodynamics. The paper mainly considers the forces produced in Magnetohydrodynamics interacting with magnetic field. The aim of this paper is to make the measurement essentially independent of the fluid electrical conductivity. The flowmeter used in this study includes two coils and the forces generated by these coils are recognized in time. As a result, it is concluded that the forces produced in the coils can accurately measure the flowrate of a flow. This result can be developed to simulate the reliability and calibration parameters of the measurement.

Keywords: magnetohydrodynamic effect, flow measurement, Lorentz force, liquid metal flow, electrical conductivity.

1 Introduction

A key feature of electromagnetism is that a force is generated when an electrical conductor moves through a magnetic field. If the material is in a fluid state, this principle can be used to determine its flowrate. At low temperatures, flowrates can be measured through inductive flowmeters [1]. By contrast, measurements in metallurgical flows of liquid metals at high temperatures cannot be carried out using conventional inductive flowmeters, since electrodes cannot be inserted in the flow. The present work is devoted to a non-contact electromagnetic flow measurement technique called Magnetohydrodynamic flowmeter (MF) [2,3]. It is based on measuring the force acting upon a magnet system that interacts with the flow of an electrically conducting fluid.

More precisely, the purpose of the present study is to improve the existing device, in order to make the measurement essentially independent of the fluid electrical conductivity. This is highly desirable in metallurgy, where the temperature and composition of the alloy can vary significantly in time and space. In turn, these variations bring uncertainties on the value of the fluid electrical conductivity. The proposed Magnetohydrodynamic flowmeter is based on temporal correlations, taken from force measurements at two locations. The feasibility of this novel version of Magnetohydrodynamic flowmeter is demonstrated entirely numerically.

2 Basic Principle

A Magnetohydrodynamic flowmeter measures the integrated Lorentz force, resulting from the interaction between a liquid metal in motion and an applied magnetic field. In the present manuscript, the magnet system consists in two current-carrying coils placed around a circular pipe and generates the so-called primary magnetic field \mathbf{B} , given by Biot-Savart's law, [4]

$$\mathbf{B}(\mathbf{r}) = \sum_{i=1,2} \mathbf{B}_i(\mathbf{r}) = \sum_{i=1,2} \frac{\mu_0 J_i}{4\pi} \oint \frac{dl \times (\mathbf{r} - \mathbf{r}')}{|\mathbf{r} - \mathbf{r}'|^3} \quad (1)$$

where J_i is the magnitude of the primary electric current circulating in the i^{th} coil, $\mu_0 = 4\pi \times 10^{-7}$ H/m is the vacuum permeability, dl is a length element of the coil, \mathbf{r}' is the position of the coil and \mathbf{r} denotes the location where the magnetic field is evaluated. The magnetic field lines are sketched in Fig. 1 for a pipe of length L and two coils separated by a distance Δ . The currents flowing through the coils have same signs (left figure) or opposite signs (right figure). Since the magnetic field interacts with the flow velocity \mathbf{u} , eddy currents, also called secondary currents, are induced in the liquid metal. These in turn create an induced magnetic field \mathbf{b} , referred to as the secondary magnetic field. In this work, the magnetic diffusion time is assumed much smaller than the timescale of large eddies. Therefore, the secondary magnetic field becomes negligible with respect to the primary magnetic field, namely $|\mathbf{b}| \ll |\mathbf{B}|$. This is referred to as the quasi-static approximation [5]. In this framework, eddy currents are described by a simplified Ohm's law, for moving electrically conducting fluids, and has the form

$$\mathbf{j} = \sigma(-\nabla\phi + \mathbf{u} \times \mathbf{B}) \quad (2)$$

The fluid electrical conductivity is denoted σ and the electric field is assumed to be the gradient of the electrical potential ϕ . According to the conservation of electric charge, eddy currents are divergence-free. Hence, the electrical potential satisfies the Poisson equation, $\nabla^2\phi = \nabla \cdot (\mathbf{u} \times \mathbf{B})$. In addition, eddy currents are maximum where the angle between \mathbf{u} and \mathbf{B} is large, see Fig. 1.

The interaction between the primary magnetic field \mathbf{B}_i , generated by the i^{th} coil, and the eddy current \mathbf{j} , induced by all coils, yields a Lorentz force,

$$\mathbf{F}_{Li} = \mathbf{j} \times \mathbf{B}_i \quad (3)$$

which globally brakes the flow. Furthermore, the secondary magnetic field magnetic field \mathbf{b} interacts with the primary current and induces a reaction force, acting on the i^{th} coil. By virtue of the reciprocity principle [3], the following integrated Lorentz force,

$$F_i = \frac{1}{V} \int \mathbf{F}_{Li} dV = -F_i^r \quad (4)$$

is equal in magnitude but opposite in direction to the reaction force F_i^r acting upon the i^{th} coil. In addition, F_i is proportional to the mean velocity of the flow and the electrical conductivity of the fluid. Previous works have shown that F_i , or equivalently F_i^r , can be used to determine the mean flowrate assuming the fluid conductivity is known. [2,3]

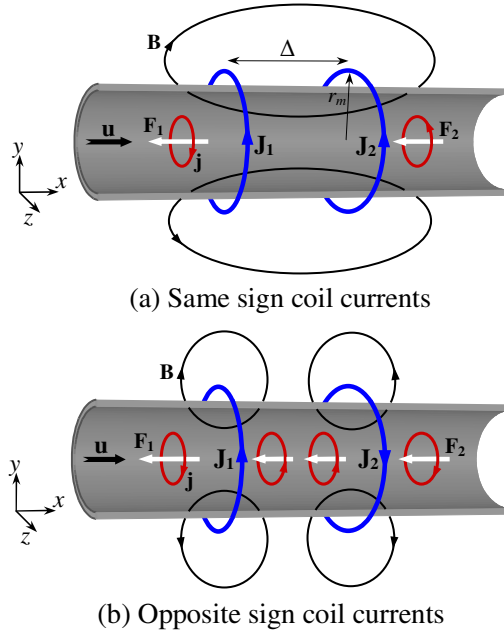


Fig. 1. Energy Principle of Magnetohydrodynamic flowmeter. Two current-carrying coils produce the primary magnetic field \mathbf{B} , which interacts with the flow \mathbf{u} of an electrically conducting fluid and induces eddy currents \mathbf{j} . The coil currents have either same (left) or opposite (right) signs. The force acting upon the coils is equal in magnitude (but opposite in direction) to the sum of the Lorentz forces F_1 and F_2 acting on the flow.

However, the electrical conductivity of the fluid is often unknown or fluctuates in time. It is therefore desirable to develop Magnetohydrodynamic flowmeters which operate independently of the electrical conductivity of the fluid.

To remove this dependency, a variant of flowmeter is investigated. It focuses on the time evolutions of the Lorentz forces, which are cross-correlated. By definition, the location of the maximum correlation gives the time shift for which the two forces are most similar. Therefore, information about the mean flowrate can be obtained. The main advantage of this technique is that the resulting flowrate is independent on the fluid properties. In the present application, the challenge stands in using the coils as sensors.

The quality of the measurement is assessed in two ways. First, its reliability is analyzed by quantifying the amplitude of the correlation peak. Second, the measured time shift is compared to its exact value, in order to determine the calibration factor. The investigation is performed for different coil radii r_m , separations Δ and signs of the coil-carrying currents.

3 Governing Equations and Numerical Method

In the proposed device, cross-correlations are performed between the Lorentz forces due to each coil. Since the Lorentz forces depend on the electric potential and the

velocity field, these quantities are needed at each time step. In this manuscript, we assume that the flow is unaffected by the Lorentz force. For the parameters considered here, the maximum streamwise Lorentz force is indeed less than 5% of the driving force. It is thus expected to have a weak influence on the flow. With this assumption, the incompressible flow dynamics are governed by the Navier-Stokes equations, as in classical hydrodynamics. The equations of motion are thus given by

$$\frac{\partial \mathbf{u}}{\partial t} + (\mathbf{u} \cdot \nabla) \mathbf{u} = -\nabla p + \nu \nabla^2 \mathbf{u}, \quad \nabla \cdot \mathbf{u} = 0 \quad (5)$$

p being the kinematic pressure (i.e. divided by the fluid density) and ν the fluid kinematic viscosity. These equations are discretised spatially using an unstructured finite volume method based on a collocated formulation. The method is analogue to that used in previous studies [6], and it is thus not detailed here. Briefly, the velocity and pressure fields at time $n+1$ are computed using a fractional-step method. First, Eq. 5 is solved for the velocity field at an intermediate time step $\mathbf{u}^{(*)}$. Then, the pressure field $p^{(n+1)}$ at time $n+1$ is computed through the following Poisson system,

$$\nabla^2 p^{(n+1)} = \nabla \cdot \mathbf{u}^{(*)} \quad (6)$$

so as to ensure that $\mathbf{u}^{(n+1)}$ is divergence-free. The velocity field $\mathbf{u}^{(n+1)}$ is finally obtained as $\mathbf{u}^{(n+1)} = \mathbf{u}^{(*)} - \Delta t \nabla p^{(n+1)}$ (Δt is the time step). The electrical potential satisfies the following Poisson equation

$$\nabla^2 \phi = \nabla \cdot (\mathbf{u} \times \mathbf{B}) \quad (7)$$

and it is computed explicitly using $\mathbf{u}^{(n+1)}$.

The computational domain consists in a circular pipe, characterized by no-slip and insulating walls located at $r=R$, which yields

$$\mathbf{u} \Big|_{r=R} = 0, \quad (\mathbf{j} \cdot \mathbf{n})_{r=R} = 0, \quad \left. \frac{\partial \phi}{\partial n} \right|_{r=R} = 0 \quad (8)$$

where \mathbf{n} is the unit vector normal to the wall. Moreover, periodic boundary conditions are applied at the inlet and outlet. In order to solve the Poisson system for the potential, the following boundary conditions are applied,

$$\phi \Big|_{r=0} = 0, \quad \left. \frac{\partial \phi}{\partial r} \right|_{r=R} = 0 \quad (9)$$

4 Simulation Settings

The input parameters for the flowmeter are the coil radius r_m (both coils being assumed to be equal in size), the coil separation Δ and the currents J_1 and J_2 flowing through each coil. Both same-sign currents ($J_1=J_2$) and opposite-sign currents $J_1=-J_2$ are considered, see Fig. 1. The primary magnetic field is computed through Biot-Savart's law, see Eq. 1, by discretising each coil in 1000 segments. The coil radii and separations equal twice the pipe radius, namely $r_m=\Delta=2R$.

The pipe is ten times longer than its radius, i.e. $L=10R$, and it is discretised with 65 points in the streamwise direction. The mesh resolutions in the radial and azimuthal directions vary with the azimuthal angle since the mesh is unstructured. However, the pipe wall is discretised with 64 points in the azimuthal direction and the numbers of points along the pipe diameter is approximately 50.

The flow is initialized with the following turbulent-like velocity profile on which random perturbations are superposed,³⁾

$$u_x = U_c \beta(\alpha) \ln \left[1 + \alpha \left(1 - \frac{r^2}{R^2} \right) \right], u_r = u_\theta = 0 \quad (10)$$

where

$$\beta(\alpha) = \frac{\alpha}{(1+\alpha)\ln(1+\alpha)-\alpha} \quad (11)$$

and $\alpha=1000$. Furthermore, the flow is driven by a constant pressure gradient such that the bulk Reynolds number fluctuates around $Re_b=2U_b R/\nu \approx 3600$, $U_b=1/V \int u dV = 2/R^2 \int_0^R \langle u_x \rangle r dr$ being the bulk velocity, V the pipe volume, and $\langle u_x \rangle$ the mean streamwise velocity profile in the radial direction. The mean value of the bulk velocity is fixed through

$$U_b^2 = \frac{4R}{\rho f} \left(\frac{\partial p}{\partial x} \right) \quad (12)$$

where f is the friction factor [7].

5 Results

The integrated forces produced by each coil and acting upon the flow in the streamwise direction, \tilde{F}_{1x} and \tilde{F}_{2x} , are non-dimensionalised by removing their mean and dividing by their root-mean-square. Their evolutions in time are shown by Fig. 2, for same-sign currents (left) and opposite-sign currents (right) flowing through the coils. For clarity, the time history is limited to three crossing of the mean flow through the pipe. Since the flow is turbulent, the forces exhibit several fluctuations and they are statistically shifted in time.

The cross-correlations of the forces produced by each coil are illustrated by Fig. 3. Two characteristics of the correlations are of particular interest: the time shift T_p associated to their main peak, and the peak magnitude C_M , which indicates the reliability of the measurement. The time T_p is compared to the time needed for the mean flow to travel from the upstream to the downstream coil, namely

$$T_b = \frac{\Delta}{U_b} \quad (13)$$

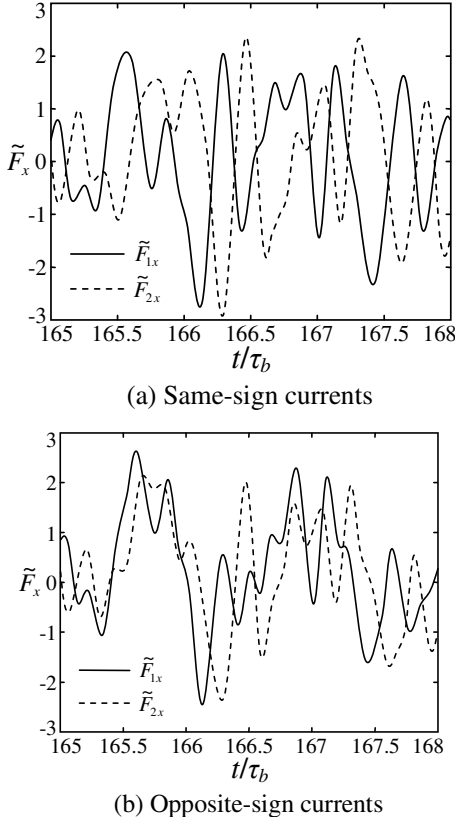


Fig. 2. Time evolutions of the integrated forces produced by each coil when a turbulent flow moves through the flowmeter: same-sign currents (left) and opposite-sign currents (right). Times are non-dimensionalised by the crossing time of the mean flow through the pipe, $\tau_b=L/U_b$, where U_b is the bulk velocity.

The ratio T_p/T_b is defined as the calibration factor of the measurement. In turn, the flowrate measured by the Magnetohydrodynamic flowmeter is given by

$$U_{MF} = \frac{T_b}{T_p} U_b \quad (14)$$

where U_b is the exact flow rate.

Table 1 shows the results of the cross-correlations between the forces produced by each coil when a turbulent flow moves through the flowmeter. C_M is the magnitude of the correlation peak and T_p/T_b is the ratio between the time shift associated to the peak and the time-of-flight of the mean flow between the coils. The ratio of the measured to the exact flowrate is U_{MF}/U_b . In both cases, the main peak of the correlation is well distinguishable from the secondary oscillations. Moreover, it is slightly larger and sharper with same-sign currents than with currents of opposite sign. Remarkably, the calibration factor T_p/T_b is almost independent of the current signs.

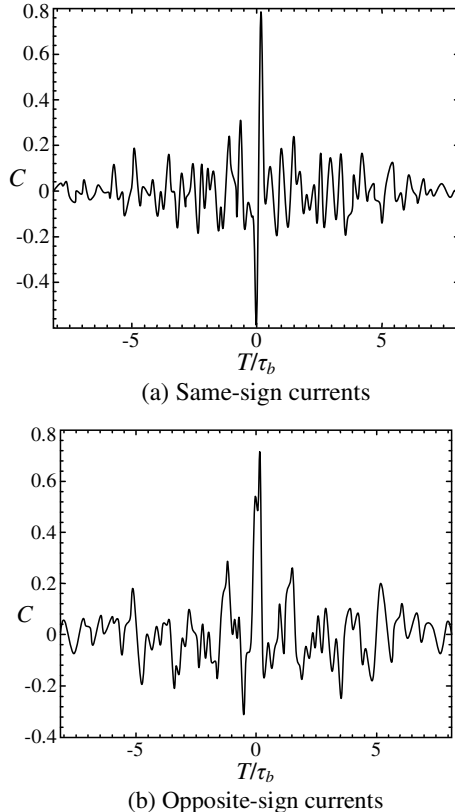


Fig. 3. Cross-correlations of the integrated forces produced by each coil when a turbulent flow moves through the flowmeter: same-sign currents (left) and opposite-sign currents (right). The time shifts T are non-dimensionalised by the crossing time of the mean flow through the pipe, $\tau_b=L/U_b$, where U_b is the bulk velocity.

Table 1. Results of the cross-correlations between the forces

Sign of (J_1, J_2)	C_M	T_p/T_b	U_{MF}/U_b
Same	0.79	0.87	1.15
Opposite	0.71	0.84	1.2

6 Conclusions

This preliminary study demonstrated numerically the feasibility of a two-coil Magnetohydrodynamic flowmeter, based on time-correlations of the Lorentz forces produced by each coil. The proposed technique was validated with coil radii and separation equal to twice the pipe radius. Particular attention was given to the magnitude of the correlation peak and its associated time. Currents of same- and opposite-sign, flowing through the coils, were investigated. In both cases, the flowrate

of a three-dimensional turbulent flow can be successfully measured. More precisely, the determination of the correlation peak is reliable and the calibration factor is almost insensitive to the sign of the currents.

Future works will aim at analyzing systematically the reliability and calibration factor of the measurement for a wide range of coil parameters. The region of maximum sensitivity of the flowmeter should also be identified. Finally, the effect of the magnetic field on the flow will be quantified through dynamic simulations, in which the momentum balance accounts for the Lorentz force as an explicit source term.

References

- [1] Minchenya, V., Karcher, C., Kolesnikov, Y., Thess, A.: Calibration of the Lorentz force flowmeter. *Flow Measurement and Instrumentation* 22(3), 242–247 (2011)
- [2] Thess, A., Votyakov, E.V., Kolesnikov, Y.: Lorentz force velocimetry. *Physical Review Letters* 96(16), 164501 (2006)
- [3] Thess, A., Votyakov, E., Knaepen, B., Zikanov, O.: Theory of the Lorentz force flowmeter. *New Journal of Physics* 9, 299 (2007)
- [4] Jackson, J.D.: *Classical Electrodynamics*, ch. 5, 3rd edn., p. 133. John Wiley & Sons Inc., New York (1999)
- [5] Davidson, P.A.: *An Introduction to Magnetohydrodynamics*, ch. 5, 1st edn., p. 118. Cambridge University Press, New York (2001)
- [6] Shen, W.Z., Michelsen, J.A., Sørensen, J.N.: A collocated grid finite volume method for aeroacoustic computations of low-speed flows. *Journal of Computational Physics* 196(1), 348–366 (2004)
- [7] Romeo, E., Royo, C., Monzón, A.: Improved explicit equations for estimation of the friction factor in rough and smooth pipes. *Chemical Engineering Journal* 86(3), 369–374 (2002)

Enhancing Total Transfer Capability via Optimal Location of TCSC in Deregulated Electricity Market

ThanhLong Duong^{1,2}, Yao JianGang¹, LeAnhTu Nguyen², and Guo ZhenWei¹

¹ Department of Electrical Engineering, Hunan University, Changsha, Hunan, China

² Department of Electrical Engineering, Industrial University of Hochiminh City, Vietnam
`{thanhlong802003,yaojiangan126,tunguyen8x,guozhenwei}@yahoo.com`

Abstract. In deregulated electricity market, most of the power transferred through the wheeling transaction. Hence, it is very important and necessary to determine the transfer capability of the transmission system before the power dispatch. Series FACTS devices such as Thyristor controlled series compensators (TCSC), with its ability to directly control the power flow can be very effective to total transfer capability of transmission network. Proper location of TCSC plays key role in improving total transfer capability (TTC). From the viewpoint, this paper focuses on the evaluation of the impact of TCSC on TTC via optimal location. Evaluation total transfer capability using TCSC requires a two-step approach. First, the optimal location of the TCSC in the network must be ascertained by Min cut algorithm and then, the mathematical formulation of TTC using Repeated Power Flow (RPF) with fixed TCSC parameters is solved. The proposed method is tested and validated for locating TCSC in IEEE 14-, IEEE-30 bus test systems. Results show that the proposed method is capable of finding the best location for TCSC installation to improve total transfer capability.

Keywords: Deregulated power system, FACTS, TCSC, RPF and TTC.

1 Introduction

Deregulation of power system has brought the trading of significant amounts of electrical energy and major changes in the system operation and control. In open access environment, consumers are allowed to choose their provider for electrical energy and consequently one and more transactions are possible in the transmission system. Therefore, the system Operator should have knowledge about power dispatch and total transfer capability (TTC).

TTC is a measure of the transfer capability remaining in the physical transmission network for further commercial activity over and above all ready committed uses. According to the report of NERC [1], TTC is defined as the amount of electric power that can be transferred while meeting all of specific set of defined pre and post contingency system condition transferred over the interconnected transmission network in a reliable. TTC can be calculated by several power flow solution methods such as 1) linear ATC (LATC) method [2], 2) continuation power flow (CPF) method

[3], 3) repetitive power flow (RPF) method [4], and 4) optimal power flow (OPF) based methods [5].

In practice, an infinite transfer capacity of the network is impossible due to transfer limit of the transmission lines. Various factors, such as environmental, right-of-way and cost constraints have limited the expansion of the transmission networks. This makes transmission lines are often driven close to or even beyond their thermal limits in order to satisfy the increased power demand and trades due to increase of the unplanned power exchanges. If the exchanges were not controlled, some lines located on particular paths may become overloaded and this has led to bottleneck on the power system. The existence of bottlenecks in the transmission line affects direct on market transactions and decrease transfer capability of power system [6]. Using TCSC seems to be a promising strategy to eliminate /alleviate the transmission congestion and to increase available transfer capability of the existing lines. This device is not an alternative to constructing new transmission networks or upgrading transmission links but make it possible to use existing transmission network up to or close to their thermal limits.

Because of cost for these devices is high and effectiveness of the controls for different purposes mainly depends on the location of control device [7]. Therefore, optimization of location of the FACTS controllers has become the important issue for system Operators in the electricity market. Determining the bottleneck of power system plays key role in reducing search space and number of FACTS devices need to be installed. However, it is difficult to implement if there is not an effective method. This paper has applied Min cut algorithm that can be used to determined bottleneck in such effective away.

Various sensitivity methods are used to determine the optimal locations of FACTS devices to achieve different objectives. In [8], Genetic algorithm (GA) was used to determine the optimal location and parameter of TCSC for maximizing power transfer capability. Evolutionary Programming (EP) was proposed to obtain optimal placement of multi-type FACTS devices for simultaneously maximizing the total transfer capability whereas minimizing the total system real power loss and the results are better when compared to loss sensitivity index method [9]. In [10], Particle Swarm Optimization (PSO) is used to determine the optimal allocation of multitype FACTS controllers to enhance power transfer capability of power transactions between sources and sink areas in power systems. In [11], the real power flow performance index (PI) was used to determine the suitable locations of TCSC and TCPAR for TTC enhancement. In [12], RPF method combined with the sensitivity index of the loading margin to transmission line impedances were used to determine the location of TCSC for maximizing TTC.

In this paper, TCSC, which is one of the most effective FACTS devices, is selected to study. The objective of this paper is to improve transfer capability through the optimal utilization of TCSC. Proper location of TCSC is determined base on bottleneck of power system. In order to evaluate the suitable location of TCSC, the Min-cut algorithm has been proposed to determine optimal location of TCSC. The proposed method can identify the weakest location of the system in terms of transfer

capability of the lines and therefore helps the System Operators to operate the system in a more secure and sufficient way.

2 Problem Formulations Using RPF with TCSC

Repeated power flow (RPF) enables transfers by increasing, the complex load with uniform power factor at every load bus in the sink area and increasing the injected real power at generator buses in the source area in incremental steps until limits are incurred [4].

The mathematical formulation of TTC using RPF without TCSC can be expressed as follows:

Maximize λ

Subject to:

$$P_{Gi} - P_{Di} - \sum_{j=1}^n V_i V_j (G_{ij} \cos \delta_{ij} + B_{ij} \sin \delta_{ij}) = 0 \quad (1)$$

$$Q_{Gi} - Q_{Di} - \sum_{j=1}^n V_i V_j (G_{ij} \sin \delta_{ij} - B_{ij} \cos \delta_{ij}) = 0 \quad (2)$$

$$V_i^{\min} \leq V_i \leq V_i^{\max} \quad (3)$$

$$S_{ij} \leq S_{ij}^{\max} \quad (4)$$

Where

λ is scalar parameter representing the increase in bus load or generation. $\lambda = 0$ (λ_0) corresponds to no transfer (base case) and $\lambda = \lambda_{\max}$ corresponds to the maximal transfer. P_{Gi} and Q_{Gi} are the real and reactive power generation at bus i; P_{Di} and Q_{Di} are the real and reactive power demand at bus i; V_i and V_j are the voltage magnitude at bus i, j; G_{ij} , B_{ij} are real and imaginary part of the ij^{th} element of bus admittance matrix; δ_{ij} is the voltage angle difference between bus i and bus j; S_{ij} is the apparent power flow of transmission line i; n is bus number of the system.

In the above power flow equations (1) and (2), P_{Gi} (generator real output in source area), P_{Di} (real load in sink area), and Q_{Di} (reactive load in sink area) are changed in the following way [13]:

$$P_{Gi} = P_{Gi}^0 (1 + \lambda K_{Gi}) \quad (5)$$

$$P_{Di} = P_{Di}^0 (1 + \lambda K_{Di}) \quad (6)$$

$$Q_{Di} = Q_{Di}^0 (1 + \lambda K_{Di}) \quad (7)$$

Where: P_{Gi}^0 is original real power generation at bus which is in source area; P_{Di}^0 , Q_{Di}^0 are original real and reactive load demand at bus which is in sink area; K_{Gi} , K_{Di} are constants used to specify the change rate in generation and load as λ varies.

TTC level in each case (normal or contingency case) is calculated as follows

$$\text{TTC} = \sum_{i \in \text{Sink}} P_{Di} (\lambda_{\max}) - \sum_{i \in \text{Sink}} P_{Di}^0 \quad (8)$$

Where

$\sum_{i \in \text{Sink}} P_{Di}(\lambda_{\max})$ is sum of load at sink area when $\lambda = \lambda_{\max}$; $\sum_{i \in \text{Sink}} P_{Di}^0$ is sum of load at sink area when $\lambda = 0$.

The effect of TCSC on the network can be seen as a controllable reactance inserted in the related transmission line. Series capacitive compensation works by reducing the effective series impedance of the transmission line by canceling part of the inductive reactance. Hence the power transferred is increased. The model of the network with TCSC is shown in Figure 1.

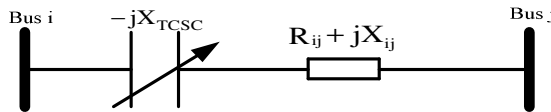


Fig. 1. Model of transmission line with TCSC

The maximum compensation by TCSC is limited to 70% of the reactance of the un-compensated line where TCSC is located. A new line reactance (X_{new}) is given as follows.

$$X_{\text{New}} = X_{ij} - X_{\text{TCSC}}$$

$$X_{\text{New}} = (1 - k)X_{ij}$$

Where $k = X_{\text{TCSC}}/X_{ij}$ is the degree of series compensation and X_{ij} is the line reactance between bus-i and bus-j.

The formulation of TTC using RPF with TCSC can be represented as follows:

Maximize λ

Subject to:

$$P_{Gi} - P_{Di} - \sum_{j=1}^n V_i V_j (G_{ij}^{\text{new}} \cos \delta_{ij} + B_{ij}^{\text{new}} \sin \delta_{ij}) = 0 \quad (9)$$

$$Q_{Gi} - Q_{Di} - \sum_{j=1}^n V_i V_j (G_{ij}^{\text{new}} \sin \delta_{ij} - B_{ij}^{\text{new}} \cos \delta_{ij}) = 0 \quad (10)$$

$$V_i^{\min} \leq V_i \leq V_i^{\max} \quad (11)$$

$$S_{ij} \leq S_{ij}^{\max} \quad (12)$$

Where

$$G_{ij}^{\text{new}} = \frac{R_{ij}}{R_{ij}^2 + X_{\text{New}}^2} \quad \text{and} \quad B_{ij}^{\text{new}} = \frac{X_{\text{New}}}{R_{ij}^2 + X_{\text{New}}^2}$$

3 Optimal Location of TCSC

Because of cost for these devices is high, the best location of TCSC is an important issue in the deregulated electricity markets. In order to reduce search space and improve transfer capability, TCSC need to be installed at the bottleneck location of power system. This is the location that demonstrates maximum possible power flow from source(s) to sink(s). When the system load is increased, the bottleneck is the first location where congestion occurs. Therefore, in order to eliminate/alleviate congestion, the transfer capability at the bottleneck should be examined.

3.1 Min Cut Algorithm

Using the Min-cut algorithm to find the minimum cut has been introduced in [14]. In this paper, the Min-cut algorithm will be used to determine the minimum cut of power system. The basic idea of the algorithm is to find the cut that has the minimum cut value over all possible cuts in the network. That is the cut which contains bottleneck branches with sum of capacity through its smallest. In other words, the power system can satisfy sufficient the power to the loads, but due to the limit of the minimum cut, so maximum possible power flow from source(s) to sink(s) equals the minimum cut value for all the cuts in the network. Therefore, if the minimum cut is identified, the branch that has the ability to install TCSC will be recognized.

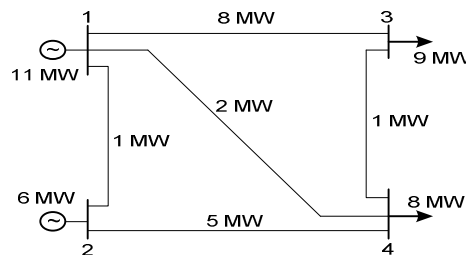


Fig. 2. Example power system with generators of 11 at 1 and 6 at 2 and loads of 9 and 8

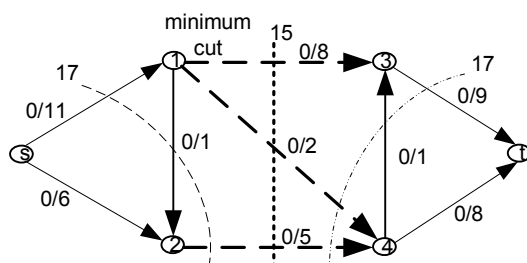


Fig. 3. The modeling of an example power system

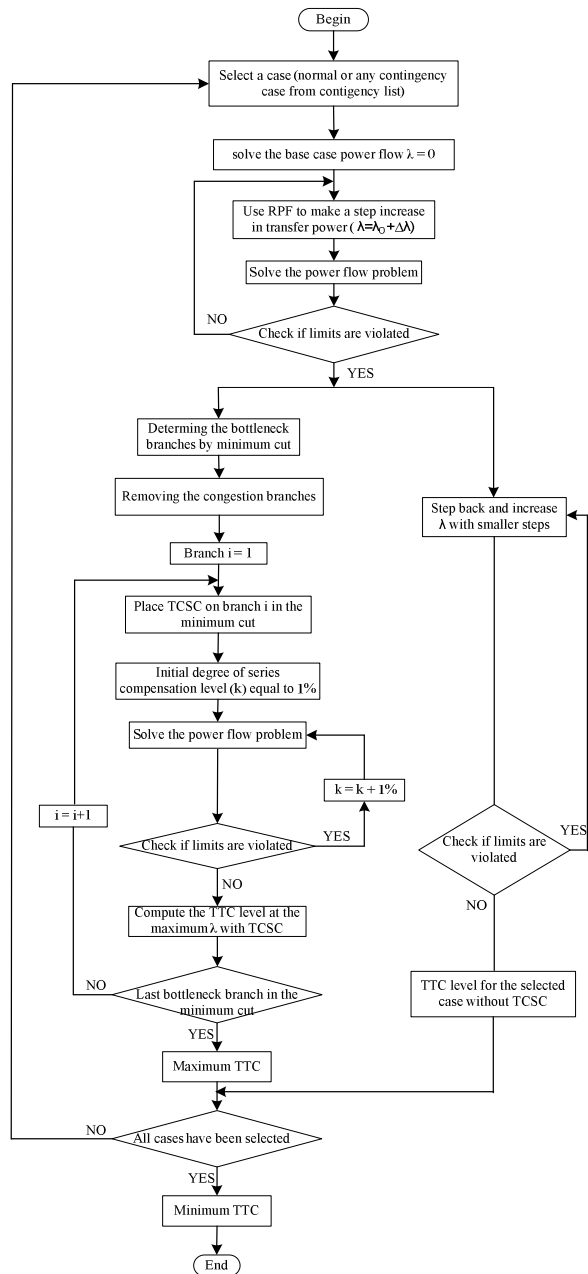


Fig. 4. Flow chart for power transfer capability with TCSC and without TCSC

3.2 Modeling Power Network Using Min Cut Algorithm

The power system is modeled as a directed network $G(N,A)$ where defined by a set N of n nodes and a set A of m directed arcs. Each arc $a_{ij} \in A$ has a capacity u_{ij} that shows the maximum amount that can flow between node i and j . The Min cut algorithm is added two nodes, the virtual source and the virtual sink, representing the combination of the generators and loads, respectively. Each line out of the virtual source has a maximum flow that matches the generation of the connected node, and each line into the virtual sink represents the load demanded by the connected node. The modeling of an example power system depicted in Figure 2 is shown in Figure 3. The details for determination the bottleneck of power system by Min cut algorithm can refer in [15]. The flow chart of the proposed method for the calculation of total transfer capability with and without TCSC is given in Figure 4.

4 Case Study and Discussions

The proposed method for the optimal location of the TCSC to evaluate TTC has been implemented on IEEE 14- and IEEE 30- bus test systems. The TTC is computed for a set of source/sink transfers (bus to bus, area to area, contingencies).

4.1 IEEE 14-Bus Test System

System data can be found in [8].

Table 1. TTC from bus to bus without and with TCSC placed in best location in the minimum cut

Source/Sink Bus No.	TTC (MW) without TCSC	Violated limits	TTC with TCSC	TCSC Location	Compens ation	Minimum cut
1/9	51.3	Line 8	69.98	Line 9	-0.086	Line 8, 9,11,12
1/10	45.9	Line 8	63.75	Line 12	-0.075	Line 8, 9,11,12
1/12	32.6	Line 8	48.13	Line 9	-0.122	Line 8, 9,11,12
1/13	32.8	Line 8	49.52	Line 9	-0.122	Line 8, 9,11,12
1/14	41.3	Line 8	58.36	Line 12	-0.115	Line 8, 9,11,12
1/4	239.7	Line 1	256.11	Line 3	-0.074	Line 1, 3,4,5
1/3	164.6	Line 2	216.84	Line 6	-0.083	Line 2, 3,5,6

According to Table 1, when TCSC is not placed, the TTC (from bus to bus) can only be achieved as shown in Table 1(Column 2). With this TTC level, it was found that the some lines in Table 1 (Column 3) are violated line thermal limit. This impeded transfer capability of power system. Therefore, by placing TCSC on proper location (the branch with great capacity in the minimum cut) to redirect the power flow through un-congested transmission line(s) is a method which rapidly rebalances the power and improve TTC.

When the minimum cut is not considered, there are 20 possible locations to place one unit of TCSC. However, the number of branches which need to be investigated to determine the location of TCSC has significantly been decreased after the minimum cut is considered. Observation of Table 1 shows that the location in Column 5 is the best location for placement TCSC since it giving maximum TTC. It can be observed from Table 1 (Column 4) that, after optimal placement of TCSC, the TTC has been improved which is more than as compared with the result in [8].

4.2 IEEE 30-Bus Test System

The network and load data for IEEE 30-bus are given in [16].

Table 2. Test results of bilateral transaction from bus 2(area 1) to bus 21(area 3) of the IEEE 30 bus test system

Objective function	Without TCSC	With TCSC	TCSC Location	TCSC setting (p.u.)	Minimum cut
Max. TTC	26.68	33.42	Line 28-27	-0.3369	Line 28-27, 10-9, 10-6

Table 2 shows the test results of bilateral transaction from bus 2 to bus 21. From this Table it can be observed that, TTC in the case without TCSC is obtained 26.68 MW. However, it is improved after installing TCSC at suitable location by using the minimum cut. As per the procedure mentioned in the previous sections, line 28-27 is one of the lines in the minimum cut which have a direct effect on TTC. Therefore this line is selected to install TCSC. The degree of series compensation for improving TTC was taken as -0.3369 pu. According to the Table 2 it can see that, the TTC in the case with TCSC is increased to 33.42MW without violating system constraints.

Table 3. Test results of multilateral transaction from area 3 to area 2 of the IEEE 30 bus test system

Case	TTC level without TCSC	TTC without TCSC	TCSC Location	TCSC setting (p.u.)	TTC level with TCSC	TTC with TCSC	Minimum cut
Normal	76.52		Line 23-24	-0.1143	85.6		
Largest generator G6 outage in area 2	56.23	56.23	Line 10-17	-0.2109	62.41	62.41	Line 10-17, 10-20, 23-24
Tie-line 23-24 outage	56.85		Line 10-20	-0.1148	65.25		

Furthermore, results of multilateral transaction from area 3 to area 2 are showed in Table 3. It was observed from this Table that, TTC value in the case without TCSC is obtained 56.23 MW. However, it is increased to 62.41 MW after placing TCSC on the line in the minimum cut. Optimal TCSC setting is -0.2109 p.u and location is line 10-17.

It can be observed from Table 3 (Column 3) and Table 3 (Column 7) that, the proposed method also captures the best location for the placement of TCSC as compared with the result in [16]. However, the number of branches which need to be investigated to determine the location of TCSC has reduced which is less than as compared with [16].

5 Conclusions

In deregulated power systems, System Operators face the challenge of finding effective ways of enhancing total transfer capability for congestion management. TCSC has been considered one of the effective methods to solve this issue. An efficient solution for the transfer capability enhancement in deregulated electricity market has been presented.

The study results on IEEE14- and IEEE 30-bus system have proved the effectiveness of the method. The proposed method is capable of finding the best location for TCSC installation to enhance the TTC. Only some lines in the minimum cut need to be examined in detail to assess the best location. Using this method, the search scope is limited hence the number of branches which need to be investigated to determine the location of TCSC has been significantly decreased.

References

1. Available transfer capability definitions and determination. NERC Report (June 1996)
2. Ejebe, G.C.: Available transfer capability calculations. IEEE Transactions on Power Systems 13(4) (November 1998)
3. Gravener, M.H., Nwankpa, C.: Available transfer capability and first order sensitivity. IEEE Transactions on Power Systems 14 (May 1999)
4. Ou, Y., Singh, C.: Assessment of available transfer capability and margins. IEEE Transactions on Power Systems 17 (May 2002)
5. Lee, K.Y., Mohamed, A.E.: Modern Heuristics Optimization Techniques. John Wiley & Sons, New York (2008)
6. Berizzi, A., Delfanti, M.: Enhanced security-constrained OPF with FACTS devices. IEEE Trans. Power Syst. 20(3), 1597–1605 (2005)
7. Okamoto, H., Kurita, A., Sekine, Y.: A method for identification of effective locations of variable impedance apparatus on enhancement of steady-state stability in large-scale power systems. IEEE Trans. Power Syst. 10(3), 1401–1407 (1995)
8. Feng, W., Shrestha, G.B.: Allocation of TCSC devices to optimize total transmission capacity in a competitive power market. In: Proceedings of IEEE Power Engineering Society Winter Meeting (January 28, 2001)

9. Ongsakul, W., Jirapong, P.: Optimal allocation of FACTS devices to enhance total transfer capability using evolutionary programming. In: IEEE International Symposium on Circuits and Systems, ISCAS, vol. 5, pp. 4175–4178 (May 2005)
10. Chansareewittaya, S., Jirapong, P.: Power transfer capability enhancement with multitype FACTS controllers using particle swarm optimization. Proceedings of IEEE (2010) 978-1-4244-6890-4
11. Verma, K.S., Singh, S.N., Gupta, H.O.: FACTS devices location for enhancement of total transfer capability. In: Proceedings of the IEEE Power Engineering Society Winter Meeting, Columbus, USA (January 28, 2001)
12. Leonidaki, E.A., Hatziargyriou, N.D., Manos, G.A., Papadias, B.C.: A systematic approach for effective location of series compensation to increase available transfer capability. In: Proceedings of the IEEE Porto Power Tech, Porto, Portugal, September 10-13
13. Chiang, H., Flueck, A.J., Shah, K.S., Balu, N.: CPFLOW: A practical tool for tracing power system steady-state stationary behavior due to load and generation variations. IEEE Trans. Power Syst. 10, 623–634 (1995)
14. John, W.: Chinneck.: Practical Optimization: a Gentle Introduction. In: Systems and Computer Engineering Carleton University Ottawa, Canada,
<http://www.sce.carleton.ca/faculty/chinneck/po.html>
15. Duong, T., JianGang, Y., Truong, V.: A new method for secured optimal power flow under normal and network contingencies via optimal location of TCSC. Electrical Power and Energy Systems 52, 68–80 (2013)
16. Joshi, S.K., Pandya, K.S.: Optimal placement of TCSC for Total Transfer Capability enhancement using particle swarm optimization. In: The 8th International Conference on Advances in Power System Control, APSCOM 2009, Hong Kong, China, November 8-11 (2009)

Augmented Lagrange Hopfield Network Based Method for Multi-objective Hydrothermal Scheduling

Nguyen Trung Thang¹ and Vo Ngoc Dieu²

¹ Faculty of Electrical and Electronics Engineering, Ton Duc Thang University, No. 19 Nguyen Huu Tho Street, Tan Phong Ward, District 7, Ho Chi Minh City, Vietnam
trungthangttt@tdt.edu.vn

² Department of Power Systems, Ho Chi Minh City University of Technology, Vietnam
vndieu@gmail.com

Abstract. The insufficient hydropower resources along with the environmental effects of thermal generations necessitate a proper scheduling scheme to comply with the growing power demand. In fact, the water resource at reservoirs has been affected by fluctuation of whether while exhausting fossil fuels and polluted emissions from thermal plants have become a serious problem. Therefore, the hydrothermal scheduling considering environment constraint becomes a very important problem. This paper proposes an augmented Lagrange Hopfield network (ALHN) for solving the multi-objective short-term hydrothermal scheduling (MOSTHS) problem. In the proposed method, ALHN is used to find a set of non-dominated solutions and the fuzzy decision-making methodology is then exploited to determine the best compromise solution among the obtained ones. The proposed method has been tested on different systems and the obtained results in terms of total fuel cost, emission, and computation time have been compared to those other methods in the literature. The result comparisons have indicated that the proposed method is effective for solving the MOSTHS problem.

Keywords: Augmented Lagrange Hopfield network, multi-objective, fixed head, hydrothermal scheduling.

1 Introduction

The short term hydro-thermal scheduling (HTS) problem is to determine the power generation among the available thermal and hydro power plants so that the total fuel cost of thermal units is minimized over a schedule time of a single day or a week while satisfying both equality and inequality constraints including power balance, available water, and generation limits of both thermal and hydro plants. In practical systems, thermal power generating stations are the sources of carbon dioxide (CO_2), sulfur dioxide (SO_2), and nitrogen oxides (NO_x) causing atmospheric pollution. Therefore, the optimal scheduling of generation in a hydrothermal system involves the allocation of generation among the hydro and thermal plants to simultaneously

minimize the fuel cost and emission level of thermal plants satisfying the various constraints on the hydraulic and system network becomes a practical requirement.

Several optimization techniques have been proposed to deal with the multiobjective programming problems. Improved quantum-behaved particle swarm optimization (IQPSO) [1] has been applied for short-term combined economic emission hydrothermal scheduling. In this paper, quantum-behaved particle swarm optimization is improved employing heuristic strategies in order to handle the equality constraints especially water dynamic balance constraints and active power balance constraints. As a result, the method has obtained quality solutions. A novel multi-objective optimization procedure based on probability security criteria for optimal generation dispatch has been proposed to obtain a set of non-inferior solutions [2]. Nondominated sorting genetic algorithm-II (NSGA-II) [3] has been used for solving dynamic economic emission dispatch problem. NSGA-II is proposed to handle dynamic economic emission dispatch problem as a true multi-objective optimization problem with competing and noncommensurable objectives. Two novel search methods have been presented in [4] for dealing the problem those are hybrid algorithm and heuristic searches with genetic algorithm (GA). Both techniques can obtain a low maximum generation. However, the computation time of the heuristic searches with GA is very long compared to the hybrid algorithm. An improved bacterial foraging algorithm (BFA) has been applied to solve the short-term HTS problem considering the environmental aspects given in [5]. The research has carried out optimization for each of the objectives individually and optimization of the four objectives. However, the best compromise solution for the combined four objectives is not provided in [5]. Another method, non-dominated sorting genetic algorithm-II (NSGA II) [6] has been applied to economic environmental dispatch of fixed head hydrothermal scheduling problem with both convex and non-convex fuel cost and emission functions. The effectiveness of NSGA-II has been verified on two systems and compared to other methods of real-coded genetic algorithm (RCGA), strength Pareto evolutionary algorithm 2 (SPEA2) and multi-objective differential evolution (MODE). NSGA-II seems to be a powerful method through the comparisons in terms of cost, emission and computation time. However, the computation time is still long and both cost and emission are still high.

In this paper, an augmented Lagrange Hopfield network (ALHN) has been proposed for solving multi-objective short term fixed head hydrothermal scheduling problem. ALHN is a combination of augmented Lagrange relaxation and continuous Hopfield neural network where the augmented Lagrange function is directly used as the energy function of the continuous Hopfield network. ALHN is tested on two systems and the results are compared to those from BFA [5], and NSGA-II, SPEA 2, RCGA, and MODE in [6].

2 Problem Formulation

Consider an electric power system network having N_1 thermal plants and N_2 hydro plants; N is the total number of plants. The basic problem is to find the active power

generation of each plant in the system as a function of time over a finite time period from 0 to M .

2.1 Thermal Model

The objective function to be minimized is the total system operating cost, represented by the fuel cost of thermal generation, over the optimization interval.

$$F_{1sk} = a_{1s} + b_{1s}P_{sk} + c_{1s}P_{sk}^2 \quad (\$/h) \quad (1)$$

where a_{1s} , b_{1s} , c_{1s} are cost coefficients for thermal unit s ,

2.2 Emission Model

The atmospheric pollutants such as nitrogen oxides (NOx), sulphur oxides (SO2) and carbon oxides (CO2) caused by fossil-fueled thermal generator can be modeled separately. The NOx, SO2, CO2 emission objective can be defined as:

$$F_{2sk} = \alpha_{1s} + \beta_{1s}P_{sk} + \gamma_{1s}P_{sk}^2 \quad (\text{Kg/h}) \quad (2)$$

$$F_{3sk} = \alpha_{2s} + \beta_{2s}P_{sk} + \gamma_{2s}P_{sk}^2 \quad (\text{Kg/h}) \quad (3)$$

$$F_{4sk} = \alpha_{3s} + \beta_{3s}P_{sk} + \gamma_{3s}P_{sk}^2 \quad (\text{Kg/h}) \quad (4)$$

where α_{1s} , β_{1s} , γ_{1s} are NOx emission coefficients; α_{2s} , β_{2s} , γ_{2s} are SO2 emission coefficients; α_{3s} , β_{3s} , γ_{3s} are CO2 emission coefficients.

2.3 Hydro Model

Relationship between water discharge and power generated was proposed by Glimm-Kirchmayer [7].

$$q_{hk} = a_h + b_h P_{hk} + c_h P_{hk}^2 \quad (5)$$

where q_{hk} is rate of water flow ; t_k is duration of subinterval k ; a_h , b_h , c_h are water discharge coefficients for hydro unit h .

2.4 Equality and Inequality Constraints

1. Load demand equality constraint:

$$\sum_{s=1}^{N_1} P_{sk} + \sum_{h=1}^{N_2} P_{hk} - P_{Lk} - P_{Dk} = 0 ; k = 1, \dots, M \quad (6)$$

$$P_{Lk} = \sum_{i=1}^{N_1+N_2} \sum_{j=1}^{N_1+N_2} P_{ik} B_{ij} P_{jk} + \sum_{i=1}^{N_1+N_2} B_{0i} P_{ik} + B_{00} \quad (7)$$

where P_{Dk} , P_{Lk} are load demand, transmission loss during subinterval k , in MW; P_{hk} , P_{sk} are generation output of hydro unit h , thermal unit s during subinterval k , in MW; B_{ij} , B_{0i} , and B_{00} are loss formula coefficients of transmission system.

2. Water availability constraints:

$$\sum_{k=1}^M t_k q_{hk} = W_h \quad (8)$$

where W_h is volume of water available for generation by hydro unit h during the scheduling period.

3. Generator operating limits:

$$P_s^{\min} \leq P_{sk} \leq P_s^{\max}; s = 1, \dots, N_1; k = 1, \dots, M \quad (9)$$

$$P_h^{\min} \leq P_{hk} \leq P_h^{\max}; h = 1, \dots, N_2; k = 1, \dots, M \quad (10)$$

where P_h^{\min} , P_h^{\max} and P_s^{\min} , P_s^{\max} are lower and upper generation limits of hydro unit h and thermal unit s respectively.

3 ALHN for the Problem

To generate the non-inferior solution to the multi-objective problem, the weighting method is applied. In this method the problem is converted into a scalar optimization as given below [8]:

$$\text{Minimize } \sum_{j=1}^4 w_j F_j \quad (11)$$

subject to (4)-(7) and satisfying

$$\sum_{j=1}^4 w_j = 1; \quad w_j \geq 0 \quad (12)$$

where weighting factors, w_j is determined based on the relative importance of objective j , which may vary from place to place and utility to utility.

The augmented Lagrange function L of the problem is formulated as follows:

$$\begin{aligned} L = & \sum_{k=1}^M \sum_{s=1}^{N_1} t_k (a_s + b_s P_{sk} + c_s P_{sk}^2) + \sum_{k=1}^M \lambda_k \left(P_{Lk} + P_{Dk} - \sum_{s=1}^{N_1} P_{sk} - \sum_{h=1}^{N_2} P_{hk} \right) \\ & + \sum_{h=1}^{N_2} \gamma_h \left[\sum_{k=1}^M t_k (q_{hk} - r_{hk}) - W_h \right] + \frac{1}{2} \sum_{k=1}^M \beta_k \left(P_{Lk} + P_{Dk} - \sum_{s=1}^{N_1} P_{sk} - \sum_{h=1}^{N_2} P_{hk} \right)^2 \\ & + \frac{1}{2} \sum_{h=1}^{N_2} \beta_h \left[\sum_{k=1}^M t_k (q_{hk} - r_{hk}) - W_h \right]^2 \end{aligned} \quad (13)$$

where: λ_k , γ_h are Lagrangian multipliers associated with power balance and water constraint, respectively. β_k , β_h are penalty factors associated with power balance and water constraint, respectively, and

$$a_s = w_1 a_{1s} + w_2 \alpha_{1s} + w_3 \alpha_{2s} + w_4 \alpha_{3s} \quad (14)$$

$$b_s = w_1 b_{1s} + w_2 \beta_{1s} + w_3 \beta_{2s} + w_4 \beta_{3s} \quad (15)$$

$$c_s = w_1 c_{1s} + w_2 \gamma_{1s} + w_3 \gamma_{2s} + w_4 \gamma_{3s} \quad (16)$$

The energy function E of the problem is described in terms of neurons is determined as:

$$\begin{aligned} E = & \sum_{k=1}^M \sum_{s=1}^{N_1} t_k \left(a_s + b_s V_{sk} + c_s V_{sk}^2 \right) + \sum_{k=1}^M V_{\lambda k} \left(P_{Lk} + P_{Dk} - \sum_{s=1}^{N_1} V_{sk} - \sum_{h=1}^{N_2} V_{hk} \right) \\ & + \sum_{h=1}^{N_2} V_{\gamma h} \left[\sum_{k=1}^M t_k (q_{hk} - r_{hk}) - W_h \right] + \frac{1}{2} \sum_{k=1}^M \beta_k \left(P_{Lk} + P_{Dk} - \sum_{s=1}^{N_1} V_{sk} - \sum_{h=1}^{N_2} V_{hk} \right)^2 \\ & + \frac{1}{2} \sum_{h=1}^{N_2} \beta_h \left[\sum_{k=1}^M t_k (q_{hk} - r_{hk}) - W_h \right]^2 + \sum_{k=1}^M \left(\sum_{s=1}^{N_1} \int_0^{V_{sk}} g^{-1}(V) dV + \sum_{h=1}^{N_2} \int_0^{V_{hk}} g^{-1}(V) dV \right) \end{aligned} \quad (17)$$

where: $V_{\lambda k}$, $V_{\gamma h}$ are outputs of the multiplier neurons associated with power balance and water constraint, respectively; V_{hk} , V_{sk} are output of continuous neuron hk , sk representing P_{hk} , P_{sk} , respectively.

The dynamics of the model for updating neuron inputs are defined as follows:

$$\frac{dU_{sk}}{dt} = -\frac{\partial E}{\partial V_{sk}} \quad (18)$$

$$\frac{dU_{hk}}{dt} = -\frac{\partial E}{\partial V_{hk}} \quad (19)$$

$$\frac{dU_{\lambda k}}{dt} = \frac{\partial E}{\partial V_{\lambda k}} \quad (20)$$

$$\frac{dU_{\gamma h}}{dt} = \frac{\partial E}{\partial V_{\gamma h}} \quad (21)$$

The inputs of neurons at step n are updated:

$$U_{sk}^{(n)} = U_{sk}^{(n-1)} - \alpha_{sk} \frac{\partial E}{\partial V_{sk}} \quad (22)$$

$$U_{hk}^{(n)} = U_{hk}^{(n-1)} - \alpha_{hk} \frac{\partial E}{\partial V_{hk}} \quad (23)$$

$$U_{\lambda k}^{(n)} = U_{\lambda k}^{(n-1)} + \alpha_{\lambda k} \frac{\partial E}{\partial V_{\lambda k}} \quad (24)$$

$$U_{\gamma h}^{(n)} = U_{\gamma h}^{(n-1)} + \alpha_{\gamma h} \frac{\partial E}{\partial V_{\gamma h}} \quad (25)$$

where $U_{\lambda k}$, $U_{\gamma h}$ are inputs of the multiplier neurons; U_{sk} , U_{hk} are inputs of the neurons sk and hk respectively; $\alpha_{\lambda k}$, $\alpha_{\gamma h}$ are step sizes for updating of multiplier neurons; α_{sk} , α_{hk} are step sizes for updating of continuous neurons.

The outputs of continuous neurons and multiplier neurons:

$$V_{sk} = g(U_{sk}) = \left(P_s^{\max} - P_s^{\min} \right) \left(\frac{1 + \tanh(\sigma U_{sk})}{2} \right) + P_s^{\min} \quad (26)$$

$$V_{hk} = g(U_{hk}) = \left(P_h^{\max} - P_h^{\min} \right) \left(\frac{1 + \tanh(\sigma U_{hk})}{2} \right) + P_h^{\min} \quad (27)$$

$$V_{\lambda k} = U_{\lambda k} \quad (28)$$

$$V_{\gamma h} = U_{\gamma h} \quad (29)$$

where σ is slope of the sigmoid function.

3.1 Initialization

The initial outputs of continuous neurons are set at their middle limits and the multiplier neurons are set as follows:

$$V_{\lambda k}^{(0)} = \frac{1}{N_1} \sum_{s=1}^{N_1} t_k \left(b_s + 2c_s V_{sk}^{(0)} \right) \left/ \left(1 - \frac{\partial P_{Lk}}{\partial V_{sk}} \right) \right. \quad (30)$$

$$V_{\gamma h}^{(0)} = \frac{1}{M} \sum_{k=1}^M V_{\lambda k}^{(0)} \left(1 - \frac{\partial P_{Lk}}{\partial V_{hk}} \right) \left/ \left(t_k \frac{\partial q_{hk}}{\partial V_{hk}} \right) \right. \quad (31)$$

3.2 Stopping Criteria

The algorithm will be terminated when either the maximum error Err_{max} is lower than a predefined threshold ϵ or maximum number of iterations N_{max} is reached.

4 Best Compromise Solution by Fuzzy-Based Mechanism

In this paper, the best compromise solution for the problem is determined using fuzzy satisfying method [9]. The fuzzy goal is represented in linear membership function as follows [9]:

$$\mu(F_j) = \begin{cases} 1 & \text{if } F_j \leq F_j^{\min} \\ \frac{F_j^{\max} - F_j}{F_j^{\max} - F_j^{\min}} & \text{if } F_j^{\min} \leq F_j \leq F_j^{\max} \\ 0 & \text{if } F_j \geq F_j^{\max} \end{cases} \quad (32)$$

where F_j is the value of objective j ; $F_{j\max}$ and $F_{j\min}$ are maximum and minimum values of objective j , respectively. For each k non-dominated solution, the membership function is normalized as follows [9]:

$$\mu_D^k = \sum_{i=1}^{N_{obj}} \mu(F_i^k) / \sum_{k=1}^{N_p} \sum_{i=1}^{N_{obj}} \mu(F_i^k) \quad (33)$$

where μ_D^k is the cardinal priority of k th non-dominated solution, $\mu(F_j)$ is membership function of objective j , N_{obj} is number of objective functions, and N_p is number of Pareto-optimal solutions. The solution that attains the maximum membership μ_D^k in the fuzzy set is chosen as the ‘best’ solution based on cardinal priority ranking [8]:

$$\text{Max } \{\mu_D^k: k = 1, 2, \dots, N_p\} \quad (34)$$

5 Numerical Results

The proposed method has been tested on two test systems. The first test system consists of two thermal and two hydropower plants from [5]. The second system comprises of two hydro plants and two thermal plants in [6]. The proposed algorithm has been coded in Matlab 7.2 programming language and executed on an Intel 2.0 GHz PC. For termination criteria, the maximum tolerance Err_{max} is set to 10^{-4} and 10^{-3} for the first and second system respectively.

5.1 The First System

For this system, the emissions consist of NO_x , SO_2 and CO_2 . The optimization for each of the objectives is individually carried out. The results of the fuel cost and each emission with computation time are given in Table 1. The result comparison between ALHN and BFA is given in Table 2. For all cases, the proposed ALHN method can obtain better solution than BFA except for the case of CO_2 emission individual optimization.

5.2 The Second System

In this system, the objective includes one total cost and one emission. The obtained economic distich and emission dispatch from the proposed method are compared to those from RCGA [6] as in Table 3. From the table, the proposed method obtains better results than RCGA method in all cases. Moreover, the proposed method is also much faster than RCGA method for both cases.

Table 1. Total cost and emission minimization of individual objective for the first system

	Min F_1 (\$)	Min F_2 (kg)	Min F_3 (kg)	Min F_4 (kg)
F_1 (\$)	51891.4144	54294.5255	53,104.1251	54,221.8203
F_2 (kg)	27443.0377	18,958.608	20,822.2018	18,963.2433
F_3 (kg)	73381.1457	72,416.895	71,641.9112	72,358.5684
F_4 (kg)	442113.2112	335,810.13	357,415.3897	335,764.1868
CPU time (s)	1.29	1.53	1.79	1.11

Table 2. Comparison of the individual minimization of each objective for the first system

	BFA [5]	ALHN
Min F_1 (\$)	52,753.291	51,891.414
Min F_2 (Kg)	19,932.248	18,958.608
Min F_3 (Kg)	71,988.754	71,641.911
Min F_4 (Kg)	334,231.219	335,764.187

Table 3. Result comparison for economic and emission dispatch of the second system

Method	Economic dispatch			Emission dispatch		
	Cost (10^4 \$)	Emis. (lb)	CPU (s)	Method	Cost (10^4 \$)	Emis. (lb)
RCGA [6]	6.6031	681.1655	21.64	RCGA [6]	6.6892	586.1481
ALHN	6.4576	668.9824	2.84	ALHN	6.5797	585.6592

Table 4. Comparison of economic emission dispatch for the second system

Method	Cost (10^4 \$)	Emission (lb)	CPU (s)
MODE [6]	6.6354	619.4280	30.72
SPEA2 [6]	6.6332	618.4580	34.88
NSGA-II [6]	6.6331	618.0660	27.86
ALHN	6.4778	615.1773	2.01

For the case of economic emission dispatch, we have determined 11 non-dominated solutions to form Pareto optimal front with the change of weights associated with objectives from 0 to 1 satisfying (12). The best compromise solution from the obtained 11 non-dominated solution is determined by fuzzy based mechanism in Section 4. The obtained the best compromise solution from the proposed method is compared to that from MODE, SPEA2, and NSGA II in [6]. Obviously, the proposed method can obtain better solution than the other methods for both total cost and emission. Moreover, the proposed method is also much faster than the others. Note the computational time in the table is for obtaining one solution and the CPU times of the methods in [6] were from a Pentium-IV, 80 GB, 3.0 GHz. Therefore, the proposed method is very effective and efficient for obtaining the best compromise solution for the problem.

6 Conclusion

The paper has been implemented an augmented Lagrange neural network based method for solving the multi-objective short-term hydrothermal scheduling problem. In the proposed method, the ALHN method is implemented for obtaining non-dominated solution and a fuzzy based mechanism is applied for determining the best compromise solution. The ALHN method is an improvement of continuous Hopfield neural network with its energy function based on augmented Lagrange function. Moreover, the ALHN method is recurrent network so it can obtain an optimal solution for an optimization problem in a very fast manner. The proposed method has been tested on two systems with different number of objectives and the obtained results have been compared to those from other methods in the literature. The result comparison has indicated that the proposed method can obtain better solution than other methods with faster computational time. Therefore, the proposed method can be very favorable for solving the multi-objective short-term hydrothermal scheduling problems.

References

- [1] Sun, C., Lu, S.: Short-term combined economic emission hydrothermal scheduling using improved quantum-behaved particle swarm optimization. *Expert Systems with Applications* 37, 4232–4241 (2010)
- [2] Yokoyama, R., Bae, S.H., Morita, T., Sasaki, H.: Multi-objective optimal generation dispatch based on probability security criteria. *IEEE Trans. PWRS-3*, 317–324 (1988)
- [3] Basu, M.: Dynamic economic emission dispatch using nondominated sorting genetic algorithm-II. *Electrical Power and Energy Systems* 30, 140–149 (2008)
- [4] George, A., Channa Reddy, M., Sivaramakrishnan, A.Y.: Multi-objective, short-term hydro thermal scheduling based on two novel search techniques. *International Journal of Engineering Science and Technology* 2(11), 7021–7034 (2010)
- [5] Farhat, I.A., El-Hawary, M.E.: Multi-objective short-term hydro-thermal scheduling using bacterial foraging algorithm. In: 2011 IEEE Electrical Power and Energy Conference, pp. 176–181 (2011)
- [6] Basu, M.: Economic environmental dispatch of fixed head hydrothermal power systems using nondominated sorting genetic algorithm-II. *Applied Soft Computing* 11, 3046–3055 (2011)
- [7] Sasikala, J., Ramaswamy, M.: PSO based economic emission dispatch for fixed head hydrothermal systems. *Electr. Eng.* 94, 233–239 (2012)
- [8] Dhillon, J.S., Parti, S.C., Kothari, D.P.: Fuzzy decision-making in stochastic multiobjective short-term hydrothermal scheduling. In: IEE Proc. Gener. Transm. and Distrib., vol. 149, pp. 191–200 (2002)
- [9] Dhillon, J.S., Parti, S.C., Kothari, D.P.: Fuzzy decision making in multiobjective long-term scheduling of hydrothermal system. *Electrical Power and Energy Systems* 24, 19–29 (2001)

Technical Efficiency for Selection and Estimation Quality of Distance Relay Protection Setting

Tran Hoang Quang Minh

Faculty of Electrical and Electronics Engineering,
Ton Duc Thang University, No. 19 Nguyen Huu Tho Street, Tan Phong Ward, District 7,
Ho Chi Minh City, Vietnam
thqminhtk@tdt.edu.vn

Abstract. Among the relay protections, line distance relay protections have a large proportion. Distance relay protections have some special features compared with the current relay protections. To study and develop technical effect criterion for selection of distance relay protection settings (high-voltage lines) and technical efficiency criterion for estimating this setting is main purpose of this paper. The probability statistical algorithms are used to calculate the above criteria. Finally base on these criteria, search and estimate effective ways to set lines distance relay protection.

Keywords: technical effect, technical efficiency, distance relay protection, setting, criterion, criteria.

1 Introduction

In the modern world of relay protection (RP), due to electrical networks found metrological advances (inhibition of the currents, the configuration of the characteristics of operating in the complex plane of the resistance, the drop voltage negative and zero sequence on the lines), and circuit solutions almost entirely (differential relay protection) or partially (distance relay protection). These eliminated the refusals of work, false and excessive actions. For relay protection with the exchange information on operation between these ends of lines, the operation principles are spread on the principle of differential relay protection, and achieved similar performance. However there is not small quantity class steps current and distance relay protection (first line), in which the property is a failure for external faults is achieved by temporary blocking system levels. These actions take place unrecoverable loss of functioning relay protection like: refusals of work, false and excessive actions. These actions are depending on the classification regime -switching states of the network, the types of faults, interference, generally expressed as a function of the selected setting [1,3,4].

The technical efficiency estimation of functioning relay protection (RP), as differences potentially possible effect in the form of an index of faults on protected object and losses (refusals of work, false and excessive actions) are carried to

potential effect, is an actual problem for designing and operation relay protection of an electric equipment and electric networks. Therefore to this question the attention was always paid at the statistical analysis of features of relay protection work, for example [1]. However there are problems of imposing appearance different components of statistical data. Some data, for example, faults are mass enough, but such events as refusals of operation relay protection, false actions at asynchronous modes, etc. are very rare. In this connection it is wrongful to use statistical characteristics with different reliability in interesting criteria functional. Therefore there is an actual problem of support statistical adequacy of all components in considered functional. This problem was solved in [2]. To present in [2] solutions of this problem and in this article this problem is analyzed, used and developed.

2 Main Part

In this paper, the definition and the analysis criterion of technical efficiency, and also numerator of this criterion (a difference of potential effect and losses) which is called as technical effect for distance relay protection lines is considered. Losses can be subdivided into three components, which are caused by refusals of equipment, mistake servicing personnel and by functioning relay protection. In the given work last component (functioning relay protection) is considered, which is defined by different topology of a network, modes of sources, switching conditions, types faults, abnormal modes, etc., i.e. Such choice is made because a number of operational conditions can be changed the operational personnel at use of the same equipment. Hardware refusals depend on element base of manufacturers and devices and mistake servicing personnel depends on the qualification and psychological factors of people [5.6.7].

Parameter resistance from a relay protection installation place on the ends of a line to place fault is distributed on the most simple and with final concrete borders uniform probability distribution law (PDL) on space of each line and other components of the network. In connection with this algorithm of technical efficiency is constructed with obligatory preservation use of the uniform probability distribution law. This recommendation concerns all steps of distance relay protection, however most simply and unequivocally it is realized at measurements of resistance to places faults on a protected line. At measurement in the fault conditions on previous lines (opposite substations departing from buses) in a direction of distance relay protection action of network elements, it is necessary to consider feeds of place fault from the additional sources connected to opposite substation. And at measurement fault on previous line to the previous components, which are fixed by reserving step distance relay protection, the account of feeds from the sources connected to opposite substations of the previous elements is necessary considered. Under uniform law PDL on all element of the network appears the natural requirement to convert the borders of the stages distance protection lines in coordinate's external (previous and adjacent) elements. Since infeeds continuously change, borders also change continuously. For accounting these changes in the calculation of technical efficiency, need to know the

range of these boundaries, especially maximum and minimum values. These boundaries can be determined by converting the captured spaces (resistance) of the external elements through the current distribution coefficients between the protected line and the previous lines. Expressions of criteria technical effect and its components are given below:

1. For first zone (stage) of distance relay protection:

$$E_{N\acute{e}1}^I = p(A_{N\acute{e}}^I) - p(O_{N\acute{e}1}^I) - \sum_{1pi=1}^{n_p} p(I_{N\acute{e}1-1pi}^I) \quad (1)$$

2. For second zone (stage) of distance relay protection:

$$E_{N\acute{e}1}^{II} = p(A_{N\acute{e}}^{II}) - p(O_{N\acute{e}1}^{II}) - \sum_{1pi=1}^{n_p} p(I_{N\acute{e}1-1pi}^{II}) \quad (2)$$

3. For back-up zone (stage) of distance relay protection:

$$\begin{aligned} E_{N\acute{e}1}^{III} = & p(A_{N\acute{e}}^{III}) + \sum_{1pi=1}^{n_{1pi}} p(A_{1pk}^{III}) - p(O_{N\acute{e}1}^{III}) - \sum_{1pk=1}^{n_{1pk}} p(O_{1pk}^{III}) \\ & - \sum_{jpi=1}^{n_{jpi}} \sum_{jpi=1}^{n_{jpi}} \sum_{jpi=1}^{n_{jpi}} p(I_{N\acute{e}1-jpi}^{III}) \end{aligned} \quad (3)$$

Where the lower indexes: $N\acute{e}$ - protected line, p – previous lines (elements), pp – previous (elements) of previous lines (elements) (Figure 1). The letter p designates probabilities of events: A – faults on a protected line, O – operation refusals, I – excessive actions;

4. Probabilities faults $p(A)$: for the first stage $p(A_{N\acute{e}}^I) = \omega_{N\acute{e}} m(T_{N\acute{e}}^I)$, for the second stage $p(A_{N\acute{e}}^{II}) = \omega_{N\acute{e}} m(T_{N\acute{e}}^{II})$, Where $\omega_{N\acute{e}}$ – the flow parameter of interest fault types on the protected lines, $m(T_{N\acute{e}}^I)$ и $m(T_{N\acute{e}}^{II})$ – average duration of detection (lock) fault channels of the first and second stages (substantially the setting time of the first and second stages). And for third stage $p(A_{N\acute{e}}^{III}) + \sum_{1pi=1}^{n_{1pi}} p(A_{1pk}^{III}) = \omega_{N\acute{e}} m(T_{N\acute{e}}^{III}) + \sum_{1pi=1}^{n_{1pi}} \omega_{1pk} m(T_{1pk}^{III})$,

where ω_{1pk} – the flow parameter of fault types on $1pk$ -th line, and $m(T_{N\acute{e}}^{III})$, $m(T_{1pk}^{III})$ – average duration of detection (lock) fault channels of the third stages (third stage time setting).

5. Excessive actions of the first stage take place in the external fault 1) as a joint action with isochronous speed protections (the first stage, the protection on the differential principle) for faults on previous lines, 2) as refusals of the first stages on the previous lines. Proceeding from the above, to the probability of excessive action of the first stage of the protected line should be show below:

$$\sum_{1pi=1}^{n_p} p(I_{N\acute{e}1-1pi}^I) = \sum_{1pi=1}^{n_p} \left[\frac{1}{2} p(\Delta_{N\acute{e}1pi} / BK_{1pi}) p(BK_{1pi}) + p(O_{N\acute{e}1pi} / BK_{1pi}) p(BK_{1pi}) \right] \quad (4)$$

Where Δ , O - joint action, refusals of protection for the 1pi-th elements, BK - faults on the 1pi-th elements.

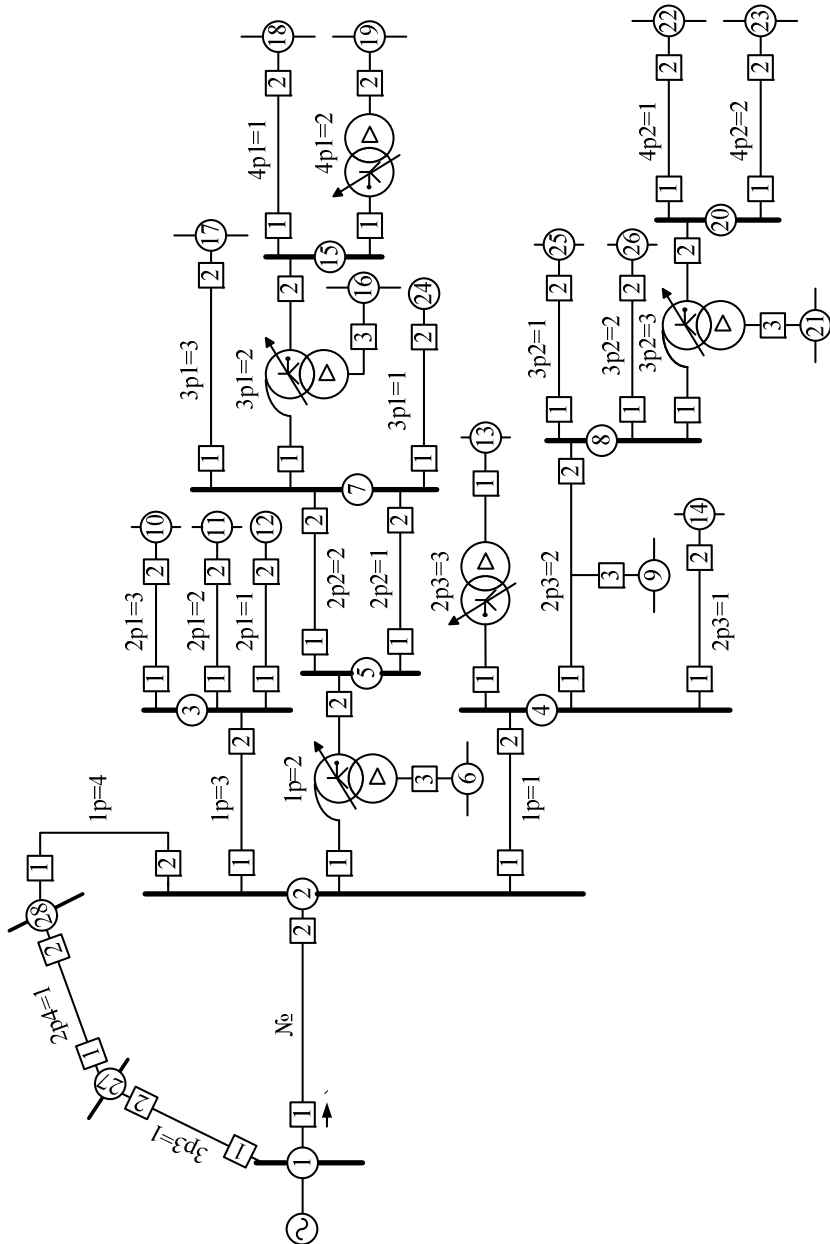


Fig. 1. Scheme of a predetermined network

The definition of conditional probabilities of the joint action, refusals of the previous elements protections (first stage) are show in (5).

$$\begin{aligned} p(\Delta_{N \in 1pi}^I / BK_p) &= [p_{\max}(\Delta_{N \in 1pi}^I / BK_p) + p_{\min}(\Delta_{N \in 1pi}^I / BK_p)] / 2, \\ p(O_{N \in 1pi}^I / BK_p) &= [p_{\max}(O_{N \in 1pi}^I / BK_p) + p_{\min}(O_{N \in 1pi}^I / BK_p)] / 2 \end{aligned} \quad (5)$$

Where maximum (max) and minimum (min) are the maximum and minimum boundaries of the first stage (protection of the protected line) in the space of each the previous elements. Conditional probabilities are the formulas on the basis of uniform PDL resistance from the start of the previous element to the fault.

The unconditional probability of the external faults at 1pi-th previous elements $p(BK_{1pi}) = \omega_{1pi} m(T_{1pi}^I)$ determined by the product of the flow parameter fault on the previous line ω_{1pi} and the average average duration of detection (lock) fault channels of the first stage (protection) of the previous line $m(T_{1pi}^I)$.

Excessive actions of the second stage take place if the setting is selected on the basis of sensitivity. These losses are due to the action of the second stages isochronous protected and previous appearance of lines and areas of action the second stage of the protected line faults in the space of the previous short lines above the parameter response (measured resistance) range of the first stages of the lines and within their space (the action of the second stages preceding lines), and if the second coverage level line protected by short circuiting the space is more than the previous line coverage will be the second stage of the lines within their area (second speed earlier failures lines). Calculations done similar calculations for the first stage:

$$\sum_{1pi=1}^{n_p} p(I_{N \in 1-1pi}^II) = \sum_{1pi=1}^{n_p} [\frac{1}{2} p(\Delta_{N \in 1pi}^I / BK_{1pi}) p(BK_{1pi}) + p(O_{N \in 1pi}^I / BK_{1pi}) p(BK_{1pi})] \quad (6)$$

The definition of conditional probabilities of the joint action, refusals of the previous elements protections (second stage) are show in (7).

$$\begin{aligned} p(\Delta_{N \in 1pi}^II / BK_p) &= [p_{\max}(\Delta_{N \in 1pi}^II / BK_p) + p_{\min}(\Delta_{N \in 1pi}^II / BK_p)] / 2, \\ p(O_{N \in 1pi}^II / BK_p) &= [p_{\max}(O_{N \in 1pi}^II / BK_p) + p_{\min}(O_{N \in 1pi}^II / BK_p)] / 2 \end{aligned} \quad (7)$$

Where maximum (max) and minimum (min) are the maximum and minimum boundaries of the second stage (protection of the protected line) in the space of each the previous elements. Conditional probabilities are the formulas on the basis of uniform PDL resistance from the start of the previous element to the fault.

The unconditional probability of the external faults at 1pi-th previous elements $p(BK_{1pi}) = \omega_{1pi} m(T_{1pi}^II)$ determined by the product of the flow parameter fault on the previous line ω_{1pi} and the average average duration of detection (lock) fault channels of the second stage (protection) of the previous line $m(T_{1pi}^II)$.

Mechanism of excessive actions of the third stages is similar formation of excessive action of the second stage. However, unlike the main stages in which the same names delay stages are almost identical, in meshed networks setting time of the back-up stages may be different: setting time of the back-up stage of considered protected line and back-up stages of the peripheral elements may be equal or greater than the considered back-up stage of the protected line stage. Therefore it is necessary to consider separately these cases mentioned by the time the interaction with all elements of the network:

$$\sum_{jn=1}^{n_{jn}} \sum_{jni=1}^{n_{jni}} \sum_{jnik=1}^{n_{jnik}} p(I_{Nel1-jnik1}^{\text{III}}) = \sum_{jn=1}^{n_{jn}} \sum_{jni=1}^{n_{jni}} \sum_{jnik=1}^{n_{jnik}} [\frac{1}{2} p(\Delta_{Nel1jnik1}^{\text{III}} / BK_{jnik}) p(BK_{jnik}) + p(O_{Nel1jnik1}^{\text{III}} / BK_{jnik}) p(BK_{jnik})] \quad (6)$$

Algorithm and methods of calculating technical effect for setting and technical efficiency for estimating quality setting of distance relay protection allowed recommending: 1) setting options of second and third stages based on the sensitivity and starting from the minimum of excessive actions; 2) setting the first stage by optimizing the technical efficiency, taking into account all the components of losses, setting of the first stage with an enhanced high-speed operation area. This reduces the complexity of choosing settings, and technical efficiency of the tool allows to choose the desired quality of the distance relay protection functioning.

A numerical results with using the developed algorithms are shown below on the example of the calculation and analysis of distance relay protection line 220 kV Substation Surgust – Substation Contur (Distance relay protection on side of the substation Surgust) on one of the Russian power system. The topology of the analyzed area is shown in Figure 2. Line p1, p2 and p3 are previous lines (the first periphery); pp1 and pp2 lines are lines of second peripheral.

The settings of the first and second stages of the distance relay protection on the lines p1, p2, p3 are chosen by the guidelines [1,3]. For the considered № 1 distance relay protection №,1, setting the first and second stages are based on the high technical efficiency at the opposite end of the line №. The results of calculation technical efficiency by varying the settings are presented in the tables 1 and 2.

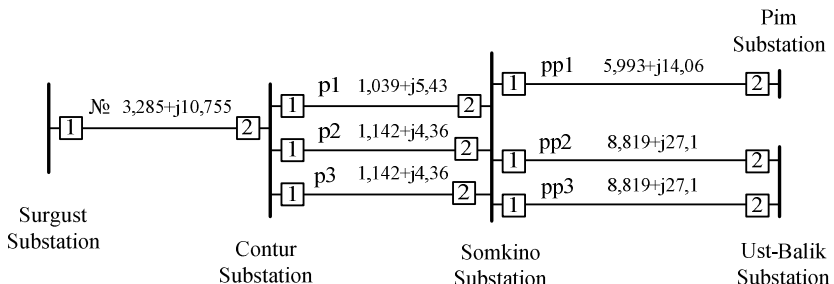


Fig. 2. The topology of the analyzed area

Table 1. The numerical results of technical efficiency by varying the setting of the first stage distance relay protection №,1

Setting of the first stage (Ohm)	Probability of refusals	Probability of excessive actions	Technical effect	Technical efficiency (%)
9,5	$0,932 \cdot 10^{-11}$	0	$5,093 \cdot 10^{-11}$	84,53
10	$0,664 \cdot 10^{-11}$	0	$5,361 \cdot 10^{-11}$	88,98
10,5	$0,396 \cdot 10^{-11}$	0	$5,629 \cdot 10^{-11}$	93,43
11	$0,128 \cdot 10^{-11}$	0	$5,897 \cdot 10^{-11}$	97,88
11,238	0	0	$6,025 \cdot 10^{-11}$	99,5
11,5	0	$0,217 \cdot 10^{-11}$	$5,808 \cdot 10^{-11}$	96,39
12	0	$0,632 \cdot 10^{-11}$	$5,393 \cdot 10^{-11}$	89,5
12,5	0	$1,047 \cdot 10^{-11}$	$4,978 \cdot 10^{-11}$	82,62
13	0	$1,462 \cdot 10^{-11}$	$4,563 \cdot 10^{-11}$	75,74

Table 2. The numerical results of technical efficiency by varying the setting of the second stage distance relay protection №,1

Setting of the second stage (Ohm)	Probability of refusals	Probability of excessive actions	Technical efficiency (%)
14,048	0	0	99,6
14,5	0	0	99,44
15	0	0	99,16
15,5	0	$0,25 \cdot 10^{-10}$	96,22
16	0	$0,559 \cdot 10^{-10}$	91,55
16,5	0	$1 \cdot 10^{-10}$	84,9
17	0	$1,44 \cdot 10^{-10}$	78,26

The numerical results under specific restrictions confirm derived from the phenomenological analysis of the findings of the maximum technical efficiency and its changes. It is evident that excessive actions in the second stage there are no set-point until it reaches the end of the first stages of previous lines and will not begin the second stage of action isochronous protect the protected line № 1 with the second stage of the protection p11, p21, p31 previous lines p1, p2 and p3. With these results, may be recommending: 1) increase setting of the first stage to the resistance equal to resistance of all line or to near this value; 2) setting of the second and third stages with the minimum of excessive actions, proceeding from their sensitivity. Positive values of technical efficiency, which are near to the one unit, are the highest technical quality of distance relay protection.

3 Conclusion

The presented technical effect and efficiency criteria analysis of line distance protection stages allows:

1) recommending: 1) setting options of second and third stages based on the sensitivity and starting from the minimum of excessive actions; 2) setting the first stage by optimizing the technical efficiency, taking into account all the components of losses, setting of the first stage with an enhanced high-speed operation area. This reduces the complexity of choosing settings, and technical efficiency of the tool allows you to choose the desired quality of the distance relay protection functioning.

2) Positive values of technical efficiency near to the one unit are the highest technical quality of distance relay protection.

3) The development of the full program, which is realizing offered probabilistic algorithm of the setting of relay protection, will allow shortening or completely excluding the stale labor of the calculation setting value relay protection. Such program can serve the instrument for designing, usages and adjustments of relay protection and automatics.

References

- [1] Fedoseev, A.M.: Relay protections power system, p. 520. M. Energoatomizdat (1984)
- [2] Minh, T.H.Q., Shmoilov, A.V.: Technical efficiency of line distance relay protection. In: The Fifth International Forum on Strategic Technology (IFOST 2010), pp. 335–340. Ulsan University of Technology, Ulsan Korea (2010)
- [3] Prutik, A.F., Minh, T., Shmoilov, A.V.: The selectivity and the technical efficiency of relay protection and automatics. Journal “Energy Problems”, 154–163 (2010)
- [4] Schneerson, E.M.: Digital relay protection, p. 549. M. Energoatomizdat (2007)
- [5] Nudelman, G.S., Shalin, A.I.: Microprocessor-based relay protection. News of Electrical Engineering, 74–79 (2008)
- [6] Shmoilov, A.V.: Probability technologies in electric power industry. In: Proc. 6th Russian-Korean Intern. Symp.on Science and Technology, KORUS 2002, Novosibirsk, vol. 2, pp. 421–424 (2002)
- [7] Shmoilov, A.V., Krivova, L.V., Stoyanov, E.I., Ignatiev, K.V.: Probabilistic method select of the borders interval data for electroenergetic problems. In: Proc. the High School, Problems of Energy–2008, vol. 7(8/1), pp. 146–157 (2008)

Optimal Load Shedding Based on Frequency, Voltage Sensitivities and AHP Algorithm

Huy Anh Quyen, Quang Anh Bui, Trong Nghia Le, and Tan Thanh Tung Le

University of Technical Education, Ho Chi Minh City, Viet Nam
anhqh@hcmute.edu.vn

Abstract. Voltage and frequency are the two important parameters affecting the maintenance of the power system stability. This paper presents the load shedding methodology based on frequency and voltage. The level of disturbance is estimated by using the rate of frequency change, and the location, number of loads shed at each bus has been determined based on the calculated voltage sensitivity at each bus in steady state. In the competitive electricity market, load shedding/not shedding Decision Support Systems are needed to find economical ways to serve critical loads with limited sources under various uncertainties. Decision - making is significantly affected by limited energy sources, generation cost, and network available transfer capacity. The load shedding program taking into account the importance and position of the load, investment rates per unit load, and the constraint conditions based on Analytic Hierarchy Process (AHP) algorithm to process when the system there are many different types of load.

Keywords: Load shedding, under frequency load shedding (UFLS), voltage sensitivities, Analytic Hierarchy Process (AHP), Linear Program.

1 Introduction

The two most important parameters to monitor are the system voltage and frequency. If the generators in the system are unable to supply the power needed, then the system frequency begins to decline, and when all the available controls cannot maintain stable frequency electrical systems, fired load will be used as a last resort to restore the limited frequency norms. The fired load optimization should consider the economic indicators and the importance of the load, and when all the available controls cannot maintain the stable frequency of electrical systems, load shedding will be used as a last resort to restore the limited frequency norms. The optimal load shedding should consider the economic indicators and the importance of the load.

Although there is some success, the load shedding the traditional load shedding based on under frequency or voltage relay have the following disadvantages: only consider the frequency reduction [2] or voltage in the power system, in this case the results are often less accurate, the mount of load is shed sometimes so large in a step, it causes excessive load shedding, the next planning does not have the flexibility to

increase the number of load steps shed [3], [4]. To increase the efficiency of load shedding, some load shedding methods based on frequency or the rate of change of frequency (df/dt) [5], voltage, sensitivities QV at load bus. However, this case shows the processing speed algorithm is too slow [1].

The load shedding proposed algorithm below aims to optimize load shedding based on frequency, voltage sensitivities at the nodes, considering the importance of the load, the investment rate/unit load and constraint conditions to resolve the limitations of previous studies.

2 Approach Method

2.1 The Load Shedding Based on Frequency and Voltage Sensitivities

The proposed load shedding combined two parameters: frequency and voltage sensitivities at bus provide the mount and location of load to shed [1]. The first step is determination the equations of swing of the rotor:

$$\frac{2H_{eq}}{f_0} \frac{df_n}{dt} = P_{diff} = P_{mn} - P_{en} \quad (1)$$

Where: H_{eq} is the equivalent inertia constant of the generators; f_0 is the nominal frequency of the system; P_{diff} is the difference in the generated power and the load power; P_{mn} is the mechanical shaft power for n machines, P_e is the electrical power for n machines.

The next step calculates dV/dt value to determine the order of load shedding. Buses with large dV/dt biggest listed at the top of the list and then arranged in descending order. The equation for reactive power, active power, and voltage sensitivities is:

$$P_i = \sum_{j=1}^n |V_i V_j Y_{ij}| \cos(\delta_{ij} - \theta_{ij}) \quad (2)$$

$$Q_i = \sum_{j=1}^n |V_i V_j Y_{ij}| \sin(\delta_{ij} - \theta_{ij}) \quad (3)$$

$$\frac{dQ_i}{dV_i} = 2|V_{ii} Y_{ii}| \cos(\theta_{ii}) + \sum_{\substack{j=1 \\ j \neq i}}^n |V_j Y_{ij}| \sin(\delta_{ij} - \theta_{ij}) \quad (4)$$

Where: P_i , Q_i are the powers incoming to the i^{th} node; V_i , V_j are the voltages at the i^{th} and j^{th} node; Y_{ij} is impedance matrix; δ_{ij} is the phase angle difference of the voltage at the i^{th} and j^{th} ; θ_{ij} phase angle of line ij .

The sensitivities voltage of each bus and the load which is shed from a bus based on equation:

$$\frac{\frac{dV_i}{dQ_i}}{\left(\frac{dV_1}{dQ_1} + \frac{dV_2}{dQ_2} + \dots + \frac{dV_n}{dQ_n} \right)} \quad (5)$$

$$S_i = \frac{\left(\frac{dV_i}{dQ_i} \right)}{\left[\sum_{i=1}^n \left(\frac{dV_i}{dQ_i} \right) \right]} P_{diff} \quad (6)$$

The algorithm load shedding flowchart is presented in Fig.1 [1].

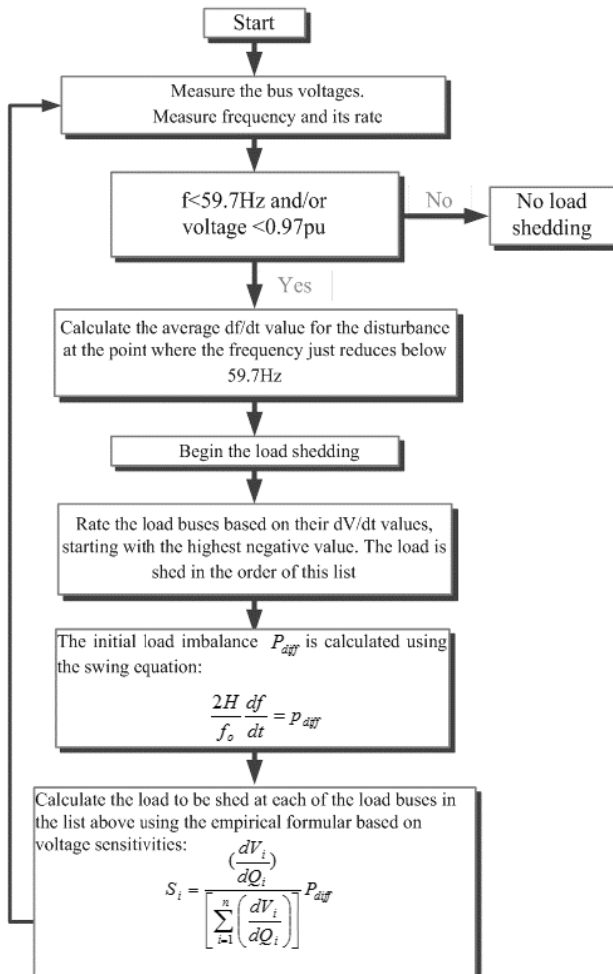


Fig. 1. Flowchart algorithm load shedding based on frequency and voltage sensitivities

2.2 Load Shedding Consider the Importance of the Load Based on AHP Algorithm

The load shedding program combinations of parameters: The importance of load, the investment rate/unit load, the load changes on time of day, the constraint conditions of power, thereby making the decision variables and calculates the maximum benefit achieved through the objective function.

1) Objective Function

$$\text{Max } H_i = \sum_{j=1}^{ND(K)} w_{ij} v_{ij} x_{ij} \quad (7)$$

Where: x_{ij} is decision variable (it equals 0 or 1) on load bus j at the i^{th} time stage; $ND(k)$ is total number of load sites in load center k; w_{ij} is load priority to indicate the importance of the j^{th} load site of the i^{th} time stage; v_{ij} the investment rate/unit load (or compensation cost/kW power failure) on load j^{th} at the i^{th} time stage (\$/kW or \$/MW); H objective function.

2) Analytic Hierarchy Process (AHP) Algorithm

Step 1: The hierarchical network model

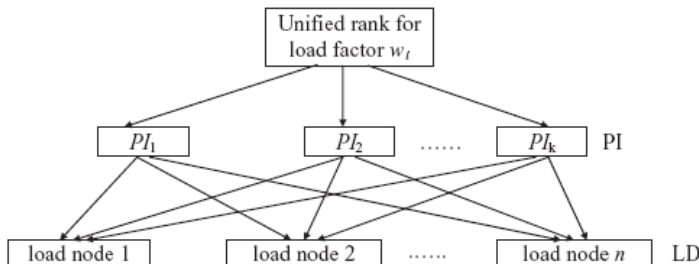


Fig. 2. Hierarchical network model

Analytical Hierarchy Process (AHP) is a method for ranking decision alternatives and selecting the best one when the decision maker has multiple criteria [6].

Step 2: Building judgment matrix A-PI and A-LD reflects the relative importance of load centers and loads in each of load center. The value of elements in the judgment matrix reflects the user's knowledge about the relative importance between every pair of factors. The judgment matrix A - PI can be written as follows:

$$A - PI = \begin{bmatrix} w_{K1}/w_{K1} & w_{K1}/w_{K2} & \dots & w_{K1}/w_{Kn} \\ w_{K2}/w_{K1} & w_{K2}/w_{K2} & \dots & w_{K2}/w_{Dn} \\ \vdots & \vdots & \ddots & \vdots \\ w_{Kn}/w_{K1} & w_{Kn}/w_{K2} & \dots & w_{Kn}/w_{Kn} \end{bmatrix} \quad (8)$$

Where: w_{ki} is the importance of the i^{th} load center, this value is unknown; w_{ki} / w_{kj} which is the element of judgment matrix A - PI, represents the relative importance of the i^{th} load center compared with the j^{th} load center. The value of w_{ki} / w_{kj} can also be obtained according to the experience of electrical engineers or system operators using some ratio “1-9” scale methods.

The judgment matrix A-LD:

$$A - LD = \begin{bmatrix} w_{D1}/w_{D1} & w_{D1}/w_{D2} & \dots & w_{D1}/w_{Dn} \\ w_{D2}/w_{D1} & w_{D2}/w_{D2} & \dots & w_{D2}/w_{Dn} \\ \vdots & \vdots & \ddots & \vdots \\ w_{Dn}/w_{D1} & w_{Dn}/w_{D2} & \dots & w_{Dn}/w_{Dn} \end{bmatrix} \quad (9)$$

Where: w_{Di} is the importance of i^{th} load, this value is unknown; w_{Di}/w_{Dj} which is the element of the judgment matrix A-LD, represents the relative importance of the i^{th} load compared with the j^{th} load. The value of w_{Di}/w_{Dj} can be obtained according to the experience of electrical engineers or system operators using some ratio “0-9” scale methods.

It is very difficult to compute exactly the weight factor of each load. The reason is that the relative importance of these loads is not the same, which is related to the power market operation conditions. According to the principle of AHP, the weight factor s of the loads can be determined through the ranking computation of a judgment matrix, which reflects the judgment and comparison of a series of pair of factors.

The unified weight factor of the load w_{ij} can be obtained from the following equation:

$$w_{ij} = w_{kj} \times w_{Di} \quad D_i \in K_j \quad (10)$$

Where: $D_i \in K_j$ means load D_i is located in load center K_j .

After calculation of the critical load factors and load centers, plans to load shedding optimization and achieve maximum benefits are calculated through the approach proposed.

Step 3: Calculate the maximal eigenvalues and the corresponding eigenvector of the judgment matrix.

Step 4: Hierarchy ranking and consistency check of results.

3 Calculation, Experiments, the Simulation on System

3.1 In Case of Study Load Shedding Based on Frequency and Voltage Sensitivities

Experiments on typical systems IEEE with $f= 60\text{Hz}$ include 37 buses 9 generators. Consider the case of loss of a generator at bus 4, simulate with POWERWORLD software and observe getting results when applying the program conventional load shedding and proposed load shedding program. Using the equations of swing of the rotor, calculates as reduction of about 185MW. Results frequency graph when does not load shedding is shown in Fig. 3.

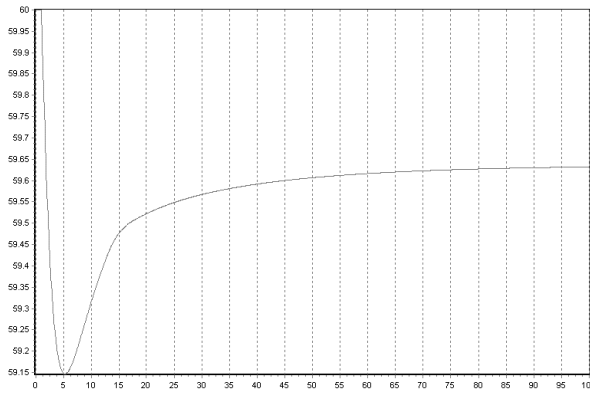


Fig. 3. Frequency system in case of failure at the generator bus 4

When no load shed, value frequency reduced 59.6 Hz is lower than the standard limit requirement. Therefore, should have solutions to restore system frequency back to the permitted limit value. The value of at the load buses are calculated and arranged in order beginning with the largest negative value. Load will be shed by order of the list presented in Table 1 and increased of 0.05s to avoid sudden loss of load. The increase in the number of load steps and load shedding in small steps avoid shedding too much load.

Table 1. The order of arrange in dv/dt at the bus

Bus	The order	dV/dt	Bus	The order	dV/dt
4	1	-0.04125	8	14	-0.01933
30	2	-0.03828	9	15	-0.01900
32	3	-0.03628	10	16	-0.01825
34	4	-0.03485	16	17	-0.01755
35	5	-0.03450	11	18	-0.01750
3	6	-0.03200	13	19	-0.01750
2	7	-0.02975	22	20	-0.01725
25	8	-0.02650	15	21	-0.01625
6	9	-0.02600	14	22	-0.01575
7	10	-0.02575	19	23	-0.01475
36	11	-0.02450	23	24	-0.01475
5	12	-0.02250	12	25	-0.01325
37	13	-0.02177	12	25	-0.01325

Shed power value at each bus will be based on its voltage sensitivities. The value of was calculated separately for each load bus at the operation steady state. The values of are applied to the voltage sensitivities formula to be calculate how much load will be shed at each bus. Frequency graph after applying load shed program is shown in Fig.4. The obtained results, the frequency before using the load shedding program is

59.6 Hz, after application proposed load shedding program, the frequency has improved to a stable value near 60 Hz (59.995 Hz) in 32s.

Comparison the case load shedding is not order sorted value, load is shed in this order: load smallest value shed before increasing order. The frequency after the load shedding is shown in Fig.4. The value frequency recovery is 59.87 Hz, and recovery time to the frequency stability is 50 seconds.

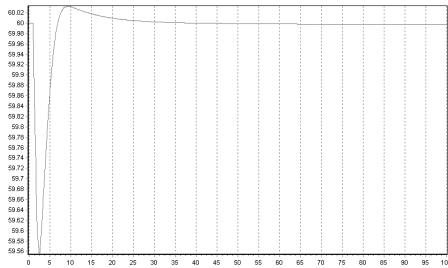


Fig. 4. Freq. of system after using load shedding based on freq. and voltage sensitivities

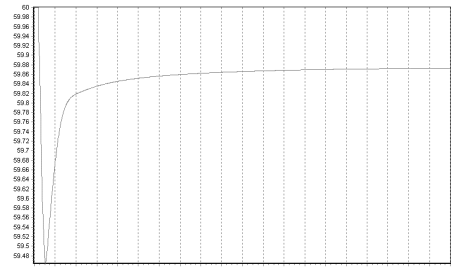


Fig. 5. Frequency of system after applying the load shedding no order dV/dt

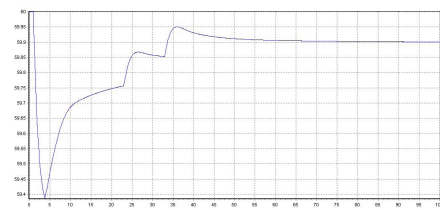


Fig. 6. Freq. of system after application load shedding by steps the decline of freq

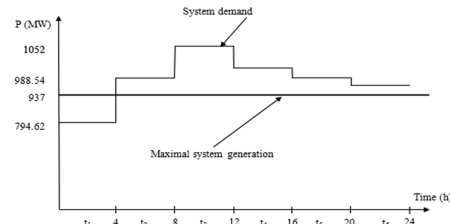


Fig. 7. Maximum system generation and load demands

Comparison with the case load shedding by steps based on the decline of frequency [3], the frequency of systems is shown in Fig. 6. In conclusion, the program loads shedding based on frequency and voltage sensitivities has faster recovery time, power load shedding less than traditional methods.

3.2 Load Shedding Consider the Importance of the Load Based on AHP Algorithm

The case study considered the 37 bus 9 generators system. The total generation power of source and load demand in the stages is shown in Fig. 7.

At first, the judgment matrices A-LD and A-PI. After calculating the value of the weight factors of each unit load at each time stage can be calculated from AHP method, ranking the unit load in order of descending priority is presented in Table 2. Load has weight factor W_{ij} larger is more important.

Table 2. Reduced ranking weight factors W_{ij} computed by AHP

Load center	Weighting Factor W_{kj} (A-PI)	Load Node	v_{ij} (\$/kW)	Weighting Factor W_{di} (A-LD)	Unified Weighting Factor W_{ij}
CK1	0.49421	PD5	300	0.09518	0.047039008
CK1	0.49421	PD7	300	0.07729	0.038197193
CK1	0.49421	PD6	300	0.06821	0.033709162
CK1	0.49421	PD4	280	0.06306	0.031163832
CK1	0.49421	PD2	280	0.06165	0.030469937
CK1	0.49421	PD8	280	0.05830	0.028811996
CK1	0.49421	PD9	280	0.05180	0.025600079
CK1	0.49421	PD3	300	0.04724	0.023347549
CK3	0.25112	PD22	220	0.04180	0.010496781
CK3	0.25112	PD16	220	0.02940	0.007381787
CK3	0.25112	PD15	280	0.02608	0.006548176
CK3	0.25112	PD19	245	0.02410	0.006050998
CK2	0.11346	PD10	245	0.04994	0.005665628
CK2	0.11346	PD13	280	0.04936	0.005600806
CK4	0.14122	PD25	300	0.03434	0.004848719
CK3	0.25112	PD23	280	0.01822	0.004576043
CK4	0.14122	PD35	245	0.02566	0.003623070
CK4	0.14122	PD32	220	0.02524	0.003564782
CK4	0.14122	PD36	300	0.02524	0.003564782
CK4	0.14122	PD34	220	0.02094	0.002957412
CK4	0.14122	PD37	220	0.02069	0.002922123
CK4	0.14122	PD30	220	0.01980	0.002796493
CK2	0.11346	PD11	280	0.02357	0.002674183
CK2	0.11346	PD14	220	0.02234	0.002534066
CK2	0.11346	PD12	300	0.02055	0.002331816

Ranking of all loads in the order of priority for each time stage and rule - based system decides the commitment or load shedding. This priority rank considers does not involve the constraints of power balance and reserve requirements when increase or decrease the load. So the final results are obtained through the combination between AHP and rule - based constraints checking. The calculation results are presented in Table 3. By the table, the decision variable $x_{ij} = 1$ means that this load is committed at the time stage t , and $x_{ij} = 0$ means that this load is shed at the time stage t .

The conventional load shedding LP method does not consider the importance of the loads as well as their relationship with each other load sites. The result comparison shows that the load shedding based on AHP is more optimal. It not only benefits the maximum load capacity of not less than layoffs, but also attention to the importance and location of the load.

Table 3. Comparison load shedding at the stages based on AHP (1) and LP (2)

LOAD SITE	STAGE T1		STAGE T2		STAGE T3		STAGE T4		STAGE T5		STAGE T6	
Methods	(1)	(2)	(1)	(2)	(1)	(2)	(1)	(2)	(1)	(2)	(1)	(2)
PD2	1	1	1	0	1	0	1	0	1	0	1	0
PD3	1	1	1	1	1	0	1	0	1	1	1	1
PD4	1	1	1	1	1	1	1	1	1	1	1	1
PD5	1	1	1	1	1	1	1	1	1	1	1	1
PD6	1	1	1	1	1	1	1	1	1	1	1	1
PD7	1	1	1	1	1	1	1	1	1	1	1	1
PD8	1	1	1	1	1	1	1	1	1	1	1	1
PD9	1	1	1	1	1	1	1	1	1	1	1	1
PD10	1	1	1	1	1	1	1	1	1	1	1	1
PD11	1	1	1	1	1	1	1	1	1	1	1	1
PD12	1	1	1	1	1	1	1	1	1	1	1	1
PD13	1	1	1	1	0	1	1	1	1	1	1	1
PD14	1	1	0	0	1	0	0	0	0	0	0	0
PD15	1	1	1	1	1	1	1	1	1	1	1	1
PD16	1	1	1	1	1	0	1	1	1	1	1	1
PD19	1	1	1	1	1	1	1	1	1	1	1	1
PD22	1	1	1	1	1	0	1	1	1	1	1	1
PD23	1	1	1	1	1	1	1	1	1	1	1	1
PD25	1	1	1	1	1	1	1	1	1	1	1	1
PD30	1	1	1	1	1	1	1	1	1	1	0	1
PD32	1	1	1	1	1	1	0	1	1	1	1	1
PD34	1	1	0	0	1	1	0	1	1	0	1	1
PD35	1	1	1	1	1	1	1	1	1	1	1	1
PD36	1	1	1	1	0	1	1	1	1	1	1	1
PD37	1	1	0	0	1	0	1	0	0	0	1	0

Table 4. Summary results compare between method conventional load shedding LP and AHP

Methods	Time stage	Max system generation (MW)	System demands (MW)	Total load shedding (MW)	Objective H_i	Benefit $\sum V_{ij}P_{ij} \times 10^3 \$$
AHP	t_1	937	794.62	0.00	94.78	213658
LP	t_1	937	794.62	0.00		213658
AHP	t_2	937	988.54	51.54	92.93	254655
LP	t_2	937	988.54	67.28		250246
AHP	t_3	937	1052	115.10	92.74	255142
LP	t_3	937	1052	116.20		254974
AHP	t_4	937	1000	63.31	92.79	255205
LP	t_4	937	1000	65.86		252308

Table 4. (*continued*)

AHP	t_5	937	988.54	51.54	93.58	254655
LP		937	988.54	67.28		250246
AHP	t_6	937	977.13	42.25	93.61	253639
LP		937	977.13	47.87		251467

4 Conclusion

The load shedding based on frequency and voltage sensitivities with frequency recovery time faster than traditional methods. However, this method isn't to mention the economic criteria and apply for emergency situations such as the loss of a generator or the loss of transmission lines.

Using the program loads shedding based on AHP algorithm considering load shedding problem considering the importance of the load, the investment rate/unit load, the load changes according to time of day and the constraint conditions allow load shedding is less than traditional methods and maximize the objective function.

References

1. Anh, B.Q.: Optimal Load Shedding. Master's Thesis at HCMUTE (2011)
2. Mahat, P., et al.: Under frequency Load Shedding for an Islanded Distribution System With Distributed Generators. IEEE Transactions on Power Delivery 25, 911–918 (2010)
3. Florida Reliability Coordinating Council Inc., FRCC standards handbook (2011)
4. The Northern Regional Power Committee (NRPC), Under frequency load shedding scheme in Northern Region (NR) (2010)
5. Hooshmand, R.: Optimal design of adaptive under frequency load shedding using artificial neural networks in isolated power system. Electrical Power and Energy Systems 42, 220–228 (2012)
6. Ung, L.C.: AHP Approach for Load Shedding Scheme of an Islanded Power System. Master's Thesis at University Tun Hussein Onn Malaysia (2012)

Modeling a Wind Turbine System Using DFIG and Realization of Current Control on the Model with Fuzzy Logic Controller

Ho-Ling Fu and Huynh Thanh Thien

Graduate Institute of Digital Mechatronic Technology, Chinese Culture University,
Taipei, Taiwan
{fuhl1123, thanhthien173}@gmail.com

Abstract. In this work, the modeling of wind turbine systems applying Doubly Fed Induction Generator is proposed. The mathematical model and control are investigated by analyzing theory and simulating performed in LabVIEW environment. All of characteristic parameters as well as the power generation process can be observed easily on LabVIEW. Besides, a comparison of reference current responses on the rotor side converter using conventional PI, PID and fuzzy controllers is also realized in this paper. The results obtained from the system with the presented control technologies indicated that the fuzzy logic controller has current response faster with almost no steady-state error than the conventional PI and PID controllers.

Keywords: The Human-machine interface, general model, vector control, fuzzy inference, active and reactive power, the center of area.

1 Introduction

Nowadays, the consumption of the electrical energy on the world rises considerably. Wind energy has become one of an alternative energy with many advantages such as safety, clean renewable-energy source and economic benefits. Wind turbines have two main types: fixed speed and variable speed wind turbine. The fixed speed wind turbines are effectively and efficiently used in several wind turbine system (WTS) because of simple control laws, low maintenance cost and simplicity. However, this kind of wind turbine supplies the low efficient performance and no capability to support reactive power because the rotor speed has no ability to adjust. The variable speed wind turbines are used more popular because the variable speed generators have ability to adjust rotor speed to absorb maximum electric power from various wind speed.

The generator are used in WTS have an important role to affect on the performance of the WTS. There have many kinds of generators such as Squirrel Cage Induction Generators (SCIG), Permanent Magnet Synchronous Generators (PMSG) and Doubly Fed Induction Generator (DFIG). To absorb maximum power extract from various wind velocity, DFIG seems to be the best choice. Mathematical model and control of DFIG is mentioned in [1], [2], and [3]. DFIG has advantages such as: reduced

mechanical stress especially is on the mechanical parts, reduced noise sound and allowed to operate both active and reactive modes [3].

In the industry, we will encounter applications in control fields using conventional Proportional (P), Proportional Integral (PI), and Proportional Integral Derivative (PID) controllers because they have simple structures and can easily use. However, they just can tune for linear models [3]. So, these controllers come up against difficulty in disturbances and variable parameters processing. This causes oscillations in responses which should be overcome in control process. Using single fuzzy controller to improve output voltage and fuzzy control combined with inner PI control at rotor side converter (RSC) to improve output current have been investigated in [4] and [5] for the both active and reactive power. However, there has been no combination between using controllers with modeling of the whole WTS.

In the scope of this study, the WTS based on DFIG is modeled using the LabVIEW program. As a result of using this platform, the interface for monitor and control would be helped user convenient to check, import and edit control parameters of system. Besides, a comparison of the current output responses of PI, PID and fuzzy controllers performed flexibly because control and environment parameters could be easily changed on interface.

2 Model and Control of the WTS Using DFIG

2.1 General Model of WTS

The mechanical power of the WTS extracted from the wind is given by:

$$P_{MECH} = \frac{1}{2} \rho_{AIR} \pi R^2 C_p(\lambda, \theta) V_{WIND}^3 \quad (1)$$

The tip speed ratio is obtained from:

$$\lambda = \frac{\omega_{turb} R}{V_{WIND}} \quad (2)$$

With characteristic parameters are the air density (ρ_{AIR}) at temperature 25°C, the rotor radius (R), the wind speed (V_{WIND}), the power efficiency coefficient (C_p), wind turbine speed (ω_{turb}), the tip speed ratio (λ) and the pitch angle (θ).

The C_p value of the turbine rotor is approximated according to [6].

$$C_p(\lambda, \theta) = C_1 \left(\frac{C_2}{\lambda_i} - C_3 \theta - C_4 \theta^{C_5} - C_6 \right) \exp \left(\frac{-C_7}{\lambda_i} \right) \quad (3)$$

The value λ_i is given by:

$$\frac{1}{\lambda_i} = \frac{1}{\lambda + C_8 \theta} - \frac{C_9}{\theta^3 + 1} \quad (4)$$

In there, the value C_i ($i = 1, \dots, 9$) is coefficients in (3) and (4) are {0.5, 116, 0.4, 0, 0, 5, 21, 0.08, 0.035}, respectively.

In this work, driving shafts are assumed that to be absolute stiffness, the relative angular displacement of the output shaft and generator's mechanical resistance torque can be ignored. Model of the gear train can be given as:

$$\frac{d\omega_g}{dt} = \frac{n(T_r - nT_e)}{(J_r + n^2 J_g)} = \frac{\left(\frac{T_r}{n} - T_e\right)}{\left(\frac{J_r}{n^2} + J_g\right)} \quad (5)$$

Where J_r : the rotation inertia of wind rotor, T_r : the torque of wind rotor, J_g : the rotation inertia of the generator, n : the gear box ratio, T_e : the electromagnetic torque.

The WTS using DFIG basically includes generator, drive train system, controllers of RSC, grid side converter (GSC), pitch angle; DC-link capacitor and grid. The DFIG is a wound rotor induction generator with the stator and rotor connected as shows in Fig. 1.

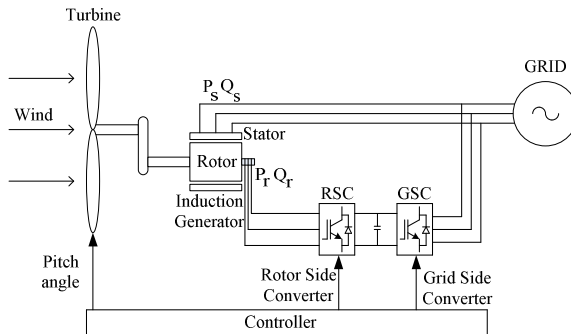


Fig. 1. WTS with DFIG

The WTS model based on DFIG using q-d arbitrary reference frame with Park and Clarke transformation is also proposed in [1], [2] and [3]. The voltages, flux equations, active, reactive power and electromagnetic torque of the DFIG are:

$$\begin{cases} u_{ds} = \frac{d\varphi_{ds}}{dt} - \omega\varphi_{qs} + R_s i_{ds} \\ u_{qs} = \frac{d\varphi_{qs}}{dt} + \omega\varphi_{ds} + R_s i_{qs} \\ u_{dr} = \frac{d\varphi_{dr}}{dt} - (\omega - \omega_r)\varphi_{qr} + R_r i_{dr} \\ u_{qr} = \frac{d\varphi_{qr}}{dt} + (\omega - \omega_r)\varphi_{dr} + R_r i_{qr} \end{cases} \quad (6)$$

$$\begin{cases} \varphi_{ds} = L_s i_{ds} + L_m i_{dr}; \varphi_{qs} = L_s i_{qs} + L_m i_{qr} \\ \varphi_{dr} = L_m i_{ds} + L_r i_{dr}; \varphi_{qr} = L_m i_{qs} + L_r i_{qr} \end{cases} \quad (7)$$

$$\begin{cases} P_s = u_{qs} i_{qs} + u_{ds} i_{ds}; Q_s = u_{qs} i_{ds} - u_{ds} i_{qs} \\ P_r = u_{dr} i_{dr} + u_{qr} i_{qr}; Q_r = u_{qr} i_{dr} - u_{dr} i_{qr} \end{cases} \quad (8)$$

$$T_e = \varphi_{ds} i_{qs} - \varphi_{qs} i_{ds} \quad (9)$$

Where u : the voltage, φ : the flux, i : the current, ω : the synchronous angular velocity, P and Q : active and reactive power, L_m : the mutual inductance, R : the resistance, the terms of s and r are stator and rotor, respectively.

2.2 Control Model of WTS Applying Oriented Vector on Stator Flux

In DFIG model, the direction of the stator flux vector is oriented from the d-axis of the synchronous frame [7]. The simplification and combination of voltage, flux and power are presented at previous part to get the active (P_s) and reactive (Q_s) powers:

$$P_s = -u_s \frac{L_m}{L_s} i_{qr} \quad (10)$$

$$Q_s = \frac{u_s L_m (i_{ms} - i_{dr})}{L_s} \quad (11)$$

Where u_s : the stator voltage, i_{ms} : the stator magnetizing current, i_{dr} and i_{qr} : the rotor currents on d and q axis, L_m and L_s : the mutual and stator inductance. The PI (or PID) controller minimize error at signal output to zero and this controller output is called the reference rotor current i_{dr}^{ref} and i_{qr}^{ref} . The control diagram using conventional PI (or PID) controller at RSC is showed in Fig. 2. From (10) and (11), the active and reactive powers are independently controlled by the vector control techniques.

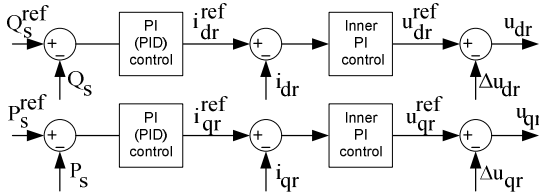


Fig. 2. The PI or PID controller for active and reactive power at RSC

3 Realization of Current Control with Fuzzy Logic Control

Due to the nonlinear characteristics of DFIG as uncertain load and variable parameters, calculating gain parameters for the conventional PI, PID feedback control using in mathematical modeling has been a difficult work. In this scheme, the PI (or PID) controller will be replaced by a fuzzy controller. It is mean that a fuzzy controller is cascaded with a fixed inner PI current controller. The fuzzy controller output is the reference current i_{dr}^{ref} and i_{qr}^{ref} can be showed in the block diagram in Fig. 3.

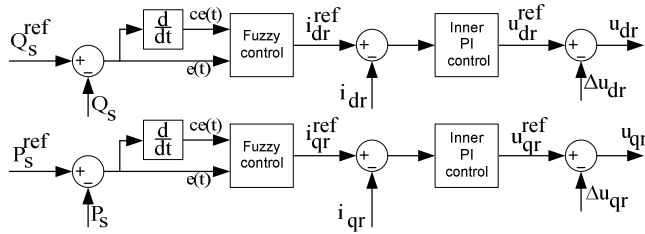


Fig. 3. The fuzzy controller for active and reactive power at RSC

The design for fuzzy control is realized by understanding the converter's characteristic and linguistic rules of the type: "If the error of the output is positive, then the duty cycle slightly" [5]. The fuzzy controller regulate the reference output current i_{dr}^{ref} and i_{qr}^{ref} , the fuzzy controller uses 2 variables for input, the error in power of reactive power, $e(t)$ and the change in error, $ce(t)$ of the stator reactive power output of DFIG, which is defined as:

$$e(t) = Q_{ref} - Q_s \quad (12)$$

$$ce(t) = e(nT_s) - e((n-1)T_s) \quad (13)$$

The output error and the change in error at reactive power have three subsets are (S, M, B) and (VS, ZE, VB) with the triangle membership function, with {S, M, B} are {Small, Medium, Big} and {VS, ZE, VB} are {Very Small, Zero, Very Big}. The output has five subsets are VS, S, M, B and VB with the triangle membership function.

The fuzzy rule table for the output current regulation is shown in Table 1. It has 9 rules of the following type: Rule i : IF (the error $e(t)$ is S (Small) AND the change in the error $ce(t)$ is VB (Very Big) THEN the change of the command is M (Medium), where $i = 1, \dots, 9$. Then, the fuzzy output is defuzzified to get the output value, the fuzzy inference process uses the center of area (COA) method [8]:

$$dz = \frac{\sum_{i=1}^n Z_i \mu_{out}(Z_i)}{\sum_{i=1}^n \mu_{out}(Z_i)}$$

Table 1. Rule base for the fuzzy controller on both active and reactive power

$\begin{matrix} u(t) \\ ce(t) \end{matrix}$	S	M	B
VB	M	S	VS
ZE	B	M	S
VS	VB	B	M

Subsets of the output error and the change in error, the fuzzy rule as well as the defuzzification method at active power are the same at reactive power.

4 Simulation Results and Discussions

In this section, by basing on above mathematical models of WTS, a human-machine interface (HMI) is written by LabVIEW platform can be indicated in Fig. 4.

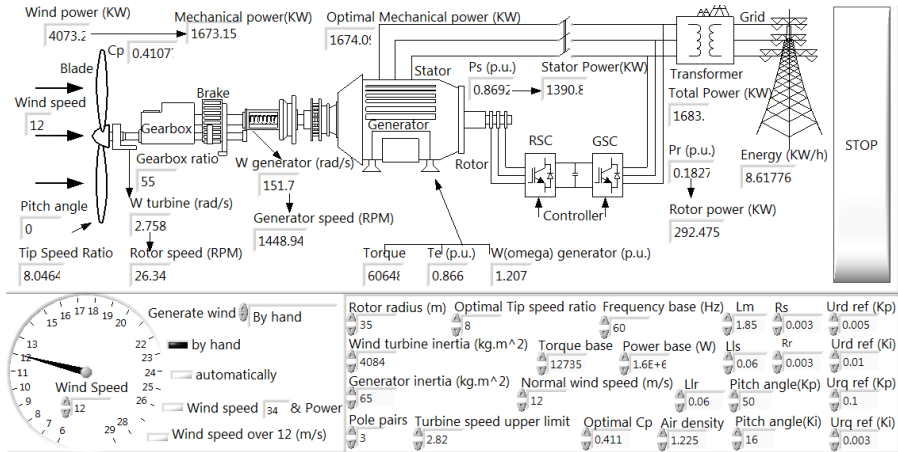


Fig. 4. The human-machine interface of WTS

The main HMI includes different parts of virtual devices with parameters of the system attached on it. This HMI not only shows the extensive look of the whole system but also allows the user to import or editing parameters for calculation, monitor and control of system. Besides, the status information and warnings make the system more convenient in monitoring and controlling. From this HMI program, the process of electric power conversion and generation also could be clearly viewed. The charts display curves of characteristic parameters such as power, stator, rotor current and voltage, characteristic curves of wind power. Moreover, a comparison of conventional PI, PID and fuzzy controller is also observed through a chart diagram in order to see the advantages and drawbacks of these controllers.

Simulation results show the various responses of the reference current i_{dr}^{ref} based on the conventional PI, PID and fuzzy controllers and the current calculated from (10), (11) equations based on the reference active and reactive stator power. All of them are shown in Fig. 5, at wind velocity is 12 m/s. Where a, b, c and d present PI, PID, fuzzy and reference responses, respectively. In Fig. 5, Fuzzy response has faster response than PI and PID, so it is the best among three.

Fig. 6 shows the responses of the reference current i_{qr}^{ref} at the various wind velocity from 10 to 14 m/s. The current response of the PID control approaches the reference current but it creates more error than fuzzy control. The current response of PI control cannot respond in time with the change of wind velocity. With the help of additional fuzzy controllers, the reference rotor current response approaches the reference rotor current more quickly. This shows that the fuzzy controller controls more accuracy, the system response can be improved. The fuzzy control obtained faster system response with almost no overshoot, shorter settling time, faster rise time and no steady-state error.

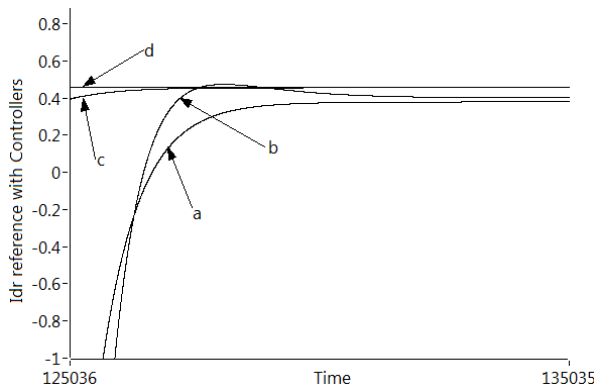


Fig. 5. The reference current responses i_{dr}^{ref} at wind speed 12 m/s

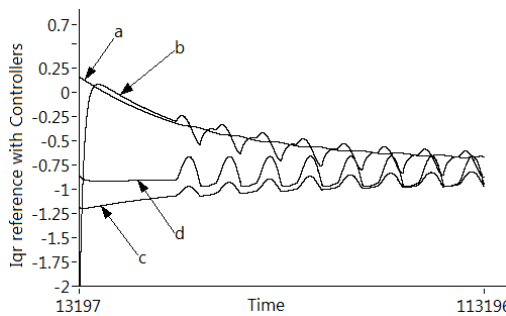


Fig. 6. The reference current responses i_{qr}^{ref} at the various wind speed [10 m/s – 14 m/s]

5 Conclusion

The HMI designed based on LabVIEW offers a graphic example in the controlling and monitoring of system. This system could be used for researcher make the test of WTS more financially benefit and convenient before production without study on large-size and costly devices in Lab. On the another side, the system helps the staff, trainee and workers comprehend quickly the basic knowledge of WTS, helps them to more understand the characteristic parameters, control process and the operation condition. There have a lot of dangers and difficulties for study in the real WTS such as the variable considerable wind speed in each area, the wrong operation, the time and location limit. So this system seems to be the promising system in reducing the costs of training, the safety of researchers and the maintenance of the system.

The new control technology based on LabVIEW with fuzzy inference makes the system more accurate and reliable. The additional fuzzy controller improves the current response of the DFIG as comparing to that of using conventional PI or PID controller.

References

1. Balogun, A., Ojo, O., Okafor, F., Karugaba, S.: Determination of Steady State Control Laws of Doubly Fed Induction Generator using Natural and Power Variables. In: 2010 IEEE on Energy Conversion Congress and Exposition, pp. 4099–4106. IEEE Press, Georgia (2010)
2. Lu, Z., Jin, X., Zhan, L.: A Novel LVRT Control Strategy of DFIG based Rotor Active Crowbar. In: 2011 Asia-Pacific on Power and Energy Engineering Conference, pp. 1–6. IEEE Press, China (2011)
3. Belmokhtar, K., Doumbia, M.L., Agbossou, K.: Modeling and Fuzzy Logic Control of DFIG Based Wind Energy Conversion Systems. In: International Symposium on Industrial Electronics, pp. 1888–1893. IEEE Press, China (2012)
4. Sastrowijoyo, F., Choi, J., Chung, G.-B.: Fuzzy Control for Back to Back Converter in DFIG for Wind Power Generation. In: 8th International Conference on Power Electronics and ECCE Asia, pp. 1337–1343. IEEE Press, Korea (2011)
5. Sastrowijoyo, F., Yim, K., Choi, J.: Comparative Study of PI and Fuzzy Controller for Rotor Side Converter of DFIG. In: 7th International on Power Electronics and Motion Control Conference, pp. 1440–1445. IEEE Press, China (2012)
6. Uma Maheswari, R., Tamilvendhan, J.: Analysis of Modelling of Active Stall Controlled and Active Pitch controlled Variable Speed Wind Turbines. International Journal of Modern Engineering Research, 2662–2667 (2012)
7. Lv, Y., Xi, P., Li, N., Fan, X.: Research of VSCF Wind Power Generation Training System Based on Matlab/LabVIEW. In: IEEE International Conference on Automation and Logistics, pp. 1592–1597. IEEE Press, China (2009)
8. Bose, B.K.: Modern Power Electronics and AC Drivers, the United States of America (2002)

Combining the Daylight and Artificial Light Based on Fuzzy Logic

Huy Anh Quyen¹, Tan Thanh Tung Le¹, Trong Nghia Le¹, and Thi Minh Thuy Pham²

¹ University of Technical Education, Ho Chi Minh City, Vietnam

² Hue Industrial College, Hue, Vietnam

anhqgh@hcmute.edu.vn

Abstract. The paper present a strategy of artificial lighting control to respond the natural state of daylight based on fuzzy logic control. After building the fuzzy logic controller, the simulations using Matlab program in two scenarios are built. For each scenario, the output responses were surveyed with the whole range of daylight corresponding to each of input statement. The simulation results show that the output of the fuzzy controller is good responsive the equilibrium when the input illumination changes, while the 4 zones scenario have more sensitive result than the 3 zones scenario.

Keywords: intelligent lighting, daylight strategy, fuzzy logic.

1 Introduction

As economies and populations grow, so will energy needs, the overall energy demand in buildings is considered and optimized in order to minimize energy requirements. Although lighting system is a very small part of energy consumption in buildings, it plays an important role in making workplaces more comfortable. Thus the lighting system needed to be studied seriously. In addition to the technical solutions are currently being used such as high performance lights, taking advantage of the natural light should be considered because of the continuous and available properties during working hours.

A controller which meets the constantly changing of the natural light during the day is required to combine the daylight with artificial light. Due to the flexibility of the control system based on the knowledge base, the fuzzy controller is proposed to meet the changes of daylight which changing with time of day. In addition, because of nonlinear output function, the fuzzy controller is capable of reducing environmental noise such as cloud-shading effect.

2 Combining the Daylight and Artificial Light in Buildings

The daylight illumination diagram (Fig. 1) shows the intensity of solar radiation increases from morning to noon, and decreases from noon to night. We could use this

chart to determine the potential time for daylight and artificial lighting in buildings. In particular, the Limit Outdoor Illumination (E_{LOI}) is illumination in which the indoor lighting must be provided, i.e. the limit illumination exceeds 85% [5] in working time from 9am to 5pm on all days of the year.

In Fig. 1, when choosing $E_{LOI} = 5.000$ lux corresponds to the period from 7am to 5pm, the condition is satisfied in:

- During 8 months in Northern.
- During 9 to 10 months in Central.
- Almost all year round in Southern.

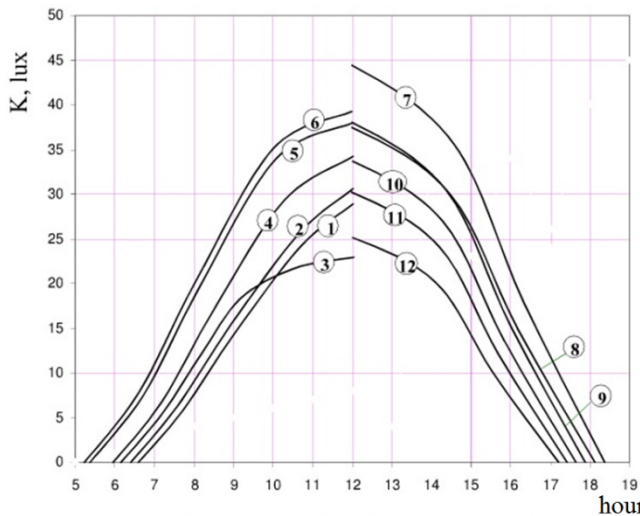


Fig. 1. Daylight illumination diagram on a horizontal surface in Hanoi [1]

When choosing $E_{LOI} = 3.000$ lux corresponds to the period from 7am to 5pm this condition is satisfied in:

- Almost all year round in the area from Quang Nam province to Southern.
- During 11 months in the area from Thanh Hoa province to Da Nang city (except Dec or Jan).
- During 10 months in the remaining local in Northern.

With daylight, the control system cannot adjust the intensity in the direction of increasing, it can only adjust the receiving point to decrease received light. Therefore, it's very passive and ineffective if you only rely on the natural light. Combining the daylight and artificial light will complement each other and increase the initiative in controlling the lighting system, take it easy response the different activities in buildings at various times.

The combination of natural lighting and artificial lighting must ensure lighting performance index, illumination and luminance according to requirements and used function in buildings.

3 Optimal Control Zoning Strategy

The depth of the optimal lighting zone depends on the shape, the height and the physical properties of window materials, direction of the window or outdoor illumination. Natural illumination is very high, but it will decrease quickly and be unevenly distributed on the working plane from the window position when going through the window. The positions which are near the window will have a very high illumination, and the illumination of the positions which are away from the window will decrease rapidly. Natural light is only significant influence in the optimal lighting zones. Depending on the feature of the buildings such as shading or no shading, the depth of the optimal lighting zone will range from 1.5 to 2.5 times height of the window. For this reason, control zoning strategy in the room is very important.

Because the positions which are near the window are affected by the rapid and significant impact of the natural light while the positions which are away from the window hardly change, control strategy will be applied in each region are different. The border zones of the room match on – off control while the central regions are more in line with dimming control [4]. The result of paper is the simulations based on scenarios of three zones scenario and four zones scenario.

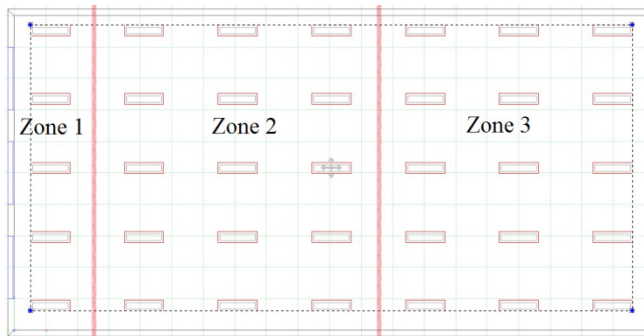


Fig. 2. The three zones scenario

The simulation performed on the model of “standard room”, in which, the size of the room is chosen 10m x 20m to consider the depth of natural lighting to 20m. The room receives the light from one direction with windows located in zone 1. The artificial lighting system is designed based on DIALux software with artificial light illumination (Eal) requires 500 lux and 35 fluorescent lamps 54W. Due to the depth of optimal lighting is about 1.5 to 2.5 times of the window height, zone 1 is selected is the first array near the window. The remaining zone is divided into 2 control zones to match with the strategy of on – off and dimming control [3].

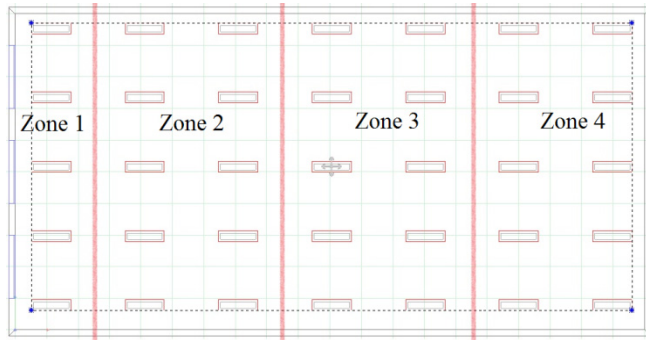


Fig. 3. The four zones scenario

The four zones scenario is built by dividing one more control zone to observe responses between zone 2 and 3. Splitting control zones allows the system response to meet closer to the influence of input [2].

4 Building Fuzzy Algorithm

4.1 The Model of Control Subject

System response is controlled by open – loop fuzzy controller. Controller input receive the signal from photo sensor which measure natural lighting illumination outside. After going through fuzzy controller, the signal is sent to dimmer which control lamps. After building control model, the knowledge base which is formed based on the results of specific states is solved by Matlab [2]. These results are the base to form the inference.

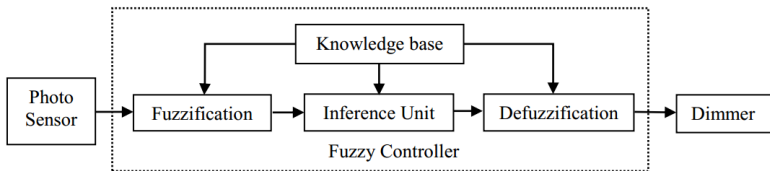


Fig. 4. Block diagram of fuzzy control system

Fuzzification and defuzzification are made by building input and output statements.

4.2 Input Statements

As daylight illumination diagram, natural lighting illumination is up to 40.000 lux in Viet Nam [1], ELOI is selected 5.000 lux according to Viet Nam Building Code (VNBC). In this way, input statements are presented in the Table 1.

Table 1. The Input/ Output Statements

Input Statements				Output Statements			
Statement s	Min	Values	Max	Statement s	Min	Values	Max
VL (very low)	0 (0)	5.000 (0.125)	5.000 (0.125)	VL (very low)	0.0	0.2	0.2
L (low)	5.000 (0.125)	13.000 (0.325)	20.000 (0.5)	L (low)	0.2	0.35	0.5
M (medium)	13.000 (0.325)	20.000 (0.5)	27.000 (0.675)	M (medium)	0.35	0.5	0.65
H (high)	20.000 (0.5)	27.000 (0.675)	34.000 (0.85)	H (high)	0.5	0.65	0.8
VH (very high)	34.000 (0.85)	34.000 (0.85)	40.000 (1)	VH (very high)	0.8	0.8	1.0

The lower statement (5.000 lux) and the upper statement (40.000 lux) are defined by Trapmf functions corresponding to VL and VH levels. The statements in the range of 5.000 lux and 40.000 lux are defined by Trimf function corresponding to L, M and H levels. Thus, the lighting system could be controlled by on – off controller when illumination is beyond control zone and by dimmer when illumination is located in control zone.

4.3 Output Statements

The output is divided into 5 state levels are: VL (very low), L (low), M (medium), H (high), and VH (very high). Output statements are identical for zone 1, zone 2 and zone 3.

The VL and VH statements are defined by Trapmf functions because the system will be turned off if control level is under 20% and be turned on if control level is over 80%. The lamp life will be improved since the system is not too sensitive to VL and VH levels. These values are selected as Table 1.

4.4 Building Rules

Building identification of membership functions for output U_i is to identify C1, C2, C3, C4, and C5. Fuzzy rules are made based on lighting scenarios which is built based on “knowledge base”. These scenarios are the basis for fuzzy logic infer based on the centroid method.

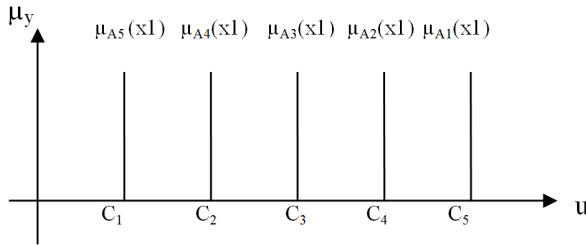


Fig. 5. The fuzzy coefficients

Defuzzifying by using centroid method:

$$u1 = \frac{c_5\mu_{A_1}(x_1) + c_4\mu_{A_2}(x_1) + c_3\mu_{A_3}(x_1) + c_2\mu_{A_4}(x_1) + c_1\mu_{A_5}(x_1)}{\mu_{A_1}(x_1) + \mu_{A_2}(x_1) + \mu_{A_3}(x_1) + \mu_{A_4}(x_1) + \mu_{A_5}(x_1)} \quad (1)$$

Given

$$\begin{aligned} \varphi 1 &= \frac{\mu_{A_1}(x_1)}{\mu_{A_1}(x_1) + \mu_{A_2}(x_1) + \mu_{A_3}(x_1) + \mu_{A_4}(x_1) + \mu_{A_5}(x_1)} & \varphi 2 &= \frac{\mu_{A_2}(x_1)}{\mu_{A_1}(x_1) + \mu_{A_2}(x_1) + \mu_{A_3}(x_1) + \mu_{A_4}(x_1) + \mu_{A_5}(x_1)} \\ \varphi 3 &= \frac{\mu_{A_3}(x_1)}{\mu_{A_1}(x_1) + \mu_{A_2}(x_1) + \mu_{A_3}(x_1) + \mu_{A_4}(x_1) + \mu_{A_5}(x_1)} & \varphi 4 &= \frac{\mu_{A_4}(x_1)}{\mu_{A_1}(x_1) + \mu_{A_2}(x_1) + \mu_{A_3}(x_1) + \mu_{A_4}(x_1) + \mu_{A_5}(x_1)} \\ \varphi 5 &= \frac{\mu_{A_5}(x_1)}{\mu_{A_1}(x_1) + \mu_{A_2}(x_1) + \mu_{A_3}(x_1) + \mu_{A_4}(x_1) + \mu_{A_5}(x_1)} \end{aligned}$$

Thus

$$u1 = \left[\begin{matrix} \varphi_1 & \varphi_2 & \varphi_3 & \varphi_4 & \varphi_5 \end{matrix} \right] \begin{bmatrix} c_5 \\ c_4 \\ c_3 \\ c_2 \\ c_1 \end{bmatrix} = \varphi^T \theta \quad (2)$$

The formula of fuzzy sets which identify output U_i is:

$$\hat{\theta} = (\varphi^T \varphi)^{-1} (\varphi^T m1) \quad (3)$$

Rules in case of three control zones are:

- If (X_1 is VL) then (U_1 is VH) (U_2 is VH) (U_3 is VH)
- If (X_1 is L) then (U_1 is M) (U_2 is VH) (U_3 is VH)
- If (X_1 is M) then (U_1 is M) (U_2 is H) (U_3 is VH)
- If (X_1 is H) then (U_1 is VL) (U_2 is M) (U_3 is H)
- If (X_1 is VH) then (U_1 is VL) (U_2 is L) (U_3 is M)

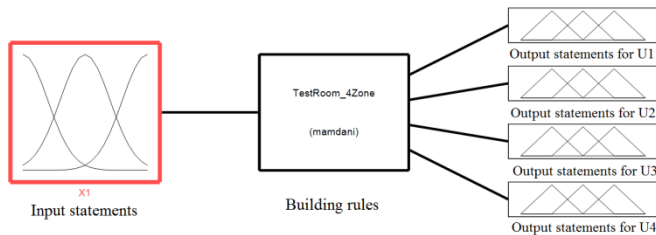


Fig. 6. Fuzzy controller in case of four zones scenarios

5 Simulation Results

5.1 Simulation Result in Case of Three Zones Scenario

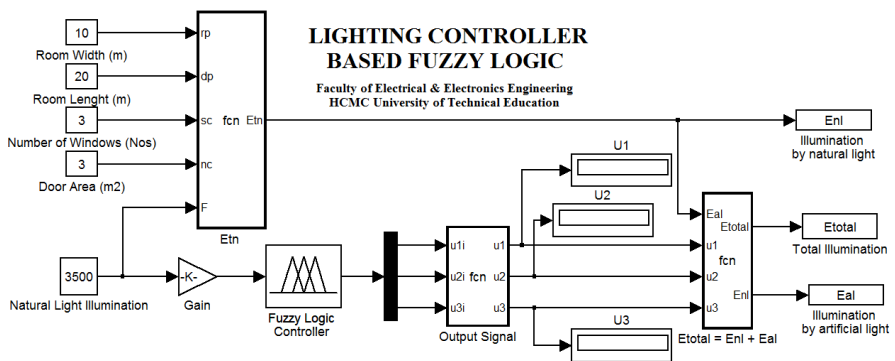


Fig. 7. Model in case of three zones scenario

Table 2. Output Results Of Lighting Controller Based On Fuzzy Logic

Case	U1	U2	U3
Case 1 (3.500 lux)	1	1	1
Case 2 (8.000 lux)	0.5	1	1
Case 3 (18.000 lux)	0.5	0.73	1
Case 4 (25.000 lux)	0.23	0.55	0.73
Case 5 (30.000 lux)	0	0.5	0.65
Case 6 (40.000 lux)	0	0.35	0.5

5.2 Simulation Result in Case of Four Zones Scenario

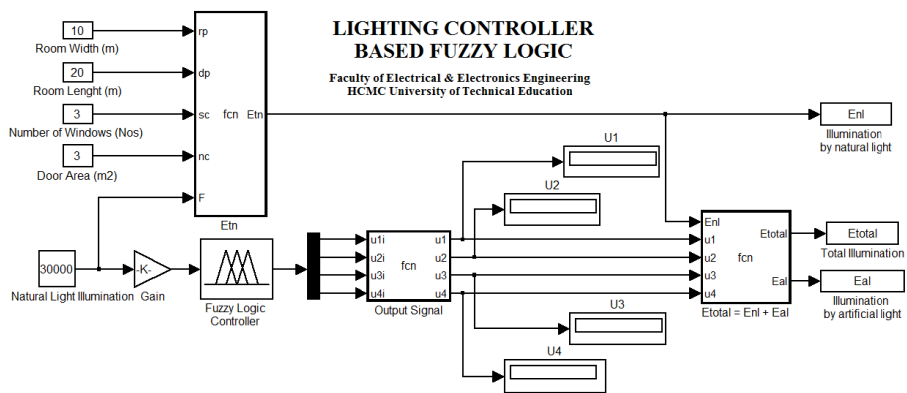


Fig. 8. Model in case of four zones scenario

Table 3. Output Results Of Lighting Controller Based On Fuzzy Logic

Case	U1	U2	U3	U4
Case 1 (3.500 lux)	1	1	1	1
Case 2 (8.000 lux)	0.5	0.65	1	1
Case 3 (18.000 lux)	0.5	0.65	0.73	1
Case 4 (25.000 lux)	0.5	0.65	0.65	1
Case 5 (30.000 lux)	0.5	0.5	0.5	0.5
Case 6 (40.000 lux)	0	0	0.35	0.43

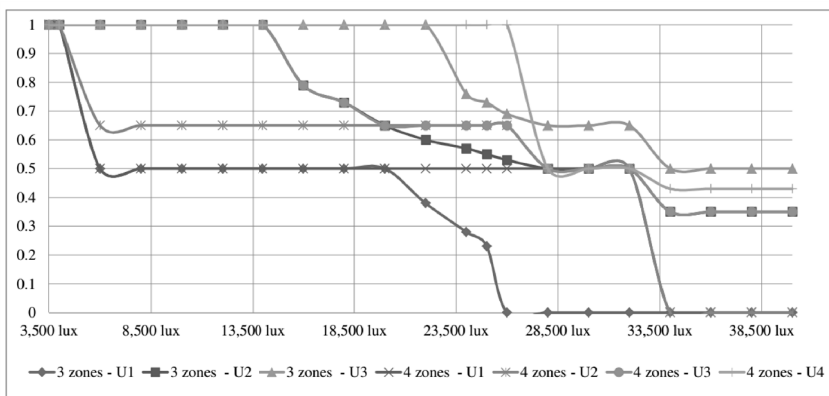
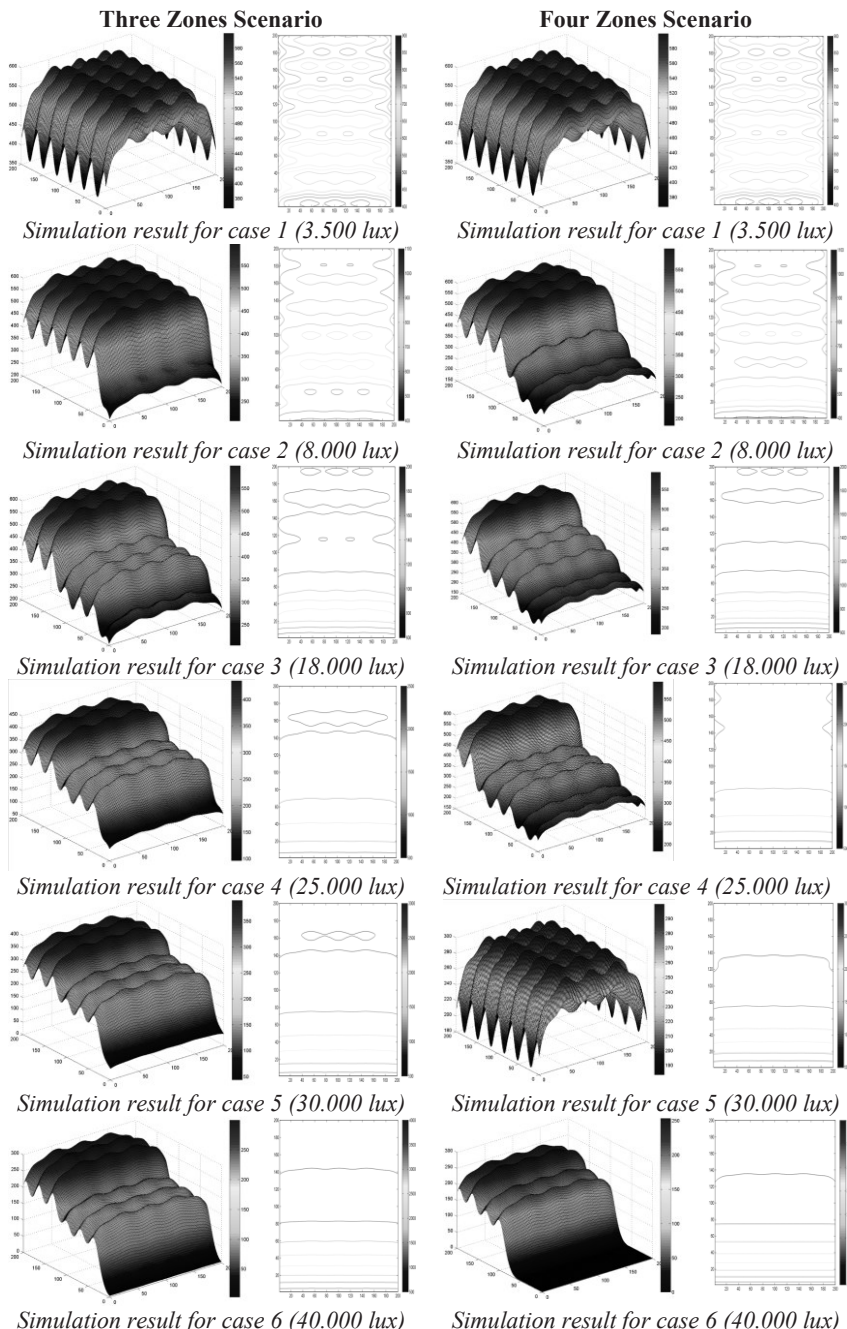


Fig. 9. System output response

The simulation results show that fuzzy controller indeed efficient in optimal lighting zone corresponding to dimming control. On other hand, on – off control is more suitable for zones which close to windows or away from windows.

Table 4. Results of artificial lighting system response and illumination plane

6 Conclusion

The simulation results of combining artificial lighting and natural lighting in cases show that illumination of artificial lighting system is significantly reduced in zones near window and optimal lighting zones.

The zoning method which is promoted based on the depth of natural lighting is suitable for most types of buildings that use natural lighting. Dividing lighting zones is to make artificial lighting control strategy be more suitable to natural lighting conditions.

System response is better by using fuzzy algorithm. Simulation results of combining artificial lighting and natural lighting show that this system is significantly save energy.

References

1. Nguyen, D.D.: Study on natural light property in Vietnam to improve the natural light zoning and proposed the lighting calculation method using natural light in Vietnam
2. Cziker, A., Chindris, M., Miron, A.: Fuzzy controller for indoor lighting system with daylighting contribution. Technical University of Cluj-Napoca / Power System Department, Cluj-Napoca, Romania, ELECO (2007)
3. Cziker, A., Chindris, M., Miron, A.: Fuzzy Controller for a Shaded Daylighting System. Technical University of Cluj-Napoca / Power System Department, Cluj-Napoca, Romania (2008)
4. Cziker, A., Chindris, M., Miron, A.: Implementation of Fuzzy Logic in Daylighting Control. Technical University of Cluj-Napoca / Power System Department, Cluj-Napoca, Romania, INES (2007)
5. Matta, S., Mahmud, S.M.: An Intelligent Light Control System. for Power Saving, Wayne State University, Detroit, Michigan, IECON 2010 (2010)
6. Kulkarni, G.H., Waingankar, P.G.: Fuzzy Logic Based Traffic Light Controller. Unique Academy, Nashik (2011)

Improved Pitch Angle Control for Variable-Speed Wind Turbine System

Tan Luong Van¹, Buu Pham Nhat Tan Nguyen², Trung Hieu Truong³,
and Tran Thanh Trang^{4,5,*}

¹ Department of Electrical Engineering, Ho Chi Minh City Electric Power College

² Department of Power System, Ho Chi Minh City Electric Power College

³ Department of Electrical-Mechanical Engineering, Ho Chi Minh City Electric Power College,
554 Ha Huy Giap, District 12, Ho Chi Minh City, Vietnam

{luongees2, trunghieubm}@yahoo.com, buutan2005@yahoo.co.nz

⁴ Department of Electronics and Telecommunication Engineering, Van Hien University,
665-667-669 Dien Bien Phu, District 3, Ho Chi Minh City, Vietnam
trangtt@vhu.edu.vn

⁵ National Key Lab of Digital Control and System Engineering, University of Technology,
Vietnam National University Ho Chi Minh City,
268 Ly Thuong Kiet, District 10, Ho Chi Minh City, Vietnam
trangtranthanhh1979@gmail.com

Abstract. In this paper, a pitch angle control scheme based on the fuzzy logic is proposed for the variable-speed wind turbine systems. The generator output power and rotor speed are used as control input variables for the fuzzy logic controller (FLC), which are effective to compensate for the nonlinear characteristic of the pitch angle to the wind speed. Also, a speed sensorless technique estimating the rotational speed is employed for the proposed control method. The effectiveness of the proposed method is verified by MATLAB simulation results for a 2-MW PMSG wind turbine system.

Keywords: Fuzzy logic, pitch angle, sensorless, wind turbine.

1 Introduction

Due to the energy shortage and environmental concern, the renewable energy, especially wind energy, has paid much attention in the world. In the wind power generation, the variable-speed wind turbine systems are more attractive than the fixed-speed ones due to the improvement of more wind energy production and the reduction of the flicker [1]. Also, the variable-speed wind turbine itself can reduce the stress, and achieve the maximum efficiency under any various wind conditions.

The variable-speed wind turbines today are equipped with the blade pitch control mechanism in all operating regions of the wind speed. The partial load region composed of the wind speeds between the cut-in wind speed, v_{in} , and the rated-wind

* Corresponding author.

speed, v_{rated} , in which the turbine speed should be controlled so that the maximum energy is extracted. As a result, the energy efficiency of the turbine is considerably increased with the increase of the power ripples. To decrease the ripples, the method employing the pitch angle has been performed [2], [3]. In the full load region where the wind speed is between the rated and cut-off wind speed, v_{out} , the generator output power and generator speed are controlled at the rated values by controlling the pitch angle. If there is any change of the pitch angle, the output power can be affected.

Several methods have been suggested to control the pitch angle for the variable-speed wind turbines. The proportional integral (PI) and proportional integral derivative (PID) controllers, within the power or speed control loops have been extensively used for the power regulation through the control of the blade pitch angle [1], [4]-[5]. However, the performance of these linear controllers is limited by the highly nonlinear characteristics of the wind turbine. Also, the gain scheduling control has been presented for compensating for the system nonlinearity, where the controller gains are continuously updated with the change of the system operating conditions [6]. However, a major drawback is the selection of the scheduling variable, to maintain the non-linearity of the system and to vary slowly.

A fuzzy logic control has been applied for controlling the pitch angle [7]. This method is simple, robust, and reliable since it can solve a wide range of the control problems. However, it is not realistic in practice since the measurement of the wind speed is required.

In this paper, a new pitch angle control scheme based on the fuzzy logic control is proposed for limiting the turbine output power and the generator speed in the high wind speed region. The generator output power and the rotational speed are used as the input variables of the fuzzy, instead of the wind speed, which can eliminate the use of an expensive anemometer. Also, a speed sensorless technique is applied to estimate the generator speed. The simulation results for a 2-MW PMSG wind turbine system shows the effectiveness of the proposed method.

2 Pitch Servo System

The block diagram of the typical pitch controller is shown in Fig. 1, in which the pitch servo system is included.

The pitch servo is modeled as an integrator or a first-order delay system, with a time constant (τ_c), and the saturation in the amplitude and derivative of the pitch angle, β . The dynamic behavior of the pitch servo is described as [1]

$$\frac{d\beta}{dt} = -\frac{1}{\tau_c}\beta + \frac{1}{\tau_c}\beta_{ref} \quad (1)$$

The time constant of the servo system can be selected to be 0.2 sec to accelerate the servo so fast. The rate pitch commanded by the pitch actuator is limited to the maximum value. The larger pitch rate ($d\beta/dt$) gives, the better transient performance is. Typically, the β ranges from -2 to 30 degrees and varies at the maximum rate of ± 10 deg/sec. To decrease the risks of the fatigue damage, the limits are not reached during the normal operation of the wind turbine.

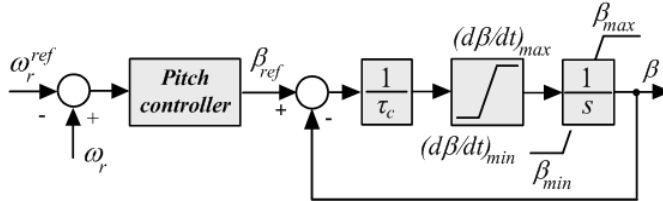


Fig. 1. Block diagram of the typical pitch angle controller

3 Proposed Pitch Angle Control Scheme

As mentioned in [8], the pitch angle is a nonlinear function of the generator speed, and generator power. Thus, the FLC uses the generator output power and estimated rotor speed as the controlling inputs, in which the rotor speed estimation will be described in detail in the following section.

3.1 Sensorless Control Method

The block diagram of the generator speed estimation is illustrated in Fig. 3. As can be seen, the stator flux, λ_s^s , in the stationary reference frame is obtained.

Then, a high-pass filter, whose cut-off frequency, ω_0 , is selected to be one-third of the generator rated speed, is employed to solve the drift and the saturation problems due to the integration. Also, to eliminate a delay problem due to the filter, the magnitude component, $\sqrt{\hat{\omega}_p^2 + \omega_0^2} / \hat{\omega}_p$, and phase component, $e^{(\phi-\frac{\pi}{2})}$, are multiplied with the transfer function, $\frac{\lambda_s^s}{v_s}$, for compensation, in which $\phi = \arctan(\hat{\omega}_p / \omega_0)$ is the phase angle, and $\hat{\omega}_p$ is an estimated synchronous angular speed. Next, the magnetic flux linkage λ_f , is calculated, from which the rotor position angle is obtained from the dq-axis components of the rotor flux as [9]

$$\hat{\theta}_r = \arctan(\lambda_{df}^s / \lambda_{qf}^s) \quad (2)$$

where λ_{df}^s and λ_{qf}^s are d- and q-axis rotor flux, respectively.

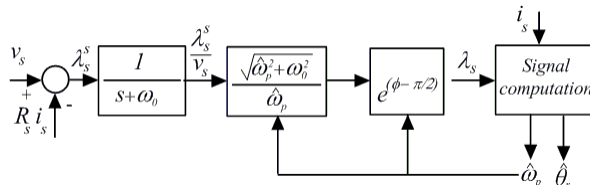


Fig. 2. Block diagram of generator speed estimation

By integrating the term of $\cos(\hat{\omega}_p t)$ in $[t_0, t_1]$ and calculating the approximate area for the integration, $\int_{t_0}^{t_1} \cos(\hat{\omega}_p t) dt$, the estimated speed is obtained as [9]

$$\hat{\omega}_p = \frac{\sin \hat{\theta}_{r1} - \sin \hat{\theta}_{r0}}{(\cos \hat{\theta}_{r1} + \cos \hat{\theta}_{r0}) T_s / 2} \quad (3)$$

where $\hat{\theta}_{r1} = \hat{\omega}_p t_1$, $\hat{\theta}_{r0} = \hat{\omega}_p t_0$, and T_s is a sampling time.

To reduce the speed ripple at the high frequencies, a low-pass filter is applied, which gives the average speed, $\hat{\omega}_d$. As aforementioned, this value is used as a control input of the pitch angle controller.

3.2 Design of Pitch Angle Control

The proposed fuzzy logic controller is shown in Fig. 3, in which the P_{ref} is selected to be 2[MW], the P_g is the measured generator output power and the $\hat{\omega}_d$ is the estimated wind speed. To find the pitch angle reference (β_{ref}), the design process for a fuzzy logic controller consists of determining the inputs, setting up the rules and designing a method to convert the fuzzy result of the rules into the output signal.

To design the proposed FLC for the pitch angle control, the input and output variables of the FLC have to be determined. In this paper, the error of the generator power, ΔP , variation of the power error, $\delta(\Delta P)$, and estimated rotational speed, $\hat{\omega}_d$ are considered as the controller inputs, in which the ΔP and $\delta(\Delta P)$ are defined as

$$\Delta P = P_g(k) - P_{ref}(k) \quad (4)$$

$$\delta(\Delta P) = \Delta P(k) - \Delta P(k-1) \quad (5)$$

The pitch angle reference is considered as the controller output, which provides to the mechanical servo system.

The triangular membership functions with the overlap used for the fuzzy sets of the inputs and output are illustrated in Fig. 4, in which the linguistic variables

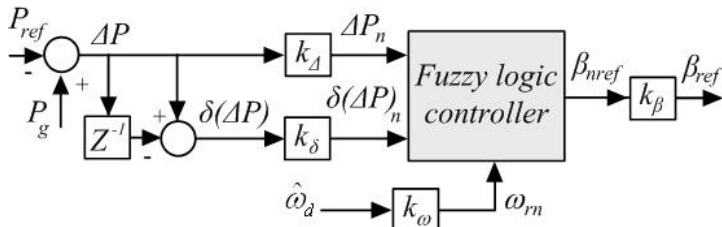


Fig. 3. Block diagram of proposed fuzzy logic control

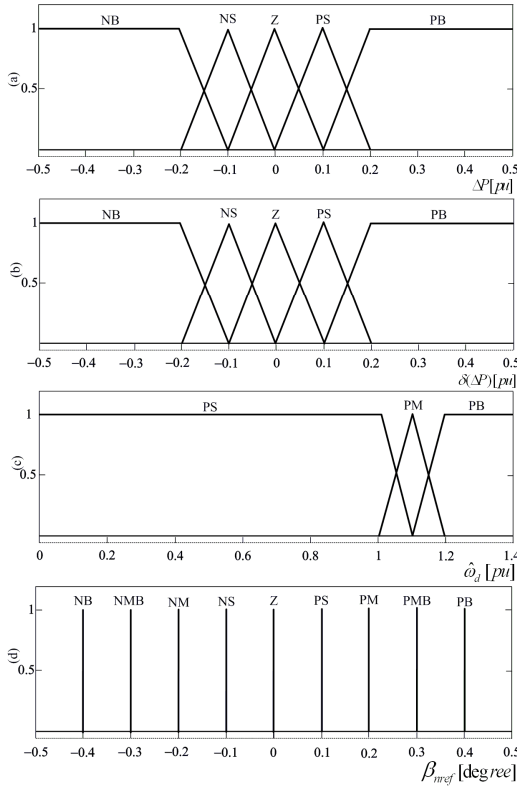


Fig. 4. Membership functions of proposed fuzzy logic controller for (a) Generator output error. (b) Variation of power error. (c) Rotational speed. (d) Pitch angle reference.

are represented by NB (Negative Big), NMB (Negative Medium Big), NM (Negative Medium), NS (Negative Small), Z (Zero), PS (Positive Small), PM (Positive Medium), PMB (Positive Medium Big), and PB (Positive Big). The width of variation can be adjusted according to the system parameters.

The grade of the input membership functions is obtained as:

$$\mu(z) = 1 - \frac{|z - m|}{0.5w} \quad (6)$$

where $\mu(z)$ is the value of the grade of the membership, w is the width, m is the coordinate of the point at which the grade of the membership is 1, and z is the value of the input variable.

The control rules are derived from the experience or knowledge on the control system. The fuzzy mapping of the input variables to the output is represented by the following rules

$R_i : \text{IF } \hat{\omega}_d(k) \text{ is } A_i \text{ and } \Delta P(k) \text{ is } B_i \text{ and } \Delta P(k-1) \text{ is } C_i \text{ THEN } \beta_{nref} \text{ is } D_i$.
where A_i, B_i , and C_i are the fuzzy subset, D_i is a fuzzy singleton.

The entire rules of the fuzzy are given in Table 1. The fuzzy with the Sugeno-type is applied for the inference mechanism [10], [11]. Each rule is weighted by the weighting factor, W_i , of the rule.

The weighted average of all rule outputs which expresses the variation of the pitch angle reference, β_{nref} , is calculated as:

$$\beta_{nref} = \sum_{i=1}^N W_i D_i / \sum_{i=1}^N W_i \quad (7)$$

where N is the total number of the rules, and D_i is the coordinate corresponding to the respective output or consequent membership function. The actual pitch angle reference is obtained from multiplying β_{nref} by k_β .

Table 1. Rules of fuzzy logic controller

$\hat{\omega}_d$		PS					PM					PB				
ΔP		NB	NS	Z	PS	PB	NB	NS	Z	PS	PB	NB	NS	Z	PS	PB
$\delta\Delta P$	NB	Z	Z	Z	Z	Z	NB	NM	NM	NS	PS	NMB	NM	NS	NS	PS
	NS	Z	Z	Z	Z	Z	NMB	NM	NS	PS	PM	NMB	NM	NS	Z	PS
	Z	Z	Z	Z	Z	Z	NM	NS	Z	PS	PM	NM	NS	Z	PS	PM
	PS	Z	Z	Z	Z	Z	NM	NS	PS	PM	PMB	NS	Z	PS	PM	PMB
	PB	Z	Z	Z	Z	Z	NS	PS	PM	PM	PB	NS	PS	PS	PM	PMB

4 Simulation Results

To verify the validity of the proposed method, the simulation has been performed using MATLAB/SIMULINK for 2[MW] PMSG wind power system. The parameters of the wind turbine and PMSG are listed in Table 2 and 3, respectively. The sampling time of the delay for the fuzzy logic controller is 50[μ s]. In the simulation, the pitch rate is limited to ± 10 (deg/sec).

Fig. 5 shows the wind speed, in which two operating regions are divided. In the region when the wind speed is higher than the rated value, 10.6 [m/s], between 27 [sec] and 70 [sec], this region is considered as the full load region. In the remaining region, when the wind speed is below the rated value, the region is the partial load one.

Fig. 6 (a) and (b) show the estimated rotor speed and position angle, respectively. As can be seen, both the rotor speed and position angle are well estimated.

Fig. 7 shows the simulation results of the pitch angle control, employing the PI control method with and without gain scheduling, and the proposed fuzzy logic control method. For the conventional PI controller, the generator power is considered as the controlling input variable. Meanwhile, the controlling input variables applying the proposed fuzzy logic control method are the generator power and estimated rotor speed.

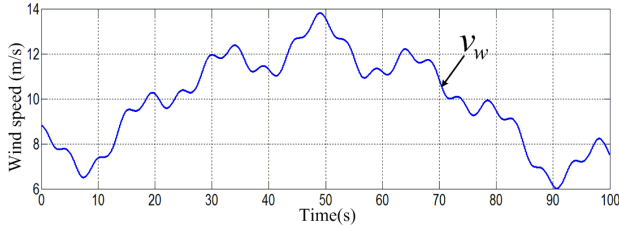


Fig. 5. Wind speed

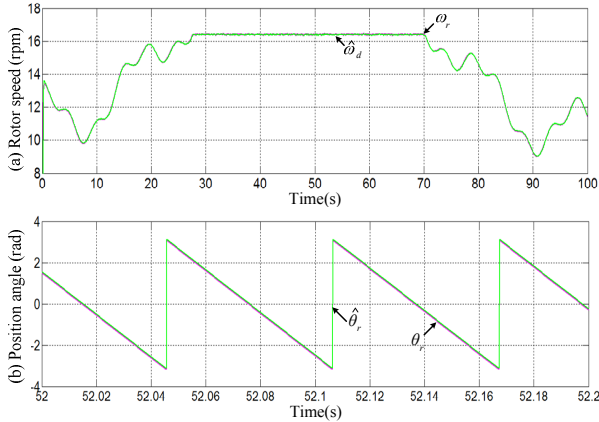


Fig. 6. Rotor speed estimation. (a) Estimated ($\hat{\omega}_d$) and real (ω_r) rotor speed. (b) Estimated ($\hat{\theta}_r$) and real (θ_r) rotor position.

As can be seen, at the rated wind speed, v_{rated} , of 10.6 [m/s], the rotational speed, ω_{rated} , is 16.66 [rpm]. In the partial load region ($\omega_r \leq \omega_{rated}$), the rotor speed is controlled so that the maximum power is extracted from the wind turbines.

While $\omega_r > \omega_{rated}$ at the time from 27 [sec] to 70 [sec], the pitch angle is activated to regulate the generator output power. Compared with the PI control method with and without gain scheduling, the generator output power is more ripples than the one in the proposed fuzzy logic control strategy, as shown in Fig. 7(a). Fig. 7(b) illustrates the estimated rotor speed for both the PI controller with and without gain scheduling, and the proposed FLC. In the PI control strategy, with and without gain scheduling, the ripples for the rotational speed are high. Also, the mechanical torque in the proposed method gives the better performance than that in the PI control one, as shown in Fig. 7(c). As shown in Fig. 7 (d), the power conversion coefficient keeps the maximum value at 0.411, before 27 [sec] and after 70 [sec], and it is changeable during the remaining time, when the rotational speed is higher than its rated value. In the full load region, the pitch angle is controlled so that the generator output power is limited to the rated value. It means that the rotational speed is also regulated to be its

rated one. By controlling the pitch angle, as shown in 7 (d), the generator output power and rotational speed are controlled to be rated, at the time from 27 to 70 [sec]. As can be seen in Fig. 7(e), the pitch angle in the proposed FLC, gives lowest ripples, compared with other controllers. Thus, the proposed fuzzy logic control method is better than others.

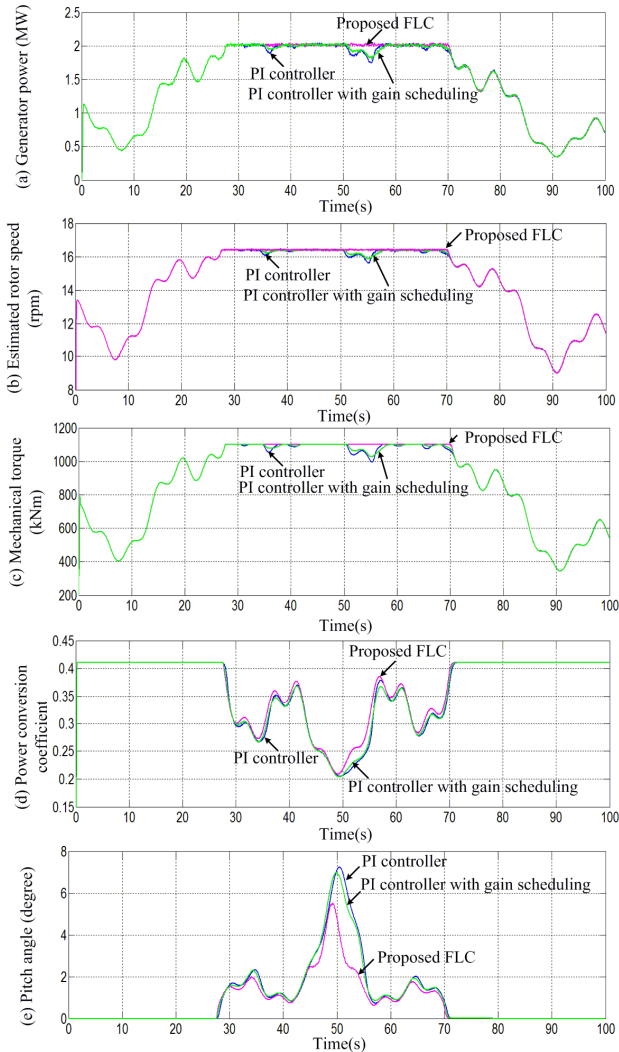


Fig. 7. Simulation results for PI controller with and without gain scheduling, and proposed fuzzy logic controller. (a). Generator power. (b). Estimated rotor speed. (c). Mechanical torque. (d). Power conversion coefficient. (e). Pitch angle (β).

The average generator output powers at the time from 27 s to 70 s (43 s) in the proposed method are 1.548 % and 0.4% higher than that of the PI control method without and with the gain-scheduling. Also, with the same pattern of wind speed, the C_P is increased by 3.019% and 1 %, compared with the C_P in the PI control method without and with gain-scheduling. As a result, more turbine power can be captured.

For pitch angle control, using the PI controller with constant gains does not give a good performance in the different operating points. Meanwhile, for PI controller with gain scheduling, even though it improves the control performance of the nonlinear system, it is not so easy to design the scheduling function updating the controller gains at the different operating points. With FLC, although the membership functions are designed, based on trial and error method, their width of variation is properly adjusted according to the system parameters. Thus, the proposed FLC is more effective for the pitch angle control, regardless to every different operating point.

5 Conclusion

In this paper, a pitch control scheme employing the fuzzy logic control for the PMSG wind turbine system is proposed, which it does not need to know well about the wind turbine dynamics as well as wind speed. A sensorless technique is applied to estimate the rotor speed without any encoder, which makes the system cost lower. The simulation results show that the pitch angle controller using the proposed fuzzy logic control, is more effective than the PI control method.

Appendix

This appendix gives the parameters of wind turbine and generators using for simulation (see Tables 2-3).

Table 2. Parameters of wind turbine for simulation

Rated power	2 [MW]
Blade radius	45 [m]
Air density	1.225[kg/m ³]
Max. power conv. coefficient	0.411
Cut-in speed	3[m/s]
Cut-out speed	25[m/s]
Rated wind speed	10.6[m/s]
Blade inertia	6.3x10 ⁶ [kg.m ²]

Table 3. Parameters of 2[MW] PMSG for simulation

Rated power	2 [MW]
Grid voltage	690 [V]
Stator voltage/frequency	690[V]/60[Hz]
Stator resistance	0.008556[Ω]
d-axis inductance	0.00359[H]
q-axis inductance	0.00359[H]

Acknowledgment. This research is mainly supported by Van Hien University, Ho Chi Minh city, Vietnam and partially supported by the National Key Lab of Digital Control and System Engineering-University of Technology-Vietnam National University Ho Chi Minh city.

References

1. Akhmatov, V.: Analysis of dynamic behavior of electric power systems with large amount of wind power. Ph.D. dissertation, Technical University of Denmark, Kgs. Lyngby, Denmark (2003)
2. Senju, T., Sakamoto, R., Urasaki, N., Funabashi, T., Fujita, H., Sekine, H.: Output power leveling of wind turbine generator for all operating regions by pitch angle control. IEEE Trans. Energy Convers. 21(2), 467–475 (2006)
3. Kamel, R.M., Chaouachi, A., Nagasaka, K.: Wind power smoothening using fuzzy logic pitch controller and energy capacitor system for improvement micro-grid performance in islanding mode. Energy 35(5), 2119–2129 (2010)
4. Hand, M.M.: Variable-speed wind turbine controller systematic design methodology: a comparison of nonlinear and linear model-based designs, NREL report TP-500-25540, National Renewable Energy Laboratory, Golden, CO (1999)
5. Qu, L., Qiao, W.: Constant power control of DFIG wind turbines with supercapacitor energy storage. IEEE Trans. Ind. Appl. 47(1), 359–367 (2009)
6. Muando, E.B., Senju, T., Uehara, A., Funabashi, T.: Gain-scheduled H_∞ control for WECS via LMI techniques and parametrically dependent feedback Part II: Controller design and implementation. IEEE Trans. Ind. Electron. 58(1), 57–65 (2011)
7. Zhang, J., Cheng, M., Chen, Z., Fu, X.: Pitch angle control for variable speed wind turbines. In: Third International Conference on DRPT 2008 (2008)
8. Lee, S.-H., Joo, Y., Back, J., Seo, J.-H., Choy, I.: Sliding mode controller for torque and pitch control of PMSG wind power systems. Journal of Power Electronics 11(3), 342–349 (2011)
9. Nguyen, T.H., Jang, S.-H., Park, H.-G., Lee, D.-C.: Sensorless control of PM synchronous generators for micro wind turbines. IEEE PECON, 936–941 (2008)
10. Van, T.L.: Power quality control of variable-speed wind turbine systems. Ph.D. dissertation, Yeungnam University, Gyeongsan, Korea (2013)
11. El-Hawary, M.E.: Electric power applications of fuzzy systems. Dalhousie Univ. IEEE Press, New York (1998)

Nonlinear Control of PMSG Wind Turbine Systems

Tan Luong Van¹, Trung Hieu Truong², Buu Pham Nhat Tan Nguyen³,
and Tran Thanh Trang^{4,5,*}

¹ Department of Basics, Ho Chi Minh City Electric Power College

² Department of Electrical-Mechanical Engineering, Ho Chi Minh City Electric Power College

³ Department of Power System, Ho Chi Minh City Electric Power College,

554 Ha Huy Giap, District 12, Ho Chi Minh City, Vietnam

{luongees2, trunghieubm}@yahoo.com, buutan2005@yahoo.co.nz

⁴ Department of Electronics and Telecommunication Engineering, Van Hien University,
665-667-669 Dien Bien Phu, District 3, Ho Chi Minh City, Vietnam

trangtt@vnu.edu.vn

⁵ National Key Lab of Digital Control and System Engineering, University of Technology,
Vietnam National University Ho Chi Minh City,
268 Ly Thuong Kiet, District 10, Ho Chi Minh City, Vietnam
trangtranthanh1979@gmail.com

Abstract. This paper proposes a control scheme for the permanent magnet synchronous generator (PMSG) wind power system. The DC-link voltage can be controlled at the machine-side converter (MSC), while the grid-side converter (GSC) controls the grid active power for a maximum power point tracking (MPPT). At the grid fault condition, the DC-link voltage controller is designed using a feedback linearization (FL) theory. For the MPPT, it is also developed for the PMSG wind turbines to continuously generate the maximum electrical power without any sensor. The validity of this control algorithm has been verified by simulation 2-MW PMSG wind turbine system.

Keywords: DC-link voltage, feedback linearization, MPPT, sag, sensorless, PMSG.

1 Introduction

Wind energy has paid much attention in the world due to the energy shortage and environmental concern. Compared with the fixed-speed types, the variable-speed wind turbine (VSWT) systems have a wide speed range of operation and provide 10%-15% higher energy capture from the wind turbine (WT) [1]. Also, the VSWT itself can reduce the stress, and achieve the maximum efficiency under any various wind conditions.

For grid voltage sags, in the conventional control method, the grid-side converter (GSC) may be out of control since the DC-link voltage and active power are

* Corresponding author.

controlled by the GSC and machine-side converter (MSC), respectively. When the grid fault happens, the DC-link voltage is increased due to the continuous operation of WT and generator. In the proposed method, the MSC controls the DC-link voltage, and the GSC controls the active power for the MPPT.

In some cases, the DC-link voltage control and MPPT control methods are not regarded as the nonlinear characteristics of wind power system [2], [3]. By using feedback linearization (FL), a linearized system is obtained and then the DC-link voltage and MPPT control can be designed by the classical linear control theory.

For MPPT, the optimal tip-speed ratio (TSR) method is used for the practical system where the wind speed and turbine speed are needed [4]. This method gives good performance with fast response and high efficiency. However, the performance of the TSR control depends on the anemometer accuracy. Also, these mechanical sensors increase the cost and reduce the reliability of the overall system.

Similarly to the DC-link voltage control, the FL is applied to deal with the nonlinear nature of wind energy conversion system (WECS). Also, a novel sensorless control is proposed for PMSG wind turbine system, without wind speed. First, the rotor speed is estimated without any delay problem. Second, based on the generator torque and estimated rotor speed, the turbine torque is obtained. Third, the wind speed is estimated with the information of the estimated turbine speed and turbine torque by using support vector regression (SVR). Then, the estimated wind speed is used to determine the optimal turbine speed reference. Based on the proposed estimation algorithms, a sensorless control is developed for PMSG wind turbines (WTs) to continuously generate the maximum electrical power without using any wind speed or rotor position sensors. To verify the effectiveness of the proposed algorithm, the simulation results for the 2-MW PMSG wind turbine system are provided.

2 Modeling of Wind Turbine Systems

2.1 Modeling of Wind Turbines

The output power of WTs (P_t) is determined as [1]

$$P_t = 0.5 \rho \pi R^2 V^3 C_p(\lambda, \beta) \quad (1)$$

where ρ is the air density [kg/m^3], R is the radius of blade [m], V is the wind speed [m/s], and $C_p(\lambda, \beta)$ is the power conversion coefficient which is a function of the TSR ($\lambda=R\omega/V$) and the pitch angle (β).

The $C_p(\lambda, \beta)$ is expressed as

$$C_p(\lambda, \beta) = c_1(c_2/\wedge - c_3\beta - c_4\beta^{c_5} - c_6)\exp(-c_7/\wedge) \quad (2)$$

where $1/\wedge = 1/(\lambda + 0.08\beta) - 0.035/(1 + \beta^3)$ and c_1-c_7 are the constants [5].

The turbine torque can be expressed as

$$T_t = 0.5 \rho \pi R^3 V^2 C_p(\lambda, \beta)/\lambda \quad (3)$$

The WT is characterized by ($P_t - \omega_m$) and ($C_p - \lambda$) curves as shown in Fig. 1. In Fig. 1(b), the power coefficient, C_{pmax} , has its maximum value at the optimal TSR, λ_{opt} . Thus, to maximize the C_p , the WECS must operate at the λ_{opt} . However, when the wind speed changes, the TSR is out of the optimal value. To keep the optimal TSR, the rotational speed needs to be adjusted by the control system.

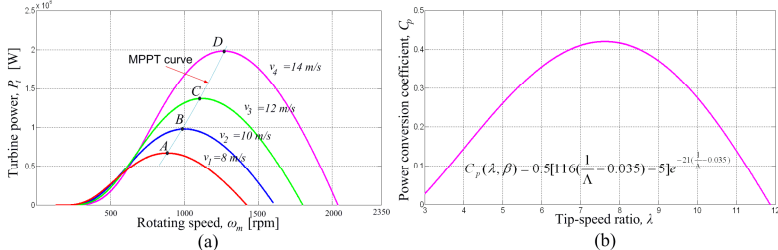


Fig. 1. Wind turbine characteristics. (a) $P_t - \omega_m$ curve. (b) $C_p - \lambda$ curve.

2.2 Modeling of PMSG

Fig. 2 shows the d - q equivalent circuits of the PMSG. The stator voltage equations of the PMSG are expressed in the synchronous d - q coordinates as [6]

$$v_{ds} = R_s i_{ds} + L_s di_{ds}/dt - \omega_r L_d i_{qs} \quad (4)$$

$$v_{qs} = R_s i_{qs} + L_s di_{qs}/dt + \omega_r L_d i_{ds} + \omega_r \lambda_f \quad (5)$$

where i_{ds} and i_{qs} are d , q -axis stator currents, R_s and L_s are stator resistance and inductance, L_d and L_q are d , q -axis inductance, λ_f is magnet flux, and ω_r is electrical angular speed.

For the generator with surface-mounted permanent magnets, d - and q -axis inductances are the same. Then, the electromagnetic torque T_e is expressed as

$$T_e = (3p/4)\lambda_f i_{qs} \quad (6)$$

where p is the number of poles.

The output electrical power can be calculated as

$$P_e = 1.5(v_{qs} i_{qs} + v_{ds} i_{ds}) \quad (7)$$

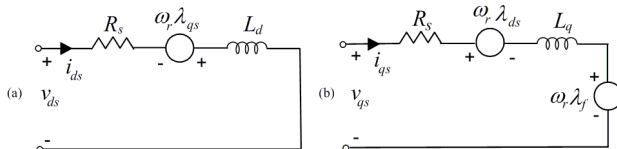


Fig. 2. Equivalent circuits of PMSG. (a) d-axis. (b) q-axis.

2.3 Modeling of the Shaft System

The turbine torque with one-mass modeling of WT systems is expressed as [1]

$$J_t d\omega_t / dt = T_t - B_t \omega_t \quad (8)$$

where J_t is the combined inertia of the turbine and generator, B_t is the damping coefficient of turbine, ω_t is the turbines speed of and T_g is the generator torque.

3 PMSG Control System

3.1 Nonlinear Modeling

To design the controllers, the dynamic characteristics of WTs in the PMSG wind power system are considered. Neglecting the converter loss, the generator power, P_g , and the DC-link capacitor power, P_{cap} , can be expressed as

$$P_g = P_t - J \omega_m d\omega_m / dt - P_{g,loss} \quad (9)$$

$$P_{cap} = CV_{dc} dV_{dc} / dt = P_g - P_{grid} \quad (10)$$

where J is the moment of inertia, P_{grid} is the grid power, $P_{g,loss}$ is the generator loss, V_{dc} is the DC-link voltage, C is the DC-link capacitor.

(9) and (10) are linearized using a FL theory, described in the next section.

3.2 Feedback Linearization

An single-input and single-output (SISO) nonlinear system is expressed as [7]

$$\dot{x} = f(x) + g(x)u \quad (11)$$

$$y = h(x) \quad (12)$$

where x is the state vector, u is the control input, y is the output, f and g are the smooth vector fields, respectively, and h is the smooth scalar function.

The nonlinear equations in (9) and (10) are expressed in the form of (11) as

$$\begin{bmatrix} \dot{V}_{dc} \\ \dot{\omega}_m \end{bmatrix} = \begin{bmatrix} -P_{grid} / CV_{dc} \\ P_t / J \omega_m - P_{g,loss} / J \omega_m \end{bmatrix} + \begin{bmatrix} 1 / CV_{dc} \\ -1 / J \omega_m \end{bmatrix} \cdot P_g \quad (13)$$

For the linearization, a relation between input and output should be delivered. So, the output of the system is obtained as [7]

$$\dot{y} = A(x) + E(x)u \quad (14)$$

where

$$A(x) = \begin{bmatrix} A_1(x) \\ A_2(x) \end{bmatrix} = \begin{bmatrix} -P_{grid}/CV_{dc} \\ P_t/J\omega_m - P_{g,loss}/J\omega_m \end{bmatrix} \quad \text{and} \quad E(x) = \begin{bmatrix} E_1(x) \\ E_2(x) \end{bmatrix} = \begin{bmatrix} 1/CV_{dc} \\ -1/J\omega_m \end{bmatrix}$$

If a control input u is chosen as

$$u = E^{-1}(x)[-A(x) + v] \quad (15)$$

where v is the equivalent control input to be specified. The resultant dynamics become linear as

$$\dot{y} = v \quad (16)$$

To eliminate the tracking error in the presence of parameter variations, the new control input with an integral control is given by

$$v = \dot{y}_{ref} - k_1 e - k_2 \int e dt \quad (17)$$

where $e = y - y_{ref}$, y_{ref} is the tracking reference, and k_1 and k_2 are the controller gains. The controller gains are determined by a pole placement technique [8].

3.3 Control of Machine-Side Converter for Constant DC Voltage

The operation of the GSC is directly affected by grid voltage unbalance, where the power delivered to the grid is restricted. In this duration, the WT and generator keep operating as if it is in normal condition. Thus, in the DC-link, power delivered from the generator side may increase the DC-link voltage excessively high. Differently from the conventional control of the AC/DC converter, the DC-link voltage for back-to-back converters is controlled by the MSC.

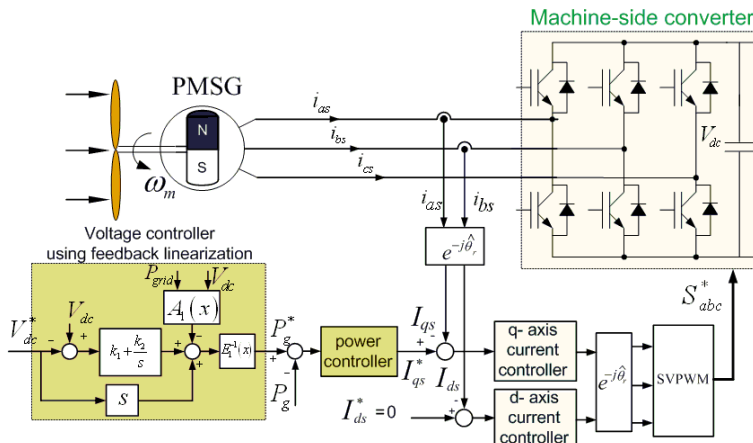


Fig. 3. Control block diagram of the machine-side converter

From (15) to (17), the block diagram of the proposed nonlinear DC-link voltage control is partially shown in Fig. 3. As can be seen, the control structure of the MSC consists of the outer power control loop and the inner current control loop.

3.4 Control of Grid-Side Converter for MPPT

In this section, the turbine torque and turbine speed are firstly estimated. Next, the wind speed is estimated to generate the optimal turbine speed reference. Finally, the MPPT method based on FL is applied to achieve the maximum power.

3.4.1 Turbine Torque Estimation

The wind speed estimation algorithm needs the information of the turbine torque. The turbine torque can be estimated in the discrete time form as:

$$\hat{T}_t = J_t \frac{\hat{\omega}_t(t) - \hat{\omega}_t(t-1)}{T_s} + T_g + B_t \hat{\omega}_t \quad (18)$$

3.4.2 Turbine Speed Estimation

A sensorless control method based on rotor flux observer and induced EMF is employed [6]. The block diagram of the generator speed estimation is shown in Fig. 4. As can be seen, the stator flux, λ_s^s , is obtained. Then, a high-pass filter, whose cut-off frequency, ω_0 , is selected to be one-third of the generator rated speed, is used to solve the drift and the saturation problems due to the integration. Also, to eliminate a delay problem due to the filter, the magnitude component, $\sqrt{\hat{\omega}_p^2 + \omega_0^2} / \hat{\omega}_p$, and phase component, $e^{(\phi-\pi/2)}$, are multiplied with the transfer function, λ_s/v_s , for compensation, in which $\phi = \arctan(\hat{\omega}_p/\omega_0)$ is the phase angle. Next, the flux linkage λ_f , is calculated from the d, q-axis rotor flux, λ_{df}^s and λ_{qf}^s , from which the rotor position angle is obtained as [6]

$$\hat{\theta}_r = \arctan\left(\lambda_{qf}^s / \lambda_{df}^s\right) \quad (19)$$

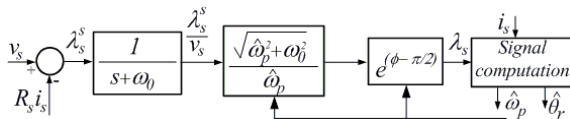


Fig. 4. Block diagram of generator speed estimation

By integrating the term of $\cos(\hat{\omega}_p t)$ in $[t_0, t_1]$ and calculating the approximate area for the integration, $\int_{t_0}^{t_1} \cos(\hat{\omega}_p t) dt$, the estimated speed is obtained as [6]

$$\hat{\omega}_p = \frac{\sin \hat{\theta}_{r1} - \sin \hat{\theta}_{r0}}{(\cos \hat{\theta}_{r1} + \cos \hat{\theta}_{r0}) T_s / 2} \quad (20)$$

where $\hat{\theta}_{r_1} = \hat{\omega}_p t_1$, $\hat{\theta}_{r_0} = \hat{\omega}_p t_0$, and T_s is a sampling time.

To reduce the speed ripple at the high frequencies, a low-pass filter is applied, which gives the average generator speed, $\hat{\omega}_r$. The estimated turbine speed, $\hat{\omega}_r$, can be directly obtained from $\hat{\omega}_r$.

3.4.3 Wind Speed Estimation

Based on SVR, the training samples for inputs (turbine torque and speed), output (wind speed) and kernel function (radial bias function) should be initially selected. In this paper, turbine torque ($T_{t\leftarrow}$) and turbine speed ($\omega_{t\leftarrow}$) are both estimated, instead of being measured by sensors. Parameters C and ε are selected by users based on a priori knowledge. During the off-line training, kernel function $K(x_i, x_j)$ is computed for all support vectors (SVs). Then the Lagrange multipliers (LMs) α_i, α_i^* are determined [9]. Only the training samples whose LMs $(\alpha_i - \alpha_i^*)$ are non-zero are really related to the solution, and these samples are considered as SVs. The bias term b is computed as [9]

$$b = \text{mean} \left(\sum_{i=1}^n \{y_i - (\alpha_i - \alpha_i^*) K(x_i, x_i)\} \right) \quad (21)$$

Hence, (22) is used online for any inputs (estimated turbine torque and turbine speed) to compute the output (wind speed), \hat{V} , as shown in Fig. 5.

$$\hat{V} = \sum_{i=1}^n (\alpha_i - \alpha_i^*) \cdot K(x_i, x) + b \quad (22)$$

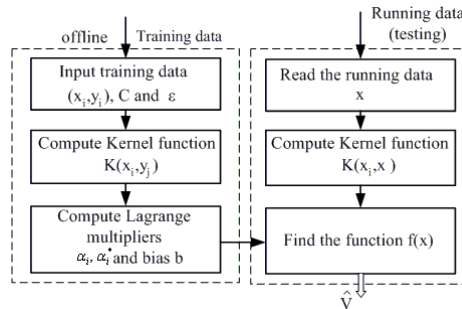


Fig. 5. Flowchart of wind speed estimation using SVR

3.4.4 Grid-Side Converter Control

As shown in Fig. 6, both the rotor position and speed are firstly estimated. Then, the estimated rotor position, turbine speed, turbine torque and wind speed lead to a sensorless control for the PMSG wind turbine. Next, the estimated wind speed is used to generate the optimal rotor speed reference. The speed control tracks the optimal turbine speed reference to maintain the optimal TSR.

From (15) to (19), the block diagram of the proposed nonlinear speed control is partially shown in Fig. 6. By using FL, the power is well captured from the WT. As can be seen, the control structure of the GSC consists of the inner current control loop and the outer speed control loop.

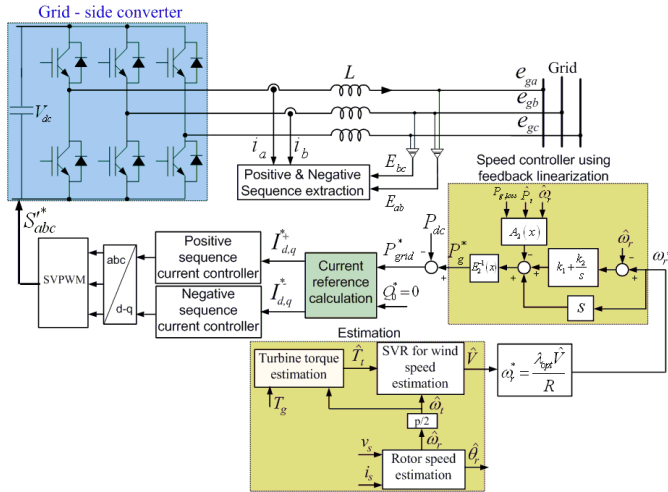


Fig. 6. Control block diagram of the grid-side converter

3.5 Simulation Studies

To verify the effectiveness of the proposed method, the simulation has been carried out using PSIM software for a 2-MW PMSG wind turbine. For WT: $R = 45.7[\text{m}]$; $\rho = 1.225[\text{kg}/\text{m}^3]$; $\lambda_{opt} = 8$. For the PMSG: the rated power is 2 [MW], $R_s=0.00856[\Omega]$; $L_d=L_q=0.00359[\text{H}]$; $\lambda_f=5.15[\text{V}\cdot\text{s}]$; $p=120$; and $J=48000[\text{kg}\cdot\text{m}^2]$.

Fig. 7 shows the system performance for the proposed MPPT method, in which the grid is assumed to be normal for easy investigation. Figs. 7 (a)-(d) illustrate the actual and estimated values of wind speed, turbine speed, turbine torque, and turbine power. The results show that the proposed algorithms accurately estimate these quantities, which are employed for real-time control of the PMSG and converters. With the change of the wind speed, the power coefficient varies, as shown in Fig. 7(e). In Fig. 7(f), the turbine speed is controlled to track its reference with high accuracy by using the estimated rotor speed (Fig. 8(a)) and rotor position (Fig. 8(b)). The tip-speed ratio varies in a small range around the optimal TSR of 8, which is illustrated in Fig. 7(g). The errors between the real and optimal tip-speed ratios are caused by fast wind speed variations and relatively slow responses of the WT generator system. This result demonstrates that the WT generator is correctly controlled to generate the maximum power by using the estimated wind speed. By applying the FL at the MSC, the generator is controlled to keep the DC-link voltage constant, of which variation is less than 1%, as shown in Fig. 7(h).

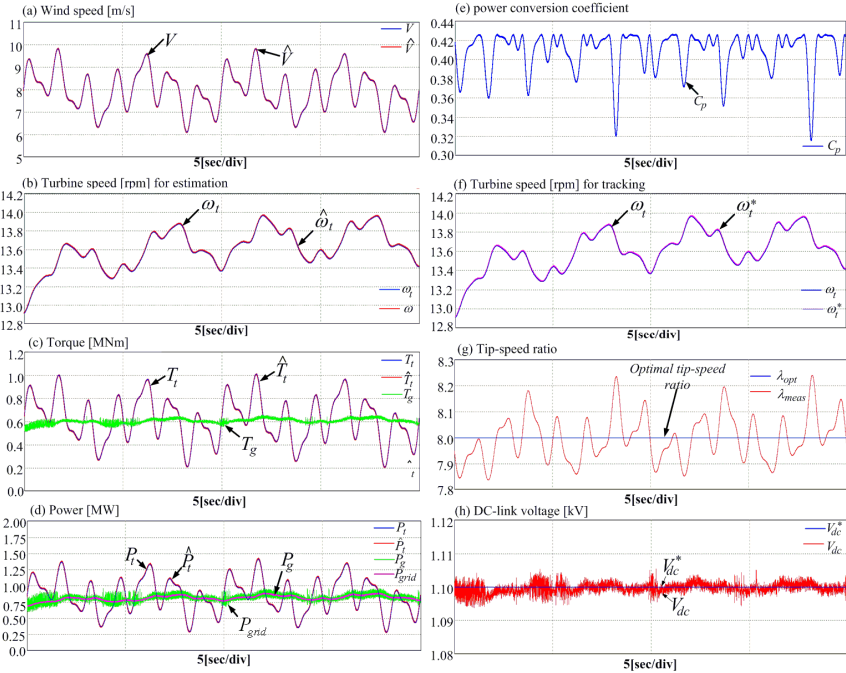


Fig. 7. System performance applying MPPT at the normal grid condition: (a). Wind speed and its estimated value. (b) Turbine speed and its estimated value. (c) Generator, turbine torque and its estimated value. (d) Grid power, generator power, turbine power and its estimated value. (e) Turbine speed reference (f) Power conversion coefficient. (g) Optimal TSR and its measured value. (h) DC-link voltage.

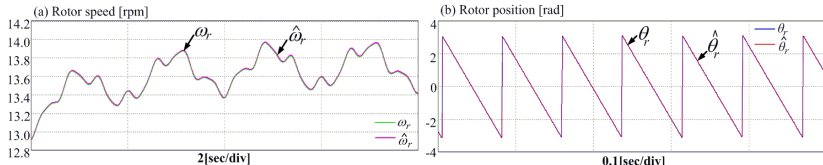


Fig. 8. Rotor speed estimation. (a) Estimated ($\hat{\omega}_r$) and actual (ω_r) rotor speed. (b) Estimated ($\hat{\theta}_r$) and actual (θ_r) rotor position.

Fig. 9 shows the system performance for a grid unbalanced voltage sag, where the wind speed is assumed to be constant (8[m/s]) for easy examination. The fault condition is 70% sag in the grid A-phase voltage for 1 sec (60 cycles), which is between the point (a) to (b) as shown in Fig. 9(a). Fig. 9(b) shows the magnified grid voltages for 6 cycles just before and after fault. The positive- and negative-sequence d-q axis voltages are shown in Fig. 9(c). Due to the grid unbalanced voltage sag, the positive-sequence q-axis voltage is reduced and the negative-sequence d-q voltage

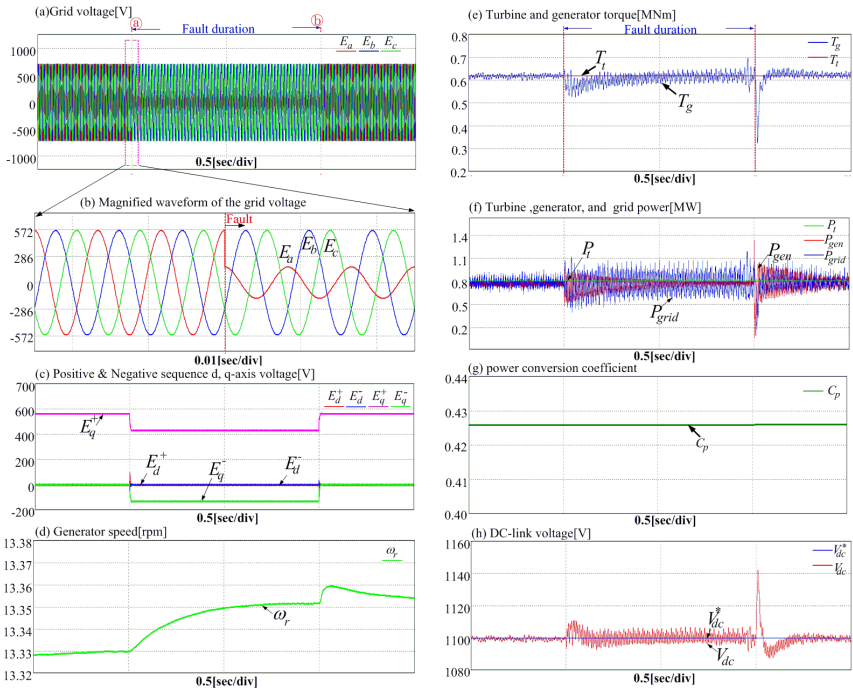


Fig. 9. Wind generation performance for grid phase-A voltage sag (70%). (a) Grid voltage. (b) Magnified waveform of the grid voltage. (c) Positive and negative sequence d-q axis voltage. (d) Generator speed. (e) Turbine and generator torque. (f) Turbine, generator and grid power. (g) Power conversion coefficient. (h) DC-link voltage.

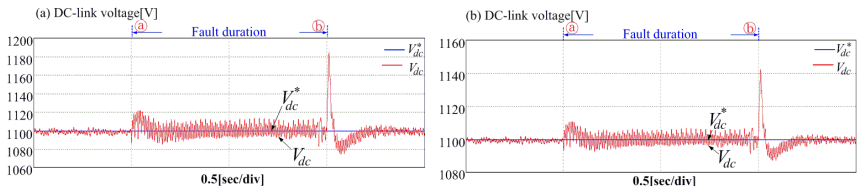


Fig. 10. Performance of DC-link voltage control: (a) PI control. (b) FL control

components appear. During the grid fault, grid and generator powers have high ripples, as shown in Fig. 9(f) and the generator speed is increased as shown in Fig. 9(d). The turbine power is not changed since the turbine speed is controlled at the optimal value for MPPT. Likewise, the generator torque has ripple, as illustrated in Fig. 9(e), where turbine torque is constant. Fig. 9(g) shows the C_p which is almost not changed during the fault. In this voltage event, the variation of the DC-link voltage is controlled within 3.6 [%]. Fig. 10 shows the DC-link voltage responses for the two controllers (PI control and FL control). The proposed method gives faster transient response and lower overshoot.

4 Conclusions

This paper proposed the control strategies of the variable speed WT with PMSG for the grid voltage sags and for the MPPT. At the grid fault, a method is based on the DC-link voltage control at the MSC, using FL technique. With this technique, the MPPT strategy is developed to control the grid power at the GSC without any sensors. The validity of the control algorithm has been verified by simulation results for 2MW PMSG wind power system. The simulation results have shown that the DC-link voltage has been controlled within less than 4[%] for 70% drop of the grid voltage for 1 second and the maximum error of the TSR is obtained to be 0.25 for the MPPT.

Acknowledgment. This research is mainly supported by Van Hien University, Ho Chi Minh city, Vietnam and supported in part by the National Key Lab of Digital Control and System Engineering-University of Technology-Vietnam National University Ho Chi Minh city.

References

1. Akhmatov, V.: Analysis of dynamic behavior of electric power systems with large amount of wind power. Ph.D. dissertation, Technical University of Denmark, Kgs. Lyngby, Denmark (2003)
2. Hansen, A.D., Michalke, G.: Multi-pole permanent magnet synchronous generator wind turbines' grid support capability in uninterrupted operation during grid faults. *IET Renew. Power Gener.* 3(3), 333–348 (2009)
3. Kim, K.-H., Van, T.L., Lee, D.-C., Song, S.-H., Kim, E.-H.: Maximum output power tracking control in variable-speed wind turbine systems considering. *IEEE Trans. Ind. Electron.* 60(8), 3207–3217 (2013)
4. Abo-Khalil, A.G., Lee, D.-C., Seok, J.-K.: Variable speed wind power generation system based on fuzzy logic control for maximum output power tracking. In: Proceedings of 2004 IEEE 35th Annual Power Electronics Specialists Conference, PESC 2004, vol. 3, pp. 2039–2043 (2004)
5. Lubosny, Z.: Wind turbine operation in electric power system, ch. 5. Springer, Heidelberg (2003)
6. Nguyen, T.H., Jang, S.-H., Park, H.-G., Lee, D.-C.: Sensorless control of PM synchronous generators for micro wind turbines. In: Proc. of IEEE PECON, pp. 936–941 (2008)
7. Slotine, J.J.E., Li, W.: Applied nonlinear control, pp. 207–271. Prentice-Hall, Englewood Cliffs (1991)
8. Lee, D.-C., Lee, G.-M., Lee, K.-D.: DC-bus voltage control of three-phase ac/dc PWM converters using feedback linearization. *IEEE Trans. Ind. App.* 36(3), 826–833 (2000)
9. Van, T.L., Nguyen, T.H., Kim, K.-H., Lee, D.-C.: SVR-based flicker estimation for wind power systems. In: IPEC Proc., pp. 1824–1829 (2010)

Optimization of Water Cooling for a Converter

Roman Sprlak and Petr Chlebis

VSB – Technical University of Ostrava, Faculty of Electrical Engineering
and Computer Science, Department of Electronics, Ostrava, Czech Republic
{roman.sprlak,petr.chlebis}@vsb.cz

Abstract. In construction of converters, there are still increasing demands for smaller dimensions of these converters. This fact leads to increased density of power dissipation on one square mm of a heat sink. The heat raised by this effect has to be removed and the structure of the heat sink must be properly designed to deal with this problem. This article is based on this topic and also it is focused to analysis of thermal field of the heat sink. The analysis, which was executed by multi-physics software with finite elements methods, counts with various placements of power modules. To execute this analysis, 3D models were created in 3D CAD software, transported to multi-physics software and described with other parameters, which specify the whole heat sink to details. In simulations, we counted with changes in initial temperature, various placement of power modules and changes in flow rate of cooling water. Simulations were performed without power modules. Based on previous steps, simulation with power modules was performed to compare the influence of the power modules to thermal field on a heat sink. Results of these simulations can serve to optimization in construction of converters before real construction.

Keywords: heat sink, thermal field, thermal analysis.

1 Introduction

In industry, the water cooling is preferred over air cooling. The design of a power converter consists in selection of a suitable heat sink. If we choose wrong heat sink, over-heat will occur or, in the worst case, the whole converter will be destroyed. The aim of this paper is thermal analysis of a water heat sink. Semikron WP16 heat sink was chosen for the analysis. This heat sink is available in various lengths. Models were created in 3D CAD software. Simulations of steady power dissipation with steady flow rate of cooling medium were performed on models without power modules. The results of these simulations for different lengths and flow rates are shown in figures 2 to 6. [1, 2, 3, 4].

2 Definition of Power Dissipation

The power dissipation has to be determined before the thermal simulation. The definition of power loss was performed from following variables.

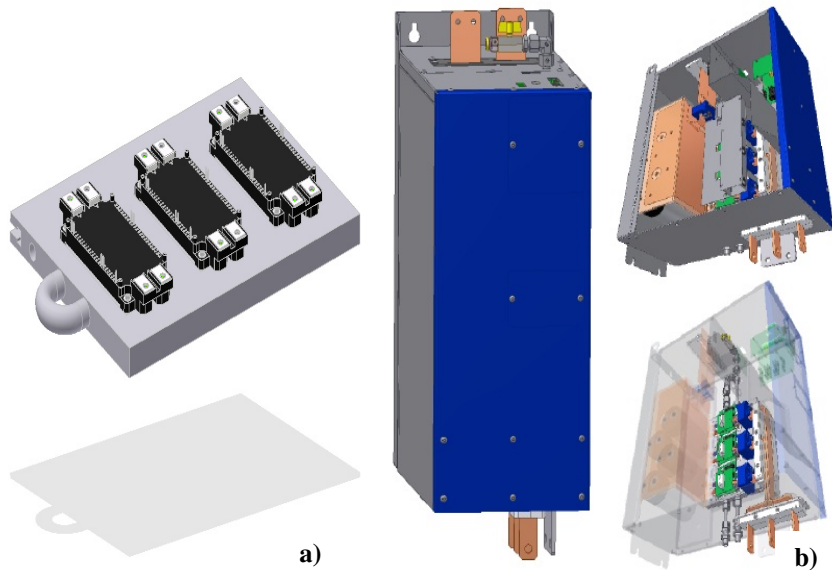


Fig. 1. (a) Water cooling WP16 with power modules and (b) power converter [8]

2.1 Effective Value of Line Voltage Inverter

Calculation of effective voltage is described in [5, 7, 9, 10]. If this literature is used so called modulation factor, which is defined in equation (1):

$$M = \frac{U_{AB}}{U_d} \quad (1)$$

Where U_{AB} is effective line voltage and U_d is dc-link voltage. The effective voltage value is calculated from the equation (5):

$$U_{ABef} = U_d \sqrt{\frac{2}{\pi} M} = 0,7979 \cdot U_d \cdot \sqrt{M} \quad (2)$$

2.2 Mean Current of the Transistor and the Diod

Collector current of transistor and zero diode has unipolar pulse shape. The general calculation of the mean value of this signal is as follows:

$$I_{avg} = \frac{1}{T} \int_0^{T_1} i(t) \cdot s(t) dt \quad (3)$$

The function $i(t)$ specifies the height of the envelope function and $s(t)$ instantaneous impulses of duty cycle. [9]

$$I_{avg} = I_{mA} \left(\frac{1}{2\pi} + \frac{M}{4\sqrt{3}} \cdot \cos \varphi \right) \quad (4)$$

2.3 The Effective Current Value of a Transistor and Diodes

For unipolar current pulses can be used general expression:

$$I_{ef} = \sqrt{\frac{1}{T} \int_0^{T_1} i^2(t) \cdot s(t) dt} \quad (5)$$

2.4 Losses Caused by the Current Conduct

The calculation of current losses can be done by:

$$P_{cond} = U_p \cdot I_{avg} + R_d \cdot I_{ef}^2 \quad (6)$$

U_p is the threshold voltage and R_d is dynamic resistance. This formula is the same as for the calculation of the transistors and for the calculation of diodes.

2.5 Switching Losses

Switching power can be determined from the relation: [9,10]

$$P_{sw} = \frac{1}{T} \int_0^{T_1} W_{sw} [i_z(t)] f(t) dt \quad (7)$$

In the case when the frequency and energy are constant, equation is adapted to the form:

$$W_{sw} = \frac{E_{max}}{I_{Cnom}} \cdot I_z \quad (8)$$

I_z is the load current. E_{max} , E_{on} and E_{off} are catalog data, which indicate the energy loss. I_{Cnom} is the current of the transistor. We define the current utilization factor of the transistor by following:

$$K = \frac{I_{Zmax}}{I_{Cnom}} = \frac{I_{mA}}{I_{Cnom}} \quad (9)$$

If the carrier frequency in equation (7) is constant, we can modify this equation to form [9]:

$$E_{max} = W_{sw} [I_{Cnom}] = E_{on} + E_{off} \quad (10)$$

$$P_{sw} = \frac{1}{\pi} \cdot f \cdot E_{max} \cdot \frac{I_{mA}}{I_{Cnom}} \quad (11)$$

2.6 Total Losses in the Inverter

The total loss P_T of the transistor is the sum of losses caused by the leadership of current and switching losses.

3 Modeling of Thermal Processes

Modeling of thermal processes is performed by program, which works with finite element analysis. Size and number of the elements are the most significant factors, which determine size and number of linking points of 3D model on which calculations are performed. Thus, more points mean more precision. For modeling of complex systems or for the reducing the simulation time, it is possible to split the 3D model into several parts. These parts are described by these parameters: [1, 2, 3]

- Temperature $T_{v,k} = {}^{\circ}\text{C}$
- Thermal capacity $C_n = \text{Ws.K}^{-1}$
- Lost power $P_n = \text{W}$
- Thermal conduction A_{mm} , $[A_{mm}] = \text{W.K}^{-1}$

4 3D Model of the Heat Sink

We can split the 3D model into several parts. On these parts we can define thermal capacity, thermal resistance a thermal inductance. On each part were not the same conditions, because in the area under power modules have the highest temperature. This heat was conducted by aluminum material dissipated to the surroundings.

5 Simulation Results

The analyses were performed to analyze thermal behavior of water cooling of IGBT modules. IGBT modules were operated with constant load. Power dissipation was set from simulation on 700W per module. The size of the model was variable depending on size of the heat sink. Distribution of power modules was symmetrical to use the whole thermal capacity of the heat sink. Water was used as a cooling medium with temperature set to 30°C . For simulations was no environment considered. This fact simulates the most negative scenario, where all of dissipation must be accumulated in the heat sink or dissipated away by water. [3, 4, 5, 6, 7]

The first simulation is performed for the heat sink with dimensions 300x225x20mm. Space between the modules is 35mm and their distance from the edge of the heat sink is 22mm. Starting temperature of the heat sink is 30°C and flow rate of the cooling medium is set to 6 and 8 l.s⁻¹.

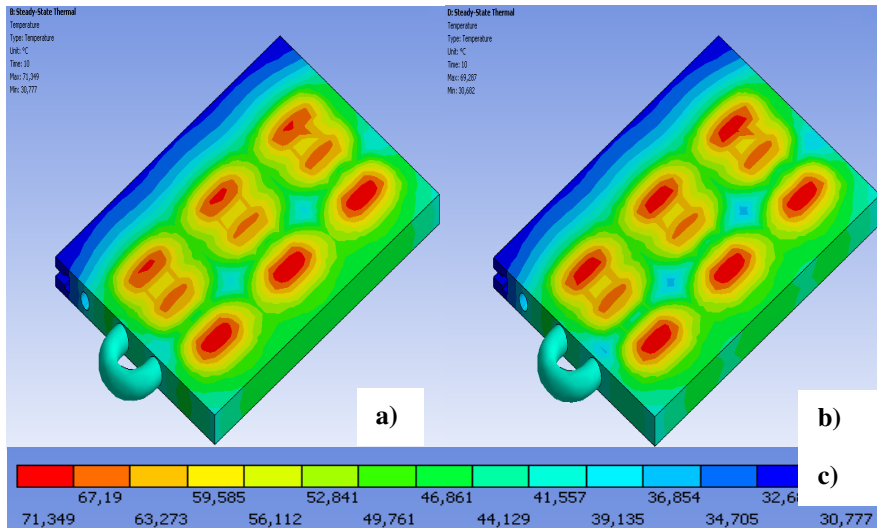


Fig. 2. (a) Thermal field at initial temperature 30°C and flow rate 6 l.s⁻¹ (b) Thermal field at initial temperature 30°C and flow rate 8 l.s⁻¹ (c) Temperature scale

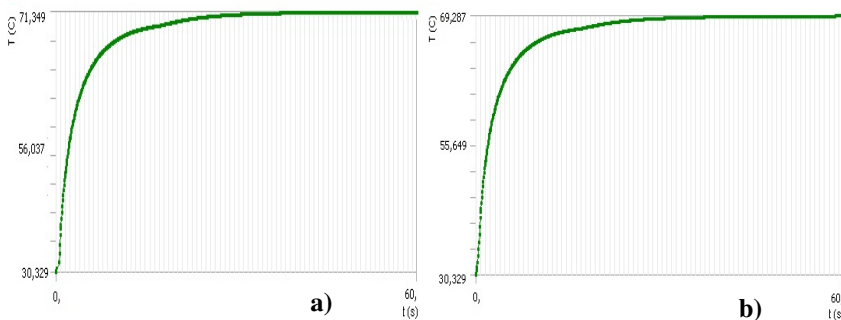


Fig. 3. (a) Temperature at initial temperature 30°C and flow rate 6 l.s⁻¹ (b) Temperature at initial temperature 30°C and flow rate 8 l.s⁻¹

The second simulation is performed for dimensions 320x225x20mm. Space between the modules is now 42 mm and distance from the edge is 25mm. Starting temperature is also set to 30°C and the flow rate of cooling medium have the same values as in the first simulation. The results of this simulation are shown in figures 4(a, b) and 5(a, b).

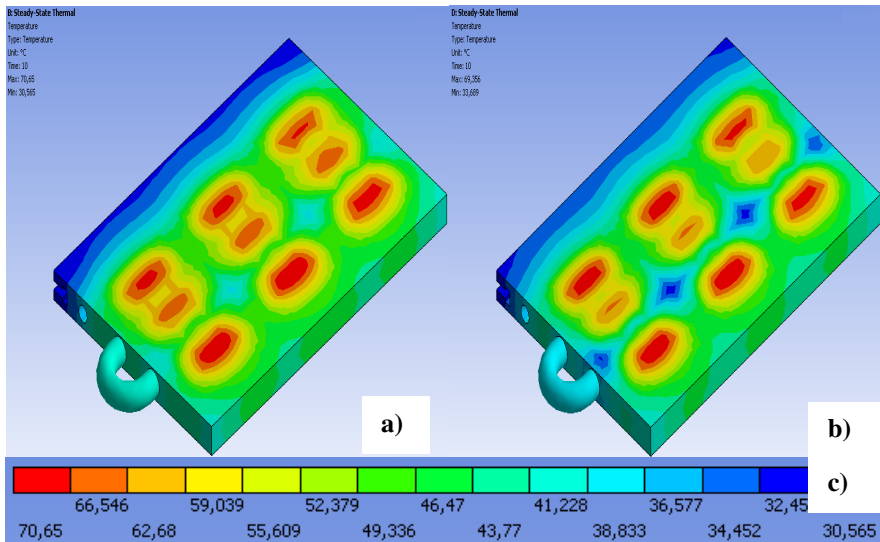


Fig. 4. (a) Thermal field at initial temperature 30°C and flow rate 6 l.s^{-1} (b) Thermal field at initial temperature 30°C and flow rate 8 l.s^{-1} (c) Temperature scale

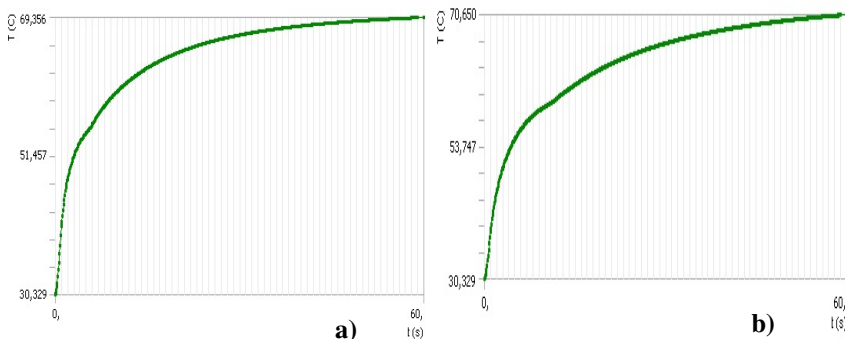


Fig. 5. (a) Temperature at initial temperature 30°C and flow rate 6 l.s^{-1} (b) Temperature at initial temperature 30°C and flow rate 8 l.s^{-1}

6 Thermal Field with Consideration of Power Modules

This simulation was created to determine the influence of power modules to thermal field distribution. The dimensions of power modules are 122x62 mm. Modules are not created in detail to simplify the simulation. Simulation was performed using flow 8 l.s^{-1} and stating temperature 30°C . Power dissipation was concentrated on the whole bottom side of the modules, because we don't know the module from the inside.

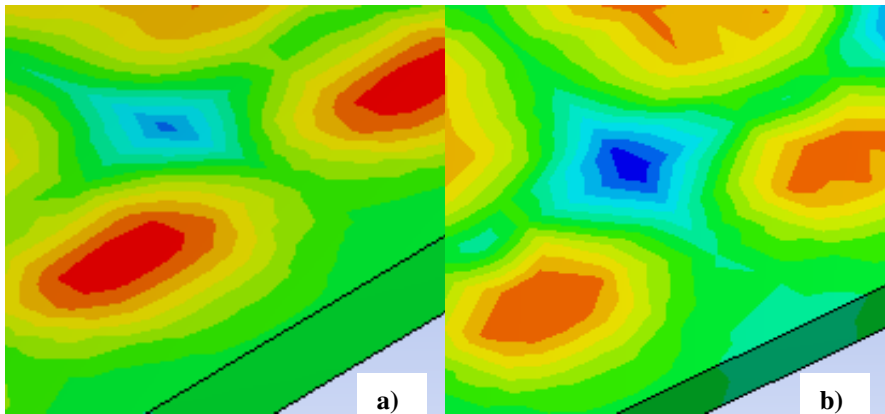


Fig. 6. (a) Detail of thermal field between power modules (heat sink has 300mm). (b) Detail of thermal field between power modules (heat sink has 320mm).

If we look at the results in detail (as shows figures 6 (a) and (b)), we can see considerable differences in temperature at this small parts of the heat sink. This difference between the hottest and the coldest spot is nearly 20°C at the heat sink with length 300mm, and almost 28°C at heatsink with length 320mm. This different temperature at this small place can result in changes of the heat sink structure followed by its deformations.

7 Evaluations of the Results

Simulations were set with omission of ambient environment, which simulates the worst scenario. All dissipation has to be taken away by the heat sink. From the results we can see that the thermal fields under the power modules are separating with increasing distance between them. From the other results we can compare maximal temperatures of the heat sink when we change the flow rate of cooling medium. These results are shown in the table.

Table 1. Simulation results

Dissipation power	Length heat sink	Initialization temperature	Max temperature	Flow rate cooling medium
P_{tot} (W)	d (mm)	t_a ($^{\circ}\text{C}$)	T_{tot} ($^{\circ}\text{C}$)	Q (l.s^{-1})
3x700	300	30	71,349	6
		30	69,287	8
3x700	320	30	70,650	6
		30	69,356	8

8 Conclusions

The aim of this paper was to show changes in maximal temperature of the heat sink when changing the length of it. The simulations were performed to determine the distribution of thermal field. Every simulation counts with other length of the heat sink and flow rate of a cooling medium. Table 1 shows the results from these simulations. If we change length of heat sink used in simulations by nearly 7 %, the maximal temperature changes only by 2 %. Next simulation was performed to determine the cold spot on the heat sink using heat sink with length 300 and 320 mm. From results of this simulation we can see problematic spot on the heat sink, which can cause deformations of the heat sink.

Acknowledgments. The research described in this paper was supported by these projects:

- SGS project SP2013/80 – Utilizing of Modern SiC Components for MF – Power Semiconductor Converters.
- ENET CZ.1.05/2.1.00/03.0069 – Energy Units for Utilization of non Traditional Energy Sources.

This research was supervised by prof. Ing. Petr Chlebiš, CSc from Department of Electronics, VSB - TU Ostrava.

References

- [1] Jaluria, Y., Torrance, K.E.: Computational Heat Transfer. Taylor and Francis, New York (2003) ISBN 1-56932-477-5
- [2] Madeci, E., Guven, I.: The Fienite Element Method and Applications in Engineering Using ANSYS. Springer, New York (2006) ISBN 0-387-28289-0
- [3] Salem, T.E.: Thermal Performance of Water-Cooled Heat Sinks: A Comparison of Two Different Designs. In: 2005 IEEE Twenty First Annual IEEE Semiconductor Thermal Measurement and Management Symposium, March 15-17, p. 264 (2005) ISSN : 1065-2221, Print ISBN: 0-7803-8985-9
- [4] Bolte, E., Kipp, B.: Transient Thermal Field Modelling. In: Proceedings of the International Conference on Electrical Machines, IEEE 2008, Paper ID 873 (2008) ISBN 978-1-4244-1736-0
- [5] Chlebis, P., Havel, A., Vaculik, P., Pfof, Z.: Modern Instruments for increasing the Efficiency of the Energy Transfer in Electric Vehicles. In: 14th EPE-PEMC 2010 International Power Electronics and Motion Control Conference, Republic of Macedonia, September 6-8, vol. 14, pp. 89–93 (2010) ISBN 978-1-4244-7854-5
- [6] Chlebis, P., Dudek, J.: Comparison of Power Losses and Quality of Output Voltage from Different Types of Inverters. In: 35th Annual IEEE Power Electronics Specialists Conference, Achen, Germany, vol. 1-6, pp. 3120–3126 (2004) ISBN 0-7803-8399-0
- [7] Osmancik, L., Polak, M., Simonik, P., Hrdina, L., Skotnica, P., Palacky, P.: Digital Signal Processor TMS320F2812 and its Application in Electric Drives. In: International Conference on Applied Electronics 2006, Pilsen, Czech Republic, pp. 129–132 (2006) ISBN 978-80-7043-442-0

- [8] Tvrdoň, M.: Design and Construction Power Converter with the Aid of 3D CAD System. In: Wofex 2012, Ostrava, Czech Republic, pp. 190–195 (2012) ISBN 978-80-248-2769-8
- [9] Valsa, J., Patočka, M.: Computer Simulation of Power Electronic Converters with Ideal Switches. In: Computer Simulation of Power Electronic Converters with Idea.Košice. SK.The Technical University of Košice. p. 398 ISBN: 80-967249-
- [10] Brandstetter, P., Chlebis, P., Simonik, P.: Active Power Filter with Soft Switching. International Review of Electrical Engineering. IREE 5(6), 2516–2526 (2010) ISSN 1827- 6660

Approximate 2DOF Digital Controller for Interleaved PFC Boost Converter

Yuto Adachi¹, Yohei Mochizuki¹, Kohji Higuchi¹, and Kosin Chamnongthai²

¹ The University of Electro-Communications 1-5-1,
Chofu-ga-oka, Chofu-shi, Tokyo 182-8585, Japan

adachi@francis.ee.uec.ac.jp, higuchi@ee.uec.ac.jp

² KMUTT, 126 Pracha-uthit Rd., Bangmond, Tungkru, Bangkok 10140, Thailand

Abstract. In recent years, improving of power factor and reducing harmonic distortion in electrical instruments are needed. In general, a current conduction mode boost converter is used for active PFC (Power Factor Correction). In a PFC boost converter, if a duty cycle, a load resistance and an input voltage are changed, the dynamic characteristics are varied greatly. This is the prime reason of difficulty of controlling the interleaved PFC boost converter. In this paper, the robust digital controller using an A2DOF (Approximate 2-Degree-Of-Freedom) method for suppressing the variation of output voltage in dynamic load response with high power factor and low harmonic is proposed. Experimental studies using a micro-processor for controller demonstrate that this type of digital controller is effective to improve power factor and to suppress output voltage variation.

Keywords: Power factor correction (PFC), Boost converter, Approximate 2DOF, Digital robust control, Micro-processor.

1 Introduction

In recent years, improving of power factor and reducing harmonic of power supply using nonlinear electrical instruments are needed. A passive filter and an active filter in AC lines are used for improving of the power factor and reducing the harmonic [1]. Generally a current conduction mode boost converter is used for an active PFC (Power Factor Correction) in electrical instruments. Especially, an interleaved PFC boost converter is used in order to make size compact, make efficiency high and make noise low. In the interleaved PFC boost converter, if a duty cycle, a load resistance and an input voltage are changed, the dynamic characteristics are varied greatly, that is, the interleaved PFC converter has non-linear characteristics. In many applications of the interleaved PFC converters, loads cannot be specified in advance, i.e., their amplitudes are suddenly changed from the zero to the maximum rating. This is the prime reason of difficulty of controlling the interleaved PFC boost converter.

Usually, a conventional Lag-Lead, an analog IC controller, a gain-scheduled controller designed to the approximated linear controlled object at one operating point is used for the PFC converter [2]. In the nonlinear interleaved PFC boost converter

system, those controllers are not enough for attaining good performance [3]. In this paper, the robust controller for suppressing the change of step response characteristics and fluctuation of output voltage with high power factor and low harmonic is proposed. An approximate 2-degree-of-freedom (A2DOF) method [4] is applied to the interleaved PFC boost converter. The PFC converter is a nonlinear system and the models are changed at each operation point. The design and combining methods of two A2DOF controllers which can cope with nonlinear system or changing of the models with one controller is proposed. These two controllers are actually implemented on one microprocessor and connected to the PFC converter and the load. Experimental studies demonstrate that the digital controllers designed by proposed method satisfy the desired performances and are useful.

2 Interleaved PFC Boost Converter

2.1 Modeling of Interleaved Boost Converter

The interleaved PFC boost converter shown in Fig. 1 is manufactured.

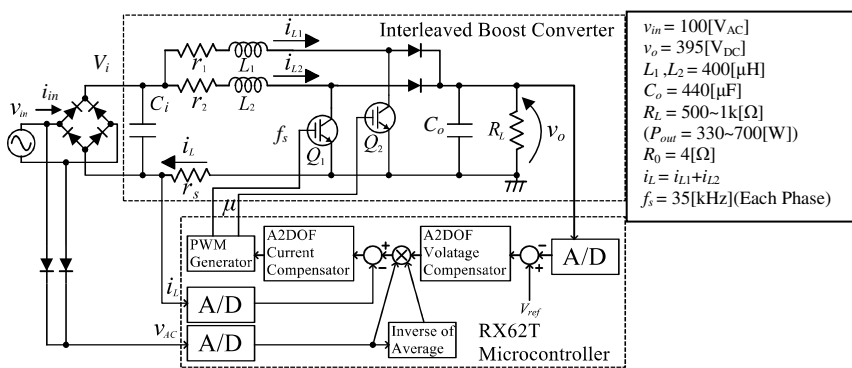


Fig. 1. Interleaved PFC boost converter

In Fig. 1, v_{in} is an input AC voltage, v_{AC} is an absolute value of the input AC voltage, i_{in} is an input AC current, C_i is a smoothing capacitor, V_i is a rectified and smoothed input voltage, and v_o is an output voltage. Q_1 and Q_2 are IGBTs, L_1 and L_2 are boost inductors, r_1 and r_2 are ESRs of inductors, D_1 and D_2 are diodes and i_L is the sum of inductor current, C_o is an output capacitor. R_L is an output load resistance. The inductor current i_L is controlled to follow the rectified input voltage v_{AC} for improving power factor, reducing harmonics and stabilizing the output voltage. Using the state-space averaging method, the state equation of the interleaved boost converter becomes as follows [5]:

$$\frac{d}{dt} \begin{bmatrix} i_L \\ v_o \end{bmatrix} = \begin{bmatrix} -\frac{R_0}{L_0} & -\frac{1}{L_0} \\ \frac{1}{C_0} & -\frac{1}{R_L C_0} \end{bmatrix} \begin{bmatrix} i_L \\ v_o \end{bmatrix} + \begin{bmatrix} \frac{V_i}{L_0} \\ 0 \end{bmatrix} + \begin{bmatrix} v_o \left[\frac{1}{L_0} \right] \\ 0 \end{bmatrix} + i_L \begin{bmatrix} 0 \\ -\frac{1}{C_0} \end{bmatrix} \mu \quad (1)$$

Here μ is duty cycle. When controlling the current of the sum of each phase, R_0 is $r_1 r_2 / (r_1 + r_2)$ and L_0 is $L_1 L_2 / (L_1 + L_2)$. The boost converter has non-linear characteristics because this equation has the product of state variable v_o , i_L and duty cycle μ .

2.2 Dynamic Characteristics of Boost Converter

At some operating point of eq. (1), let v_o , i_L and μ , be V_s , I_s and μ_s , respectively. Then the linear approximate state equation of the boost converter using small perturbations $\Delta i_L = i_L - I_s$, $\Delta v_o = v_o - V_s$ and $\Delta \mu = \mu - \mu_s$ is as follows:

$$\begin{aligned} \dot{x}(t) &= A_c x(t) + B_c u(t) \\ y(t) &= C_c x(t) \end{aligned} \quad (2)$$

where

$$A_c = \begin{bmatrix} -\frac{R_0}{L_0} & -\frac{1-\mu_s}{L_0} \\ \frac{1-\mu_s}{C_0} & -\frac{1}{R_L C_0} \end{bmatrix} \quad B_c = \begin{bmatrix} \frac{V_s}{L_0} \\ -\frac{I_s}{C_0} \end{bmatrix} \quad x(t) = \begin{bmatrix} \Delta i_L(t) \\ \Delta v_o(t) \end{bmatrix} \quad y = \begin{bmatrix} y_i \\ y_v \end{bmatrix} \quad u(t) = \Delta \mu(t) \quad C_c = [1 \quad 0]$$

From this equation, matrix A_c and B_c of the boost converter depends on duty cycle μ_s . Therefore, the converter response will be changed depending on the operating point and other parameter variations. The changes of the load R_L , the duty cycle μ_s , the output voltage V_s and the inductor current I_s in the controlled object are considered as parameter changes. Such parameter changes can be replaced with the equivalent disturbances inputted to the input and the output of the controlled object. Therefore, what is necessary is just to constitute the control systems whose pulse transfer functions from equivalent disturbances to the output y become as small as possible in their amplitudes, in order to robustize or suppress the influence of these parameter changes.

3 Digital Robust Current Controller

3.1 Discretization of Controlled Object

The continuous system of eq. (2) is transformed into the discrete system as follows:

$$\begin{aligned} x(k+1) &= A_d x(k) + B_d u(k) \\ y(k) &= C_d x(k) \end{aligned} \quad (3)$$

where

$$A_d = [e^{A_c T}] B_d = \left[\int_0^T e^{A_c \tau} B_c d\tau \right], C_d = C_c$$

Here, in order to compensate the delay time by A/D conversion time and microprocessor operation time etc., one delay (state ξ_1) is introduced to input of the controlled object. Then the state-space equation is described as follows:

$$\begin{aligned} x_{dt}(k+1) &= A_{dt}x_{dt}(k) + B_{dt}v(k) \\ y(k) &= C_{dt}x_{dt}(k) \end{aligned} \quad (4)$$

where

$$\begin{aligned} A_{dt} &= \begin{bmatrix} e^{A_c T_s} & e^{A_c(T_s-L_d)} \int_0^{L_d} e^{A_c \tau} B_c d\tau \\ 0 & 0 \end{bmatrix} = \begin{bmatrix} a_{11} & a_{12} & a_{13} \\ a_{21} & a_{22} & a_{23} \\ 0 & 0 & 0 \end{bmatrix} \\ B_{dt} &= \begin{bmatrix} \int_0^{T_s-L_d} e^{A_c \tau} B_c d\tau \\ 1 \end{bmatrix} = \begin{bmatrix} b_{11} \\ b_{21} \\ 1 \end{bmatrix} \quad x_{dt}(k) = \begin{bmatrix} x(k) \\ \xi_1(k) \end{bmatrix} \quad C_{dt} = [C_c \ 0] = [1 \ 0 \ 0] \end{aligned}$$

3.2 Design Method for A2DOF Digital Current Controller

The transfer function from the reference input r'_i to the output y_i is specified as follows:

$$W_{r'_i y_i}(z) = \frac{(1+H_1)(1+H_2)(1+H_3)(z-n_{1i})(z-n_{2i})}{(z+H_1)(z+H_2)(z+H_3)(1-n_{1i})(1-n_{2i})} \quad (5)$$

Here H_i , $i=1,2,3$ are the specified arbitrary parameters, n_{1i} and n_{2i} are the zeros of the discrete-time controlled object. This target characteristic $W_{r'_i y_i}$ is realizable by constituting the model matching system shown in Fig. 2 using the following state feedback to the controlled object.

$$v = -Fx_{dt} - G_i r'_i \quad (6)$$

Here $F = [f_1 \ f_2 \ f_3]$ and G_i are selected suitably. In Fig. 2 q_v and q_{yi} are the equivalent disturbances with which the parameter changes of the controlled object are replaced.

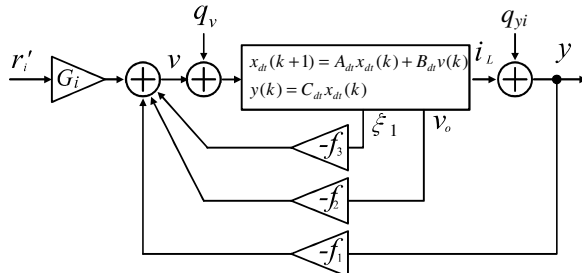


Fig. 2. Model matching system using state feedback

It shall be specified that the relation of H_1 and H_3 become $|H_1| \gg |H_3|$ and $n_{1i} \approx H_2$. Then $W_{ri'yi}$ can be approximated to the following first-order discrete-time model:

$$W_{ri'yi}(z) \approx W_{mi}(z) = \frac{1+H_1}{z+H_1} \quad (7)$$

The transfer function $W_{Qyi}(z)$ between the equivalent disturbance $Q_i = [q_v \ q_{yi}]^T$ to y_i of the system in Fig. 2 is defined as

$$W_{Qyi}(z) = [W_{qvi}(z) \ W_{qyi}(z)] \quad (8)$$

The system added the inverse system and the filter to the system of Fig. 2 is constituted as shown in Fig. 3.

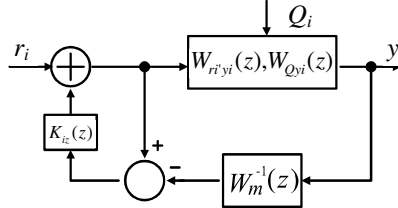


Fig. 3. System Reconstituted with Inverse System and Filter

In Fig. 3, the transfer function $K_i(z)$ is as follows:

$$K_i(z) = \frac{k_{zi}}{z-1+k_{zi}} \quad (9)$$

The transfer functions between $r_i - y_i$, $q_{ui} - y_i$ and $q_{yi} - y_i$ of the system in Fig. 3 are given by

$$y_i = \frac{1+H_1}{z+H_1} \frac{z-1+k_{zi}}{z-1+k_{zi}W_{si}(z)} W_{si}(z) r_i \quad (10)$$

$$y_i = \frac{z-1+k_{zi}}{z-1+k_{zi}} \frac{z-1+k_{zi}}{z-1+k_{zi}W_{si}(z)} W_{Qyi}(z) Q_i \quad (11)$$

where

$$W_{si}(z) = \frac{(1+H_3)(z-n_{1i})}{(z+H_3)(1-n_{1i})}$$

Here, if $W_{si}(z) \approx 1$, then eq. (10) and eq. (11) are approximated, respectively as follows:

$$y_i = \frac{1+H_1}{z+H_1} r_i \quad (12)$$

$$y_i = \frac{z-1}{z-1+k_{zi}} W_{Qyi}(z) Q_i \quad (13)$$

From eq. (12) and eq. (13), it turns out that the characteristics from r to y can be specified with H_1 and the characteristics from Q_i to y_i can be independently specified with k_{zi} . That is, the system in Fig. 3 is an A2DOF system, and its sensitivity against disturbances becomes lower with the increase of k_{zi} . If equivalent conversion of the controller in Fig. 3, we obtain Fig. 4. Then, substituting a system of Fig. 2 to Fig. 4, A2DOF digital integral type control system will be obtained as shown in Fig. 5. In Fig. 5, the parameters of the controller are as follows:

$$\begin{aligned} k_1 &= -f_1 - \frac{Gk_{zi}}{1+H_1}, \quad k_2 = -f_2 \\ k_3 &= -f_3, \quad k_{ii} = G_i k_{zi}, \quad k_{ri} = G_i \end{aligned} \quad (14)$$

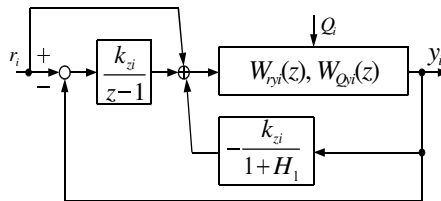


Fig. 4. Equivalent Conversion of the Robust Digital Controller

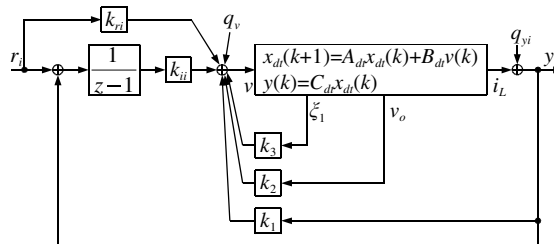


Fig. 5. Approximate 2DOF Digital Integral Type Current Control System

4 Digital Robust Voltage Controller

4.1 Addition of u_v and v_{ac} to r_i

Add the multiplier in front of the reference input r_i of the current control system. Let the inputs of the multiplier be v_{ac} and u_v as shown in Fig. 6. In Fig. 6, v_{ac} is the absolute value of the input voltage v_{in} and u_v is a new input. This addition is for making the inductor current i_L follow the AC voltage v_{ac} .

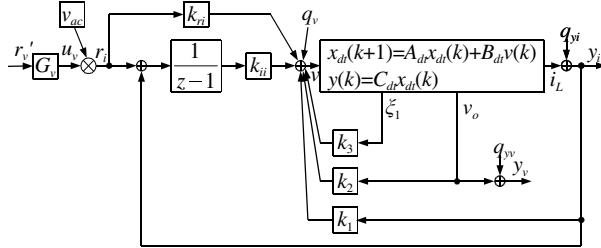


Fig. 6. Current Control System Added Multiplier

4.2 Approximate Controlled Object for Voltage Controller

The system of Fig. 6 becomes a controlled object for a voltage controller. Derive an approximated controlled object from this system for designing the voltage controller. In Fig. 6, u_v is a control input, and $v_o = y_v$ is an output of the controlled object. When u_v is set to 0, $u_v = G_{vv}'$, the transfer function from r_v' to v_o is as follows:

$$v_o = \frac{(1+H_2)}{(z+H_2)} \frac{(1+H_1)}{(z+H_1)} \frac{(1+p_{1i})}{(z+p_{1i})} \frac{(1+p_{2i})}{(z+p_{2i})} \frac{(z-n_{1v})}{(1-n_{1v})} \frac{(z-n_{2v})}{(1-n_{2v})} r_v' = W_{ryv} r_v' \quad (15)$$

where

$$G_v = \frac{1}{G_{uv}} = \frac{a_{21} + \frac{a_{23}}{G_{ui}} + \frac{b_{21}}{G_{ui}}}{1 - a_{22}}, G_{ui} = \frac{1}{C_{dt}(I - A_{dt})^{-1} B_{dt}}$$

G_{uv} is DC gain between u_v to v_o . n_{1v}, n_{2v} are zeros of the transfer function from u_v to v_o .

In eq. (15) $|H_2| \gg (|H_1|, |p_{1i}|, |p_{2i}|)$, so the controlled object W_{ryv} for the voltage controller is approximated as

$$W_{ryv}(z) \approx W_{mv}(z) = \frac{1+H_2}{z+H_2} \quad (16)$$

4.3 Design Method of A2DOF Voltage Controller

The inverse system $W_{mv}^{-1}(z)$ and the filter $K_v(z)$ are added to the system of eq. (16) like Fig. 3. Here $K_v(z)$ is as follows:

$$K_v(z) = \frac{k_{zv}}{z-1+k_{zv}} \quad (17)$$

In Fig. 3, $r_i, y_i, Q_i, q_v, K_i, W_{ryi}, W_{mi}^{-1}$, and W_{Qyi} are replaced with $r_v, y_v, Q_v, q_v, q_{yv}, K_v, W_{ryv}, W_{mv}^{-1}$, and W_{Qyy} , respectively. Then the transfer functions between r_v-y_v , q_v-y_v and $q_{yv}-y_v$ of the system like Fig. 3 are given by

$$y_v \approx \frac{1+H_2}{z+H_2} r_v \quad (18)$$

$$y_v \approx \frac{z-1}{z-1+k_{zv}} W_{Q_v y_v}(z) Q_v \quad (19)$$

The A2DOF digital integral type control system will be obtained from the equivalent conversion of the controller like Fig. 4 as shown in Fig. 7.

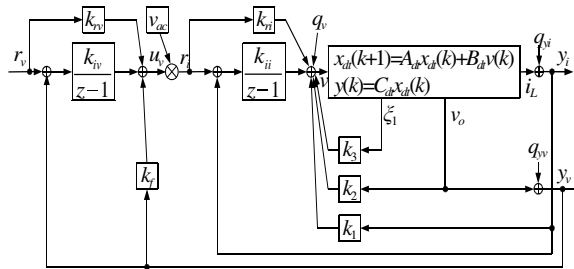


Fig. 7. Approximate 2DOF Digital Integral Type Control System Including the Current Controller and the Voltage Controller

In Fig. 7, the parameters of the voltage controller are as follows:

$$k_f = -\frac{G_v k_{zv}}{1+H_2} \quad k_{iv} = G_v k_{zv} \quad k_{rv} = G_v \quad (20)$$

5 Experimental Studies

All experimental setup system is shown in Fig. 8. A micro-controller (RX62T) from Renesas Electronics is used for the digital controller. Two digital controllers for the current and voltage were implemented on one Micro Controller.



Fig. 8. Experimental setup system

In this experiment, the sampling frequency is $2f_s$ (f_s is a switching frequency) and the design parameters are set up as follows.

$$H_1 = -0.8 \quad H_2 = -0.9988 \quad H_3 = -0.1 \quad k_{zi} = 0.04 \quad k_{zv} = 0.85$$

From eq. (14) and eq. (20), the controller parameters are obtained as follows.

$$\begin{array}{lll} k_1 = -0.0139755 & k_2 = 0.000139848 & k_3 = 0.0476263 \\ k_{ii} = 0.0024912 & k_{ri} = 0.06228 & k_f = -5.70004 \\ k_{iv} = 0.00684005 & k_{rv} = 0.00804711 & \end{array}$$

The experiment result of the steady state using the proposed controller is shown in Fig. 9. The input current waveform and the phase are almost same as the input voltage, and the power factor at 500[Ω](300[W]) is 0.983. The experimental result of the steady state using the conventional digital Lag-Lead controller is shown in Fig. 10. The input current waveform is distorted more than the one in Fig. 9. at the zero cross point. That is, the proposed controller can reduce harmonics. The experimental result of dynamic load response using the proposed controller and the conventional digital Lag-Lead controller are shown in Fig. 11 and Fig. 12, respectively. The output voltage fluctuations in dynamic load response of both results are less than 9[V](2.5[%] of v_o), but the oscillation is not seen in the result of the proposed method. It turns out that proposed method is better than the conventional method in the performance of the output regulation in dynamic load response.

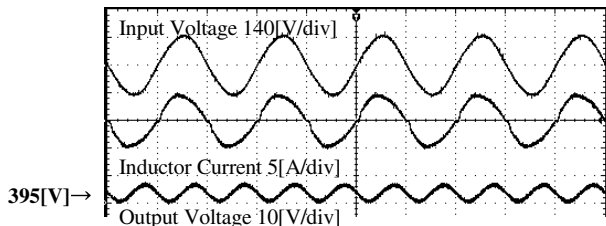


Fig. 9. Experimental Results of Steady State Waveforms using of the proposed A2DOF current and voltage controller PF = 0.98 (x-axis 10[ms/div])

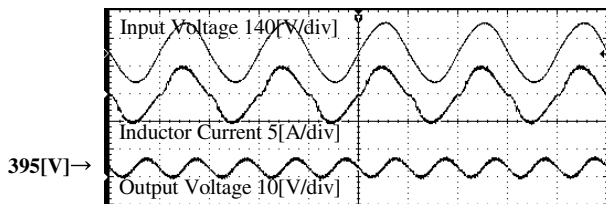


Fig. 10. Experimental Results of Steady State Waveforms using of the conventional Lag-Lead controller PF = 0.98 (x-axis 10[ms/div])

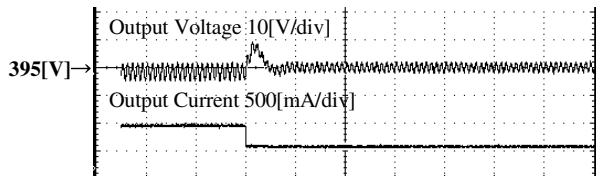


Fig. 11. Experimental Results of dynamic load response $R_L = 1000[\Omega]$ to $500[\Omega]$ using of the proposed A2DOF current and voltage controller (x-axis 100[ms/div])

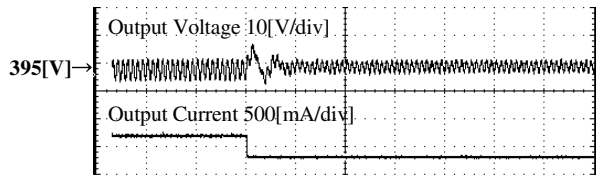


Fig. 12. Experimental Results of dynamic load response $R_L = 1000[\Omega]$ to $500[\Omega]$ using of the conventional Lag-Lead controller (x-axis 100[ms/div])

6 Conclusion

In this paper, the concept of the digital controller which attains good robustness for the interleaved PFC boost converter was given. The proposed digital controller was implemented on the micro-processor. The PFC boost converter built-in this micro-processor was manufactured. It was shown from experiments that the digital controller which combined two A2DOF can suppress the output voltage variations in dynamic load response while attaining the high power factor and the low harmonic. This fact demonstrates the usefulness and practicality of our proposed method. A future subject is checking experimentally the change of the output voltage when the input voltage is changed.

References

1. Rossetto, L., Spiazzi, G., Tenti, P.: Control Techniques for Power Factor Correction Converters. In: Proc. PEMC 1994, pp. 1310–1318 (1994)
2. Zhang, W., Feng, G., Liu, Y., Wu, B.: A Digital Power Factor Correction (PFC) Control Strategy Optimized for DSP. IEEE Transactions on Power Electronics 19(6), 1474–1485 (2004)
3. Figueres, E., Benavent, J.M., Garcera, G., Pascual, M.: A Control Circuit With Load-Current Injection for Single-Phase Power-Factor-Correction Rectifiers. IEEE Transactions on Industrial Electronics 54(3), 1272–1281 (2007)
4. Higuchi, K., Nakano, K., Kajikawa, T., Takegami, E., Tomioka, S., Watanabe, K.: A New Design of Robust Digital Controller for DC-DC Converters. In: IFAC 16th Triennial World Congress, CD-ROM (2005)
5. Sasaki, S., Watanabe, H.: Analysis of Multiple Operating Points for Dynamical Control of Switching Power Converters. IEIC Technical Report, pp. 33–38 (2005)

A Study of Virtual Model of Power Supply Laboratory

Pham Thanh Nhan^{1,2}, Nguyen Thanh Nghia^{1,2}, Huynh Xuan Dung^{1,2},
Quyen Huy Anh³, Bui Huu Phu², and Tran Thanh Trang^{1,2,4,5,*}

¹ The Electronics Engineering Department, Cao Thang College of Technology,
Ho Chi Minh City, Vietnam

² The National Key Lab of Digital Control and System Engineering, University of Technology,
Vietnam National University Ho Chi Minh City, Vietnam
trangtrantranh1979@gmail.com

³ The Electrical-Electronics Engineering Department, University of Technical Education
Ho Chi Minh City, Vietnam

⁴ The Electrical Engineering Department, Ho Chi Minh City Open University, Vietnam

⁵ The Electronics & Telecommunication Engineering Department, Van Hien University,
Ho Chi Minh City, Vietnam
trangtt@vhu.edu.vn

Abstract. This paper presented the method of creating virtual models of power supply laboratory in the Matlab environment based on the physical model of LD Didactic GmbH Company. A study created virtual models that had all the features of the physical model. Thus, experiment on the virtual models was similar to experiment on the physical models.

Keywords: Physical model, virtual model, transformer, transmission line, synchronous generator.

1 Introduction

Power supply laboratory is necessary to universities and colleges. Most universities and colleges have invested a lot of money in equipping power supply laboratory with physical models. However, a few universities and colleges had ability to invest, because of the high cost of physical model. Another way to create a power supply laboratory with low cost is building virtual model [1 - 3].

This paper describes the development of the virtual models based on physical models of the LD Didactic GmbH. These virtual models have high flexibility and accuracy that can substitute the physical models.

* Corresponding author.

2 Materials and Methods

2.1 Experiment on the Physical Models

Synchronous generator model, Three phase transformer model, Transmission line model to collect data.

2.2 The Creation of Mathematical Model of Three Phase Transformer

The equivalent circuit diagram for the transformer operating under load is reproduced in figure 1:

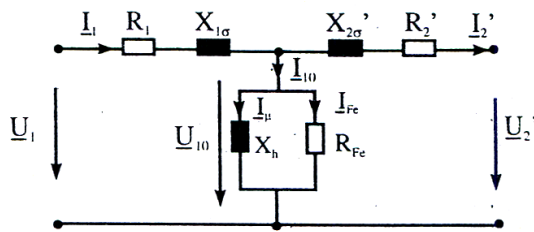


Fig. 1. Equivalent circuit diagram for the transformer operating under load

R_2 : Ohmic resistance of the secondary side

R'_2 : Value of R_2 converted to the primary side in accordance with expression:

$$R'_2 = R_2 t^2 \quad (1)$$

$X_{1\sigma}$: Leakage reactance of the primary side

$X_{2\sigma}$: Leakage reactance of the secondary side

X'_2 : Value of $X_{2\sigma}$ converted to the primary side in accordance with expression:

$$X_{2\sigma} = X'_2 t^2 \quad (2)$$

$$\frac{U_1}{U_2} = \frac{W_1}{W_2} = t \quad (3)$$

To calculate the value showed in figure 1, first of all, experiments with performance at no-load and calculated the following: $\cos\phi_0$, I_{Fe} , I_μ , R_{Fe} , X_h [4].

Then, conduct further experiments with performance at short - circuit, the parameters of the specifications are formulated by:

$$\cos\phi_k = \frac{P_{lk}}{U_{lk} \cdot I_1} \quad (4)$$

$$u_k = \frac{U_{lk}}{U_{1N}} \quad (5)$$

$$u_r = u_k \cos \varphi_k \quad (6)$$

$$u_x = u_k \sin \varphi_k \quad (7)$$

$$R_{lk} = \frac{U_{1k} \cos \phi_k}{I_l} \quad (8)$$

$$X_{lk} = \frac{U_{1k} \sin \phi_k}{I_l} \quad (9)$$

Draw a complete equivalent circuit diagram of the transformer and enter all of the measured or calculated quantities in figure 2. The following applies approximately: $R_1 = R_2 = R_{lk} / 2$ and $X_{1\sigma} = X_{2\sigma} = X_{lk} / 2$ [4].

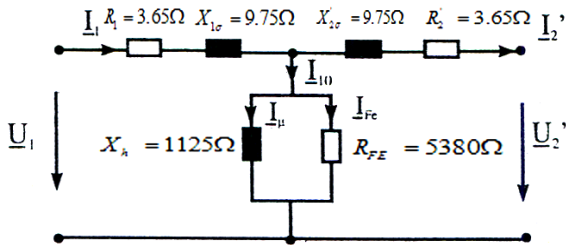


Fig. 2. A complete equivalent circuit diagram for the transformer operating under load

2.3 The Creation of Mathematical Model of Transmission Line

When operating a transmission line with three-phase current, the leakage losses (G) and the inductive and capacitive properties (L and C) of the arrangement, as well as the resistance of the conductor material (R) must be taken into consideration. As these values are evenly distributed along the transmission line in the form of quantities per unit length, the equivalent circuit diagram in figure 3 with concentrated circuit component only applies to short lines [5]:

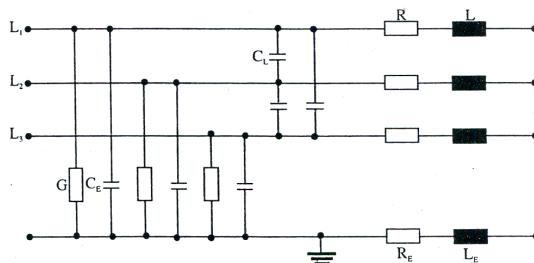


Fig. 3. Equivalent circuit diagram of a three-phase transmission line

$$R = \frac{l}{\chi A} \quad (10)$$

l : Line length

A : Line cross-section

χ : Specific at a temperature of conductor material

$$L = \frac{1000\mu_0}{2\pi} \left(\ln \frac{d_{gmi}}{r_B} + \frac{0.25}{n} \right) \quad (11)$$

d_{gmi} : The geometrical mean value for the conductor spacing. For this the following applies:

$$d_{gmi} = \sqrt[3]{(d_{12} \cdot d_{23} \cdot d_{31})} \quad (12)$$

d_{12} etc: Spacing of the conductor cables from each other

n : Number of subconductors

r_B : Equivalent radius for multiple conductor lines

$$r_B = \sqrt[n]{(n \cdot r \cdot a^{n-1})} \quad (13)$$

r : Radius of a conductor cable

a : Spacing of the subconductors of a multiple conductor line

μ_0 : Permeability of free space = $1,257 \cdot 10^{-6}$ Vs/Am

$$C_L = \frac{1000 \cdot 2\pi \cdot \epsilon_0 \cdot \ln \frac{2h}{d_{gmi}}}{3 \ln \frac{2h}{d_{gmi}} \ln \frac{2h}{\sqrt[3]{r_B \cdot d_{gmi}^2}}} \quad (14)$$

$$C_E = \frac{1000 \cdot 2\pi \cdot \epsilon_0}{3 \left(\ln \frac{2h}{\sqrt[3]{r_B \cdot d_{gmi}^2}} - \frac{\left(\ln \frac{h+h_0}{d_0} \right)^2}{\ln \frac{2h_0}{r_0}} \right)} \quad (15)$$

$h = \sqrt[3]{(h_1 h_2 h_3)}$: Geometrical average of the line height

h_0 : Medium height of the earth wire

$d_0 = \sqrt[3]{d_{10} \cdot d_{20} \cdot d_{30}}$: Geometrical average distance from earth wire to the other conductors

r_0 : Radius of the earth wire

r_B : Equivalent radius as in calculation of the inductance

ϵ_0 : Permittivity of free space = $8,86 \cdot 10^{-12}$ As/Vm

In the transmission line model, condensed circuit element was used to simulate a transmission line with three possible lengths: 144km, 216 km, 360 km, as indicated in table 1:

Table 1. The technical data of transmission line

Length in Km	360	216	144
Length in %	100	60	40
R in Ω	13	8	5
L in mH	290	174	116
C _B in nF	5000	3000	2000

2.4 The Creation of Mathematical Model of Synchronous Generator

The circuit is based on a star configuration of the stator (see figure 4):

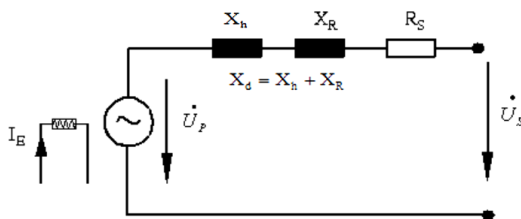


Fig. 4. Single-phase equivalent circuit diagram of the turbo generator in stationary operating mode

I_E : Exciter current in rotor

\dot{U}_p : Synchronous generated voltage in stator

\dot{U}_s : Stator voltage

X_h : Main field reactance of the stator winding

X_R : Leakage reactance of the stator winding

R_s : Resistance of the stator winding

Accordingly the two reactances are defined X_h and X_R , the two in conjunction constitute the synchronous reactance X_d , which is also referred to as armature reactance [4].

$$X_d = X_h + X_R \quad (16)$$

The resistance R_s of the stator winding is designed as small as possible by selecting the appropriate diameter for the copper windings. Thus, for rough observations, R_s can be ignored in comparison with the synchronous reactance X_d .

The value of the synchronous reactance X_d is obtained by performing current and voltage measurements during a short-circuit experiment whereby the resistance of the stator winding is neglected. The measurement is carried out with reduced exciter current and with all three phases of the stator winding short-circuit current. There is an almost linear relationship between the exciter current and the short-circuit current. Furthermore, unlike the no-load voltage, the short-circuit current is nearly independent of the machine's speed, as both the synchronous generated voltage and the synchronous reactance are proportioned to the frequency, thus making the quotient of both quantities frequency-dependent.

The curve of a no-load and a short-circuit characteristic is reproduced in figure 5:

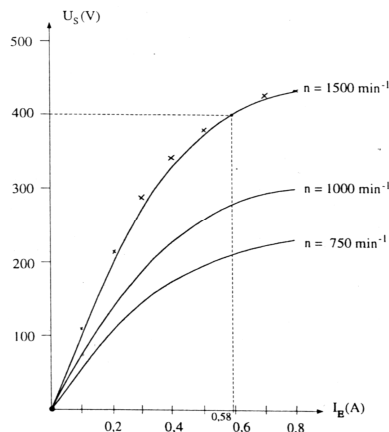


Fig. 5a. No-load characteristic of the turbo generator

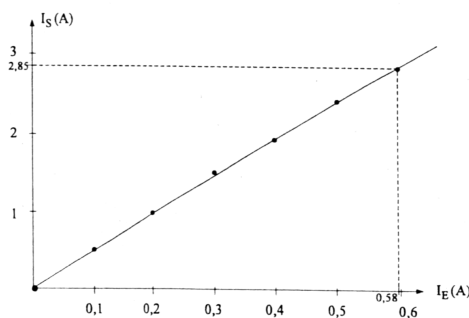


Fig. 5b. Short-circuit characteristic of the turbo generator

The no-load nominal exciter current $I_{E0} = 0.58$ (A) is that particular current in the rotor which supplies the nominal voltage during generator operation under no-load condition. If the machine is short-circuited at this current level, then the so-called no-load steady short-circuit current I_{K0} flows in the stator. The synchronous reactance can be determined. For a star connection of the stator this amounts to:

$$X_d = \frac{U_N}{\sqrt{3}I_{K0}} = \frac{400}{\sqrt{3} \cdot 2.85} = 81\Omega \quad (17)$$

2.5 The Creation of Virtual Model

Building the electric circuit of the physical model on Simulink with all the information have been received from the mathematical model [6 - 7] (see figure 6, figure 7, figure 8):

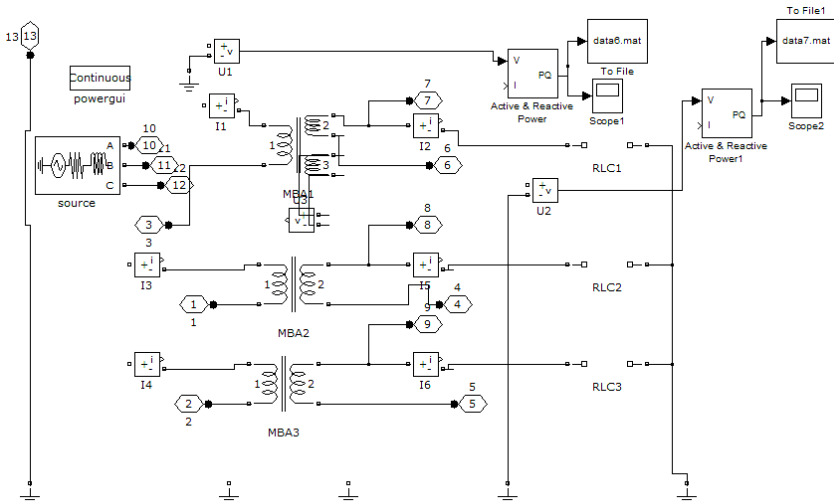


Fig. 6. Circuit diagram of three-phase transformer model

In figure 6, the circuit used the Transformer models and Three-Phase Source model, Series RLC Branch models, these models used varying parameter to from mathematical models and physical models. The Transformers model connected to Three-Phase Source model, Series RLC Branch models was correspondent with each cases of experiment selected from the interface of the virtual model. The Voltage Measurement models, Current Measurement models, and Active & Reactive Power models were measured currents, voltages, powers and results would displayed in the interface model. The circuits in figure 7, 8 show the same.

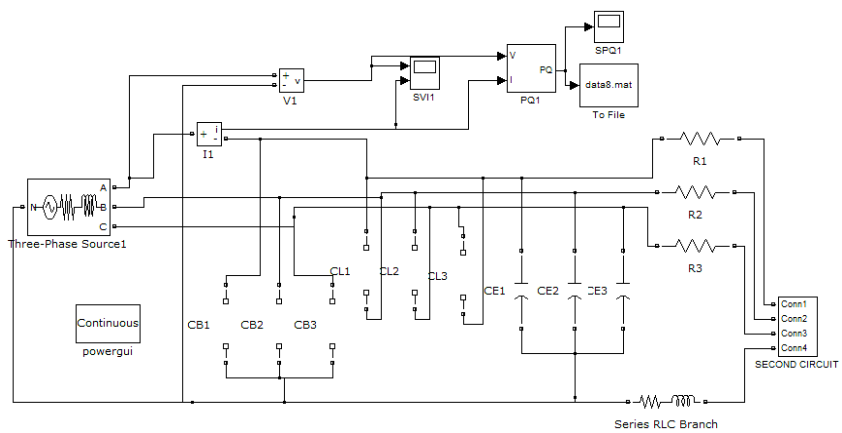


Fig. 7a. First circuit diagram of transmission line model

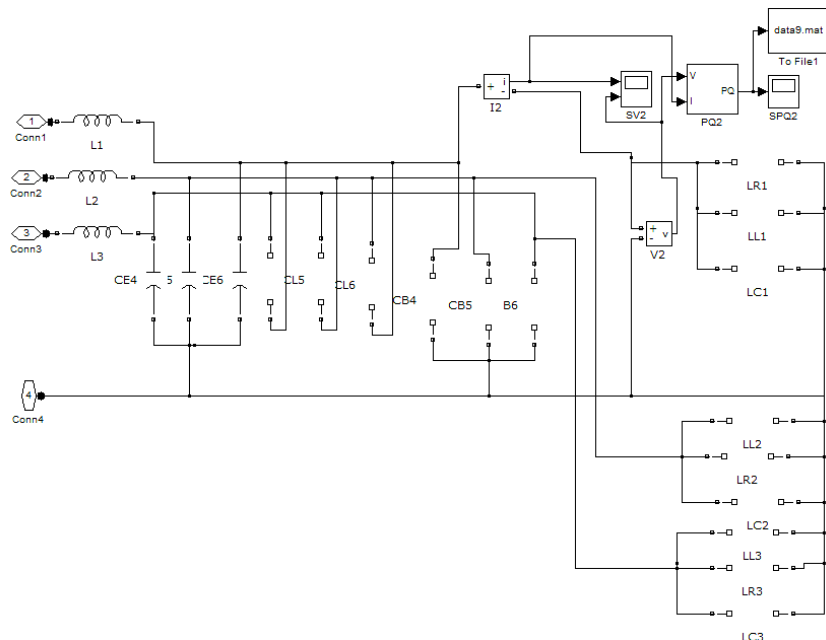


Fig. 7b. Second circuit diagram of transmission line model

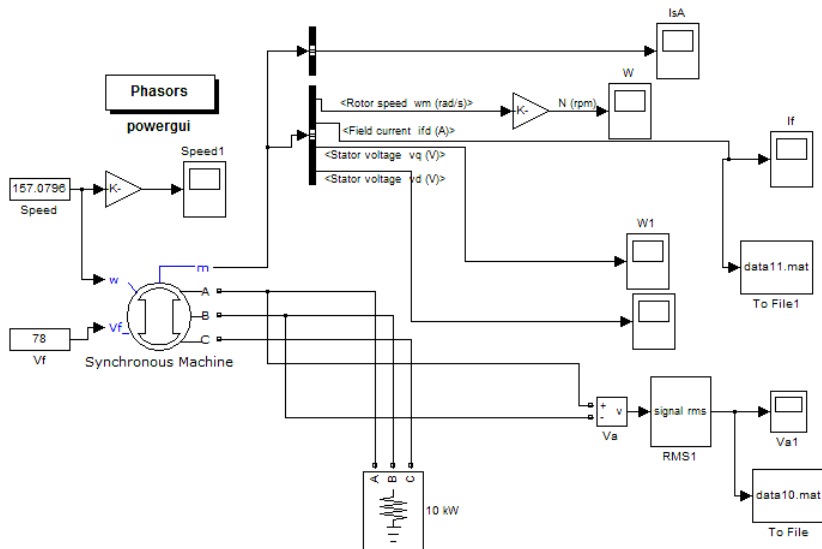


Fig. 8. Circuit diagram of synchronous generator model

The interface of virtual model was created by GUI function (see figure 9, figure 10, figure 11):

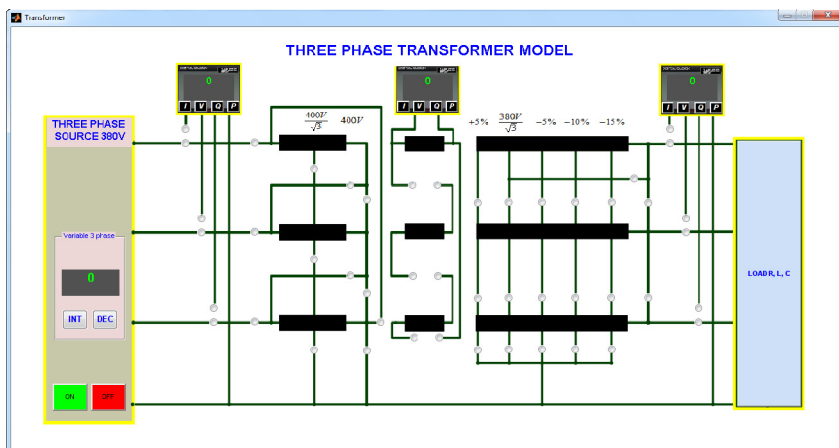


Fig. 9. The interface of three-phase transformer virtual model

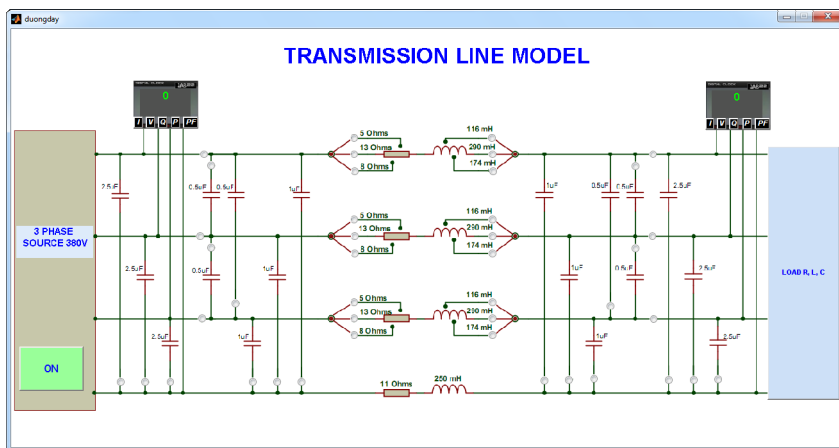


Fig. 10. The interface of transmission line virtual model

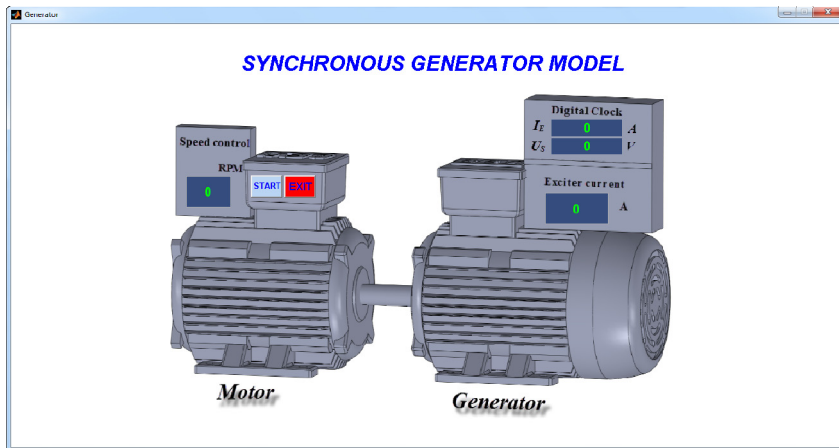


Fig. 11. The interface of synchronous generator virtual model

3 Results and Discussion

3.1 Three Phase Transformer Virtual Model

Can be carry out experiments on transformer virtual model:

- Performance at no-load: Determining the voltage transformation ratio of a transformer operating at no-load as well as measuring the consumed active and reactive power, determining equivalent circuit quantities based on these measurements.
- Performance at short-circuit: Measuring voltage, current, and active power when there is a short-circuit on the secondary side of the transformer and determining the equivalent circuit quantities based on these measurements.

- Performance at load operation: Measuring the effect of load type and magnitude on the performance of the secondary voltage and comparing this to the theoretically anticipated value, determining the efficiency.

The tolerance between experiments on virtual model and physical model, as indicated in table 2, table 3 and table 4.

Table 2. Performance at no-load

Tolerance	$U_{N+5\%}$	U_N	$U_{N-5\%}$	$U_{N-15\%}$
$U_1 (\%)$	0.27	0.27	0.27	0.27
$U_2 (\%)$	1.05	0.64	0.22	0.87
$U_3 (\%)$	-	0.63	-	-
$P_{10} (\%)$	-	0	-	-
$I_{10} (\%)$	-	1	-	-

Table 3. Performance at short-circuit

Tolerance	$U_{1k} (\%)$	$I_1 (\%)$	$P_{1k} (\%)$
	4	0	0

Table 4. Performance at load operation

Tolerance	$U_{20} (\%)$	$U_2 (\%)$	$I_2 (\%)$	$P_1 (\%)$	$P_2 (\%)$
R_1	0.40	1.07	5	3.30	3.60
R_2	0.40	0.39	4	4.60	3.40
R_3	0.40	0.39	4	4.40	3.30
R_4	0.40	0.70	4	4.60	3.30
R_5	0.40	1.09	4.30	4.30	4

3.2 Transmission Line Virtual Model

Can be carry out experiments on transmission line virtual model:

- Performance at no-load: Measurement of the voltage increase and charging power in lines of different lengths in no-load operation. Explanation of the concept of operating capacitance. Different performance characteristics of overhead transmission line and cable.
- Performance characteristics for three-phase short-circuit: Measuring and interpreting the current and voltage ratios of a transmission line during a three-phase short-circuit.

- Performance characteristics of an ohmic-inductive and pure inductive load: Measuring and interpreting the current and voltage ratios of a transmission line with mixed ohmic-inductive and pure inductive loads.

- Performance characteristics of an ohmic-capacitive and pure capacitive load: Measuring and interpreting the current and voltage ratios of a transmission line with mixed ohmic-capacitive and pure capacitive loads.

The tolerance between experiments on virtual model and physical model, as indicated in table 5, table 6.

Table 5. Performance at no-load

Tolerance	U ₁ (%)	U ₂ (%)	Q _C (%)
144 km	0.05	0.03	1.5
216 km	0.36	0.02	1.6
360 km	0.70	0.40	1.2

Table 6. Performance at load operation: An ohmic-inductive and pure inductive load

Tolerance	U ₁ (%)	I ₁ (%)	P ₁ (%)	U ₂ (%)	I ₂ (%)	P ₂ (%)
1	2	0	1.2	2	3.5	
0.8	1.6	0	1.2	2.1	2.8	
1	1.9	0	1.1	3	3.5	
1.3	1.6	0.6	0.6	2.6	2.7	

3.3 Synchronous Generator Virtual Model

Can be carry out experiments on synchronous generator virtual model:

- Performance at no-load: Measuring the exciter current and the corresponding stator voltage at various speeds. Determining the no-load nominal exciter current from the measured values.

The tolerance between experiments on virtual model and physical model, as indicated in table 7.

Table 7. Performance at no-load

P=750 (RPM)	I _E (A)	0.1	0.2	0.3	0.4	0.5	0.6
Tolerance	U _S (%)	2	2.7	3.6	2.9	2.6	2
P=1000 (RPM)	I _E (A)	0.1	0.2	0.3	0.4	0.5	0.6
Tolerance	U _S (%)	2.7	2.2	3.2	2.3	2	1.8
P=1500 (RPM)	I _E (A)	0.1	0.2	0.3	0.4	0.5	0.6
Tolerance	U _S (%)	2.5	1.8	2.2	2.	2.4	2.25

4 Conclusion

The virtual models were built with high homology with the physical models, the results of experiment on the virtual model and the physical model had low tolerance, the physical models were replaced by virtual models. Can perform the experiments on the virtual model similar to perform the experiments on the physical models and can be extended to the case of experiments, other practices by change information's the settings of the virtual model. Can be equipped the virtual models for universities, colleges cannot equipped yet with the physical model to conduct experiments.

Acknowledgements. This work is supported mainly by Van Hien University, supported by part of the National Key Lab of Digital Control and System Engineering-University of Technology-Vietnam National University Ho Chi Minh city.

References

1. Petrone, J.G., Cammarata, G.: Modelling and Simulation. InTech (2008)
2. Anh, Q.H.: Modeling and Simulation. University of Technical Education Ho Chi Minh City (2011)
3. Law, A.M., Kelton, W.D.: Simulation Modeling and Analysis. McGraw – Hill (2000)
4. Loi, B.T.: Electric Machine. Da Nang University of Technology (2005)
5. Viet, N.H., Binh, P.T.T.: Short circuit and Stability in power system. VietNam National University Publisher (2010)
6. Velten, K.: Mathematical Modeling and Simulation. Wiley (2009)
7. Hunt, B.R., Lipsman, R.L., Rosenberg, J.: A guide to Matlab for beginners and experienced users. Cambridge University Press (2006)

Neutral Point Voltage Balancing Method and the Influence of Some Parameters on Capacitor Voltage in Three-Level NPC Converter

Vo Xuan Nam^{1,2,3}, Le Van Manh Giau³, Nguyen Van Nho³,
and Tran Thanh Trang^{1,2,4,5,*}

¹ The Electronics Engineering Department, Cao Thang College of Technology,
Ho Chi Minh City, Vietnam

² The National Key Lab of Digital Control and System Engineering, University of Technology,
Vietnam National University Ho Chi Minh City, Vietnam
trangtranhanh1979@gmail.com

³ The Power Engineering Research Lab, University of Technology,
Vietnam National University Ho Chi Minh City, Vietnam

⁴ The Electrical Engineering Department, Ho Chi Minh City Open University, Vietnam

⁵ The Electronics & Telecommunication Engineering Department, Van Hien University,
Ho Chi Minh City, Vietnam
trangtt@vhu.edu.vn

Abstract. This paper presented a control method for balancing capacitor voltage of three-level neutral-point-diode-clamped (NPC) converter. This control method overcomes one of the main problems of this converter, which is the low frequency voltage oscillation that appears in the neutral point. The algorithm is based on Carrier-based Pulse Width Modulation (CPWM). This paper showed the influence of power factor, modulation index and offset limit on capacitor voltage. It also presented the optimal amplitude of offset voltage in some case of power factors and modulation indexes.

Keywords: Neutral point diode clamped converter, offset, modulation index, THD.

1 Introduction

Multilevel converters have been looked upon as a good choice for medium- and high-voltage application. There are some converter structures, such as, Neutral Point diode Clamped, Cascade, Floating Capacitor Converters. The NPC converter is generous using because of its advantage. Three level NPC converter have several advantages over traditional two-level inverters -besides better quality output voltage and current waveform, the peak transient voltage at the motor terminals is reduced, particularly for applications that use long power cables, which reduces the stress on the motor

* Corresponding author.

insulation. With certain modulation schemes, common-mode voltage and bearing currents can be considerably reduced. However, a significant problem with three-level converters is the fluctuation in the neutral-point voltage. It affects the quality of output voltage. So, the capacitor voltage balancing is needed. This paper gives a contribution to the problem of neutral-point voltage balancing in three-level NPC converter.

2 Balancing Method

Fig.1 shows the construction of three-level NPC converter. Controlling the ON/OFF states of the transistors makes changing the output voltage. As shown in fig. 1, the transistors are controlled by control Sxi signals, where $x=\{a,b,c\}$ and $i=\{1,2,3,4\}$. If Sxi is 1 then transistor xi will be “ON” state, otherwise transistor xi is “OFF” state.

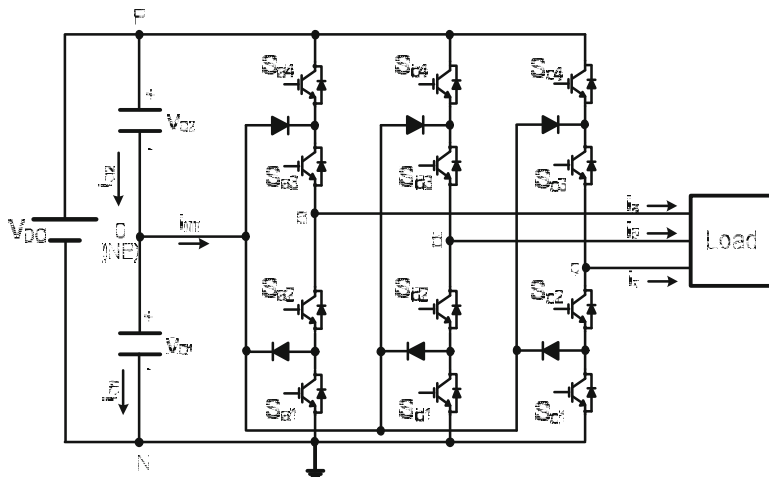


Fig. 1. Structure of three levels, three phases NPC converter

There are many modulation methods to control converters, such as space vector modulation [1] or sinusoidal modulation [2-7]. The method provided below is called modified sinusoidal modulation of sine modulation. Modulation signal of each phase is originally been splitting into two modulated signals v_{xp} and v_{xn} (where $x= \{a, b, c\}$) for each branch of the converter [3].

$$\begin{cases} v_a = v_{ap} + v_{an} \\ v_b = v_{bp} + v_{bn} \\ v_c = v_{cp} + v_{cn} \end{cases} \quad (1)$$

Where $v_{xp} \geq 0$ and $v_{xn} \leq 0$, with $x = \{a, b, c\}$. The signal with the subscript ‘ p ’ (upper control signal) will only cross the upper carrier, $v_{carrier}^p \in [0,1]$ and the signals with the subscript ‘ n ’ (lower control signal) will only cross the lower one, $v_{carrier}^n \in [-1,0]$. The modified control signal of phase x is defined by equation (2) (using Switching Frequency Optimal Pulse Width Modulation):

$$v_x = v_x - \frac{\max(v_a, v_b, v_c) + \min(v_a, v_b, v_c)}{2} \quad (2)$$

In order to preserve voltage balance, the locally-averaged NP current must be zero. Therefore, it is necessary to operate with the averaged NP current instead of the instantaneous current. The averaged NP current is obtained by using the moving average operator. The optimal values of v_{xp} and v_{xn} were showed below [3]:

$$\begin{cases} v_{xp} = \frac{v_x - \min(v_a, v_b, v_c)}{2} \\ v_{xn} = \frac{v_x - \max(v_a, v_b, v_c)}{2} \end{cases} \quad (3)$$

Where: $x = \{a, b, c\}$, and

$$\begin{cases} v_a = m \cdot \cos \omega t \\ v_b = m \cdot \cos(\omega t - 2\pi/3) \\ v_c = m \cdot \cos(\omega t + 2\pi/3) \end{cases} \quad (4)$$

The offset voltage sign depends on the direction of the NP current. Magnitude of offset voltage should be always enough to compensate. Thus, the magnitude of the offset voltage must be related to the deviation between two capacitors (Δv_c). Therefore, the equation of offset voltage should be defined as follows:

$$v_{x_off} = k_p |\Delta v_c| \cdot \text{sign} (\Delta v_c \cdot i_x) \quad (5)$$

With k_p is a parameter and needs to be adjusted. The magnitude of the offset voltage equal absolute value of capacitor voltage deviation multiplied by coefficient k_p . The $\text{sign}(\Delta v_c \cdot i_x)$ is considered as sign of the offset voltage. If wrong sign is applied to the offset voltage, it will produce voltage imbalance.

The block diagram of the control signals creating block was showed in fig. 2. The amplitude of offset voltage should be limited before taking to adder. If there is no offset limiter or the offset limit is so high, then capacitor voltage will not be balanced. Otherwise, if offset limit is so low, it will take the long time to balance capacitor voltage. This issue is concretely presented in fig. 8. Choosing value of k_p is also important because it affects the balancing time and capacitor voltage variation.

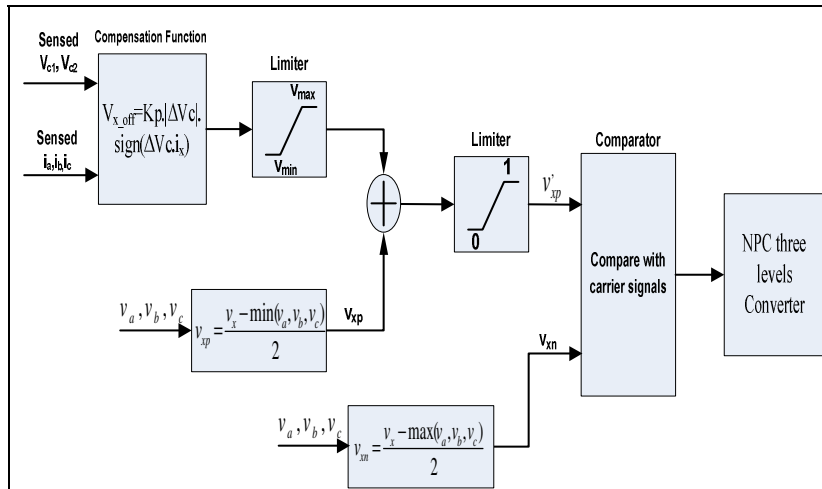


Fig. 2. Control signals creating block diagram

3 Results and Discussion

For the simulation examples, the converter is supplied by a dc source, V_{dc} equals to 1100V and the initial voltages: $V_{C1}=400V$, $V_{C2}=700V$, $C1=C2=220\mu F$, carrier frequency f_s is 5 KHz, output frequency $f_0=50$ Hz.

3.1 Results and the Influence of k_p on Capacitor Voltage

Fig.3 shows the voltage waveform of the two capacitors in some different values of k_p , where $R = 7.42\Omega$, $L = 47mH$, m equals 1. Values of k_p is in turn as 0.001, 0.5, 1

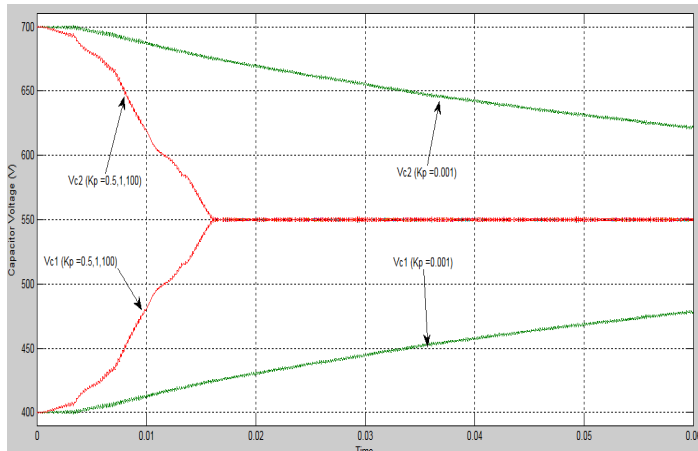


Fig. 3. Waveform of capacitor voltage by some factor k_p

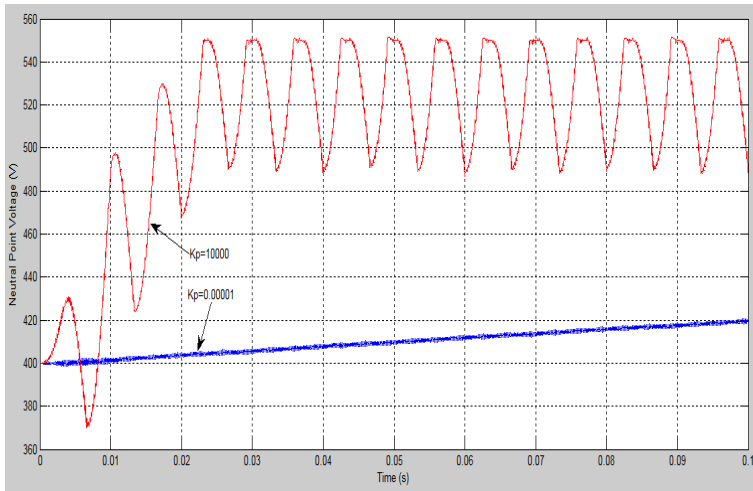


Fig. 4. Waveform of capacitor voltage in two cases of k_p (without limiter)

and 100. When k_p equals to 0.5, 1 or 100, the capacitor voltages have nearly identical waveforms and shorter balancing time than in case k_p equal to 0.001. Thus, the magnitude of k_p affects to the balancing time (t_B) and maximum capacitor voltage deviation ($\Delta V_{C_{\max}}$). However, if the correct sign is applied but not an optimal magnitude, following effects are observed (fig. 4). If the value of offset is lower than required, a slow voltage balancing dynamic on the capacitors is produce. Otherwise, if the value of offset is higher than optimal one, low frequency voltage oscillations appear in the NP.

Waveform and THD of load voltage with different k_p are showed in fig.5. And fig.6 shows the wareform and THD of load currents when k_p equal to 0.5, modulation index equal to 1 and offset limit is ± 0.2 .

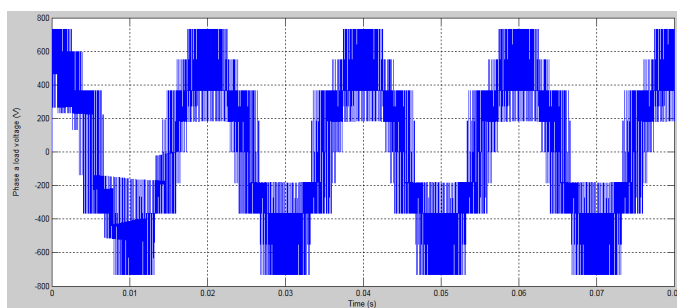


Fig. 5. Waveform of phase a load voltage

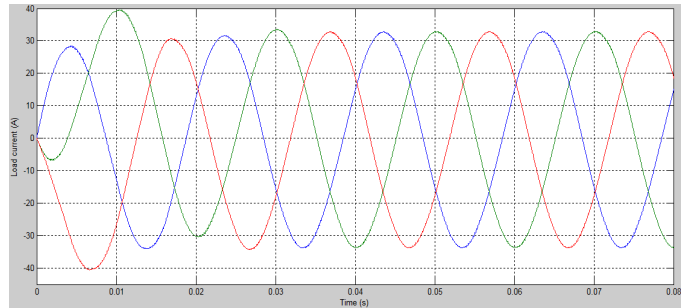


Fig. 6. Waveform of phase a load current

3.2 The Influences of Offset Limit on Capacitor Voltage

The waveform of capacitor voltage when adjusting the offset limit was showed in fig.7. The values of load are $R=7.42\Omega$, $L=47mH$ and capacity equal to $220\mu F$. Result shows that, the lower limit the higher balancing time. When offset limit is equal to ± 0.01 , the capacitor voltage is not balancing before 0.06 seconds. It can be explained that when offset limit is too low, the offset adding to upper control signal is small too. So, it spends much time to make capacitor voltage balancing. If offset limit higher than 0.2 then the balancing time in all case of offset limit is similar. But the higher offset limit, the higher capacitor voltage deviation. According to fig.8 we should choose offset limit being ± 0.2 when balancing capacitor voltage for three levels NPC converter if using this method.

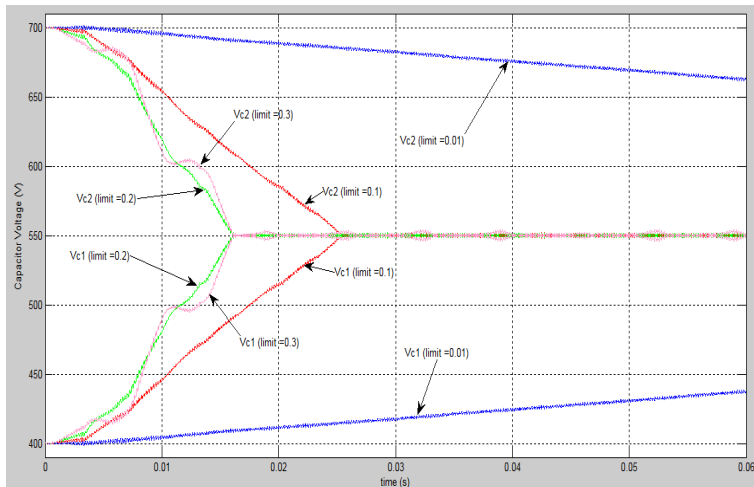


Fig. 7. Waveform of capacitor voltage in some offset limit

3.3 The Influences of Modulation Index on Capacitor Voltage

Fig.8 describes the capacitor voltage waveform in some values of m . Where k_p equals to 1, other parameters are same as Section A. The result shows that, when m equals to 1, balancing time and maximum value of capacitor voltage deviation are lowest. When m equals to 1.1547, balancing time and maximum value of capacitor voltage deviation are highest. Note that, 1.1547 is maximum value of modulation index in line near arrange when using SFO-PWM method.

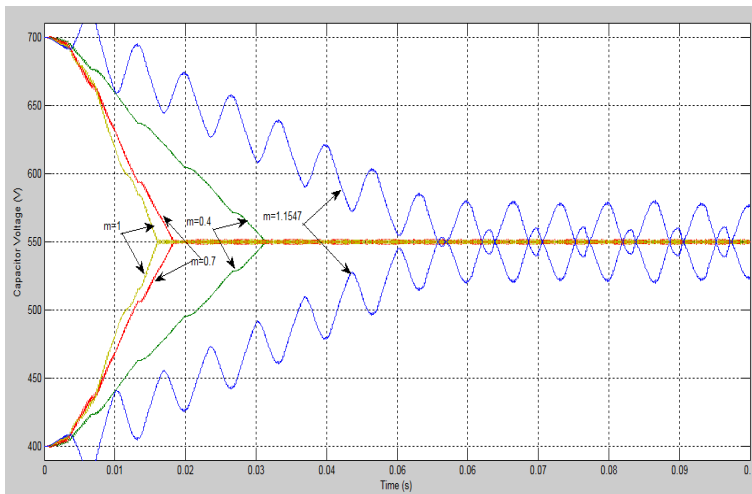


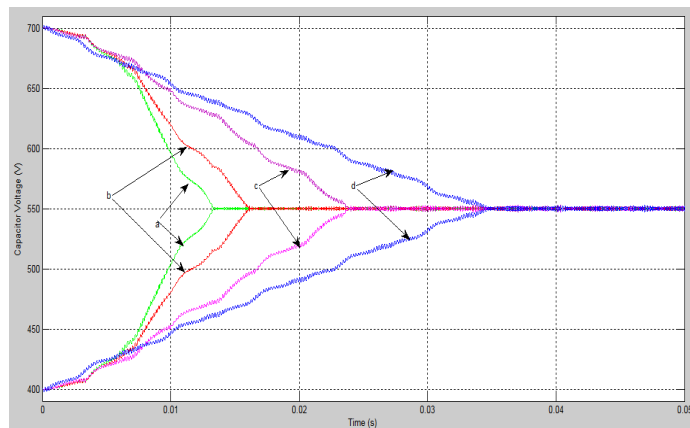
Fig. 8. Waveform of capacitor voltage with some case of modulation index

3.4 The Influences of $\cos\phi$ on Capacitor Voltage

Fig.9 shows the influence of the factor power ($\cos\phi$). In case (a) $\cos\phi$ is 0.2, case (b) $\cos\phi$ equals to 0.45 case (c) $\cos\phi$ is 0.85, case (d) $\cos\phi$ equals to 1. The waveform shows that, the greater power factor, the higher t_B . However, when the power factor is too small (case a) the variation of capacitor voltage lower than the remaining cases.

4 Optimal Value of K_p

The k_p , modulation index and power factor are all affect to balancing time and deviation between two capacitors. So, when choosing k_p for the offset function we should pay attention to modulation index and power factor. The value of k_p in which the balancing time and maximum deviation between two capacitors are lowest is called optimal value of k_p . This section presents the optimal value of k_p with some different values of power factor and modulation index. Getting optimal k_p is done by programmed and simulation in matlab. With each value of m and $\cos\phi$, increasing k_p from 0 to 10 with step by 0.01 and calculating the value of ΔV_c and t_B . The values of

**Fig. 9.** Waveform of capacitor voltage by some $\cos\phi$ **Table 1.** The relationship between optimal values of K_p and power factor in some cases of modulation index

$\cos\phi$	$m=0.4$	$m=0.8$	$m=1$	$m=1.1547$
0.00	0.33	0.14	0.25	0.20
0.05	0.31	0.22	0.21	0.21
0.10	0.31	0.15	0.15	0.25
0.15	0.46	0.16	0.18	0.25
0.20	0.42	0.19	0.19	0.26
0.25	0.39	0.16	0.22	0.27
0.30	0.36	0.14	0.19	0.31
0.35	0.34	0.12	0.28	0.32
0.40	0.37	0.16	0.14	0.29
0.45	0.35	0.08	0.13	0.46
0.50	0.32	0.09	0.11	0.44
0.55	0.32	0.07	0.13	0.42
0.60	0.32	0.08	0.12	0.13
0.65	0.35	0.09	0.12	0.15
0.70	0.43	0.07	0.11	0.39
0.75	0.55	0.10	0.20	0.25
0.80	0.49	0.11	0.15	0.25
0.85	0.43	0.15	0.31	0.11
0.90	0.46	0.13	0.29	0.12
0.95	0.47	0.15	0.29	0.11
1.00	0.42	0.16	0.16	0.10

k_p in which result has lowest value of ΔV_c and t_B is called optimal k_p . Tab. 1 shows the optimal value of k_p in some different values of m and $\cos\varphi$ varies from 0 to 1. According to the table 1, the highest optimal k_p is 0.55 and the lowest optimal k_p is 0.07. Note that, with a pair of modulation index and power factor, parameter k_p can have some value which achieves the same lowest balancing time and deviation of capacitor voltage.

5 Conclusion

This paper presents a control approach for the balancing of the dc-link capacitor voltages of three levels NPC converter. The presented balancing algorithm has achieved the purpose of balance. The simulation result showed that k_p , $\cos\varphi$, m affect balancing time and imbalance voltage. To achieve the best result, k_p must be adjusted to the best value. The best value of k_p depends on power factor and modulation index.

Acknowledgements. This work is supported mainly by Van Hien University, supported by part of the National Key Lab of Digital Control and System Engineering-University of Technology-Vietnam National University Ho Chi Minh city. The authors would also like to thank the support of the Power Engineering Research Lab-University of Technology-Vietnam National University Ho Chi Minh City.

References

1. Celanovic, N., Boroyevich, D.: A Fast Space-Vector Modulation Algorithm for Multilevel Three-Phase Converters. IEEE Transaction on Industry Applications 37(2) (2001)
2. Nho, N.V., Youn, M.J.: A Unified carrier based PWM Method in Multilevel Inverters. Journal of Power Electronics 5(2), 142–150 (2009)
3. Zaragoza, J., Pou, J., Ceballos, S., Robles, E., Jaen, C., Corbalan, M.: Voltage Balance Compensator for a Carrier Based Modulation in the Neutral Point clamped Converter. IEEE, 305–314 (2009)
4. Busquets-Monge, S., Alepuz, S., Bordonau, J., Peracaula, J.: Voltage Balancing Control of Diode-Clamped Multilevel Converters with Passive Front-Ends. IEEE (2009)
5. Ben-Brahim, L., Tadakuma, S.: A novel multilevel carrier-based PWM control method for GTO inverter in low index modulation region. IEEE Trans. Ind. 42, 121–127 (2006)
6. Ben-Brahim, L.: A Discontinuous PWM Method for Balancing the Neutral Point Voltage in Three-Level Inverter-Fed Variable Frequency Drives. IEEE Transactions on Energy Conversion 23(4) (2008)
7. Pou, J., Rodríguez, P., Sala, V., Zaragoza, J., Burgos, R., Boroyevich, D.: Fast-Processing Modulation Strategy for the Neutral Point Clamped Converter with Total Elimination of the Low-Frequency Voltage Oscillations in the Neutral Point. IEEE Trans. Ind. (2005)

TLSR: A Tree Link State Routing for Infrastructure-Based Mobile Ad Hoc Networks^{*}

Chi Trung Ngo and Hoon Oh^{**}

School of Electrical Engineering,
University of Ulsan,
Ulsan Metropolitan City, South of Korea
chitrung218@gmail.com, hoonoh@ulsan.ac.kr

Abstract. The existing protocols for the Internet connectivity of mobile ad hoc networks suffer from high overhead since they often rely on flooding in mobility management and/or route discovery. In our approach, mobility management of mobile nodes is achieved in the construction process of tree topology and also contributes to building topology information for a routing protocol, resolving the inherent problem of the excessive control overhead in link state routing protocols. The activities of the routing protocol help updating the topology information. In this way, mobility management and routing protocol collaborate to increase convergence speed of topology and reduce control overhead. In addition, a message aggregation technique is used to reduce the congestion of mobile nodes near the Internet Gateway that process much more control messages. Simulation results show that the proposed method far outperforms AODV-Hybrid and OLSR+.

Keywords: Internet Connectivity, Mobility management, Mobile ad hoc networks, Aggregation, Link state routing, Tree topology.

1 Introduction

The provision of Internet connection is an essential service for extending the usability of mobile ad hoc networks (MANETs). This service can be implemented by integrating an Internet Gateway into MANETs, referred to as Infrastructure-based mobile ad hoc networks (abbreviated to IFMANET). In IFMANET, one mandatory requirement is that IGs have to manage the mobility of the MNs via multi-hop to provide uninterrupted connections for them [1] while they moves freely, thereby causing high control overhead. Furthermore, the routing protocols for IFMANETs can be designed with a new approach to take advantage of powerful IGs.

* This research was supported by Basic Science Research Program through the National Research Foundation of Korea (NRF) funded by the Ministry of Education (2013R1A1A2013396).

** Corresponding author.

A lot of researches have been conducted for the provision of Internet connectivity for MANETs. In [1], Sun et al. discussed how Mobile IP and AODV [2] can cooperate to discover multi-hop paths between MNs and IGs. Ratanchandani et al. [3] proposed a hybrid scheme that combines some techniques, such as agent advertisements, TTL scoping, and the detection of agent advertisements, eavesdropping, and agent solicitation. M. Benzaid et al. [4] proposed a hierarchical architecture that uses a proactive scheme to integrate Mobile IP and OLSR [5] routing protocol. In this approach, control overhead can be reduced by exploiting Multipoint Relays (MPRs) technique to limit the number of retransmissions of topology control as well as advertisement messages. Recently, some adaptive gateway discovery algorithms have been considered in IFMANETs. A. J. Yuste et al. [6] proposed an adaptive scheme in which IGs dynamically adjust the interval between two consecutive advertisement messages based on a genetic algorithm to decrease network congestion and achieve lower end-to-end delay.

The aforementioned approaches use one of the ad hoc routing protocols such as AODV, DSR, OLSR, and DSDV for routing while focusing on the invention of an efficient mobility management protocol. These protocols suffer from the overhead of flooding or the low convergence speed of topology information. Furthermore, if both mobility management and routing use flooding, the performance will be worsen due to the double impact of control overhead caused by two sources of flooding. On the other hand, a tree-based approach was proposed [7], in which a number of small trees are managed to reduce tree maintenance cost and every MN in the tree maintains its own tree information such as its descendants, its parent, and its IG. This approach can reduce the control overhead of mobility management; however, the improvement is restricted since it still used flooding, although limited, for route discovery.

In this paper, we propose a tree-based link state routing protocol in which mobility management utilizes tree topology. During mobility management, a gateway can build and update tree topology by having every node send a registration message including its link states to the gateway periodically. The constructed topology information is used later when a routing function explores a routing path. Thus, the proposed approach does not pay additional cost in building the topology information for routing. More importantly, the funneling effect [8] that occurs because the nodes near the gateway process much more messages, can be alleviated significantly by employing a message aggregation technique. According to the previous study [9], message aggregation not only reduces collision, but also improves network throughput.

In what follows, Section 2 gives network model with message and graph definitions. Section 3 details a tree link state routing protocol with a message aggregation technique. Section 4 evaluates our approach and Section 5 concludes the paper.

2 Preliminary

2.1 The Network Model

The network considered in this paper consists of stationary Internet Gateways (IGs) and a number of mobile nodes (MNs). We assume that IGs share their network

management information through a high speed wired network. Every MN can act as a router to receive and forward data to other MNs. An IG is equipped with two network interface cards so that it can communicate with MNs using one interface card and also communicate with a wired host in the Internet using the remaining one. Both IG and MN have the same and limited wireless transmission range to reduce interference. An MN can not only initiate communication with any wired host or MN but also be requested for connection from wired hosts in the Internet or MNs in other wireless networks via an IG. Thus, MNs should do their best to register with the IG so that the IG can keep track of the locations of MNs. A connection between two MNs is said to be a link while a connection between an MN and its parent is to be a *tree-link*. A node is a *tree-node* if it belongs to a tree; otherwise, it is an *orphan-node*. The network forms a tree topology as shown in Fig. 1.

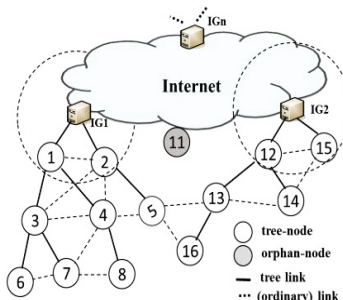


Fig. 1. The network model

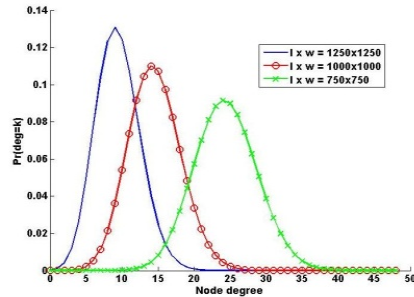


Fig. 2. The distribution of node degree with different network dimensions, $R = 250$ m, and $n = 100$ nodes

2.2 Messages and Notations

We define some notations as follows:

- HopToIG*: indicates the distance in hops from a node to its IG.
- $NS(i)$: is a set of neighbors of node i .
- $C(i)$: is a set of children of node i .
- $TS(i)$: is a set of tree-nodes in a given tree whose root is node i .
- $P(i)$: is a parent of node i .

Every node i maintains its topology graph, $TG(i)$, defined as follow.

$TG(i) = \{V(i), E(i)\}$, $V(i) = \{x, y \mid x \in TS(i), y \in NS(x)\}$, and $E(i) = \{(x, y) \mid x \in TS(i), y \in NS(x)\}$. For example, in Fig. 1, $TS(4) = \{4, 8\}$ and $TG(4) = \{(1, 2, 3, 5, 7, 8), \{(4, 1), (4, 2), (4, 3), (4, 5), (4, 7), (4, 8), (8, 7)\}\}$. We assume that IGs can share their topology graphs through a high speed network.

In addition we elucidate some messages for convenience as follows:

- $IG\text{-ADV} = (MsgId, W_1, a)$: An IG broadcasts this advertisement message to advertise its presence *periodically*, where $MsgId$ distinguishes this message from other messages, W_1 and a are the values used in a time generation function for skewed time synchronization.
- $J\text{-REQ} = (MsgId, HopToIG, W_1, a)$: An MN sends this join request message to join an IG or an MN as a primary parent
- $REG = (MsgId, NS(x))$: An MN x includes its link state, $NS(x)$, in this message.

3 Tree Link State Routing (TLSR)

3.1 Topology Management

3.1.1 Tree Construction

A tree construction is initiated by IG-ADV issued periodically by an IG. An MN receiving this message tries to join the IG by replying with J-REQ. Upon receiving the J-REQ, the IG takes the MN as its child and responds with ACK. Then, the MN becomes a tree-node as a child of the IG when it receives ACK. Similarly, another nearby orphan-node can overhear the J-REQ and thus can join the tree-node that issued the J-REQ previously. This join process continues. In this process, every MN i can maintain its $NS(i)$ by receiving or overhearing J-REQ. In addition, an MN can maintain its $C(i)$ upon receiving J-REQ or REG message from a node. The process of receiving REG is discussed in the next following sections.

A node includes a current time in its J-REQ as a timestamp. If an MN has overheard J-REQs from multiple tree-nodes, it selects a tree-node that provides the shortest distance to an IG as a primary parent. The ties are broken in the order of the timestamps. The timestamp contributes to increasing the degree of message aggregation by the principle “the early actor gets more children.” The rest of the tree-nodes with the same distance become auxiliary parents.

An MN takes an auxiliary parent with the second earliest timestamp as a primary parent if it loses its primary parent. If it does not have any auxiliary parent, it takes a neighbor that has the shortest hop distance to an IG from its neighbor list for joining. If it does not have a tree-node to join, it becomes an orphan node until the next tree construction cycle. This will not cause any serious problem, except that it loses one registration message. This way of tree construction may cause power consumption biased to a certain node; however, power consumption after next tree construction can be biased to different nodes since nodes issue J-REQ in a random order.

3.1.2 Skewed Time Synchronization

Time at which tree-nodes initiate their registration messages needs to be synchronized in a skewed manner throughout the nodes in a tree structure so that every node issues its registration message earlier than its parent. In this way, a node can maximize the degree of aggregation by performing aggregation after receiving the registration messages from all its children and this way of harmonious transmission can also reduce message collision.

Let T_{shd} be the worst case time delay for a message transmission (J-REQ and REG message) that includes transmission delay, propagation delay, processing delay, and staggering delay or small random delay used to avoid collisions between different transmissions. We denote T_{join} and T_{reg} as an amount of time for a node to finish joining its new parent and to send an REG message to its parent in the worst case, respectively

(a) Wait time generation function

During the tree construction process, MNs have to generate their transmission initiation times of REG according to a time generation function. Let $WTime(d)$ be a wait time function for generating a wait time that an MN at depth d has to wait before it issues its REG message at every registration interval. Then, this function is subject to the following requirements

Req. 1: For an MN staying at depth i and an MN staying at depth j , $WTime(i) < WTime(j)$ if $i > j$.

Furthermore, nodes near an IG compete more for channel access since they have to process more REGs or the bigger REG by aggregation delivered from their children. We define $WTime_Gap(i)$ as the wait time gap between two MNs located at two adjacent depths i and $i+1$, thus it would be desirable to have the following inequality requirement.

Req. 2: $WTime_Gap(i) \geq WTime_Gap(j)$ if $i < j$.

Considering these two requirements, we devise the following time generation function to generate the wait time of an MN at depth d .

$$WTime(d) = W_1 \times a^{d-1} \quad (1)$$

where, $d \geq 1$, W_1 is the wait time of a node at depth one and a is the base of exponential function ($0 < a < 1$). Since a is a fractional number less than *unity*, $WTime(d)$ is a decreasing function that has the maximum value W_1 , thus satisfying *Req. 1*. Since the wait time W_1 of a node located at depth 1 should be at least larger than the amount of time for the other nodes to finish joining the tree plus the amount of time to receive all REG messages from its descendants, the W_1 value has to satisfy the following condition.

$$W_1 \geq (H - 1) \times (T_{join} + T_{reg}) \quad (2)$$

where, H is a maximum tree depth. Then, we get the wait time gap between two MNs located at two adjacent depths as follows

$$WTime_Gap(d) = |WTime(d) - WTime(d + 1)|, 1 \leq d < H \quad (3)$$

Substituting Eq. (1) for Eq. (3), we get

$$WTime_Gap(d) = W_1 \times (1 - a) \times a^{d-1}, 1 \leq d < H \quad (4)$$

$WTime_Gap(d)$ is an exponentially decreasing function of a . Considering a node that stays at depth d , the value of $WTime_Gap(d)$ increases as a gets smaller and/or as depth d decreases, thus satisfying *Req. 2*. Since every node should send its REG message before nodes at the one-hop lower depth start sending REG messages in

order to maximize aggregation, the minimum of wait time gap from Eq. (4) should be at least greater than the worst case of one-hop registration transmission in one interval, hence we get the following constraint.

$$\text{Min_WTime_Gap} = \text{WTime_Gap}(H - 1) > T_{reg} \quad (5)$$

Moreover, since a node can have its neighbors over three depths, its own depth, its depth minus 1, and its depth plus 1, we simply assume that each node has approximately $nNbrs/3$ neighbors at each depth. According to the join process discussed in Subsection 3.1, a node at depth i competes with its neighbors at depth i and its neighbors at depth $(i - 1)$. Since its parent-to-be at depth $(i - 1)$ has already joined a tree, the total number of competing neighbors is $(2 \times nNbrs/3 - 1)$. In the worst case, a node can start its own join process after the join completion of all the competing neighbors. On the other hand, during the registration process, a node only competes with its neighbors that stay at the same depth as its own depth for sending the REG message. Considering that a node's parent already has joined a tree, T_{join} and T_{reg} are given as follows.

$$T_{join} = T_{shd} \times (2 \times nNbrs/3 - 1 + 1) = T_{shd} \times \left(2 \times \frac{nNbrs}{3}\right) \quad (6)$$

$$T_{reg} = T_{shd} \times (nNbrs/3 + 1)$$

Substituting Eq. (6) for Eq. (2), we get

$$W_1 \geq (H - 1) \times T_{shd}(nNbrs + 1) \quad (7)$$

(b) Estimation of depth H and nNbrs

If the IG and all mobile nodes are uniformly distributed in a square area of $m \times m$, the depth distribution of nodes in the tree topology can be obtained using the equation of cumulative distribution functions of distance l between two uniformly distributed nodes which is less than value of L in Eq. (12.1) and Eq. (12.2) in [10]. Referring to Fig. 7 in [10], we can obtain the distribution of depth according to variation of m when $R = 250$ m; for example, when the number of nodes is 100 and the transmission range of node = 250 m in area 1000 x 100 (m²). We can see that the probability of depth = 5 is approximately 3 % and it is would be reasonable to infer that the possible maximum depth in this case is $H = 5$.

Furthermore, with the given network dimension $l \times w$, transmission range R , and the number of nodes n , we can calculate the distribution of the number of neighbors, $nNbrs$, of nodes in the network using the probability mass function proposed in Eq. (11) in [11]. Fig. 2 shows the distribution of node degree according to variations of network dimension with $R = 250$ m, and $n = 100$ nodes. Since the degree of a node corresponds to the average number of neighbors, $Nbrs$, that the node can have, we obtain $nNbrs = 15$ with $l \times w = 1000 \times 1000$ (m²) and $n = 100$ nodes.

3.1.3 Aggregated Transmission

A node does not have to report its upstream tree-link to its parent that already knows the link. Thus, we defined the reduced link state of node i , $RLS(i)$, as follows.

$$RLS(i) = \{(i, j) \mid j \in (NS(i) - P(i))\}$$

We also define the aggregated link state $ALS(i)$ of node i as follows.

$$ALS(i) = \cup_{x \in C(i)} ALS(x) \cup RLS(i)$$

where, $ALS(x)$ is aggregated link state included in received REG from node x , a children of node i .

Aggregated transmission is performed as follows. Leaf node j sends REG = ($ALS(j) = RLS(j)$) to its parent as soon as its *WTime* expires. An intermediate node i saves $ALS(k)$ received from its children k until its *WTime* expires, aggregates the saved ones with $RLS(i)$ into $ALS(i)$ when its *WTime* expires, and then sends REG = ($ALS(i)$) to its parent. Any aggregated packet that exceeds the maximum transmission unit (e.g. 2272 bytes in 802.11 WLAN) is segmented into the smaller ones before transmission.

3.2 Path Management

3.2.1 Path Discovery

A node acquires a path by sending a *path calculation request* (PC-REQ) message to an IG. However, this can increase path acquisition delay and overhead for the nodes near the IG. Since every internal node in a tree maintains partial topology information, a path can be discovered in a progressive way. A *progressive path* (PP) discovery is performed as follows. A source that needs a path tries to calculate a path using its own TG. If it cannot find a valid path, it sends PC-REQ to its parent and associates a timer, *PC-RES-timer*, with that PC-REQ, waiting for a *path calculation response* (PC-RES) message. Upon receiving the PC-REQ, a node calculates a path using its TG. If it succeeds, it responds to the source with PC-RES including the obtained path. Otherwise, it continues to forward the PC-REQ to its parent. If the source receives PC-RES before the *PC-RES-timer* expires, it sends data packets using the path. Otherwise, it performs the same path discovery process after some intervals.

3.2.1 Path Recovery

During packet transmission, if a node does not receive ACK after it sends a packet to a downstream node on the path, it judges that the corresponding link is broken. Then, the node issues a *route error* (RERR) message that includes the broken link to a source and at the same time, initiates a path discovery with PC-REQ that includes the broken link to find a salvage path to salvage the undelivered packets. Upon receiving PC-REQ, every node eliminates the broken link from its TG before calculating a path. Upon receiving RERR, a source initiates a new path discovery.

4 Performance Evaluation

Firstly, we select the proper value of W_1 and a based on the above analysis in section 3.1.2. Then, *TLSR-PP* (TLSR using the Progressive Path discovery), *OLSR+* [12] and

AODV-Hybrid combining AODV [2] and Hybrid scheme [3] are evaluated comparatively.

4.1 Simulation Environment and Performance Metrics

We conducted simulations using the commercial network simulator QualNet 5.02. We used three scenarios, S1, S2, and S3 that have an IG located at the center, the middle of the top, and the corner in the rectangular terrain of 1000 x 1000 (m^2), respectively. These scenarios were selected to generate various sizes of trees and consider different flooding ranges. In order to evaluate the proposed protocol, we make data communications between 15 flows of sources and destinations chosen randomly in MANETs with 512 bytes of packet size. The packet data rate at sources was fixed at 2 packets per second. The Random Waypoint was used to model the mobility of nodes with 30 seconds of pause time. Furthermore, the wireless bandwidth and the transmission range of nodes are set 2 Mbps and 250 m, respectively. All the simulations were performed within 600 seconds and the results were averaged after 10 runs with different seeds. The performance metrics such as *Control Overhead (CO)*, *Delivery Ratio (DR)*, *End-to-end delay (E2ED)*, are used for evaluation with variation of the number of nodes ($nNodes$) and the maximum speed ($mSpeed$) of node.

4.2 Optimal Selection of W_1 and a

From the subsection 3.1.2 – (b), the maximum tree depth H and the average number of nodes $nNbrs$ are estimated to be 5 and 15 in the dimension of 1000 x 1000 m^2 . Supposing that $T_{shd} = 0.03$ sec, by applying $H = 5$ and $nNbrs = 15$ to Eq. (7), then W_1 should be greater than 1.92 (sec): $W_1 \approx 2$ (sec). Moreover, with $W_1 = 2$ (sec) and $H = 5$, from Eq. (5) we can get the appropriate range of $a = [0.6, 0.82]$ since $\text{Min_WTime_Gap} > T_{reg}$ (= 0.18 calculated from Eq. (6)).

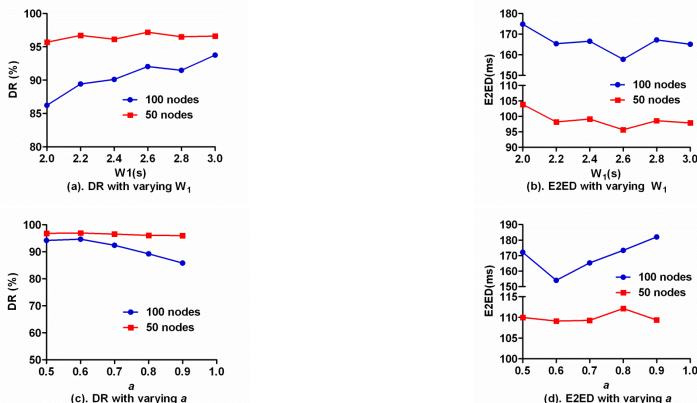


Fig. 3. Examination of W_1 and a (S3, $nNodes = 50/100$, $mSpeed = 10$ m/s)

Then, we performed simulation using the dimension and the transmission range given in section 4.1, and scenario S3 with $nNodes = 50, 100$ and $mSpeed = 10 \text{ m/s}$ in order to choose an optimal value of a in $[0.6, 0.82]$ complying with $W_1 = 2 \text{ (sec)}$.

Referring to Fig. 3-(a), the graph with 100 nodes indicates that the W_1 value should be increased as $nNodes$ increases, which well complies with our previous analysis (see Eq. (7)). According to Fig. 3-(b), E2ED has a decreasing pattern from 2 to 2.6(s) and then an increasing one from 2.6 to 3(s) for both graphs. The reason is that the large value of W_1 may lower the accuracy of topology information received at an IG due to the long waiting time. It seems that $W_1 = 2.6 \text{ (sec)}$ is appropriate overall.

To choose an optimal value of a ranging between 0.6 and 0.82, we performed simulation by fixing $W_1 = 2.6 \text{ (sec)}$. Fig. 3-(c) shows that the DR decreases sharply when a increases from 0.6 to 0.9 in the scenario with 100 nodes. On the contrary, as can be seen from Fig. 3-(d), the E2ED of scenario with 100 nodes increases significantly over $a = 0.6$, while it shows slight increase with 50 nodes. From these simulation results, we conclude that the performance of TLSR is sensitive to the values of W_1 and a , and its best results are achieved when the values of W_1 and a are set to 2.6 (sec) and 0.6, respectively, in the given scenarios.

4.3 Comparison with AODV-Hybrid and OLSR+

4.3.1 Evaluation with Varying Speed

Fig. 4 – Fig. 6 compare three protocols with varying $mSpeed$ when $nNodes$ is 50 in scenario S3. As can be seen from Fig. 4, control overhead of TLSR-PP is considerably low compared to the other two's due to the use of aggregation and the removal of flooding. Referring to Fig. 5, the delivery ratio of TLSR-PP and OLSR+ slightly decreases with the increase in node mobility since nodes fail frequently to send the registration messages to update its link state with the IG in case of high speed, thus the IG does not have enough update on network topology to find paths for sources. This leads to the decrease in performance. On the contrary, since AODV-Hybrid can explore a path on demand, it is little sensitive to mobility. That is why the performance of AODV-Hybrid is not affected by node mobility. Nevertheless, its overall performance is still lower than that of TLSR-PP. This also explains why as node speed increases, the end-to-end delay of both TLSR and OLSR+ tends to increase linearly, while it seems to keep constant in case of AODV-Hybrid (see Fig. 6).

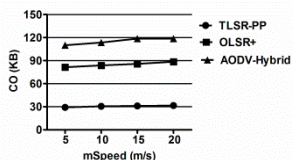


Fig. 4. Control overhead with varying $mSpeed$ ($S3, nNodes = 50$)

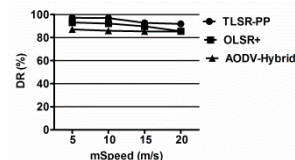


Fig. 5. Delivery ratio with varying $mSpeed$ ($S3, nNodes = 50$)

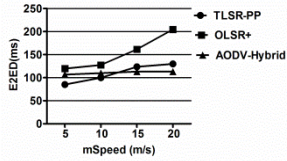


Fig. 6. End-to-end delay with varying *mSpeed* (S3, *nNodes* = 50)

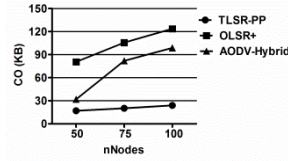


Fig. 7. Control overhead with varying *nNodes* (S1, *mSpeed* = 10 m/s)

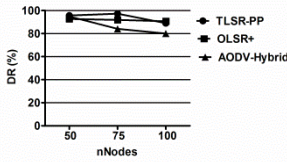


Fig. 8. Delivery ratio with varying *nNodes* (S1, *mSpeed* = 10 m/s)

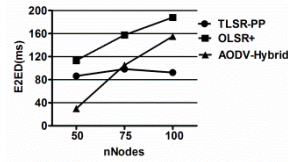


Fig. 9. End-to-end delay with varying *nNodes* (S1, *mSpeed* = 10 m/s)

4.3.2 Evaluation with Varying Node Density

Fig. 7 – Fig. 9 compare the three protocols with varying *nNodes* when *mSpeed* is fixed at 10 m/s in scenario S1. As can be seen in Fig. 7 the control overhead of TLSR-PP is sustained low compared to OLSR+ and AODV-Hybrid. This result comes from the utilization of message aggregation and the efficient topology management without using the flooding. However, because in the scenario S1 the IG is placed at the middle of the terrain, the increase in *nNodes* will increase the number of children of an IG and also increase the number of small sub-trees formed by those children. So, the TLSR-PP discovery does not make big improvement since PC-REQ will mostly reach an IG. Thus, the delivery ratio of TLSR-PP degrades slightly as *nNodes* increases.

5 Conclusion

We proposed a novel tree link state routing protocol (TLSR) in which topology management function and routing function cooperates closely. Not only do MNs exclude flooding in both mobility management and routing, but also they can make use of unicast mechanism to increase the reliability of transmission. To resolve a funneling effect, the TLSR employs a message aggregation technique that relies on skewed time synchronization to increase the degree of aggregation.

References

1. Sun, Y., Belding-Royer, E.M., Perkins, C.E.: Internet Connectivity for Ad Hoc Mobile Networks. International Journal of Wireless Information Networks 9(2), 75–88 (2002)

2. Perkins, C.E., Royer, E.M.: Ad-hoc on-demand distance vector routing. In: Proceedings of the 2nd IEEE Workshop on Mobile Computing Systems and Applications, pp. 90–100 (1999)
3. Ratanchandani, P., Kravets, R.: A hybrid approach to Internet connectivity for mobile ad hoc networks. In: Proceedings of the International Conference on Wireless Communications and Networking (WCNC), pp. 1522–1527 (2003)
4. Benzaïd, M., Minet, P., Agha, K.A., Adjih, C., Allard, G.: Integration of mobile-IP and OLSR for a universal mobility. *Wireless Networks* 10(4), 377–388 (2004)
5. Clausen, T., Jacquet, P.: Optimized link state routing protocol (OLSR). RFC 3626. IETF (2003)
6. Yuste, A.J., Trujillo, F.D., Trivi, A., Casilar, E.: An adaptive gateway discovery for mobile ad hoc networks. In: Proceedings of the 5th ACM International Workshop on Mobility Management and Wireless Access, pp. 159–162 (2007)
7. Oh, H.: A tree-based approach for the Internet connectivity of mobile ad hoc networks. *Journal of Communications and Networks* 11(3), 261–270 (2009)
8. Ahn, G.-S., Hong, S.G., Miluzzo, E., Campbell, A.T., Cuomo, F.: Funneling-MAC: a localized, sink-oriented MAC for boosting fidelity in sensor networks. In: Proceedings of the 4th International Conference on Embedded Networked Sensor Systems, Boulder, Colorado, USA, pp. 293–306 (2006)
9. Youngsoo, K., Sunghyun, C., Kyunghun, J., Hyosun, H.: Throughput enhancement of IEEE 802.11 WLAN via frame aggregation. In: Proceedings of the IEEE 60th Vehicular Technology Conference, pp. 3030–3034 (2004)
10. Dung, L.T., An, B.: A modeling framework for supporting and evaluating performance of multi-hop paths in mobile ad-hoc wireless networks. *Computers & Mathematics with Applications* 64(5), 1197–1205 (2012)
11. Lifang, G., Harfoush, K., Huimin, X.: Distribution of the Node Degree in MANETs. In: Next Generation Mobile Applications, Services and Technologies (NGMAST), pp. 162–167 (2010)
12. Yu, B., Zhang, W., Li, L.: Design and implementation of ad-hoc dynamic gateway based on OLSR and mobile IP. In: Proceedings of the 5th International Conference on Wireless Communications, Networking and Mobile Computing, pp. 2997–3000 (2009)

Selection Combining Technique and Its Real-Time FPGA Implementation for Spectrum Sensing Efficiency Improvement in Cognitive Radio

Tu T. Nguyen, Tri M. Nguyen, Khoa L. Dang, and Phuong Huu Nguyen

Faculty of Electronics and Telecommunications, University of Science HCM City, Vietnam
nttu@fetel.hcmus.edu.vn

Abstract. Reception diversity has considered as an effective way to improve the system performance. In this paper, we present a real-time hardware implementation of spectrum sensing based energy detection (ED) with multi-receive antenna technique. We only focused on Selection Combining (SC) technique due to low complexity in Radio Frequency (RF) chain (need only one RF chain). The system performance is evaluated in real-time hardware implementation over Rayleigh environment based FPGA (Field Programmable Gate Array) platform. The DVB-T (Digital Video Broadcasting - Terrestrial) signal is designed as primary signal. This is specified in draft IEEE 802.22 WRAN standard for re-utilization the TV frequency band. The target FPGA board is Stratix II EP2S180. The fixed point 32 bits (fraction: 22.10) is chosen for calculation in FPGA model. The empirical results showed that the performance of ED with selection combining technique was improved remarkably. Thus, we conclude that selection combining techniques can be used to overcome the drawbacks of ED over Rayleigh fading environment.

Keywords: CR, SS-ED, SC, multi-antenna, receiver diversity, FPGA, DVB-T, IEEE 802.22.

1 Introduction

The number of wireless devices has increased dramatically in many countries these days. Most of them operate in fixed spectrum bands. This results in low spectrum utilization in some specific spectrum bands. Cognitive Radio (CR) or Dynamic Spectrum Access (DSA) has been studied for addressing this problem. CR technology improves spectrum usage efficiency by a special policy spectrum access. It allows unlicensed users (cognitive users or secondary users – SUs) exploit spectrum resource of licensed users (Primary Users – PUs) when PU is not in demand. In such scenarios, the SUs must have ability to vacant the borrowed resources from PUs as quickly as possible. In other words, the SUs must guarantee that its harmful interference to PUs should be below a certain level. It is really a challenging problem in cognitive radio network (CRN).

In CRN, the SUs must have ability to detect whether PU signal present as quickly and exactly as possible. There are many spectrum sensing techniques have been proposed and studied well in literature [1]. Among them, Energy detection (ED) method is considered one of the best approach due to its low complexity and hardware implementation possibility [2]. Another reason is that ED does not require any prior information of primary signal. So, it can be easily implemented on hardware. However, one of the main disadvantages of ED is that its performance will degrade considerably in low signal to noise ratio (SNR) and fading environment as well [3], [4]. To overcome this issue, diversity techniques has been proposed [4]. In this paper, we employ Selection Combining (SC) technique for increasing instantaneous SNR at the SUs. In addition, SC only requires one RF chain [5] so that the complexity of system could be reduced considerably.

FPGA is used popularly for signal processing applications nowadays because of reconfiguration ability, reliability, less power consumption, high speed, etc. Moreover, FPGA has been studied and developed for idea testing and hardware verifying without going through fabrication process of application specific integrated circuits design. Most of FPGA vendors offer DSP intergrated tools that combine simulation, algorithm development, etc., with synthesys and place and route.

Major previous works on spectrum senisng in cognitive radio mainly focus on simulation by software [3], [4]. Therefore, more hardware evidences does really need for verification and implementation. Because of these reasons, we investigated real-time FPGA implementation of ED with SC technique to improve detection rate in Rayleigh fading environment. The detection rate over Rayleigh fading was analyzed based on closed form mathematical expression. After that, the FPGA implementation of spectrum sensing with SC technique was applied for DVB-T signal detection over Rayleigh fading channel. The tool we used for these works is *Synphony Model Compiler*. The performance of ED scheme with SC technique is evaluated by parameters: probability of detection (P_d) and probability of false alarm (P_f). In our work, we used the StratixII EP2S180 board as the targeted device for verification and comparison.

The outline of this paper is following. After a short introduction, the overview of energy detection algorithm and mathematical analysis of SC technique are presented in part II. Part III will illustrate hardware model and parameter for simulation. Part IV gives some of numerical results, and the last, part V will be for discussions and conclusion.

2 Spectrum Sensing Based Energy Detection with SC Technique

2.1 Single Antenna Energy Detection Model

Fig. 1 shows the basic block scheme of ED without multiple antenna technique. The band pass filter chooses the bandwidth of interest, W . A square device is following to measure the power of primary signal, an integrator determines energy of it over observation time interval, T . Finally, the output of integrator is compared with pre-determined threshold, λ , to decide whether the primary signal is appeared (hypothesis H_1) or not (hypothesis H_0).

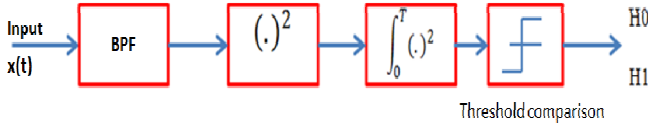


Fig. 1. Block diagram of spectrum sensing based energy detection

Let $x(t)$ is the input signal, the two hypotheses of received signal are given by:

$$\begin{cases} r(t) = h(t)x(t) + n(t) & : H_1 \\ r(t) = n(t) & : H_0 \end{cases} \quad (1)$$

Where $n(t)$ is addition zero mean white Gaussian noise, $h(t)$ is the channel gain from primary user to secondary user.

Based on Fig. 1, the normalized test statistic (Y) is defined [3]:

$$Y = \frac{1}{N_0} \int_0^T r^2(t) dt \quad (2)$$

Where N_0 is the two sided noise PSD (Power Spectral Density), n_i is the sampled noise which is obtained by sampling $s(t)$ at frequency of $2W$ (Nyquist rate), $u = TW$, $n_i \sim N(0, 2N_0 W)$ for all i .

It is well known that the test statistic Y obeys a central Chi square distribution (χ^2) under hypothesis H_0 , with degree of freedom (DoF) of $2u$. Under hypothesis H_1 , test statistic Y follows a non-central Chi square distribution, with DoF of $2u$ and non-central parameter of 2γ [4][6], where $\gamma = E_s/N_{01}$ is the signal to noise ratio, N_{01} is the one sided noise PSD. In short notation, we write:

$$Y \sim \begin{cases} \chi_{2u}^2 & \text{under } H_0, \\ \chi_{2u}^2(2\gamma) & \text{under } H_1. \end{cases} \quad (3)$$

Based on cumulative distribution function of test statistic, Y , the P_d and P_f can be inferred [4]:

$$P_d = P[Y > \lambda | H_1] = 1 - F_Y(\lambda) = Q_u(\sqrt{2\gamma}, \sqrt{\lambda}) \quad (4)$$

$$P_f = P[Y > \lambda | H_0] = \frac{\Gamma(u, \lambda/2)}{\Gamma(u)} \quad (5)$$

Where $Q_m(.,.)$ is the generalized Marcum Q function and $\Gamma(a, b)$ is the incomplete Gamma function [8]

2.2 Multi Receive Antenna – Selection Combining Technique

To address the drawback of ED in fading environment, SU employs more than one antenna to increase instantaneous SNR of received signal. Therefore, quality of received signal will be improved. We assume that the PU has only one antenna for transmission. So we have a Single-Input Multiple-Output (SIMO) system (Fig. 2).

The received signal at each antenna in SU includes signal from PU through channel H and AWGN noise. Each received signal on each antenna at SU will be processed by SC algorithm. In our work, the channel H is assumed to be *flat fading*. It means that the channel has only one *tap*. Each channel coefficient $h_i(t)$ of i^{th} receiver antenna varies randomly in time, and follows Rayleigh distribution. We also assume that channel coefficient on each antenna is known at receiver and be independent with each other. SC will select the signal on the receive antenna whose signal to noise ratio is the largest.

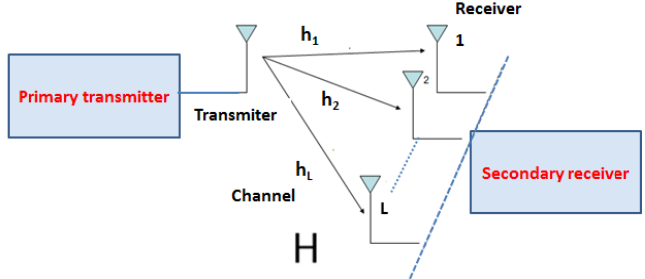


Fig. 2. The system with multiple receive antennas at SU

In SC algorithm, the SU makes final decision by comparing SNR, γ_i , of all L antennas. The antenna with maximum SNR will be selected. We assume that channel coefficients on all antennas follow i.i.d Rayleigh distribution. The PDF of maximum SNR, γ_{max} , among L antennas in SC is given [4]:

$$f_{\gamma_{max}}(\gamma) = \frac{L}{\gamma} (1 - e^{-\gamma/\bar{\gamma}})^{L-1} e^{-\gamma/\bar{\gamma}} \quad (6)$$

The average detection probability over fading environment (\bar{P}_{dsc}) can be calculated by averaging (4) over (6):

$$\bar{P}_{dsc} = \int_{\gamma} Q_u(\sqrt{2\gamma}, \sqrt{\lambda}) f_{\gamma_{max}}(\gamma) d\gamma \quad (7)$$

After some reduced operations, (7) can be evaluated [7]:

$$\bar{P}_{dsc} = L \sum_{i=0}^{L-1} \frac{(-1)^i}{i+1} \binom{L-1}{i} \bar{P}_{dRay}\left(\frac{\bar{\gamma}}{i+1}\right) \quad (8)$$

Where $\bar{P}_{dRay}\left(\frac{\bar{\gamma}}{i+1}\right)$ is the average detection probability in Rayleigh fading channel in single receive antenna case with SNR of $\left(\frac{\bar{\gamma}}{i+1}\right)$ [17].

$$P_{dRay}\left(\frac{\bar{\gamma}}{i+1}\right) = e^{-\frac{\lambda}{2}} \sum_{k=0}^{u-2} \frac{1}{k!} \left(\frac{\lambda}{2}\right)^k + \left(\frac{1+\bar{\gamma}}{\bar{\gamma}}\right)^{u-1} \left[e^{-\frac{\lambda}{2(1+\bar{\gamma})}} e^{-\frac{\lambda}{2}} \sum_{k=0}^{u-2} \frac{1}{k!} \left(\frac{\lambda\bar{\gamma}}{2(1+\bar{\gamma})}\right)^k \right] \quad (9)$$

When the primary signal is absent, the probability of false alarm in SC is exactly the same with local energy detection as in (5).

3 FPGA Implementation Model and Parameters of ED with SC Technique for DVB-T Primary Signal Sensing Purpose

In this paper, the input of ED which was used as primary signal is DVB-T signal. The specific parameters of DVB-T system in 2k mode (1705 useful sub-carriers, FFT/IFFT 2048 points) are given in Table 1. Due to DVB-T bandwidth of 6 MHz, the baseband representation of DVB-T signal is limited at ± 3 MHz [12]. It includes in-phase and quadrature components. The baseband DVB-T signal, therefore, was sampled at Nyquist rate of 6 MHz. We can easily calculate the observed time corresponding to the number of observed samples in Table 1. The number of observed samples using for DVB-T signal detection is 8, 64, 128, 512 and 1024 with QPSK (Quadrature Phase-Shift Keying) modulation. As we can see the longest sensing time corresponding with the largest number of samples is still satisfied the IEEE 802.22 sensing time requirement (below 2 second) [13].

Table 1. DVB-T Specifications and observed time T

DVB-T mode	2k
Number of sub-carriers	1705
Modulation	4QAM
Bandwidth	6 MHz
Number of Observed samples	8(1.3) μ s, 64(10.67 μ s), 128(21.3 μ s), 512(58.3 μ s), 1024(170.6 μ s)
Useful duration of OFDM Symbol	224 μ s

The hardware model of FPGA implementation system with SC is illustrated in Fig. 3. The “*PU signal generation*” block generates OFDM signal with parameters as describing in Table 1 before sending it to the receiver. The main function of “*PU transmitter*” is to generate 2048 orthogonal carrier signals by using IFFT algorithm. It converts signal from frequency domain to time domain. Because of sensing purpose only, we did not need to build channel coding, training and channel estimation functions as in DVB-T standard specification.

4 Experimental Results

4.1 Testbed Configuration

The hardware system configuration for DVB-T signal sensing purpose is shown in Fig. 4. Target FPGA device is Stratix II EP2S180 board. Fig. 5 shows real-time 6 MHz spectrum pattern of ODFM 2048 sub-carriers on spectrum analyzer. The time domain of DVB-T signal does not need to show due to uselessness to system analysis.

4.2 Hardware Numerical Performance of ED with SC Technique

Fig. 6 shows the ROC curves of FPGA implementation of ED with SC technique at the receiver of SU over Rayleigh fading channel. The number of antennas we used is 1, 2 and 3 respectively. The probability of false alarm P_f is kept below 1% (very low level). The P_f parameter illustrates how effective the cognitive users reuse spectrum resource of primary users. It means that we try to employ as much of available time slots as possible. It can be easily seen from this results that the longer sensing time we used, the better performance we obtained. For example, if we use 2 receiver antennas, the probability of detection is around 8% at SNR of -10dB in case of sensing time 1.3 μ s. This number will increase to approximately 70% if we extend the sensing time to 170.6 μ s. If we try to increase the number of receive antennas from 2 to 3, we even obtain the probability of detection over 80% at the same condition. Moreover, the ROCs curves of single antenna circumstance are given in order to compare with SC. As we can see, the detection rate of system improves considerably by employing SC technique. As the general trend, the detection rate will increase according to the number of receive antennas at SU. Comparing with one receiver antenna scenarios at sensing time of 170.6 μ s and at SNR of -10dB, around 20% and 30% of improvement are obtained when we employed SC with 2 and 3 receive antennas, respectively.

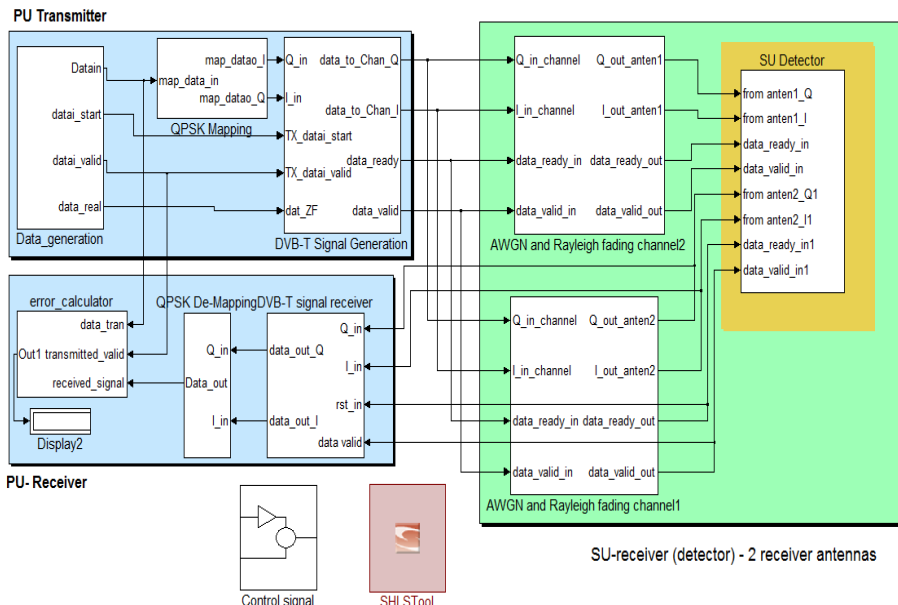


Fig. 3. FPGA block diagram of ED with SC technique – 2 receiver antennas

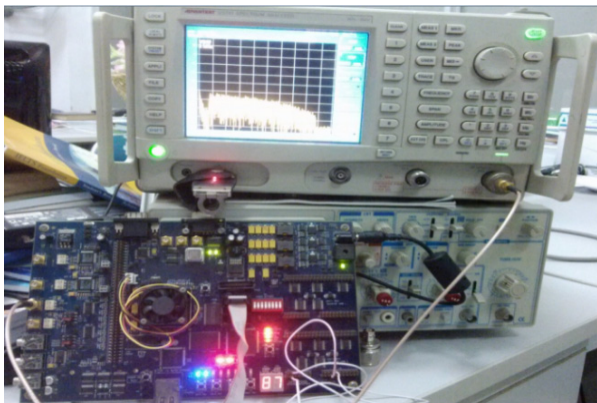


Fig. 4. Tested configuration on Stratix II EP2S180 board

The performance of system will even increase more if we increase the number of antenna at the receiver of SU. However, this will result in higher complexity of receiver at SU. Another way to improve the detection rate is that we could accept to increase the probability of false alarm to around 10%. As mentioned before, there is always a trade-off between probability of detection and probability of false alarm.

4.3 Hardware Consumption

Hardware consumption of system in FPGA Stratix II EP2S180 device is evaluated in Table 2. We chose fixed point 32 bits (fraction: 22.10) in order to increase the system accuracy. As we can see in this table that less than there are about 40% hardware resources which are used for system implementation. However, the percentage of ED with SC is just around 2% of the resources. Therefore, the ED can be easily implemented on other smaller hardware devices.

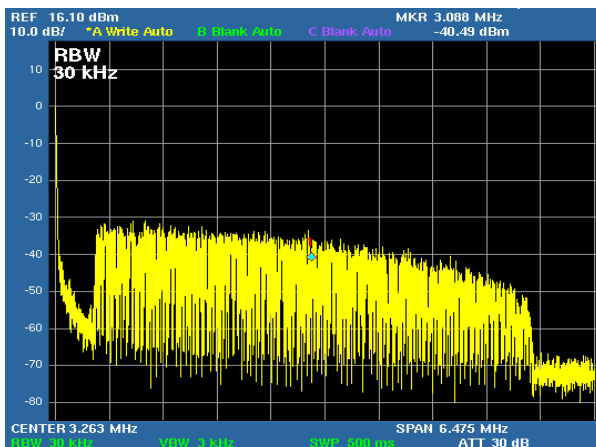


Fig. 5. Real time Spectrum of 6 MHz DVB-T signal in 2k mode

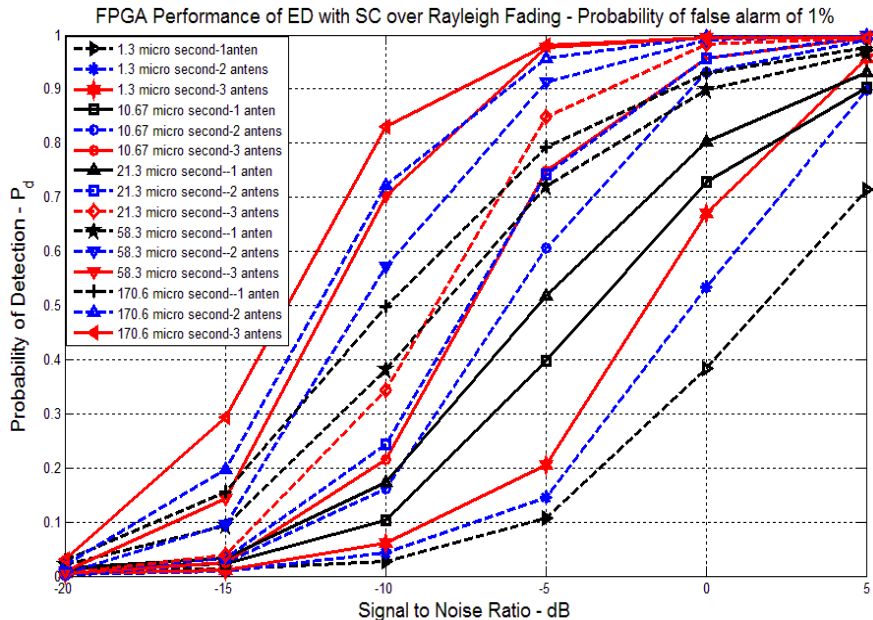


Fig. 6. The performance of FPGA implementation of ED with SC technique over Rayleigh fading channel, probability of false alarm of 1%

Block	Consumption				
	The number in Model	Max Speed (MHz)	Combinational ALUTs Max: 143520	Dedicated Logic Registers Max: 143520	DSP Block Elements Max: 768
Modulation	1	420	41 (<1%)	39 (6%)	N/A
IFFT 2048	1	145.10	3809(3%)	3654 (3%)	160 (26%)
AWGN Channel	1 -3	420	1019 (<1%)/1	303 (<1%)/1	16 (2%)/1
Rayleigh Channel	1-3	420	5004 (<2%)/1	1033 (<5%)/1	87 (8%)/1
Data generation	1	243.72	48 (<1%)	58 (<1%)	N/A
ED detection module (with SC)	1	<289	<4103(5%)	<502 (<3%)	<29 (<3%)
Total evaluation		145.10	<15%	<20%	<40%

Table 2.
Hardware consumption of sensing system in FPGA Stratix II EP2S180 board

5 Conclusion

In this paper, ED with reception diversity - SC for spectrum sensing purpose was studied and designed on hardware platform using Stratix II EP2S180 device. The DVB-T signal in 2k mode was chosen as PU signal. The real-time ED algorithm with SC technique was implemented in hardware device successfully. It was shown that the detection rate of system increased dramatically by applying SC technique.

Therefore, this technique can be employed to overcome disadvantages of ED in low SNR and Rayleigh environment as well.

References

1. Yucek, T., Arslan, H.: A survey of spectrum sensing algorithms for cognitive radio applications. *IEEE Communications Surveys & Tutorials* 11(1), 116–130 (2009)
2. Han, N., Shon, S., Chung, J.H., Kim, J.M.: Spectral Correlation Based Signal Detection Method for Spectrum Sensing in IEEE 802.22 WRAN Systems, pp. 1765–1770 (2006)
3. Ciftci, S., Torlak, M.: A Comparison of Energy Detectability Models for Cognitive Radios in Fading Environments. *Wireless Personal Communications* 68(3), 553–574 (2012)
4. Gavrilovska, L., Atanasovski, V.: Spectrum Sensing Framework for Cognitive Radio Networks. *Wireless Personal Communications* 59(3), 447–469 (2011)
5. J.G., Proakis, S.M.: Digital communications, 5th edn. McGraw-Hill (2008)
6. Urkowitz, H.: Energy Detection of Unknown Deterministic Signals. *Proceedings of the IEEE* 55(4) (1967)
7. Nuttall, A.H.: Some integrals involving the Q-function (1974)
8. I.S.G., Ryzhik, I.M.: Table of Integrals, Series, and Products, 6th edn., Section 9.2 (2000)
9. S.K., Johnson, N.B., N.L.: Continuous Univariate Distributions, vol. 2. John Wiley and Sons, New York (1995)
10. Proakis, J.G.: Digital Communications, 4th edn. McGrawHill (2001)
11. Digham, F.F., Alouini, M.-S., Simon, M.K.: On the energy detection of unknown signals over fading channels. *IEEE Transactions on Communications* 55, 21–24 (2007)
12. Broadcasting, D.V.: EN 300 744 - V1.6.1 - Digital Video Broadcasting (DVB); Framing structure, channel coding and modulation for digital terrestrial television, vol. 1, pp. 1–66 (2009)
13. IEEE Standard for Information Technology–Telecommunications and information exchange between systems Wireless Regional Area Networks (WRAN)–Specific requirements (2011)

Performance Analysis of the IEEE 802.11p under Finite Traffic Conditions

Duc Ngoc Minh Dang¹, Hanh Ngoc Dang², The Cuong Do¹, and Choong Seon Hong¹

¹ Department of Computer Engineering, Kyung Hee University,
1732 Deokyoungdaero, Giheung-gu, Yongin-si, Gyeonggi-do, 446-701, Korea
{dnmduc, dtcuong, cshong}@khu.ac.kr

² Department of Telecommunications Engineering,
Ho Chi Minh City University of Technology,
268 Ly Thuong Kiet Street, District 10, Ho Chi Minh City, Vietnam
hanhdn@hcmut.edu.vn

Abstract. Vehicular Ad hoc Network (VANET) is developed for more driving efficiency, comfort and safety. The IEEE 802.11p/WAVE is a standard intended to support wireless access in VANETs. In this paper, we propose an analytical model to evaluate the performance of the IEEE 802.11p based MAC for VANETs under non-saturation condition through the packet delivery ratio, the average delay of emergency message and the throughput of service message. The 2-D Markov model is used to model two access categories in the IEEE 802.11p. The analytical model is validated by the extensive simulation, and it shows the impact of different parameters on the performance of network.

1 Introduction

The main goal of the Intelligent Transportation System (ITS) is to improve the quality, effectiveness and safety of the future transportation systems. VANET is developed as an important part of the ITS with two types of communication: Vehicle-to-vehicle (V2V) and Vehicle-to-Infrastructure (V2I). The applications of VANETs fall into two categories, namely safety applications and non-safety applications. Safety applications, providing drivers information about critical situation in advance, have strict requirements on the communication reliability and delay. On the other hand, non-safety applications are used for improving driving comfort and the efficiency of transportation system which are more throughput-sensitive instead of delay-sensitive. Safety messages have higher priority than non-safety messages. The IEEE 802.11p [1] and the IEEE 1609 standard family are standard for VANETs. Some recent studies [2–5] try to improve the performance of VANETs.

The performance analysis of the IEEE 802.11 Distributed Coordination Function (DCF) is presented by Bianchi [6]. The Bianchi's model employs 2-D Markov chain analysis to compute the saturation throughput under ideal channel conditions. The delay analysis of the IEEE 802.11 protocol is studied in [7]. By taking account of the busy medium conditions, Ziouva *et al.* present a more analytical study of throughput and delay of the Carrier Sense Multiple Access with Collision Avoidance (CSMA/CA) protocol [8]. Different from above models, the non-saturation condition is considered

in [9]. The delay in idle state is geometric with parameter λ , which has no relationship with the load on the system. In [10], Malone *et al.* model the IEEE 802.11 DCF under non-saturated heterogeneous conditions with the post-backoff consideration. The relationship between the offered load and the model parameters is also presented in this study. For the broadcast analysis, Ma *et al.* evaluate the saturation performance of broadcast service in the IEEE 802.11 in [11].

To support MAC-level QoS, the IEEE 802.11e is proposed with the Hybrid Coordination Function (HCF). It combines the contention based Enhanced Distributed Channel Access (EDCA) and the contention-free HCF Controlled Channel Access (HCCA). The EDCA provides a priority scheme by differentiating the inter-frame space (IFS), the initial window size and the maximum window size. Yang analyzed the priority scheme with differentiating the minimum backoff window size, the backoff window-increasing factor and the retransmission limit in [12]. In [13], Wu *et al.* studied about the throughput analysis of the IEEE 802.11p EDCA by taking into account different Contention Window (CW), Arbitration Inter-frame Space (AIFS) values for each Access Categories (AC) and the internal collision.

The IEEE 802.11p uses an Enhanced Distributed Channel Access (EDCA) MAC sublayer based on the IEEE 802.11e. In the literature, there are some studies about the performance of VANET [14–16]. Broadcasting is one of the essential communication techniques in ad hoc network. The broadcast reliability is important in VANETs. While in [14, 15], the authors studied only about the broadcasting in VANETs, Han *et al.* [16] analyzed the IEEE 802.11p with four different Access Categories. In this paper, we consider two types of traffic: emergency traffic with high priority and service traffic with low priority. The 2-D Markov chain is used to model the back-off procedure for each traffic type. The probabilities of transmitting an emergency and service messages are derived. The packet delivery ratio (PDR), the average delay of emergency message and the throughput of service message are also derived to evaluate the performance of the IEEE 802.11p.

2 Analytical Model

In our analytical model, we consider the emergency and service applications as shown in Fig. 1. There are N vehicle nodes in the network, the packet arrival rate of emergency and service traffics at each node are λ_e and λ_s , respectively. Since the emergency messages are sent by broadcast mechanism, the vehicle node will not send any acknowledgement for the received emergency messages. The sender could not detect the failure of the emergency transmission and hence there is no retransmission.

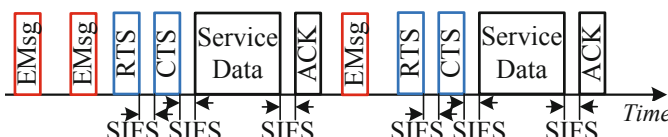


Fig. 1. Emergency and service transmissions

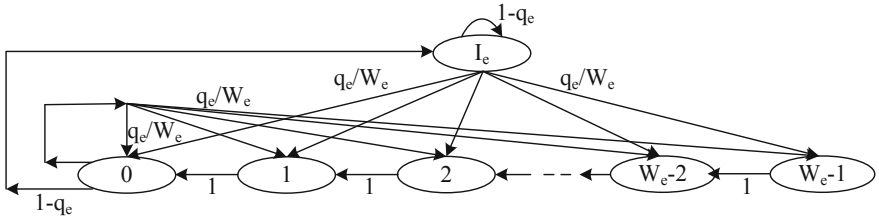


Fig. 2. Markov chain of the emergency traffic

Let $b_e(t)$ be the random process representing the back-off counter value at slot time t ; p_e be the collision probability and q_e be the probability of at least one emergency message waiting for transmitting in the buffer. The state transition diagram is shown in Fig.2. The non-null transition probabilities are

$$\begin{cases} P\{I_e|I_e\} = 1 - q_e \\ P\{I_e|0\} = 1 - q_e \\ P\{k|I_e\} = q_e/W_e, \text{ for } 0 \leq k \leq W_e - 1 \\ P\{k|0\} = q_e/W_e, \text{ for } 0 \leq k \leq W_e - 1 \\ P\{k|k+1\} = 1, \text{ for } 0 \leq k \leq W_e - 2. \end{cases} \quad (1)$$

Let $b_{e,k} = \lim_{t \rightarrow \infty} P\{b_e(t) = k\}$, for $0 \leq k \leq W_e - 1$ be the stationary distribution of the Markov chain, where W_e is the contention window of emergency traffic. From the Markov chain, we can obtain

$$(1 - q_e)b_{e,0} = q_e b_{I_e} \quad (2)$$

$$b_{e,k} = \frac{W_e - k}{W_e} b_{e,0}, \quad 1 \leq k \leq W_e - 1 \quad (3)$$

Using Eq. 3 and normalization condition $1 = b_{I_e} + \sum_{k=0}^{W_e-1} b_{e,k}$, we have

$$b_{e,0} = \left[\frac{1 - q_e}{q_e} + \frac{W_e + 1}{2} \right]^{-1} \quad (4)$$

Let τ_e be the probability that a node transmits an emergency message in a time slot

$$\tau_e = b_{e,0} = \left[\frac{1 - q_e}{q_e} + \frac{W_e + 1}{2} \right]^{-1} \quad (5)$$

Let $b_s(t)$ and $s_s(t)$ be the stochastic process representing the backoff counter and backoff stage for the service data at slot time t , respectively. Let L be the retry limit, the maximum number of trials before the packet is dropped and $W_{s,i} = 2^i W_{s,0}$ be the contention window (CW) of i^{th} backoff stage, where $i \in [0, L]$. We assume the collision probability p_s is constant and independent. Let q_s be the probability of at least one new

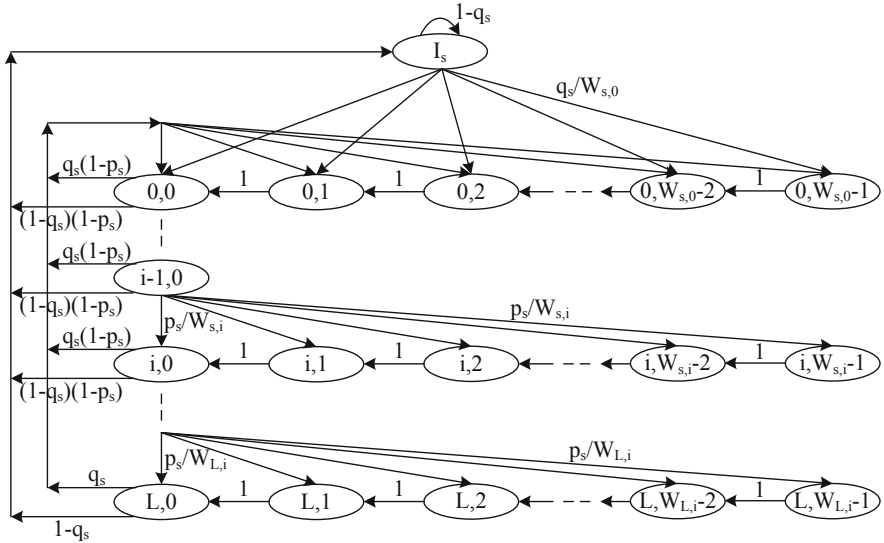


Fig. 3. Markov chain of the service traffic

service message in the buffer. So, we can model the bidimensional process $s_s(t), b_s(t)$ with the discrete-time Markov chain, as shown in Fig. 3. The only non-null one-step transition probabilities are

$$\begin{cases} P\{I_s|I_s\} = 1 - q_s, \\ P\{I_s|i,0\} = (1 - q_s)(1 - p_s), \quad \text{for } 0 \leq k \leq W_{s,0} - 1, 0 \leq i \leq L - 1, \\ P\{I_s|L,0\} = 1 - q_s, \\ P\{0,k|I_s\} = q_s/W_{s,0}, \quad \text{for } 0 \leq k \leq W_{s,0} - 1, \\ P\{0,k|i,0\} = q_s(1 - p_s)/W_{s,0}, \quad \text{for } 0 \leq k \leq W_{s,0} - 1, 0 \leq i \leq L - 1, \\ P\{0,k|L,0\} = q_s/W_{s,0}, \quad \text{for } 0 \leq k \leq W_{s,0} - 1, \\ P\{i,k|i-1,0\} = p_s/W_{s,i}, \quad \text{for } 0 \leq k \leq W_{s,i} - 1, 1 \leq i \leq L, \\ P\{i,k|i,k+1\} = 1, \quad \text{for } 0 \leq k \leq W_{s,i} - 2, 0 \leq i \leq L. \end{cases} \quad (6)$$

Let $b_{s,i,k} = \lim_{t \rightarrow \infty} P\{s_s(t) = i, b_s(t) = k\}$, $0 \leq i \leq L$, $0 \leq k \leq W_{s,i} - 1$ be the stationary distribution of the Markov chain. From the Markov chain, we can obtain

$$b_{s,i,0} = b_{s,i-1,0} \cdot p_s \rightarrow b_{s,i,0} = p_s^i \cdot b_{s,0,0}, \quad \text{for } 1 \leq i \leq L \quad (7)$$

$$\begin{aligned} q_s b_{I_s} &= \sum_{i=0}^{L-1} (1 - q_s)(1 - p_s)b_{s,i,0} + (1 - q_s)b_{s,L,0} \\ &= (1 - q_s)b_{s,0,0} \end{aligned} \quad (8)$$

Since the chain is regularity, for each $k \in (1, W_{s,i-1})$, we have

$$b_{s,i,k} = \frac{W_{s,i} - k}{W_{s,i}} b_{s,i,0}, \quad \text{for } 0 \leq i \leq L, 1 \leq k \leq W_i - 1 \quad (9)$$

All $b_{s,i,k}$ are expressed in terms of $b_{s,0,0}$ which is determined through the normalization condition $1 = b_{I_s} + \sum_{i=0}^L \sum_{k=0}^{W_{s,i}-1} b_{s,i,k}$ as follows

$$\begin{aligned} b_{s,0,0} &= \left[\frac{1-q_s}{q_s} + \sum_{i=0}^L p_s^i \left(\frac{W_{s,i}+1}{2} \right) \right]^{-1} \\ &= \left[\frac{1-q_s}{q_s} + \frac{1}{2} \left(\frac{1-p_s^{L+1}}{1-p_s} + \frac{1-(2p_s)^{L+1}}{1-2p_s} W_{s,0} \right) \right]^{-1} \end{aligned} \quad (10)$$

As a packet is transmitted when the backoff counter is zero, regardless of the backoff stage, the probability τ_s that node transmits in a time slot is given as

$$\begin{aligned} \tau_s &= \sum_{i=0}^L b_{s,i,0} = \frac{1-p_s^{L+1}}{1-p_s} b_{s,0,0} \\ &= \frac{1-p_s^{L+1}}{1-p_s} \left[\frac{1-q_s}{q_s} + \frac{1}{2} \left(\frac{1-p_s^{L+1}}{1-p_s} + \frac{1-(2p_s)^{L+1}}{1-2p_s} W_{s,0} \right) \right]^{-1} \end{aligned} \quad (11)$$

A transmitted frame collides when one more node also transmits during a slot time. The collision probabilities p_e, p_s are given as

$$\begin{aligned} p_e &= 1 - (1 - \tau_e)^{N-1} (1 - \tau_s)^N \\ p_s &= 1 - (1 - \tau_e)^N (1 - \tau_s)^{N-1} \end{aligned} \quad (12)$$

From Eqs. 5, 11 and 12, we can solve the unknowns τ_e, τ_s . The probability P_b that the channel is busy is given by

$$P_b = 1 - (1 - \tau_e)^N (1 - \tau_s)^N \quad (13)$$

The probabilities of successful transmission for emergency and service traffic are

$$\begin{cases} P_{e,suc} = N\tau_e(1-\tau_e)^{N-1}(1-\tau_s)^N \\ P_{s,suc} = N\tau_s(1-\tau_e)^N(1-\tau_s)^{N-1} \end{cases} \quad (14)$$

Let σ be the duration of slot time, $H = PHY_{hdr} + MAC_{hdr}$ be the packet header and δ be the propagation delay. Let $T_{e,suc}, T_{s,suc}, T_{e,col}$ and $T_{s,col}$ be the average time the channel is sensed busy because of the successful transmission of emergency and service traffic, the average time the channel is sensed busy during the collision caused by the emergency and service traffic, respectively

$$\begin{cases} T_{e,suc} = T_{e,col} = T_e = H + E[P_e] + DIFS + \delta \\ T_{s,suc} = RTS + SIFS + \delta + CTS + SIFS + \delta \\ \quad + H + E[P_s] + SIFS + \delta + ACK + DIFS + \delta \\ T_{s,col} = RTS + DIFS + \delta \end{cases} \quad (15)$$

The collision transmission may from only emergency traffic; only service traffic or both with the probability given as

$$\begin{cases} P_{e,col} = (1 - \tau_s)^N \left(1 - (1 - \tau_e)^N - N\tau_e(1 - \tau_e)^{N-1} \right) \\ P_{s,col} = (1 - \tau_e)^N \left(1 - (1 - \tau_s)^N - N\tau_s(1 - \tau_s)^{N-1} \right) \\ P_{es,col} = P_b - P_{e,suc} - P_{s,suc} - P_{e,col} - P_{s,col} \end{cases} \quad (16)$$

Each state may be a successful transmission, a collision or the medium being idle. The expect time spent per state E_S is given

$$E_S = (1 - P_b)\sigma + P_{e,suc}T_{e,suc} + P_{s,suc}T_{s,suc} + P_{e,col}T_{e,col} + P_{s,col}T_{s,col} + P_{es,col} \max(T_{e,col}, T_{s,col}) \quad (17)$$

From the average time slot E_S , the probability q_e and q_s can be approximated as [10, 17]

$$\begin{aligned} q_e &= 1 - e^{-\lambda_e \cdot E_S} \\ q_s &= 1 - e^{-\lambda_s \cdot E_S} \end{aligned} \quad (18)$$

The packet delivery ratio (PDR) of the emergency traffic can be calculated as [11]

$$PDR_e = \frac{P_{e,suc}}{N_e \tau_e} = (1 - \tau_e)^{N-1} (1 - \tau_s)^N \quad (19)$$

It takes the average slot of $\frac{(W_e - 1)}{2}$ for the back-off. The average time for an emergency message to finish back-off can be estimated by

$$\mu_e = E_E = \frac{(W_e - 1)}{2} E_S \quad (20)$$

For simplicity, each node can be modeled as an M/M/1 queue with an infinitive buffer size. With the packet arrival rate λ_e and service rate μ_e , the average delay of the emergency traffic including the queueing delay and the transmission delay is

$$E[D_e] = \frac{\mu_e}{(1 - \lambda_e \mu_e)} + T_e \quad (21)$$

The saturation throughput of the service traffic is calculated as

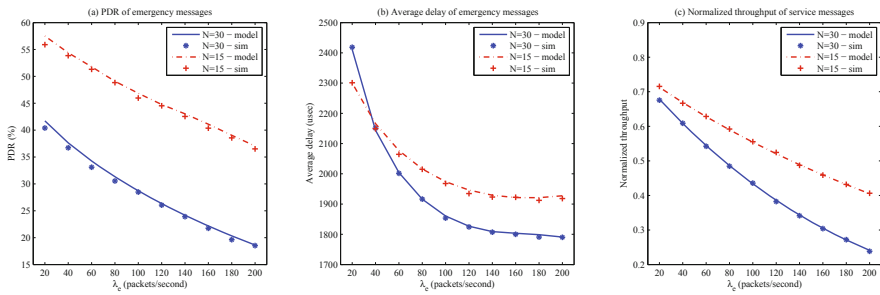
$$S_s = \frac{P_{s,suc} \cdot E[P_s]}{E_S} \quad (22)$$

3 Model Validation

To validate our model, we use the event-driven simulation program written in Matlab. Our program follows the IEEE 802.11 standard with the time resolution of microsecond. The parameters value used to obtain the numerical results for both the analytical model and simulation runs, are summarized in Table. 1. We fix the service packet arrival rate λ_s at 100 packets/second, and vary the emergency packet arrival rate λ_e and the number

Table 1. MAC parameters

Parameters	Value
Data rate	6 Mbps
RTS	20 bytes
CTS	14 bytes
Service data P_s	1000 bytes
ACK	14 bytes
Emergency data	100 bytes
Slot time σ	9 μ s
SIFS	16 μ s
DIFS	34 μ s
Propagation time δ	1 μ s
W_e	8
$W_{s,0}$	16
Retry limit L	6

**Fig. 4.** Performance analysis of the IEEE 802.11p

of nodes N to evaluate the PDR and the average delay of the emergency messages and the throughput of service messages.

Fig. 4 shows the performance of the IEEE 802.11p based MAC for VANET with varying the packet arrival rate of emergency messages when the number of nodes is 15 nodes and 30 nodes. The analytical results (lines) closely match the simulation results (symbols). Obviously, when the number of nodes in the network increases, the collision probability increases and therefore, the performance of the network decreases. And as the packet arrival rate of emergency message increases, there are more nodes having emergency messages to send, thus the collision probability also increases. That is the reason why the PDR of the emergency messages and the normalized throughput of the service messages decrease (Fig. 4(a), Fig. 4(c) respectively).

Since the average delay of the emergency messages including queueing delay is considered for both the successful and failed broadcast. This delay is calculated from the time the emergency message arrived at a node until the time this emergency message is transmitted. The average delay is the total delay over the number of transmitted emergency messages. When the collision probability is low, the successful broadcast

probability is high. In this case, an emergency message has to wait long time until it is transmitted, and the total delay increases. On the other hand, as the collision probability increases, there are more collided emergency messages and it makes the total delay decreased. So, the average delay of emergency messages decreased when the number of nodes increases and the packet arrival rate of emergency messages increases as given in Fig. 4(b).

4 Conclusion

In this paper, we proposed an analytical model to evaluate the performance of the IEEE 802.11p based MAC for VANET using the 2-D Markov chain. The numerical results show how the number of nodes and the packet arrival rate affect the network performance. According to the performance analysis, the IEEE 802.11p does not provide the emergency broadcast reliability and the high service throughput.

Acknowledgement. This research was supported by the MSIP (Ministry of Science, ICT & Future Planning), Korea, under the ITRC (Information Technology Research Center) support program supervised by the NIPA (National IT Industry Promotion Agency)" (NIPA-2013-(H0301-13-2001)). Dr. CS Hong is the corresponding author.

References

1. Wireless LAN Medium Access Control (MAC) and Physical Layer (PHY) Specifications Amendment 6: Wireless Access in Vehicular Environments (July 2010)
2. Dang, D.N.M., Dang, H.N., Do, C.T., Hong, C.S.: An enhanced multi-channel mac for vehicular ad hoc networks. In: 2013 IEEE Wireless Communications and Networking Conference (WCNC), pp. 351–355 (2013)
3. Wang, Q., Leng, S., Fu, H., Zhang, Y.: An IEEE 802.11 p-based multichannel MAC scheme with channel coordination for vehicular ad hoc networks. *IEEE Transactions on Intelligent Transportation Systems* 13(2), 449–458 (2012), doi:10.1109/TITS.2011.2171951
4. Han, C., Dianati, M., Tafazolli, R., Liu, X., Shen, X.: A novel distributed asynchronous multichannel mac scheme for large-scale vehicular ad hoc networks. *IEEE Transactions on Vehicular Technology* 61(7), 3125–3138 (2012)
5. Dang, D.N.M., Dang, H.N., Do, C.T., Hong, C.S.: An efficient and reliable mac for vehicular ad hoc networks. In: 2013 15th Asia-Pacific Network Operations and Management Symposium, APNOMS (2013)
6. Bianchi, G.: Performance analysis of the ieee 802.11 distributed coordination function. *IEEE Journal on Selected Areas in Communications* 18(3), 535–547 (2000)
7. Chatzimisios, P., Boucouvalas, A., Vitsas, V.: Packet delay analysis of ieee 802.11 mac protocol. *Electronics Letters* 39(18), 1358–1359 (2003)
8. Ziouva, E., Antonakopoulos, T.: Csma/ca performance under high traffic conditions: throughput and delay analysis. *Computer Communications* 25(3), 313–321 (2002)
9. Ergen, M., Varaiya, P.: Throughput analysis and admission control for ieee 802.11a. *Mobile Networks and Applications* 10(5), 705–716 (2005)
10. Malone, D., Duffy, K., Leith, D.: Modeling the 802.11 distributed coordination function in nonsaturated heterogeneous conditions. *IEEE/ACM Transactions on Networking* 15(1), 159–172 (2007)

11. Ma, X., Chen, X.: Performance analysis of ieee 802.11 broadcast scheme in ad hoc wireless lans. *IEEE Transactions on Vehicular Technology* 57(6), 3757–3768 (2008)
12. Xiao, Y.: Performance analysis of priority schemes for ieee 802.11 and ieee 802.11e wireless lans. *IEEE Transactions on Wireless Communications* 4(4), 1506–1515 (2005)
13. Wu, H., Wang, A., Zhang, Q., Shen, X.: Ieee 802.11e enhanced distributed channel access (edca) throughput analysis. In: *IEEE International Conference on Communications*, ICC 2006, vol. 1, pp. 223–228 (2006)
14. Hafeez, K., Zhao, L., Liao, Z., Ma, B.: Performance analysis of broadcast messages in vanets safety applications. In: *2010 IEEE Global Telecommunications Conference (GLOBECOM 2010)*, pp. 1–5 (2010)
15. Campolo, C., Vinel, A., Molinaro, A., Koucheryavy, Y.: Modeling broadcasting in ieee 802.11 p/wave vehicular networks. *IEEE Communications Letters* 15(2), 199–201 (2011)
16. Han, C., Dianati, M., Tafazolli, R., Kernchen, R., Shen, X.: Analytical study of the ieee 802.11p mac sublayer in vehicular networks. *IEEE Transactions on Intelligent Transportation Systems* 13(2), 873–886 (2012)
17. Daneshgaran, F., Laddomada, M., Mesiti, F., Mondin, M.: Unsaturated throughput analysis of ieee 802.11 in presence of non ideal transmission channel and capture effects. *IEEE Transactions on Wireless Communications* 7(4), 1276–1286 (2008)

Wireless Digital Signage for Intelligent Traffic Management System

Mukti Winanda, Nila Gita Cahyani, and Whilda Chaq

School of Electrical Engineering and Informatics, Institut Teknologi Bandung,
Bandung, Indonesia
mukti.winanda@students.itb.ac.id, gcahyani@gmail.com,
13511601@std.stei.itb.ac.id

Abstract. Wireless digital signage for intelligent traffic management system is an integrated system for traffic management purposes. Digital signage, which is made out of LED matrices, is used to display real-time traffic information sent from the police or other traffic authorities wirelessly and mobile. To show information as a real-time, it is required a system of wireless networks which is able to transmit the information quickly and actual. On a small scale, this wireless system is divided into two, delivery data that carried out by the user through the application and acceptance of that which is received by a hardware display at a same local network. The data delivery can be carried out by applying the principle of a socket programming between users as client with a hardware device on display as the server. To ensure the delivery is reliable, socket used the principle of communication through the TCP/IP. On a large scale, this network system is the integration of small scale network subsystem which every subsystem is connected by using a WiMAX network. It is intended in order that information on traffic conditions that occur can be affordable in many locations as a real-time. To be able to updates information about traffic conditions in real-time, it required mobile devices that can manage the content of the information, therefore it needs a software applications that can run on android and PC so police or authorities can update information quickly. Applications on mobile devices can access multiple digital signage displays that are scattered in various locations and also show the status of each display, whether it is online or offline.

Keywords: digital signage, wireless, real-time, mobile.

1 Introduction

Along with the increase of drivers of highways and traffic phenomena that may occur, the dissemination of information is necessary for road users. Most of the people argued that the traffic jams, one of the phenomena on traffic, is an inevitable thing while driving, but actually the traffic jams is an option. For example, if a road user has to get information about the condition of the road, then the traffic jams or other traffic phenomenon can be avoided. Thus, real- time media traffic information is needed for road users, especially drivers. Information about traffic can be spread

through the media information on the side of the road. One form of media information is digital signage. Digital signage is an electronic display that can display traffic information or any other message. Examples of traffic information, such as phone number associated on traffic, traffic jams, event of accidents, and so on. In terms to deliver information in real-time, digital signage is connected to the wireless network to update information by the police or authorities, so the information about road conditions can be delivered in real-time to road users.

2 Overview

2.1 Socket Programming

For doing communication between two or more computers, which in this case is the communication between the user application devices with display module, it can be done with socket programming. The Socket itself is a communication channel between devices (computer) based internet protocol, while the socket programming itself is how to use socket API (Application Socket Programming), to do the communication link. The API is a library of useful windows functions or to run a command that is found in all the display windows, such as screen savers and desktop display.

To create a channel of communication between devices (computer) based internet protocol, socket programming is required. It uses the terms of client and server, which the client is an application that sends the request to the server and waits for the response given by the server, in this case, the client is an application that receives data input by the user. While the server itself is an application to receive (accept) the connection provided by the client on the network and provide a response back to the client, in this case wireless communications module is a server that will forward the data to the board Arduino controller in display digital signage.

2.2 Socket in TCP (Transmission Control Protocol) Communication

In the connection socket TCP-based communication, before the client can send the data input by the user, the client and the server must be able to connect and respond to each other in advance, the following description of the process of making the socket on TCP communication:

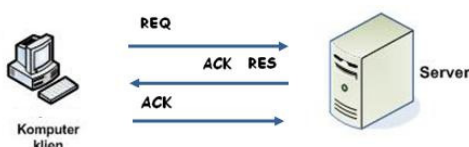


Fig. 1. TCP Communication

- Computer or client who wants to make the connection will send a segment of REQ (request) to the server that will be invited to communicate.
- Next, the server would response by sending the RES (response) and ACK (acknowledgment) to the client.
- Afterwards getting a response, then the client will begin to exchange data with the server.
- With the response and the acknowledgment from server, that is makes the TCP connection is reliable.

3 Design and Specification System

3.1 Specification

The wireless system has the following specification:

- System can transmit information that comes from a user to a network device on a display.
- Information data which sent by users is a text message.
- System can access digital signage displays which are scattered in various locations.

3.2 Design System

Based on the above specification, can be made a wireless system design, Data Flow diagrams (DFD) which shows the data flow that occurs in the system as shown in the image below.

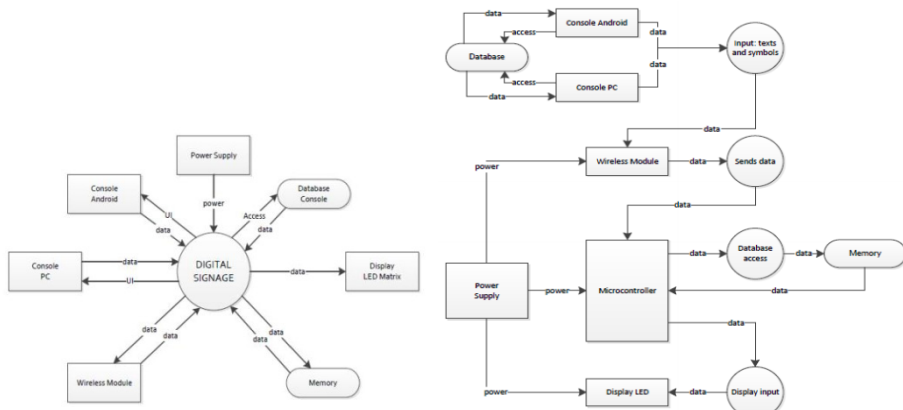


Fig. 2. DFD Level 0 and Level 1

Figure above are show the data flow diagram of the system. The information from users is delivered from console Android or PC to wireless module in display digital signage.

3.3 Flow Chart of Message Sending

Based on data flow on a DFD, it can be created the design of the message flow that comes from the user as client, through the application, to board Arduino controller in a display as a server.

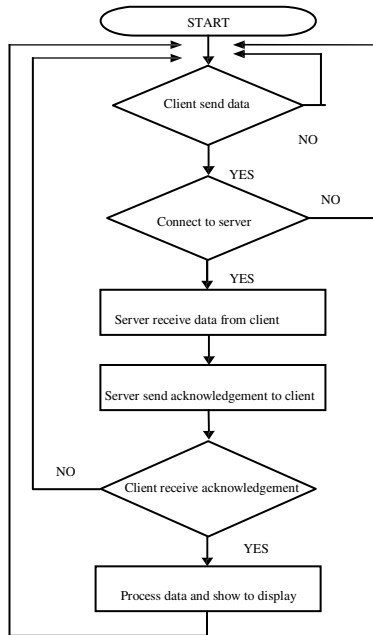


Fig. 3. Flow Chart of Message Sending

3.4 Design of Wireless Network

To reach out digital signage in various locations, it needs the design of a wireless network using WiMAX (Worldwide Interoperability for Microwave Access).

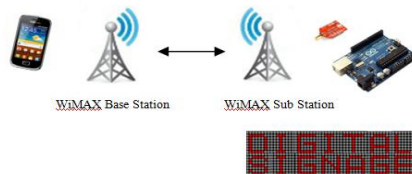


Fig. 4. Design of Wireless Network

Figure above explains the process of sending data. Firstly, applications device that are used by the user must be connected to the WiMAX network Base Station, so it can eventually sent the data to the WiMAX Sub Station which is at a different location. On the display devices section, board Arduino controller and the wifly

module must be connected to the WiMAX Subsection Station so it can receive the data that is sent by the user.

To be able to access multiple digital signage displays in various locations, the system needs a further developed design, where each of digital signage will be represented by different addresses (IP address) and accessing through the device application.



Fig. 5. Design of Wireless Network for Different Locations

4 Implementation and Result

4.1 Wireless Communication Module (Wifly)

To connect the display device to the wireless network, it required wifly as a wireless module. Wifly module is connected with board Arduino controller. Prior to testing, it needs configuration to the module with serial communication through the serial monitor it aims so wifly module can accept data in TCP/IP communication and connected to wireless network.

The implementation of the module:

```

COM23 - Tera Term VT
File Edit Setup Control Window Help
WiFly Ver 2.32, 02-13-2012 on RN-171
MAC Addr=00:06:66:71:ee:ab
Auto-Assoc gcahyani chan=WiFly Ver 2.32, 02-13-2012 on RN-171
MAC Addr=00:06:66:71:ee:ab
Auto-Assoc gcahyani chan=1 mode=OPEN SCAN OK

```

Fig. 6. Implementation of Wireless Module

In the picture above, it can be seen that the module has been successfully joined into the wifi network with SSID named gcahyani connected to WiMAX. To see the connection of the modules into the network TCP, it can be known through the LED light mounted on the wifly module. The LED is green and lights up in solid indicating that the module has been connected successfully.



Fig. 7. Module Connected Over TCP

To test the connection of the modules with the network, it can be done by simply sending packages via the command prompt to the IP address obtained on the wifly.

```
C:\Users\utari>ping 192.168.170.2 -t
Pinging 192.160.170.2 with 32 bytes of data:
Reply from 192.168.170.2: bytes=32 time=6ms TTL=255
Reply from 192.168.170.2: bytes=32 time=3ms TTL=255
Reply from 192.168.170.2: bytes=32 time=3ms TTL=255
Reply from 192.168.170.2: bytes=32 time=5ms TTL=255
Reply from 192.168.170.2: bytes=32 time=3ms TTL=255
Reply from 192.168.170.2: bytes=32 time=4ms TTL=255
Reply from 192.168.170.2: bytes=32 time=2ms TTL=255
```

Fig. 8. Testing Wireless Module

4.2 Socket Programming in TCP Communication

In creating the connected between devices application as a client, with the display device as a server, it required implementation of socket programming. On the application of the principle of the socket on the client, it needs to know that client must know IP address on server and number of port provided by the server as the place of transaction data. While on the server, it only needs to provide the number of port as a place of transaction data between client and server. The server always in available conditions to accept every new connections from the client.

Testing can be done by sending a message by the user through the application to the display which equipped with wireless module and board Arduino controller. That is the appearance of the display application while it is sending information about traffic conditions.

```
PERHATIAN!!! ADA GALIAN
Connected to:192.168.92.101 on port:1234
sending to Arduino-Server: PERHATIAN!!! ADA GALIAN
recieved from Wifly-Server: *HELLO*
```

Fig. 9. Sending Message from Application

In the picture above, it can be known that if the test is successful, the server sends a message or acknowledgment to the client, for example ‘Hello’ message. The received message by the wireless module can be seen through the serial monitor on the Arduino board controller.

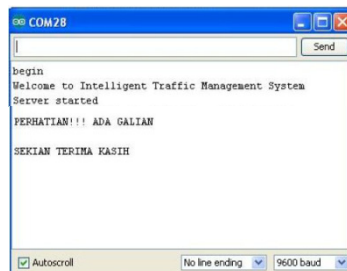


Fig. 10. Receive Message in Board Arduino Controller

In the picture above, it can be seen that the sending and receiving of data testing successfully. Text message which have come to the display device has shown in serial monitor of display.

4.3 Processing Data Information

To be able to be shown on the display the led matrix, text message that is received on the board Arduino controller must be changed first to be of type byte that represents each character of the string is received. Therefore, it required implementations of a function that is created in a program on the board Arduino controller.

That function will receive input in the form of a string, and then break it down into each character first, then change the representation of a new letter of type character with the same letter of representation of type byte.



Fig. 11. Change String Message to Each Character

Testing is done in a manner showing characters from each letter on the digital signage display.

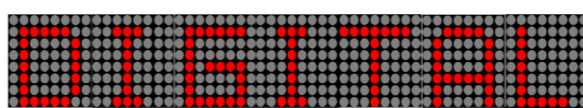


Fig. 12. Message in Digital Signage

4.4 Wireless Networking

In every WiMAX location, it equipped with a single router that can generate local wifi network that connects every device applications on users who are in the same location.

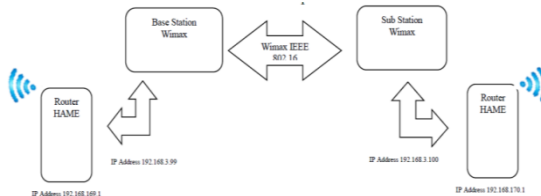


Fig. 13. Implementation in Wireless Networking

Testing is done by testing the connected of each router which separated and connected through intermediaries as the media liaison in WiMAX wireless network. Testing can be tested by send a simple package by using the command prompt. It sends to the address of the IP address of the client on each router in an area of WiMAX network.



Fig. 14. WiMAX Module

The following test results is show the data delivery from WiMAX Base Station to the WiMAX Sub Station.

```

Connection-specific DNS Suffix . :
IP Address . . . . . : 192.168.169.2
Subnet Mask . . . . . : 255.255.255.0
Default Gateway . . . . . : 192.168.169.1

C:\Users\utari>ping 192.168.170.2 -t
Pinging 192.168.170.2 with 32 bytes of data:
Reply from 192.168.170.2: bytes=32 time=6ms TTL=255
Reply from 192.168.170.2: bytes=32 time=3ms TTL=255
Reply from 192.168.170.2: bytes=32 time=3ms TTL=255
Reply from 192.168.170.2: bytes=32 time=5ms TTL=255
Reply from 192.168.170.2: bytes=32 time=3ms TTL=255
Reply from 192.168.170.2: bytes=32 time=3ms TTL=255
Reply from 192.168.170.2: bytes=32 time=2ms TTL=255
  
```

Fig. 15. Testing on WiMAX Module

It can be seen on the results above that the client which has IP address 192.168.170.2 received the packet from IP address 192.168.169.2 successfully. Client and server above is separated by a WiMAX network.

To maximize the use of WiMAX in every location, the new scheme is required in each location are attached with WiMAX, which at each router is connected with every digital signage in that location. The picture below is shown the installation of digital signage in every intersection of road.

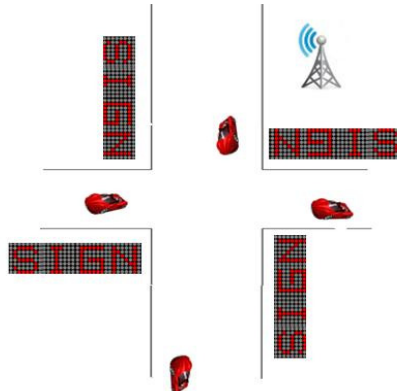


Fig. 16. Digital Signage In Every Intersection of Road

Every digital signage, which is installed in an intersection, will have a unique IP address and the same subnet mask.

5 Conclusion

Wireless network system was able to transmit information from the user application to the wireless module on a display digital signage. Information data sent by the user with Android or PC can be shown on the digital signage display.

Wireless network system enables the whole system to access digital signage displays that are scattered in various locations.

This system is used for intelligent traffic management system in Indonesia, so that can manages traffic along street. It informs congestions, accidents, vehicle breakdown and other incidents promptly, ensuring fast response to restore normal traffic flow and reduces negative impact from congestion.

References

1. Cah, N.G., Meganti, M., Winanda, M.: Dokumen B100-B500: Digital Signage untuk Intelligent Traffic Management System. Final Project, ITB (2012)

2. Carne, E. Bryan, A Professional's Guide to Data Communication in a TCP/IP World, Artech House: London, 2004.
3. Evans, M., Noble, J., Hochenbaum, J.: Arduino in Action, pp. 4–24. Manning, New York (2012)
4. Forouzan, B.A.: Data Communications and Networking, 4th edn. McGraw-Hill, New York (2007)
5. Francis, T.: Intelligent Transportation Systems Smart and Green Infrastructure Design, pp. 44–53. CRC Press, United States of America (2010)
6. Hall, B.B.J.: Beej's Guide to Network Programming Using Internet Sockets, pp. 8–66 (2012)
7. Nathan, Y., Turner, J.W., Keir, D.: The Definitive Guide to Linux Network Programming, pp. 27–87. Apress, United States of America (2004)
8. Poor, H.V., Wornell Gregory, W.: Wireless Communications Signal Processing Perspectives. Prentice Hall PTR, Upper Saddle River (1998)
9. Schaeffler, J.: Digital Signage Software, Networks, Advertising, and Displays, pp. 95–106. Focal Press, Jordan Hill (2008)
10. Wicaksono, A.: Seri PenuntunPraktisDasar-DasarPemrograman Java 2. PT Elex Media Komputindo, Jakarta (2002)
11. Wicaksono, A.: Tutorial Java Networking 13.45 WIB (January 12, 2013),
http://www.tutorialspoint.com/java/java_networking.htm
12. Wicaksono, A.: Simple Arduino TCP Server, 10.00 WIB (February 3, 2013),
<http://www.lauridmeyer.com/2012.04/simple-arduino-tcp-server-using-the-ethernetshield-and-a-java-client/>
13. Wicaksono, A.: Make a 24x6 Led Matrix 11.30 WIB (February 24, 2013),
<http://www.instructables.com/id/Make-a-24x6-LED-matrix/>

Text Similarity Based on Data Compression in Arabic

Hussein Soori¹, Michal Prilepok¹, Jan Platos¹,
Eshetie Berhan², and Vaclav Snasel¹

¹ Department of Computer Science, FEECS, IT4 Innovations, Centre of Excellence,
VSB-Technical University of Ostrava, Ostrava Poruba, Czech Republic

{sen.soori,michal.prilepok,jan.platos,vaclav.snasel}@vsb.cz

² Addis Ababa Institute of Technology, School of Mechanical and Industrial
Engineering, Addis Ababa, Ethiopia
eshetie_ethio@yahoo.com

Abstract. With the huge amount of online and offline written data, plagiarism detection has become an eminent need for various fields of science and knowledge. Various context based plagiarism detection methods have been published in the literature. This paper, tries to develop a new plagiarism detection methods using text similarity for Arabic language text with 150 documents and 330 paragraphs (159 from the source document and 171 from Al-Khaleej corpus). The findings of the study show that the similarity measurement based on Lempel Ziv comparison algorithms is very efficient for the plagiarized part of the Arabic text documents with a successful rate of 71.42%. Future studies can improve the efficiency of the algorithms by combining more sophisticated computation, statistical and linguistics hybrid detection methods.

1 Introduction

Similarity detection is considered a crucial part of document processing. It covers a wide area including spam detection, and online and offline plagiarism detection. The need for plagiarism detection tools in Arabic is growing with the growing number of natural language documents that are written in Arabic in schools and universities in the Arab world. The growing number of these documents include, students' assignments in schools, Masters' and PhD theses and dissertations. While some students resort to cut and paste methods, some other students use different ways of plagiarism including changing the sentence structure, paraphrasing and replacing the lexical meaning of words with synonyms. These require new and more sophisticated tools to detect plagiarism. This study tries to proof that similarity measurement based on Lempel Ziv comparison algorithms can be very efficient for detecting plagiarism of Arabic texts.

2 Methods of Plagiarism Detection

Traditional methods of Plagiarism detection use manual observation and comparison of documents but these methods are no longer viable due to the

tremendous number of documents available online in various fields of science and knowledge.

Context based methods are widely used and they depend on the measurement of similarity between documents where the fingerprints of each document is compared with other documents. Finger prints use representation of key contents. They are made by hashing subsets of documents. Winnowing algorithm [1] is one of the widely used algorithms. It depends on the selection of finger prints of hashes of k-grams. It is based on idea of finding the similarity of certain lengths of small partial matches where t is the guarantee threshold and k is the noise threshold. Basically the idea is based on two conditions: the substring found is at least as long as the threshold, and if there is any match that is shorter than the noise threshold k , then it is not detected.

Stanford Copy Analysis Mechanism (SCAM) [2] is based on a copy detection server which is made of a repository and a chunker. Documents are broken up into small chunks (sentences, words...etc.) and, after that, registered in the repository. Each chunk is sorted out and labeled. After that, every new unregistered document is broken up into chunks and compared with the registered documents already in the repository. It is based on the idea that smaller units of chunks increase the probability of finding similar texts. This method uses Relative Frequency Mode (RFM).

Other approaches are based on writer's style [3]. The most widely used is a stylometry statistical method, which is based on the idea that every writer has her his own style which can be detected by dividing the documents into smaller parts and comparing the linguistic features such as the length of text (sentences, paragraphs and chapter), frequency of use of punctuations, parts of speech, use of function words, richness of the vocabulary used, ... etc. This method is an intrinsic method [4] where the detection is performed within the same document and not taking into account outside references. The draw back of stylometry approach comes when the writer has more than one style then this approach can detect false-positive plagiarism.

Data compression can be used for measurement similarity of texts. There are many data compression algorithm [5] for similarity of small text files. Some of these use compression methods to detect text similarity, such as the method used by Prilepok et. al. to detect plagiarism of English Texts [6]. The main idea of this paper is inspired by that method [6] but here we adapted the method to detect plagiarism of Arabic texts.

3 Similarity of Text

The main property in the similarity is a measurement of the distance between two texts. The ideal situation is when this distance is a metric [7]. The distance is formally defined as a function over Cartesian product over set S with nonnegative real value [8] and [9]. The metric is a distance which satisfy three conditions for all :

$$D(x; y) = 0, x = y, \quad (1)$$

$$D(x; y) = D(y; x), \quad (2)$$

$$D(x; z) \leq D(x; y) + D(y; z) \quad (3)$$

The conditions 1, 2 and 3 are called: identity, symmetry and the triangle inequality respectively. This definition is valid for any metric, e.g. Euclidean Distance, but the application of this principle into document or data similarity is much complicated.

3.1 Plagiarism Detection by Compression

The main idea of this paper is inspired by a method used in Prilepok et. al. 2013 [6]. This method uses Lempel-Ziv compression method. The main principle of this method is the fact that for the same sequence of data the compression becomes more efficient. Lempel-Ziv compression method is one of the most currently used methods in data compression in various kinds of data like texts, images, audio [10], [11]. This compression was used to detect plagiarized text and detect their similarity [12].

3.2 Creating Dictionary of Document

Creating dictionary is one of the parts of the encoding process Lempel-Ziv 78 method [13]. The dictionary is created from input text, which is split into separate words. If current word from the input is not in the dictionary, then this word is added. If the current word is contained in dictionary, a next word from the input is added from the input to it. This will eventually create a sequence of words. If this sequence is found in the dictionary, then the sequence is extended with the next word from the input in a similar way. If the sequence is not in the dictionary, it is added to dictionary with the incrimination of the number of sequences property. The process is repeated until we reach the end of input text.

3.3 Comparison of the Documents

The comparison of the documents is the main task. One dictionary is created for each of the compared files. Then the dictionaries are compared to each other. The main property for comparison is the number of common sequences in the dictionaries. This number is represented by the parameter in the following formula, which is a metric of similarity two documents.

$$SM = \frac{sc}{\min(c_1, c_2)} \quad (4)$$

- sc - count of common word sequences in both dictionaries.
- c_1, c_2 - count of word sequences in dictionary of the first or the second document.

The SM value is in the interval. If $SM = 1$, then the documents are equal and they have the highest difference when the result value of $SM = 0$.

4 Linguistic Characteristics of Arabic

Unlike languages that use Roman characters, Arabic is written from right to left and has twenty eight alphabet letters (three vowels and twenty five consonants). Arabic is considered as one of the highly inflectional languages with complex morphology where affixes are added to the stem to form words. Hence, Arabic plagiarism detection tools require considering language specific features in detecting text similarity. Arabic alphabets are much different from Roman alphabets, which are naturally not linked. The shape of every letter changes according to its position in the word - initial, medial, and final. In addition to that, Arabic has eight short vowels and diacritics as shown on the figure 1 below. According to Habash [14], since diacritical problems in Arabic occur so infrequently, they are removed from the text by most researchers. Typists normally ignore putting them in a text, but in case of texts where they exist, they are pre-normalized - in value - to avoid any mismatching with the dictionary or corpus in text processing or plagiarism detection.

(ُ , ِ , َ , ِّ , َّ , ُّ , ِّّ , َّّ)

Fig. 1. Short vowels and diacritics marks

5 Experimental Setup

In our experiments we used Khaleej-2004 corpus of Arabic texts. Al-Khaleej corpus-2004 contains 5690 documents. It is divided to 4 topics: local news, economy sports and international news, of which we chose the local news category. This dataset contains only documents in Arabic language. In our experiment, we needed to have suspicious document collection to test the suggested approach. We created 150 false suspicious and 100 source documents from Khaleej-2004 corpus by using a small tool that we designed to create false suspicious documents.

5.1 False Suspicious Documents Creator Tool

The purpose of this tool is to create false suspicious documents. The tool is designed following these steps. All the documents from the corpus were split into paragraphs, and each paragraph is labeled with new line mark for a quick reference of its position in the corpus. From this paragraphs list we created two separate collections of documents. The first is a source document collection

and the other is the suspicious collection. For source documents, we randomly selected one - five paragraphs from the list of paragraphs. These paragraphs are added to a newly created document and marked as source document one. This step is repeated for all 100 documents. The collection contains 252 distinct paragraphs.

The process of creation suspicious document is very similar to process of creation the source documents. We randomly selected from each suspicious document one - five paragraphs. The tool randomly selects the paragraphs. Each document contains some paragraphs from the source document and some unused paragraphs. This step is repeated for all 150 documents. For creating a collection of suspicious documents, we used 330 paragraphs - 159 paragraphs from source documents and 171 unused paragraphs from Al-Khaleej corpus. For each created suspicious document, we created an XML description file. This file contains information about the source of each paragraph in our corpus starting and ending, byte and file name. This step is repeated for all 150 documents. Our created dataset contains 150 suspicious (24 with plagiarized part and 126 with unplagiarized parts) and 100 source documents are considered as the testing data for our algorithm.

5.2 The Experiment

The comparison of the whole documents where only a small part of the document may be plagiarized is useless, because other characteristics and the whole text of the new document may hide the characteristic of the plagiarized part. Therefore, we split the documents into paragraphs. We choose paragraphs, because we think that they are better than sentences for the reason they contain more words and should not be affected by stop words, such as, preposition, conjunctives, etc. The Paragraphs were separated by an empty line between them. We created a dictionary for each paragraph from the source document, according to the method described above. As a result of the fragmentation of the source documents, we get 252 paragraphs and their corresponding dictionaries. These dictionary paragraphs serve as reference dictionaries that we used to compare the dictionary paragraphs with the suspicious documents created.

The set of suspicious documents was processed in a similar way. Each suspicious document was fragmented into paragraphs. After fragmentation of the suspicious documents, we get 330 paragraphs. Then, we create a corresponding dictionary using the same algorithm without removing diacritics and stop words. After that, we compared this dictionary with the dictionaries from the source documents. To improve the speed of the comparison, we choose only subset of dictionaries for comparison because comparing one suspicious dictionary to all source dictionaries consume too much time. The subset is chosen according the size of a particular dictionary with tolerance rate of $\pm 20\%$. For example, if the dictionary of the suspected paragraphs contains 122 phrases, we choose all dictionaries with number of phrases between 98 and 146. This 20% tolerance significantly improves the speed of the comparison. Moreover, we believe this tolerance percentage does not affect the overall efficiency of the algorithm. We

pick up the paragraph with the highest similarity to each paragraph of the tested paragraph.

5.3 Stop Words Removal

Stop words removal has been proven to increase the accuracy level of text similarity detection. For that reason, in our method, we removed stop words from the texts used. As a source of stop words we have used two lists of stop words. Shereen Khojas list of stop words from Khoja Stemmer 2004 [15]. The list contains 168 stop words. The second list used is the final release April 2013 of the Basic Arabic Stemmer [16], which contains 1300 stop words. We found 42 common words between the two stop words lists. Our algorithm is modified in a way so that after the fragmentation of the text, all stop words are removed from the list of paragraphs and, then the rest of them are processed by the same algorithm.

6 Results

In our meaning we will consider as a plagiarized document a document in which managed to find all plagiarized parts from the attached annotation XML file. Partially plagiarized document is a document in we did not detect successfully all the plagiarized parts from annotation XML file, for example 3 from 5 parts in annotation XML file. A non-plagiarized document is a document, which did not have in the XML file an annotated plagiarized part of text.

Table 1. Table of Results

	Successful rate	
Plagiarized documents	90/126	71.42%
Partially plagiarized documents	36/126	28.58%
Non-plagiarized documents	24/24	100.00%

In our experiments we found 71.42% of plagiarized documents, 28.85% partially plagiarized documents and all 100.00% non-plagiarized documents in the suspicious collection.

In case of partially plagiarized documents, we could find suspicious paragraphs in another document, or paragraphs with higher similarity similarly as a paragraph with the same content. This case can occurs if one of the paragraphs is shorter then the other. To illustrate this case we mention a brief example.

6.1 Result Example

This first paragraph comes from one of the suspicious documents collections. Paragraph consists of two sentences. After removing stop words and diacritics we get 28 word sequences.

تشير الإحصاءات التجارية في أسواق الخليج على أنها تمتلك سوقاً مفتوحة وواعدة في مجال الأثاث والديكور حيث يبلغ مجموع الاستثمارات التي تفتخها أسواق المنطقة إلى ما يفوق الخمسة مليارات دولار سنوياً وذلك يبين حجم النشاط الذي يتمتع به سوق الأثاث في المنطقة.

Fig. 2. Source Text

The second paragraph was taken as the most similar paragraph from the source documents collection. This paragraph has the greatest similarity $SM = 1.0$, because it is an exact copy of the source paragraph.

تشير الإحصاءات التجارية في أسواق الخليج على أنها تمتلك سوقاً مفتوحة وواعدة في مجال الأثاث والديكور حيث يبلغ مجموع الاستثمارات التي تفتخها أسواق المنطقة إلى ما يفوق الخمسة مليارات دولار سنوياً وذلك يبين حجم النشاط الذي يتمتع به سوق الأثاث في المنطقة.

Fig. 3. Exact Match suspicious text

The third paragraph contains same words and sentences. This paragraph has different position of sentences of clauses to the first paragraph. This paragraph similarity with the s first paragraph is $SM = 1.0$.

تشير الإحصاءات التجارية في أسواق الخليج على أنها تمتلك سوقاً مفتوحة وواعدة في مجال الأثاث والديكور وذلك يبين حجم النشاط الذي يتمتع به سوق الأثاث في المنطقة حيث يبلغ مجموع الاستثمارات التي تفتخها أسواق المنطقة إلى ما يفوق الخمسة مليارات دولار سنوياً.

Fig. 4. Text Two with change of sentences or clauses

The fourth paragraph is one the less similar paragraphs. It has the same meaning and different used words and sentence construction. This paragraph similarity with the s first paragraph is $SM = 0.4$.

6.2 Visualization of Similarity of Documents

In the tool we use three methods for the visualization of paragraph similarities. This visualization method should give the user a simple a quick overview of the results of the suspicious document.

أشارت الإحصاءات إلى أن منطقة الخليج لذاتها أسواق تجارية مفتوحة وواحدة في مجال الديكور والأثاث و يتعدى إجمالي الاستثمارات خمسة مليارات دولار سنويًا مما يدل على حجم نشاط هذا السوق في الخليج.

Fig. 5. Text three rewritten in different words 'paraphrased'

The first method is represented by a line chart. This chart shows the similarity for each suspicious paragraph in the document. The user may easily see which part of the document is plagiarized and the number of the plagiarized parts. Higher similarities represent paragraphs with more plagiarized content.

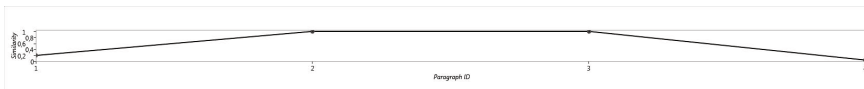


Fig. 6. This similarity for each suspicious paragraph in the document

The second method is a histogram of document similarity. The histogram shows a brief overview of how many paragraphs have the same similarity and how many parts of the suspicious document are or can be plagiarized.

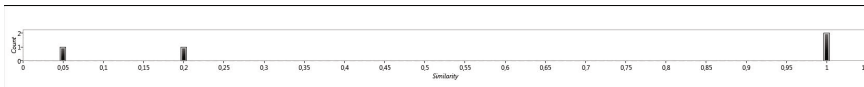


Fig. 7. The histogram document similarities

The last method presentation used to easily visualize the similarity as a form of colored text highlights. We use 4 colors for visualization. The red color means that the paragraph has a similarity rate greater than 0.2. The orange color shows the paragraphs with lower similarity ranging between 0 and less than 0.2. This paragraph has only few similar words with the source paragraphs. The green text means that the paragraph was not found in the source text and is not plagiarized.

7 Conclusion

In this paper, we applied the similarity detection algorithm by Michal Prilepok et. al. [6] on a real dataset with Arabic texts. We also confirmed the ability to detect plagiarized parts of the documents with the removal of stop words

and diacritics, as well as the viability of this approach for Arabic language. The algorithm for similarity measurement based on the Lempel Ziv compression algorithm and its dictionaries was very efficient in detection of the plagiarized parts of the documents. All plagiarized documents in a dataset were marked as plagiarized and in most cases all plagiarized parts were identified, as well as, their original version.

Acknowledgement. This work was partially supported by the Grant Agency of the Czech Republic under grant no. P202/11/P142, and by the Grant of SGS No. SP2013/70, VŠB - Technical University of Ostrava, Czech Republic, and was supported by the European Regional Development Fund in the IT4Innovations Centre of Excellence project (CZ.1.05/1.1.00/02.0070) and by the Bio-Inspired Methods: research, development and knowledge transfer project, reg. no. CZ.1.07/2.3.00/20.0073 funded by Operational Programme Education for Competitiveness, co-financed by ESF and state budget of the Czech Republic.

References

1. Schleimer, S., Wilkerson, D., Aiken, A.: Cited By (since 1996) 177, pp. 76–85 (2003), <http://www.scopus.com/inward/record.url?eid=2-s2.0-1142267351&partnerID=40&md5=9872bd8facb5cb07ff129dade9ca781f>
2. Shivakumar, N., Garcia-Molina, H.: DL (1995)
3. Haddad, H., Liebrock, L.M., Omicini, A., Wainwright, R.L. (eds.) Proceedings of the 2005 ACM Symposium on Applied Computing (SAC), March 13-17. ACM, Santa Fe (2005)
4. Maurer, H.A., Kappe, F., Zaka, B.: J. UCS 12(8), 1050 (2006)
5. Platos, J., Snásel, V., El-Qawasmeh, E.: Advanced Engineering Informatics 22(3), 410 (2008)
6. Prilepok, M., Platos, J., Snasel, V.: Similarity based on data compression. Unpublished paper (2013)
7. Tversky, A.: Psychological Review 84, 327–352 (1977)
8. Cilibarsi, R., Vitányi, P.M.B.: IEEE Transactions on Information Theory 51(4), 1523 (2005)
9. Li, M., Chen, X., Li, X., Ma, B., Vitányi, P.M.B.: IEEE Transactions on Information Theory 50(12), 3250 (2004)
10. Kirovski, D., Landau, Z.: 2004 IEEE 6th Workshop on Multimedia Signal Processing, pp. 127–130 (2004), doi:10.1109/MMSP.2004.1436438
11. Crnojevic, V., Senk, V., Trpovski, Z.: 6th International Conference on Telecommunications in Modern Satellite, Cable and Broadcasting Service, TELSIKS 2003, vol. 2, pp. 522–525 (2003), doi:10.1109/TELSIKS.2003.1246280
12. Chudá, D., Uhlík, M.: Rachev, B., Smrikarov, A. (eds.) CompSysTech, pp. 429–434. ACM (2011)
13. Ziv, J., Lempel, A.: IEEE Transactions on Information Theory 24(5), 530 (1978), doi:10.1109/TIT.1978.1055934

14. Habash, N.: Introduction to Arabic Natural Language Processing. In: Synthesis Lectures on Human Language Technologies. Morgan & Claypool Publishers (2010)
15. C.D.L. University. Stemming arabic text (1999),
<http://www.comp.lancs.ac.uk/computing/users/khoja/stemmer.ps>
(online; accessed September 22, 1999)
16. <https://arabicstemmer.codeplex.com/releases/view/105699>
(online; accessed April 26, 2013)

Peak-to-Average Power Ratio Reduction in Long Haul Coherent Optical OFDM Systems

Dang Le Khoa, Nguyen Thanh Tu, Nguyen Thi Hong Thu, and Nguyen Huu Phuong

Faculty of Electronics and Telecommunications, HCM City University of Science,
HCM City, Vietnam
`{dlkhoa, nttu, nththu, nhphuong}@fetel.hcmus.edu.vn`

Abstract. Recently, Coherent Optical Orthogonal Frequency Division Multiplexing (CO-OFDM) has been seen as a potential candidate for long haul optical transmission. It is due to OFDM technique that was proved as an effective solution for mitigating chromatic dispersion (CD) effects in optical communication systems. However, a very basic drawback of OFDM technique is large peak-to-average power ratio (PAPR) problem which requires large scale linear power amplifier and optical external modulator. The large PAPR leads to the increase of nonlinearity of optical fiber which depends on instantaneous signal power. So, the performance of CO-OFDM system is degraded. Several approaches were studied and applied in wireless communication. Among all techniques of Partial Transmit Sequence (PTS) is considered as the good method because of its distortionless characteristics. But the efficiency of this algorithm in long haul optical communication application is still an open issue. In this paper, we study PTS technique to reduce the influence of optics nonlinear effects. The Simulink simulation results are presented and discussed.

Keywords: Orthogonal Frequency Division Multiplexing, CO-OFDM, PAPR, PTS.

1 Introduction

Optical communication has been advanced to deliver the highest bit rates ever imagined, up to several hundred Gbits/s per optical wavelength channel [1] [2]. This is possible due to the significant progresses in the use of coherent detection, orthogonal frequency division multiplexing (OFDM) technique, multiplexing of polarization modes of guided optical waves in single mode optical fibers, and the employment of ultra-high speed processing in the electronic domain. OFDM technique has been demonstrated to combat fiber impairments such as fiber chromatic dispersion (CD) and polarization-mode dispersion (PMD) by splitting one high data rate stream into many lower data rate streams and then modulating each of them on corresponding subcarriers. Thus, OFDM can tolerate inter-symbol interference (ISI) caused by fiber chromatic dispersion [3], therefore, it seems quite a potential technique in high data rate optical communication. However, this technique exist

some drawbacks. One of them is a high PAPR since many subcarrier components are added via IFFT operation. The high PAPR gives rise to signal impairments which are caused by nonlinear devices' characteristics such as Analog/Digital (A/D) converter, Mach-Zehnder Modulator (MZM) as well as fiber cable[4]. In addition, the Kerr effect also makes distortions known as four-wave mixing (FWM) phenomenon between OFDM subcarriers. It makes subcarriers become dis-orthogonal. It is worth noticing that the influences of these nonlinear phenomena depend on the signal power which is measured before launching into fiber [5]. Therefore, various PAPR reduction techniques have been researched and proposed in wireless communications and recently for optical OFDM systems[3][6]-[8]. In wireless communication field, researchers already carried out many PAPR reduction methods such as filtering, clipping, coding, partial transmission sequences (PTS), selected mapping (SLM), etc[4][9]. Among these methods, the PTS scheme is considered as more efficient for PAPR reduction. The idea is to scramble an input data block of the OFDM symbols in time domain (PTS) and multiply them by a set of phase factor. Finally, the one with the minimum PAPR is transmitted. So, the probability of occurring high PAPR could be reduced before taking into Mach-Zehnder external modulation module.

In our work we use PTS reduction method applying to optical communication employing OFDM technique to reduce fiber nonlinear effects. The Simulink model is built and the experimental results are discussed. After a short introduction, the fundamental PAPR theory in CO-OFDM systems is revealed in section two. In section three, the PTS algorithm is illustrated in detail, CO-OFDM system set-up with this algorithm is discussed and showed in next part. The last one is some of the numerical simulation results and discussion.

2 PAPR of the OFDM Signal

In OFDM system with N subcarriers, if M signal are added with the same phase, they produce a peak power that is M times the average power.

Generally, even linear amplifier can cause nonlinear distortion on the output signals. It happens because of saturation characteristics of high power amplifier (HPA), external modulation MZM. In this case, the input signal power is much larger than its nominal value. However, the high input power level also causes several serious effects due to fiber nonlinearity[10] such as four-wave mixing (FWM) or self-phase modulation (SPM).

The performance of PAPR reduction algorithms could be evaluated in the following ways: (1) In-band ripple or out of band radiation which can be seen through power spectral density, (2) distribution of PAPR which is given by complementary cumulative distribution function (CCDF), and (3) is coded and uncoded BER performance. In our work, we use (2) and (3) to evaluate system's performance since PTS is a distortionless PAPR reduction method. The formula of CCDF is as follows[8]:

$$\begin{aligned} P\{PAPR > z\} &= 1 - P\{PAPR \leq z\} \\ &= 1 - (1 - e^{-z})^N \end{aligned} \quad (1)$$

3 PTS Algorithm Illustration

PTS is the most efficient approach and a distortionless scheme for PAPR reduction by optimally combining signal sub-blocks. In PTS technique, the input data block is broken up into disjoint sub-blocks in time domain. The sub-blocks are transformed into frequency domain by using IFFT, and after that they are weighted by a phase weighting factor before adding together to produce alternative transmit containing the same information (Fig. 1). However, when we have a large number of sub-blocks, finding out a best weighting factor is a complex and difficult problem [11].

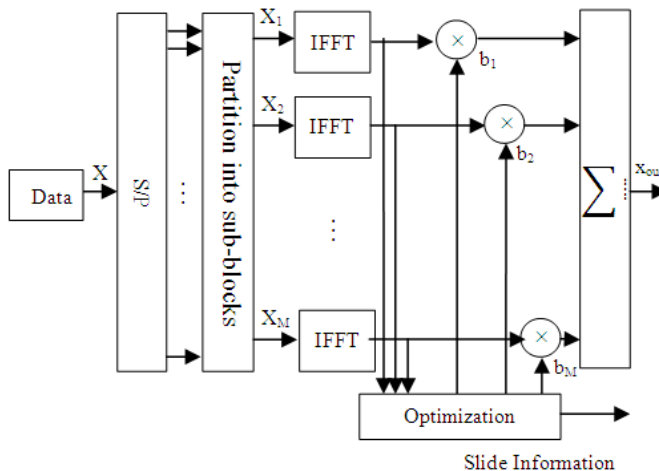


Fig. 1. The structure of transmitter site with PTS

The input data vector X in PTS algorithm is firstly partitioned into M disjointed sub-blocks $X_m = [X_{m,0}, X_{m,1}, \dots, X_{m,N-1}]^T$ such that:

$$X = \sum_{m=0}^{M-1} X^{(m)}, \quad 0 \leq m \leq M-1 \quad (2)$$

The sub-blocks are combined to minimize the PAPR. After performing the Inverse Fast Fourier Transform of X_m , we have $x_m = [x_{m,0}, x_{m,1}, \dots, x_{m,NL-1}]^T$, $0 \leq m \leq M-1$ with L is oversampling factor.

Each sub-block in time domain after that is rotated by a phase factor set $b_m = e^{j\phi m}$. In general, the phase factor set is limited with a finite number of elements to reduce the complexity. In this paper, we chose $\phi \in \{0, \pi/2, \pi, 3\pi/2\}$, this means $b_m \in \{\pm j, \pm 1\}$. Finally, the sub-blocks are summed up. After the PTS operation, the OFDM signal becomes [12]

$$x = \sum_{m=0}^{M-1} b_m x_m \quad (3)$$

Where x and x_m are the signal in the time domain.

The aim in the PTS is to find the optimal phase factors. In the phase optimization, because the phase factor of the first sub-block is taken as $b_0 = 1$, there are W^{M-1} alternative b combinations, where $b = [b_1 \dots b_{M-1}]$ and W is the number of the phase factors. In sequence b , b_m values are as follows:

$$b_m = \begin{cases} \{\pm 1\} & \text{if } W = 2 \\ \{\pm 1, \pm j\}, & \text{if } W = 4 \end{cases} \quad (4)$$

Therefore, the side information (SI) consists of the length of the SI is $R = (M - 1) \log_2(W)$ bits.

4 Long-Haul Optics Fiber Communication Setup

A single fiber transmission span consists of a Single Mode Fiber (SMF), an optical amplifier EDFA. We simulate an optical communications link over several hundred kilometers by cascading these spans from one end of the transmission link to another. The loss of each span is compensated by an EDFA.

The simulation of the optical signal which is propagated is based on the solution of the nonlinear Schrödinger equation (NES)[12].

$$\frac{\partial A}{\partial z} = -\frac{\alpha}{2} A - \beta_1 \frac{\partial A}{\partial t} - \frac{j}{2} \beta_2 \frac{\partial^2 A}{\partial t^2} + \frac{1}{6} \beta_3 \frac{\partial^3 A}{\partial t^3} - j\gamma |A|^2 A \quad (5)$$

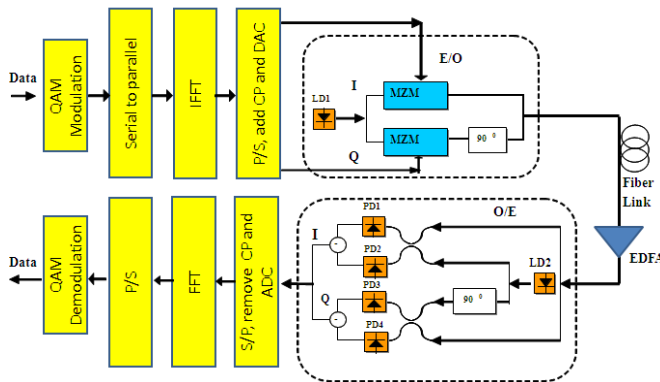
Where β_1 correspond to the various dispersion components of the fiber; β_2 , β_3 are the chromatic dispersion parameters respectively; Losses over the fiber are considered through the attenuation α parameter, and fiber non-linearity are showed by the γ term.

The parameters of a single fiber link and EDFA are shown in Table 1.

Table 1. Fiber and EDFA parameters for single span

SMF	EDFA
Loss factor: $\alpha = 0.2 \text{ dB}$	Gain: G_dB = 16(dB)
Dispersion coeff.: D = 17 (ps/nm.km)	Noise figure: NF = 5
Nonlinear coeff.: $\gamma = 1.4e^{-4} (\text{m}^{-1} \cdot \text{W}^{-1})$	
Fibre length: L = 80 km	

The block diagram of CO-OFDM is shown in Fig. 2. A very high speed data is firstly modulated by using 4-QAM. After serial to parallel conversion, IFFT algorithm is performed to convert signal from frequency domain to time domain. They are then added CP, performed DAC converter and finally converted to optical domain via external modulation MZM.

**Fig. 2.** CO-OFDM system

At the receiver, after converting the signal from optical to electrical domain by using photo-detectors, the electrical signal is processed to give back the data via de-OFDM modulation, and 4-QAM de-modulation.

In our simulation, the data rate is simulated at 10 Gbps and we have totally 256 subcarriers. It means that we use 256 points IFFT/FFT transformation.

5 Simulation Results

This part illustrates the results of Simulink simulations conducted to evaluate the performance of long-haul CO-OFDM system with and without PTS algorithm.

5.1 PTS Efficiency

The PAPR reduction performance of PTS algorithm is evaluated by the CCDF. Fig. 3 show the comparison of PAPR performance in term of CCDF of PTS.

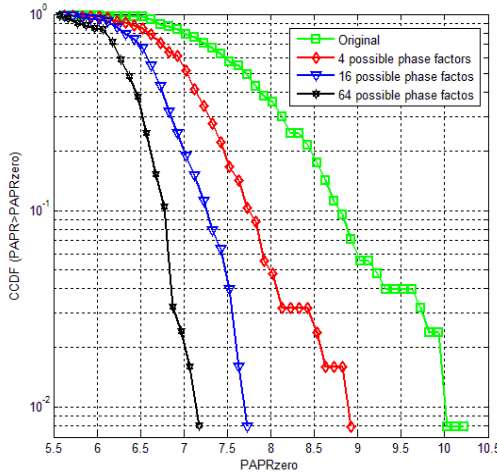


Fig. 3. CCDF comparison of PTS with different number of phase factors

Fig. 3 reveals the performance of PTS in term of number phase factor. We can see that the PTS even gives the better result when the number of combination phase factor increases. However, the system complexity becomes a big trouble as number of phase factor is large. We chose the number of combination at 16. It gave quite good performance as well as reasonable complexity.

5.2 Long Haul Optical Communication Link Experiment Results

The system is demonstrated for a transmission up to 1000 km of standard-single-mode-fiber (SSMF) without dispersion compensation at 10Gb/s. The tolerance of the models to nonlinear effects is tested by increasing the average launched power into the fiber. The nonlinear threshold which is used in this model is 10mW.

In Fig. 4, we can see that at low launched power, the system with and without PAPR reduction algorithms have similar performances. At 2.5 dBm in PTS, the performance of CO-OFDM with and without reduction methods is almost the same. The quality of system could be acceptable for around 1000 km fiber long. BER of this system is still below 10^{-9} for such a long haul optics communication link.

When we increase the launched powers, system performance is now influenced by nonlinear effects. Therefore, the efficiency of PTS is represented clearly. As we can see in Fig. 4, the performance of the system with PAPR reduction algorithm is better than system without this algorithm in nonlinear region. This number is even span to about 200 km with PTS algorithm (Fig. 4).

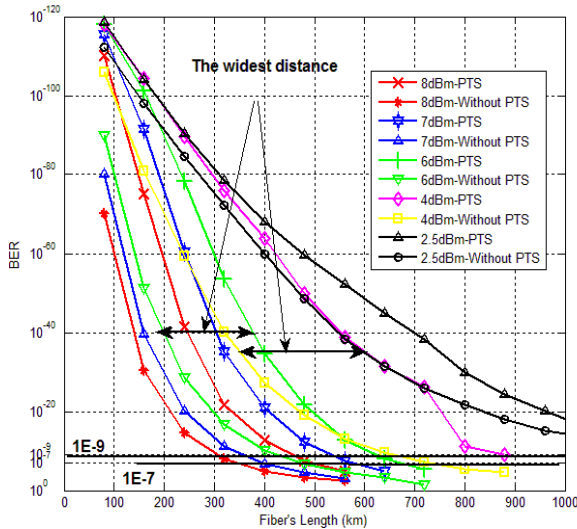


Fig. 4. BER of long haul optics fiber link with and without PTS algorithm in different average launched power values

6 Conclusion

OFDM technique is a very attractive approach for long haul high speed optical transmission system. However, the PAPR problem is one of the important aspects needed to consider. In this article, we have fundamentally simulated the algorithm for PAPR reduction purpose, namely PTS applying for point-to-point long haul coherent optical – CO-OFDM system. As a result, system tolerance of nonlinear effects increases with this algorithm. It is necessary to study some algorithms for reducing the complexity of the both PAPR reduction methods in optical OFDM communication.

References

1. Yang, Q., Tang, Y., Ma, Y., Shieh, W., Orthogonal, A.: Experimental Demonstration and Numerical Simulation of 107-Gb / s High Spectral Efficiency Coherent Optical OFDM. *Journal of Lightwave Technology* 27, 168–176 (2009)
2. Jansen, S.L., Morita, I., Schenk, T.C.W., Tanaka, H.: 121.9-Gb/s PDM-OFDM Transmission With 2-b/s/Hz Spectral Efficiency Over 1000 km of SSMF. *Journal of Lightwave Technology* 27, 177–188 (2009)
3. Shieh, W., Athaudage, C.: Coherent optical orthogonal frequency division multiplexing. *Electronics Letters* 42, 10–11 (2006)
4. Hellerbrand, S., Goebel, B., Hanik, N.: Trellis Shaping for Reduction of the Peak-to-Average Power Ratio in Coherent Optical OFDM Systems. In: Conference on Optical Fiber Communication, OFC 2009, pp. 1–3 (2009)

5. Goebel, B., Fesl, B., Coelho, L.D., Hanik, N.: On the Effect of FWM in Coherent Optical OFDM Systems. In: Conference on Optical Fiber Communication/National Fiber Optic Engineers Conference, OFC/NFOEC 2008, pp. 1–3. Ieee (2008)
6. Bulakçı, Ö., Schuster, M., Bunge, C., Spinnler, B.: Precoding Based Peak-to-Average Power Ratio Reduction for Optical OFDM demonstrated on Compatible Single- Sideband Modulation with Direct Detection. In: Conference on Optical Fiber communication/National Fiber Optic Engineers Conference, OFC/NFOEC 2008, pp. 1–3 (2008)
7. Krongold, B.S., Tang, Y., Shieh, W.: Fiber Nonlinearity Mitigation by PAPR Reduction in Coherent Optical OFDM Systems via Active Constellation Extension. In: 34th European Conference on Optical Communication, ECOC 2008, pp. 157–158 (2008)
8. Han, S.H., Lee, J.H.: An Overview Of Peak - To -Average Power Ratio Reduction Techniques For Multicarrier Transmission. IEEE Wireless Communications 56–65 (2005)
9. Wulich, D.: Definition of efficient PAPR in OFDM. IEEE Communications Letters 9, 832–834 (2005)
10. London, Y., Sadot, D.: Analysis of nonlinearity of Mach-Zehnder modulator in coherent optical OFDM in the presence of PAPR. In: 2010 IEEE 26th Convention of Electrical and Electronics Engineers in Israel, pp. 795–797 (2010)
11. Goebel, B., Member, G.S., Hellerbrand, S., Haufe, N., Hanik, N.: PAPR Reduction Techniques for Coherent Optical OFDM Transmission. In: 11th International Conference on Transparent Optical Networks, ICTON 2009, pp. 5–8 (2009)
12. Wang, J., Guo, Y., Zhou, X.: PTS-clipping method to reduce the PAPR in ROF-OFDM system. IEEE Transactions on Consumer Electronics 55, 356–359 (2009)

A Novel Wideband VHF Antenna for Impulse Ground Penetrating Radar Systems

Dong Tan Phuoc¹, Pham Minh Quang², Bui Huu Phu¹, and Lai Nguyen Duy³

¹ DCSELAB, University of Technology, Vietnam National University in Hochiminh City, Vietnam

² Post and Telecommunication Institute of Technology, Vietnam

³ Hochiminh City University of Transport, Vietnam

bhphu@dcselab.edu.vn

Abstract. In this paper, we propose a novel wideband VHF antenna operating at central frequency of 200 MHz for impulse ground penetrating radar (GPR) systems. As operating at the low frequency, impulse GPR systems can work well at the depth to 5 m. The proposed bow-tie antenna has been created based on the Lemniscate curve. This structure helps the antenna achieve better performance than conventional bow-tie antennas. In the paper, we also propose a wideband balanced-to-unbalanced (balun) transformation line to feed our antenna. The balun has good performance and matching impedance. The antenna is implemented in FR4 substrate and copper patch. Based on design, simulation, and implementation results, it has been shown that our proposed antenna has a good matched impedance, stable radiation patterns, and constant gain. Thus, it can be thoroughly applied to GPR systems in the future.

Keywords: ground penetrating radar (GPR), wideband antenna, Lemniscate curve, bow-tie antenna.

1 Introduction

Ground penetrating radar (GPR) technology has been widely studied over the world. The GPR system emits electromagnetic energy into ground and receives reflection signals to process and display images of objects underground. The technology can be applied to variety of fields such as military, constructions, geophysics, etc [1]. One important component in any GPR system is the transmit and receive antennas [2]. Antennas for GPR system should be designed to radiate pulses with given properties into the ground and receive reflected signals from subsurface objects as in [3].

The penetration depth of impulse GPR system is limited by the electrical conductivity of the ground, the radiated power, and the transmitted central frequency. The lower the operation frequency is, the deeper the signals can be penetrated, but the less the resolution of the systems has. So, antennas of GPR systems are required carefully in design to have as low central frequency and high bandwidth as possible for applications which require consideration in depth [4-14].

Recently, many studies on improving the deeper penetration for impulse GPR systems have been considered. Authors in [4] have proposed the GPR antenna suitable above dry sand with relative dielectric permittivity in the frequency range from 500 MHz to 3 GHz with a small conductivity. The antenna has a broadband, thus give GPR systems to have a high resolution. However, the UHF central frequency of this antenna does not improve the range of depth for the GPR systems. Authors in [5] have designed a loaded antenna operating in the frequency band from 0 to 300 MHz. However, the voltage standing wave ratio (VSWR) of the antenna is less than 2.5 and makes difficult in signal processing at the receiver. Authors in [6] have studied a shielded antenna for GPR systems. Although it has a good transmit signal with shielding and absorbing materials, their designed antenna is used in a GPR system working at 400MHz central frequency, and could not penetrate deeper than 3 m.

In this paper, we propose a novel wideband VHF antenna to improve the deep penetration for impulse GPR systems. Unlike above bowtie antennas, our antenna is based on Lemniscate curves to achieve a better radiation and smaller size. We also propose a broadband balun matching with the proposed antenna. The proposed antenna can work well in the bandwidth from 176 MHz to 232 MHz, and make GPR systems receive reflected signals at the depth to 5 m.

The remaining of the paper is as follows. Our proposed antenna and balun are presented in detail in Section 1. The simulation results is also shown in this section. In Section 3, the implementation and measurement results of the antenna have been provided. Finally, the conclusions are included in Section 4.

2 Proposed Wideband Antenna

The proposed antenna is designed based on FR4 dielectric substrate and copper patch for impulse GPR systems. We use the Lemniscate curve to create the structure of the antenna. This curve of the patch of antenna is shown in Fig. 1. The locus of the point P on the Lemniscate curve can be determined from two focal points F and F' such that $2OF \cdot OF' = a^2$ (where a is the distance from O to the center focal point F). The equation of Lemniscate curve in Cartesean coordinate is shown as followings [7]:

$$(x^2 + y^2)^2 - 2a^2(x^2 - y^2) = 0 \quad (1)$$

and the form in plolar coordinate is given by:

$$r^2 = 2a^2 \cos(2\theta) \quad (2)$$

The curve Lemniscate of the designed antenna has length $La = 541.3$ mm, width $Wa = 182$ mm, and the gap between the two wings of the antenna is 5 mm, as shown in Fig. 2.

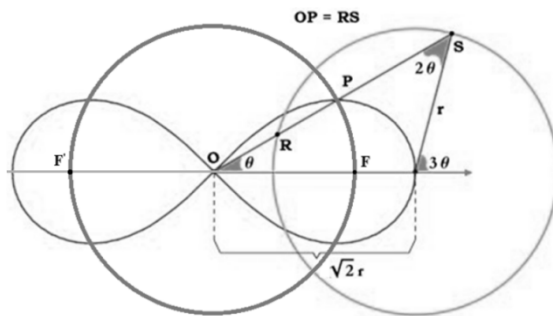


Fig. 1. The Lemniscate curve

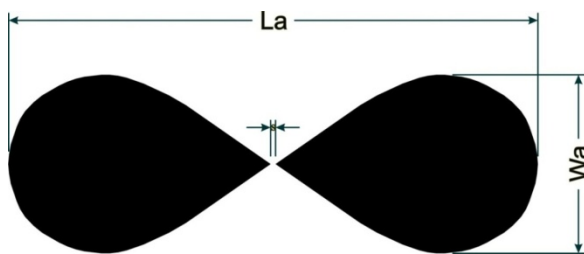


Fig. 2. Geometry and configuration of the proposed antenna

The distance of Lemniscate curve for this antenna is designed $\sqrt{2}r = 268.15$ mm and $OF = 186.61$ mm. Like the dipole antenna, the feed line of the Lemniscate antenna is located in middle of the wings at S opened point. Proposed antenna is designed by using FR4 dielectric material has a length L_s is 546.3 mm, width W_s is 192 mm, the thickness of FR4 dielectric substrate h is 1.6 mm, dielectric constant ϵ_r is 4.6, loss tangent $\tan \delta$ is 0.02, and the thickness of the copper patch t of 35 μm , as shown in Fig. 3.

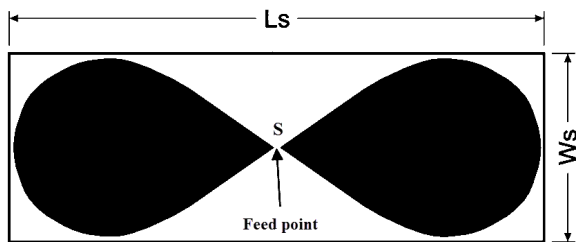


Fig. 3. Geometry and configuration of the proposed antenna

The proposed microstrip taper balun is designed to transform from the unbalanced structure of the coaxial cable 50 Ω impedance to the antenna structure balance in the 200 MHz frequency is shown in Fig. 4. This taper-line balun has two sections: the

balanced line portion which matches the antenna impedance to 50 ohm and a portion which actually performs the mode transduction. The dimensions of the balun are shown in Fig. 5 and its values are shown in Table 1.

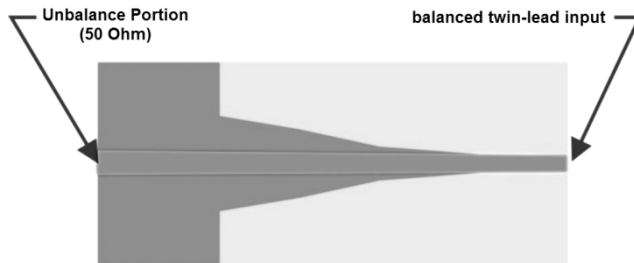


Fig. 4. Configuration of the microstrip taper balun

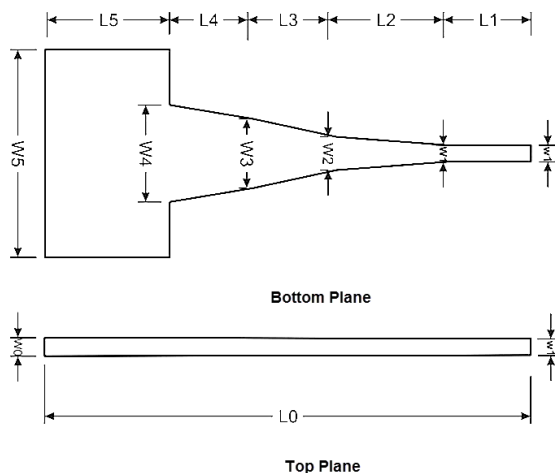


Fig. 5. The dimensions of balun

Table 1. The Dimension Values of Balun

n	W_n (mm)	L_n (mm)
0	3	300
1	3	60
2	6	90
3	12	60
4	25	60
5	40	30

Firstly, we simulate our proposed antenna without the balun. The value of reflection coefficient S_{11} is equal to -21.1 dB at the central frequency of 200 MHz, and S_{11} is less than -10 dB and VSWR is less than 2 in the frequency range from 184.38 MHz to 221.6 MHz, as shown in Figs. 6 and 7. Input impedance of the designed antenna $Z = 42.52 + 3.24*j \Omega$ at frequency 200 MHz. The real part and the imaginary part of the impedance respectively is presented in Figs. 8 and 9.

Secondly, we connect our proposed balun to the designed antenna to make a good match impedance and increase performance of antenna, as shown in Fig. 10. The simulation results of the antenna with balun is shown in Figs. 11 and 12.

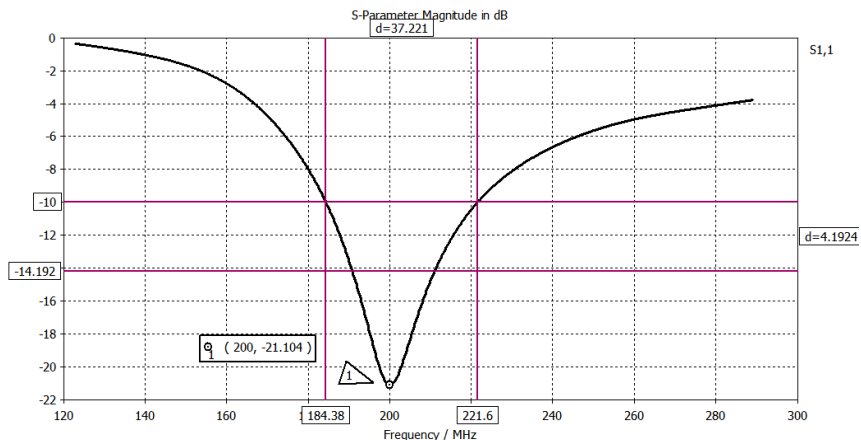


Fig. 6. Return loss S_{11} of the antenna without balun

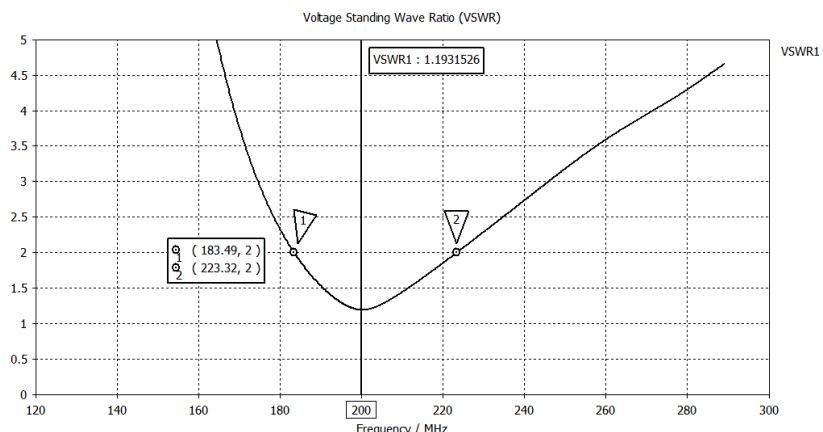


Fig. 7. VSWR of the antenna without balun

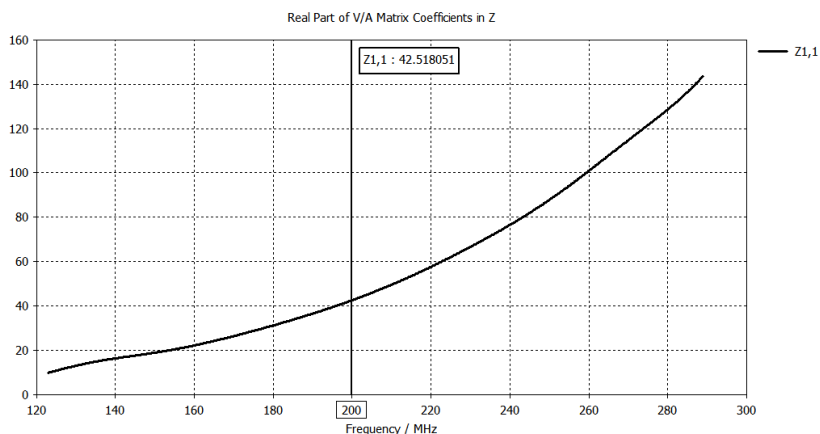


Fig. 8. The real part of the impedance

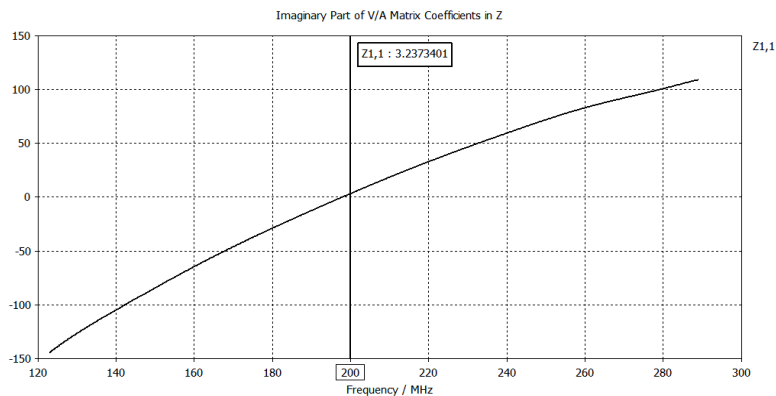


Fig. 9. The imaginary part of the impedance

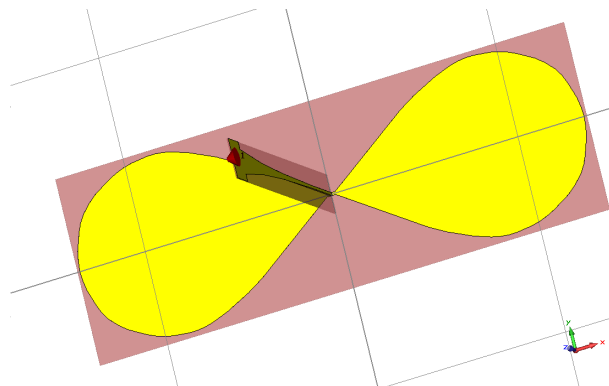


Fig. 10. Antenna with balun in simulation environment of CST software

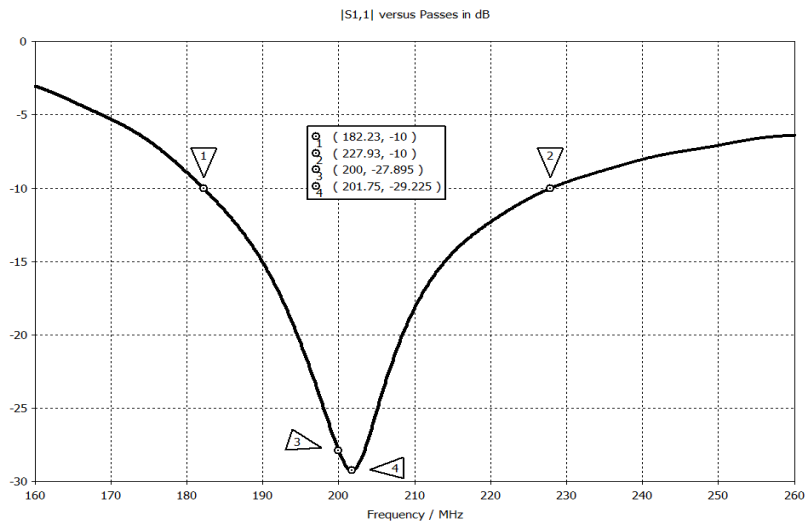


Fig. 11. Return loss of antenna with balun

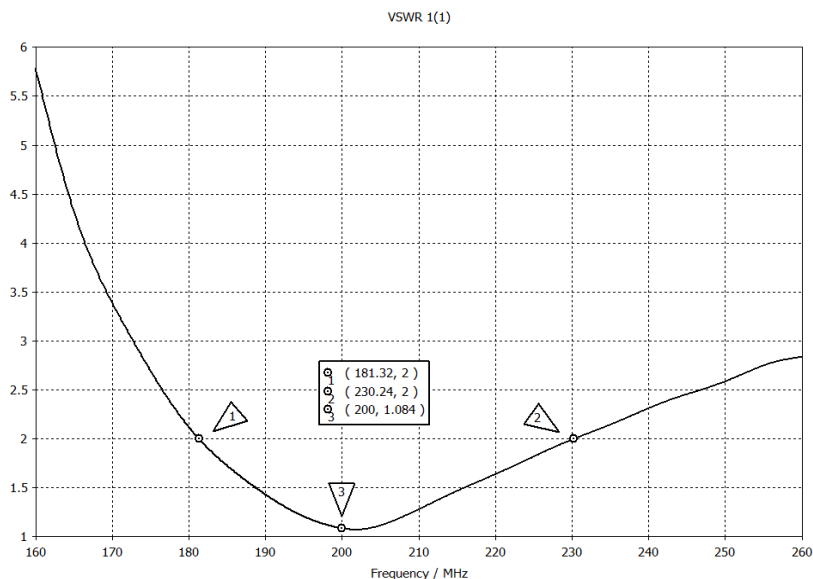


Fig. 12. VSWR of the antenna with balun

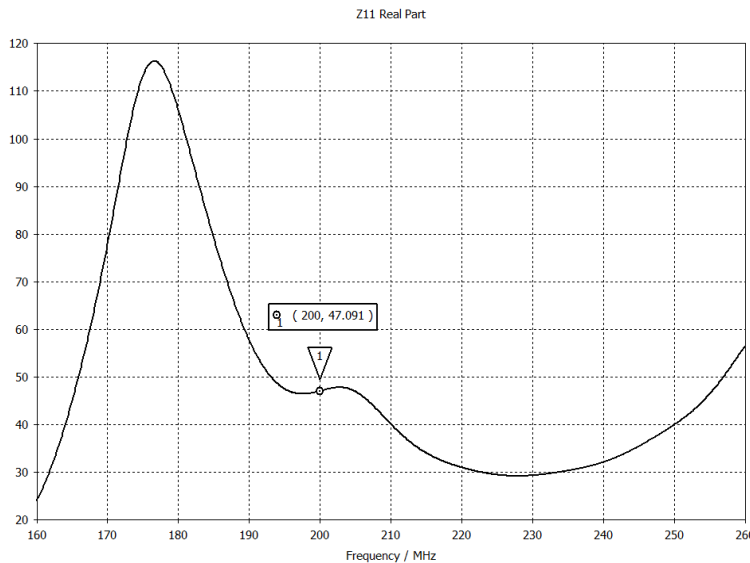


Fig. 13. The real part of impedance in case the antenna with balun

According to the above simulation results at the central frequency of 200 MHz, S11 is less than -25 dB and the real part of the impedance is 47Ω . The bandwidth can be extended to 49 MHz, equivalent to 25% of the central frequency 200 MHz. The simulation results have shown that the matching impedance in this case is better than the case of the antenna without balun. So, the designed balun helps to increase the performance of antenna.

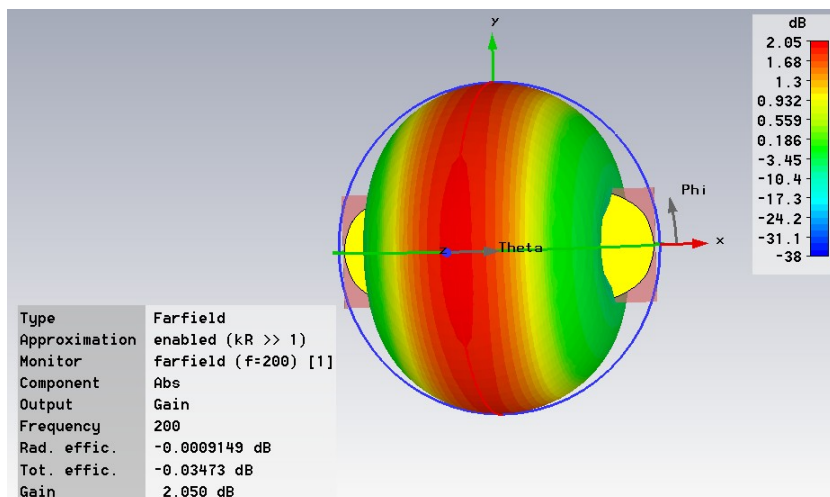


Fig. 14. 3D radiation pattern of antenna at 200 MHz

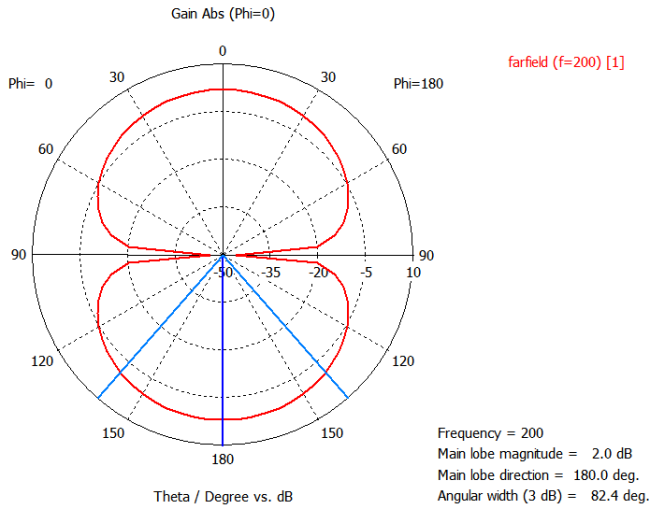


Fig. 15. Polar radiation pattern of antenna at 200 MHz

3D and Polar radiation patterns of the proposed antenna at 200 MHz are shown in Fig. 14 and 15, respectively. The antenna gain can be reached to 2 dB.

3 Experimental Results

Based on the design and simulation results, we have implemented the proposed antenna and balun in FR4 material. In this section, we will show the results of its implementation and measurements. The implemented antenna is shown in figure 16.

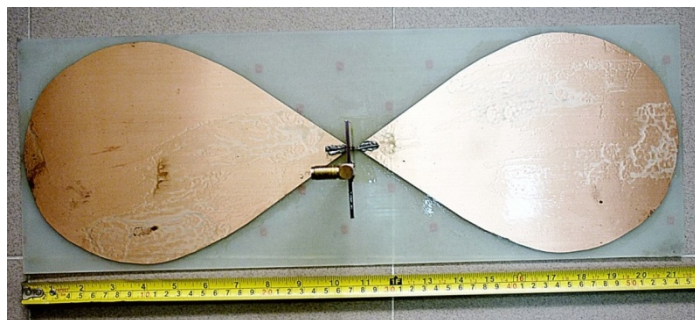


Fig. 16. Geometry of the implemented antenna

The measured reflection coefficient S11 and VSWR with wideband balun transformer line are shown in Fig. 17 and 18. It can be seen that our proposed antenna can work in the frequency band from 176 MHz to 232 MHz. The Smith Chart measurement of the proposed antenna is shown in Fig. 19. It has shown a good matching impedance. A comparison between simulation results and implementation results of S11 and VSWR values are shown in Tables 1 and 2. It can be seen that the performance of implementation is better than in simulation. This may be the difference from the characteristics of real FR4 material and parameters in simulation.

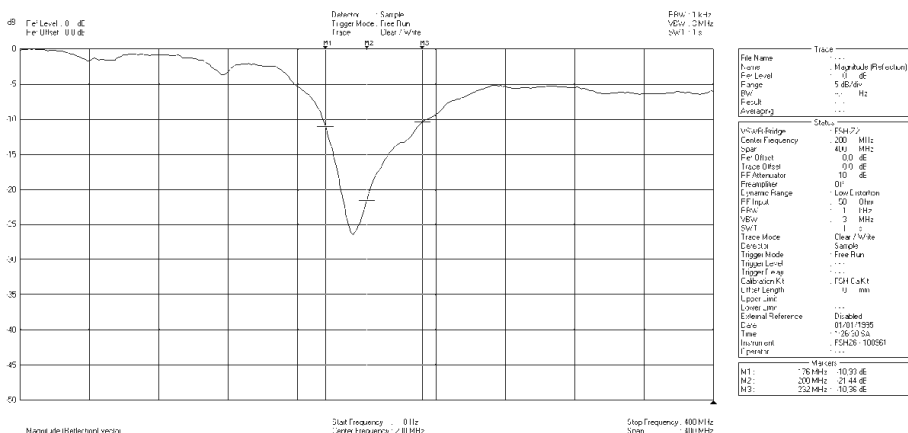


Fig. 17. Measured reflection coefficient S11

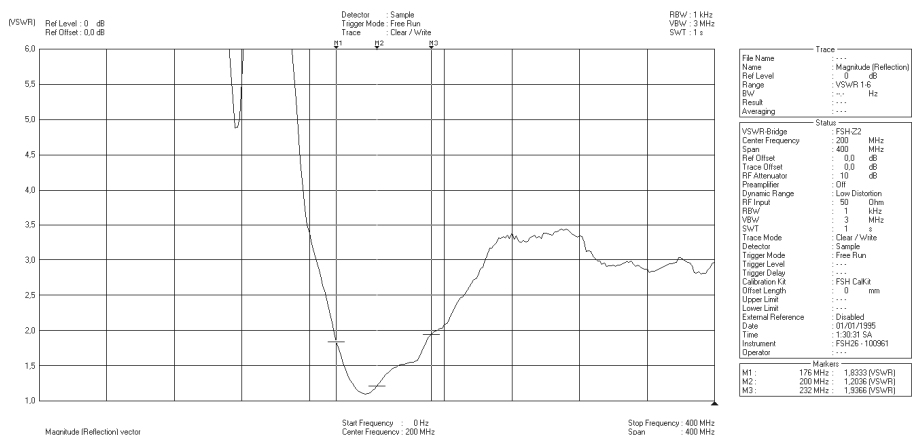
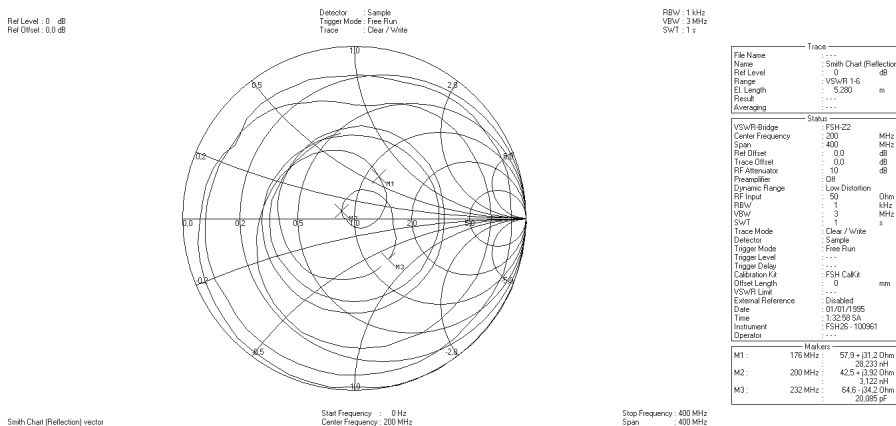


Fig. 18. VSWR measurement

**Fig. 19.** Smith Chart measurement**Table 2.** Comparison Results between Simulation and Measurement of S11

Frequency (MHz)	Simulated S11 (dB)	Frequency (MHz)	Measured S11 (dB)
182.23	-10	176	-10.93
200	-27.9	200	-21.44
227.93	-10	232	-10.36

Table 3. Comparison Results between Simulation and Measurement of VSWR

Frequency (MHz)	Simulated VSWR	Frequency (MHz)	Measured VSWR
181.32	2	176	1.833
200	1.084	200	1.204
230.24	2	232	1.972

4 Conclusions

In the paper, a proposed novel wideband VHF antenna has been presented. We have designed, simulated, and implemented the antenna and a wideband balun. The measured results have shown that the proposed antenna has a wide frequency band from 176 MHz to 232 MHz, equivalent to 28% of the central frequency 200 MHz.

The wideband balun has also been designed to make a good matching impedance of the antenna. The patch antenna is designed based on the Lemniscate curve. The implementation of the antenna is extremely low cost, small size, and high gain. This proposed antenna is very suitable for wideband systems such as impulse GPR.

References

- [1] Wilson, M.G.C., Henry, G., Marshall, T.R.: A review of the alluvial diamond industry and the gravels of the North West Province, South Africa. *South African Journal of Geology* 109, 301–331 (2006)
- [2] Pramudita, A.A., Kurniawan, A., Bayu Suksmono, A.: Hexagonal monopole strip antenna with rectangular slot for 100-1000MHz SFCW GPR applications. *International Journal of Antennas and Propagation*, 1–6 (2008)
- [3] Yarovoy, A.G., Lighthart, L.P.: Ultra-wideband antennas for ground penetrating radar. In: International Research Centre for Telecommunications-transmission and Radar, Faculty of Information Technology and Systems, TU Delft (2003)
- [4] Lestari, A.A., Yarovoy, A.G., Lighthart, L.P.: Adaptive wire bow-tie antenna for GPR applications. *IEEE Trans. Antennas and Propagation* 53, 174–1754 (2005)
- [5] Zou, A., Li, J., Wang, K., Cheng, D.: Investigations of RL-Loaded Bowtie Antenna for Low-Resolution GPR. In: 5th International Conference on Wireless Communications, Networking and Mobile Computing, WiCom 2009 (2009)
- [6] Guo, C., Liu, R.C.: Design of a shielded antenna system for ground penetrating radar applications. *IEEE Trans. Antennas and Propagation Society International Symposium*, 1–4 (2009)
- [7] Dennis Lawrence, J.: A catalog of special plane curves, pp. 4–5, 121–123, 145, 151, 184. Dover Publications (1972)
- [8] Turk, A.S., Sen, B.: Ultra wide band antenna designs for ground penetrating impulse radar systems. In: IEEE EMC Symposium Records, Istanbul, Turkey (2003)
- [9] Kiminami, K., Hirata, A., Shiozawa, T.: Double-sided printed bow-tie antenna for UWB communications. *IEEE Antennas and Wireless Propagation Letters* 3, 152–153 (2004)
- [10] Lestari, A.A., Bharata, E., Suksmono, A.B., Kurniawan, A., Yarovoy, A.G., Lighthart, L.P.: A modied bow-tie antenna for improved pulse radiation. *IEEE Transactions on Antennas and Propagation* 58(7), 2184–2192 (2010)
- [11] Lestari, A.A.: RC-loaded bow-tie antenna for improved pulse radiation. *IEEE Transactions on Antennas and Propagation* 52(10), 2555–2563 (2004)
- [12] Pramanick, P., Bhartia, P.: Tapered Microstrip Transmission Line. In: IEEE MTT-S Int. Microwave Symp. Dig., pp. 242–244 (1983)
- [13] Pramanick, P., Bhartia, P.: A GeneralizedTheory of Tapered Transmission Line Matching Transformers and Asymmetric Couplers Upporting Non-TEM Modes. *IEEE Trans. Microwave Theory Tech.* 87(1), 361–364 (1987)
- [14] Romano, N., Soldovieri, F., Persico, R.: Design and numerical analysis of a new reconfigurable antenna for georadar applications. In: 13th International Conference on Ground Penetrating Radar, GPR 2010, June 21-25, pp. 1–5 (2010)

TOA Estimation Algorithm Based on Shift-Invariant Technique for Multi-band Signals

Ying-chun Li, Seungryeol Go, Hyung-ryeol Yoo, Sang-deok Kim,
and Jong-Wha Chong

Hanyang University, Seoul, Korea
lyc.workhard@gmail.com

Abstract. This paper proposes a new TOA estimation algorithm based on shift invariant structure for multi-band signals. The performance of the proposed method is compared with Cramer-Rao lower bound (CRLB) and the conventional algorithms such as MUSIC, matrix pencil, TLS-ESPRIT in additive white Gaussian noise (AWGN) and multipath channel.

1 Introduction

Wireless location has drawn considerable research and provided numbers of application, such as target finding, mine rescuing and navigating. The main technique utilized in wireless location is parameter estimation include time-of-arrival (TOA) estimation, time difference of arrival (TDOA) estimation, received signal strength interference (RSSI) estimation and angle-of-arrival (AOA) estimation.

TOA estimation is an important signal processing problem with applications in many areas, such as radar, sonar, and wireless communications. How is the TOA estimation organized? Two kinds of approaches exist for TOA estimation. The first one is the maximum-likelihood (ML) method, which investigates the correlation function of a received signal as in [1]-[2]. Therefore, the resolution is limited by the inverse of the signal bandwidth, and it is always used with a narrow band signal. The second one is the shift invariant method, which transforms the received signal to a sinusoidal signal and handles the received signal in the frequency domain. In previous work, parameter estimation techniques can be divided into two types: one-dimensional parameter estimation and two-dimensional parameter estimation. First kind of parameter estimation techniques, which are one dimensional, such as MULTiple Signal Classification (MUSIC) [3], Matrix Pencil (MP) [4] and Total Least Square ESPRIT (TLS-ESPRIT) [5], were applied to the transformed signals. Second kind of parameter estimation techniques, such as 2-dimensional MUSIC, and joint angle and frequency estimation, have only been used for the estimation of TOA parameters in uniform or non-uniform arrays.

Although the performances of the conventional algorithms can approximate the CRLB, higher computational complexities and support of different auxiliary information are in demand [5]. Therefore, more efficient and robust TOA estimation techniques still require further research. In this paper, a new TOA estimation by using shift-invariant technique was proposed.

2 Proposed Method

2.1 Signal Model

The received signals can be changed into a form of sinusoids for shift invariant TOA estimation. Our algorithm transforms the received samples by a DFT and a deconvolution, as in [3-4] and [6].

We assume that K multiple symbols are transmitted at different frequency bands, and the discrete time model for the k -th received signals $y_k(t)$ is given by $y_k[n]=y_k(nT_s)$ for $n=0,1,\dots,N-1$ where $T_s=1/f_s$ is the sampling period, such that $T_{sym}=NT_s$. The sampling period T_s is determined in such a way that the Nyquist criterion is met. For a given sequence of $y_k[0], y_k[1], \dots, y_k[N-1]$ from the k -th symbol, a sequence of the data for the estimated channel frequency response(CFR) by N -point DFT and deconvolution is modeled from [4] by

$$x_k[l] = \sum_{m=0}^{M-1} a_m \exp(j2\pi(f_k + l\Delta f)\tau_m) \text{ for } l = 0, \dots, N-1, \quad (1)$$

where a_m and τ_m denote the complex amplitude and TOA of the m -th path, respectively; M is the number of the received paths; the frequency spacing Δf is determined by f_s/N and f_k denotes the center frequency of the k -th symbol. For convenience without loss of generality, we assume that $f_k=(k-1)B$ where B denotes the bandwidth for a symbol. By the transformation, a sequence of the received samples $y_k[n], n=0, \dots, N-1$ in the time domain is changed into a sequence of the samples $x_k[l], l=0, \dots, N-1$ in the frequency domain. The transformation using the N -point DFT is based on the shifting property of the Fourier transform. Since the transformed samples are composed of M sinusoids whose frequency is a function of τ_m , it is also possible to estimate the TOA of the received paths by frequency estimation of $x_k[l], l=0, \dots, N-1$.

2.2 Shift-Invariant Technique

In this section, the small-scaled phase shift is defined by ϕ_m of (2). Using the transformed samples of the k -th symbol, $x_k[l]$ for $l=0, \dots, N-1$, the Hankel snapshot matrix is defined as

$$X_k = \begin{bmatrix} x_k[0] & x_k[1] & \cdots & x_k[L_r - 1] \\ x_k[1] & x_k[2] & \cdots & x_k[L_r] \\ \vdots & \vdots & \ddots & \vdots \\ x_k[L_c - 1] & x_k[L_c] & \cdots & x_k[N - 1] \end{bmatrix}, \quad (2)$$

where L_r and $L_c=N-L_r+1$ are selection parameters, referred to as pencil parameter in [7], satisfying the condition $L_r \geq M$ and $L_c \geq M$. Let us define the steering matrices P and

\mathbf{Q} , which contain the corresponding M sinusoids in its columns and rows, respectively, such that,

$$\mathbf{P} = \begin{bmatrix} 1 & 1 & \cdots & 1 \\ \phi_0 & \phi_1 & \cdots & \phi_{M-1} \\ \vdots & \vdots & \ddots & \vdots \\ \phi_0^{L_c} & \phi_1^{L_c} & \cdots & \phi_{M-1}^{L_c} \end{bmatrix} \text{ and } \mathbf{Q} = \begin{bmatrix} 1 & \phi_0 & \cdots & \phi_0^{L_r-1} \\ 1 & \phi_1 & \cdots & \phi_1^{L_r-1} \\ \vdots & \vdots & \ddots & \vdots \\ 1 & \phi_{M-1} & \cdots & \phi_{M-1}^{L_r-1} \end{bmatrix}, \quad (3)$$

where $\phi_m = \exp(j2\pi\Delta f\tau_m)$ for $m=0, \dots, M-1$. Let us define the diagonal matrix \mathbf{R}_k whose elements on its diagonal represents the complex amplitude of the m -th path multiplied with the TOA-induced phase shift $\varphi_{m,k} = \exp(j2\pi f_k \tau_m)$, such that

$$\mathbf{R}_k = \text{diag} [a_0 \varphi_{0,k}, a_1 \varphi_{1,k}, \dots, a_{M-1} \varphi_{M-1,k}], \quad (4)$$

and $\text{diag}[\cdot]$ denotes the diagonal matrix. As proven in [7], \mathbf{X}_k is factorized in terms of \mathbf{P} , \mathbf{Q} and \mathbf{R}_k by

$$\mathbf{X}_k = \mathbf{P} \mathbf{R}_k \mathbf{Q} \text{ for } k=1, \dots, K-1. \quad (5)$$

Let us define two matrices $\mathbf{X}_{k,0}$ and $\mathbf{X}_{k,1}$, which are the partitioned sub-matrix of \mathbf{X}_k with the last row deleted and the first row deleted, respectively, such that

$$\mathbf{X}_{k,0} = \mathbf{J}_0 \mathbf{X}_k \text{ and } \mathbf{X}_{k,1} = \mathbf{J}_1 \mathbf{X}_k \quad (6)$$

where $\mathbf{J}_0 = [\mathbf{I}_{N-Lr}, \mathbf{0}_{N-Lr \times 1}]$, $\mathbf{J}_1 = [\mathbf{0}_{N-Lr \times 1}, \mathbf{I}_{N-Lr}]$, \mathbf{I}_{N-Lr} denotes the identity matrix of $N-L_r$ by $N-L_r$, and $\mathbf{0}_{N-1 \times 1}$ denotes the zero matrix of $N-1$ by 1. Substituting \mathbf{X}_k with $\mathbf{P} \mathbf{R}_k \mathbf{Q}$ in (5), the sub-matrices $\mathbf{X}_{k,0}$ and $\mathbf{X}_{k,1}$ are represented by

$$\mathbf{X}_{k,1} = \mathbf{J}_1 \mathbf{P} \mathbf{R}_k \mathbf{Q} = \mathbf{P}_0 \mathbf{R}_k \mathbf{Q}, \quad (7)$$

where $\mathbf{P}_0 = \mathbf{J}_0 \mathbf{P}$ and

$$\mathbf{X}_{k,1} = \mathbf{J}_1 \mathbf{P} \mathbf{R}_k \mathbf{Q} = \mathbf{P}_1 \mathbf{R}_k \mathbf{Q} = \mathbf{P}_0 \boldsymbol{\Phi} \mathbf{R}_k \mathbf{Q}, \quad (8)$$

where $\mathbf{P}_1 = \mathbf{P}_0 \boldsymbol{\Phi}$ and $\boldsymbol{\Phi} = \text{diag}[\phi_0, \phi_1, \dots, \phi_{M-1}]$. The factorizations in (7)-(8) are quite similar to the factorization used in [7]. Based on the factorizations in (7)-(8), the generalized EVD on $\mathbf{X}_{k,0}$ and $\mathbf{X}_{k,1}$ can be derived by

$$\begin{aligned} (\mathbf{X}_{k,1} - \lambda \mathbf{X}_{k,0}) \boldsymbol{\beta} &= 0 \Leftrightarrow (\mathbf{P}_0 \boldsymbol{\Phi} \mathbf{R}_k \mathbf{Q} - \lambda \mathbf{P}_0 \mathbf{R}_k \mathbf{Q}) \boldsymbol{\beta} = 0 \\ &\Leftrightarrow (\mathbf{P}_0 [\boldsymbol{\Phi} - \lambda \mathbf{I}_M] \mathbf{R}_k \mathbf{Q}) \boldsymbol{\beta} = 0 \end{aligned} \quad (9)$$

where λ and $\boldsymbol{\beta}$ denote the eigenvalue and the corresponding eigenvector, respectively. In (9), one can demonstrate that, in general, the rank of $(\mathbf{X}_{k,1} - \lambda \mathbf{X}_{k,0})$ will be M . However, if $\lambda = \phi_m$, $m=0, 1, \dots, M-1$, the i -th row of $(\mathbf{X}_{k,1} - \lambda \mathbf{X}_{k,0})$ equal to

$(\mathbf{P}_0[\Phi \cdot \lambda \mathbf{I}_M] \mathbf{R}_k \mathbf{Q})$ becomes zero and the rank of this matrix is $M-1$. Through the generalized EVD on $X_{k,0}$ and $X_{k,1}$, this rank reducing numbers are given by the eigenvalues, i.e., $\lambda_m = \phi_m$ for $m=0, \dots, M-1$. Based on the estimated ϕ_m , we can achieve the estimated TOA for the m -th path such that

$$\hat{\tau}_m = \frac{1}{2\pi\Delta f} \arg(\phi_m) \quad (10)$$

3 Simulation Results

The simulation results of Monte Carlo averaged over 10,000 estimates for the AWGN and multipath channel (two-path, herein). In the simulation results, the TOA estimation performance of our proposed algorithm is compared with that of the conventional algorithms such as the ML-based method, MUSIC, MP and TLS-ESPRIT. The ML-based TOA estimation method developed for multicarrier signals in [2] is used here. Since the TOA of the first arrival path is meaningful in wireless localization, only the RMSE for the first arrival path is considered. The received signal spassed through the multipath channel are normalized to have unit power in average, and AWGN signals with the specified variance is added for Monte-Carlo simulations.

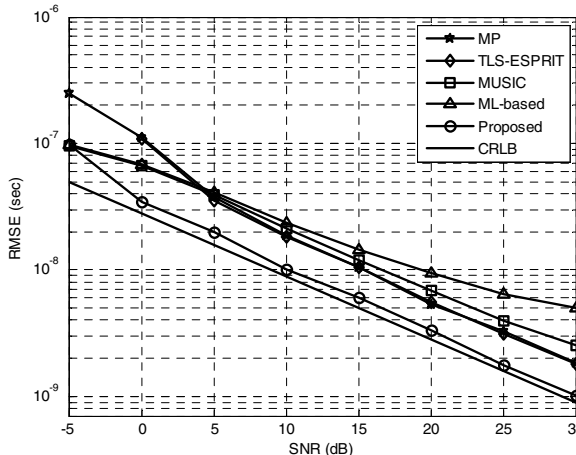


Fig. 1. Comparsion of RMSEs with CRLB in AWGN channel

In Fig. 1, the performance of the proposed algorithm is compared with that of the conventional shift invariant algorithms and CRLB in the AWGN channel. Among the conventional algorithms, the proposed one exhibits the most accurate TOA estimation performance, since it exploits the dual shift invariant structure of the multi-band signals while the others are constrained to the single shift invariant structure. The

ML-based estimation algorithm shows the worst performance in the AWGN channel due to its low resolution.

By the two-path channel simulation, the decomposition capability of the algorithms can be compared to each other. The proposed method shows the most superior performance among the algorithms as shown in Fig. 2. For the case of ML-based method, it shows the worst performance in two-path channel, since its bandwidth is too small to decompose the received paths.

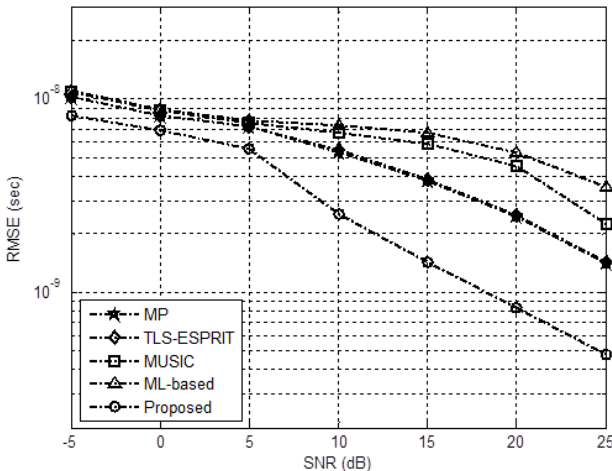


Fig. 2. Comparsion of RMSEs in two-path channel

4 Conclusion

We proposed an accurate shift invariant TOA estimation for multiple reference signals in multipath channels. Performance improvement is observed in the TOA estimation results based on the proposed transformation.

Acknowledgement. This work was supported by the IT R&D program of MKE/KEIT. [10035570, Development of self-powered smart sensor node platform for smart&green building]. This work was sponsored by ETRI SW-SoC R&BD Center, Human Resource Development Project.

References

- [1] Haneda, K., Takizawa, K., Takada, J., Dashti, M., Vainikainen, P.: Performance evalution of threshold-based UWB ranging methods - Leading edge vs. search banck -. In: 3rd European Conf. Antennas and Propagation, EuCAP 2009, pp. 3673–3677 (2009)

- [2] Yasir, K., Davide, D., Antonio, A., Umberto, M.: Range Estimation in Multicarrier Systems in the Presence of Interference: Performance Limits and Optimal Signal Design. *IEEE Trans. Wireless Commun.* 10(10), 3321–3331 (2011)
- [3] Sarkar, T.K., Pereira, O.: Using the matrix pencil method to estimate the parameters of a sum of complex exponentials. *IEEE Antennas Propag. Mag.* 37(1), 48–55 (1995)
- [4] Li, F., Vaccaro, R.J., Tufts, D.W.: Performance Analysis of the State-Space Realization (TAM) and ESPRIT Algorithms for DOA Estimation. *IEEE Transactions on Antennas and Propagation* 39, 418–423 (1991)
- [5] Guvenc, I., Chong, C.: A Survey on TOA Based Wireless Localization and NLOS Mitigation Techniques. *IEEE Communications Surveys & Tutorials* 11(3), 107–124, 3rd Quarter (2009)
- [6] Li, X., Pahlavan, K.: Super-resolution TOA estimation with diversity for indoor geolocation. *IEEE Trans. Wireless Commun.* 3(1), 224–234 (2004)
- [7] Boumard, S., Mammela, A.: Robust and Accurate Frequency and Timing Synchronization Using Chirp Signals. *IEEE Transactions on Broadcasting* 55, 115–123 (2009)

PWM Noise Reduction in OFDM-Based Power Supply Overlaid Communication System for Industrial Machine Control

Hidetsugu Koga^{1,2}, Masayuki Kurosaki², and Hiroshi Ochi²

¹ Technology & Development Division / Corporate Research & Development Center,
Yaskawa Electric Corporation,
12-1, Otemachi, Kokurakita-ku, Kitakyushu, Fukuoka, 8038530, Japan
hks@yaskawa.co.jp

² Department of Computer Science and Electronics, Kyushu Institute of Technology,
680-4, Kawazu, Iizuka, Fukuoka, 8028502, Japan
[{kuroasaki,ochi}@cse.kyutech.ac.jp](mailto:hkoga@dsp.cse.kyutech.ac.jp)

Abstract. This paper presents a design and prototyping of power supply overlaid communication system for industrial machine. In industrial machine, the control signals require for real-time and reliable. However, there is no power supply overlaid communication system for industrial machine to meet such requirements with current technology. We have developed a power supply overlaid communication system to meet the demands of these two. We also report to develop a channel emulation system using power line model for industrial machine, since the evaluation of the proposed system.

Keywords: PWM Noise, Power supply overlaid communication, Industrial machine control.

1 Introduction

Represented by the industrial machine, industrial robot is constructed by many actuators. Used only for communication lines that are routed to the actuator from the controller this controls the whole machine of the actuator. In addition, the actuator power supply lines and the controller power supply lines are wired separately from this. For this reason, many cables are used for the control signal and power supply, in the industrial robot. The cables gradually deteriorate from twisting and bending from the robot position, expansion and contraction. As a result, the cable is disconnected, and it will waste the cost of the replacement cables. Thus industrial machine is necessary to wire saving. In addition, if could wire saving, it is able to contribute to saving resources of copper material.

Previously we explain the communication cables and power supply cables is distributed to industrial machine. The method of wire saving is communication on the power supply cables. It enables to control industrial machine over one power supply cable. However, the power supply cable has a number of branches, so the superposed signal is reflected [1]. This makes the power supply overlaid

communication channel multipath. Then receiver receives signal which added multipath signals. If these signals delay long, receiving characteristic deteriorates by Inter-Symbol Interference (ISI) [2] [3]. In the power supply overlaid communication, Orthogonal Frequency Division Multiplexing(OFDM) modulation method enables high throughput communication against multipath channel[4]. OFDM modulation is also used by wireless LAN (WLAN) system including IEEE802.11a system [5]. OFDM divides high throughput data into low throughput data. Then transmit in parallel by using lots of sub-carriers. This enables to reduce multipath distortion and to complement channel condition flexibility. Sub-carriers are orthogonal each other, so it enables to communicate in high frequency usage efficiency. Moreover the inserted redundant signals called guard interval (GI) between the symbols avoid multipath delay interference efficiently and the received sub-carriers are just influenced by attenuation. Although the attenuated sub-carrier is susceptible to the noise effect, it enables to correct code error by combine with error correction. On the other hand, within the multipath channel, a bit loading algorithm to maximize the bit rate has been proposed in the simulation [6]. For this reason, we need to develop a power supply overlaid communication system for industrial machine control [7][8].

However, the noise is assumed Gaussian white noise in these systems, the impulse noise generated from the actuator of the machines is also present in practice. In such environment, the bit error rate much degrades because the affection of impulse noise spreads all carriers in OFDM. As a proposal to a power supply overlaid communication system in impulse noise environment, by using a limiter amplifier, it is shown that it can improve the BER deterioration due to impulse noise [9], Method of re-modulated in the OFDM time domain signal samples, it has been degraded by impulse noise [10]. There is nothing that can ensure communication reliability and real-time either.

This paper is a proposal for improvement of communication reliability. This paper is organized as follows. In the section 2, shows the impulse noise occurs in industrial machinery. The section 3 describes the proposed method. The section 4 shows the construction of the proposed power supply overlaid communication system for industrial machine control. The section 5 shows the result of the proposed system performance. Finally in section 6, we describe some of the challenges and future works.

2 System Specification

Fig.1 shows the basic robot control system. The basic robot control system controls the attitude of the robot. First, the robot controller sends position information request from the servo amplifier to the encoder. Then, position information requested encoder responds position information. Next, the robot controller controls attitude of the robot using by this position information.

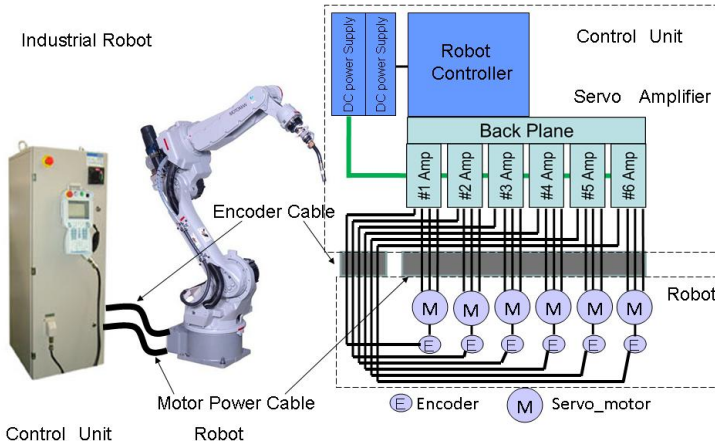
Fig.2 shows a schematic diagram of the basic robot control system which is applied by the proposed power supply overlaid communication system for industrial machine control. The new system saves the use of encoder cables.

Table 1. Rate- Dependent Parameter

Data Rate [Mbits/s]	Modulation	Coding Rate	Coded bits per sub-carrier	Data bits OFDM symbol
81	64QAM	3/4	6	216

Fig.3 shows details of the wire-saving on encoder cable. The left side shows the structure of conventional encoder cables. Three pairs of wires are necessary for one encoder communication: one pair of DC power supply wires, one pair of battery power supply wires and one pair of serial communication wires. So the whole encoder cable that used to connect all six encoders consists of six lines of such bundled wires (Total 18 pairs). The right side shows the structure of encoder cables used by the proposed new system. By communalizing the communication line and power supply line between controller and encoder, the power supply lines which are connected to the encoder are reduced from threes pairs to two pairs. Additionally, because all six encoders are connected by Bus connection method, the whole encoder cable consists of only two pairs of wires.

On the industrial robot, the control period shifts from msec to μ sec, so control signals are required to be sent at high data rate to control multi-axial robot. For this reason, considering the safety of robot control, the data rate is set to 81Mbps. On this system, 48 data sub-carriers for data transmission and 4 pilot sub-carriers for detecting frequency offset are used, OFDM symbols are modulated by 64 point Fourier fast transmission (FFT). Then, the robot power supply line channel is showed Fig4. The robot power supply line channel uses band width of 30 MHz, each sub-carrier frequency space gets into 0.469 MHz. Depending on this space, FFT period gets into 2.13 μ sec as the reciprocal of this space.

**Fig. 1.** The basic robot control system

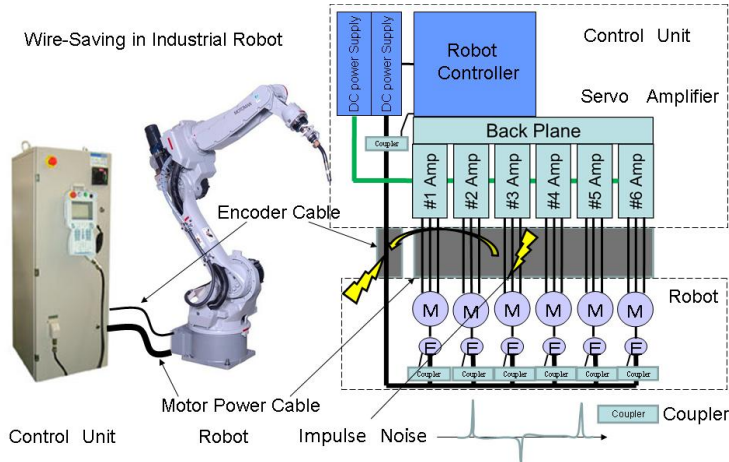


Fig. 2. Applying by the proposed power supply overlaid communication system for industrial machine control

As shown in Figure 2, the impulse noise is generated from the servo amplifier, however BER is significantly reduced. Fig.5 shows a general circuit configuration of the actuator used for industrial robots. This circuit is called a voltage output inverter. By comparing the voltage command value (triangle wave) and carrier frequency, this circuit generates PWM signal and carries out switching operation according to the PWM signals[11]. With the switching operation, voltage which is proportional to the voltage command is applied to the motor. Fig.6 shows the PWM signal which is generated by comparing the voltage command value (triangle wave) and carrier frequency. This signal is the gate signal of switching devices($a^+, a^-, b^+, b^-, c^+, c^-$) showed in Fig.5. These switching devices turn on and off according to the PWM signal and drive the induction motor. Fig.7 shows

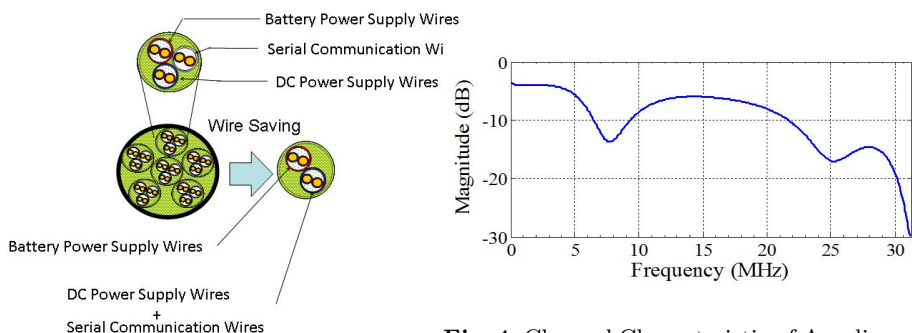


Fig. 4. Channel Characteristic of Amplitude

Fig. 3. Detail of the wiring-saving

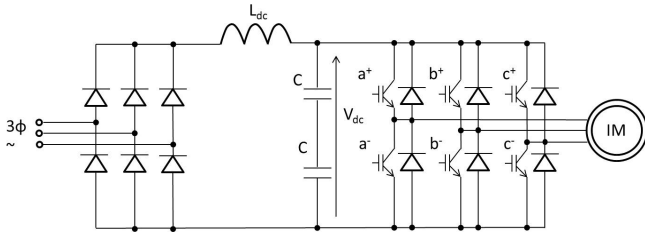


Fig. 5. Main power converter structure of widely utilized diode-rectifier front-end-type PWM-VSI drive

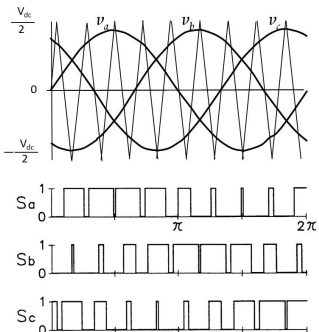


Fig. 6. Relation of Voltage command and PWM

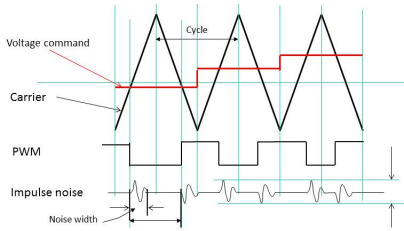


Fig. 7. Voltage Command, Carrier and PWM Signals

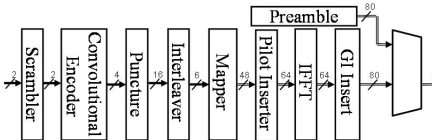
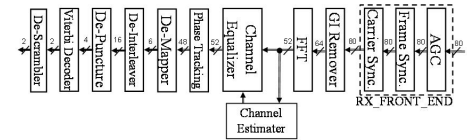
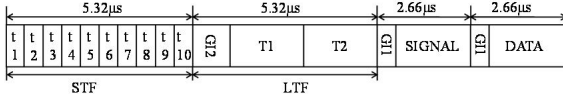
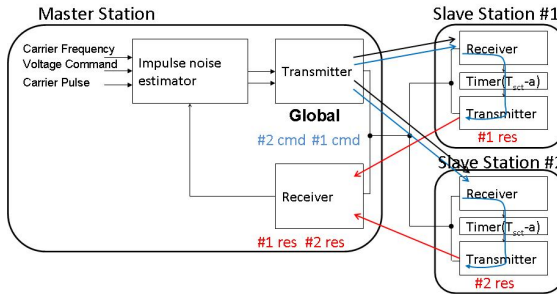
the impulse noise which is induced by encoder communication cable laid with the motor power supply cable. Impulse noise generates by the rising and falling edges of the PWM signal.

3 System Architecture

Fig.8, 9 and 10 shows the proposed system of transmitter receiver and packet format. The proposed system is developed with a based on IEEE802.11a circuit. The bandwidth of the proposed system is extended from 20MHz to 30MHz. The proposed system is improved data rate from 54Mbps to 81Mbps.

3.1 Impulse Noise Estimator

Generation timing of impulse noise can be expected if you know the timing of the triangular wave and frequency(f) of the triangular wave voltage command(η)

**Fig. 8.** Proposed Transmitter**Fig. 9.** Proposed Receiver**Fig. 10.** Packet Format**Fig. 11.** Diagram of a power supply overlaid communication system

value. Equation.1 indicates the non-impulse noise time interval, T_{sca} : Safety Communication Area.

$$T_{sca} = (1 - \eta)/2 \times 1/f_c - \pi t_r \quad (1)$$

This equation can be derived useful starting time for communication from the peak and valley of the triangle wave. Equation.2 estimates useful starting time for communication by the peak and valley of the triangle wave, T_{sct} : Start Communication Timing.

$$T_{sct} = 1/(2 \times f_c) - (1 - \eta)/2 \times 1/2f_c + \pi t_r \quad (2)$$

T_{sca} is required 24.03μsec according to the Fig.10. Voltage command (η) derive ≤ 0.38 at 10kHz and ≤ 0.75 at 4kHz. Fig.11 shows a configuration diagram of a power supply overlaid communication system proposed. Master station is located on the controller, the slave station is placed in the actuator unit. Slave station 1 is in the actuator 1. Slave station 2 is in the actuator 2. Fig.12 shows the communication protocol of the proposed system. The first signal indicates multicast

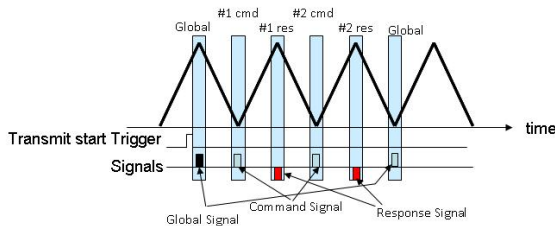


Fig. 12. The proposed system of protocol

frame. The second signal(#1 cmd) indicates the command to the slave station 1. The third signal(#2 cmd) indicates the command to the slave station 2. The signal(#1 res) indicates response to the master station from the slave station 1. The signal(#2 res) indicates response to the master station from the slave station 2. These behaviors are described in the following issues. Master station estimates the communication time(T_{sct}) from the voltage command and carrier frequency, whenever the carrier pulse is input to the impulse noise estimator. T_{sct} time after starting from the peak or valley of career, master station transmits a signal to the global time zone that is not the generation of impulse noise. When receiving the global signal, the slave station sets the T_{sct} the internal timer. Then, the master station receives a time period that does not occur in the impulse noise from the impulse noise estimator, it transmits a command(#1 cmd) to the slave station 1. The slave station 1 received command signals, and then it starts the internal timer. The time is reached not generated the impulse noise, the slave station 1 responds signals(#1 res) to the master station. Even if other slave station is there, data communication of this command response is carried out. The proposed system performs cyclic communication in this step. In this paper, a method of activation timing of this cyclic communication is proposed.

4 Evaluation System

Fig.13 shows an outline of the developed transmission line emulator system. The developed system consists of a transmitter unit and receiver unit and channel simulator unit and two selector units. The transmitter unit and the channel simulator unit are connected by the left side selector, and that the channel simulator unit and the receiver unit are connected by the right side selector. The transmitter unit and receiver unit functions are achieved by MATLAB®/Simulink®, or Verilog HDL simulator, or the circuit board. Fig.14 shows construction of channel simulator unit in Fig.13. Channel simulator unit is composed of back-end unit and transmission line unit and front-end unit. Back-end unit convert the real signal component from the complex signal that is output from the transmission unit. Transmission line unit achieves the characteristics of any channel, and add the Gaussian noise according to SNR and impulse noise. Fig.15 shows the measured values used for impulse noise model. Front-end unit convert the

complex signal from the real signal component. By switching the selector, the combination of transmit and receive units are determined. Channel simulator unit construct of a complex signal to real component signal processing back-end unit that signal is output from the transmission unit.

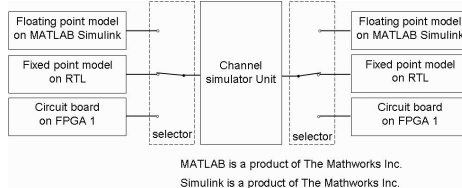


Fig. 13. Transmission Line Emulator System

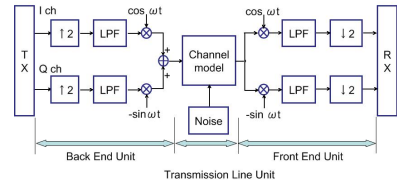


Fig. 14. Channel Simulator Unit

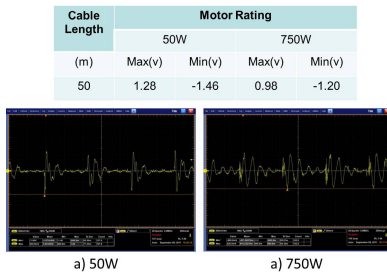


Fig. 15. Impulse noise

Fig.16 shows the construction of the transmission line emulator system using the circuit board. The system consists of two circuit boards, instrument, and PC. The circuit boards 1 and 2 mount FPGA and CPU chips. Transmitter and receiver of the proposed communication system have implemented in the circuit boards 1 and 2, respectively. The CPU mounted on the circuit boards 1 and 2 takes control of the FPGA. The instrument (TLA7012) consists of the logic analyzer unit (TLA7NA3) and data generator unit (TLA7PG2). The logic analyzer unit is sampling the signal output from the FPGA of the circuit board 1. We treated the signal from the circuit board 1 and inputted the signal into the FPGA of the circuit board 2. The signal processing is applied to the channel characteristics (AWGN, Robot power line) and noise transmission path by the channel simulator unit. This signal processing was simulated using the MATLAB®/Simulink® simulator on the PC in the middle of Fig.16.

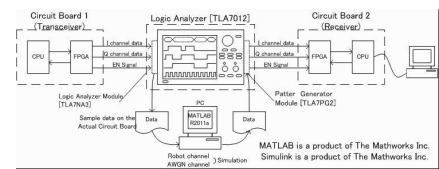


Fig. 16. Transmission Line Emulator System Using FPGA

5 Performance Examination

We verified the real-time and reliability communication performance of the proposed system. The proposed system was verified real-time performance and reliability performance by actual circuit and transmission line emulator System.

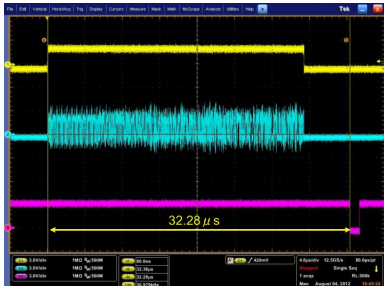


Fig. 17. Real Time Result (Transmit and Receive Time)

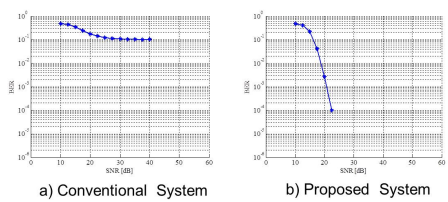
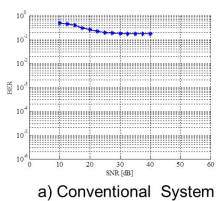
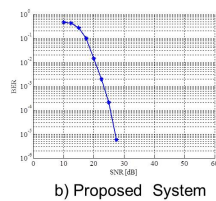


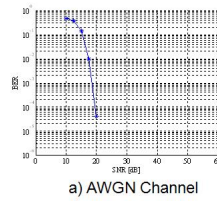
Fig. 18. Simulation Result (AWGN Channel)



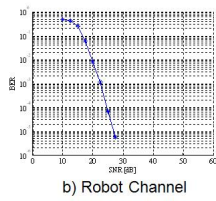
a) Conventional System



b) Proposed System



a) AWGN Channel



b) Robot Channel

Fig. 19. Simulation Result (Robot Power Line Channel)

Fig. 20. Simulation Result (without impulse noise)

Fig.17 shows real-time performance of the proposed system. Ch1 signal indicates the signal of the start of transmission, ch2 is a communication signal, ch3 is a signal indicating that reception has completed. Time to complete the start of transmission received from $32.28 \mu\text{sec}$ is understood.

From Fig.18 to Fig.20 shows the results when the simulation model to a floating point number in the proposed system. Fig.18 shows the characteristics of AWGN channel. Fig.19 shows the characteristics of robot power line channel characteristics. Fig.20 shows the characteristics of AWGN channel and robot power line channel without impulse noise. Three validations carried out a hard decision Viterbi decoding circuit in error correction circuit.

As a result of the verification, It was confirmed that the proposed system is superior performance the conventional systems on BER vs SNR. On the AWGN channel, conventional systems are pulling the floor in the performance of $\text{BER} = 10^{-1}$, at $\text{SNR} = 25\text{dB}$, the proposed system is $\text{BER} = 10^{-5}$ or less. On the robot power line channel, conventional systems are pulling the floor in the performance of $\text{BER} = 2.0 \times 10^{-1}$ at $\text{SNR} = 25\text{dB}$, the proposed system is $\text{BER} = 2.0 \times 10^{-4}$ or less. On the non-impulse noise channel, AWGN showed the performance of $\text{BER} = 4.0 \times 10^{-5}$ at $\text{SNR} = 20\text{dB}$ and the robot power line channel showed the performance of $\text{BER} = 7.0 \times 10^{-5}$ at $\text{SNR} = 25\text{dB}$. It can be seen that conventional system can not communicate in impulse noise environment. However, the proposed system was found to be a communication performance similar to the non-impulse noise conditions. Fig.4 shows amplitude frequency

Table 2. Simulation Parameter

Parameter	Value
Band Width	30[Mbit/s]
Carrier Frequency	15[MHz]
Data Rate	81[Mbit/s]
FFT point	64
Modulation	64-QAM
Coding Rate	3/4
Transmitted bit	10^8 [bit]
Channel	AWGN or Industry Robot Power Supply Line
Noise	AWGN

response of robot channel model. This channel model is identified by measured value of actual robot power supply line reflective characteristic. Simulation parameter is showed in Table 2.

6 Conclusion

We proposed a power supply overlaid communication system for industrial robot control. The system can reduce PWM noise. Then, we reported on the feasibility study of power supply overlaid communication system, using the transmission line emulator system. We verified real-time communication performance and that real-time μ sec order could be confirmed. The proposed system is able to communicate $BER=2.0 \times 10^{-4}$ $SNR=25dB$ on the robot power line channel. In the future, we plan to examine a method to bring maximum voltage command.

References

1. Katayama, M.: Power-Line Communications. Measurement and Control 44(6), 378–383 (2005)
2. Morikura, M.: 802.11 High-Speed Wireless Lan Textbook. Impress (January 2005)
3. Zimmermann, M., Dostert, K.: A multipath model for the powerline channel. IEEE Trans. on Commun. 50(4), 553–559 (2002)
4. Mori, A.: OFDM Signal Transmission Characteristics for Power Line Model Using High-Speed PLC Modem. IEICE Trans. Commun. j-90-B(11), 1179–1186 (2007)
5. Supplement to IEEE Standard for Information technology Telecommunications and information exchange between systems Local and metropolitan area networks Specific requirements. IEEE Std 802.11a-1999 (R2003) (June 2003)
6. Hayasaki, T., Umehara, D., Denno, S., Morikura, M.: A bit-loaded OFDMA for in-home power line communications. In: Proc. IEEE ISPLC 2009, Dresden, Germany, pp. 171–176 (March/April 2009)
7. Yamaguchi, Y., Koga, H., Kurosaki, M., Ochi, H.: Power Supply Overlaid Communication System with OFDM Modulation for Robot Control. In: SISA 2011, Nagasaki, Japan, October 31-November 2 (2011)

8. Koga, H., Kurosaki, M., Ochi, H.: Power Supply Overlaid Real Time Communication System with OFDM for Industrial Robot Control. In: ISCIT 2012, Gold Coast, Australia, vol. 2-5(3), pp. 215–220 (October 2012)
9. Aiichiro, T., Goh, M., Yukio, Y.: A study of the influence of the impulse noise on the OFDM transmission. ITE Technical Report, vol. 25(7), pp. 41–46, BFO2001-26, ROFT2001-26 (January 2001)
10. Tatsuya, H., Masahiro, F., Makoto, I.: Reducing Influence of Impulse Noise on OFDM Signal by Recovering Time Domain Samples. ITE Trans. 60(5), 757–764 (2006)
11. Hava, A.M., Kerkman, R.J., Lipo, T.A.: Carrier Based PWM-VSI Overmodulation Strategies: Analysis, Comparison, and Design. IEEE Transactions on Power Electronics 13, 674–689 (1998)

Measuring and Control Central Based on Digital Signal Controller

Josef Oplustil, Roman Sprlak, Daniel Kalvar, Miroslav Uchoc, Petr Palacky,
and Vaclav Sladecek

VSB – Technical University of Ostrava, Faculty of Electrical Engineering and
Computer Science, Department of Electronics, Ostrava, Czech Republic
Josef.oplustil@vsb.cz

Abstract. The article is dealing with construction of the measuring and control central for electric accumulation systems. The structure and the purpose of all convertors are introduced here together with their integration in the accumulation system. Next there are introduced the functions and abilities of this measuring and control central which is based on digital signal controller TMS32 0F28335.

Keywords: Measuring Central, TMS320F28335, Texas Instruments, Digital Signal Controller.

1 Introduction

Because there are bigger requirements for utilization of renewable energy sources we need to handle with this type of energy. Usually, when we have plenty of this energy we have no use for it and when we want to use it, it is not available. Therefore, we need to store this energy and use it when we need. There are several ways how to store the electric energy. Every technique is composed from transformation of electricity into another type of energy when we need to store it, and from opposite transformation when we want to use it. There are three types of energy transformation like an example. Those are: accumulators, flywheels and hydrogen. Flywheels use transformation from electricity to motion energy. It is quite simple but we can store only low amount of energy for a short time. Storing the energy in hydrogen is very modern, but it is too complex and it has low efficiency. The simplest way is to store the electric energy in accumulator. It is quite simple, cheap and the amount of the energy is restricted only by quantity of the accumulators [5].

2 Concept of the Accumulating Unit

Our concept uses transformation of the electric energy, which is produced from any energy source, to alternating voltage 3x400V, 50Hz. This voltage is connected to

central alternating bus. As the energy sources we can use solar cells, AC generators, DC generators, hydrogen cells and other sources and this energy can be transformed by conventional convertors to AC voltage. The central AC bus can be connected directly to the grid and we can provide the electricity to the customers or we can take the electricity from this bus and store it in accumulators of our accumulation system.

Figure 1 shows the connection of the photo-voltaic source with our accumulation system. The DC energy is transformed by conventional convertor (convertor 1) to AC energy and it is connected to the central bus.

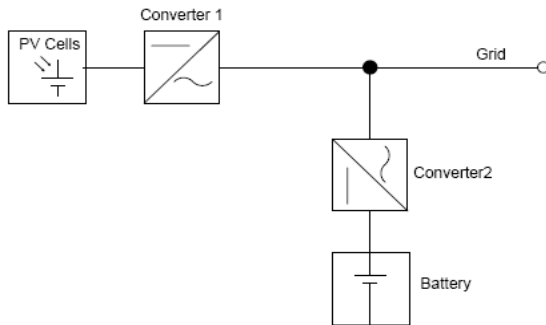


Fig. 1. Accumulation system with PV power source

When there is shortage of energy in the grid we can provide whole produced energy to the customers. But when there is surplus of the energy in the grid, we can transform our energy to DC by convertor 2 and we can store it in the accumulators [4].

If we want to store only our energy, it is important to measure the energy produced by PV source. The other possibility is that we have no energy produced from our source and at the same time, there is a surplus of the energy in the grid. So we can accumulate some energy from the grid and when there is shortage of the energy in the grid, we can provide our energy from accumulators [6].

This system does not use classical concept of the convertors but it use interconnection of the parallel active power filter and serial active power filter. These active filters use lead-acid accumulators like power banks. Primary function of these power filters isn't improvement of voltage waveforms, but it is to act like convertors and to provide energy to the grid. This energy can flow both ways, from grid to battery and from battery to grid. Currently, the whole system is composed from two of these function blocks. Every function block has serial active power filter (SAPF), parallel active power filter (PAPF) and accumulator [1].

When there is no utilization for energy from PV cells, we can accumulate whole amount of this energy and in addition, we can take some amount of energy from the grid and accumulate it as well. When we need to provide some energy, we can do it

from accumulators. The biggest advantage of providing energy from batteries is that the startup time is minimal and we can cover also the short lacks in power grid. The advantage of combination the serial and parallel convertor is that we can assign tasks between both convertors and we can ensure best quality and efficiency.

On Figure 2, you can see block diagram of our accumulating system. PAPF is converter which is based on parallel active power filter [2]. Its output is connected through coupling transformer TRxP. SAPF is convertor which works like serial active power filter and it is connected to central bus through coupling transformer TRxS. In this diagram, there are not all of components of the system. Because all of devices in this system work with pulse width modulation (PWM) there are more additional filters to deal with switching frequency. Both, parallel and serial convertor, are made like stand-alone devices. In fact, they are both the same device. The only difference is in software and in their connection to the system.

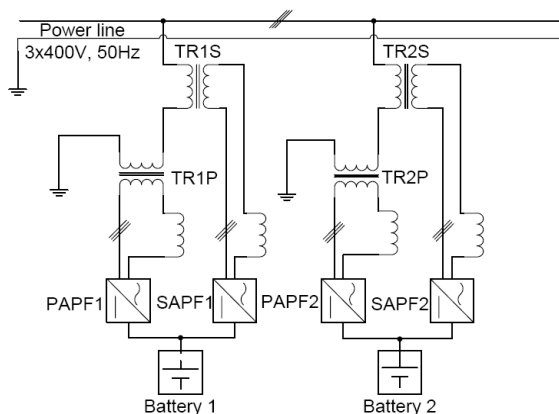


Fig. 2. Concept of the accumulating system

Before construction of these convertors, there was made their design. We designed electric parts of the convertors, i.e. voltage, current and power specifications for all components and capacity of the DC link.

Next we made 3D models of all electrical and mechanical components of the convertor. From these components we assembled the whole 3D model of the convertor. This method is more complicated but it has benefits in easy creation of the documentation and data for manufacturing. In Figure 3, there is 3D model of the convertor which was made in Autodesk Inventor cad software. In this figure you can see front and side views to the convertor and view to the inside of the convertor. From this model we can obtain information about size of all components like metal sheets, screws and others and information about position of the transistors, capacitors and other electric components.

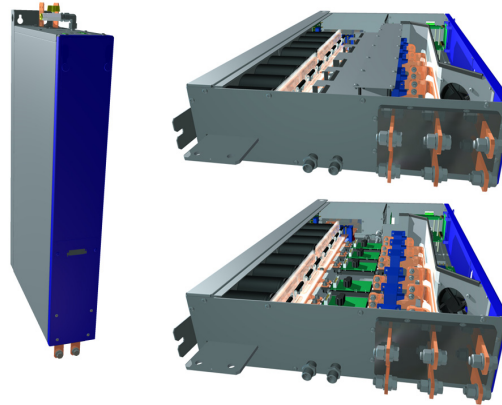


Fig. 3. 3D model of the converter

3 Simulation of the Convertor

To ensure that all components work properly we performed some simulations in Matlab Simulink software. Like an example, there is simulation of the serial active power filter, see figure 4 [9].

Because this type of convertor will be mostly working like power conditioner, we performed our simulations exactly for this case. AC voltage is connected at the input of this convertor. This voltage has ideal harmonic shape. In parallel to this AC voltage is connected block Fault. This block can simulate faults in the three phase systems.

Vector control strategy [7], [8] was used for simulation of this convertor. We performed three types of faults in the simulation:

- Voltage sag
- Voltage swell
- Harmonic distortion

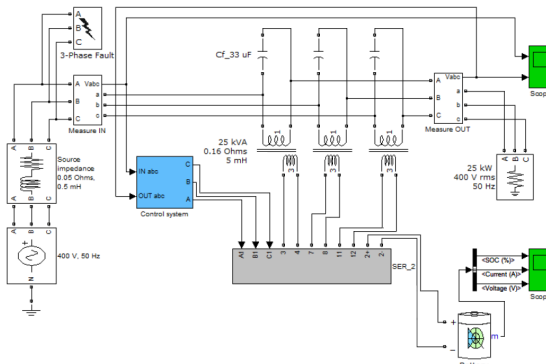


Fig. 4. Simulation diagram of the converter

Simulation result from the third case is shown in next figure. We added five harmonic components to the input harmonic voltage. These components were:

- 3rd harmonic component (12%)
- 5th harmonic component (8%)
- 7th harmonic component (5%)
- 11th harmonic component (2%)
- 13th harmonic component (1%)

Total harmonic distortion from FFT analysis was 15.5%.

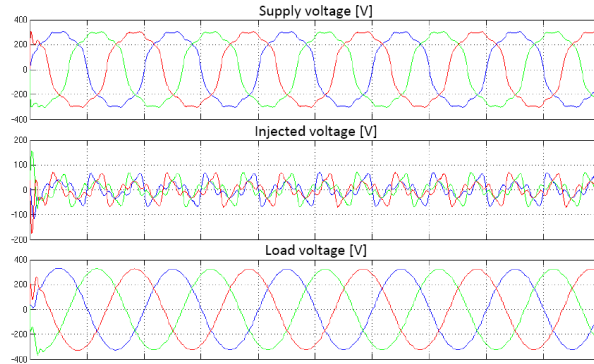


Fig. 5. Simulation results

This input voltage waveform is in upper part of the Figure 5. In middle of Figure 5, you can see reaction of the convertor. It is trying to preserve pure harmonic waveform and it need to add some voltage to the input voltage waveform. This voltage is in Figure 5 called injected voltage. At the waveform in bottom of this figure, you can see voltage waveform at the output of the convertor. Total harmonic distortion of this waveform was 1.7%.

This simulation was performed because we supposed that the parallel converter will work like the invertor with the simplest possible control algorithm and serial convertor will be improving the output waveform from the parallel one. To control these tasks we need some device which can gather information from this system and which will decide how the convertors will work.

Beside this simulation we performed other different simulations like simulation for charging and discharging of accumulators, simulation of parallel convertor and simulation of thermal processes in convertors. The results from these simulations are presented in other articles [3].

4 Measuring and Control Central

Measuring and control central is a device which is collecting data from the system and from this data it is computing quantity and direction of produced or consumed energy. Next it performs monitoring and data backup for later application and analysis

of collected data. The most significant task is to perform real-time analyses of measured data and to control all convertors in system on the bases of these analyses. Block diagram of this measuring and control central is shown in figure 6.

This measuring and control central consists from several basic parts. First of these parts is processor module. This module is based on digital signal controller TMS320F28335. It is digital signal controller from Texas Instruments and it works with floating-point data representation. This processor runs at 150MHz and it has 68KB data memory which is externally extended by 512KB. This processor is controlling whole system of measuring and control central and it performs mathematical operations with data. Also it ensures communication with convertors and with remote terminal.

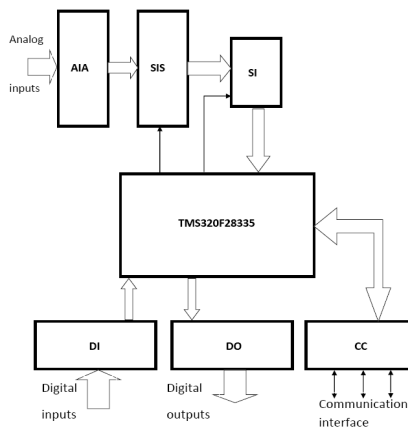


Fig. 6. Block diagram of the measuring central

Definitions of acronyms:

AIA – Analog Inputs Adjusting

SIS – Sampling of the Input Signals

SI – Switching of the Inputs

DI – Digital Inputs

DO – Digital Outputs

CC – Communication Circuits

Next parts of this central are circuits for analog input signal adjustment and measuring. These circuits serve to extension of input channels from 16 to 32 and for adaptation of input ranges. Extension of input channels is performed by multiplexors and sample/hold circuits. This structure makes possible to sample all inputs simultaneously.

In addition, the measuring central has 12 digital general purpose inputs and 12 digital outputs. Inputs can be used for signalization from contactors and output can be used to control them. These digital inputs and outputs are adjustable. Currently, we are using one digital input for external synchronization for measuring.

Measuring and control central is equipped by RS422 communication interface. This interface serves for communication between this central and convertors. The measuring central sends required values of voltage, current and shape of the output waveforms by this interface. RS422 can be used to communication between convertors as well.

Next interface of measuring central is universal serial bus (USB). This interface can serve to controlling this central and to reading values and setting the parameters of this central. Nevertheless, this interface is meant to be for debugging only. USB interface is composed from standard SCI interface and from convertor FT232. For controlling of this measuring central is primary assigned Profibus interface.

The last part of measuring and control central is power source. This power source is placed on one board of the measuring central and it provides supply voltages for all functional blocks. The input voltage is 24V DC.

This power source provide voltage 3.3V, 5V, 15V and -15V. Voltages 3.3V and 5V serve to supply the logical circuits like processor and communication interfaces. Voltage 15V and -15V serve for analog circuits. All of these voltages are made by switched mode power supplies.

For better quality of supply voltage for analog circuits we performed experiment. We did want to find best possible power supply for analog circuits, because the switched supply has high level of noise and linear supply has high power dissipation. So we made our power supply like a combination of these two types. Switched power supply provides 15V and -15V and these voltages are processed by linear stabilizers to 12V and -12V. This solution guarantees low level of noise and low power dissipation. You can see prototype of our measuring central in figure 7. It is made on three circuit boards. Front board is equipped with connectors for analog and digital inputs and outputs and with connectors for communication interfaces and supply voltage.

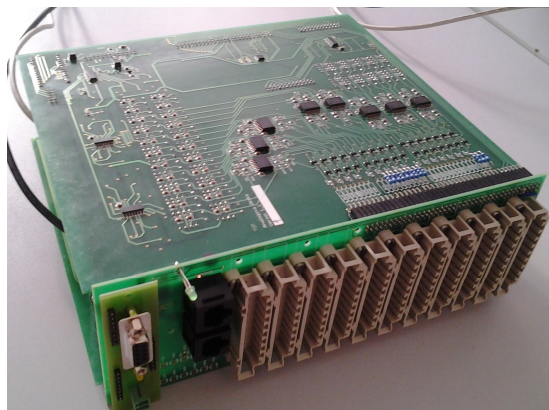


Fig. 7. Measuring central

Voltages and currents are not measured directly by the measuring and control central, but they are measured by current and voltage sensors. The outputs of these sensors are connected into measuring central. Measuring central provides capability for both, voltage and current output from these sensors. Input ranges for voltage and

current are configurable. Currently, the input range for voltage inputs is $\pm 10V$ and input range for current input is $\pm 150mA$. These ranges are adapted to sensors CV3 and ITB300 from LEM.

Voltage sensors measure voltage on batteries and at the output of converters. Current sensors measure current from battery and output currents of the convertors. From measured values, we can compute the magnitude of the energy and we can perform the analysis of input data. Measuring and control central can decide, from these data, how to control the convertors, how to achieve the best possible quality of the output waveforms and how to achieve the best possible efficiency of the convertors and whole system.

5 Conclusion

In this article, we presented the concept of the system for electric power production which cooperates with the accumulation unit. This accumulation system was lately developed on department of electronics VSB-TUO with help of ENET project. The substantial part of the article is oriented to design and to function of measuring and control central because this central will be the most significant part of the whole system. Data measuring and data analyzing can lead to determination of next generation of these systems.

Data measuring is important part how to discover all processes inside the convertors and inside the systems which are using these convertors. Therefore, the next step of the research is to bring the system completely in function and to start to debug the whole system to achieve the best possible results.

This concept is used to control of the collaboration of four convertors which works with two accumulator blocks. Our measuring and control central is compact device which includes all functions in one device. Devices, which are commonly used for this purpose in industry, are based on module conception compared to our device which is “all in one” concept.

Acknowledgments. The research described in this paper was supported by these projects:

- SGS project SP2013/80 – Utilizing of Modern SiC Components for MF – Power Semiconductor Converters.
- ENET CZ.1.05/2.1.00/03.0069 – Energy Units for Utilization of non Traditional Energy Sources.

This research was supervised by prof. Ing. Petr Chlebiš, CSc. and Ing. Petr Vaculík, Ph.D. from Department of Electronics, VSB - TU Ostrava.

References

- [1] Brandstetter, P., Chlebis, P., Simonik, P.: Active Power Filter with Soft Switching. International Review of Electrical Engineering, IREE 5(6), 1827–6660 (2010) ISSN 1827- 6660

- [2] Brandstetter, P., Chlebis, P., Palacky, P., Simonik, P.: Unconventional Soft Switched Parallel Active Power Filter. In: 10th International Scientific Conference Electric Power Engineering, Kouty nad Desnou, Czech Republic, pp. 347–351 (2009) ISBN 978-80-248-1947-1
- [3] Vaculik, P., Havel, A., Tvrdon, M., Hromjak, M.: The Design and Construction of a Reversible Voltage Inverter Prototype. In: 13th International Scientific Conference Electric Power Engineering 2012, Brno, Czech Republic, May 23-25, pp. 1059–1062 (2012) ISBN 978-80-214-4514-7
- [4] Tan, N.M.L., Abe, T., Akagi, H.: Design and Performance of a Bidirectional Isolated DC-DC Converter for a Battery Energy Storage System. IEEE Transactions on Power Electronics 27(3), 1237–1248 (2012)
- [5] Naish, C., McCubbin, I., Edberg, O., Harfoot, M.: Outlook of Energy Storage Technologies. European Parliament Study (2007)
- [6] Ribeiro, P.F., Johnson, B.K., Crow, M.L., Arsoy, A., Liu, Y.: Energy Storage Systems for Advanced Power Applications. Proceedings of IEEE 89(12), 1744–1756 (2001)
- [7] Zhan, C., Ramachandaramurthy, V.K., Arulampalam, A., Fitzer, C., Kromlidis, S.: Dynamic Voltage Restorer Based on Voltage-Space-Vector PWM Control. IEEE Actions on Industry Applications 37(6), 1855–1863 (2001)
- [8] Meyer, C., Doncker, R.W., Li, Y.W., Blaabjerg, F.: Optimized Control Strategy for a Medium-Voltage DVR. IEEE Transactions on Power Electronics 23(6), 2746–2754 (2008)
- [9] The MathWorks, Inc.: SimPowerSystems User's Guide. USA (September 2011)

Autocorrelation Properties of Walsh Function for Logic Synthesis FPGA

Nguyen Huu Khanh Nhan

The Department of Electrical - Electronic, Ton Duc Thang University,
Ho Chi Minh City, Vietnam
khanhnhan@tdt.edu.vn

Abstract. The objective of multi-level logic synthesis of FPGA is to find the “best” multi-level structure, where “best” in this case means an equivalent presentation that is optimal with respect to various parameters such as size, speed or power consumption. Four basic operations are used in order to reach this goal: decomposition, extraction, covering and substitution. In this paper we propose a novel application of Walsh spectral transformation to the evaluation of Boolean function autocorrelation. The methods, operations in the transform domain has appeared to be more advantageous than traditional approaches, using operations in the Boolean domain, concerning both memory occupation and execution time on some classes of functions.

Keywords: logic synthesis, Walsh spectral, Boolean function, decomposition, autocorrelation function.

1 Introduction

Field programmable gate arrays (FPGA) technology is static memory (SRAM), is programmed for solving a wide range of tasks. In this case, the contents of SRAM can be changed, resulting in a FPGA can be reprogrammed by the user [1]. Note that the basic logic element of FPGA is the 2^k bit memory cell, which can be realized by any k -input Boolean function (BF) by loading in the cell truth table function. In [2] proposed a classification of the FPGA, they are divided into two major groups - the architecture of Table Look-Up (TLU) or LUT - Look-Up Table) and the architecture Multiplexer based (MB).

Thus, the analysis of architecture and technology of FPGA allows us to conclude that, in addition to common for the entire microelectronics industry trends to increase the degree of integration, improving overall performance, reduce costs, etc., the new trend is the increased ease of design and debug circuits. However, with increasing complexity of both the crystals and projects to the fore front more and more are questions of design and development of algorithms for automatic logic synthesis. It follows that the main problem of logic synthesis in the basis of FPGA is minimize the number of used logic blocks and reducing the complexity of the trace.

When logic synthesis FPGA often use the technique of design separation into two distinct phases [3], the technology-independent and technology-dependent (technology mapping). We describe in more detail the mathematical problems that arise when consider the basis of FPGA as well as possible and suggest solutions. Based on an analysis of FPGA architecture, we use methods based on five basic mathematical problems [4]: Decomposition, covering (factoring), extraction and substitution. These studies showed promise using spectral analysis of BF for solving problems of use FPGA. In this case, the gain occurs mainly in the processing of large amounts of input data.

2 Spectral and Correlation Analysis of Boolean Functions

We use the definition of BF in the monographs [5], where they are treated as multi-dimensional functions with m -inputs and k -outputs, and carry out mapping of the form $f : \{0,1\}^m \rightarrow \{0,1\}^k$. Set of outputs is denoted as BF f_{k-1}, \dots, f_0 , and used the decimal indices $x = (X_{m-1}, \dots, X_0) \in \{0,1\}^m$ are calculated the formula:

$$x = \sum_{i=0}^{m-1} x_i 2^i \quad (1)$$

$$f = (f_{k-1}, \dots, f_0) \in \{0,1\}^k, f = \sum_{i=0}^{k-1} f_i 2^i \quad (2)$$

where x and f can be interpreted as the coordinates of the binary vectors to decimal numbers. Note that the expressions (1) and (2) describe the BF as a piecewise constant function $F(x)$ of real argument on the half-open interval $[0, 2^m]$. With this notation system of BF can be represented as a lattice of $y = f(x)$, defined at the points $0, 1, \dots, 2^m - 1$ interval $[0, 2^m]$. Extend the function $y = f(x)$ to piecewise constant function $F(x)$ as follows:

$$F(x) = f(\delta) \text{ variations } x \in [\delta, \delta + 1] \quad (3)$$

We say that a piecewise constant function $F(x)$ represents the original system of BF, if it satisfies the condition (3) and $f(x)$ is constructed by formulas (1) and (2). Thus, the foundation can be described as a vector $F = [f(0), f(1), \dots, f(2^m - 1)]^T$, where $X = (x_{m-1}, \dots, x_0)$, $(0 < x < 2^m - 1)$ - a set of input vectors, and $f(x)$ is an integer value, where $F_i = [f_i(0), f_i(1), \dots, f_i(2^m - 1)]^T$, and $f_i(x)$, $0 < i < k - 1$, a binary value.

It is known that between BF and Walsh functions, there is a relationship, which explains the possibility of effective use of spectral analysis in the basis of Walsh functions to analyze the fleet. In order to determine this relationship, we consider details of the Walsh function. These functions are piecewise constant and are given on the half-open interval $[0, 2^m]$ expression:

$$W_{\omega}(x) = (-1)^{\sum_{i=0}^{\omega-1} \omega_{(m-1-i)} x_i} \quad (4)$$

where $0 < \omega < 2^m - 1$, $m \in N$, and ω_i and x_i are determined from the binary representations ω and x .

Autocorrelation function of BF $f(x_0, x_1, \dots, x_{m-1})$ is determined on the basis of relations:

$$B_2^{(f:f)}(\tau) = \sum_{x=0}^{2^m-1} f(x)f(x \oplus \tau), \quad (5)$$

where $\tau \in \{0, 1, \dots, 2^m - 1\}$. As seen from (5), the original function is related to the autocorrelation function of convolution transforms. Cross-correlation or simply the correlation function of two BF $f_1(x)$ and $f_2(x)$ is the function:

$$B_2^{(f_1:f_2)}(\tau) = \sum_{x=0}^{2^m-1} f_1(x)f_2(x \oplus \tau), \quad (6)$$

where $\tau \in \{0, 1, \dots, 2^m - 1\}$. Establish a connection between the correlation functions and features considered earlier Walsh. Also known as Wiener-Khinchin theorem [6].

$$B_{2,2}^{(f_1,f_2)} = 2^{2m} W(W(f_1)W(f_2)). \quad (7)$$

Properties of the correlation characteristics of BF determined by the properties of convolution transforms of the original features. In particular, the form of these transformations implies the invariance of the correlation characteristics to shift the argument of the original. Converse is also true that the autocorrelation function of the original function can be restored up to a shift of the argument.

The complexity of BF is usually understood as the minimum number of two-input elements necessary for the construction of the scheme; it realizes that the complexity criteria are now known a lot. The simplest and most natural criterion of BF $f(x_0, x_1, \dots, x_{m-1})$, $x_i \in \{0, 1\}$, $i = 1, \dots, n-1$ is the number $\mu_0(f)$, $(\mu_0(f) \leq m)$, which equals the number of arguments to this function, from which it depends, it is assumed that the function essentially depends on the arguments x_i , if there are $\alpha, \beta \in \{0, 1\}$, such that for any set of arguments $(x_0, \dots, x_{i-1}, x_{i+1}, \dots, x_{m-1})$ value with $f(x_0, \dots, x_{i-1}, \alpha, x_{i+1}, \dots, x_{m-1}) \neq f(x_0, \dots, x_{i-1}, \beta, x_{i+1}, \dots, x_{m-1})$ [7, 8]. This criterion is called the μ_0 , we note that this assessment is quite easy to get, but it is μ_0 criterion of BF very weakly associated with specific properties of the original BF.

Frequently uses criterion of BF μ_1 . To determine this, we use the notion of Hamming distance in the discrete Euclidean space, i.e. If $x_1 = (x_1^0, \dots, x_1^{m-1})$ and $x_2 = (x_2^0, \dots, x_2^{m-1})$; $(x_1^{(i)}, x_2^{(i)} \in \{0, 1\})$ then the Hamming distance between x_1 and x_2 will be:

$$d(x_1, x_2) = \sum_{i=0}^{m-1} |x_1^{(i)} - x_2^{(i)}|. \quad (8)$$

Then the complexity of BF $\mu_1(f)$, we mean the number of vectors pairs $\{x_1, x_2\}$ with Hamming distance between them $d(x_1, x_2) = 1$ such that $f(x_1) \neq f(x_2)$. Similarly, we introduce criteria of BF μ_r , where $r = d(x_1, x_2)$. Strength criteria with increasing r , but also increases the complexity of their calculation are determined by $C_m \cdot r \cdot 2^m$. Note that μ -criteria of BF may be related to their correlation functions. Indeed, since the number of true minterm at a distance, for example, 1 corresponds to the values of the autocorrelation function of BF in points $\tau = 1, 2, 4, \dots, 2^{m-1}$, then the function.

$$\psi(f) = \sum_{\tau=1,2,4,\dots,2^{m-1}} B^{(f,f)}(\tau), \quad (9)$$

can be regarded as a measure of simplicity of this function, and, as shown in [6] $\mu(f) = km2^{m-1} - \psi(f)$. Consider a set of m linear transformations of the arguments of the original BF $f(z)$. BF obtained to be denoted as $f_i(z)$, and their autocorrelation functions - as $B_i(\tau)$; moreover,

$$B(\tau) = \sum_{i=0}^{m-1} B_i(\tau). \quad (10)$$

Denote

$$B(T) = \sum_{s=0}^{m-1} B \left(\sum_q \tau_{q,s} 2^{m-1-q} \right) \quad (11)$$

where $T = (\tau_{qs})$, $\tau \in \{0,1\}$, and $(q, s = 0, 1, \dots, m-1)$. It is obvious that the function $B(T)$ holds Karpovsky theorem [6], whose formulation is given below.

Let $\max_{|T| \neq 0} B(T) = B(T_\eta)$ then $\sigma_\eta + T_\eta = E_m \pmod{2}$. Here $|T|$ - determinant T , E_m - identity matrix size $m \times m$. The importance of this theorem is due to the fact that its use can introduce the concept of an optimal linear transformation of the arguments given BF σ_η . It consists of the following: conversion σ_η , corresponding theorem Karpovsky, considered the optimal linear transformation of the arguments of BF by the criterion η .

3 Decomposition Problems of Boolean Functions

The theorem Karpovsky [6] allows find the linear transformation σ_η , construct the autocorrelation function $B(t)$ is the original BF and m linearly independent samples of its arguments, such that the sum of $B(t)$ for these samples is maximal. These m samples can be found as follows: if we find s samples ($1 \leq s \leq m$), which is denoted as t_0, t_1, \dots, t_{s-1} , then $(s+1)$ - reading t_s from the condition:

$$B(\tau_s) = \max_{r \in Q_s} B(r), \quad (12)$$

where Q_s - the set of all linear combinations of vectors $\vec{\tau}_0, \vec{\tau}_1, \dots, \vec{\tau}_{s-1}$ and vector (00 ... 0) modulo 2; τ_i - vector of the binary expansion of t_i . We can show that found $\vec{\tau}_0, \vec{\tau}_1, \dots, \vec{\tau}_{s-1}$ thus form the columns of T_η . Then the transformation matrix σ_η , the optimal criterion η , can be determined by T_η . In addition, to find a linear transformation σ_η , the optimal criterion η , can use the following recursive procedure: Let T - matrix of size $m \times m$, such that $T = \tau_0, \tau_1, \dots, \tau_{m-1}$, (τ_i - raw size $m \times 1$), other τ_0 is found from the expression:

1. $B(\tau_0) = \max_{|r| \neq 0} B(r)$
2. Take $L_0 = \{C_0 \tau_0 \mid C_0 \in \{0; 1\}\}$, so $L_0 = \{0; \tau_0\}$. τ_1 is as $B(\tau_1) = \max_{|r| \neq L_0} B(r)$.
3. When $\tau_0, \tau_1, \dots, \tau_{s-2}$ found, take $L_{s-2} = \left\{ \bigoplus_{i=0}^{s-2} C_i \tau_i \right\}, C_i \in \{0; 1\}$, and τ_{s-1} defined as $B(\tau_{s-1}) = \max_{|r| \neq L_{s-2}} B(r)$.
4. Desired transformation $\sigma_\eta = T^{-1}$

Thus, the linear transformation of the BF arguments, the optimal criterion η , is given by:

$$z_i = \bigoplus_{j=0}^{m-1} \sigma_{ij} x_{m-1-j}, \quad 0 \leq i \leq m-1. \quad (13)$$

In this case, the sum modulo 2 can be realized in z_i , require many inputs, how many units contained in the i -th row, that is σ_η , in the worst case complexity of linear part of the BF is proportional to the square of the number of input variables, since the matrix σ_η can contain $m * (m-1)$ of non-zero values. The nonlinear part f_σ of BF can be calculated by multiplying each minterm (x_{m-1}, \dots, x_0) in the matrix σ . The resulting vector will be minterm nonlinear part f_σ of the BF.

To illustrate this fact consider the following example. Assume that the operation described by summing the decimal function $f(x_3, x_2, x_1, x_0) = 2(x_3 + x_1) + x_2 + x_0$. Construct a function $F = [f(0), f(1), \dots, f(2^m-1)]^T = [0, 1, 2, 3, 1, 2, 3, 4, 2, 3, 4, 5, 3, 4, 5, 6]^T$; We note that the i -th column of F - is the decimal representation of the binary digital signal in the output of three bit adder contained in the i -th column of the truth table.

Calculating the autocorrelation function F on Wiener-Khinchin theorem, we have $B = [22, 8, 10, 6, 8, 16, 6, 14, 10, 6, 18, 4, 6, 14, 4, 12]$. Next, we use the linearization procedure of BF, as described above: after deleting the coefficient $B(0)$, we find that the maximum coefficient of the autocorrelation function of BF is 18 with the number of columns (address) $\tau_0 = 10$, which corresponds to the binary representation of 1010. Thus, $L_0 = \{0, 10\}$. Then, strike out from the vector in the term L_0 find that following

its maximum rate is 16 and is located at 5. Thus, $\tau_1 = 5 = 0101$, $L_1 = \{0, 10, 5, 15\}$. Similarly, we find that $\tau_2 = 7$ or 13. Arbitrarily choose a value. Let it be 13 (1101); $L_2 = \{0, 10, 5, 15, 13, 7, 8, 2\}$. Note that the L_2 will remain the same regardless of the choice, because it contains a linear combination of 13 and 7. Similarly, we have $\tau_3 = 1 = 0001$. Then

$$T = \begin{bmatrix} 1 & 0 & 1 & 0 \\ 0 & 1 & 1 & 0 \\ 1 & 0 & 0 & 0 \\ 0 & 1 & 1 & 1 \end{bmatrix} = [\tau_0, \tau_1, \tau_2, \tau_3] \quad \sigma = T^{-1} = \begin{bmatrix} 1 & 0 & 1 & 0 \\ 0 & 1 & 1 & 0 \\ 1 & 0 & 0 & 0 \\ 0 & 1 & 1 & 1 \end{bmatrix}$$

Thus, during decomposition of BF initially implemented block σ , which translates as if the original set of input variables X in a different set of z , conversion between them is as follows: $f_\sigma(z) = f_\sigma(x) = f_\sigma(\sigma x)$, $f_o(\sigma x) = f(T_z)$. As an example, consider $z = (0010) = 2$;

$$T = \begin{bmatrix} 1 & 0 & 1 & 0 \\ 0 & 1 & 1 & 0 \\ 1 & 0 & 0 & 0 \\ 0 & 1 & 1 & 1 \end{bmatrix} \cdot \begin{bmatrix} 0 \\ 0 \\ 1 \\ 0 \end{bmatrix} = \begin{bmatrix} 1 \\ 1 \\ 0 \\ 1 \end{bmatrix}$$

Thus, $f(1101) = f_\sigma(0010) = f_\sigma(2) = 4$, a F_σ described as $[0, 1, 4, 3, 2, 1, 2, 3, 4, 5, 4, 3, 6, 5, 2, 3]^T$.

4 The Covering Problem Using Spectral Representations

Problem solved in this paper, equivalent to the problem of packing a backpack, known from combinatory, and operations research. In the most general form, it is stated as follows: there are n items, the i -th object has a mass m_i , volume v_i , price c_i and usefulness of p_i . You need to dial a set of objects with numbers i_1, \dots, i_k (k -not fixed) so that their total mass and volume did not exceed the specified weight values M and volume V . While the total price $c_{i1} + \dots + c_{ik}$ should aspire to the minimum value, and the total utility $p_{i1} + \dots + p_{ik}$ - to the maximum. Solutions to the problem are possible sets of items, all admissible sets satisfy the above constraints on the mass and volume, but among them there are the best kits that provide the greatest usefulness of the criteria of price and utility. To solve this problem using two objective functions - the total cost and total utility, which is a multi-objective problem.

As applied to cover the formulation of packing a backpack is somewhat simplified in comparison with its classical formulation. The variables of BF can be interpreted as packaged items that have the same volume and price (a lot can be disregarded). The total volume of objects is interpreted as the number of input variables in the CLB, and the utility for compliance with the autocorrelation function of BF. The steps of the algorithm for solving the covering problem is as follows:

1. Calculated autocorrelation coefficient of BF $B(\tau_0) = \max_{|\tau| \neq 0} B(\tau)$ which is interpreted as the utility function.
2. Determined $L_0 = \{C_0 \tau_0 \mid C_0 \in \{0;1\}\}$, i.e. $L_0 = \{0; \tau_0\}$, where τ is a $B(\tau_1) = \max_{|\tau| \neq L_0} B(\tau)$.
3. Determined $\|\tau\| = x_{i1}, \dots, x_{in}$.
4. Verified that the inequality $\sum_{j=1}^n x_{ij} \leq M$.
5. After determining the $\tau_0, \tau_1, \dots, \tau_{s-2}$, computed $L_{s-2} = \left\{ \bigoplus_{i=0}^{s-2} C_i \tau_i \right\}$ $C \in (0,1)$ and τ_{s-1} is defined as $B(\tau_1) = \max_{|\tau| \neq L_{s-2}} B(\tau)$;

In the above procedures sequence $\|\tau\|$ - capacity expansion, τ - binary address, M - number of inputs of CLB. As an example, consider the case $M = 2$. Assume that the operation described by summing the decimal function $f(x_3, x_2, x_1, x_0) = 2(x_3 + x_1) + x_2 + x_0$. Construct a function $F = [f(0), f(1), \dots, f(2^m - 1)]^T$, i.e. $F = [0, 1, 2, 3, 1, 2, 3, 4, 2, 3, 4, 5, 3, 4, 5, 6]^T$, Where the i -th column of F - decimal output of three bit adder binary in the i -th column of the truth table. We calculate the autocorrelation function of F ; in accordance to the Wiener-Khinchin theorem, we have $B = [22, 8, 10, 6, 8, 16, 6, 14, 10, 6, 18, 4, 6, 14, 4, 12]$.

After deleting the coefficient $B(0)$, we find that the maximum is 18 and it is in column number (address) 1010 (binary). Weight variables used does not exceed two, which should be in agreement to limit the number of input variables in the specified condition.

5 Problems of Extraction and Substitution

Based on the autocorrelation function of a Boolean function (BF) considerations, the authors propose an algorithm for solving the problem of extraction, described below. Initially formed by the coefficients of the autocorrelation function of BF. Then take into account factors "first tier", ie depending on one variable, and among them is sought with a minimum rate. If you have coefficients with the same value, then made advanced search of the coefficients of the relevant variables at the next tier. Depending on the results of this search and select and the minimum ratio. After finding the minimum rate and to determine the original function arguments, on which it depends, there is a transition to the coefficients of the "second tier", that is dependent on two variables. In this case the coefficients in the formation of which was attended by the same arguments as in the formation of a minimum ratio of the first tier, we seek the minimum ratio. Then jumps to the next tier, etc... After completing the loop through all tiers of the above algorithm is repeated for the other variables. Thus, the proposed algorithm for solving the division consists of the following:

1. Verified by the fulfillment of conditions $B(\tau_0) = \max_{|\tau|=0} B(\tau)$ and $\|\tau\| = 1$;
2. Determined $\|\tau\| = x_{i_1}, \dots, x_m$;
3. Verified that the inequality $\sum_{j=1}^n x_{ij} \leq M$ and $\tau \leq n$;
4. Determined $B(\tau_i) = \min_{|\tau| \leq i} B(\tau)$;
5. Go to step 1.

In the above procedures sequence $\|\tau\|$ - capacity expansion, τ - binary address, M - number of inputs of CLB. We describe an algorithm for extraction example of the following functions: $f(x_3, x_2, x_1, x_0) = (x_0 \oplus x_1) \& (x_2 \oplus x_3)$. Define $F = [0, 0, 0, 0, 0, 1, 1, 2, 0, 1, 1, 2, 0, 2, 2, 4]^T$, that is $B = [36, 24, 24, 16, 24, 12, 12, 8, 24, 12, 12, 8, 16, 8, 8, 4]$. From the analysis in that all the functions of the first tier of the same, ie value of the autocorrelation function of BF in these points is 24. By viewing the advanced find out that the function is symmetrical. Therefore, as the first variable we take x_0 , having minimum values of the autocorrelation of the variables x_3 and x_2 . This means that the separation (cutting) of the original BF should be performed by separating the variable x_0 from x_3 and x_2 . After a similar operation for the variable x_1 , we obtain a similar result: x_1 requires separation of x_3 and x_2 . Given the fact that the restriction on the number of variables is two, we find that this feature should be implemented by cutting into two parts - x_3 and x_2 , as well as x_0 and x_1 .

Another task logic synthesis FPGA is the substitution (merge) - is proposed to solve by analyzing the autocorrelation function of the table corresponding BF. In this case there are two possible levels of addressing the merge. At a higher level problem is solved not only the merge of the original BF, but also because of previously conducted its decomposition. The task becomes much more complicated because of the substantial increase in the number of searched options.

6 Simulation Results

Software program will be implementation algorithms for spectral processing functions, the problem of the linear functions decomposition, heuristic algorithms for the BF synthesis, based on the spectral paradigm. The author has been designed and implemented a class Vector, organizes an array of disk space and works with them to the cache lines. When programming is given by the size and number clipboards in the data file. By default, the array is created with two buffers, capable of accommodating 512 elements. In the case where the dimension of the array does not exceed 1024, a disk file is created, and work with the data is only in memory. This could makes use this class to represent all the arrays of the program without loss of efficiency. At the entrance of an algorithm to compute the spectrum or the autocorrelation function must have the truth table of the analyzed function 2^n values, where n - number of variables of the function. The output of the algorithm is the spectrum or the autocorrelation function with the same number of values.

Buffer - memory for copying from one file to another; Cache - memory for faster file reading; M - Number of variables in functions.

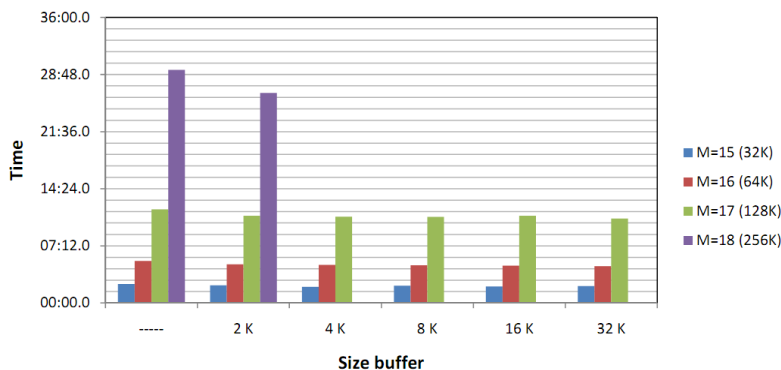


Fig. 1. The dependence on the speed of operation of the buffer size

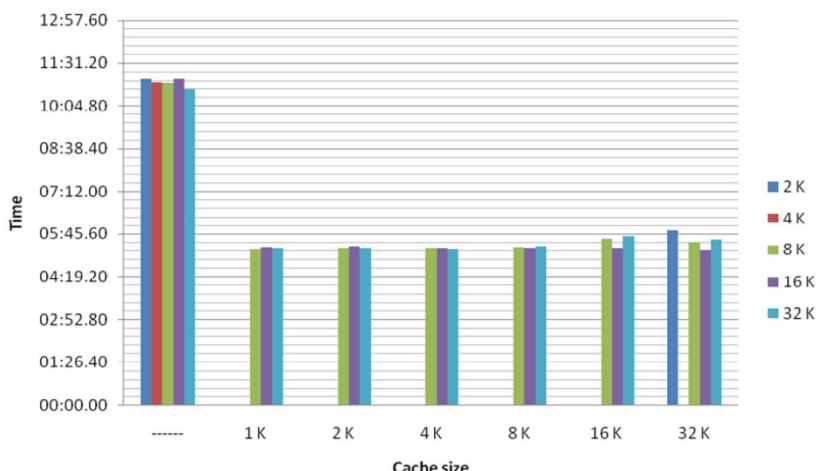


Fig. 2. Dependence on the building range from the size of the buffer and cache, for M = 17

The average time for calculating the spectrum of 5 experiments. The buffer size is 4 K and the cache size is 16K. Calculations show that the average improvement of the program through the use of buffering technology is not less than 8% (on average 10-12%). Due to the caching technology, as shown in Table 1, accelerates work an average of two times. Moreover, the size of the cache speed is virtually independent.

Table 1. Average Execution-time for 5 experiments

Experience	M					
	14	15	16	17	18	19
1	00:25,10	00:55,75	02:12,59	05:17,52	14:31,06	37:17,39
2	00:24,88	00:55,75	02:08,97	05:13,18	15:15,72	
3	00:24,88	00:55,91	02:22,86	05:16,98	14:15,96	
4	00:24,99	00:55,81	02:13,35	05:12,80	13:50,31	
5	00:24,93	00:55,75	02:08,74	05:14,12	14:05,25	
Average	00:24,96	00:55,79	02:13,30	05:14,92	14:23,66	37:17,39
Without the buffer	01:03,94	02:23,91	05:17,36	11:47,00	29:23,00	
Acceleration	2,5621	2,5793	2,3808	2,2450	2,0413	

7 Conclusion

The analyzes of the basic mathematical problems arising in the development of methods for logic synthesis FPGA, showed that the complexity of their solutions can be significantly reduced with the use of fast spectral transforms of Boolean functions (BF), implemented in the base logic cells FPGA. It is possible to formulate the basic problems, which consists in developing methods for logic synthesis FPGA based on new algorithms for analysis and synthesis using the Walsh spectra of BF, with low complexity in comparison with the case using traditional methods.

References

1. Karplus, K.: Using if-then-else DAG's for multi-level minimization. In: Decennial Caltech Conf. on VLSI (May 1989)
2. Murgai, R., Nishizaki, Y., Shenoy, N., Brayton, R.K., Sangiovanni-Vlncentelli, A.: Logic synthesis algorithms for programmable gate arrays. In: Proc. of the CM/IEEE Design Autom., Orlando, FL, pp. 620–625 (June 1990)
3. Mailhot, F., De Micheli, G.: Algorithms for technology mapping based on binary decision diagrams and on Boolean operations. IEEE Trans. on CAD 12(3), 599–620 (1993)
4. Karp, R.M.: Functional decomposition and switching circuit design. J. SIAM 11(2), 291–335 (1963)
5. Darrlner, J., Joyner, W., Berman, L., Trelyan, L.: Logic Synthesis through local transformation. IBM J. Res. Develop. 25(4), 272–280 (1981)
6. Karpovsky, M.G.: Finite Orthogonal Series in the Design of Digital Devices. Wiley, New York (1976)
7. Keren, O.: Efficient linear decomposition of multi output Boolean functions represented in SOP form. WSEAS Transactions on Circuits and Systems 5(2), 219–226 (2006)
8. Keren, O., Levin, I., Stankovic, R.S.: Linearization of Functions Represented as a Set of Disjoint Cubes at the Autocorrelation Domain. In: Proc. of the 7th International Workshop on Boolean Problems, pp. 137–144 (September 2006)

Application of Street Tracking Algorithm in a Feedback Configuration for an Integrated INS/GPS Navigation System

Nguyen Van Thang¹, Chu Duc Trinh², and Tran Duc Tan²

¹ Broadcasting College 1, Ha Nam, Viet Nam

² VNU University of Engineering and Technology, Hanoi, Vietnam
nguyenvanbathanh@gmail.com, {trinhcd, tantd}@vnu.edu.vn

Abstract. When satellite's signal outage occurs, a single GPS receiver will be unable to provide a reliable solution, and an INS/GPS system would continue to use the raw IMU data to compute a solution. Several complementary methods have been proposed to provide a system with highly accurate position, velocity, and attitude in challenging GPS environments. In our previous study [1], we have proposed new algorithm called Street Tracking Algorithm (STA) to enhance the correctness of the integrated system. However, this algorithm can only improve the accuracy of the position of the vehicle due to its feed-forward configuration. This paper is an extended work of [1] when we proposed a feedback scheme that combines STA with the conventional INS/GPS system. In this novel configuration, both velocity and position parameters are enhanced. The experimental result has showed that when GPS signal is lost, we can control the position error is around 2.5 m, and the velocity error is around 3.2 m/s.

Keywords: Inertial Navigation System (INS), Global Positioning System (GPS), Inertial Measurement Unit (IMU), Street Tracking Algorithm (STA), Kalman.

1 Introduction

Recently, INS/GPS integrated systems have been popularly used in navigation and guidance field. However, selecting low-cost or high-cost INS/GPS integrated systems depends on each specific application. We combine INS with GPS to make use of advantages and limit disadvantages of them. It means that when GPS signal is available, information determined by INS is always combined with one determined by GPS to find out the most precise parameters such as attitude, velocity, position of moving object [2], [3]. In case of unreliable GPS signal or GPS outage, INS will directly provide those parameters. From advantages and disadvantages of INS and GPS lead to novel methods to minimize limitations of each system or integrated system. We can consider some approaches:

The system improves accuracy by implementing a technique known as “Zero Velocity Update” (ZUPT). The ZUPT technique combine with related signal

processing algorithms, typical errors of proposed system are around 2% of distance traveled for short walks. When walking continuously for a few minutes, the error increases gradually beyond 2%. So, the system can utilize in military, security personnel as well as emergency responders [4].

Another method can help a quad-rotor helicopter flying autonomously during GPS outage is to use a motion planning algorithm [5]. This novel algorithm permits the vehicle to have ability to localize itself varies across the environment, different features of environment provide different degrees of position. Consequently, an extended study that combined this algorithm with the Unscented Kalman Filter (UKF), and described a sampling algorithm that minimizes the number of samples required to choose the best path for flying [6].

In order to performance improve of a low-cost INS/GPS, Ruijie et. al. proposed Adaptive Kalman filtering techniques use the residual sequences to adapt the stochastic properties of the filter on line to correspond to the temporal dependence of the errors involved [7]. That proposal uses three adaptive filtering techniques that are artificially scaling the predicted Kalman filter covariance, the Adaptive Kalman Filter and Multiple Model Adaptive Estimation.

In this paper, we proposed an integrated system that utilized an algorithm named Street Tracking Algorithm that improves both position and velocity information of the land vehicle during GPS outage. The paper is organized as following: Section 2 presents the working principles of GPS, INS and INS/GPS integrated system. Section 3 presents the proposed configuration scheme and its operating principle. Results and discussions are mentioned in Sect. 4 and conclusion is given in Sect. 5.

2 Working Principles

2.1 Global Position System (GPS)

Principle of determining the coordinates of the GPS receiver (R) bases on the formula $\text{distance} = \text{velocity} \times \text{time}$. Satellites (Sats) emit signals including their location, and the signal emitting time. The GPS receiver calculates the distance from the satellites to its position. The GPS receiver location is the point of intersection of spheres with center is satellites, and the radius is the signal broadcasting time from the satellite to the GPS receiver multiple velocity of electromagnetic wave rate. However, in order to find out longitude, latitude, and height the receiver needs to see at least four satellites (see Fig. 1).

2.2 Inertial Navigation System (INS)

An inertial navigation system normally consists of three parts such as an inertial measurement unit (IMU), support electronic elements, and a navigation computer. The IMU utilizes gyroscopes and accelerometers to maintain an estimate of the position, velocity, and attitude of the moving object equipped itself. This object could be

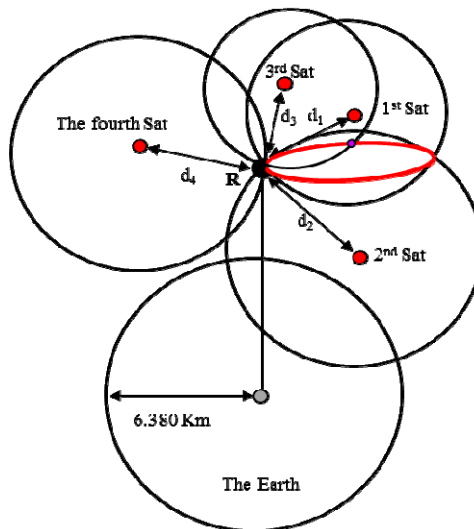


Fig. 1. Determination of the GPS receiver's position

aircraft, spacecraft, surface ship, a land vehicle etc. Fundamental principle of INS can be explained as follows: Before working, INS is set up standard information about position (latitude, longitude and height), and attitude. When INS starts working, gyroscopes and accelerometers in an IMU provide velocity and angular (pitch, roll and yaw) increments to navigation computer. Computer bases on these increments and the above standard information to determine information about position, velocity and attitude at the present time (t_1). Familiar to this determining, the position information at the next time (t_2) will be found out via the position information at the latest time (t_1) and increment or decline of parameters of velocity, acceleration, and angle during the period from t_1 to t_2 .

2.3 INS/GPS Integrated System

With a view to integrate INS and GPS, it can use one in three basic integration methods such as loosely-coupled, tightly-coupled, and deeply-coupled. However, this study utilizes the loosely-coupled integration method (see Fig. 2) [8].

In this scheme, after receiving and processing information come from satellites, the processed information is put into the navigation processor inside the GPS receiver to calculate position (P_{GPS}) and velocity (V_{GPS}) of moving object when GPS signal is available. P_{GPS} and V_{GPS} continue to be processed one time again in external navigation processor before outputting the most precise navigation parameters about position P and velocity V . In case of GPS outage, accelerometers and gyroscopes in IMU will provide angular increment, velocity increment respectively to navigation processor so as to calculate three parameters such as velocity, attitude, and position. After that these are output directly without combining with information provided by GPS.

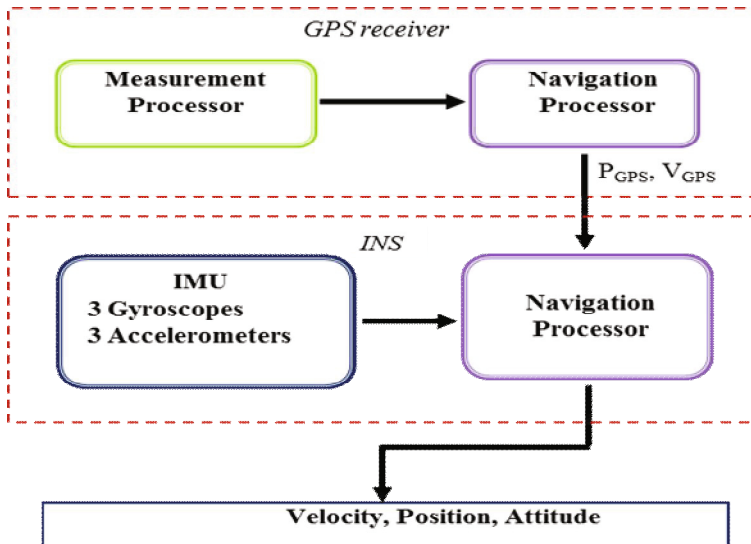


Fig. 2. The INS/GPS system using loosely-coupled integration method

An external navigation filter computes position (P_{INS}), velocity (V_{INS}) and attitude (A_{INS}) from the raw inertial sensor measurements and uses the GPS position and velocity to correct INS errors. An advantage of a loosely coupled system is that the GPS receiver can be treated as a black box. The blended navigation filter will be simpler if using GPS pre-processed position and velocity measurements. However, if there is a GPS outage, the GPS stops providing processed measurements and the inertial sensor calibration from the INS/GPS filter stops as well.

In an INS/GPS integrated system, when working in common mode INS is always supported by GPS. It means that the GPS position and velocity are used to correct INS errors. But in case of GPS outage, INS will computer, output parameters without supporting of GPS [2]. The reason why the use of kind of this combination is INS having high-speed update, self-contained navigation ability while GPS has low-speed update and depends on the weather condition, environment condition, seeing how many satellites etc. It is clear that this integrated system could bring into play advantages and limit disadvantages of each system.

3 Proposed Configuration Scheme

The proposed INS/GPS/feedback P_{STA} system is shown in Fig. 3. It should be presented here for complete understanding:

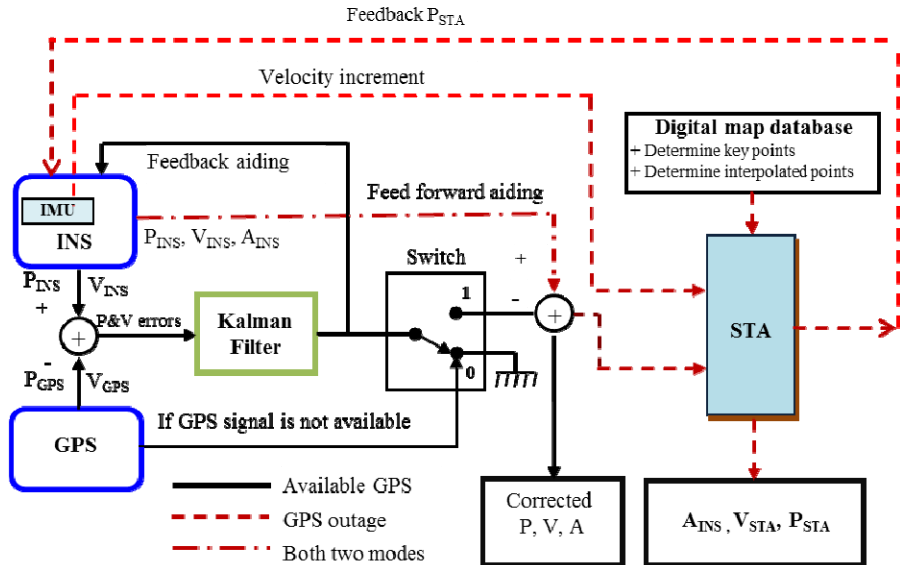


Fig. 3. The proposed INS/GPS/feedback P_{STA} system

When GPS signal is available, the state of the switch is “1” and the system would run in the solid lines and dotted line. It means that the system can work well without STA and digital map. However, if GPS signal is lost, the state of the switch is “0” and the system would run in the dotted line and dashed lines. In this scenario, the Kalman filter will work in prediction mode, and the Street Tracking Algorithm would enable to assist position information based on digital map.

In the computer, we have to store the information of the trajectory of the vehicle. The data is prepared in two steps. The first step is determination of key points based on digital map. The second step is determination of interpolated points based on above key points. The aim of the second step is to increase the reference points (key points or interpolated points). It supposed that d_{ref} is reference distance; this means that d_{ref} is distance from starting position of the vehicle to any reference point. The distance of d_{ref} is the sum of the line segments between two consecutive reference points since starting point. Before GPS outage, the STA block stores the last reliable location of the vehicle at the time of t_s having distance of d_s (distance from starting position of the vehicle to the last reliable location) (see Fig. 4). The distance of vehicle ran to the time of t_k is calculated by:

$$d = d_s + d(t_k), \quad (1)$$

where $d(t_k)$ is the distance of the vehicle from the moment the GPS signal is lost to the epoch t_k . Note that this distance is computed by integrating the velocity provided directly by the IMU:

$$d(t_k) = \int_{t_s}^{t_k} v(t) dt. \quad (2)$$

It is easy to see that $d(t_k)$ is only the distance from t_s to t_k . It cannot provide the information of longitude or latitude. The STA will determine its longitude and latitude by comparison of d with the reference distances d_{ref} . It will search which value of d_{ref} would have nearest distance to d (to ensure that ε is smallest):

$$|d - d_{ref}| < \varepsilon. \quad (3)$$

After that, we will obtain the corrected position of the vehicle as the longitude and latitude of reference point having distance of found d_{ref} . It means that the vehicle will be pulled to the fixed location determined in the database.

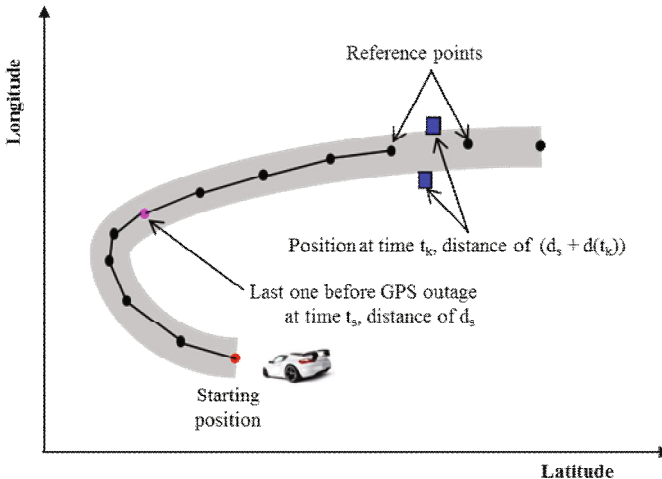


Fig. 4. Determination of corrected positions to replace the wrong ones

It is clear that when amount of the reference points increased the performance would be improved. However, it also needs to have a balance between the performance and the complexity.

The limitation of integrated system without feedback P_{STA} is that it could not improve information of velocity. Thus an integration scheme using feedback P_{STA} is proposed as shown in Fig. 3. After obtaining corrected position P_{STA} from output of STA block, this information is feedback to INS to continue to correct parameter of velocity. The different between two continuous P_{STA} divide the updated period T_S would provide the velocities V_N and V_E :

$$V_N(t_k) = \frac{P_{STA}^N(t_k) - P_{STA}^N(t_{k-1})}{T_S}, \quad (4)$$

$$V_E(t_k) = \frac{P_{STA}^E(t_k) - P_{STA}^E(t_{k-1})}{T_S}. \quad (5)$$

Note that we should not use the position information as the longitude and latitude because the change of the position in degree is very small. In (4) and (5), the positions (P_{STA}^N and P_{STA}^E) are measured by the distance in the North and the East.

4 Results and Discussions

Hardware configuration used in this study includes a computer, a GPS receiver, an IMU named MICRO-ISU BP3010 consisting of three ADXRS300 gyros and three ADXL210E accelerometers (as shown in Fig. 5). The calibration process for this IMU is presented in [9, 10]. From the digital map, we determined 92 key points and 410 interpolated points for STA block. Trajectory of line segments is formed via those reference points. The moving trajectory of the vehicle; trajectory of line segments, and trajectory drawn by GPS in open-sky condition are shown in the Fig. 6.

In this scenario, GPS signal was assumed to be lost within 200 seconds from the 900th to 1100th second. The output parameters of the system in this scenario will be compared with the actual GPS's output.



Fig. 5. The hardware configuration of the INS/GPS integrated system

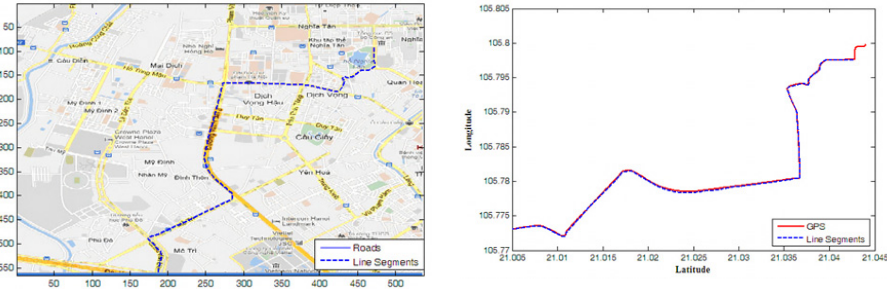


Fig. 6. The trajectories of roads and line segments (a) and the trajectories of GPS and line segments (b)

We can observe the velocities in the North and the East (V_N and V_E) in Fig. 7. It is easy to see that the system could not adapt with the real moving. The velocities are nearly unchanged until the GPS signal is available again.

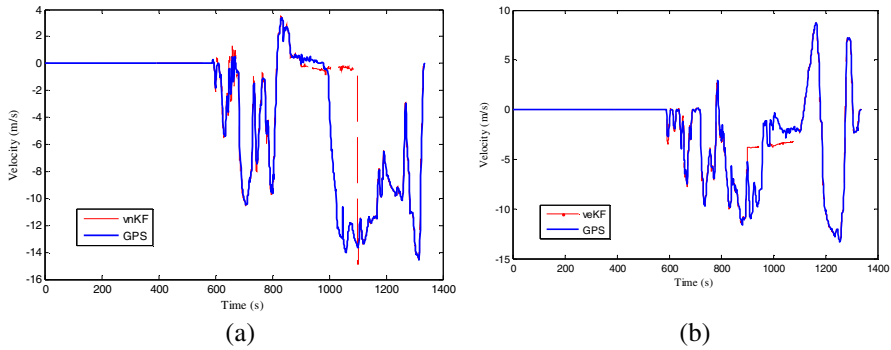


Fig. 7. The velocity in the North (a) and the East (b) without feedback P_{STA}

Even if we use STA with feed forward configuration, we could not obtain the information of the velocity. It means that the velocity of the INS/GPS system with STA in feed forward mode is the same Fig. 7. Using STA with feedback configuration, the velocities have been estimated as shown in Fig. 8. Obviously, the velocities can adapt with real moving. The result would be better if we increase the number of the key points and interpolated points.

The positions of the vehicle before using STA are shown in Fig. 9.a. When GPS signal is available, the integrated system offers positions matched with reference curve. However, when GPS signal is lost, the integrated system (the dotted curve) is bias from the reference trajectory (the solid curve). The maximum position error caused by INS is over 1000 meters in the North and about 50 meters in the East during the period of 200 seconds and this error is unacceptable. However, this is

improved a lot after using feedback P_{STA} (see Fig. 9.b). In order to quantify the performance of this system, we calculated the error as:

$$e = \frac{1}{N} \sum_{i=1}^N \left| \hat{P}_i - P_i^{ref} \right|, \quad (6)$$

where \hat{P}_i and P_i^{ref} are estimated and reference values, and N is total number of samples. Consequently, we can calculate the position and velocity errors based on the data as shown in Fig. 8 and Fig. 9. The position error is 2.5 meters and the velocity error is 3.2 m/s. These errors are entirely acceptable.

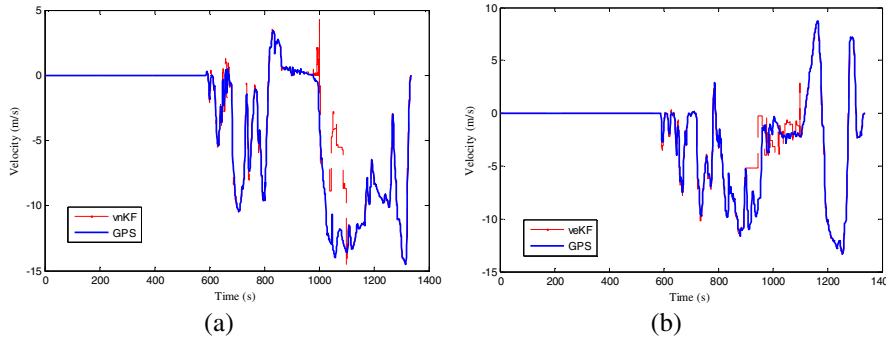


Fig. 8. The velocity in the North (a) and the East (b) using feedback P_{STA}

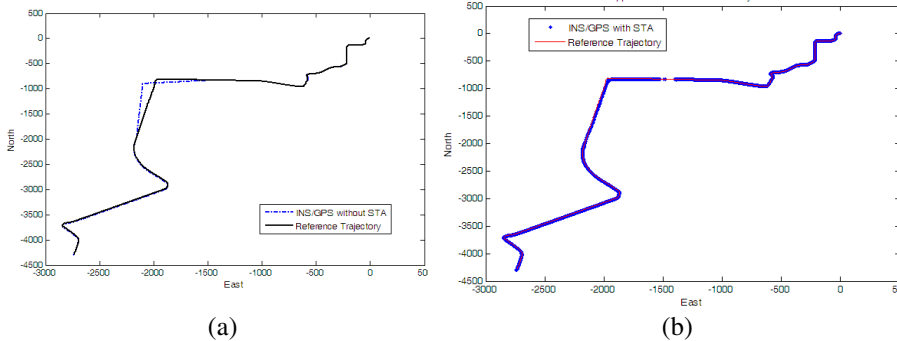


Fig. 9. The trajectory of the INS/GPS system before (a) and after (b) using STA

5 Conclusion

In this paper, we have proposed a Street Tracking Algorithm in a feedback configuration in order to accurately improve the both position and velocity of the land vehicle when the GPS signal is lost. This algorithm works based on INS position output, velocity increment from the IMU and a digital map. The performance of the

proposed system has been verified with experimental data. The position error of the system is controlled around 2.5 meters and the velocity error is controlled around 3.2 m/s. This system can be applied in vehicle navigation, railway transportation navigation, etc.

References

1. Van Thang, N., Trinh, C.D., Tan, T.D.: Application of Street Tracking Algorithm to Improve Performance of a Low-cost INS/GPS System. *Journal of Automation and Control Engineering* 1(3), 1–5 (2013)
2. Tan, T.D., Ha, L.M., Long, N.T., Tue, H.H., Thuy, N.P.: Feedforward Structure of Kalman Filters For Low Cost Navigation. In: International Symposium on Electrical-Electronics Engineering (ISEE 2007), Ho Chi Minh City, Viet Nam, pp. 1–6 (2007)
3. Tan, T.D., Ha, L.M., Long, N.T., Duc, N.D., Thuy, N.P.: Integration of Inertial Navigation System and Global Positioning System: Performance analysis and measurements. In: International Conference on Intelligence and Advance Systems, Malaysia, pp. 1047–1050 (2007)
4. Ojeda, L., Borenstein, J.: Personal Dead-reckoning System for GPS-denied Environments. In: IEEE International Workshop on Safety, Security, and Rescue Robotics (SSRR 2007), Rome, Italy, September 27-29 (2007)
5. Prentice, S., Roy, N.: The belief roadmap: Efficient planning in linear POMDPs by factoring the covariance. In: Kaneko, M., Nakamura, Y. (eds.) *Robotics Research*. STAR, vol. 66, pp. 293–305. Springer, Heidelberg (2010)
6. He, R., Prentice, S., Roy, N.: Planning in Information space for a Quad rotor Helicopter in a GPS-denied Environment. In: The IEEE International Conference on Robotics and Automation, ICRA 2008 (2008)
7. Hide, C., Moore, T., Smith, M.: Adaptive Kalman Filtering for Low-cost INS/GPS. *The Journal of Navigation* 56, 143–152 (2003)
8. Sung, W., Dong-H wan, H., Tae, K., Sang, J.: Design and Implementation of an Efficient Loosely-Coupled INS/GPS Integration Scheme. Chungnam National University, Korea (2002)
9. Ha, L.M., Tan, T.D., Long, N.T., Duc, N.D., Thuy, N.P.: Errors Determination of The MEMS IMU. *Journal of Science VNUH*, 6–12 (July 2007)
10. Tan, T.D., Tue, H.H., Long, N.T., Thuy, N.P., Chuc, N.V.: Designing Kalman Filters for Integration of Inertial Navigation System and Global Positioning System. In: The 10th Biennial Vietnam Conference on Radio & Electronics, REV 2006, Hanoi, November 6-7, pp. 266–230 (2006)

EEG Data Similarity Using Lempel–Ziv Complexity

Ibrahim Salem Jahan, Michal Prilepok, and Vaclav Snasel

VSB – Technical University of Ostrava,
17. listopadu 15, 708 33 Ostrava – Poruba, Czech Republic
Jahan_nw@yahoo.com, {michal.prilepok, vaclav.snasel}@vsb.cz

Abstract. Today still big challenge in world is to find efficient technique for perform recognition on mental tasks and distinguish between them. These allow us to use Brain Computer Interface applications to help disabled people to interact with environment and control external devices such as wheel chair. In this article we used EEG data from National University of Sciences and Technology, Pakistan, which are available online. We made our experiments on signals from one subject performing hand movement task. First we applied Faster Fourier Transformer (FFT), removing the EEG higher frequencies, applying the inverse Fourier transformer then converting EEG data into graphics by turtle graphics, then find the similarity between these trials by Lempel–Ziv complexity, to find maximum similarity between EEG data for same mental task. Our model reached average accuracy up to 52.63%.

Keywords: Electroencephalograph (EEG), Neuron, Lempel–Ziv Complexity, Turtle Graphics, EEG Data Similarity.

1 Introduction

There are several algorithms to analyze similarity and recognition of mental tasks, but still remains big challenge in world to find very efficient method for analysis and recognition human mental tasks. We will use Lempel–Ziv Complexity technique to finding similarity between EEG data and distinguish between human mental tasks. There are several approaches to classify EEG signal, they include Support Vector Machines (SVM), L1 regularized logistic regression and non-negative matrix factorization (NMF) [1]. In this paper we will give some glance at EEG, Lempel–Ziv Complexity, Turtles graphics and applying proposed method for Electroencephalograph (EEG) data similarity.

2 Introduction to EEG

EEG include on complex irregular signals that may provide useful information denote about underlying neural activities of the brain [2]. The human brain electrical activity has been recognized from more than a century. It is defined as that variation of the surface potential distribution on the scalp that reflects functional activities emerging from the underlying brain [3]. This electrical surface potential variation can be

recorded by placing set of sensors on the scalp, and measuring the electrical signal between couples of these sensors after that filtered, amplified, and recorded these electrical signals. The final result of these data is called the Electroencephalograph (EEG) [3].

2.1 Source of EEG Generating

The EEG signals define as measurements of the currents when flowing during synaptic excitations of the dendrites of multiple pyramidal neuron in the cerebral cortex. When brain cells are activated, the synaptic currents are produced within the dendrites. Normally this current producing a magnetic field can be measurable by electromyogram (EMG) machines and an electrical field over the scalp measurable by EEG techniques. Basically the current in each neuron cell of brain is produced from pumping the positive ions of calcium, sodium, and potassium, and negative ions of chlorine, through the neuron membranes in the direction governed by the membrane potential, as structure of neuron in figure (1) [4].

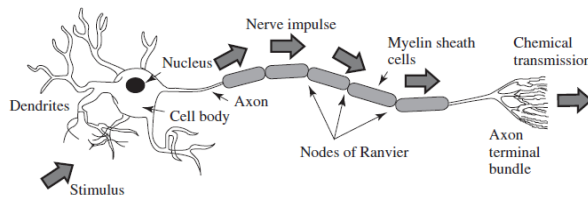


Fig. 1. Structure of Neuron [4]

3 Faster Fourier Transform (FFT)

A Fourier transform, converting a function from time domain to frequency domain and vice versa. The faster Fourier Transform (FFT) is algorithm that can compute the discrete Fourier transform (DFT) and inverse of DFT, also FFT is an efficient to compute the discrete Fourier transform (DFT). The FFT is important in field frequency analysis, because it takes a discrete signal in time domain and converts this signal to discrete frequency domain representation [5]. FFT and IFFT algorithms have been well known and widely used in several applications due to their efficiency [6].

4 Turtle Graphic

The Turtles graphic is an easy way for representation complicated geometric object. Turtle Graphic or L-systems method is used for making the graphics. The basic idea to make graphics by turtle is convert the graphic into sequence of commands, which control turtle and allow to making the specific graphic [7]. Turtle geometry has been used to study and representation many various subjects from simple polygons to

complex fractals [8]. To understand turtle geometry, we will explain that it by a virtual turtle. The virtual turtle must know own position, facing direction, and step size, it to follow some commands to change own position, or heading, or notion scale [8]. For example we have a turtle on a plane. The location of turtle on the plane can be represented by a point A given by pair of (a_1, a_2) , also the turtle heading can represent by vector V given by pair of (v_1, v_2) , the length of vector V denote on turtle step size, the pair (A, V) denote on turtle state.

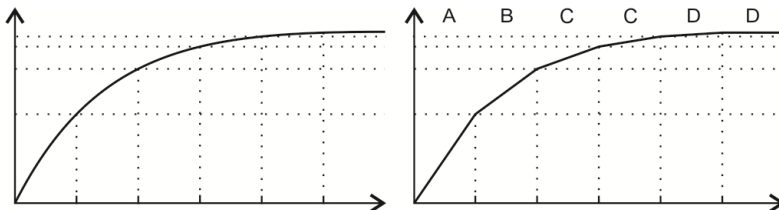


Fig. 2. Data conversion

On the left figure on Fig. 2 we can see interpretation in a line chart of the measured raw data. The right figure shows interpretation measured after conversion into turtle graphic command. The command are on the top edge of figure. The final commands sequence for our example is ABCCDD. In this example we have only four commands. The C and D commands doubled, because third and fourth angles have same value. In case of D command is the situation same to command C.

5 Lempel–Ziv Complexity

The Lempel–Ziv (LZ) complexity for sequences of finite length was suggested by Lempel and Ziv [9]. It is a non-parametric, simple-to-calculate measure of complexity in a one-dimensional. LZ complexity is related to the number of distinct substrings and the rate of their recurrence along the given sequence [10], with larger values corresponding to more complexity in the data. It has been applied to study the brain function, detect ventricular tachycardia, fibrillation and EEG [11]. It has been applied to extract complexity from mutual information time series of EEGs in order to predict response during isoflurane anaesthesia with artificial neural networks. [12]

LZ complexity analysis is based on a coarse-graining of the measurements, so before calculating the complexity measure $c(n)$, the signal must be transformed into a finite symbol sequence. In this study we have used turtle graphic for conversion measured data into finite symbol sequence P .

The sequence P is scanned from left to right and the complexity counter $c(n)$ is increased by one unit every time a new subsequence of consecutive characters is encountered. The complexity measure can be estimated using the following algorithm [9] and [12]:

1. Let S and Q denote two subsequences of P and SQ be the concatenation of S and Q , while sequence $SQ\pi$ is derived from SQ after its last character is deleted (π means the operation to delete the last character in the sequence). Let $v(SQ\pi)$ denote the vocabulary of all different subsequences of $SQ\pi$. At the beginning, $c(n) = 1$, $S = s(1)$, $Q = s(2)$, therefore, $SQ\pi = s(1)$.
2. In general, $S = s(1), s(2), \dots, s(r)$, $Q = s(r+1)$, then $SQ\pi = s(1), s(2), \dots, s(r)$; if Q belongs to $v(SQ\pi)$, then Q is a subsequence of $SQ\pi$, not a new sequence.
3. Renew Q to be $s(r+1), s(r+2)$ and judge if Q belongs to $v(SQ\pi)$ or not.
4. Repeat the previous steps until Q does not belong to $v(SQ\pi)$. Now $Q = s(r+1), s(r+2), \dots, s(r+i)$ is not a subsequence of $SQ\pi = s(1), s(2), \dots, s(r+i-1)$, so increase $c(n)$ by one.
5. Thereafter, S is renewed to be $S = s(1), s(2), \dots, s(r+i)$, and $Q = s(r+i+1)$.

These procedures have to be repeated until Q is the last character. At this time the number of different subsequences in P – the measure of complexity – is $c(n)$.

In our experiment we do not deal with measure of the complexity. From the individual subsequences we create a list of them. One list is created for each data file with turtle commands of the compared commands files.

5.1 Comparing Data Using LZ Complexity and Turtle Graphics Commands

The comparison of the LZ sequence lists is the main task. The lists are compared to each other. The main property for comparison is the number of common sequences in the lists. This number is represented by the sc parameter in the following formula (1), which is a metric of similarity between two turtle commands lists.

$$SM = \frac{sc}{\min(c_1, c_2)} \quad (1)$$

Where

- sc Count of common LZ sequences in both dictionaries.
- c_1, c_2 Count of LZ sequences in list of the first or the second file.

The SM value is in the range between 0 and 1. If $SM = 1$, then the commands lists are equal and they have the highest difference (have nothing common), when the result value of $SM = 0$.

6 EEG Experiments

6.1 EEG Data

In our experiment we used EEG data that available online from National University of Sciences and Technology, Pakistan, we choosing Dataset 2 - 2D motion. The EEG

data raw was recorded at 500Hz, from a subject male 21 years old using 19 electrodes FP1 FP2 F3 F4 C3 C4 P3 P4 O1 O2 F7 F8 T3 T4 T5 T6 FZ CZ PZ, consisting on several trials of hand and leg movements. In our experiments we used left hand back movement trial - LeftBackward1, left hand back movement trial - LeftBackward2, left hand back movement trial - LeftBackward3, left hand back Imaging movement - Left Backward Imagined.

6.2 EEG Data Preparation

The EEG data are prepared in following steps. As a first step separate dataset into individual mental tasks, trials and sensors. We got 122 data parts. In the second step of our process we applied Faster Fourier Transform to transform raw sensor data from time domain into frequency domain. In the frequency domain we removed higher frequencies above than 150Hz. In the next step we applied Inverse FFT to convert data back from frequency domain into time domain. This filtered data we converted using turtle graphics into text format. For the turtle graphic we used 128 commands. Each command represents an angle in the selected first and fourth quadrant. We used only first and fourth quadrat, because the time in data line goes from left to right and the signal does not go backwards.

After that each EEG trial were prepared by LZ complexity to get LZ subsequences from turtle commands list. For each data trial we created a list of LZ subsequences. We compared training and testing lists to find the maximum similarity between EEG trials of same mental task.

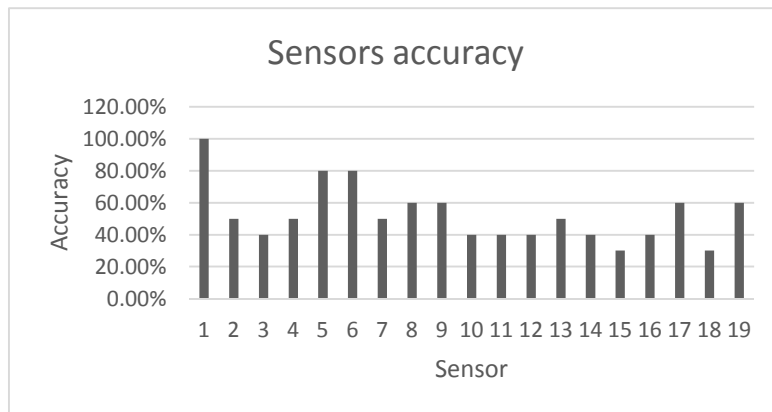
6.3 Experiment Results

We made similarity between the EEG trials for left hand back movement and imaging left hand back movement task, to find maximum similarity between different EEG trials of the same mental task. Our results are listed in the Table 1. The maximum similarity results of mental tasks by our method reached to 100.00%, minimum similarity was 30.00% and average value of similarity was 52.63%. Our suggested model reached accuracy up to 52.63%.

Table 1. Similarity results

	Minimum	Maximum	Average
Correctly identified	30.00%	100.00%	52.63%
Incorrectly identified	0.00%	70.00%	47.37%
True positive rate	0.00%	100.0%	35.53%
False positive rate	0.00%	100.0%	55.26%
Accuracy	30.00%	100.00%	52.63%

In Figure 3 we can see accuracy of all used sensors. The accuracy of sensor nr. 1 reached to 100%, sensors nr. 5 and 6 reached to 80%, the most accuracy sensors values was between 40% and 60%.

**Fig. 3.** Sensors accuracy

7 Conclusion

We made our experiments on EEG signals from one subject performing left hand back movement task in three trials, and other trial for imaging left hand back movement, we applied FFT to EEG data, removing high frequencies, applied Invers FFT, represent EEG data by turtle graphics, then finding the maximum similarity between these trials by LZ complexity. The experiment results on EEG data showed the maximum similarity results of mental tasks by our method reach to 100%, minimum similarity was 30.00% and average value of similarity was 52.63%. Our model reached accuracy up to 52.63%. In future work we will try to collect EEG data using Emotiv EEG neuroheadset, and use this data to find similarity between trials of mental tasks by our proposed method to analysis and recognition on mental tasks.

Acknowledgements. This work was partially supported by the Grant of SGS No. SP2013/70, VŠB - Technical University of Ostrava, Czech Republic, and was supported by the European Regional Development Fund in the IT4Innovations Centre of Excellence project (CZ.1.05/1.1.00/02.0070) and by the Bio-Inspired Methods: research, development and knowledge transfer project, reg. no. CZ.1.07/2.3.00/20.0073 funded by Operational Program Education for Competitiveness, co-financed by ESF and state budget of the Czech Republic.

References

1. Shin, B., Oh, A.: Bayesian Group Nonnegative Matrix Factorization for EEG Analysis (December 2012)
2. Bhattacharya, J., Petsche, H.: Universality in the brain while listening to music. Proc. the Royal Society Lond. B 268, 2423–2433 (2001)

3. Ochoa, J.B., Molina, G.G., Ebrahimi, T.: EEG Signal Classification for Brain Computer Interface Applications (2002)
4. Sanei, S., Chambers, J.A.: EEG Signal Processing. John Wiley & Sons Ltd., The Atrium (2007)
5. Garcia, J., Castillo, C.: Frequency-change Analysis of Nonlinear System Using Spectrum (Fast Fourier Transform) Theory. In: 6th International Conference Electrical Engineering, Computing Science and Automatic Control, CCE, 2009, pp. 1–6 (2009)
6. Perko, M., Fajfar, I., Tuma, T., Puhan, J.: Fast Fourier transform computation using digital CNN simulator. In: 1998 Fifth IEEE International Workshop Cellular Neural Networks and Their Applications Proceedings, London, pp. 230–235 (1998)
7. Prusinkiewicz, P.: Graphical applications of L-system. In: Graphical Interface, pp. 247–253 (1986)
8. Goldman, R., Schaefer, S., Ju, T.: Turtle geometry in computer graphics and computer-aided design, pp. 1471–1482 (2004)
9. Lempel, A., Ziv, J.: On the complexity of finite sequences, pp. 75–81 (1976)
10. Radhakrishnan, N., Gangadhar, B.N.: Estimating regularity in epileptic seizure time-series data, pp. 89–94 (1998)
11. Zhang, X.S., Roy, R.J., Jensen, E.W.: EEG complexity as a measure of depth of anesthesia for patients, pp. 1424–1433 (2001)
12. Abásolo, D., Hornero, R., Gómez, C., García, M., López, M.: Analysis of EEG background activity in Alzheimer’s disease patients with Lempel–Ziv complexity and central tendency measure, pp. 315–322 (2006)

An Energy-Aware Routing Protocol for Wireless Sensor Networks Based on K-Means Clustering

Thai T. Vu¹, Viet D. Nguyen², and Hien M. Nguyen¹

¹ Faculty of Computer Science and Engineering, Hanoi Water Resources University,
Hanoi, Vietnam
{thaivt,hiennm}@wru.vn

² Faculty of Information Technology, VNU University of Engineering and
Technology, Hanoi, Vietnam
vietnd@vnu.edu.vn

Abstract. Wireless sensor networks (WSNs) have recently gained much attention from researchers due to their large potential for practical applications. One of the most critical problems in WSN research is to prolong the network lifetime, given that sensor nodes are only equipped with energy-limited batteries. Clustering sensor nodes and then routing the transmission of data to the base station via cluster heads (CHs) is an effective approach to this problem. In this paper, we first analyze the problem of selecting cluster centers as CHs which may quickly exhaust their energy. Then we propose a new k -means-based routing (KMR) protocol, where the selection of CHs is randomized so as to better distribute the transmission load among sensor nodes of the same cluster. The simulation results on OMNeT++ show that our method KMR can make a substantial improvement in the network lifetime compared with some existing methods, including LEACH (Low-Energy Adaptive Clustering Hierarchy).

Keywords: wireless sensor network, routing, clustering, k -means.

1 Introduction

The advancements in technologies have allowed the mass production of tiny and low-cost sensors. These sensors appear in many applications (e.g., environmental monitoring and disaster mitigation) because of the need to measure and collect various kinds of data from the environment, such as temperature, humidity, light, sound, and vibration. Depending on application domains, a large number of sensor nodes can be deployed on a wide area in a random or manual fashion, and are connected together in the form of wireless sensor networks (WSNs). However, one of the most critical problems for a successful deployment of WSNs is how to optimize the transmission of data between sensor nodes and the base station (BS) so as to prolong the network lifetime, given that sensor nodes are highly limited in power supply.

In recent years, routing techniques for WSNs have gained much attention from researchers due to their effectiveness in solving the problem of energy inefficiency

in data transmission, which causes the shortening of the network lifetime. These routing techniques can generally be divided into three categories: Flat-based routing, location-based routing, and hierarchy-based routing [1, 2]. In flat-based routing, sensor nodes have the same roles for routing data, while in location-based routing, sensor nodes route data considering their geographic locations. In hierarchical routing protocols, nodes are partitioned into clusters, each of which has a member node selected as the cluster head (CH). The CH aggregates the data from member nodes so as to eliminate redundancy and reduce the number of direct transmissions to the base station, and therefore saving energy [6, 7, 10]. A distributed or centralized algorithm can be used to cluster the network. In distributed algorithms, the formation of clusters is performed over the entire network. In contrast, centralized algorithms run on the base station, and the information about clusters is sent back to all nodes of the network. Some popular clustering methods that can be applied to routing in WSNs include local search algorithms, Taboo search, simulated annealing, and k -means [3, 8].

The effectiveness of the k -means clustering algorithm has been demonstrated by many successful applications in various fields. For the problem of clustering WSNs, using k -means in a usual manner (to which we refer as *basic k-means*) can help find out an optimal clustering of sensor nodes, which is likely not to change over routing rounds. If we implement a hierarchical routing protocol where cluster centers are chosen as cluster heads, some certain nodes may die earlier than expected because they would always keep the role of cluster heads during their lifetime. Therefore, the basic k -means may be not suitable for energy-efficient routing in WSNs.

In this paper, we propose a new k -means-based routing (KMR) protocol, which considers the residual energy of nodes as well as distances between them for randomizing the selection of cluster heads. In this protocol, after the k -means clustering algorithm is finished, a new cluster head is selected for each cluster of nodes so as to avoid burdening the transmission load on the same nodes as in the previous routing round, and therefore prolonging the lifetime of the entire network.

We compare the performance of our method KMR with that of several others, including the method that directly transmits data from all sensor nodes to the base station, the basic k -means, and a well-known method for routing in WSNs called LEACH (Low-Energy Adaptive Clustering Hierarchy). The results on the OMNeT++ simulation framework show that KMR can make a substantial improvement in the network lifetime compared with the others.

The rest of the paper is organized as follows: Section 2 introduces some previous methods for routing in WSNs. Section 3 describes our method in details. Section 4 presents the simulation and comparison results. Section 5 concludes the paper.

2 Related Work

In hierarchical routing methods, nodes with higher energy can be used to receive, process, and transfer data, while lower-energy nodes can be used to sense the

environment. By organizing nodes into clusters, transmission of data from nodes to the base station through cluster heads can increase the scalability, lifetime, and energy efficiency of WSNs [2].

Low-Energy Adaptive Clustering Hierarchy (LEACH) is one of the first routing protocols for balancing energy consumption among nodes [4, 5]. In this protocol, all nodes organize themselves into clusters, each of which has one member node selected as the cluster head. Each round in the operation of LEACH has two phases: the set-up phase for forming clusters and the steady-state phase for transferring data from nodes to the corresponding cluster heads and then from these cluster heads to the base station. LEACH combines the ideas of energy-efficient cluster-based routing and application-specific data aggregation in order to maximize the system lifetime.

LEACH-Centralized (LEACH-C) [5], which is a derivation from LEACH, was proposed to solve two limitations of LEACH: the fluctuating number and the poor distribution of cluster heads. LEACH-C consists of two phases which are similar to those of LEACH: the set-up phase and the steady-state phase. In the former, LEACH-C uses a centralized clustering algorithm, and in the latter, data is transferred from nodes to the corresponding cluster heads, and then from these cluster heads to the BS. At the beginning of the set-up phase, all nodes send information about their positions and residual energy to the BS. Based on such information, the BS uses the simulated annealing algorithm [8] to find the best clusters.

3 K-Means-Based Routing Protocol

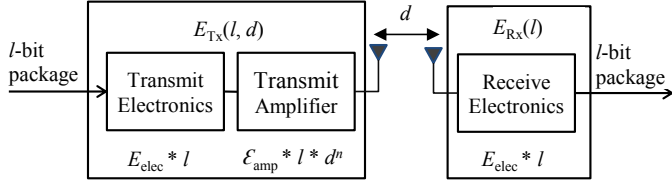
3.1 Network Models

Models for wireless sensor networks can vary according to application domains. For the development of our routing protocol, we make assumptions about network models, as follows:

- The base station is a high-energy node, which is capable of computing highly complex operations. This node is not moving and located far away from the sensor field.
- Sensor nodes in the network are homogeneous and have a fixed location. They are highly limited in power supply, but can transmit data to the BS with enough power if needed.
- Sensor nodes are aware of their locations and residual energy, which are sent to the BS at the beginning of each round in the routing process. In order to know their locations, nodes can be equipped with a low-power GPS device or a localization algorithm [9].

3.2 Radio Models

Radio models play an important role in the construction and operation of routing protocols. Different assumptions about radio characteristics, such as energy

**Fig. 1.** First-order radio model

dissipation in transmit and receive modes, will change the effectiveness of the protocols. In this paper, we use the first-order radio model from the literature [4], as shown in Fig. 1.

The amount of energy consumption in transmitting data of l bits over a distance d can be represented by (1):

$$E_{\text{Tx}}(l, d) = \begin{cases} E_{\text{elec}} \times l + \epsilon_{\text{fs}} \times l \times d^2 & \text{if } d < d_0 \\ E_{\text{elec}} \times l + \epsilon_{\text{mp}} \times l \times d^4 & \text{if } d \geq d_0 \end{cases} \quad (1)$$

where $d_0 = \sqrt{\epsilon_{\text{fs}}/\epsilon_{\text{mp}}}$, E_{elec} is the transmitter and receiver electronics' consumed energy, ϵ_{fs} and ϵ_{mp} are the radio frequency (RF) amplifier's consumed energy for free space and multi-path fading channel models, respectively. The receiver node consumes the following amount of energy:

$$E_{\text{Rx}}(l) = E_{\text{elec}} \times l . \quad (2)$$

When the BS is far from the network area, to save nodes' energy, cluster heads receive and aggregate data from the corresponding member nodes, and then send only useful information to the BS. According to the experimental results in [11], the energy for data aggregation is set as $E_{\text{DA}} = 5 \text{ nJ/bit/signal}$.

3.3 Timeline Operation of Proposed Method

Like LEACH, the lifetime of the network in our proposed method is divided into rounds. Each round has a set-up phase for organizing sensor nodes into clusters, followed by a steady-state phase for collecting and sending data to the BS. At the beginning of each round, all nodes send information about their locations and residual energy to the BS. In the set-up phase, the BS uses the k -means clustering algorithm to divide nodes into clusters, and then sends information about these clusters back to the nodes.

Figure 2 shows the operation of our method. A steady-state phase consists of a number of frames. Each node sends information about the surrounding environment to the BS via cluster heads at a fixed time slot in the frames.

3.4 K-Means Clustering Algorithm

K-means [3] is a popular clustering algorithm in machine learning, which can be used to automatically partition a data set into k disjoint subsets (or clusters). In

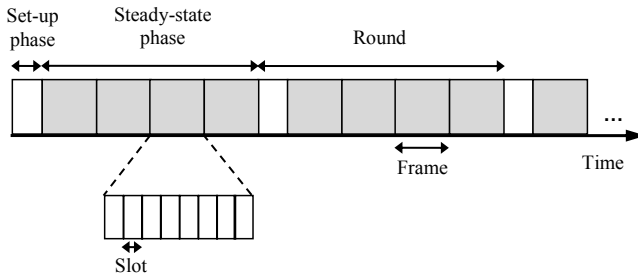


Fig. 2. Timeline for operation of proposed method: Set-up phase for forming clusters and steady-state phase for transmitting data from nodes to CHs and then from CHs to BS

the WSN clustering problem for energy-efficient routing, the k -means algorithm can be used to cluster sensor nodes based on information about their positions. However, simply using k -means and choosing cluster centers as CHs may cause shortening of the network lifetime. If we assume that the results of clustering sensor nodes do not change over routing rounds (in fact, the resulting clusters will be slightly varying due to the random initialization of cluster centers), there will be the fixed k nodes (i.e., k cluster centers) that are always selected as CHs over the network lifetime. These nodes will quickly run out of energy due to constant far transmissions of data to the BS. In other words, the lifetime of the entire network will be dramatically shortened because the burden of transmitting data to the BS is imposed only on a small number of nodes, which are cluster centers.

3.5 Energy-Aware K-Means-Based Routing Protocol

We propose a new k -means-based routing (KMR) protocol, in which the selection of CHs is adjusted appropriately using information about the residual energy and distances of nodes to cluster centers. In our proposal, only nodes with energy not lower than the average energy of nodes in the network have a chance of becoming a CH.

Our method is presented in Algorithms 1 and 2. In our method, instead of selecting cluster centers as cluster heads for transmitting data to the BS, a post-processing stage (after clustering with k -means) re-elects a new cluster head for each cluster without changing cluster members. The chance for each node to become a CH is based on its score that is given by a scoring function proportional to the residual energy of this node but inversely proportional to the distance between this node and the corresponding cluster center. Therefore, our protocol can avoid burdening transmission load on a small number of cluster centers; instead this load is more evenly distributed among nodes in a cluster, and thus prolonging the lifetime of the entire network.

Algorithm 1. *Proposed_Algorithm(S, k)*

Input: Set of sensor nodes $S = \{x_1, x_2, \dots, x_n\}$ and number of clusters k
Output: Clustering of sensor nodes $C = \{C_1, C_2, \dots, C_k\}$

- 1: Calculate average energy E_{avg} of all nodes alive
- 2: Select k cluster centers randomly from nodes with energy $E_{cur} \geq E_{avg}$
- 3: **repeat**
- 4: Assign each node to the cluster whose center is closest to that node
- 5: Re-calculate cluster centers as the mean of locations of cluster-member nodes
- 6: Select nodes with $E_{cur} \geq E_{avg}$ and closest to cluster centers as new centers
- 7: **until** no changes in clusters
- 8: Call *Post_Kmeans_Processing(C)*

Algorithm 2. *Post_Kmeans_Processing(C)*

Input: Clustering of sensor nodes $C = \{C_1, C_2, \dots, C_k\}$
Output: Clustering of sensor nodes $C' = \{C'_1, C'_2, \dots, C'_k\}$

- 1: **for** $i \leftarrow 1, \dots, k$ **do**
- 2: $score(C_i) \leftarrow 0$
- 3: **for all** $x_j \in C_i$ with $E_{cur}(x_j) \geq E_{avg}$ **do**
- 4: Calculate $score(x_j)$
- 5: $score(C_i) \leftarrow score(C_i) + score(x_j)$
- 6: **end for**
- 7: **for all** $x_j \in C_i$ with $E_{cur}(x_j) \geq E_{avg}$ **do**
- 8: $f(x_j) \leftarrow score(x_j)/score(C_i)$
- 9: **end for**
- 10: $pos \leftarrow$ generate a random number in $[0, 1]$
- 11: $total_f \leftarrow 0$
- 12: **for all** $x_j \in C_i$ with $E_{cur}(x_j) \geq E_{avg}$ **do**
- 13: $total_f \leftarrow total_f + f(x_j)$
- 14: **if** $total_f \geq pos$ **then**
- 15: $C'_i \leftarrow C_i$
- 16: Set x_j as cluster head for cluster C'_i
- 17: **break**
- 18: **end if**
- 19: **end for**
- 20: **end for**

4 Simulation and Results

4.1 Experimental Setup

To evaluate the performance of our proposed method for routing in WSNs, we conducted experiments using the OMNeT++ simulator [12].

To select cluster heads, we give each sensor node x_i a score using a function that is proportional to its residual energy (E_{cur}) and inversely proportional to the distance from x_i to the corresponding cluster center ($d_{toCenter}$). In the experiments, we chose the following scoring function:

$$score(x_i) = \frac{E_{\text{cur}}(x_i)}{d_{\text{toCenter}}(x_i) + \varepsilon} \quad (3)$$

where ε is a small positive constant (set to 0.001 in our experiments) for avoiding a zero denominator. The probability for each node to become the head of its cluster can be calculated as follows:

$$f(x_i) = \frac{score(x_i)}{\sum_{x_j \in \text{Cluster}} score(x_j)} . \quad (4)$$

We compared our method (KMR) with several other routing methods, including the method (DT) that directly transmits data from all sensor nodes to the base station, the basic k -means (BKM) that is similar to KMR but uses cluster centers as cluster heads, and a well-known method for routing in WSNs called LEACH (Low-Energy Adaptive Clustering Hierarchy).

We simulated a WSN by randomly and uniformly generating 100 sensor nodes with 2 J of initial energy in an area with size of 100 m \times 100 m. The BS is located at the location with coordinates $x = 175$ and $y = 50$. Each data message is 2000 bits long. Each protocol compared was run 100 times with different random seeds varying from 1 to 100. Then, the results were taken over all these runs in order to increase the reliability of the reported results.

The costs for sending, receiving, and aggregating data are calculated using the formulas given in Sect. 3.2. The other parameters for the simulation are shown in Table 1.

Table 1. Simulation parameters

Parameter	Value
Network size	100 m \times 100 m
Nodes	100
Cluster heads	1 ~ 10
Base station's location	(175, 50)
Data message size l	2000 bits
E_{elec}	50 nJ/bit
E_{DA}	5 nJ/bit/signal
ϵ_{fs}	10 pJ/bit/m ²
ϵ_{mp}	0.0013 pJ/bit/m ⁴
Distance threshold d_0	87.7 m
Initial energy of nodes	2 J
Frames per round	20

4.2 Experimental Results

Three cluster-based routing protocols, LEACH, BKM, and KMR, were simulated to assess the impact of the number of clusters upon the network lifetime. The

number of clusters was varied from one to ten. Figure 3 shows the number of routing rounds with all nodes alive. The lifetime of KMR is substantially longer than that of LEACH and BKM. For example, in case of five clusters, nodes begin to die after 65 rounds for BKM, 315 rounds for LEACH, and 390 rounds for KMR. BKM is the worst among the methods compared, with the longest network lifetime being only 79 rounds (in case of nine cluster heads). As was discussed previously, the reason for this poor performance of BKM is that cluster centers are always to be selected as cluster heads for transmitting data to the BS, and therefore they would quickly run out of energy.

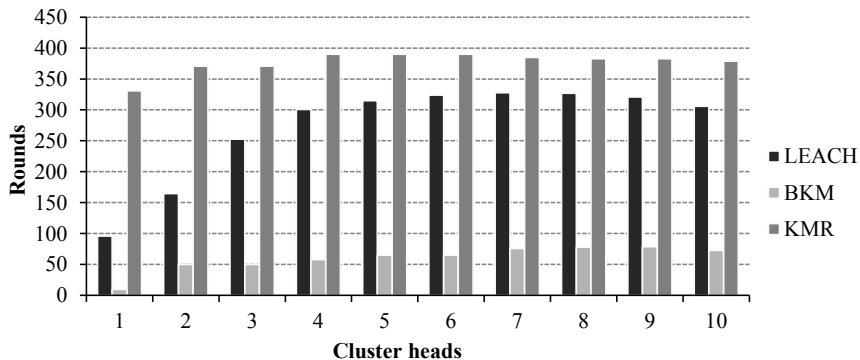


Fig. 3. Number of routing rounds before the first node dies

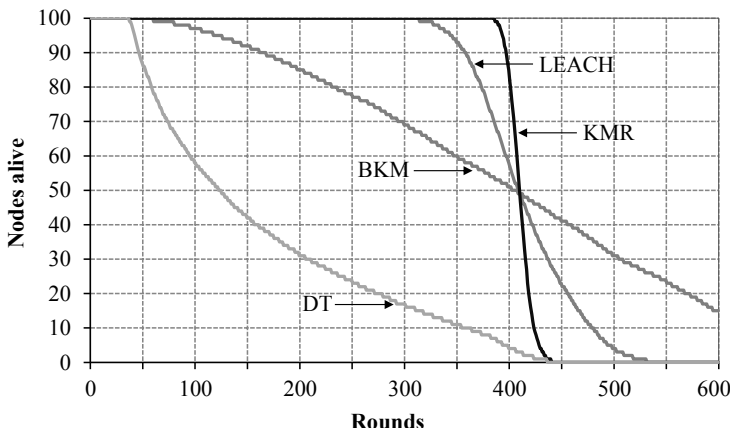


Fig. 4. Number of nodes alive over rounds in case of five cluster heads

Figure 4 shows the detailed results of different routing protocols when the number of clusters was set to five. As can be seen, our method KMR has the

longest lifetime of the network due to better load balancing among sensor nodes. One remarkable point from the results is that our strategy for randomizing the selection of cluster heads has led to a significant improvement of KMR over BKM, which simply selects cluster centers as cluster heads.

5 Conclusion

In this paper, we have presented a novel approach (KMR) to the energy-efficient routing problem in WSNs. To optimize the performance of WSNs in terms of lifetime, KMR first constructs clusters of sensor nodes by using the k -means clustering algorithm. Then, a post-processing stage is performed to randomize the selection of cluster heads, considering nodes' residual energy and distances to cluster centers. The purpose of KMR is to avoid burdening the transmission load on only several nodes, which are cluster centers after clustering with k -means. The simulation results on the OMNeT++ framework show that KMR can substantially increase the network lifetime compared with existing routing methods, including LEACH.

There are several directions for further study of this k -means-based routing problem. The KMR method may be sensitive to the scoring function, and therefore our future work is to investigate the impact of different scoring functions on the performance of KMR. It is an observation that sensor nodes in real WSNs may not be uniformly distributed; instead they may be clustered in a number of natural groups, and this number is usually not known in advance. Thus, automatically identifying such natural clusters of nodes may be an important research problem for further improving the performance of KMR in particular and cluster-based routing protocols in general.

References

1. Akkaya, K., Younis, M.: A Survey on Routing Protocols for Wireless Sensor Networks. *Ad Hoc Networks* 3(3), 325–349 (2005)
2. Al-Karaki, J.N., Kamal, A.E.: Routing Techniques in Wireless Sensor Networks: A Survey. *IEEE Wireless Communications* 11(6), 6–28 (2004)
3. Duda, R.O., Hart, P.E., Stork, D.G.: Pattern Classification, ch. 10. Wiley (2001)
4. Heinzelman, W.B., Chandrakasan, A., Balakrishnan, H.: Energy-Efficient Communication Protocol for Wireless Microsensor Networks. In: 33rd Annual Hawaii International Conference on System Sciences, pp. 1–10 (2000)
5. Heinzelman, W.B., Chandrakasan, A.P., Balakrishnan, H.: An Application-Specific Protocol Architecture for Wireless Microsensor Networks. *IEEE Transactions on Wireless Communications* 1(4), 660–670 (2002)
6. Krishnamachari, L., Estrin, D., Wicker, S.: The Impact of Data Aggregation in Wireless Sensor Networks. In: 22nd International Conference on Distributed Computing Systems Workshops, pp. 575–578 (2002)
7. Mahfoudh, S., Minet, P.: Survey of Energy Efficient Strategies in Wireless Ad Hoc and Sensor Networks. In: 7th International Conference on Networking, pp. 1–7 (2008)

8. Murata, T., Ishibuchi, H.: Performance Evaluation of Genetic Algorithms for Flowshop Scheduling Problems. In: 1st IEEE Conference on Evolutionary Computation, vol. 2, pp. 812–817 (1994)
9. Patwari, N., Ash, J.N., Kyperountas, S., Hero, A.O., Moses, R.L., Correal, N.S.: Locating the Nodes: Cooperative Localization in Wireless Sensor Networks. *IEEE Signal Processing Magazine* 22(4), 54–69 (2005)
10. Rajagopalan, R., Varshney, P.K.: Data Aggregation Techniques in Sensor Networks: A Survey. *Electrical Engineering and Computer Science*, paper 22 (2006)
11. Wang, A., Heinzelman, W.B., Sinha, A., Chandrakasan, A.P.: Energy-Scalable Protocols for Battery-Operated Microsensor Networks. *Journal of VLSI Signal Processing Systems for Signal, Image, and Video Technology* 29(3), 223–237 (2001)
12. OMNeT++ Simulation Framework, <http://www.omnetpp.org>

Neighboring Pixels Based on a Log-linearized Gaussian Mixture Model for Image Segmentation

Khoa Anh Tran and Gueesang Lee^{*}

Department of Electronics and Computer Science,

Chonnam National University,

Gwangju, South Korea

anhkhoayy@gmail.com, gslee@chonnam.ac.kr

Abstract. An advanced probabilistic algorithm developed based on log-linearized Gaussian mixture model aims to estimate posteriori probability of neighboring pixel method in image segmentation. We firstly apply the log-linearized Gaussian mixture to develop and determine the mixture and the mixture component of the Gaussian mixture model. Then, the posterior probabilities of each pixel are also identified by using neighboring pixel method. Secondly, employing maximum likelihood technique to simulate the statistic model under our algorithm framework aims to improve accuracy of segmented images and to reduce impacts of noise during image segmentation process. Our research results present good segmentation yields, and the segmented images are more accuracy comparing to the segmented images which obtained by other segmentation methods.

Keywords: Neighboring pixels, Log-linearized, Gaussian Mixture Model (GMM), Image Segmentation, Maximum Likelihood.

1 Introduction

Today, color image segmentation is useful in many applications in image processing and image recognition systems. The good segmentation results would help to identify regions of interest and objects in the scenes that is very beneficial to the subsequent image analysis or annotation. For example, many communication tasks require high compression ratio to save network resource. One possible way to realize the higher compression ratio is to discriminate objects in an image and compress only the targeted objects toward user's concerns. This makes image segmentation extremely important role in providing the necessary information. Several previous works have been carrying out for image segmentation by using threshold method [1]. However, it is not easy to determine and identify a proper threshold value. This is also the large disadvantage to threshold method, and in some cases a bad choice of a certain thresholds could alternate the quality of the segmentation and probably leads to a worse interpretation. An artificial neutral network is an approach applied in image

* Corresponding author.

segmentation in order to avoid this disadvantage. In the paper [2], the authors applied a feature vectors that are extracted from an image using a neural network. This method and model simulation do not place out spatial information, the spatial attributes of pixels are maximally used in this method. This method would help to minimize the distance between the feature vectors. The experiment results indicate that this method work well and lead to sub-optimal image segmentation.

Recently, with the expansion application of Gaussian mixture model (GMM), image segmentation based on GMM has become popular [3]. In this approach a mixture of multi-variant densities and the mixture parameters are estimated by using EM algorithm. However, a main drawback of this method is that the number of Gaussian mixture components is assumed known as prior, resulting not sensitive to noise of segmentation. The spatially variant finite model was proposed in [4]. In this model a maximum-a-posteriori (MAP) estimation is determined by using Markov random fields (MRF). The main advantage of MRF models is that prior information of the pixel labels can be imposed locally through clique potentials. Importantly, segmentation accuracy is quite sensitive to the initialization of segmentation algorithm, because of using the local optimization parameter estimation algorithms such as EM. Therefore, the initializations for these local algorithms have to be well selected and determined. This approach works well in minimizing the impacts of noise though the image segmentation process.

An advanced algorithm based on the GMM and the log-linear model is necessarily to be developed to improve image segmentation. Therefore our study objectives aim: 1) applying the log-linear model to a product of the mixture coefficient and the mixture component of the GMM. 2) using the local spatial interactions between neighboring pixels to reduce impacts of noise in image segmentation. The proposed method will be applied for segmenting synthetic and real world grayscale images. The robustness, accuracy and effectiveness of proposed model and other methods such as standard GMM, and K-means, and Mean-shift are compared to evaluate the advantages of the proposed method.

This paper is organized as follows. In section 2, the segmentation algorithm for image is presented. In section 3, the experimental results are presented and discussed. Finally, the conclusions are given in section 4.

2 Proposed Approach

2.1 Neighboring Pixels

In this paper, we use the local spatial interaction between neighboring pixels in a 3×3 window. For each of the i^{th} window, neighboring pixels are denoted by

$$X = (x_1x_1, x_1x_2, \dots, x_1x_d, x_2x_2, x_2x_3, \dots, x_2x_d, \dots, x_dx_d) \quad (1)$$

where x_2x_2 is the central pixel of k -th window and $x_1x_1, x_1x_2, x_1x_3, x_2x_1, x_2x_3, x_3x_1, x_3x_2, x_3x_3$ are called the neighboring pixels of the x_2x_2 .

For each window, the posterior probability $P(k \mid x)$ for all classes. with the central pixel x_2x_2 will belong to an certain class that has the largest posterior probability.

2.2 Log-linearized Gaussian Mixture Model

Here, a PDF $f(x)$ of a feature vector $x \in \Re^d$ is represented by a GMM with K classes:

$$f(x) = \sum_{k=1}^K \sum_{m=1}^{M_k} \alpha_{k,m} g(x; \mu^{(k,m)}, \Sigma^{(k,m)}) \quad (2)$$

$$\sum_{k=1}^K \sum_{m=1}^{M_k} \alpha_{k,m} = 1 \quad (3)$$

$$g(x; \mu^{(k,m)}, \Sigma^{(k,m)}) = (2\pi)^{-\frac{d}{2}|\Sigma^{(k,m)}|^{-\frac{1}{2}}} \times \exp \left[-\frac{1}{2} (x_2x_2 - \mu^{(k,m)})^T (\Sigma^{(k,m)})^{-1} (x_2x_2 - \mu^{(k,m)}) \right] \quad (4)$$

where $M_k (k=1, \dots, K)$ denotes the number of components of the class k ; $\alpha_{k,m}$ denotes a mixture coefficient or a mixing proportion of each component $\{k, m\}$ and $\mu^{(k,m)} \in \Re^d$ and $\Sigma^{(k,m)} \in \Re^{d \times d}$ represent the mean vector and the covariance matrix of each component $\{k, m\}$. Note that $|\cdot|$ represents the determinant.

Let us consider a problem to classify an observed vector x into one of K classes. The Bayes decision theory determines a specific class if a posteriori probability of the vector belonging to the class is larger than the ones to any other classes. Using the GMM of the PDF of x , the posteriori probability $P(k \mid x) (k=1, \dots, K)$ is given as

$$P(k \mid x) = \sum_{k=1}^K P(k, m \mid x) = \sum_{m=1}^{M_k} \frac{P(k, m) P(x, x \mid k, m)}{P(x)} \quad (5)$$

where $P(k, m)$ is the a priori probability of the class k and the component m , which corresponds to the mixing coefficient $\alpha_{k,m}$; and $P(x \mid k, m)$ is the PDF of x conditioned by the class k and the component m . Then, using Eq. (l), the posteriori probability $P(x \mid k, m)$ can be expressed as

$$\begin{aligned}
P(k, m | x) &= \frac{P(k, m) P(x | k, m)}{\sum_{k'=1}^K \sum_{m'=1}^{M_k} P(k' | m') P(x | k', m')} \\
&= \frac{\alpha_{k,m} g(x; \mu^{(k,m)}, \Sigma^{(k,m)})}{\sum_{k'=1}^K \sum_{m'=1}^{M_k} \alpha_{k',m'} g(x; \mu^{(k',m')}, \Sigma^{(k',m')})} \quad (6)
\end{aligned}$$

Since $g(x; \mu^{(k,m)}, \Sigma^{(k,m)})$ is the d-dimensional Gaussian distribution given as Eq. (3), using the mean vector $\mu^{(k,m)} = (\mu_1^{(k,m)}, \dots, \mu_d^{(k,m)})^T$ and the inverse of the covariance matrix $\Sigma^{(k,m)-1} = [s_{ij}^{(k,m)}]$, the numerator of the right side of Eq. (5) can be represented as $\alpha_{k,m} g(x; \mu^{(k,m)}, \Sigma^{(k,m)})$

$$\begin{aligned}
&g(x; \mu^{(k,m)}, \Sigma^{(k,m)}) \\
&= \exp\left[-\frac{1}{2} \sum_{j=1}^d \sum_{l=1}^j (2 - \delta_{jl}) s_{jl}^{(k,m)} x_j x_l + \sum_{j=1}^d \sum_{l=1}^d s_{jl}^{(k,m)} \mu_j^{(k,m)} x_l\right. \\
&\quad \left.- \frac{1}{2} \sum_{j=1}^d \sum_{l=1}^j \delta_{jl} s_{jl}^{(k,m)} \mu_j^{(k,m)} \mu_l^{(k,m)} - \frac{1}{2} \log |\Sigma^{(k,m)}| + \log \alpha_{(k,m)}\right] \quad (7)
\end{aligned}$$

where δ_{jl} is the Kronecker delta: $\delta_{ij} = 1$ when $i = j$ and $\delta_{ij} = 0$ when $i \neq j$.

Let us consider to linearize the right side of Eq. (6). Taking a logarithm of Eq. (6), we can get

$$\zeta_{k,m} \triangleq \log \alpha_{(k,m)} g(x; \mu^{(k,m)}, \Sigma^{(k,m)}) = \beta^{(k,m)^T} X \dots \dots \quad (8)$$

Where $X \in \Re^H$ and $\beta^{(k,m)} \in \Re^H$ are defined as from Eq. (1)

$$X = (x_1 x_1, x_1 x_2, \dots, x_1 x_d, x_2 x_2, x_2 x_3, \dots, x_2 x_d, \dots, x_d x_d)$$

$$\begin{aligned}
\beta^{(k,m)} &= (\beta_0^{(k,m)}, \sum_{j=1}^d s_{jl}^{(k,m)} \mu_j^{(k,m)}, \dots, \sum_{j=1}^d s_{jd}^{(k,m)} \mu_j^{(k,m)} \\
&\quad - \frac{1}{2} s_{l1}^{(k,m)}, -s_{l2}^{(k,m)}, -s_{ld}^{(k,m)}, \dots, -\frac{1}{2} s_{dd}^{(k,m)})^T \quad (9)
\end{aligned}$$

$$\begin{aligned}\beta_0^{(k,m)} = & -\frac{1}{2} \sum_{j=1}^d \sum_{l=1}^j \delta_{jl} s_{jl}^{(k,m)} \mu_j^{(k,m)} \mu_l^{(k,m)} \\ & -\frac{d}{2} \log 2\pi - \frac{1}{2} \log |\Sigma^{(k,m)}| + \log \alpha_{(k,m)}\end{aligned}\quad (10)$$

And the dimensionally is H defined as $H = 1 + d(d + 3)/2$. We can see that $\zeta_{k,m}$ can be expressed as a product of the coefficient vector $\beta^{(k,m)}$ and the modified input vector $X \in \Re^H$.

However, since $\sum_{k=1}^K \sum_{m=1}^{M_k} P(k, m | x) = 1$, the variable is $\zeta_{k,m}$ redundant. Then, a new variable $Y_{k,m}$ and a new coefficient vector $w^{(k,m)} \in \Re^H$ are introduced:

$$Y_{k,m} \triangleq \zeta_{k,m} - \zeta_{M,M_k} = (\beta^{(k,m)} - \beta^{(K,M_k)^T}) X = w^{(k,m)} X \quad (11)$$

where $w^{(K,M_k)} = 0$. It should be noted that $w^{(k,m)}$ becomes a weight coefficient with no constraints. Then the posterior probability

$$P(k, m | x) = \frac{\exp[Y_{k,m}]}{\sum_{k'=1}^K \sum_{m'=1}^{M_{k'}} \exp[Y_{k',m'}]} \quad (12)$$

As mentioned above, by taking a logarithm of the PDF of each component, the posterior probability can be expressed using the variable $Y_{k,m}$ that is a linear sum of the modified input vector X and the coefficient vector $w^{(k,m)}$: that is, the GMM is log-linearized.

Using the data image, a log-likelihood function L can be derived as

$$E = -\ln L - \sum_{k=1}^K \ln \left\{ \sum_{m=1}^{M_k} g(x; \mu^{(k,m)}, \Sigma^{(k,m)}) P(k, m | x) \right\} \quad (13)$$

3 Experimental Results

In this section, we evaluate the segmentation performance of the proposed algorithm by using a subset of the Berkeley image segmentation dataset and benchmark [8] (Fig. 1). This benchmark dataset consists of a set of natural images along with their ground truth segmentation maps which were provided by different individuals. In this experiment, we employ the probabilistic rand (PR) index [9] to quantitatively evaluate the performance of the proposed algorithm. Let $GT = \{GT_1, GT_2, \dots, GT_k\}$ denote a set of

ground truth images and G the segmentation result to be evaluated the PR index is given by

$$PR(G_s, GT) = \frac{2}{M(M-1)} \sum_{i,j} [c_{ij} p_{ij} + (1 - c_{ij})(1 - p_{ij})] \quad (14)$$

where $c_{ij}=1$ if pixels i and j belong to the same class in G_s , otherwise. M is the number of image pixels, and p_{ij} is the ground truth probability of pixels i and j belong to the same class. The PR index takes values between 0 and 1 with the values close to 1 means a good segmentation result, and close to 0 means a bad result. Unnikrishnan and Hebert in [10] have proved that the PR index is robust to segmentation maps resulting from ground truth segment splitting or merging.

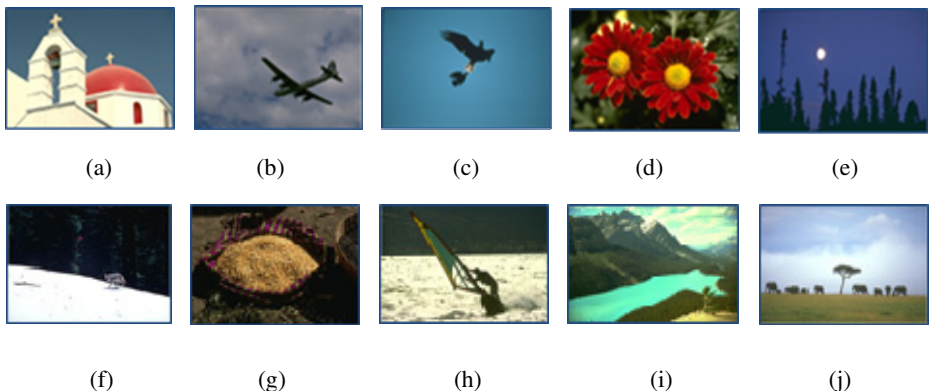


Fig. 1. Images from the Berkeley's image segmentation dataset. (a) 118035, (b) 2096, (c) 135069, (d) 124084, (e) 238011, (f) 167062, (g) 58060, (h) 62096, (i) 176035, (j) 253036.

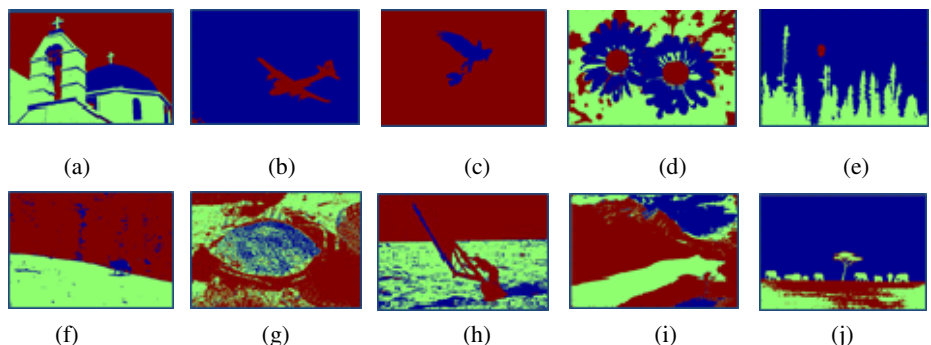


Fig. 2. Image segmentation results obtained by employing the proposed method. (a) 118035, (b) 2096, (c) 135069, (d) 124084, (e) 238011, (f) 167062, (g) 58060, (h) 62096, (i) 176035, (j) 253036.

Figure 3 presents the segmentation results obtained from our proposed method and 4 other methods by using the real world image as the input.

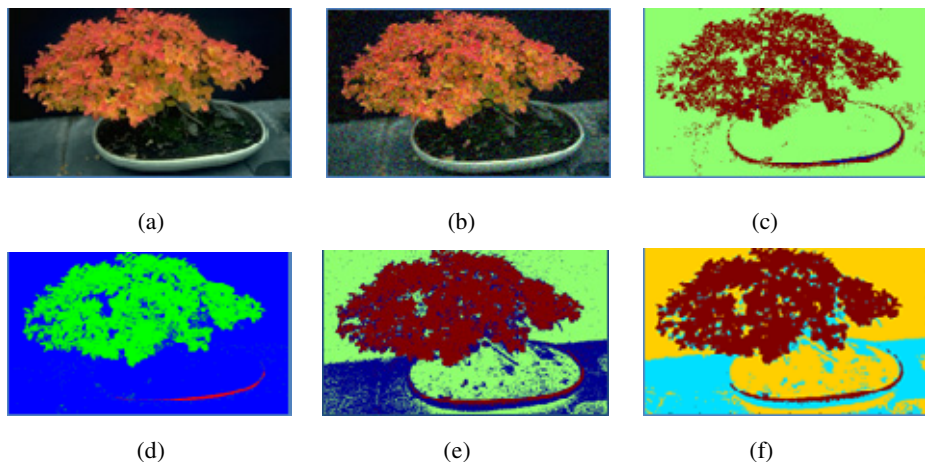


Fig. 3. 481x321 color testing data, (a) Original image, (b) Standard deviation of Gaussian noise (0 mean, 0.001 variance), (c) K-means (PR=0.670), (d) Mean shift (PR=0.691), (e) Standard GMM (PR=0.723), (f) Our method (PR=0.8184).

Table 1. The PR indexes of segmentation applying our proposed method and other 4 methods on Berkeley images

PR indexes					
Image	k	K-means	Mean-shift	Standard GMM	The proposed algorithm
118035	3	0.624	0.688	0.706	0.784
2096	2	0.980	0.980	0.982	0.984
135069	2	0.983	0.983	0.983	0.985
124084	3	0.520	0.624	0.663	0.730
238011	3	0.714	0.769	0.800	0.815
167062	3	0.630	0.635	0.720	0.786
58060	3	0.552	0.588	0.596	0.605
62096	3	0.601	0.615	0.628	0.642
176035	3	0.754	0.760	0.769	0.771
253036	3	0.630	0.635	0.635	0.660
Mean	-	0.688	0.727	0.748	0.762

Table 1 presents the PR values indicating the efficiencies of image segmentation obtained from our proposed algorithm and from other algorithms, namely K-means, Mean-shift and Standard GMM. These show that using the same number of segmentation, presented in Eq. 8, the PR values obtained from our method is slightly

higher than the PR values obtained from other methods for the same tested images. Importantly, by comparing the images in Figure 1 and 2, our method results in Figure 2 show that the developed algorithm is efficiently applied for image segmentation at different class regions results, as well as can preserve well boundary information for all cases.

In another experiment, our method is tested robustness and efficacy with 10 iterations though the segmentation process, and the testing process is implemented by adding noise into the original images. Figure 3 presents the image segmentation results of our research method and other methods for the same one image extracted from the Berkeley Segmentation Dataset. Figure 3a shows the original image with 3 classes. Figure 3b is the result that obtained by using Gaussian noise (0 mean, 0.001 variance). Figure (3c-3e) present results obtained from 3 methods (with 15 iterations for each method). Figure 3f presents our study result. Although the tested images during our experiment process are somehow degraded by adding high levels of noise, the results show that our method provides better images than other methods. Moreover, our proposed method demonstrates robustness with respect to noise yielding a better segmentation result.

4 Conclusions

In this paper, we proposed a new mixture model based on the log-linearized Gaussian mixture model, which can estimate the posterior probability for image segmentation. Here we have presented experimental results of the proposed model and also presented a comparison of image segmentation results between our method and three other algorithms to validate our research method. Experimental results show that the proposed algorithm has generally satisfying properties for image segmentation, and it outperforms the competing algorithms in terms of robustness to efficiency and preservation of target boundary information. Finally, in this paper, the number of classes (K) is manually selected. In the future, we would like to further our study on how to automatically optimize this parameter.

Acknowledgments. This work was supported by the National Research Foundation of Korea (NRF) grant funded by the Korea government (MEST)(2013-006535). Also this research was supported by the MSIP (Ministry of Science, ICT&Future Planning), Korea, under the ITRC (Information Technology Research Center) support program (NIPA-2013-H0301-13-3005) supervised by the NIPA (National IT Industry Promotion Agency).

References

- [1] Glasbey, C.A.: An Analysis of Histogram-based Thresholding Algorithm. *CVGIP: Graphical Model and Image Processing* 55, 532–537 (1993)
- [2] Amartur, S.C., Piraino, D., Takefuji, Y.: Optimization neural networks for the segmentation of magnetic resonance images. *IEEE Transaction on Medical Imaging* 11, 215–220 (1992)

- [3] MacLachlan, G., Peel, D.: Finite Mixture Models. John Wiley and Sons, New York (1997)
- [4] Sanjay-Gopal, S., Hebert, T.: Bayesian pixel classification using spatially variant finite mixtures and the generalized EM algorithm. *IEEE Trans. Image Process.* 7(7), 1–14 (1998)
- [5] Gonzalez, R., Woods, R.E.: Digital Image Processing, 3rd edn. Pearson (2010)
- [6] Tosuji, T., Ichinobe, H., Fukuda, O., Kaneko, M.: A Maximum Likelihood Neural Network Based on a Log-linearized Gaussian Mixture Model. In: Proc. IEEE Conf. Neural Network, vol. 3, pp. 1293–1298 (1995)
- [7] Bishop, C.M.: Pattern Recognition and Machine Learning, pp. 240–242. Springer (2006)
- [8] Martin, D., Fowlkes, C., Tal, D., Malik, J.: A database of human segmented natural images and its application to evaluating segmentation algorithms and measuring ecological statistics. In: Proc. Int. Conf. Comp Vision, Canada, pp. 416–423 (July 2001)
- [9] Unnikrishnan, R., Pantofaru, C., Hebert, M.: A measure for objective evaluation of image segmentation algorithms. In: Proc. IEEE Conf. Comp. Vis. Pattern Recog., vol. 3, pp. 34–41 (June 2005)
- [10] Unnikrishnan, R., Hebert, M.: Measures of similarity. In: Proc. IEEE Workshop Comput. Vis. Appl., pp. 394–400 (January 2005)

Uncertainty Analysis of LIDAR and Panoramic Camera Calibration

Angel-Iván García-Moreno, José-Joel Gonzalez-Barbosa,
Francisco-Javier Ornelas-Rodriguez, and Juan B. Hurtado-Ramos

Research Center for Applied Science and Advanced Technology (CICATA)
Instituto Politécnico Nacional, Cerro Blanco 141 Col. Colinas del Cimatario, Querétaro, México
jgonzalezba@ipn.mx

Abstract. Terrestrial platforms for 3D reconstruction typically combine several data acquisition systems such as lasers, cameras and inertial systems. However the geometrical combination of different sensors requires their calibration and data fusion. These topics are an important task for vision-based systems since it estimates the values of sensor model parameters, such as cameras. The uncertainty of these parameters must be known in order to evaluate the error of the final calibration and their applications. The aim of this paper is to present a method to compute the calibration of both sensors. A new calibration pattern, visible to both sensors is used. Correspondence is obtained between each laser point and its position in the image, the texture and color of each point of LIDAR can be know. Experimental results are presented for data collected with the platform integrated with a 3D laser scanner and a panoramic camera system.

1 Introduction

Nowadays the urban environment reconstruction has rapidly grown using terrestrial platforms for the scanning process. One of the most important challenges is the fusion of information from multiple sensors in which the main step is the calibration of sensors. The calibration process works as a closed form solution followed by a non linear refinement to give the best solution for a given set of data. Different sensors are used recently to get information like depth laser sensors, CCD cameras and inertial systems primarily [7] [14]. For example, camera parameters are used in many applications which involve geometric computation to extract metric information from images, these parameters are used to estimate the tridimensional position of a feature in the image. The precision of the position of the feature in the image in the 3D scene depends on the accuracy of the computed parameters which tend to vary for many reasons, such as lens distortion or the camera focus calculation.

The estimation of LIDAR (Light Detection and Ranging) and camera intrinsic parameters is a nonlinear problem that can be solved in different ways. A novel algorithm has been proposed [8] for joint estimation of both the intrinsic parameters of the laser sensor and the LIDAR-camera transformation. Specifically, measurements of a calibration plane are used at various configurations to establish geometric constraints between the LIDARs intrinsic parameters and the LIDAR-camera 6 degrees of freedom (d.o.f.) relative transformation. These measurement constraints are processed to estimate the

calibration parameters as follows: First, an initial estimate for the intrinsic and extrinsic calibration parameters are computed in two steps. Then, a batch iterative (nonlinear) least-squares method was employed to refine the accuracy of the estimated parameters. Another method uses a planar checkerboard pattern proposed in [9] [10], the authors defines the rotation matrix between the sensor laser and camera as achieved moving the platform and observing the resulting motion of the sensors, this step attempts to solve the well-known homogeneous transform, translation is calculated using a commonly least-squares estimation algorithm according to the corners of the pattern, detected by both sensors. Besides the problem of calibration in [13] provide a solution for the occlusion problem that arises in conjunction with different view points of the fused sensors, they approach first performs a synchronization of both sensors to allow for moving objects which incorporates an inertial correction of the LIDAR data and an automatic trigger mechanism depending on the view direction of the camera, the occlusion detection algorithm uses 2D convex hulls derived from a 3D object segmentation to allow for a visibility check of projected 3D LIDAR data.

Not only square flat patterns are used for calibration between these two sensors, in [12] they use a circle-based calibration object because its geometry allows to obtain an accurate estimation pose in the camera frame and the camera intrinsic parameters. Authors use a linear minimization of the Euclidian distance error between the 3D circle center point sets, and then they first generate the 3D circles of the n poses estimated by the camera, which consists in computing m points of each estimated circle pose by using the 3D circle center and an orthonormal base lying in circle's plane. Another approach uses a conic based geometry object to calibrate 2D/3D laser sensors [2].

2 Platform Projection Model

In this work, two types of sensors are used, *Velodyne HDL-64E* laser scanner and *Point Grey Ladybug2* spherical digital camera. The laser scanner operates by pulsing a laser diode for a short duration (typically 4 nanoseconds) and precisely measuring the amount of time it takes for the pulse to travel to an object, reflect off that object and return to a highly sensitive photodetector and camera system is a high resolution omnidirectional sensor, it has six 0.8 – *Megapixel* cameras, with five CCDs positioned in a horizontal ring and one positioned vertically, that enables the system to collect video from more than 75% of the full sphere.

The goal of the method is to find homogeneous transformation between the pinhole camera and the LIDAR in order to fuse the measurements from both sensors in urban digitalized environment applications.

Data are collected by a mobile platform using the data collection vehicle shown in Figure 1. This mobile mapping system is composed of a LIDAR sensor and a video camera.

This research focuses the uncertainty analysis of the registration of LIDAR and panoramic images.

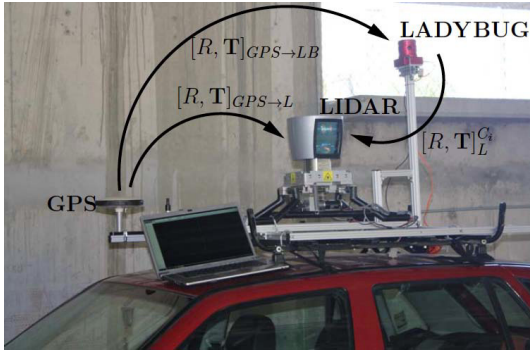


Fig. 1. Sensor platform composed of LIDAR Velodyne HDL-64E (L) *Ladybug2* (LB) and GPS. *Ladybug2* spherical digital video camera system has six cameras (C_i). $[R, T]_L^{C_i}$ represent translation and rotation of the LIDAR and six camera frames of the *Ladybug2*.

2.1 Panoramic Camera and LIDAR Model

The six cameras frames of the *Ladybug2* are represented by C_i (where $i = 1, \dots, 6$). The 3D points acquired by the LIDAR (\mathbf{X}^L) are transformed from LIDAR frame to camera frames by $[R_L^{C_i}, \mathbf{T}_L^{C_i}]$, called the extrinsic parameters (see Figure 2).

A 2D point in the camera C_i is denoted by $\mathbf{u}^{C_i} = [u^{C_i} \ v^{C_i}]^T$. A 3D point in the LIDAR frame is denoted by $\mathbf{X}^L = [X^L \ Y^L \ Z^L]^T$. We use $\hat{\mathbf{x}}$ to denote the augmented vector by adding 1 as the last element: $\hat{\mathbf{u}}^{C_i} = [u^{C_i} \ v^{C_i} \ 1]^T$ and $\hat{\mathbf{X}}^L = [X^L \ Y^L \ Z^L \ 1]^T$. A camera is modeled by the usual pinhole: The image \mathbf{u}^{C_i} of a 3D point \mathbf{X}^L is formed by an optical ray from \mathbf{X}^L passing through the optical center C_i and intersecting the image plane. The relationship between the 3D point \mathbf{X}^L and its image projection \mathbf{u}^{C_i} is given by

$$s\hat{\mathbf{u}}^{C_i} = A^{C_i}[R_L^{C_i}, \mathbf{T}_L^{C_i}]\hat{\mathbf{X}}^L = P_L^{C_i}\hat{\mathbf{X}}^L \quad (1)$$

$$\text{with } A^{C_i} = \begin{bmatrix} -k_u & f & 0 & u_0 & 0 \\ 0 & k_v & f & v_0 & 0 \\ 0 & 0 & 1 & 0 & 0 \end{bmatrix}^{C_i}$$

$$\text{and } P = A^{C_i}[R_L^{C_i}, \mathbf{T}_L^{C_i}]$$

where s is an arbitrary scale factor, $[R_L^{C_i}, \mathbf{T}_L^{C_i}]$, called the extrinsic parameters, is the rotation and translation which relates from LIDAR system L to camera system C_i , and A^{C_i} is called intrinsic matrix for the camera C_i , with (u_0, v_0) the coordinates of the principal point, $f k_u(\alpha)$ and $f k_v(\beta)$ the scale factors in image u and v axes. The 3×4 matrix $P_L^{C_i}$ is called the camera projection matrix, which mixes both intrinsic and extrinsic parameters.

3 Sensors Calibration and Uncertainty

The importance of the small errors in the feature points on the calibration process and the influence of the incorrect estimation of some camera parameters on the final calibration are addressed in this section. The uncertainty assessment of the calibration parameters, are important in high-accuracy dimensional measurement and data fusion.

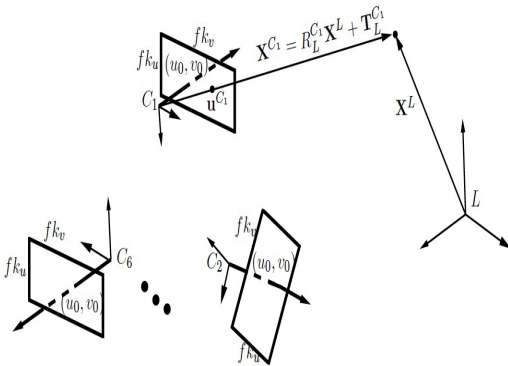


Fig. 2. LIDAR frame L and the six pinhole camera model

Since the noise from the digital camera and other environment conditions are random, the extracted feature points are considered to be random measurements. Camera parameters obtained by minimizing an objective function have a level of uncertainty. Vision-based measurement is a process that transforms the target from the image coordinate system to the C_i according to the camera parameters. Therefore, the variations in the estimated parameters affect all the measurements that are subjected to this transformation, and the knowledge of the camera parameters uncertainties plays a key role in the design of measurement systems with high-precision requirements [16] [6].

According to [5] to perform this analysis it is necessary to know the value of the uncertainty of input quantities:

- uncertainty of input pixel localization (σ_{2d})
- uncertainty of target point coordinates (σ_{3d})

The σ_{2d} depends on the image acquisition system and the algorithm used to extract the pixel coordinates. The uncertainty is due to many factors such as lens diffraction and propagates through subsequent algorithms, such as edge detectors. Although an analytical evaluation of the uncertainty of the pixel coordinates would not be straightforward, it can be easily determined experimentally. This procedure includes two steps: 1) image acquisition of a view of the target and 2) localization of the reference target points. These two steps are repeated several times. Then, σ_{2d} is evaluated as standard deviations of the pixel coordinates of the target points. The value of σ_{3d} depends on the technical characteristics of the realization of the target and of the instrument used in measuring the coordinates of its points.

To evaluate the uncertainty in this work, the variances of the camera parameters are estimated by Monte Carlo simulations, adding Gaussian noise to the extracted feature points. These noisy points are utilized to determine the camera parameters. The simulation was performed 2,000 times (n) and the dispersion for each camera parameter is obtained by calculating the standard deviation.

Algorithm 1. Algorithm used to compute the uncertainty dispersion.

Monte Carlo simulation
Input: world and image feature points matrix to compute Pd
Output: intrinsic parameters matrix $[\sigma_{2d}^p]_{9 \times n}$

```

 $\xi \leftarrow std(Pd)$ 
 $tam \leftarrow sizeof(P_{CS})$ 
for all  $i \leftarrow 1 : n$  do
     $n_r \leftarrow randomNoise(tam)$ 
     $N \leftarrow \frac{n_r}{std(n_r)}$ 
     $P_n \leftarrow P_i + \xi \cdot n_r$ 
     $x_{p,i} \leftarrow getCalibration(P_n, Pe)$ 
end for
 $\sigma_{2d}^p = std(x_p)$ 

```

The six cameras of the *Ladybug2* are calibrated with Zhang's method [15], in which the intrinsic parameters (A^{C_i}) of the cameras are computed. The LIDAR is calibrated using the method proposed in [3]. We use a pattern which facilitates the extraction of the same point in camera and LIDAR data. This pattern is shown in Figure 6 and it is composed of white rhombuses and rhombus voids which have the black appearance of the background. Figure 3 shows the relationship between the pattern W_i camera C_i and LIDAR L . The transformation between LIDAR and cameras shown in the equation 1 is computed by:

$$[R_L^{C_i}, \mathbf{T}_L^{C_i}] = [R, \mathbf{T}]_W^{C_i} * ([R, \mathbf{T}]_W^L)^{-1} \quad (2)$$

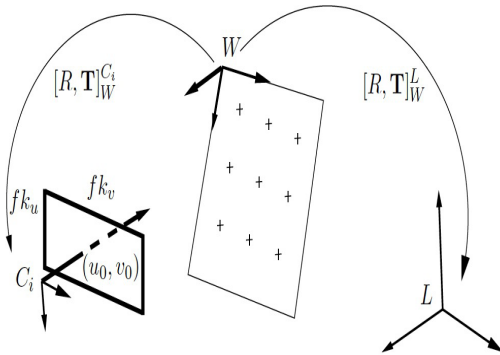


Fig. 3. The extrinsic parameters $[R, \mathbf{T}]_W^{C_i}$ are computed by Zhang's method and $[R, \mathbf{T}]_W^L$ are computed with the Algorithm shown in Algorithm 2

In the algorithm shown in Algorithm 2, the function *transform_to_XYZ* transform the LIDAR data to X, Y, Z points using the method proposed in [3]. RANdom SAMple Consensus (RANSAC) algorithm is widely used for plane detection in point cloud

Algorithm 2. Algorithms used in this work.

For each camera C_i do:

Algorithm to get of extrinsic LIDAR parameters.

Input: raw point clouds data

Output: extrinsic parameters between LIDAR and world framework

for all nRawPointCloud **do**

$nPointCloud \leftarrow transform_to_XYZ(nRawPointCloud)$

$(nPatterPointCloud, \Pi) \leftarrow RANSAC(nPointCloud)$

$nProjPattern \leftarrow proj_to_normal_pattern(nPatterPointCloud)$

$[R, T]_W^L \leftarrow MaximizingFunction(nProjPattern, \Pi)$

end for

Algorithm to get extrinsic and intrinsic Ladybug2 parameters.

Input: pattern images

Output: intrinsic and extrinsic parameters between camera and world framework

for all nImage **do**

$[R, T]_W^{C_i}, A^{C_i} \leftarrow use\ Bouguet's\ camera\ calibration\ Toolbox$

end for

LIDAR and Ladybug2 calibration

Input: extrinsic parameters for both sensors

Output: extrinsic parameters between camera and LIDAR

for all nImage **do**

$[R_L^{C_i}, T_L^{C_i}] = [R, T]_W^{C_i} * ([R, T]_W^L)^{-1}$

end for

data. The principle of *RANSAC* algorithm consists to search the best plane among a 3D point cloud. For this purpose, it selects randomly three points and it calculates the parameters of the corresponding plane. Then it detects all points ($nPatternPointCloud$) of the original cloud belonging to the calculated plane (Π), according to a given threshold. The *proj_to_normal_pattern* algorithm projected the points $nPatternPointCloud$ to plane Π . In function *MaximizingFunction*, we build an artificial calibration pattern ($Pattern(radius, \theta)$) using the dimension of the pattern calibration. The artificial pattern can be moved on the plane Π rotating an angle θ and moving a distance $radius$ in the direction of rotation. The $nProjPattern$ points are comparing with the artificial pattern plane, the maximum comparison allows us to calculate the distance ($radius$) and angle (θ) in the plane where the reference pattern placed. Using the plane equation Π and ($radius, \theta$) we compute the $[R, T]_W^L$ parameters.

4 Results

The results are presented in three stages, the computation of extrinsic parameters of the LIDAR, extrinsic parameters between each camera and LIDAR and the uncertainty analysis. For practical purposes, we show the results for only one camera, however the *Ladybug2* is formed by six cameras.

4.1 Algorithm for Computing of Extrinsic LIDAR Parameters

Figure 4 shows the extracted points (blue points) using the *RANSAC* algorithm projected onto plane Π using the *project_to_normal_pattern* algorithm. The red circle in Figure 4 represent the position of the artificial pattern plane. This position is computed with the algorithm *MaximizingFunction*. The *MaximizingFunction* computes the matches between the real pattern data and the synthetic pattern, this is shown in Figure 5. The rotation and translation are performed on the plane Π , and the translation is carried out in θ orientation.

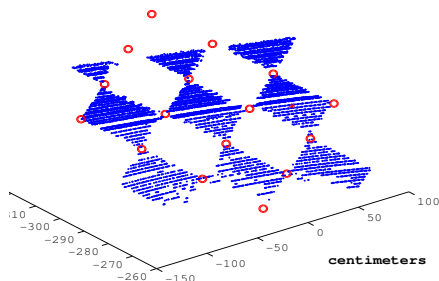


Fig. 4. Extraction of the calibration pattern using the *RANSAC* algorithm and projection onto the plane Π

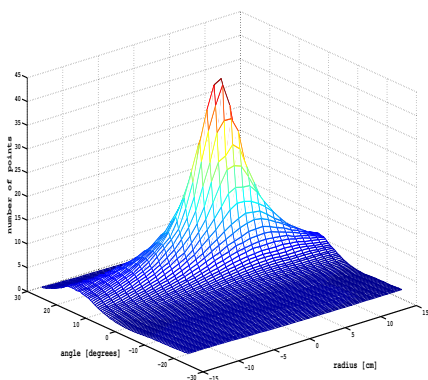


Fig. 5. The maximization function computes the number of points of the real pattern matches with the synthetic pattern

The rigid transformation of a 3D point in the LIDAR frame, L , into the world frame (pattern frame) is defined by the rotation matrix and translation vector ($[R, \mathbf{T}]_W^L$):

$$R_W^L = \begin{bmatrix} 0.7395 & 0.6724 & -0.0272 \\ 0.6713 & -0.7399 & -0.0420 \\ -0.0484 & 0.0127 & -0.9987 \end{bmatrix}; \quad \mathbf{T}_W^L = \begin{bmatrix} 137.98 \\ 1212.81 \\ 5476.10 \end{bmatrix}$$

4.2 LIDAR and Ladybug2 Calibration

The rigid transformation between camera and LIDAR frame was computed using Equation 2. In Figure 6, the pattern acquired by the LIDAR is transformed onto the image frame using the extrinsic parameters $[R_L^{C_i}, \mathbf{T}_L^{C_i}]$. This transformation allows us to reference in the camera the points acquired by the LIDAR. The projection is completed using the intrinsic camera parameters A^{C_i} . Figure 7 (a) shows the LIDAR data projected onto the image that corresponds to a wooden plank (our test data). A better view of the accuracy of our work is shown in Figure (b). In order to evaluate the calibration between the LIDAR and camera transformation, we acquired a plank with both sensors. The plank is segmented in the point cloud and the image. The 3D data of the plank is projected onto the image data and the matches are computing. The number of points that correspond to the plank are 1,859, however 34 points are not matches with their respective data in the image, which represents an error of 1.89%.

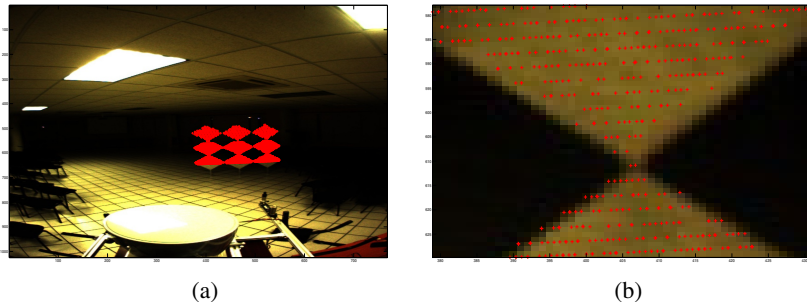


Fig. 6. (a)The red points are acquired by the LIDAR and projected onto the image. (b) Zoom on one section of the image target.

4.3 Uncertainty Analysis

According to the standard [1], the uncertainty indicates the interval of the values that the quantity to be measured (the measurand) may assume after all systematic biases have been corrected. When uncertain data are used as inputs to a numerical algorithm, the standard uncertainty of the algorithms results can be evaluated either with an *a posteriori* approach, i.e., with a statistical analysis of the sample of results obtained with a significant number of repeated runs of the algorithm, or with an *a priori* or analytical approach, i.e., developing analytical relationships describing how uncertainty propagates through the algorithm from inputs to outputs. The latter requires only one

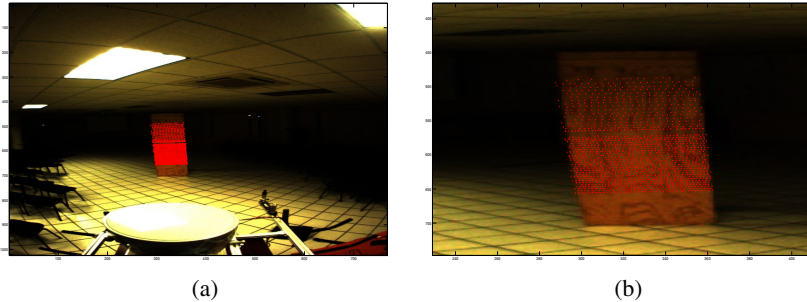


Fig. 7. (a) Image and point cloud test data matched. (b) Zoom-in over our test data

run of the algorithm and then is the preferred approach when measurement times are constrained, such as in online measurements.

Algorithm 1 shows an algorithm to compute the uncertainty, where Pd are the differences of the feature points in the camera system and the coordinates of feature points in world camera system transformed with the original intrinsic and extrinsic parameters. tam is the size of the camera system feature point matrix, $randomNoise$ function generate normally distributed pseudorandom numbers. P_n are the new feature points with noise, $x_{p,i}$ has the new calculated parameters after each iteration and σ_{2d}^p are the uncertainty value.

After Monte Carlo simulation we obtained the results shown in Table 1, in which we computed the intrinsic parameters, principal point (u_0, v_0) , focal length (α, β) , and distortion coefficients.

Table 1. Uncertainty camera extrinsic and intrinsic parameters

	Translation (mm)		Rotation (rad)		Focal (mm)	Image center (px)
mean	-125.82 -21.50 339.43		-2.22 -2.14 -2.13		(551.34, 550.81)	(388.61, 506.62)
std	0.0012 0.0017 0.0075		3.88 4.37 $\times 10^{-6}$ 4.44		(0.0013, 0.0013)	(0.0025, 0.0029)

Table 2. Uncertainty LIDAR-Ladybug2 extrinsic parameters $[R, T]_L^{C_i}$

	Translation (mm)		Rotation (rad)	
mean	-179.13 20.26 409.45		-2.00 -2.18 0.25	
std	0.0003 0.0034 0.0034		0.049 0.095 $\times 10^{-6}$ 0.071	

5 Conclusions and Future Work

Typically, sensor calibration in a surveying applications is performed once, and the same calibration is assumed to be constant for rest of the life of that particular sensor platform. However, for reconstruction applications where the sensors are used in urban terrain, with accident conditions, the assumption that the sensor calibration is not altered during a task is often not true. Although we should calibrate the sensors before every task, it is typically not practical if it is necessary to setup a calibration environment every time. Our method, being free from any such constraints, can be easily used to fine tune the calibration of the sensors *in situ*, which makes it applicable to in-field calibration scenarios.

We provide a uncertainty analysis for a new extrinsic calibration method for a multiple sensor platform. By using a plane calibration target, extrinsic calibration between sensors and intrinsic camera calibration can be effectuated simultaneously. The results obtained in real data tests illustrate an appropriate and accurate projection of the LiDAR data. Future work is oriented toward the estimate of the confidence intervals in the calibration method and the propagation error in data sensor fusion for texture 3D data.

In addition future work focus on the calibration of the sensors online and the 3D data texturization in large scale environments.

References

1. Evaluation of Measurement Data—Guide to the Expression of Uncertainty in Measurement. JCGM (2008)
2. Almeida, M., Dias, P., Oliveira, M., Santos, V.: 3d-2d laser range finder calibration using a conic based geometry shape. In: Campilho, A., Kamel, M. (eds.) ICIAR 2012, Part I. LNCS, vol. 7324, pp. 312–319. Springer, Heidelberg (2012)
3. Atanacio-Jiménez, G., González-Barbosa, J.J., Hurtado-Ramos, J.B., Ornelas-Rodríguez, F.J., García-Ramírez, H., Jiménez-Hernández, T.F.J., González-Barbosa, R.: Lidar velodyne hdl-64e calibration using pattern planes. Int. J. Adv. Robot. Syst. 8, 70–82 (2011)
4. Bouguet, J.Y.: Camera calibration toolbox for Matlab (2008)
5. Di Leo, G., Liguori, C., Paolillo, A.: Covariance propagation for the uncertainty estimation in stereo vision. IEEE Transactions on Instrumentation and Measurement 60(5), 1664–1673 (2011)
6. Koppaparu, S., Corke, P.: The effect of noise on camera calibration parameters. Graphical Models 63(5), 277–303 (2001)
7. Mei, C., Rives, P.: Calibration between a central catadioptric camera and a laser range finder for robotic applications. In: Proceedings 2006 IEEE International Conference on Robotics and Automation, ICRA 2006, pp. 532–537. IEEE (2006)
8. Mirzaei, F.M., Kottas, D.G., Roumeliotis, S.I.: 3d lidar-camera intrinsic and extrinsic calibration: Observability analysis and analytical least squares-based initialization. International Journal of Robotics Research 31(4), 452–467 (2012)
9. Nunez, P., Drews Jr., P., Rocha, R., Dias, J.: Data fusion calibration for a 3d laser range finder and a camera using inertial data. In: European Conference on Mobile Robots, vol. 9, p. 9 (2009)

10. Pandey, G., McBride, J., Savarese, S., Eustice, R.: Extrinsic calibration of a 3d laser scanner and an omnidirectional camera. In: Intelligent Autonomous Vehicles, vol. 7, pp. 336–341 (2010)
11. Ricolfe-Viala, C., Sánchez-Salmerón, A.-J.: Uncertainty analysis of camera parameters computed with a 3d pattern. In: Roli, F., Vitulano, S. (eds.) ICIAP 2005. LNCS, vol. 3617, pp. 204–211. Springer, Heidelberg (2005)
12. Rodriguez, F., Fremont, V., Bonnifait, P., et al.: Extrinsic calibration between a multi-layer lidar and a camera. In: IEEE International Conference on Multisensor Fusion and Integration for Intelligent Systems, MFI 2008, pp. 214–219. IEEE (2008)
13. Schneider, S., Himmelsbach, M., Luettel, T., Wuensche, H.J.: Fusing vision and lidar-synchronization, correction and occlusion reasoning. In: 2010 IEEE Intelligent Vehicles Symposium (IV), pp. 388–393 (2010)
14. Underwood, J., Scheding, S., Ramos, F.: Real-time map building with uncertainty using colour camera and scanning laser. In: Proceedings of the 2007 Australasian Conference on Robotics and Automation (2007)
15. Zhang, Z.: A flexible new technique for camera calibration. IEEE Transactions on Pattern Analysis and Machine Intelligence, 1330–1334 (2000)
16. Zhu, L., Luo, H., Zhang, X.: Uncertainty and sensitivity analysis for camera calibration. Industrial Robot: An International Journal 36(3), 238–243 (2009)

An Implementation of High Speed DCT and Hadamard Transform for H.264

Bui An Dong and Huynh Quoc Thinh

Faculty of Electronics and Telecommunications, HCMC University of Science, Vietnam
badong@hcmus.edu.vn

Abstract. The focus of this paper is the improvement of performance of the high speed forward integer DCT architecture for H.264 and Hadamard for luma in intra prediction. The DCT and Hadamard architecture are the same architectures, a serial architecture and pipeline processing, includes two 1-D architectures. Each architecture uses six adders and four shifters (DCT) or one shifter (Hadamard). They can operate simultaneously for high-throughput processing. The proposed DCT and Hadamard algorithms are verified by Matlab and VCS tool of Synopsys. Then the design is synthesized by Design Compiler with 90nm CMOS technology. The DCT and Hadamard core requires only 5103 logic cells (DCT core uses 2170 logic cells; Hadamard core uses 2392 logic cells, and other cores use 540 logic cells) and needs 24 clock cycles to finish one 4x4 DCT or Hadamard block at pipeline mode. Its frequency can operate at 250MHz.

Keywords: DCT, Hadamard, H.264, HDTV, MPEG.

1 Introduction

H.264, an advanced compression standard currently being developed by the JVT (Joint Video Team) and was standardized in 2003, is widely used as: HDTV, mobile digital TV, satellite TV, TV conference ... By the transmission bit rate can be reduced by 50% compared with the previous standards, H.264 requires high complexity of encoding and decoding system. In addition to other complex algorithms, H.264 uses the Integer Discrete Cosine transform. It is performed on integer more accurate and faster than the calculation of the real numbers with floating point or static point.

The parallel DCT architecture is high-speed. In contrast, the serial DCT architecture saves more power. Today, mobile applications require high speed and low-power. Therefore, this paper proposes a new serial DCT architecture. These architectural design test algorithms in Matlab and the results are compared with hardware design simulate in Synopsys tools with process 90nm of Synopsys.

As a result, the DCT hardware resources are reduced more than 58% compared with parallel DCT architecture [5] and its clock cycle is reduced more than 14.6% compared with serial DCT architecture [3]. Besides, Hadamard hardware resources are less than approximate 60% compared with architecture [6] and speed increases of 2.5 times and 1.7 times compared with architecture [6] and [8].

This paper is organized as follows: in section 2, the background of DCT transforms and Hadamard transforms for 16x16 block in intra prediction, as supported by the H.264 standard and the hardware architecture of forward DCT and Hadamard transforms. Results of simulation and synthesis are described in section 3. Section 4 is conclusions.

2 Experimental

2.1 Algorithms

The 4x4 forward DCT transforms is defined as:

$$Y_{ij} = C X C^T \quad (1)$$

Where X is a 4x4 pixel block; C is:

$$C = \begin{pmatrix} 1 & 1 & 1 & 1 \\ 2 & 1 & -1 & -2 \\ 1 & -1 & -1 & 1 \\ 1 & -2 & 2 & -1 \end{pmatrix}$$

The 4x4 forward DCT transform is used for all of intra and inter mode. Similarly, the 4x4 forward Hadamard transform is only used for luma mode in intra prediction and it is defined as:

$$K_{ij} = (K M K^T)/2 \quad (2)$$

Where M is 4x4 DC block, includes DC values which is transformed DCT in luma mode of intra prediction; K is:

$$K = \begin{pmatrix} 1 & 1 & 1 & 1 \\ 1 & 1 & -1 & -1 \\ 1 & -1 & -1 & 1 \\ 1 & -1 & 1 & -1 \end{pmatrix}$$

2.2 Experimental

To further simplify the computation, the scalar multiplication is integrated into the quantization unit in H.264/AVC. We have only to implement $CX C^T$ in the transform engine.

The 2D-DCT is separated into two 1D-DCTs. Firstly, the input data is transformed by column, and then the obtained results are transposed. Finally, they are transformed again by row.

Consider 1D-DCT and 2D-DCT as figure 1. The transform is separate from two stages: buffer stage and record stage. The algorithm is shown below figure with one node is an addition, and the multiplication with 2 is replaced by a shifter.

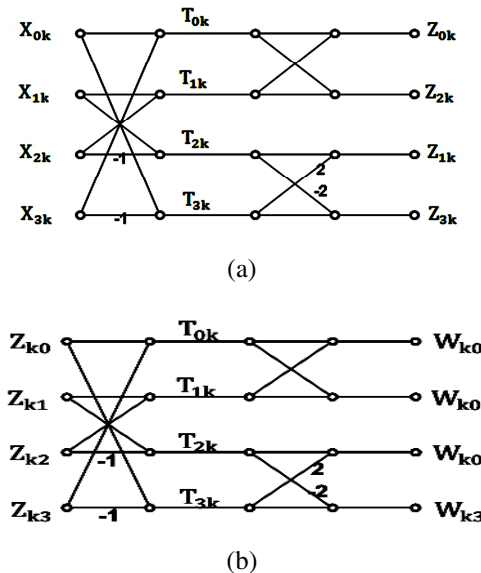


Fig. 1. (a) The algorithm of 1-D DCT (b) The algorithm of 2-D DCT

Figure 2 shows the 1D-DCT architecture, includes the ping-pong buffer, the adder-subtractors, the sign-extended and the left-shifter.

The ping-pong buffer holds data while input data is being written serially. The adder-subtractors are built from carry look ahead adder to get high speed. The shifters operate as a multiplier by 2. The sign-extended convert signed 9-bit data to sign 12-bit data.

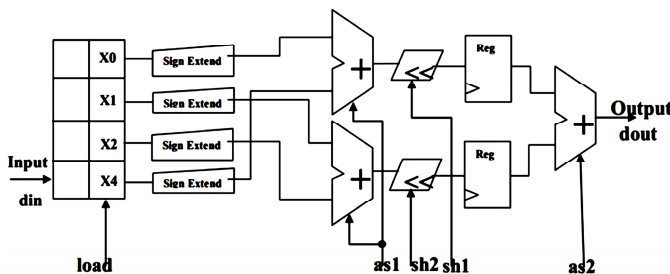
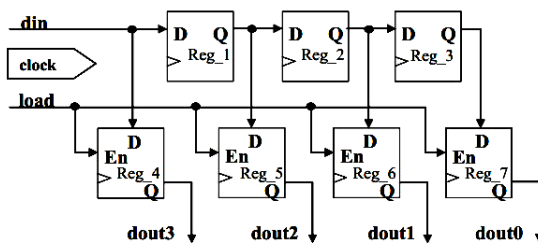


Fig. 2. The 1D-DCT architecture

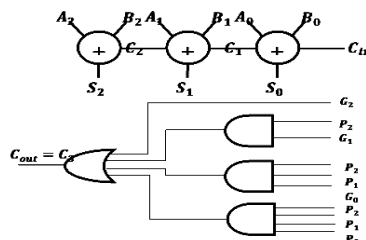
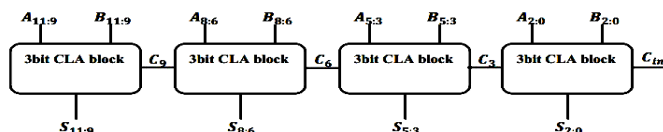
We can use 1D-DCT to compute second dimension of DCT by a multiplexor. This saves area and power, but speed will be decreased a half. To improve throughput, we can construct a pipeline architecture as figure 3. The 1D-DCT and 2D-DCT can work simultaneously so speed of the circuit will be increased two times.

**Fig. 3.** The system of 2D-DCT

Ping-pong Buffer. The ping-pong buffer (figure 4) is the array of registers with serial input data to be converted to parallel data. When the rising edge of the clock, serial input data is written to the registers Reg_1, Reg_2 and Reg_3. When the load signal to 1, it enables the registers Reg_4, Reg_5, Reg_6 and parallel Reg_7 record and hold data until new data are written to. A special feature of this register array is able to calculate the value maintained while data continues to be included the serial.

**Fig. 4.** Ping-pong Buffer

Adder-Subtractor. The adder-Subtractor, Carry Look-Ahead Adder (CLA), is not only high speed but also low power. We group 3 or 4 bits into a small block; carry number of each block is calculated directly from the Pi, Gi of block and it is Cin for next block. At the 3-bit CLA block, in Figure 5 (a), C1, C2 are calculated by CLA, and Cout is calculated by P1, P2, G1, G2 and Cin without waiting for the C1 and C2. While the first 3-bit block is calculating, C3 is calculated from Cin, C6 is calculated from C3 and etc.... Therefore, the Adder performs faster.

**Fig. 5. (a)3-bit CLA Adder****Fig. 5. (b)12-bit CLA Adder**

Left Shifter. The left shifter is same multiply 2. When sh = 0, data passes through, and when sh = 1, the shifter performs 1-bit left shift.

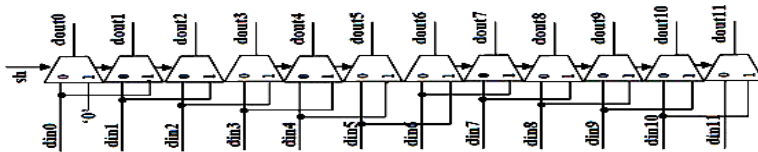


Fig. 6. Shifter

Matrix Transpose. The Matrix Transpose in Figure 7 is two parallel register arrays, each array is designed according to the serial input or output data. When the load signal is 1, t registers is received values corresponding to the r registers. Finally, the data in t registers is shifted and put out sequentially. The matrix transpose needs 16 cycles to receive serial data, 1 cycle to transpose and 16 cycles to put out the serial data.

The advantage of this matrix transpose is able to write and put out data in the same time. This improves speed but it needs more resource than the RAM transpose because the memory cell of the RAM is less transistor than the register, uses Flip-flop.

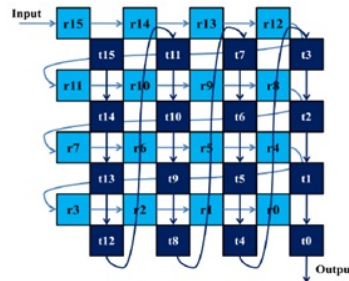


Fig. 7. Matrix Transpose

Operation. The datapath of 1D-DCT is divided into two-stage correlations with the algorithm. In the first four clock cycles, data is entered into the first register array of ping-pong buffer. The next cycle, data is simultaneously loaded into remain the next register array of ping-pong buffer and held during these cycles. In these cycles, the circuit operates as follows

- The 6th cycle, the 1-D DCT calculates and records result into register,
- The 7th cycle, the 2-D DCT calculates and outputs the first result. In the also 7th cycle, the 1-D DCT calculates the second data and records into register.
- The process is continued until completing a 4x4 block. This circuit takes 21 cycles to finish.

The process is indicated in the table 1.

Table 1. The operation of DCT architecture

Cycles	Operation	Cycles	Operation
0	Reset	11	T_{01}, T_{11}, W_{11}
1	Input x_{00}	12	T_{21}, T_{31}, W_{21}
2	Input x_{10}	13	T_{02}, T_{12}, W_{31}
3	Input x_{20}	14	T_{22}, T_{32}, W_{02}
4	Input x_{30} , Load data to the second floor of ping-pong register	15	T_{02}, T_{12}, W_{12}
5	T_{00}, T_{10}	16	T_{22}, T_{32}, W_{22}
6	T_{20}, T_{30}, W_{00}	17	T_{02}, T_{12}, W_{32}
7	T_{00}, T_{10}, W_{10}	18	T_{23}, T_{33}, W_{03}
8	T_{20}, T_{30}, W_{20}	19	T_{03}, T_{13}, W_{13}
9	T_{01}, T_{11}, W_{30}	20	T_{23}, T_{33}, W_{23}
10	T_{21}, T_{31}, W_{01}	21	T_{03}, T_{13}, W_{33}

Because the Hadamard transform for luma in intra prediction is calculated similarly DCT transform, the Hadamard architecture and operating are similarly DCT architecture and operating. The 16 DC values, after DCT calculation, are written to another DC matrix to calculate Hadamard, in figure 8.

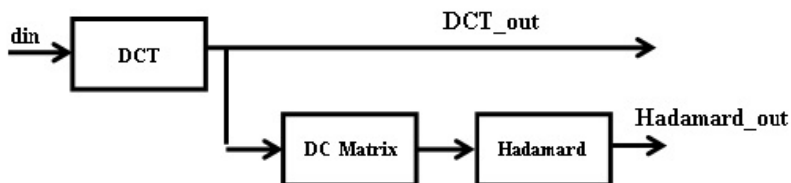


Fig. 8. DCT and Hadamard Architecture

These values put in Hadamard transforms to calculate and the Hadamard transform needs also 21 cycles to finish. At this time, DCT transforms is still processing.

3 Results

Data after prediction, estimation and motion compensation creates a residual matrix with one element is a signed 9-bit. This is also the input of DCT.

$$\begin{bmatrix} 41 & 92 & 92 & 50 \\ 37 & 43 & 44 & 29 \\ 96 & 49 & 38 & 58 \\ 49 & 43 & 49 & 74 \end{bmatrix} \xrightarrow{\text{DCT}} \begin{bmatrix} 703 & -93 & 45 & -54 \\ -147 & 125 & -37 & 60 \\ 37 & -55 & 71 & 10 \\ -6 & -69 & 54 & -100 \end{bmatrix}$$

The DCT result simulated by Matlab is matched with VCS and Design Compiler in figure 9 and figure10:

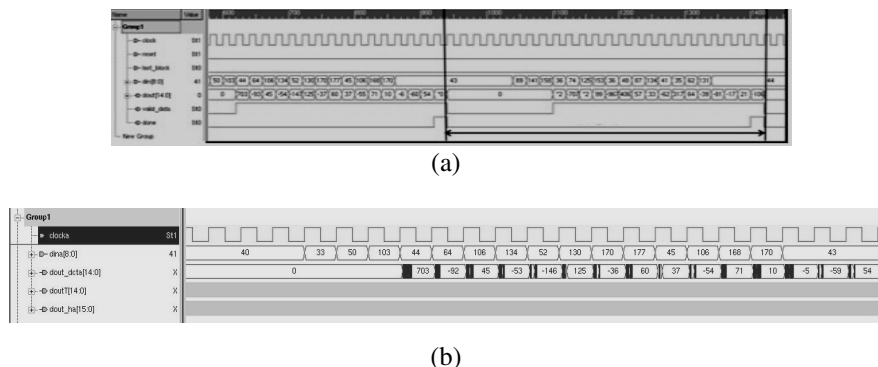


Fig. 9. The result of 2D-DCT is simulated by VCS: (a) Before synthesis (b) After synthesis

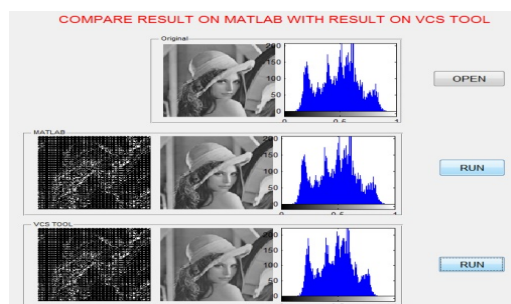


Fig. 10. Compare the results on Matlab and results on Modelsim

The Hadamard result, simulated by Matlab, is matched with VCS and Design Compiler in figure 11:

$$\begin{bmatrix} 703 & 1592 & 1393 & 686 \\ 894 & 1997 & 2684 & 2053 \\ 1075 & 2602 & 2810 & 2480 \\ 2324 & 2619 & 2660 & 2197 \end{bmatrix} \xrightarrow{\text{Hadamard}} \begin{bmatrix} 15425 & -1538 & -3013 & -882 \\ -3423 & -92 & -318 & 227 \\ -1250 & 1840 & 659 & 867 \\ -2004 & 222 & -520 & -578 \end{bmatrix}$$

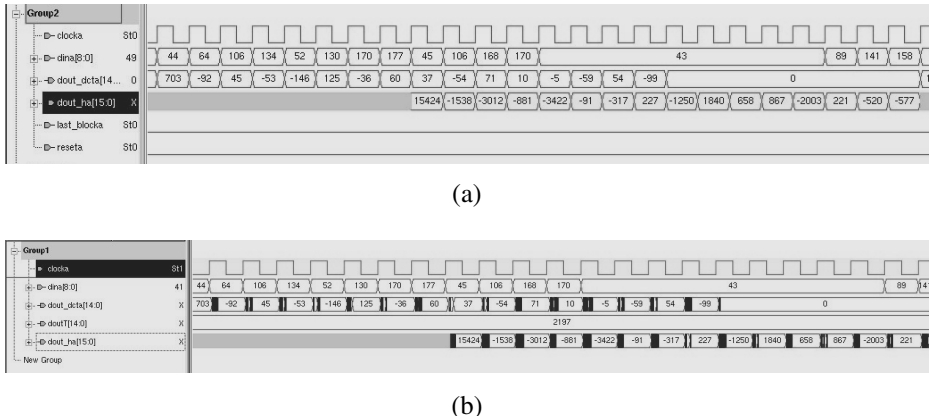


Fig. 11. The result of Hadamard is simulated by VCS: (a) Before synthesis (b) After synthesis

The circuit is synthesized base on Design Compiler and generic 90nm library of Synopsys at 250MHz frequency, follow a top-down method. Condition of the circuit: Vdd=0.7V, T=125oC. The result of the top module:

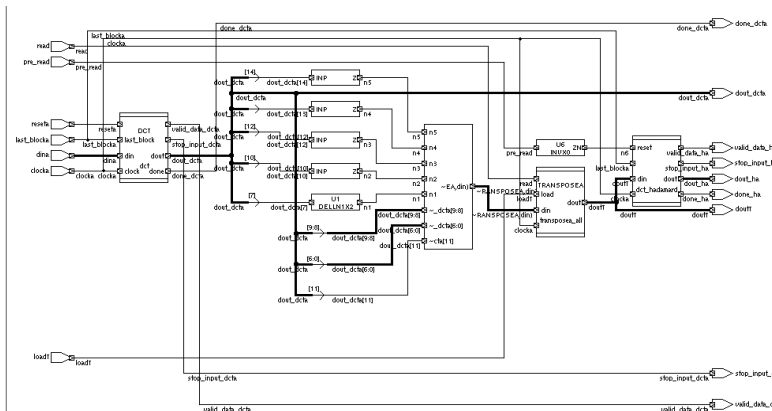


Fig. 12. The DCT and Hadamard datapath for luma mode in intra prediction

Table 2. The characteristic of design

Characteristic	frequency	Leaf Cell	Cell area	Circuit area	Dynamic power	Leakage power
Unit	MHz		μm^2	μm^2	μW	μW
Value	250	5103	83278	89127	130.1335	327.157

This work constructs a serial architecture combine with pipeline to increase speed of calculation. The DCT circuit needs 21 clock cycles to finish 4x4 residual block. The DCT system includes in 6 adder-subtractor 4 shifter so the area and power will be improved.

Table 3. Comparison the DCT design with other designs

Research	Architecture	No. of clock	No. of gate or cell	Component of datapath	
[3]	Serial	164	1189	1 add-sub, 2 Mux, 1 shifter, rom 16x16	Non-pipeline
[4]	parallel	12	FPGA	10 add-sub, 4 shifter	pipeline
[5]	parallel	8	3737		
DCT in this work	serial	24	2170 (leaf cell)	6 add-sub, 4 shifter	pipeline

4 Conclusion

This paper has analyzed and constructed a serial and pipeline architecture of DCT and Hadamard transform for luma in intra prediction. The system is described by Verilog HDL, simulated, synthesized base on 90nm library. The architecture requires 5103 logic cells and 21 clock cycles to calculation DCT or Hardamard for a 4x4 block at pipeline mode. Its frequency can operate at 250MHz and power is 327μW. Our DCT hardware resources are reduced more than 58% compared with parallel DCT architecture [5] and its clock cycle is reduced more than 14.6% compared with serial DCT architecture [3]. Our Hadamard hardware resources are less then approximate 60% compared with architecture [6] and speed increases of 2.5 times and 1.7 times compared with architecture [6] and [8].

References

- Lin, Y.-L.S., Kao, C.-Y., Kuo, H.-C., Chen, J.-W.: VLSI Design for Video Coding - H.264/AVC Encoding from Standard Specification to Chip. Springer, Heidelberg (2010) ISBN 978-1-4419-0958-9
- Hallapuro, A., Karczewicz, M.: Low Complexity Transform and Quantization – Part I: Basic Implementation, Joint Video Team (JVT) of ISO/IEC MPEG & ITU-T VCEG (ISO/IEC JTC1/SC29/WG11 and ITU-T SG16 Q.6) (2002)
- Prasoon, A.K., Rajan, K.: 4×4 2-D DCT for H.264/AVC. In: International Conference on Advances in Computing, Communication and Control, ICAC3 2009 (2009)
- Sun, S., Qi, H.: A Pipelining Hardware Implementation of H.264 Based on FPGA. In: International Conference on Intelligent Computation Technology and Automation (2010)
- Wang, T.-C., Huang, Y.-W., Fang, H.-C., Chen, L.-G.: Parallel 4X4 2D trans-form and inverse transform architecture for MPEG-4 AVC/H.264. In: Proceedings of the 2003 International Symposium on Circuits and Systems, vol. 2, pp. II-800–II-803 (2003)
- Chen, L.-F., Li, K.-H., Huang, C.-Y., Lai, Y.-K.: Analysis and architecture design of multi-transform architecture for h.264/avc intra frame coder. In: ICME (2008)
- Tran, X.-T., Tran, V.-H.: An Efficient Architecture of Forward Transforms and Quantization for H.264/AVC Codecs. REV Journal on Electronics and Communications 1(2) (April–June 2011)

8. Huang, Y.Q., Liu, Q., Ikenaga, T.S.: Highly parallel fractional motion estimation engine for super hi-vision 4kx4k@60fps. *IEEE Int. Works. Multimedia Signal Processing* (2009)
9. Malvar, H.S., Hallapuro, A., Karczewicz, M., Kerofsky, L.: Low-Complexity Transform and quantization in H.264/AVC. *IEEE Transactions on Circuits and Systems for Video Technology* 13(7) (2003)
10. Agostini, L., Porto, R., Porto, M., Silva, T., Rosa, L., Guntzel, J., Silva, I., Bampi, S.: Forward and Inverse 2-D DCT Architectures Targeting HDTV For H.26/AVC Video Compression Standard. *Latin American Applied Research* (2007)
11. EL-Banna, H., EL-Fattah, A.A., Fakhr, W.: An Efficient Implementation of the 1D DCT using FPGA Technology. In: *Proceedings of the 11th IEEE International Conference and Workshop on the Engineering of Computer Based Systems (ECBS 2004)*, pp. 356–360 (2004)
12. Xiuhua, J., Caiming, Z., Yanling, W.: Fast Algorithm of the 2-D 4x4 Inverse Integer Transform for H.264/AVC. In: *IEEE Innovative Computing, Information and Control International Conference, ICICIC* (2007)
13. Owaida, M., Koziri, M., Katsavounidis, I., Stamoulis, G.: A High Performance and Low Power Hardware Architecture for The Transform & Quantization Stages In H.264. In: *ICME* (2009)
14. Liu, Z., Wang, D., Ikenaga, T.: Hardware optimizations of variable block size hadamard transform for h.264/avc frext. In: *ICIP* (2009)

Dynamic Identity-Based Authentication Scheme with Perfect Forward Secrecy Session Key

Toan-Thinh Truong¹, Minh-Triet Tran¹, and Anh-Duc Duong²

¹ University of Science, VNU-HCM, Hochiminh City, Vietnam

{ttthinh, tmtrie}@fit.hcmus.edu.vn

² University of Information Technology, VNU-HCM, Hochiminh City, Vietnam

daduc@uit.edu.vn

Abstract. Password is one of the simple and efficient methods to protect the transactions in insecure network environments. There are many authors researching in this area to suggest the protocols preventing illegitimate users from accessing the systems. In 2013, Y-H An proposed the scheme to isolate some problems which exist in Khan et al.'s scheme. In this paper, we demonstrate that Y-H An's scheme is vulnerable to server forgery attack and cannot provide user's anonymity. Furthermore, we also propose the modified scheme to overcome these limitations.

Keywords: Dynamic identity, Mutual authentication, Remote communication, User anonymity, Security.

1 Introduction

Several insecure wireless environments, such as GSM and CDPD, need an authentication scheme to defend against some adversaries. Such schemes play important role in the remote systems because they will protect the transactions from illegal accessing.

There are many approaches to construct a secure authentication. In 1981, Lamport [1] is the pioneer using one-way hash function in authentication scheme. In his scheme, there is the password table for checking user's legality at login phase. Therefore, if this table is revealed, service provider and registered users will be damaged by adversaries. Recently, Das et al. proposed the scheme [2] with some improved ideas. Their scheme do not maintain password table for verification and use dynamic identity to resist ID-theft and forgery attack. In 2005, I-En Liao [3] proved Das's scheme is not able to withstand password-guessing attack and cannot provide mutual authentication. Additionally, password in Das's scheme is submitted in raw form at registration phase. In 2006, E-J Yoon discovered that I-En Liao's scheme is still vulnerable to password guessing attack, and he proposed the scheme [4] to improve I-En Liao's scheme. Yoon utilizes random values with password when using one-way hash function. Hence, this makes the adversaries not to exactly guess true user's password. In 2010, Khan et al. suggested the scheme [5]. In this scheme, he distributes the shared secret information to all users and use time-stamp to confront impersonation and replay

attack. However, in 2013, Y-H An showed that Khan's scheme cannot protect the users from password guessing and forgery attacks. Moreover, it cannot provide user's anonymity. He also proposed an improved scheme [6] to isolate the weaknesses of Khan et al.'s. Nevertheless, in this paper, we prove that Y-H An's scheme has inability to provide user's anonymity. Furthermore, it also cannot prevent adversaries from impersonating the server. Ultimately, we propose the modified version to recover the problems mentioned.

Rest of this paper is organized as follows: section 2 quickly reviews Y-H An's scheme and discusses its limitations. Then, our proposed scheme is presented in section 3, while section 4 discusses the security and efficiency of the proposed scheme. Our conclusions are presented in section 5.

2 Review and Cryptanalysis of Y-H An's Scheme

In this section, we review Y-H An's scheme and show his scheme cannot resist server impersonation attack and cannot provide user's anonymity.

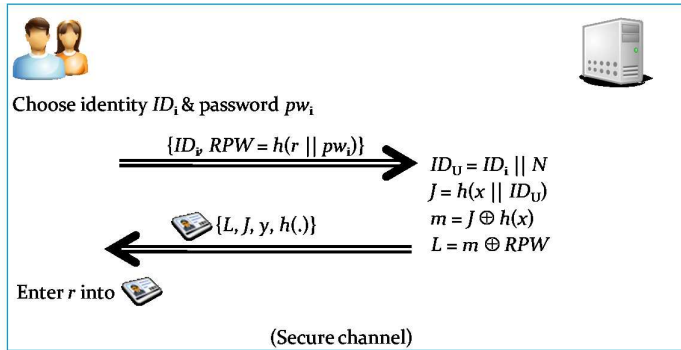
2.1 Review of Y-H An's Scheme

His scheme includes three phases: registration phase, login phase, and authentication phase. Some important notations are listed as follow:

- U_i : User i^{th}
- S : Remote server
- pw_i : Password of U_i $h(.)$: The one-way hash function
- x : The secret key kept by the remote server
- y : The common secret number kept by the users
- T : The timestamp
- N : The number of times a user registers
- SC : The smart card
- SK : The common session key
- \oplus : The exclusive-or operation
- \parallel : Concatenation operation

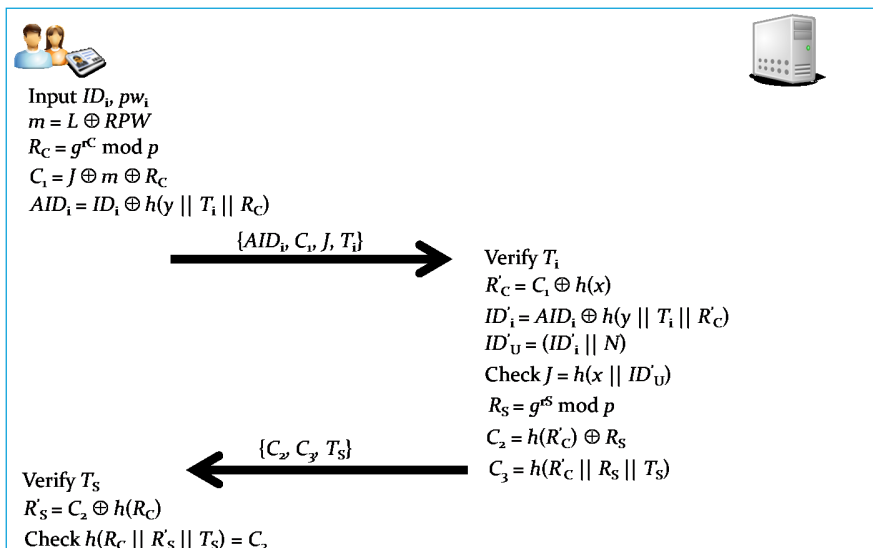
Registration Phase. First of all, S chooses a large prime p and finds a primitive element in $GF(p)$. Afterwards, U_i starts to register to S (Illustrated in Figure 1).

1. U_i freely chooses ID_i and pw_i . Then, U_i sends masked password $RPW = h(r \parallel pw_i)$ and ID_i to S over secure channel, where r is the random value chosen by U_i .
2. After receiving registration message from U_i , S computes $ID_U = (ID_i \parallel N)$, $J = h(x \parallel ID_U)$, $m = J \oplus h(x)$, and $L = m \oplus RPW$.
3. S issues the SC containing $\{L, J, y, h(.)\}$ to U_i over secure channel.
4. U_i enters random number r in the SC .

**Fig. 1.** Y-H An's registration phase

Login Phase. This phase is performed when U_i logs in to S (Illustrated in Figure 2).

1. U_i inserts SC into another card-reader. Then he enters pw_i & ID_i .
2. SC generates a random number r_C and computes $R_C = g^{r_C} \bmod p$.
3. Then, SC computes $m = L \oplus RPW$, $C_1 = J \oplus m \oplus R_C$ and $AID_i = ID_i \oplus h(y \parallel T_i \parallel R_C)$, where T_i is the current timestamp.
4. Finally, U_i sends a login request message $\{AID_i, C_1, J, T_i\}$ to S .

**Fig. 2.** Y-H An's login and authentication phases

Authentication Phase. This phase is performed when S receives the user's login request message.

1. S picks the current T' and verifies the user's T_i . If $T' - T_i \leq \Delta T$, S accepts the login request, where ΔT denotes the expected valid time interval for transmission delay.
2. S computes $R'_C = C_1 \oplus h(x)$, $ID' = AID_i \oplus h(y \parallel T_i \parallel R'_C)$ and $ID'_U = ID' \parallel N$.
3. Then, S checks if $J = h(x \parallel ID'_U)$ or not. If they are equal, S successfully authenticates U_i .
4. S generates a random value r_S and computes $R_S = g^{r_S} \bmod p$.
5. Continually, S computes $C_2 = h(R'_C) \oplus R_S$ and $C_3 = h(R'_C \oplus R_S \oplus T_S)$ to U_i .
6. Once receiving the message from S , SC verifies T_S by picking current T'' . If $T'' - T_S \leq \Delta T$, SC accepts the message.
7. SC computes $R'_S = C_2 \oplus h(R_C)$ and checks if $C_3 = h(R_C \oplus R'_S \oplus T_S)$ or not. If they are the same, U_i successfully authenticates S .
8. Finally, after obtaining mutual authentication, S and U_i can share a common $SK = (R'_S)^{rc} = (R'_C)^{rs} = g^{rsr_c} \bmod p$ for secrecy communication.

2.2 Cryptanalysis of Y-H An's Scheme

In this subsection, we prove that Y-H An's scheme fails to provide user's anonymity and withstand server impersonation attack.

Inability to Protect User's Anonymity. In Y-H An's scheme, any user can know the identities of other users. From the SC , he or she can compute the server's secret information $h(x)$. With this key, legal user can capture any login message of other users and find their identities. Following are some steps which another user can perform.

1. He computes masked password $RPW = h(r \parallel pw_i)$. Then he computes $m = L \oplus RPW$ and finds server's secret information $h(x) = m \oplus J$.
2. With this $h(x)$, he will capture any login message $\{AID_i, C_1, J, T_i\}$. Then, he computes $m = h(x) \oplus J$, $R_C = C_1 \oplus m \oplus J$.
3. Finally, with R_C of other users, he can detect identity $ID_i = AID_i \oplus h(y \parallel T_i \parallel R_C)$.

The main reason why Y-H An's scheme cannot provide user's anonymity is that this scheme distributes the same $h(x)$ to all users. Therefore, if another user know this information, he or she will detect identity of other users with above steps.

Server Impersonation. In Y-H An's scheme, any user can impersonate remote server to cheat other users. Similarly, another user also computes $h(x)$. Next, the user captures any login message from another user $\{AID_i, C_1, J, T_i\}$ and finds R_C . All steps is the same as the steps in finding identity except some next steps below:

1. He can generate a random value r_A and compute $R_A = g^{r_A} \bmod p$.
2. Next, he computes $C^*_2 = h(R_C) \oplus R_A$ and $C^*_3 = h(R_C \oplus R_A \oplus T_A)$, where T_A is the current timestamp.
3. He sends $\{C^*_2, C^*_3, T_S\}$ to waiting user.
4. Waiting user will re-compute $R'_A = C^*_2 \oplus h(R_C)$, then check if $C^*_3 = h(R_C \oplus R'_A \oplus T_S)$ or not.
5. Finally, waiting user computes a common $SK = (R_A)^{r_C} \bmod p$ and malicious user also computes $SK = (R_C)^{r_A} \bmod p$

The main reason why Y-H An's scheme cannot resist server impersonation is that his scheme distributes the same $h(x)$ to all users. Furthermore, the authentication key J is directly transmitted through a common channel. Consequently, with that supportive message-package, malicious user easily computes secret information of other users.

3 Proposed Scheme

Our scheme includes four phases: registration phase, login phase, authentication phase, and password-update phase. Similarly to Y-H An's scheme, remote system needs to choose large prime p and primitive element in $GF(p)$. Then, U_i starts to register to S .

3.1 Registration Phase

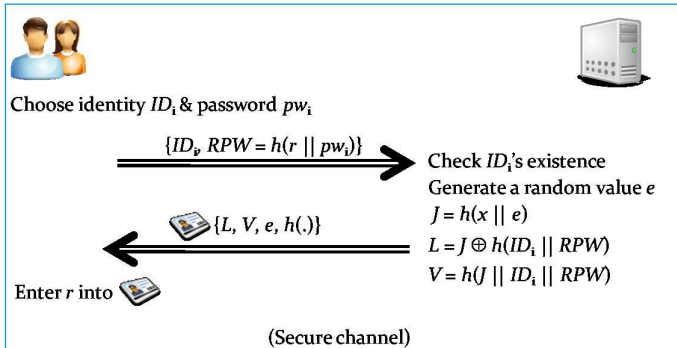
This phase is performed when U_i registers to S (Illustrated in Figure 3).

1. U_i chooses ID_i and pw_i . Then, U_i submits ID_i and $RPW = h(r \parallel pw_i)$ to S through a secure channel, where r is a random value chosen by U_i .
2. When receiving $\{ID_i, RPW\}$ from U_i , S checks ID_i 's existence. If this ID_i is exist, S asks U_i to choose another identity. Otherwise, S continues to go next step.
3. S generates a random value e and computes $J = h(x \parallel e)$, $L = J \oplus h(ID_i \parallel RPW)$ and $V = h(J \parallel ID_i \parallel RPW)$.
4. S sends the SC including $\{L, V, e, h(\cdot)\}$ to U_i through a secure channel.
5. After receiving SC from S , U_i securely enters random value r into SC .

3.2 Login Phase

U_i inserts SC into card reader, and enters ID_i and pw_i to login to S . Next, SC performs:

1. Compute $RPW = h(r \parallel pw_i)$ and $J = L \oplus h(ID_i \parallel RPW)$.
2. Verify if $V \stackrel{?}{=} h(J \parallel ID_i \parallel RPW)$ or not. If this condition is hold, SC continues to go next step. Otherwise, SC terminates this session.
3. Generate a random value r_C . Then SC computes $R_C = g^{r_C} \bmod p$, $C_1 = J \oplus R_C$, $AID_i = ID_i \oplus h(R_C)$ and $C2 = h(J \parallel ID_i \parallel R_C)$
4. Finally, SC sends $\{AID_i, C_1, C_2, e\}$ to S through a common channel.

**Fig. 3.** Proposed registration phase

3.3 Mutual Authentication Phase

S receives U_i 's login message $\{AID_i, C_1, C_2, e\}$ and performs following steps (Illustrated in Figure 4).

1. S computes $R_C = h(x \parallel e) \oplus C_1$ and uncovers $ID_i = AID_i \oplus h(R_C)$. Then, S checks identity's validity. If this identity is not valid, S terminates this session. Otherwise, S goes to next step.
2. S continues to verify if $C_2 = h(h(x \parallel e) \parallel ID_i \parallel R_C)$ or not. If this condition does not hold, S terminates this session. Otherwise, S generates a random value r_S and computes $R_S = g^{rs} \bmod p$, $C_3 = h(R_C) \oplus R_S$, $C_4 = h(R_C \parallel R_S \parallel h(x \parallel e) \parallel ID_i)$.
3. S sends $\{C_3, C_4\}$ to U_i through a common channel.
4. After receiving $\{C_3, C_4\}$ from S , U_i computes $R_S = C_3 \oplus h(R_C)$ and check if $C_4 = h(R_C \parallel R_S \parallel J \parallel ID_i)$. If this condition does not hold, U_i terminates the session. Otherwise, U_i successfully authenticates S . U_i sends $C_5 = h(R_C \parallel R_S)$ to S through a common channel and computes $SK = (R_S)^{rc}$.
5. When receiving $\{C_5\}$ from U_i , S checks if $C_5 = h(R_C \parallel R_S)$. If this condition does not hold, S terminates the session. Otherwise, S successfully authenticates U_i . And S also computes $SK = (R_C)^{rs}$.

3.4 Password Update Phase

When U_i changes password pw_i . He can perform following steps:

1. Insert SC into card reader, enter ID_i , pw_i and choose a new password pw_{inew} .
2. SC computes $RPW = h(r \parallel pw_i)$ and $J = L \oplus h(ID_i \parallel RPW)$. Then, SC checks if $V = h(J \parallel ID_i \parallel RPW)$. If this condition does not hold, SC terminates the session. Otherwise, SC computes $L_{new} = J \oplus h(ID_i \parallel RPW_{new})$ and $V_{new} = h(J \parallel ID_i \parallel RPW_{new})$, where $RPW_{new} = h(r \parallel pw_{inew})$.
3. Finally, SC replaces L with L_{new} , V with V_{new} .

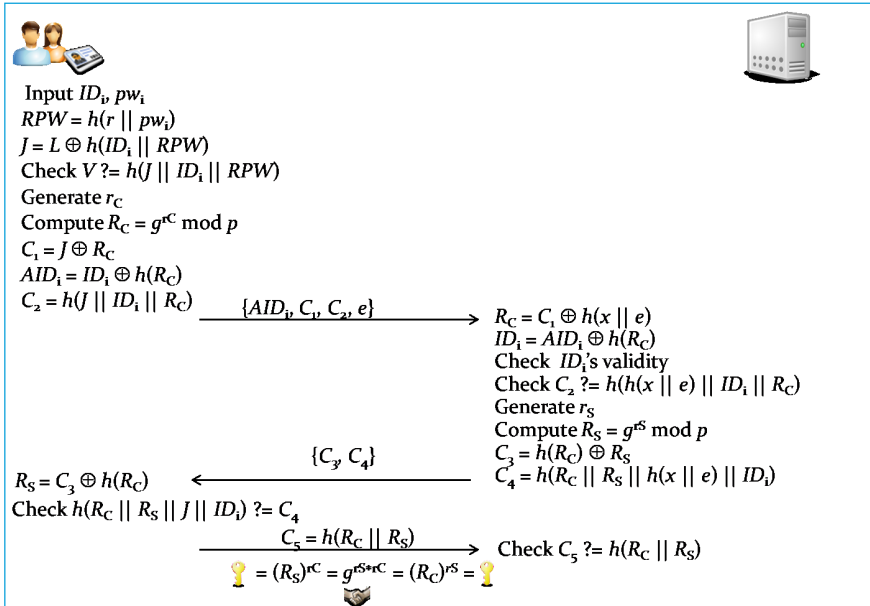


Fig. 4. Proposed login and authentication phases

4 Security and Efficiency Analysis

In this section, we analyze our scheme on two aspects: security and efficiency.

4.1 Security Analysis

In this subsection, we present security analyses and show that proposed scheme can resist many kinds of attacks. Assuming that wireless communication is insecure and that there exists an adversary, he has capability to intercept or hear all messages transmitted between server and user. Besides, we assume that the adversary can steal smart-card's information.

Forgery Attack. In our scheme, attacker cannot impersonate user because he fails to compute authentication key J , random value R_C or identity ID_i . Similarly, attacker cannot impersonate server to cheat other users because he also fails to compute random value R_S . In our design, we use a random value r instead of distributing common secret information to all users. Hence, each user has a different key at different time and other users have no chance to exploit constant clues in their smart cards. Finally, proposed scheme can completely resist forgery attack.

Password Guessing Attack. In our scheme, we also use random value r with user's password in cryptographic hash function. Therefore, attacker is hard to

exactly guess user's password from hashing-output. Furthermore, in our design, masked password RPW does not participate in login and authentication phases. Hence, attacker has no chance to computes anything from $\{AID_i, C_1, C_2, e\}$ and $\{C_3, C_4\}$. Ultimately, proposed scheme successfully withstands this kind of attack.

User Anonymity. In our scheme, user's identity is concealed by using user's random value R_C . To compute this random value, attacker needs to have user's authentication key $J = h(x \parallel e)$. Clearly, knowing server's master key x is impossible. Attacker can exploit login-message $\{AID_i, C_1, C_2, e\}$ and response-message $\{C_3, C_4\}$ to figure something about J . We see that there are three clues: AID_i , C_1 and C_3 which can be used to compute. However, attacker cannot find anything from them and our scheme completely protects user's anonymity.

Session-Key Agreement. Our proposed scheme provides session key agreement during the authentication phase. Session key $SK = (R_S)^{rc} \bmod p = (R_C)^{rs} \bmod p = g^{rs*rc} \bmod p$ is shared between U_i and S . Apparently, even R_C and R_S are revealed due to leaking master key x , attacker cannot compute this key because he must face Diffie - Hellman problem. Consequently, our scheme not only provides session key agreement but also satisfies perfect forward secrecy considered in some schemes using elliptic curve [7, 8, 9, 10].

Table 1. A comparison between our scheme & Y-H An's for withstanding various attacks

Kinds of Attacks	Schemes	
	Y-H An's	Ours
Forgery attack	No	Yes
Password guessing attack	Yes	Yes
User anonymity	No	Yes
Secret key forward secrecy	Yes	Yes
Session key agreement	Yes	Yes

4.2 Efficiency Analysis

To compare efficiency between our scheme and Y-H An's, we reuse the method which is used in Y-H An's scheme to appraise computational complexity. That is, we ignore cost of concatenation and XOR operations because they are not time or energy-consuming operations. Additionally, we let T_h denote the computing-time of one-way hash function. Y-H An's scheme needs $3 \times T_h$ in registration phase, and $9 \times T_h$ in login and authentication phases. Our scheme needs $4 \times T_h$ in registration phase and $12 \times T_h$ in login and authentication phases.

Table 2. A comparison of computation cost

Schemes \ Phases	Registration	Login & Authentication
Y-H An's	$3 \times T_h$	$9 \times T_h$
Ours	$4 \times T_h$	$12 \times T_h$

Because our scheme and Y-H An's are based on smart-card, we compare the storage capacity of smart-card. To do that, we assume output hash function is 160 bit long, for example SHA-1. Moreover, we also would like to consider communication cost between user and server in term of authentication in two schemes. In Table 3, we see that the bits in smart-card of our schemes and Y-H An's are the same. Besides, in authentication phase, our scheme also only needs the same bits as Y-H An's scheme.

Table 3. A comparison of communication cost and storage capacity

Schemes \ Capacity & Communication	Y-H An's	Ours
Bits in smart-card	800	800
Bits in authentication	1120	1120

5 Conclusions

In this paper, we re-consider Y-H An's scheme. Although his scheme can withstand some attacks, we see that his scheme is still vulnerable to server impersonation attack. Besides, his scheme does not provide user's anonymity. Consequently, we propose an improved scheme to eliminate such problems. With our improvement, the schemes can be applied in many applications, especially in financial area.

In the near future, we intend to employ visual cryptography with elliptic curve to store user's authentication key. By approaching this new method, authentication scheme can easily store authentication key in smart-card and user does not have to remember this long key. Therefore, the scheme has been more secure and convenient than previous schemes.

References

- [1] Lamport, L.: Password authentication with insecure communication. Communications of the ACM 24, 770–772 (1981)
- [2] Das, M.L., Saxena, A., Gulati, V.P.: A dynamic id-based remote user authentication scheme. IEEE Transactions on Consumer Electronics 50(2), 629–631 (2004)

- [3] Liao, I.-E., Lee, C.-C., Hwang, M.-S.: Security enhancement for a dynamic id-based remote user authentication scheme. *IEEE Transactions on Consumer Electronics* 50, 629–631 (2004)
- [4] Yoon, E.-J., Yoo, K.-Y.: Improving the dynamic id-based remote mutual authentication scheme. In: Meersman, R., Tari, Z., Herrero, P. (eds.) OTM 2006 Workshops. LNCS, vol. 4277, pp. 499–507. Springer, Heidelberg (2006)
- [5] Khan, M.K., Kimb, S.-K., Alghathbara, K.: Cryptanalysis and security enhancement of a more efficient & secure dynamic id-based remote user authentication scheme. *Computer Communications* 34(3), 305–309 (2010)
- [6] An, Y.-H.: Security improvements of dynamic id-based remote user authentication scheme with session key agreement. In: 2013 15th International Conference on Advanced Communication Technology (ICACT), pp. 1072–1076 (2013)
- [7] Yang, J.-H., Chang, C.-C.: An id-based remote mutual authentication with key agreement scheme for mobile devices on elliptic curve cryptosystem. *Computers and Security* 28(3-4), 138–143 (2009)
- [8] Yoon, E.-J., Yoo, K.-Y.: Robust id-based remote mutual authentication with key agreement scheme for mobile devices on ecc. In: IEEE International Conference on Computational Science and Engineering, vol. 2, pp. 633–640 (2009)
- [9] Islam, S.H., Biswas, G.P.: A more efficient and secure id-based remote mutual authentication with key agreement scheme for mobile devices on elliptic curve cryptosystem. *Journal of Systems and Software* 84(11), 1892–1898 (2011)
- [10] Debiao, H., Jianhua, C., Jin, H.: An id-based client authentication with key agreement protocol for mobile clientserver environment on ecc with provable security. *Information Fusion* (2011)

Automated Face Comparison with Facebook Friend's Faces and Flickr Photos

Petr Šaloun, Jakub Stonawski, and Ivan Zelinka

Faculty of Electrical Engineering and Computer Science,
VSB-Technical University of Ostrava,
Czech Republic

{petr.saloun, ivan.zelinka}@vsb.cz, stonawski.jakub@gmail.com

Abstract. Automated comparison of photographs of faces is a well established discipline. We describe our approach using freely available faces comparator Betaface together with automated processing of Facebook profile of a user. Research interesting task is to compare the facial images of friends in a social network, in our case is described an automated search in the social network Facebook with images from Flickr. Comparison results are very good and conform to the usual tasks based on a comparison of faces. The method of automated comparison and links to social networks Facebook are part of the paper.

Keywords: face comparison, Betaface, Facebook, law aspects, Flickr, automation, C#, .NET Framework.

1 Introduction and State of the Art

Nowadays web contains uncounted number of pictures, lot of them contain faces of people. The first question to appear is "how we can find next photography of selected person". Since this task is still not common enough we have to deal with a number of problems, mostly related to reliability of recognize algorithms. There are a lot of algorithms for face detection but mostly they are provided as paid services. As we focus on *freeware services* we have to find algorithm which mets such a requirement. Our approach is engineering one. If there is defined input/output of selected face recognition algorithm, it encapsulate its and creates a *black box* which can be replaced inside by better algorithm to provide more better/precise service in the future.

Very close to our work is *Friends with faces* [15]. It is a part the project FaceBots: Social Robots utilizing Facebook [16]. The goal of whole project was to develop a robot with face recognition ability and dialog capabilities that is connected into the social database. With these features the robot is able to analyze information in the social network and use them in the real world. The face recognition can be done above real world photos captured by robot's cameras or above photos downloaded from Facebook. After the analysis the robot can decide who is friend of who.

In our approach we would like to replace the analysis of a social context by the analysis of common available photos which we can either match together nor not match and use it as a tool for any usage in this field.

2 Law Aspect of Face Recognize

All applications that used face recognition are now in the viewfinder of organizations which protecting personal data of the users of social networks. Especially in case when explicit agreement of the user, whom face is analyzed, is not given. Since clear law boundaries where the algorithms can operate is still not established the approval of acceptability (from law point of view) is given ad hoc. This fact could be also reason why faces recognize applications are not included in social network yet. As the example of a problematic law aspect Facebook vs. European Commission affair is shown.

2.1 Example of Problems with Law Aspect – Facebook Tag Suggestions Service

New service called Tag Suggestions was introduced in the first half of December 2010 by Facebook's official blog [1]. Main goal of the new service was to facilitate user with tagging people in new photos. The Tag Suggestions works on background and when the user upload new photos the service goes through the photos and all faces try to be found. If the search is successful analysis phase begin. In the analysis phase the service try to parse correct names with detected faces based on pre-collected data.

This service piqued the interest of the Data protection working party (European Union) after the complain to the Office of the Data protection commissioner was sent [2]. Excessive intervention to the personal biometric data of users was expected to be proved by European representatives. Facebook argued that no user's right is exceeded since every user have to agree with the terms of use where the Tag Suggestions is explained sufficiently. Anyway European representatives started to examined the service and final audit was published where the main problems was explained [3].

Main problems with the Tag Suggestions:

- Facebook does not explicitly admits that its service works with biometric data of a users
- re-approval with corrected terms of use is not required from all current users
- no detail information about functionality of the new service is provided to users
- deactivation of the service is not enough user friendly and there is no proof that after deactivation all collected data about a user is deleted

Facebook finally succeed and approval to use the service on the territory of European Union was given. But Facebook has to improve its terms of use as well as redesign deactivation of the service. Also recommendation about getting explicit approval for working with biometric data of the users was issued.

2.2 Recommendation for Development

Recommendation for future developers of face-compare applications is that explicit agreement with the processing of biometric data should be received from the user. Despite the fact that in current situation biometric data is not in every country included

in category that needs to be specially protected¹. Also the Terms of use should be created precisely and as many details about the face compare service as possible should be included in it. With the solution of these issues the three main principles of the best practices during face recognition also can help us [14]. These principles deal with facts that the privacy of the users should be considered in each phase of the development, that all collected information should be transparent to the users and simplified user's choice related with use of an application.

3 Face Recognition Techniques

Nowadays a specific *primary objects in face* is used for face recognition in most of the current algorithms [4]. The primary objects are for example eyes, nose or ears. When these objects are found in a face the algorithms usually compares positions and sizes of the objects and then these data are used for face comparation. Many problems such a occultation of part of the face can occur. Success in dealing with these problems depends on fact how each algorithm can adapt in not ideal conditions.

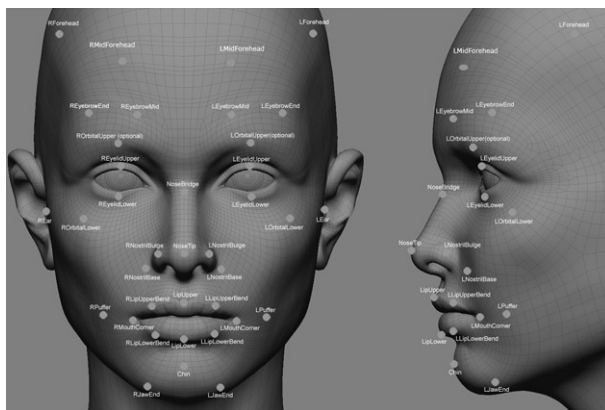


Fig. 1. Primary objects for face comparation algorithms

3.1 Basic Classification of the Algorithms

The algorithms for face comparation can be divided to following groups (depends on how adaptive they are).

a) *Semiautomatic algorithms*: These algorithms represent the easiest way how the face recognition can be done. Interaction with the users is required before recognition can starts. The user have to mark the primary objects in face or if there is some of these objects missing mark approximate area of occurrence (see Figure 1). After this phase computation above the primary objects begin [5]. First who tried to implement this

¹ Irish Data Protection Acts and EU Data Protection Directive.

system was W.W. Bledsoe [6]. The whole system was then improved in Bell Labs where the vector composed of the primary objects was determined. The improvement leads to better results during analysis phase [7]. Algorithms based on these systems is still used but for our purposes are inappropriate since the user interaction during face recognition needs to be eliminated.

b) Automatic algorithms: Similar comparation techniques like in previous group are essentially used also in automatic algorithms. Only manually mark of the primary objects is replaced by automatic detection of these objects. This automatic detection was first implemented by Fichler and Elschlager [8]. Their algorithm was then improved and worked with parametric model of human face [9] where primary objects were detected more reliably since parameter of this model was determined for each photo individually. Level of errors during comparation of faces is also unsatisfactory in this group of algorithms. Especially if the picture of face is taken in bad conditions (for ex. some parts of face is missing or covered by shadows).

c) Self-learning algorithms: The algorithms what are able to self-learning is the best option for our porpoyses because problems mentioned above can be solved by them. Problems with emotion in a face can be solved by them as well. In beginnings an associative networks which implemented basic self-learning algorithms were used [10]. This was then improved by using recursive results propagation [11]. When the neural networks began to be used the algorithms become more effective. The results of self-learning is shown in Figure 2.

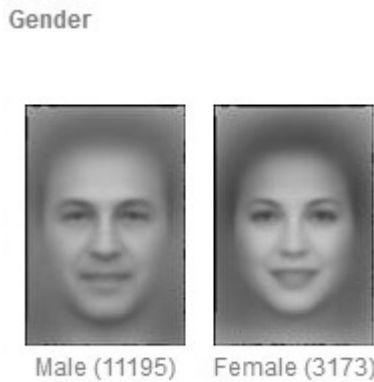


Fig. 2. Interpretation of gender by self-learn algorithm

4 Test of Betaface Algorithms for Face Recognition

In our solution the Betaface service is taken as a black box but for further possibility to replace it by better solutions basic test of its algorithm was done. Betaface says² that

² Information provided by Oleksandr Kazakov - CTO Betaface.

its algorithms reaches 90 % ID rate at 1 % FA rate for single faces per person in its internal tests that are similar to LFW³ test protocols. For our test the dataset of images with faces provided by Ralph Gross from Carnegie Mellon University⁴ was used. This set of the picture was taken during two months when 63 people was photographed in more than 4000 images [13]. In our experiment three random persons (two men and one woman) were choosen and their images created in different lights and angles conditions were analyzed. The example of different conditions is shown in Picture 3.



Fig. 3. Test data provided by Carnegie Mellon University

The results of this test are shown in Table 1. The problems occured mainly during analysis of the pictures taken in the big angles between face and camera. In most of this situations the faces were captured almost from the side and the algorithm cannot find critical points in the face (see Figure 1). On the other hand susceptibility of the algorithms to the different light condition has not been proven.

The results for person A and B is same only difference is person C. It is caused by the smaller height of the person C. The face is captured in low part of the image and the face is less susceptible to bigger angles between face and camera. The result shows that average success rate of Betaface service during face recognition is 58 percent.

Table 1. Successful recognition of the faces during test of Betaface service

Situation	Person A	Person B	Person C
reference picture	N.A.	N.A.	N.A.
normal	100 %	100 %	67 %
big angles	0 %	0 %	14 %
different lights	100 %	100 %	100 %

³ Labeled Faces in the Wild - <http://vis-www.cs.umass.edu/lfw/>

⁴ http://www.ri.cmu.edu/research_project_detail.html?project_id=418&menu_id=261

5 External Service's Communication

The communication layer with services and social networks is implemented inside our new application without usage of external libraries because it allows better control over the various phases of communication, and less data traffic in most situations. The only exception was Flickr, where an external communication library was used because the authentication phase in this service is quite specific.

5.1 Betaface Communication

Basic interface is through XML documents. Even as Betaface authors offers library for .NET Framework, it is too complex even when basic functions are called and moreover there is huge data transfer. For this reason we decided to implement our own communication layer.

Pictures have to be encoded to *base64Binary* and serialized in data stream, see Listing 1.1. For this purposes our own *BetafaceImage* class was implemented.

Listing 1.1. JPEG encode into base64Binary coded text string

```
private string convertImage(Stream s=null)
{
    Image im;
    if (s!=null)
    {
        im=Image.FromStream(s);
    }
    else
    {
        im=Image.FromFile(imPath);
        LoadTagsFromImage(im);
    }
    using (MemoryStream ms = new MemoryStream())
    {
        // Convert Image to byte[]
        im.Save(ms, ImageFormat.Jpeg);
        byte[] iB = ms.ToArray();

        // Convert byte[] to Base64 String
        string result = Convert.ToBase64String(iB);
        return result;
    }
}
```

5.2 Facebook Communication

Facebook's developer pages give full description of communications methods. All queries could be transfer as standard GET and POST methods, moreover they can be done via HTTPS with SSL, see Tab.2. Data format is JSON mostly, see Listing 1.2.

Facebook user is identified by unique ID, the user's name could be ambiguous in case of common names. User's details answered by Facebook could be as on Listing 1.2.

Listing 1.2. Users's info given by Facebook

```
{
  "id": "100003085620908",
  "name": "Jakub Stonawski",
  "first_name": "Jakub",
  "last_name": "Stonawski",
  "link": "http://www.facebook.com/jakub.stonawski.7",
  "username": "jakub.stonawski.7",
  "gender": "male",
  "locale": "cs_CZ" }
```

Table 2. Example of specific requests to Facebook's servers

URL format	Action
https://graph.facebook.com/ <i>ID</i>	basic info about a user
https://graph.facebook.com/ <i>ID</i> /picture?type=large	return profile picture of a user
https://developers.facebook.com/tools/explorer	get access token
https://graph.facebook.com/ <i>ID</i> /friends?accesstoken= <i>T</i>	list of user's friends

Specific token allows more details about the user, his permission is necessary when detailing information is required.

Each external application needs to be registered in Facebook which allows communication and data analysis. Registration of our application is shown in Picture 5

The analysis of existing friends is shown in Figure 4. Once the friends list of a particular user is obtained, the details about each friend (such a name and profile picture) must be requested separately. Then follows a pairing of profile picture and data of specific person, and if the face is recognized, the entire record is stored for later processing. Friends, that cannot be recognize by theirs faces are avoided in this way.

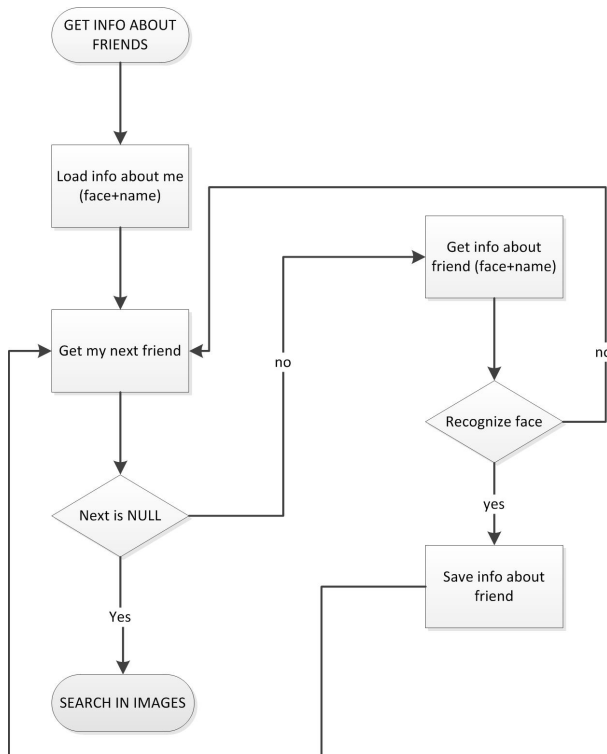
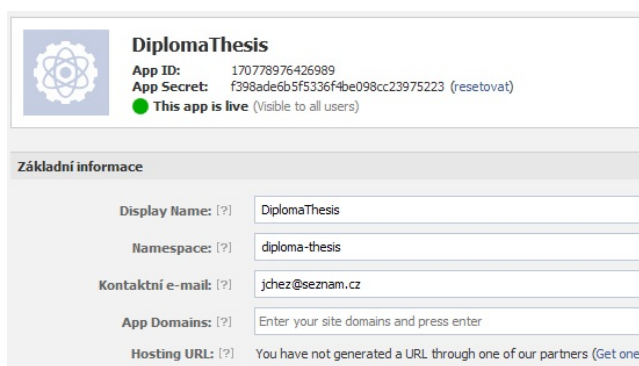
Note: By highest privacy setting reasons is not allowed to track particular friends with such a setting. There is no way how to track them.

5.3 Flickr Communication

With this service is only used external library for communication that is designed for .NET Framework⁵. Each external third-party application that wants to communicate with a network of Flickr, must be also registered on the Flickr web sites, see Figure 6, similar as in Facebook case. After registration application is assigned a unique ID and secret key by which this application also communicates with Flickr network.

Flickr due to security reasons does not support the automatic logging of user in third-party applications. In the new application is not possible for the user only once

⁵ <http://flickrnet.codeplex.com/releases/view/92730>

**Fig. 4.** Facebook's friends analyze algorithm**Fig. 5.** Registered application in Facebook

The App Garden

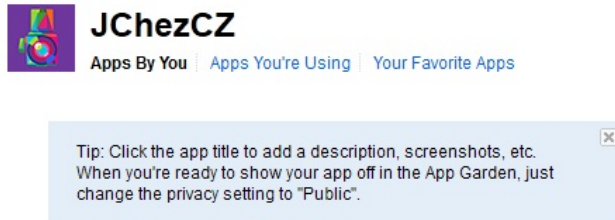


Fig. 6. New app registration by Flickr

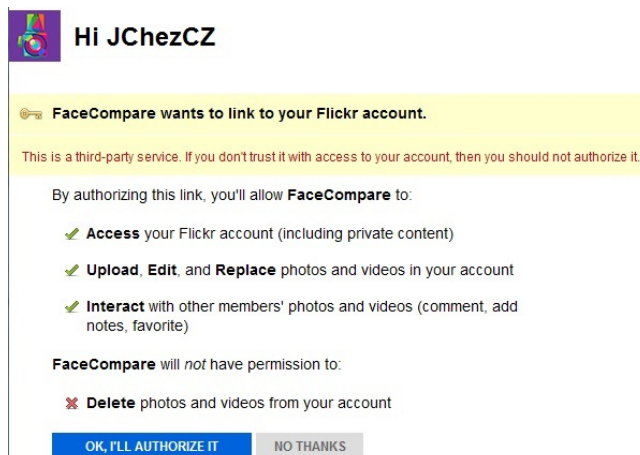


Fig. 7. Authorization of our application by the user against Flickr

filled login information into the service and used them automatically. It is necessary that during each new access to the network, when the login is required, the user must be re-authorized through a Web interface (see Figure 7). In our application .NET *Web-Browser* object was used so we can integrate Internet browser to our application. This is prevented from opening an external web browser that would otherwise be used.

The feedback information, if the authorization was successful is resolved in a way that shows Listing 1.3. The specific form contains an event that is invoked when closing a web browser. The method *wvAuthorizationCompleted* is connected to this event. Final check if the user give to our application requested permissions is done in *GetPermission* method.

Listing 1.3. Flickr login code

```
//WebView is a form that includes WebBrowser
// object for displaying web pages
...
    WebView vv = new WebView();
    vv.Url = user.url;
    vv.AuthorizationCompleted
        += vvAuthorizationCompleted;
    vv.ShowDialog();

    void vv_AuthorizationCompleted(object sender,
        EventArgs e)
    {
        user.GetPermission();
        FillData();
    }
}
```

6 Case Study: Facebook's Friends and Flickr Pictures

As a real world case study Flickr and Facebook were selected. Author's own accounts were used. Facebook's account contains 77 friends in total, 75 of them could be possible to track due to security (see Section 5.2).

Table 3. Results of our application

Pic	New faces	Current friends	Faces detected	New links		Tags added	
				O.K.	bad	O.K.	bad
1	0	2	2	0	0	1	0
2	0	3	3	0	0	0	2
3	0	2	3	0	0	0	0
4	1	0	1	0	0	0	1
5	2	1	4	1	0	1	1
6	1*	0	1	0	0	0	0
7	1*	0	1	0	0	0	0
8	0	1	3	0	0	1	0
9	3*	0	2	0	0	0	0
10	1*	0	1	0	0	0	0
11	0	1	2	0	0	0	0
12	0	4	0	0	0	0	0
13	0	6	6	0	0	1	2
14	2	0	2	2	0	2	0
15	2*	7	9	0	0	1	3
16	0	2	2	0	0	0	1
17	(4+1*)	0	6	0	0	0	2
18	1*	0	1	0	0	0	0
19	1	0	1	1	0	1	0
20	0	2	2	0	0	0	0

After an initial filtering, in which friends where the algorithm could not detect a face on the profile photo were removed, left to test 51 users. In the Flickr, a series of 20 photos that captures the user of our service with other people was created. The entire series was divided into two parts, 10 photos in each one. In the first, there were only included those contained in its tag information on the names of the persons who appear in them. Of these ten, five photos were with current Facebook friends of our user. Remaining five photos were with strangers. The second part of a series includes only those photos with names listed in the object tag. Again, five of them were photographs with existing friends on Facebook and five with previously unknown people. This whole series of photos was presented to the input of our application and the results are shown in Table3.

The names of the persons referred to in the object tag each photo was in a format that allow you to find people on the social network. If the image contains an unknown person in column *new faces* number equal to the number of such persons. Furthermore, if an asterisk at the numbers, it indicates that the person cannot be found (tag photo does not name these people). An example of one photo that contains new person with information about his name is shown in Picture 8. In this photography one new friend was provided to a user of our application.

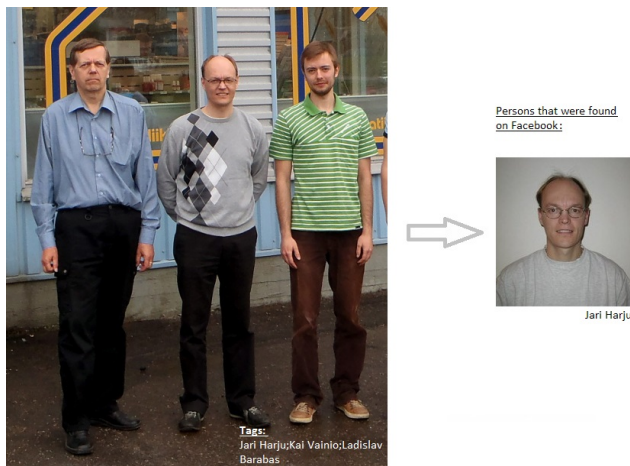


Fig. 8. Example of results: 1 new friend found on Facebook

7 Conclusions

The main goal of our work was to create new experimental algorithm that can be used for face recognition and comparing of pictures with faces on the web, in our case study in Flickr and Facebook.

As is evident from the test results in 20 photographs were ideally detectable ten new people. The faces of all these people in the photographs were detected, which is

a success of Betaface algorithms. A total of four people out of ten of these were successfully identified on the social network Facebook and has been so designed four new connection to the application user. Satisfactory results can also indicate the fact that it has not been implemented by one faulty design a new connection. Larger errors but was detected in the creation of new object tag describing the persons who appear in the photographs. In seven of the 20 photographs have appeared at least one erroneous information about a person, which is reflected on them. However these errors can be eliminated by better face-recognize algorithm in a future. Additionally, since this function is complementary to more important feature of the new proposals connection of the entire experimental algorithm described as successful.

Acknowledgement. The following grants are acknowledged for the financial support provided for this research: Grant Agency of the Czech Republic - GACR P103/13/08195S, by the Development of human resources in research and development of latest soft computing methods and their application in practice project, reg. no. CZ.1.07/2.3.00/20.0072 funded by Operational Programme Education for Competitiveness, co-financed by ESF and state budget of the Czech Republic, and by Grant of SGS No. SP2013/114, VŠB - Technical University of Ostrava, Czech Republic.

References

1. Facebook. Facebook Blog (March 10, 2013),
<http://blog.facebook.com/blog.php?post=467145887130>
2. Office of the Data Protection Commissioner. Complaint against Facebook Ireland Ltd. (March 10, 2013),
http://europe-v-facebook.org/Complaint_09_Face_Recognition.pdf
3. Data Protection Commissioner. Facebook Ireland Audit Report (March 10, 2013),
<http://www.dataprotection.ie/docs/Facebook-Ireland-Audit-Report-December-2011/1187.htm>
4. Turk, M., Pentland, A.: Eigenfaces for Recognition. *Journal of Cognitive Neuroscience*, 71–86 (1991)
5. Bledsoe, W.W.: The model method in facial recognition. Panoramic Research Inc., Palo Alto (1966)
6. Bledsoe, W.W.: Man-Machine facial recognition. Panoramic Research Inc., Palo Alto
7. Goldstein, A.J., Harmon, D.L., Lesk, B.A.: Identification of human faces. *Proc. IEEE* 59, 748–756 (1971)
8. Fischler, A.M., Elschlager, A.R.: The Representation and matching of pictorial structures. *Proc. IEEE c-22*, 67–92 (1973)
9. Yuille, L.A., Cohen, S.D., Hallinan, W.P.: Feature extraction from faces using deformable templates. *International Journal of Computer Vision*, 99–111 (1992)
10. Kohonen, T., Oja, E., Lehtio, P.: Storage and processing of information in distributed associative memory systems. In: Chapter from *Parallel Models of Associative Memory*, pp. 105–143. Lawrence Erlbaum Associates, Publishers Hillsdale (1981)
11. Fleming, K.M., Cottrell, W.G.: Categorization of faces using unsupervised feature extraction. In: *IJCNN International Joint Conference*, pp. 65–70 (1990)
12. Facebook. Graph Search (April 07, 2011),
<https://www.facebook.com/about/graphsearch>

13. Sim, T., Baker, S., Bsat, M.: The CMU Pose, Illumination, and Expression (PIE) Database of Human Faces, 18 pages. Carnegie Mellon University (CMU-RI-TR-01-02) (2001)
14. Federal Trade Commission. Best Practices for Common Uses of Facial Recognition Technologies (Staff Report). Federal Trade Commission, 30 pages (2012)
15. Mavridis, N., Kazmi, W., Toulis, P.: Friends with Faces: How Social Networks Can Enhance Face Recognition and Vice Versa. In: Chapter from Computational Social Network Analysis, pp. 453–482. Springer-Verlag London Limited (2010)
16. Mavridis, N., Datta, C., Emami, S., Tanoto, A., BenAbdelkader, C., Rabie, T.: FaceBots: Social Robots Utilizing FaceBook. In: ACM/IEEE 4th International Conference on Human-Robot Interaction Human-Robot Interaction, 195 pages (2009)

A Hybrid Genetic Algorithm – Sequential Quadratic Programming Approach for Canting Keel Optimization in Transverse Stability of Small Boat Design

Tat-Hien Le^{1,2}, Vo Hoang Duy³, Pham Nhat Phuong³, and Jong-Ho Nam⁴

¹ Department of Naval Architecture and Marine Engineering,
Ho Chi Minh City University of Technology, Vietnam
hienlt@hcmut.edu.vn

² National Key Lab. of Digital Control & System Engineering, Viet Nam National University
³ Faculty of Electrical and Electronics Engineering

Ton Duc Thang University, No. 19 Nguyen Huu Tho Street, Tan Phong Ward,
District 7, Ho Chi, Minh City, Vietnam
{vhduy, pnphuong}@tdt.edu.vn

⁴ Division of Naval Architecture and Ocean Systems Engineering, Korea Maritime University,
Busan, Korea
jongho@alum.mit.edu

Abstract. The transverse stability is one of the most important characteristics of the ship in survivability. This factor can be influenced by wind, moving cargoes and passengers. In order to avoid maritime accidents due to parametric rolling, several ways are considered in the practical situation such as active and passive anti rolling method. The canting keel is a practical tool for the enhancement of ship stability. In the early ship design stage, this problem is considered to be multimodal objective problem. In the present research, a hybrid optimization technique, genetic algorithm – sequential quadratic programing (GA-SQP) is developed to determine the appropriate parametric values of design of canting keel.

Keywords: genetic algorithm, SQP, canting keel, ant rolling.

1 Introduction

According to classical ship stability, a ship assumed to be in an equilibrium state if the sum of weight and buoyancy is balanced. According to Archimedes theory, a floating body displaces volume water equal to its own weight. The center of gravity (CG) is unchanged unless weight changes or moves. Raising the CG reduces the stability while lowering the CG improves the stability. However, the freeboard is reduced by adding ballast for lowering the CG. In this case, the problem of down-flooding occurs at smaller heel angle. Next, there is the center of buoyancy (CB), which is the geometric center of the immersed hull. It moves as the vessel heels. The Fig. 1 shows that when a boat is upright, the CG is above the CB, it is stable. If the

boat is heeled by some external forces (eg: waves, wind), CG and CB no longer act along the same vertical line and moment can be up-righting or overturning heeling. As a result, the ship is stable or unstable.

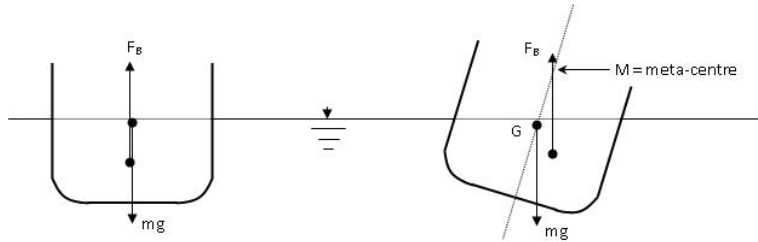


Fig. 1. Forces acting on a ship floating at the upright position

When a ship is inclined, the restoring moment is appeared due to the change of the geometry of the ship. The restoring moment should be equal to the heeling moment to ensure that the ship is in the equilibrium state. The general transverse stability was estimated mainly based on meta center at a small roll angle. In 1757, the relationship between the meta centric height (GM) and roll period of ships was founded by Bernoulli. Next in 1939, Rahola analyzed the still water level arm curves that are acceptable according to the experts' opinion[1,2]. Basically, the stability of ship is considered by using righting arm GZ curve, as shown in Fig. 2. If the righting arm GZ is large, a ship will return the equilibrium state immediately. The objective of the present work is to obtain genetic algorithm and SQP technique to determine the canting keel to generate the restoring moment effectively.

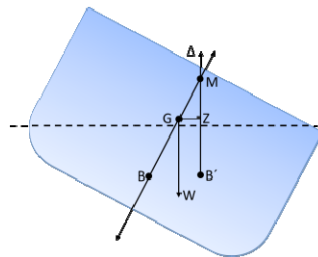


Fig. 2. Righting arm GZ

2 Hybrid GA-SQP Optimization for Canting Keel Design

For a range of small boats, canting keel has been used to increase transverse stability. This is achieved by small increasing in weight of the keel bulb (Fig. 3). As for a fixed keel, a restoring moment is based on the keel length and weight of canting keel. Obviously, these variables should be as large as possible to increase the restoring moment under a number of design load conditions. However, it leads to some limitations of ship design requirement such as longer keel, heavier weight, and greater drag. They also tend to be less maneuverable. A swing canting keel can be suitable in these cases.



Fig. 3. Canting keel system

Our design goal is to minimize keel length, keel bulb weight and rotating angle of keel. Conventional optimization techniques, called steepest descent method, such as gradient-based method, Levenberg-Marquardt method (Rao1999), have been used for a long time[3].

2.1 Sequential Quadratic Programming (SQP)

SQP techniques are used for optimization problems whose objective function and constraints must be continuous and differentiable. A nonlinear programming problem has a form:

$$\min \quad \begin{cases} f(x) \text{ subject to} \\ b(x) \geq 0 \end{cases} \quad (1)$$

Our objective function is obtained by approximating the Lagrangian function with m constraints and Lagrange multiplier variable λ .

$$L(x, \lambda) = f(x) + \sum_{i=1}^m \lambda_i b_i(x) \quad (2)$$

In our canting keel design, the objective functions are f_{weight} , f_{length} , f_{angle} . All of objective functions should be minimized as far as possible.

$$f(x) = [keel_length(x) * keel_weight(x) * \tan(keel_angle(x)) - unbalanced\ weight * level\ arm]^2 \quad (3)$$

where *keel_weight* and *keel_length* are the weight and length of the canting keel, *keel_angle* is the rolling angle of the canting keel to provide a better stable for a boat. These values should be as small as possible.

Next, the constraints of canting keel are limited as size of canting keel.

$$keel_length(x) \leq limitationoflength \quad (4)$$

SQP is fast when the number of objective functions is not too large[4]. However, SQP would get trapped in local minimums in some cases.

2.2 Genetic Algorithm

Evolutionary algorithms, such as GA, however, have been recognized to be possible to solve multi-objective problems[5]. The GAs were invented by John Holland at the University of Michigan in the 1960s and popularized by his student, Goldberg (1989). Holland presented GA as a mechanism of natural adaptation and imported to computer systems. His GA is a method for moving one population (strings or bits) to a new population by using a kind of “natural selection” together with crossover and mutation processes. Today, the researchers use the term “GA” to describe something far from Holland’s conception. Instead of using bits in crossover and mutation process, a real coded GAs was introduced for some applications[6,7,8]. The general multi-objective problem is written in Eq (3).

2.2.1 Encoding for Initial Population

The standard GA method use a bit pattern (each gene has a value equal 0: knot-put out or 1: knot-put in). In our present work, GA with individuals using a real value is composed. A set of values in this chromosome is exchanged during the GA mechanism to generate a new chromosome in the next generation. Three major elements such as keel weight, keel length and angle encoded are illustrated in Fig. 4 to form chromosomes.

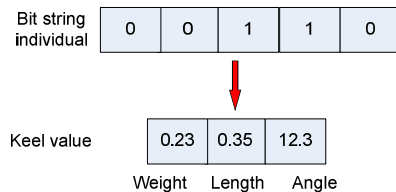


Fig. 4. Real coded individual

2.2.2 Reproduction Process

The steady-state selection is not a particular method (Whitley and Kauth 1988). Each individual in population has a fitness value. First, the individuals are sorted from lowest to highest fitness values. The main idea of this selection is that the good 80% individuals in population (good group) are selected to produce and the rest (bad group) are discarded. Also, in the good group, a few best individuals will be retained at each generation by elitism method. It is recommended that the number of elite individuals is 5% of the number of individuals in a good group. In addition, the bad group in current population will be replaced by the individuals that are executed by the crossover and mutation processes in the good group of current population. A replacement/deletion strategy is more practical than other methods because some characters of good individuals can be lost if they are not selected to produce or if they are destroyed by crossover or mutation processes.

2.2.3 Crossover Process

Crossover is explorative. The encoded design variables are arranged in a dimensional form as a “string” (individual). The individuals divide a string into sub-strings

(weight, length, keel) and swap the sub-strings to create new individuals using the crossover process (see Fig. 5). After that, the next population will be generated.

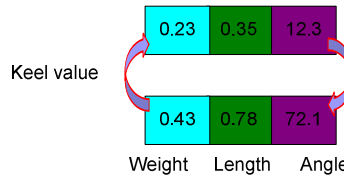


Fig. 5. Crossover mechanism

2.2.4 Mutation Process

The role of mutation is to understand how GA solves complex problems. Mutation is exploitation; it creates a small deviation on the surface. The role of mutation in GA has been considered as preventing premature convergence of the solution (see Fig. 6).



Fig. 6. Mutation mechanism

2.3 Hybrid GA-SQP

A major disadvantage of GA is the convergence speed. The hybrid GA-SQP is considered an effective optimization solver that can enhance the convergence speed. In the present study, GA is applied first to generate the initial point. Then, the calculations would shift to SQP. When objective values close to the local minimum based on our specified tolerance are achieved, our process returns to GA to escape from this local minimum. The basic structure of GA-SQP is illustrated in Fig. 7.

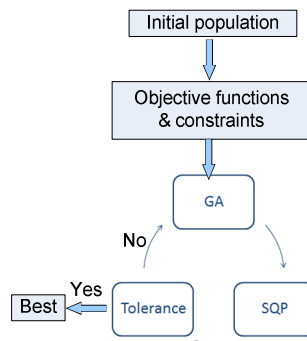


Fig. 7. Hybrid GA-SQP algorithm

3 Numerical Study

By using GA-SQP technique for canting level design, we obtained the following control variables. In order to demonstrate the results, the transverse stability of boat with and without canting keel is calculated by measuring the GZ curve. In this study, our optimization code was written in MATLAB and GZ curve is generated from MAXSURF ship design software. The small boat in our example is obtained as Fig.8 and Table 1

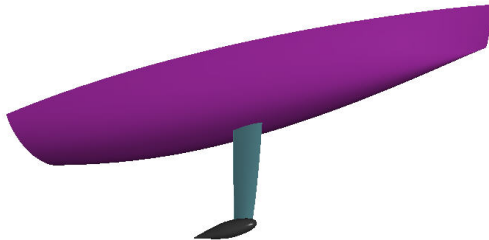


Fig. 8. Small boat with canting keel system

Table 1. Assumption of load case condition in small boat

	Weight [ton]	Long.Arm [m]	Vert.Arm [m]	Trans.Arm [m]
Full ship	6.401	6.460	1.020	0.000
Moving weight	0.5000	6.460	1.020	1.000
	6.901	LCG=6.460	VCG=1.020	TCG=0.072

As shown in Figs.9,10 and Table 2, the GZ curves were generated to demonstrate the efficiency of hybrid GA-SQP for canting keel optimization. The SQP technique reaches the local optimum very fast while the GA technique finds the optimum point slowly. Theoretically, the GZ curve generated from the SQP technique is the greatest. However, the weight of keel bulb is very large and it is not practical in design compared to the weight of full ship. The GZ curve from GA-SQP seems to achieve the global optimum in this case.

Other optimization techniques such as differential equation (DE), gradient-based methods work well and fast but there is no guarantee that an optimal solution will be reached. Simulated annealing (SA) is very slow if the objective functions are complicated. SOMA is able to solve even highly complex optimization problems [9]. The hybrid GA-SQP has been recognized to be possible simply to solve multi-objective problems while reducing the convergence speed.

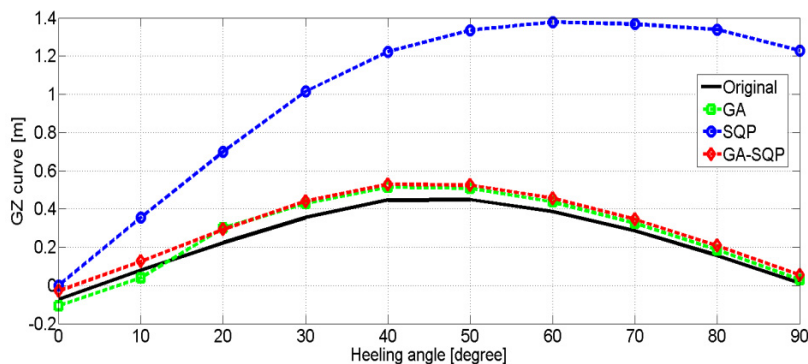


Fig. 9. GZ stability curve using optimization techniques

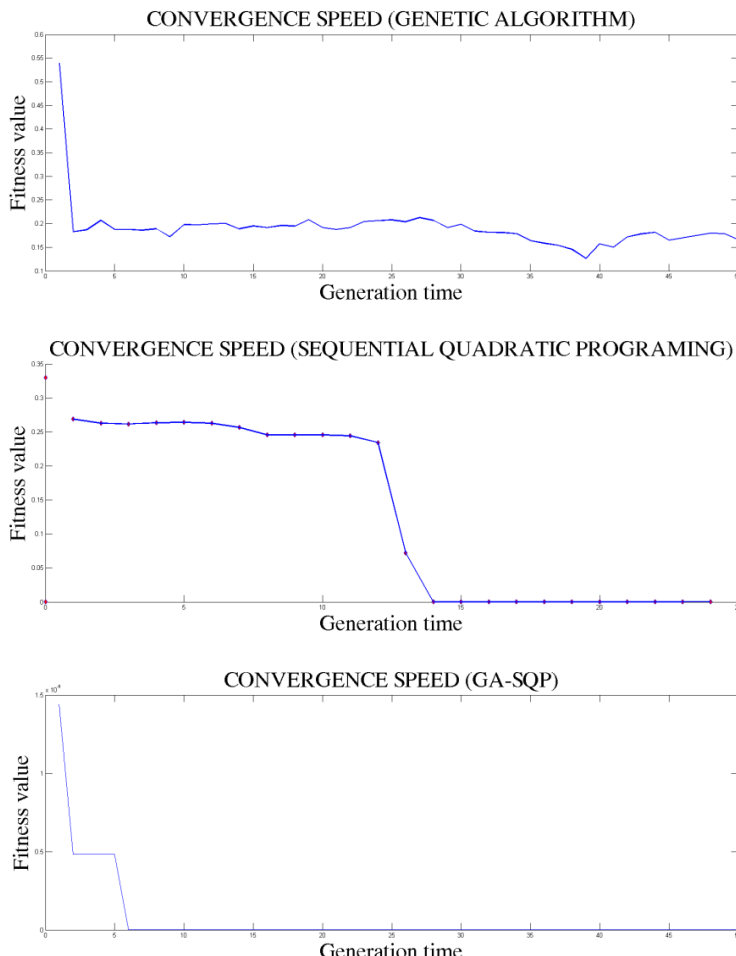


Fig. 10. Convergence of objective value (a) GA technique, (b) SQP technique, (c) GA-SQP

Table 2. Design variables using optimization techniques

	Keel bulb [ton]	Keel angle [degree]	Keel length [m]	Objective value
GA	0.1300	82.3000	3.8810	0.0000
SQP	5.0508	2.8062	2.0223	0.0000
GA-SQP	0.2450	82.3795	2.0589	0.0000

4 Conclusion

The presented hybrid GA-SQP technique represents the best performance in GZ stability calculation. The accuracy of modeling is dependent on the generation time of the process. This procedure is able to shift to the SQP technique to get the process faster and shift back to the GA technique to find other better solutions until the convergent solution is guaranteed within the required precision. For future research, the emphasis should be on performing an experiment of controllable canting keel system.

Acknowledgments. This paper was partially supported by National Key Lab. of Digital Control & System Engineering, Hochiminh City University of Technology, Viet Nam National University.

References

1. Biran, A.: Ship hydrostatics and stability. Butterworth-Heinemann (2003)
2. Watson, D.: Practical ship design. Elsevier Ocean Engineering Book Series (2002)
3. Whitley, D., Kauth, J.: GENITOR: A different Genetic Algorithm. In: Proceedings of the RockyMountain Conference on Artificial Intelligence, pp. 118–130 (1988)
4. Hwang, J., Roh, M., Lee, K.: Determination of the optimal operating conditions of the dual mixed refrigerant cycle for the LNG FPSO topside liquefaction process. Computers and Chemical Engineering 49, 25–36 (2013)
5. Goldberg, D.: Genetic algorithm in search, optimization, and machine learning. Addison-Wesley (1989)
6. Nam, J., Le, T.: Automatic interior space arrangement of mid-sized superyachts using a constraint-based genetic algorithm. Journal of Marine Science and Technolog 17, 481–492 (2012)
7. Chiu, C., Hsu, P.: A constraint-based genetic algorithm approach for mining classification rules. IEEE Transactions on Systems, Man, and Cybernetics 35, 205–220 (2005)
8. Le, T., Kim, D.: Application of a real-coded genetic algorithm for the fitting of a ship hullsurface through a single non-uniform B-spline surface. Journal of Marine Science and Technolog 16, 226–239 (2011)
9. Ivan, Z., Sergej, C., Hendrik, R., Guanrong, C.: Evolutionary algorithm and Chaotic systems. Springer, Heidelberg (2010)

Evolutionary Control of Chaotic Lozi Map by Means of Chaos Driven Differential Evolution

Roman Senkerik¹, Michal Pluhacek¹, Ivan Zelinka², Donald Davendra²,
Zuzana Kominkova Oplatkova¹, and Roman Jasek¹

¹ Faculty of Applied Informatics, Tomas Bata University in Zlin
T.G. Masaryka 5555, 760 01 Zlin, Czech Republic

{senkerik, pluhacek, kominkovaoplatkova, jasek}@fai.utb.cz

² Technical University of Ostrava, Faculty of Electrical Engineering and Computer Science,
17. listopadu 15, 708 33 Ostrava-Poruba, Czech Republic
{ivan.zelinka, donald.davendra}@vsb.cz

Abstract. In this paper, Differential Evolution (DE) is used for the evolutionary optimization of control of chaotic Lozi map system. The novelty of the approach is that the identical selected discrete dissipative chaotic system is used as the chaotic pseudo random number generator to drive the mutation and crossover process in the DE. The optimization was performed for two types of case studies and developed cost functions.

Keywords: Differential Evolution, Optimization, Chaos control, Evolutionary algorithms, Lozi map.

1 Introduction

These days the methods based on soft computing such as neural networks, evolutionary algorithms, fuzzy logic, and genetic programming are known as powerful tool for almost any difficult and complex optimization problem.

The interest about the interconnection between evolutionary techniques and control of chaotic systems is spread daily. First steps were done in [1], [2], [3] where the control law was based on Pyragas method: Extended delay feedback control – ETDAS [4], [5], [6]. These papers were concerned to tune several parameters inside the control technique for chaotic system. The big advantage of the Pyragas method for evolutionary computation is the amount of accessible control parameters, which can be easily tuned by means of evolutionary algorithms (EA).

This paper is aimed at investigating the chaos driven Differential Evolution (DE). Although a number of DE variants have been recently developed, the focus of this paper is the embedding of chaotic systems in the form of chaos pseudo random number generator (CPRNG) for DE and its application to optimization of chaos control.

Firstly, the problem design is proposed. The next sections are focused on the description of used cost functions, evolutionary algorithm DE and the concept of chaos driven DE. Results and conclusion follow afterwards.

2 Motivation

This research is a continuation of the previous successful initial application based experiment with chaos driven DE [7], [8].

This paper extends the research of evolutionary chaos control optimization by means of both SOMA or DE algorithm [3] and initial experiment with chaos driven DE [9].

In this paper the DE/rand/1/bin strategy driven by Lozi chaotic map (system) was utilized to solve the issue of evolutionary optimization of chaos control for the very same chaotic system. Thus the idea was to utilize the hidden chaotic dynamics in pseudo random sequences given by chaotic Lozi map system to help Differential evolution algorithm in searching for the best controller settings for the very same chaotic system.

Recent research in chaos driven heuristics has been fueled with the predisposition that unlike stochastic approaches, a chaotic approach is able to bypass local optima stagnation. This one clause is of deep importance to evolutionary algorithms. A chaotic approach generally uses the chaotic map in the place of a pseudo random number generator [10]. This causes the heuristic to map unique regions, since the chaotic map iterates to new regions. The task is then to select a very good chaotic map as the pseudo random number generator.

Several papers have been recently focused on the connection of DE and chaotic dynamics either in the form of hybridizing of DE with chaotic searching algorithm [11] or in the form of chaotic mutation factor and dynamically changing weighting and crossover factor in self-adaptive chaos differential evolution (SACDE) [12].

The focus of this paper is the embedding of chaotic systems in the form of chaos pseudo random number generator for DE.

The chaotic systems of interest are discrete dissipative chaotic systems. The Lozi map chaotic system was selected as the chaos pseudo random number generator for DE based on the successful results obtained with DE [13] or PSO algorithm [14].

3 Selected Chaotic System

The chosen example of discrete dissipative chaotic system used both as a CPRNG and within the evolutionary optimization of chaos control problem was the two-dimensional Lozi map system.

The Lozi map is a simple discrete two-dimensional chaotic map. The map equations are given in (1). The parameters used in this work are: $a = 1.7$ and $b = 0.5$ as suggested in [15].

For these values, the system exhibits chaotic behavior. The example of this behavior is depicted in the numerical simulation of direct system output (x or y) in the uncontrolled state (Fig. 1).

$$\begin{aligned} X_{n+1} &= 1 - a|X_n| + bY_n \\ Y_{n+1} &= X_n \end{aligned} \tag{1}$$

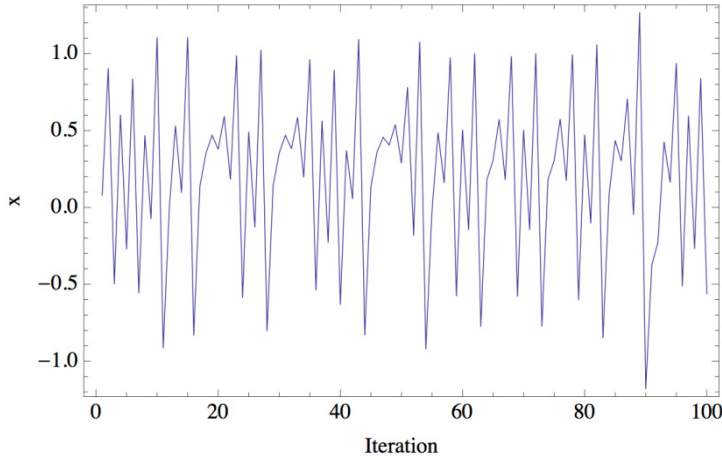


Fig. 1. Iterations of the uncontrolled Lozi map (variable x)

4 Original ETDAS Chaos Control Method

This work is focused on the utilization of the chaos driven DE for tuning of parameters for ETDAS control method to stabilize desired Unstable Periodic Orbits (UPO). In the described research, desired UPO was p-1 (stable state). The original control method – ETDAS in the discrete form suitable for Lozi map has the form (2).

$$\begin{aligned} x_{n+1} &= aX_n - Y_n^2 + F_n \\ F_n &= K[(1-R)S_{n-m} - x_n] \\ S_n &= x_n + RS_{n-m} \end{aligned} \quad (2)$$

Where: K and R are adjustable constants, which have to be evolutionary tuned. F is the perturbation; S is given by a delay equation utilizing previous states of the system, m is the period of m-periodic orbit to be stabilized. The perturbation F_n in equations (2) may have arbitrarily large value, which can cause diverging of the system outside the output interval of Lozi map system $\{-1.4, 1.4\}$. Therefore, F_n should have a value between $<-F_{\max}, F_{\max}>$. The suitable F_{\max} value was also obtained from evolutionary optimization process.

5 Cost Functions

This research utilizes and compares two cost function design.

The proposal of the first basic cost function (CF) is in general based on the simplest CF, which could be used problem-free only for the stabilization of p-1 orbit. The idea

was to minimize the area created by the difference between the required state and the real system output on the whole simulation interval – τ_i . The simple CF is given in (3).

$$CF_{SIMPLE} = \sum_{t=0}^{\tau_i} |TS_t - AS_t| \quad (3)$$

Nevertheless this simple approach has one big disadvantage, which is the including of initial chaotic transient behavior of not stabilized system into the cost function value. As a result of this, the very tiny change of control method setting for extremely sensitive chaotic system causing very small change of CF value, can be suppressed by the above-mentioned including of initial chaotic transient behavior.

Another universal cost function had to be used for securing the stabilization of either p-1 orbit (stable state) or higher periodic orbit and having the possibility of adding penalization rules. It was synthesized from the simple CF and other terms were added.

This CF is in general based on searching for desired stabilized periodic orbit and thereafter calculation of the difference between desired and found actual periodic orbit on the short time interval - τ_s (approx. 20 - 50 iterations) from the point, where the first min. value of difference between desired and actual system output is found (i.e. floating window for minimization). The CF_{UNI} has the form (4).

$$CF_{UNI} = pen_1 + \sum_{t=\tau_1}^{\tau_2} |TS_t - AS_t| \quad (4)$$

Where:

TS - target state, AS - actual state

τ_1 - the first minimal value of difference between TS and AS

τ_2 – the end of optimization interval ($\tau_1 + \tau_s$)

$pen_1 = 0$ if $\tau_1 - \tau_2 \geq \tau_s$; $pen_1 = 10 * (\tau_1 - \tau_2)$ if $\tau_1 - \tau_2 < \tau_s$ (i.e. late stabilization)

6 Differential Evolution

DE is a population-based optimization method that works on real-number-coded individuals [16]. DE is quite robust, fast, and effective, with global optimization ability. It does not require the objective function to be differentiable, and it works well even with noisy and time-dependent objective functions. Description of the utilized DERand1Bin strategy is presented in [16], [17], [18] and [19] together the description of all other strategies.

7 Chaos Driven DE

The main principle of this concept is the embedding of chaotic systems in the form of chaos pseudo random number generator (CPRNG) for DE. In this research, direct output iterations of the chaotic map were used for the generation of real numbers in

the process of crossover based on the user defined CR value and for the generation of the integer values used for selection of individuals. The initial concept of embedding chaotic dynamics into the evolutionary algorithms is given in [20].

8 Experimental Results

Within the research a total number of 50 simulations with chaos driven DE by means of Lozi map system were carried out for each CF design. All simulations were successful and have given new optimal settings for ETDAS control method securing the fast stabilization of the chaotic system at required behaviour (p-1 orbit).

Following Tables 2 and 4 contains the simple statistical overview of optimization/simulation results. Tables 3 and 5 contain the best founded individual solutions of parameters set up for ETDAS control method, corresponding final CF value, also the *Istab. value* representing the number of iterations required for stabilization on desired UPO and further the average error between desired output value and real system output from the last 20 iterations.

Graphical simulation outputs of the best individual solutions for both case studies are depicted in Fig. 2 and Fig. 4, whereas the Fig. 3 and Fig 5 shows the simulation output of all 50 runs of CHAOS DE, thus confirm the robustness of this approach.

For the illustrative purposes, all graphical simulations outputs are depicted only for the variable x of the chaotic Lozi map system.

Settings of EA parameters for both processes were based on performed numerous experiments with chaotic systems (Table 1).

Based on the mathematical analysis, the real p-1 UPO for unperturbed Lozi map system has following value: $x_S = 0.4545$.

The ranges of all estimated parameters were these:
 $-2 \leq K \leq 2$, $0 \leq F_{\max} \leq 0.9$ and $0 \leq R \leq 0.99$,

Table 1. CHAOS DE settings

DE Parameter	Value
PopSize	25
F	0.8
CR	0.8
Generations	250
Max. CF Evaluations (CFE)	6250

8.1 Case Study 1 – Simple Cost Function

From the results presented in the Tables 2 and 3, it follows that the CF-simple is very convenient for evolutionary process, which means that repeated runs of EA are giving identical optimal results (i.e. very close to the possible global extreme). This is graphically confirmed in the Figure 3 when all 50 simulations are basically merged into the one line. On the other hand the disadvantage of including of initial chaotic

transient behavior of not stabilized system into the cost function value and resulting very tiny change of control method setting for extremely sensitive chaotic system is causing suppression of stabilization speed and numerical precision.

Table 2. CF-simple values statistic

Statistical data	CF Value
Min	0.520639
Max	0.520639
Median	0.520639
Std.Dev.	$2.41 \cdot 10^{-15}$
Avg. Full Stab. (Iteration)	32

Table 3. Characteristics of the best solution

Parameter	Value
K	-1.11259
F_{\max}	0.9
R	0.289232
CF Value	0.520639
$I_{stab.} Value$	21
Avg. error per iteration	$7.21 \cdot 10^{-15}$

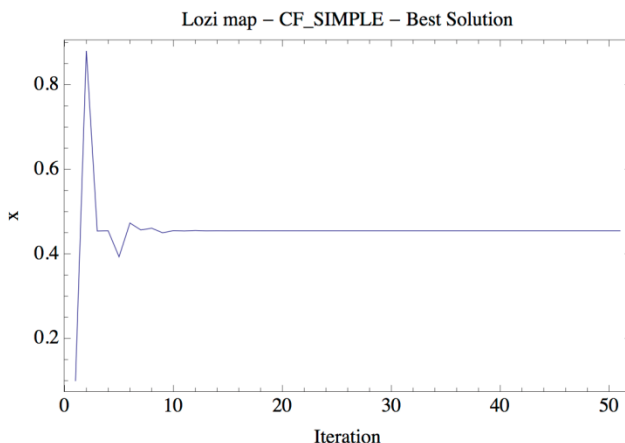


Fig. 2. Simulation of the best individual solution, CHAOS DE - CF Simple

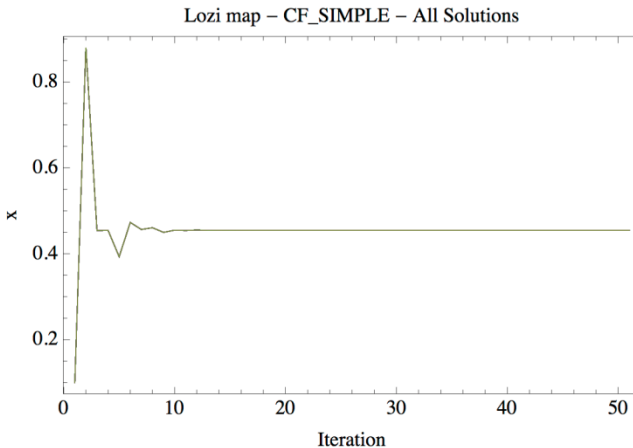


Fig. 3. Simulation of the all 50 solutions, CHAOS DE - CF Simple

8.2 Case Study 2 – Universal Cost Function

Results obtained in this case study lend weight to the argument, that the technique of pure searching for periodic orbits is advantageous for faster and more precise stabilization of chaotic system.

Table 4. CF-universal values statistic

Statistical data	CF Value
Min	$3.5331 \cdot 10^{-15}$
Max	$4.0551 \cdot 10^{-15}$
Average	$3.8063 \cdot 10^{-15}$
Std.Dev.	$1.19 \cdot 10^{-16}$
Avg. Stab. (Iteration)	11

Table 5. Characteristics of the best solution

Parameter	Value
K	-0.859989
F_{\max}	0.643099
R	0.065669
CF Value	$3.5331 \cdot 10^{-15}$
$Istab.$ Value	9
Avg. error per iteration	0

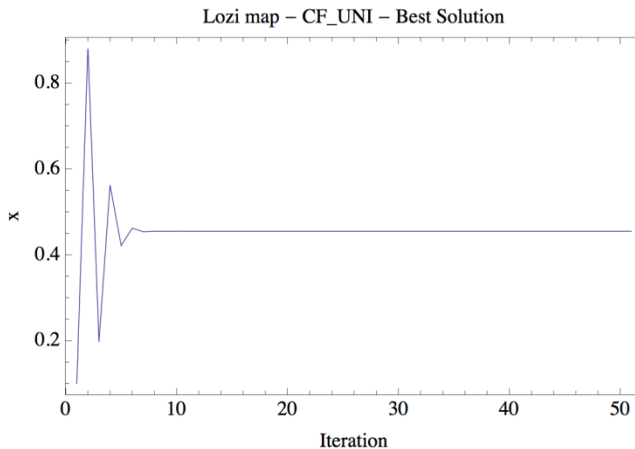


Fig. 4. Simulation of the best individual solution, CHAOS DE - CF Universal

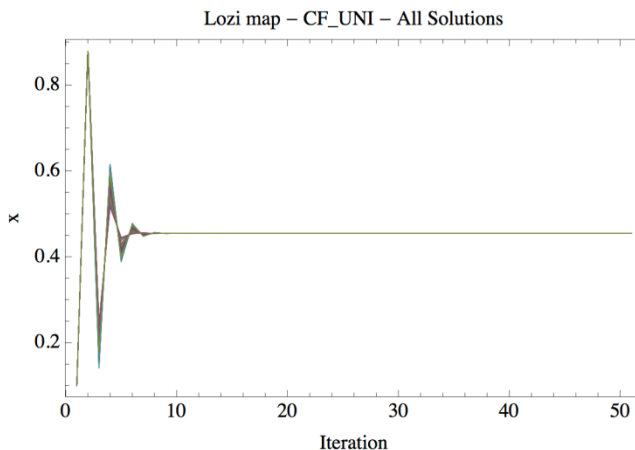


Fig. 5. Simulation of the all 50 solutions, CHAOS DE - CF Universal

9 Conclusions

Based on obtained results, it may be claimed, that the presented Chaos DE driven by selected discrete dissipative chaotic system has given satisfactory results in the chaos control optimization issue.

The results show that embedding of the chaotic dynamics in the form of chaotic pseudo random number generator into the differential evolution algorithm may help to improve the performance and robustness of the DE. Thus to obtain optimal solutions securing the very fast and precise stabilization for both convenient CF surface in case of the CF-simple and very chaotic and nonlinear CF surface in case of the CF-universal.

When comparing the both CF designs, the CF-simple is very convenient for evolutionary process (i.e. repeated runs are giving identical optimal results), but it has many limitations.

The second universal CF design brings the possibility of using it problem free for any desired behavior of arbitrary chaotic systems, but at the cost of the highly chaotic CF surface. Nevertheless the embedding of the chaotic dynamics into the evolutionary algorithms helped to deal with such an issue.

The primary aim of this work was not to develop any new pseudo random number generator, which should normally pass many statistical tests, but to show that through embedding the hidden chaotic dynamics into the evolutionary process in the form of chaotic pseudo random number generators may help to obtain better results and avoid problems connected with evolutionary computation such as premature convergence and stagnation in local extremes.

The issue of possible stagnation in local extremes was tested within the previous initial research with ChaosDE and CEC 2005 benchmark functions. The results lend weight to the argument that no through the distribution of pseudo-random numbers, but the hidden dynamics of chaotic systems representing the sequence of numbers may help to the evolutionary process and drives the population out of the local optimum.

Future plans include testing of different chaotic systems, either manually or evolutionary tuning of chaotic maps parameters, comparisons with different heuristics and obtaining a large number of results to perform statistical tests.

The future research will include the development of better cost functions, testing of different AP data sets, and performing of numerous simulations to obtain more results and produce better statistics, thus to confirm the robustness of this approach.

Acknowledgements. This work was supported by Grant Agency of the Czech Republic- GACR P103/13/08195S, by the project Development of human resources in research and development of latest soft computing methods and their application in practice, reg. no. CZ.1.07/2.3.00/20.0072 funded by Operational Program Education for Competitiveness; by the European Regional Development Fund under the project CEBIA-Tech No. CZ.1.05/2.1.00/03.0089, by the Technology Agency of the Czech Republic under the Project TE01020197, and by Internal Grant Agency of Tomas Bata University under the project No. IGA/FAI/2013/012.

References

1. Zelinka, I., Senkerik, R., Navratil, E.: Investigation on evolutionary optimization of chaos control. *Chaos, Solitons & Fractals* 40(1), 111–129 (2009)
2. Senkerik, R., Zelinka, I., Davendra, D., Oplatkova, Z.: Evolutionary Design of Chaos Control in 1D. In: Zelinka, I., Celikovsky, S., Richter, H., Chen, G. (eds.) *Evolutionary Algorithms and Chaotic Systems. SCI*, vol. 267, pp. 165–190. Springer, Heidelberg (2010)
3. Senkerik, R., Zelinka, I., Davendra, D., Oplatkova, Z.: Utilization of SOMA and differential evolution for robust stabilization of chaotic Logistic equation. *Computers & Mathematics with Applications* 60(4), 1026–1037 (2010)

4. Pyragas, K.: Control of chaos via extended delay feedback. *Physics Letters A* 206, 323–330 (1995)
5. Just, W.: Principles of Time Delayed Feedback Control. In: Schuster, H.G. (ed.) *Handbook of Chaos Control*. Wiley-Vch (1999)
6. Pyragas, K.: Continuous control of chaos by self-controlling feedback. *Physics Letters A* 170, 421–428 (1992)
7. Davendra, D., Zelinka, I., Senkerik, R.: Chaos driven evolutionary algorithms for the task of PID control. *Computers & Mathematics with Applications* 60(4), 898–1221 (2010) ISSN 0898-1221
8. Senkerik, R., Davendra, D., Zelinka, I., Oplatkova, Z., Pluhacek, M.: Optimization of the batch reactor by means of chaos driven differential evolution. In: Snasel, V., Abraham, A., Corchado, E.S. (eds.) *SOCO Models in Industrial & Environmental Appl. AISC*, vol. 188, pp. 93–102. Springer, Heidelberg (2013)
9. Senkerik, R., Davendra, D., Zelinka, I., Oplatkova, Z.: Chaos Driven Differential Evolution in the Task of Chaos Control Optimization. In: Proceedings of 2010 IEEE World congress on Computational Intelligence, 2010, pp. 1408–1415 (2010) ISBN-ISSN 978-1-4244-6910-9
10. Aydin, I., Karakose, M., Akin, E.: Chaotic-based hybrid negative selection algorithm and its applications in fault and anomaly detection. *Expert Systems with Applications* 37(7), 5285–5294 (2010)
11. Liang, W., Zhang, L., Wang, M.: The chaos differential evolution optimization algorithm and its application to support vector regression machine. *Journal of Software* 6(7), 1297–1304 (2011)
12. Zhenyu, G., Bo, C., Min, Y., Binggang, C.: Self-Adaptive Chaos Differential Evolution. In: Jiao, L., Wang, L., Gao, X.-b., Liu, J., Wu, F. (eds.) *ICNC 2006, Part I. LNCS*, vol. 4221, pp. 972–975. Springer, Heidelberg (2006)
13. Senkerik, R., Davendra, D., Zelinka, I., Pluhacek, M., Kominkova Oplatkova, Z.: Investigation on the Differential Evolution Driven by Selected Six Chaotic Systems in the Task of Reactor Geometry Optimization. In: 2013 IEEE Congress on Evolutionary Computation (CEC 2013), Cancún, MX (2013) ISBN 978-1-4799-0452-5
14. Pluhacek, M., Senkerik, R., Davendra, D., Kominkova Oplatkova, Z., Zelinka, I.: On the behavior and performance of chaos driven PSO algorithm with inertia weight. *Computers and Mathematics with Applications* 66, 122–134 (2013) ISSN 0898-1221
15. Sprott, J.C.: *Chaos and Time-Series Analysis*. Oxford University Press (2003)
16. Storn, R., Price, K.: Differential evolution - a simple and efficient heuristic for global optimization over continuous spaces. *Journal of Global Optimization* 11, 341–359 (1997)
17. Price, K.: An Introduction to Differential Evolution. In: Corne, D., Dorigo, M., Glover, F. (eds.) *New Ideas in Optimization*, pp. 79–108. McGraw-Hill, London (1999) ISBN 007-709506-5
18. Price, K., Storn, R.: Differential evolution homepage (2001), <http://www.icsi.berkeley.edu/~storn/code.html>
19. Price, K., Storn, R., Lampinen, J.: *Differential Evolution - A Practical Approach to Global Optimization*. Springer (2005) ISBN: 3-540-20950-6
20. Caponetto, R., Fortuna, L., Fazzino, S., Xibilia, M.: Chaotic sequences to improve the performance of evolutionary algorithms. *IEEE Trans. Evol. Comput.* 7(3), 289–304 (2003)

Arnold Cat Map and Sinai as Chaotic Numbers Generators in Evolutionary Algorithms

Lenka Skanderova and Ivan Zelinka

Department of Computer Science, VSB - Technical University of Ostrava, 17. listopadu 15,
708 33 Ostrava-Poruba Czech Republic

{lenka.skanderova, ivan.zelinka}@vsb.cz

Abstract. It is commonly known that evolutionary algorithms use pseudorandom numbers generators. They need them for example to generate the first population, they are necessary in crossing or perturbation process etc. In this paper chaos attractors Arnold Cat Map and Sinai are used as chaotic numbers generators. The main goal was to investigate if they are usable as chaotic numbers generators and their influence on the cost functions convergence's speed. Next goal was to compare reached values of Arnold Cat Map and Sinai and assess which attractor is better from the view of cost function convergence's speed.

1 Introduction

Differential evolution (DE) and Self migrating algorithm (SOMA) belong to the great family of evolutionary algorithms. Evolutionary algorithms are based on three basic principles - natural selection, crossing and mutation. They work with population of individuals, which is developing during generation cycles. DE is typical example of the evolutionary algorithm, because in its principle we can find each aspect mentioned above. There is the population of individuals, individuals are crossed and mutated. Best survive while worse die [12]. On the other hand the principle of SOMA is different. There is the population of individuals too but individuals migrate in space of possible solutions. There is no offspring. The individuals just change their positions. Generation cycles are replaced by migration cycles and crossing is replaced by perturbation.

For DE and SOMA, generator of pseudorandom numbers is necessary in many steps of the algorithms. The first population of individuals is created randomly. Each individual is created by parameters and fitness value. Each parameter has its own lower and upper bound. The parameters of individuals in the first population in these algorithms are generated randomly in that bounds. It is not possible to cross over these bounds. Pseudorandom numbers generators are necessary for example in crossing, perturbation vector creating etc. In this paper Sinai and Arnold Cat Map have been chosen as the chaotic numbers generators. As the cost functions 1st de Jong's, Schwefel's and Ranna's function have been chosen.

In 2013 papers [1]-[5] have been written in connection with DE. In [6]-[9] DE and SOMA are connected with chaos. In [10] we can find a pseudorandom number generator of q-Gaussian random variables based on chaotic map dynamics.

2 Evolutionary Algorithms

As it was mentioned above, evolutionary algorithms are based on three basic principles according to Darwin's and Mendel's theory. The family of these algorithms is very robust. In this paper, DE and SOMA have been chosen because their main principles are different.

2.1 Differential Evolution

Differential evolution works with population of individuals. These individuals are crossed and mutated and best survive while worse die. At beginning the first population is generated randomly. The number of individuals is given by parameter NP . As it was mentioned above individuals are created from parameters and fitness value. Fitness value says how good is this individual in population. When the first population is generated, reproduction cycle can begin:

- For each individual three next random individuals are chosen.
- Mutation is realized according to the Eq.1, where v_j denotes noise vector, $r1, r2, r3$ are three randomly chosen individuals from the population and F denotes mutation constant, its values can move in interval $[0,2]$.
- New individual creating. For each parameter random number r from interval $[0,1]$ is generated. If r is smaller than crossing probability CR the value from the noise vector is chosen as a parameter of new individual, else parameter from the actual individual is chosen.
- The fitness value of new individual is computed. If it is smaller than fitness of actual individual, new individual will replace actual individual, else, new individual will be forgotten and actual individual will stay in the population.

There are many types of DE. These types usually differ in noise vector computation. In this paper DE/rand/1/exp is used [11].

$$v_j = x_{r3,j}^G + F(x_{r1,j}^G - x_{r2,j}^G) \quad (1)$$

2.2 Self Organizing Migrating Algorithm (SOMA)

The principle of SOMA differs from DE. There is no offspring, individuals just migrate in the space of possible solutions. The begin of the algorithm is same like in DE. First population is generated randomly. Next steps differs according to the type of SOMA. In this paper SOMA AllToOne is used. Except this, AllToAll, AllToOne Random, All-ToAll Adaptive and AllToOne Adaptive exist. In the case of AllToOne next steps are realized [13]:

- *Leader*, the individual with best fitness, is chosen.
- Each individual migrates to the *Leader* – for each individual perturbation vector α is created. Perturbation vector consists of 0 and 1, and says in which direction the individual will migrate to the *Leader*.

- Individual migrate to the *Leader* in steps. The value of parameter t which denotes step is usually 0.11. Migration of individual is realized according to the Eq.2 where r is a new candidate solution, r_0 denotes actual individual, m is a difference between *Leader* and start position of individual and t is the step, $t \in [0, PathLength]$.

$$r = r_0 + mt\alpha \quad (2)$$

2.3 Chaos

There is no precise definition of chaotic system, we can find just some conditions to classify the system as chaotic:

- The system must be sensitive to initial conditions. This condition is very well known as a "butterfly effect" [14].
- The system must be topologically mixing. The typical example of chaotic system is mixing of colored dyes or fluids[15].
- The system's periodic orbits must be dense. Every point in the space is approached arbitrary closely by periodic orbits.

Chaotic map is defined such that:

Definition 1. A map: $f : X \rightarrow X$ of a metric space is said to exhibit sensitive dependence on initial conditions if there is a $\Delta > 0$, called a sensitivity constant, such that for every $x \in X$ and $\varepsilon > 0$ there exists a point $y \in X$ with $d(x, y) < \varepsilon$ and $d(f^N(x), f^N(y)) \geq \Delta$ for $N \in \mathbb{N}$ [14].

According to [14] this means that "the slightest error (ε) in any initial condition (x) can lead to a macroscopic discrepancy (Δ) in the evolution of the dynamics. Δ does not depend on x , nor on ε but only on the system."

Theorem 1. Chaotic maps exhibit sensitive dependence on initial conditions, except when the entire space consists of a single periodic orbit [14].

To visualize the chaotic movement phase diagram of movement is usually used. Time is implicit in this diagram and each axis represents one dimension of the state. If the graph creates the closed curve, this curve will be called orbit. It can be very often seen that the system ends in the same movement for all beginning states in the area around this movement - it seems that this system is attracted to this movement. This movement is called attractor of the system [16]. In [17] author says about attractor: "If one considers a system and its phase space, then the initial conditions may be attracted to some subset of the phase space (attractor) at time $t \rightarrow \infty$." Next author says about strange attractor: "For many other attractors the attracting set can be much more irregular (some would say pathological) and, in fact, can have a dimension that is not an integer. Such sets have been called fractal and, when they are attractors, they are called strange attractors."

In this paper Sinai attractor (Eq. 3) and Arnold Cat Map (Eq. 4) have been chosen. Sinai billiard is mentioned in [21] and [22]. In [18], [19] and [20] we will find Arnold Cat Map's using.

$$\begin{aligned}x_{n+1} &= (x_n + y_n + \sigma \cos(2\pi y_n)) \bmod 1, \\y_{n+1} &= (x_n + 2y_n) \bmod 1\end{aligned}\tag{3}$$

$$\begin{aligned}x_{n+1} &= (x_n + y_n) \bmod 1, \\y_{n+1} &= (x_n + ky_n) \bmod 1\end{aligned}\tag{4}$$

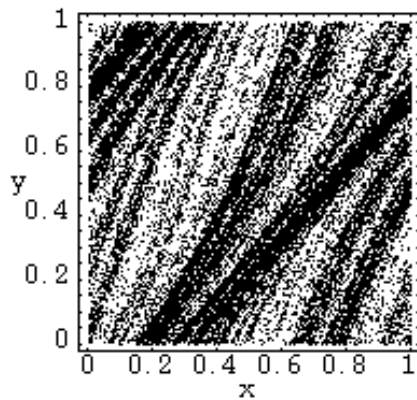


Fig. 1. Sinai map

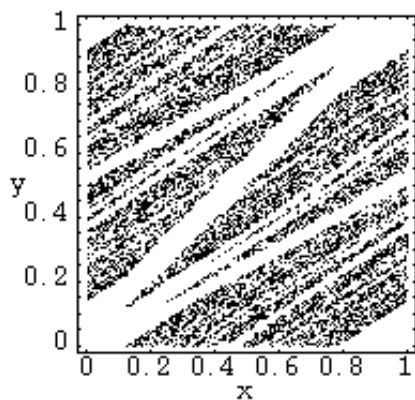


Fig. 2. Arnold Cat Map

3 Motivation

The main goal was to find out if Sinai and Arnold Cat map are useful as a generators of chaotic numbers and comparison of these chaotic equations each other. These equations have been compared from the view of the evolutionary algorithms (DE and SOMA) cost functions convergence's speed.

4 Experiments Design

For experiments HP Pavilion dv7-6050 with processor Intel Core i7 with frequency 2 GHz, 4 GB RAM and graphic card AMD Radeon HD 6770M and Microsoft Visual Studio 2010 have been used. The experiments have been processed by Mathematica 8 and Gnuplot 4.6. Precise setting of DE is mentioned in Table 1 and precise setting of SOMA in Table 2. Schwefel's function, 1st de Jong's function and Ranna's function have been chosen as the testing functions. Schwefel's function has many local extremes while 1st de Jong is not so jagged. And Ranna's function has been chosen because there is no global extreme described in the literature. For each function and chaos equation special experimental set has been created. For each equation, Sinai and Arnold Cat Map, one set of experiments has been created. In each set each experiment has been repeated one hundred times.

Table 1. DE setting

Parameter	Value
<i>NP</i>	100
<i>D</i>	20
<i>Migrations</i>	300
<i>PathLength</i>	3
<i>Step</i>	0.11
α	0.1

Table 2. SOMA setting

Parameter	Value
<i>NP</i>	50
<i>D</i>	20
<i>Generations</i>	1800
<i>F</i>	0.9
<i>CR</i>	0.4

5 Results

Results are mentioned in Tab. 3, where we can see minimum, maximum and average reached values for DE and SOMA, where 1st de Jong's, Ranna's and Schwefel's functions have been used as testing functions. In Fig. 3 comparison of Arnold Cat Map and Sinai used as chaotic numbers generators in DE, where 1st de Jong's function has been used as testing function is depicted. Fig. 4 shows the comparison, where SOMA has been used as the evolutionary algorithm and Ranna's function has been used as the cost function and in Fig. 5 comparison of both chaotic numbers generators used in DE, where Schwefel's function has been chosen as the cost function is depicted.

Table 3. Comparison of chaotic numbers generators Sinai and Arnold Cat Map, from the view of evolutionary algorithm convergence's speed. For better illustration there is smaller numbers in the rows with 1st de Jong's function. Settings of evolutionary algorithms are mentioned in Tables 1 and 2.

Evolutionary algorithm	Pseudorandom numbers generator	Function	Min	Max	Average
DE	Sinai	1st de Jong	6.963×10^{-9}	7.015×10^{-8}	2.530×10^{-8}
		Ranna	-6220.839	-5240.327	-5641.828
		Schwefel	-8379.658	-8379.658	-8379.658
	Arnold Cat Map	1st de Jong	9.343×10^{-9}	9.634×10^{-8}	3.859×10^{-8}
		Ranna	-6359.965	-5048.777	-5460.802
		Schwefel	-8379.658	-8379.658	-8379.658
SOMA	Sinai	1st de Jong	3.021 10^{-33}	1.020 10^{-31}	2.199 10^{-32}
		Ranna	-9065.627	-8477.0319	-8789.540
		Schwefel	-8379.658	-8261.219	-8377.289
	Arnold Cat Map	1st de Jong	4.569 10^{-33}	1.185 10^{-31}	3.509 10^{-32}
		Ranna	-8967.828	-8402.458	-8669.560
		Schwefel	-8379.658	-8261.219	-8376.105

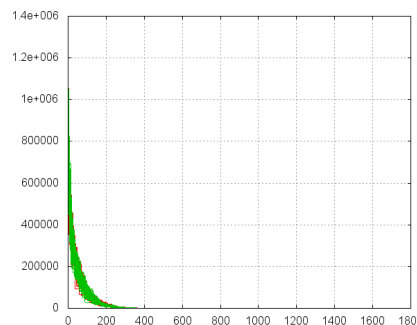


Fig. 3. DE, 1st de Jong's function, comparison of Arnold Cat Map (red) and Sinai (green)

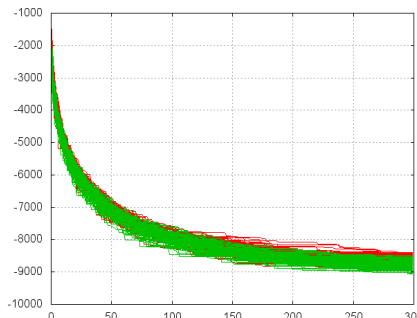


Fig. 4. SOMA, Ranna's function, comparison of Arnold Cat Map (red) and Sinai (green)

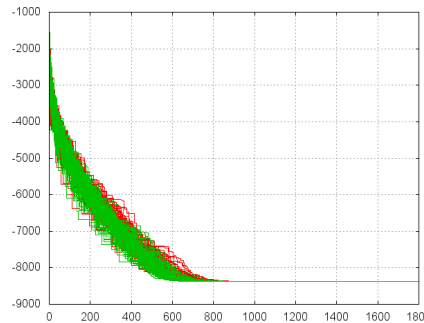


Fig. 5. DE, Schwefel's function, comparison of Arnold Cat Map (red) and Sinai (green)

6 Conclusion

In Tab. 3 there are described minimum, maximum and average values reached during the evolution for DE and SOMA, where 1st de Jong's, Ranna's and Schwefel's functions has been used as testing function and Arnold Cat Map and Sinai have been used as pseudorandom numbers generators. From these results we can make some conclusions:

- We can say that both algorithms are usable as the generators of chaotic numbers. When we look at the Table 3 we will see that their results are comparable.
- DE, 1st de Jong's function: We can say that when Arnold Cat Map was used, 1st de Jong's function convergence has been faster. But the difference between Arnold Cat Map and Sinai is very small and we can consider it insignificant, see Fig. 3.
- DE, Ranna's function: There is no global minimum mentioned in literature by Ranna's function. As we can see both algorithms reached values around -6300. Arnold Cat Map reached smaller values than Sinai and the situation is the same like in the previous case, see Fig. 5.
- DE, Schwefel's function: Both algorithms reached the global minimum of the Schwefel's function. Their values mentioned in Table 3 are the same.
- SOMA, 1st de Jong's function: Reached values are significantly smaller than in DE. From the view of chaotic numbers generators both algorithms reached comparable values. Arnold Cat Map reached smaller values than Sinai. But the difference is insignificant.
- SOMA, Ranna's function: The same situation happened when Ranna's function has been used as the cost function. The results of both chaotic numbers generators are comparable, see Fig. 4.
- SOMA, Schwefel's function: As well as in previous cases both algorithms reached comparable values. In Schwefel's function they reached the global minimum of the cost function.
- The results of both attractors are very similar. When we look at Figs. 1 and 2 it is not surprising phenomenon, because these attractors are relatively similar.

Acknowledgements. The following grants are acknowledged for the financial support provided for this research: Grant Agency of the Czech Republic - GACR P103/13/08195S, by the Development of human resources in research and development of latest soft computing methods and their application in practice project, reg. no. CZ.1.07/2.3.00/20.0072 funded by Operational Programme Education for Competitiveness, co-financed by ESF and state budget of the Czech Republic, and by Grant of SGS No. SP2013/114, VLB - Technical University of Ostrava, Czech Republic.

References

1. Koloseni, D., et al.: Differential evolution based nearest prototype classifier with optimized distance measures for the features in the data sets. *Expert Systems with Applications* 40, 4075–4082 (2013), doi:10.1016/j.eswa.2013.01.040
2. Tasgetiren, M.F., et al.: A variable iterated greedy algorithm with differential evolution for the no-idle permutation flowshop scheduling problem. *Computers & Operations Research* 40, 1729–1743 (2013), doi:10.1016/j.cor.2013.01.005
3. De Melo, V.V., Carosio, G.L.C.: Investigating Multi-View Differential Evolution for solving constrained engineering design problems. *Expert Systems with Applications* 40, 3370–3377 (2013), doi:10.1016/j.eswa.2012.12.045
4. Depolli, M., et al.: Asynchronous Master-Slave Parallelization of Differential Evolution for Multi-Objective Optimization. *Evolutionary Computation* 21, 261–291 (2013)
5. Maione, G., Punzi, A.: Combining differential evolution and particle swarm optimization to tune and realize fractional-order controllers. *Mathematical and Computer Modelling of Dynamical Systems* 19, 277–299 (2013), doi:10.1080/13873954.2012.745006
6. Senkerik, R.: On the Evolutionary Optimization of Chaos Control - A Brief Survey. In: Zelinka, I., Snasel, V., Rössler, O.E., Abraham, A., Corchado, E.S. (eds.) *Nostradamus: Mod. Meth. of Prediction, Modeling*. AISC, vol. 192, pp. 35–48. Springer, Heidelberg (2013)
7. Senkerik, R., Oplatkova, Z., Zelinka, I.: Evolutionary Synthesis of Control Rules by Means of Analytic Programming for the Purpose of High Order Oscillations Stabilization of Evolutionary Synthesized Chaotic System. In: Zelinka, I., Snasel, V., Rössler, O.E., Abraham, A., Corchado, E.S. (eds.) *Nostradamus: Mod. Meth. of Prediction, Modeling*. AISC, vol. 192, pp. 191–201. Springer, Heidelberg (2013)
8. Zelinka, I., et al.: An Investigation on Evolutionary Reconstruction of Continuous Chaotic Systems. *Mathematical and Computer Modelling* 57, 2–15 (2013), doi:10.1016/j.mcm.2011.06.034
9. Nguyen, T.D., Zelinka, I.: Using Method of Artificial Intelligence to Estimate Parameters of Chaotic Synchronization Systems. In: Mendel 2011-17th International Conference on Soft Computing, Mendel, pp. 22–29 (2011)
10. Umeno, K., Sato, A.H.: Chaotic Method for Generating q-Gaussian Random Variables. *IEEE Transactions on Information Theory* 59, 3199–3209 (2013), doi:10.1109/TIT.2013.2241174
11. Wang, H., et al.: Gaussian Bare-Bones Differential Evolution. *IEEE Transactions on Cybernetics* 43, 634–647 (2013), doi:10.1109/TCYB.2012.2213808
12. Caamano, P., et al.: Evolutionary algorithm characterization in real parameter optimization problems. *Applied Soft Computing* 13, 1902–1921 (2013), doi:10.1016/j.asoc.2013.01.002
13. Senkerik, R., et al.: Synthesis of feedback controller for three selected chaotic systems by means of evolutionary techniques: Analytic programming. *Mathematical and Computer Modelling* 57, 57–67 (2013), doi:10.1016/j.mcm.2011.05.030
14. Hasselblatt, B., Katok, A.: *A First Course in Dynamics: With a Panorama of Recent Developments*. Cambridge University Press (2003) ISBN 0-521-58750-6

15. Vellekoop, M., Berlund, R.: Om Intervals, Transitivity = Chaos, vol. 101, pp. 353–355. The American Mathematical Monthly, JSTOR (1994)
16. Liu, C.: A novel chaotic attractor. Chaos, Solitons & Fractals 39, 1037–1045 (2009)
17. Grebogi, C., et al.: Chaos, Strange Attractors, and Fractal Basin Boundaries in Nonlinear Dynamics. In: Non-Linear Physics for Begginers: Fractals, Chaos, Pattern Formation, Solutions, Cellular Automata and Complex Systems, pp. 111–117. Word Scientific Publishing Co. Pte. Ltd. (1998)
18. Chen, F., et al.: Period Distribution of the Generalized Discrete Arnold Cat Map for N=2(e). IEEE Transactions on Information Theory 59, 3249–3255 (2013), doi:10.1109/TIT.2012.2235907
19. Bao, J.H., Yang, Q.G.: Period of the discrete Arnold cat map and general cat map. Nonlinear Dynamics 70, 1365–1375 (2012), doi:10.1007/s11071-012-0539-3
20. Kanso, A., Ghebleh, M.: A novel image encryption algorithm based on a 3D chaotic map. Communications in Nonlinear Science and Numerical Simulation 17, 2943–2959 (2012), doi:10.1016/j.cnsns.2011.11.030
21. Yang, R., et al.: Harnessing quantum transport by transient chaos. CHAOS 23 (March 2013), doi:10.1063/1.4790863
22. Pecora, L.M., et al.: Regularization of Tunneling Rates with Quantum Chaos. International Journal of Bifurcation and Chaos 22 (October 2012), doi:10.1142/S0218127412502471

Optimizing Transportation Sequence in Warehouse with Genetic Algorithms

Xuan-Thuong Tran¹, Thanh-Do Tran², and Hwan-Seong Kim³

¹ Graduate School, Korea Maritime University, South Korea

² Inria Lille – Nord Europe and Université Lille 1, France

³ Department of Logistics, Korea Maritime University, South Korea

Abstract. Optimizing transportation sequence is crucial to reduce material handling costs in warehouse operations and thus in total logistics costs. Transportation sequence is the ordering of storage and retrieval jobs that a material handling device has to perform to finish an order list. In many studies, the optimization of transportation sequence has been simplified as an order-picking problem, and accordingly solved as a classical traveling salesman problem. However, transportation sequence is a double-cycle storage and retrieval problem (DCSRP) in itself, meaning that the combination of storage and retrieval jobs into double cycles has to be considered simultaneously. In this paper, we propose formulating the DCSRPs as a permutation problem and applying several genetic algorithms to solve the formulated problem. Extensive computational experiments were performed to demonstrate the capability of the approach. The experimental analysis confirms that our approach could solve the problem efficiently on the one hand, and addresses the question of which genetic operators are best applied to the formulated DCSRPs on the other hand.

Keywords: Transportation sequence, genetic algorithms, permutation.

1 Introduction

Typical functions of a warehouse include receiving, storage, order picking, and shipping. In [3], the authors provided a comprehensive review of research on warehouse operation, in which various decision support models and solution algorithms for each of the functions were discussed. One of the repeated activities that absorbs significant costs in total warehouse operational costs is material handling. This activity comprises order picking, loading and unloading goods, and transporting to another location for unloading and loading, etc.

These material handling activities are unavoidable since Stock Keeping Units (SKUs) are stored in different locations in a warehouse while orders may come from various customers and/or departments. Transportation costs, both external and in-house transportation, contribute as the highest cost of total logistics costs (> 40%). To reduce these costs, it is required to reduce traveling distance (and also traveling time) of transporters—which are forklift trucks in our work.

In warehouses, a single transport order is described as a movement of one storage unit from one location (source) to another location (sink). Such orders are transferred to the subordinate control of a forklift operating in a warehouse aisle. Thereby the warehouse management system (WMS) can control the sequence (i.e. ordering) of operations to be performed by a forklift in an aisle. In each aisle, loads (e.g. pallets) to be stored and retrieved by the forklift are buffered in the warehouse prestorage zone [4].

A straightforward method to optimize transportation sequence in an aisle is to combine simultaneous storage and retrieval jobs into multiple cycles. Fig. 1 illustrates the comparison between single- and double-cycle operation modes. There are two transport orders in this illustration. The order 1 is a storage job and the order 2 is a retrieval job. By combining two orders into double cycle operation shown in Fig. 1b, the total traveling distance to complete two orders is 16 length units in comparison with the single-cycle case in Fig. 1a with a total of 26 length units.

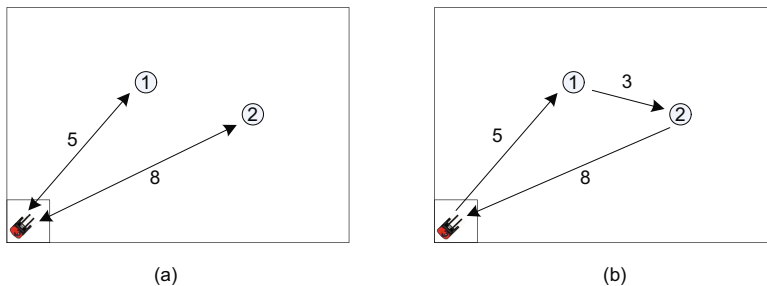


Fig. 1. Single vs double cycle operation mode

The DCSR problem is one of the sequencing problems that occurs in many fields of material flow. Another problem with similar characteristics is the well-known order-picking problem [1,2]. The objective of these problems is to find an optimal sequence of transportation (or order-picking) that yields the *minimal* total traveling distance of the material handling transporter (or picker). Such kind of sequencing problems can be considered as the traveling salesman problem (TSP), which is among the most popular NP-hard combinatorial problems [6]. In fact, several existing investigations into these sequencing problems have been formulated via the TSP [7,11].

Specifically in warehouse operations, a large portion of research has been performed to tackle the order-picking problem. For example, in [11], the authors use TSP heuristic algorithms to address the sequencing problems of order pickers in conventional multi-parallel-aisle warehouse systems. Another example is the use of TSP-based k-interchange method for solving the problem of routing order pickers in single-block warehouses [7]. Meanwhile, the issue of double-cycle transportation in warehouses has not been considered rigorously in the operations research literature. Motivated by previous research on using TSP heuristics

for solving the order-picking problem, in this paper, we discuss the optimization of transportation sequence in warehouses by solving the double-cycle storage and retrieval problem. To be more specific, we aim to find an optimal combination of all double cycles that the forklift has to follow to finish an order list with minimal traveling distance.

One of the benefits of transferring the order-picking problem into the TSP is the existence of various solution approaches for this problem. Recent development in metaheuristics, including the hybridization of evolutionary algorithms with heuristics as a local search strategy, have provided promising solution approaches to the TSP. Among evolutionary algorithms, genetic algorithms are the most popular technique and have certain success in solving NP-hard problems, including the TSP [5]. In this paper, we formulate the DCSRP as a permutation problem and employ different genetic algorithms to solve the resulting problem.

The remainder of this paper is organized as follows. In Sect. 2, the double-cycle storage and retrieval problem in a multi-parallel-aisle warehouse system is described and then formulated as permutation problem. Next, in Sect. 3, we present an approach to solving the formulated problem using genetic algorithms (GAs) and review different genetic operators to be used. Then, in order to evaluate the effectiveness of GAs to our problem, extensive computational experiments were implemented and the results are analyzed in Sect. 4. Finally, some conclusions and possible extensions for future research are discussed.

2 Problem Description and Formulation

2.1 Problem Description

A conventional multi-parallel-aisle warehouse system is shown in Fig. 2. This warehouse consists of r racks and l aisles. In this paper, we consider a warehouse containing only full-sized pallets, which are stored on the racks and in both sides of the aisles. In this figure, those pallets that need to be stored are denoted by filled rectangles and those that need to be retrieved are denoted by crossed rectangles. Buffer zone is the location where pallets are released and also where a forklift picks the pallets that need to be stored in warehouse.

A double cycle is executed as follows. First, the forklift starts from the buffer zone (B), loads a pallet, moves to the designated storage location (S), and stores the pallet. Then, it approaches the pallet to be retrieved at the retrieval location (R), picks this pallet, travels back to the buffer zone, and unloads the pallet. At this point, the forklift has completed a double cycle and the process is repeated until all transport orders are finished.

Given the DCSRP as described above, the aim of a warehouse manager is to find a sequence of transportation that minimizes the total traveling distance of the forklift. In other words, the goal is to determine a combination of double cycles that results in minimal traveling distance. Such a sequencing problem can be viewed as a permutation problem. Permutation is one of the NP-hard problems for which there does not exist any exact algorithms that can give optimal solutions in polynomial time. For this class of problem, (meta-) heuristics are

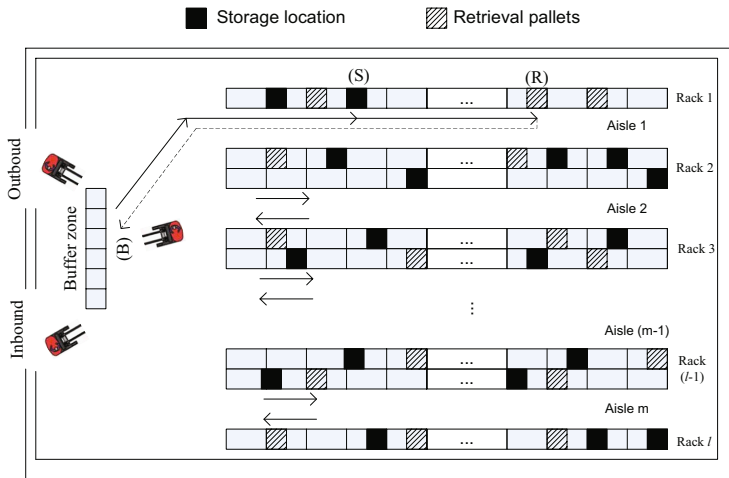


Fig. 2. Multi-parallel-aisle warehouse system

commonly employed to approximate the optimal solutions. In the following, we show that our formulated problem has the computational complexity of factorial, and thus call for the use of evolutionary algorithms as a solution approach.

Assuming that a symmetrical order volume consists of n storage and n retrieval jobs; therefore, n double cycles have to be executed by the forklift in a consecutive sequence. The first of the n storage jobs may be followed by one of the n retrieval jobs. Then, the second may be followed by one of the $(n - 1)$ remaining retrieval jobs. Similarly for the rest of the n storage jobs, there will have a total of $n!$ possible sequences of double cycles that can be chosen. Since any of the n storage jobs can be chosen first in the sequence, the number of all possible double-cycle sequences theoretically amounts to $(n!)^2$.

However, the ordering of double cycles normally has no effect on the overall distance [4]. This means that the two double-cycle sequences 1–4–7 and 7–4–1, for example, are considered to be the same. Thanks to this property, the number of possible sequences of a symmetrical order volume with n storage and n retrieval jobs is reduced to $n!$.

2.2 Problem Formulation

To facilitate the formulation, some assumptions and notations are needed.

Assumptions:

- First of all, the number of storage jobs and retrieval jobs in each aisle are equal and this symmetric order volume is known beforehand.

- The forklift starts and ends a trip at the buffer zone; so, there is no need to add the traveling cost from the ending point of a trip to the starting point of next trip.
- The forklift can identify the pallets that need to be picked up or retrieved.

Notations:

S : the set of storage jobs, with $|S| = n$ being the no. of storage jobs in S .

R : the set of retrieval jobs, with $|R| = n$ being the no. of retrieval jobs in R .

B : buffer area where stored pallets and retrieved pallets are located.

$d(B \rightarrow S_i)$: distance from the buffer area to storage position S_i , $S_i \in S$.

$d(S_i \rightarrow R_j)$: distance from storage position S_i to retrieval position R_j .

$d(R_j \rightarrow B)$: distance from retrieval position R_j to the buffer position.

P_k : the k -th permutation of the set R , indicating an ordering (i.e. sequence) of retrieval jobs, where $k = 1, 2, \dots, n!$. For example, with $R = \{R_1, R_2, R_3, R_4\}$, a permutation of R could be $\{R_2, R_1, R_3, R_4\}$. P_k is an ordered set.

P_Σ : the set of all possible permutations, i.e. $P_\Sigma = \{P_k\}_{k=1}^{n!}$

$C_j(P_k)$: the cost of double cycle j , where $j = 1, 2, \dots, n$. Note that there are exactly n double cycles in each sequence.

$TC(P_k)$: total cost to complete n double cycles associated with P_k .

With the above notations, let us consider a DCSRP with symmetrical order volume consisting of n storage jobs and n retrieval jobs. The cost of a double cycle j in the sequence corresponding to the permutation P_k , where $k = 1, 2, \dots, n!$, is calculated by Eq. 1:

$$C_j(P_k) = d(B \rightarrow S_i) + d(S_i \rightarrow R_j) + d(R_j \rightarrow B), \quad (1)$$

where $S_i \in S$ with $i = 1, 2, \dots, n$, and $R_j \in P_k$ with $j = 1, 2, \dots, n$. Finally, the total cost to complete n double cycles in permutation P_k is computed by Eq. 2:

$$TC(P_k) = \sum_{j=1}^n C_j(P_k). \quad (2)$$

The objective of solving the DCSRP is to find a permutation $P^* \in P_\Sigma$ of the set R [of retrieval jobs] that minimizes the total traveling distance of the forklift:

$$P^* = \arg \left[\min_{P_k \in P_\Sigma} (TC(P_k)) \right]. \quad (3)$$

Eventually, the optimal solution of the DCSRP is a sequence of n double cycles. Each double cycle i of the sequence consists of a pair of the storage job S_i and the retrieval job R_j , where R_j is the i -th element of P^* . Let us

consider an example with 4 storage jobs $S = \{S_1, S_2, S_3, S_4\}$ and 4 retrieval jobs $R = \{R_3, R_2, R_1, R_4\}$. Assuming that the optimal solution of this DCSR is $P^* = \{R_3, R_2, R_1, R_4\}$, then the optimal sequence of double cycles is:

$$(B \rightarrow S_1 \rightarrow R_3 \longrightarrow B \rightarrow S_2 \rightarrow R_2 \longrightarrow B \rightarrow S_3 \rightarrow R_1 \longrightarrow B \rightarrow S_4 \rightarrow R_4 \rightarrow B)$$

It is worth noting that the permutation of the set S of n storage jobs does not affect the solution of the problem. Note also that the DCSR is subject to a number of constraints. The first constraint is that each storage job position or retrieval job position can only be visited once. Second, in each double cycle, the forklift must firstly visit a storage location to unload the pallet and then move to a retrieval position to load the retrieval pallet; and this order must be respected. Third, after loading a retrieval pallet, the forklift must always move to the buffer area where the pallet is to be pre-stored. In the next section, we will discuss the use of genetic algorithms to solve the formulated DCSR.

3 Genetic Algorithms for the DCSR

Genetic algorithms (GAs) [8] are perhaps among the most widely used evolutionary optimization techniques. GAs are adaptive randomized searchers that simulate the genetic inheritance and the Darwinian principle of striving for survival in nature. One might find GAs simple to implement, fun to use, and versatile to solve a wide range of problems. GAs are often useful to problems for which there is no algorithm available or the computation to reach the exact optimum is unaffordable. The pseudocode of typical GAs is given in Alg. 1.

Algorithm 1. Pseudocode of Genetic Algorithms

- 1: INITIALIZATION: randomly generate a population of N individuals
 - 2: EVALUATION: evaluate the initial population
 - 3: **while** (not STOPPING_CRITERIA) **do**
 - 4: MATING SELECTION: select parents to reproduce offsprings
 - 5: CROSSOVER: apply crossover operator to the mating pool to generate offsprings
 - 6: MUTATION: mutate the offsprings by [genetic] mutation operator
 - 7: EVALUATION: evaluate the offspring population
 - 8: SURVIVOR SELECTION: select individuals for the next generation
 - 9: **end while**
-

First of all, we have to define how a candidate solution to the problem is represented in GAs. For the DCSR formulated in Sect. 2.2, it is quite straightforward to use integer numbers from 1 to n (with n being the number of retrieval jobs) to directly encode a retrieval job's number. By this way, a candidate solution to the DCSR is just a series of unique integers; and the ordering of the numbers in this series determines which retrieval job to be handled together with which storage job in a double cycle. More precisely, the value (from 1 to n) of an integer in the series indicates the retrieval job's number, while the position (also from 1 to n) of this integer in the series indicates the companion storage

job's number. In other words, a permutation of the series generates a candidate solution to the problem. With this encoding scheme, it is trivial to create an initial population of N individuals for GAs, just by performing N permutations.

Given a candidate solution, it is essential to compute the objective value (i.e. the cost, or the total traveling distance in this case) associated with it. Using the above-mentioned encoding strategy and the problem formulation given in Sect. 2.2, the cost of a solution is computed by summing up the costs induced by all component double cycles (see Eq. 2). The cost of each double cycle, in its turn, is—as denoted in Eq. 1—the summation of three components: the distance from the buffer to the storage location, the distance between the storage and retrieval jobs, and the distance from the retrieval job to the buffer. By these calculations, every *feasible* solution (i.e. a series of *unique* integers from 1 to n) can be evaluated for its objective value.

In addition to the representation and evaluation function, the determination of proper genetic operators, including crossover and mutation, are of paramount importance to a GA. These operators are strongly dependent on the solution representation. For the permutation encoding described above, there exist a number of crossover and mutation operators that can be applied. In this work, *five* crossover operators: (1) order crossover (OX), (2) partially mapped crossover (PMX), (3) cycle crossover (CX), (4) position-based crossover (PBX), and (5) modified order crossover (MOX); and *two* mutation operators: (1) reciprocal exchange (or swap) mutation (S) and (2) inversion mutation (I), were selected to deploy. Due to the space limitation, complete details about these operators are not given in this paper; a full description is therefore redirected to [10,8,5].

Such operators have been widely tested on the TSP and scheduling problem. As pointed out in p. 242 of [8], both problems are of sequencing type but they differ in characteristics and thus require different operators. The adjacency information (i.e. distances between cities) is important for the TSP but not applicable to the scheduling problem, while the relative order of items is not important for the TSP yet is of great concern in the scheduling problem. It is clear from the above encoding that the formulated DCSR displays different properties than both the TSP and the scheduling problem, as no adjacency information exists and the relative order of integers in the series is also not a decisive factor. The motivation here is therefore to evaluate several operators and to learn about their performance on the DCSR.

In order to complete the nuts and bolts of a GA, some other components need also to be defined. For mating selection, in this work, we employ the binary tournament selection strategy. This tournament selection could favor a low selection pressure [9], which has been known to be useful in preventing premature stagnation during the evolution. Additionally, it is required to have another selection mechanism in between two consecutive generations. In this study, when a new population is generated and evaluated, GAs evolves to the next generation by discarding the parent population except for its best individual. The best of the past population replaces the worst of the current population. This survivor selection mechanism is often referred to as the generational-with-elitism strategy.

4 Experiments and Discussions

In this section, an extensive analysis is presented to verify the validity of the proposed approach to the DCSR problem and to answer the question of which genetic operators are most suitable for the formulated problem. For problem instances, we used two real warehouse datasets, having pallets stored in one and two aisles, respectively. For the dataset of one aisle, different instances with the symmetric order volumes of 10, 20, and 30 pallets were simulated by sampling randomly from the aisle, repeated twice for each volume, resulting in six instances. The same procedure was applied to the dataset of two aisles, but with the symmetric order volumes of 10, 20, 30, 40, 50, 60, and 70 pallets being sampled, resulting in 14 instances. Consequently, we solved a total of 20 problem instances. It should be noted that the four instances with a ten-pallet volume are practically small; they are still possible to be solved to optimality by an enumeration method. Their true optimal solutions could therefore be known exactly.

For algorithms, we considered five crossovers and two mutations as listed in Sect. 3, which amounts to a total of ten GAs. Each GA is then referred to by its crossover's and mutation's abbreviations; the S+OX, for example, thereby refers to the GA using swap mutation and order crossover. All the GAs used a crossover rate $p_{cross} = 1$, a mutation rate $p_{mut} = 0.15$, and a fixed population size $popsize = 100$. On each problem instance, each GA was launched 30 times with different initial populations to mitigate its random effect. With 20 instances and ten GAs, we performed a total of 6000 runs. As a simple stopping criterion, we terminated a run after a fix number of generations, which was set empirically to 200 for those instances with a volume of 30 or less, and to 500 for those with larger volumes. It is worth noting that, for evaluating a solution, the distances in Eq. 1 were computed prior to the GA runs using a shortest path method; these distances thereby reflect the real traveling distances in the warehouse.

The performance of ten GAs on three typical instances are presented in Fig. 3. It can be clearly observed that the GAs with an OX or MOX crossover performs worst, no matter which mutation it goes with. For the GAs with PMX, CX, and PBX, the performance depends greatly on mutation: those GAs with inversion mutation perform worse than their counterparts with swap mutation; and for the GAs using swap mutation, those equipped with PMX and CX impressively outperform all the other GAs. The difference between S+PMX and S+CX is however unobvious. These trends are invariant across the three instance sizes.

Table 1 summarize the best algorithm (i.e. the winner out of the ten GAs) in terms of its median-quality solution across 30 runs. This table is compiled from the results of all the 6000 runs of the ten GAs. Three main remarks can be drawn from this table. First, the GA with swap mutation and PMX crossover perform best on most of the instances and datasets. Second, the same GA but with CX crossover perform better on the instances of size 50; and this could also be observed in the middle boxplot in Fig. 3. Interestingly, for the two 30-pallet instances from the one-aisle dataset, the two mentioned GAs dominate each other by random. Third, for small instances with only 10 pallets, all GAs could finally find the true optima. The computational budget for the GAs here

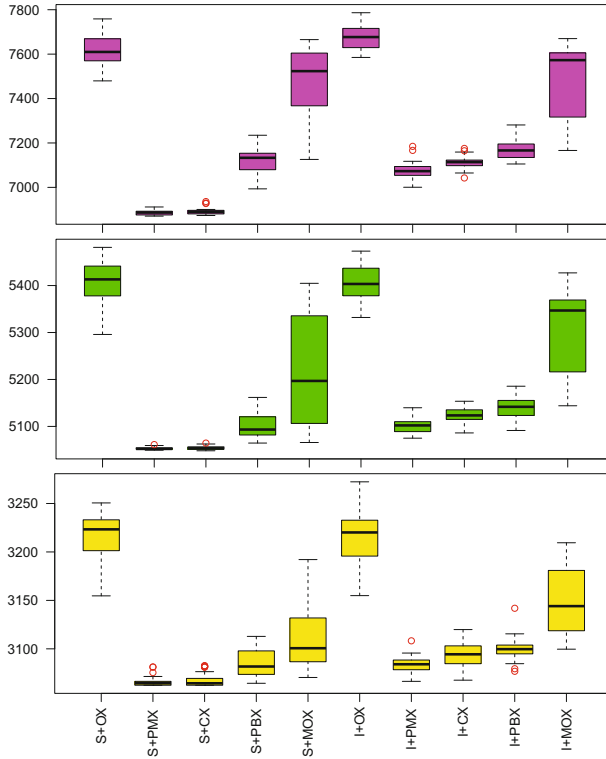


Fig. 3. Solutions in 30 runs of ten GAs across three instance sizes 30, 50, and 70, which are presented in the lower (yellow), middle (green), and upper (magenta) boxplots, respectively. In each plot, the lower a box, the better is the corresponding algorithm.

Table 1. The best algorithms in terms of median over 30 runs of the best achieved objective value in each run. For each of the datasets (one and two aisles), two random order lists were sampled to create two random instances. A ‘–’ indicates the unavailability of an instance for the corresponding size. An ‘ALL’ denotes that all ten algorithms could equally solve the instance to optimality, thus they are incomparable in the end.

Instance	10	20	30	40	50	60	70
One aisle 1	ALL	S+PMX	S+PMX	–	–	–	–
One aisle 2	ALL	S+PMX	S+CX	–	–	–	–
Two aisles 1	ALL	S+PMX	S+PMX	S+PMX	S+CX	S+PMX	S+PMX
Two aisles 2	ALL	S+PMX	S+PMX	S+PMX	S+CX	S+PMX	S+PMX

is much smaller than the enumeration method’s. These results could therefore reflect somewhat the effectiveness and efficiency of the proposed approach.

Finally, Fig. 4 provides some insight into the evolution of the ten GAs. The profiles of S+PMX and S+CX, in addition to the plots in Fig. 3, once again

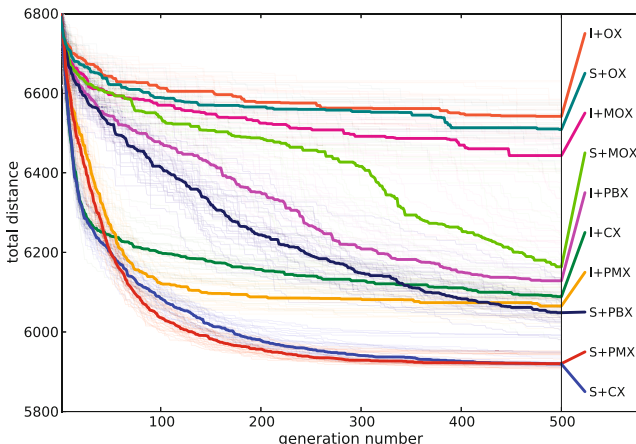


Fig. 4. The 30 run profiles of ten GAs on an instance of size 60. At each generation in a run, the best-so-far objective value of each GA was recorded, forming a profile for that run. Thirty profiles for each GA are plotted in the same transparent color in the background. The median of the 30 profiles is plotted by a thick line of the same color.

confirm their suitability for the formulated problem. The swap mutation provides better convergence than the inversion. And more importantly, the PMX and CX crossovers exhibit a persuasive success on the DCSRPs.

5 Conclusions

The double-cycle storage and retrieval problem is an important problem in warehouse operations. Notwithstanding its relevance and importance, there is a lack of general-purpose solution approaches to this problem in the literature. In this work, we have formulated the DCSRPs as a permutation problem and solved it using genetic algorithms. Since this problem was not given due attention in the evolutionary optimization community, less or no knowledge about which genetic operators work best on it. Through an extensive experiment, we could draw a conclusion that the GA equipped with a swap mutation coupled with a PMX or CX crossover clearly outperforms the GAs using any of the other genetic operators under consideration. The second conclusion is that, for instances of as small size as 10 with the exact optimum being known, GAs can efficiently solve the instances to optimality within a limited number of function evaluations. What still remain interesting to know are the impact of other GA parameters, such as crossover and mutation rates, and the effectiveness of the algorithm when the problem size grows to a much larger number of items, e.g. hundreds or even thousands. These questions deserve further investigations into the DCSRPs.

Acknowledgement. This research was supported by a grant (11 Transportation System – Logistics 02) from the Transportation System Efficiency Program funded by the Ministry of Land, Infrastructure and Transport of the Korean government. TDT is supported by the CORDI-S Doctoral Fellowship of the French National Institute for Research in Computer Science and Control.

References

1. De Koster, R., Le-Duc, T., Roodbergen, K.J.: Design and control of warehouse order picking: A literature review. *Eur. J. Oper. Res.* 182(2), 481–501 (2007)
2. Goetschalckx, M., Donald Ratliff, H.: Order picking in an aisle. *IIE Transactions* 20(1), 53–62 (1988)
3. Gu, J., Goetschalckx, M., McGinnis, L.F.: Research on warehouse operation: A comprehensive review. *Eur. J. Oper. Res.* 177(1), 1–21 (2007)
4. ten Hompel, M., Schmidt, T.: *Warehouse Management: Automation and Organisation of Warehouse and Order Picking Systems*. Intralogistik. Springer (2007)
5. Larrañaga, P., Kuijpers, C., Murga, R., Inza, I., Dizdarevic, S.: Genetic algorithms for the travelling salesman problem: A review of representations and operators. *Artificial Intelligence Review* 13(2), 129–170 (1999)
6. Lawler, E.L., Lenstra, J.K., Kan, A.R., Shmoys, D.B.: *The Traveling Salesman Problem: A Guided Tour of Combinatorial Optimization*. Wiley, New York (1985)
7. Makris, P.A., Giakoumakis, I.G.: k-interchange heuristic as an optimization procedure for material handling applications. *App. Math. Model.* 27(5), 345–358 (2003)
8. Michalewicz, Z.: *Genetic Algorithms + Data Structures = Evolution Programs*, 3rd edn. Springer, London (1996)
9. Sokolov, A., Whitley, D.: Unbiased tournament selection. In: *Proceedings of the GECCO 2005*, pp. 1131–1138. ACM, NY (2005)
10. Starkweather, T., McDaniel, S., Mathias, K., Whitley, D.: A comparison of genetic sequencing operators. In: *Proc. of 4th ICGA*, pp. 69–76. Morgan Kaufmann (1991)
11. Theys, C., Bräysy, O., Dullaert, W., Raa, B.: Using a TSP heuristic for routing order pickers in warehouses. *Eur. J. Oper. Res.* 200(3), 755–763 (2010)

Decentralized Output Feedback Control for Mismatched Uncertain Large Scale Systems: An LMI Approach

Yao-Wen Tsai¹, Huynh Van Van¹, Lee Cua Ting², and Kuo-Kai Shyu²

¹Department of Mechanical and Automation Engineering, Da-Yeh University,
Changhua 51591, Taiwan R.O.C

²Department of Electrical Engineering, National Central University, Chung-Li,
Taiwan 32054, ROC

yw.tsai@msa.hinet.net, hvvanute@gmail.com,
sob77311@hotmail.com, kkshyu@ee.ncu.edu.tw

Abstract. In this paper, a large scale systems with matched and mismatched uncertainties is considered. Based on sliding mode techniques, a decentralized control scheme, using only output information, is presented to stabilize the system globally. In addition, appropriate linear matrix inequality (LMI) stability conditions by the Lyapunov method are derived such that each subsystem in the new sliding mode is completely invariant to both matched and mismatched uncertainties. Moreover, the stability analysis of the overall system is also provided. Finally, a numerical example is used to prove the efficacy on the method.

Keywords: Large scale systems, Decentralized adaptive control, Linear matrix inequalities (LMI), mismatched uncertainties, sliding-mode control (SMC).

1 Introduction

Over the past decades, the decentralized control problem of uncertain large scale systems has attracted a lot of attention. Decentralized control issues naturally arise from the control of large complex systems found in the power industry, aerospace and chemical engineering applications, telecommunication network, etc. Several typical results have been designed in decentralized control for large scale systems with parameter uncertainties or the uncertainties to be bounded by the p th-order polynomial bounds with unknown constants [1]–[3]. Earlier works on decentralized control were developed in [4]–[5] to achieve the tracking performance for nonlinear large scale systems in the nested form with completely unknown functions. However, a major structural restriction imposed on the system in all these aforementioned schemes is that the uncertainties and interconnections are in the range space of the input matrix, which is basically the strict-matching condition. Thus they can not be applied to control those mismatched uncertain large-scale systems without satisfying the matching condition [6]–[8].

The main advantages of these direct or indirect decentralized control approaches lies in the fact that the developed controllers can deal with increasingly complex systems and to carry out controllers without explicit knowledge of the model structure of the underlying dynamic system. Theoretical validation on the use of the decentralized controllers using a state feedback approaches is valid when all of the system states are available for measurement [10]–[11]. However, for many practical applications, the full state information is not always available, and only the output is obtainable. In this situation, there are two approaches in designing the sliding mode output feedback controllers. One is to use state observers to provide an estimate of the unmeasured states [12]–[13]. The other is to utilize the output-based controllers, such as static gain and dynamic compensator types [14]–[15]. Motivated by the previous works, in this paper, we attempt to address a decentralized output feedback control for a class of matched and mismatched uncertain large-scale systems with unmeasurable states.

The main contributions of this paper lie in the following.

- 1) A new approach is developed to design sliding surface using only the output information and an precise solution parameterizing the sliding surface is given in the LMI framework.
- 2) The decentralized output feedback controller such that the motion of the closed-loop system satisfies the reaching condition is proposed. It is not only maintainable closed-loop system stability but also asymptotic zero when mismatched uncertainties are present in the subsystems. Our approach does not need the availability of the state variables so that our method is very useful and more realistic since it can be easily implemented in practice.

2 Problem Formulations and Preliminaries

Consider a class of mismatched uncertain large-scale systems that is decomposed into L subsystems. The state space representation of each subsystem is described by the following:

$$\begin{aligned}\dot{x}_i &= (A_{ii} + \Delta A_{ii})x_i + B_i u_i + \sum_{\substack{j=1 \\ j \neq i}}^L A_{ij} x_j \\ y_i &= C_i x_i\end{aligned}\tag{1}$$

where $x_i \in R^{n_i}$, $u_i \in R^{m_i}$, $y_i \in R^{p_i}$ are the state variable, control input and output of the subsystem, respectively. A_{ii}, B_i, A_{ij} are constant matrices with appropriate dimensions. The values of the parameters of uncertain matrices ΔA_{ii} are unknown.

Assumption 1: The pair (A_{ii}, B_i) is stabilizable.

Assumption 2: The input matrix B_i , C_i have full rank matrix with $m_i \leq p_i < n_i$

Assumption 3: $\Delta A_{ii} = D_{ii} F_{ii}(x_{ii}, t) E_{ii}$ where $F_{ii}(x_{ii}, t)$ is unknown but bounded $\|F_{ii}(x_{ii}, t)\| \leq 1$, and D_{ii}, E_{ii} are known matrices of appropriate dimensions.

Lemma 1 [16]: The following matrix inequality:

$$\begin{bmatrix} Q(x) & \Pi(x) \\ \Pi(x)^T & R(x) \end{bmatrix} > 0$$

Where $Q(x) = Q(x)^T$, $R(x) = R(x)^T$ and $\Pi(x)$ depend affinity on x , is equivalent to

$$R(x) > 0, \quad Q(x) - \Pi(x)R(x)^{-1}\Pi(x)^T > 0$$

Lemma 2 [15]: Let X, Y, F be real matrices of suitable dimension with $F^T F < I$ then

$$X F Y + Y^T F^T X^T \leq X X^T + Y^T Y$$

Lemma 3 [9]: Let X, Y be real matrices of suitable dimension then

$$X Y^T + Y X^T \leq X X^T + Y^T Y$$

3 Sliding-Mode Decentralized Output Feedback Controller Design

In this section, we design a decentralized output feedback controller for the system (1). The first, we select an appropriate sliding surface, which should have the property that the desired performance can be achieved by only using output information. The second, we organize a decentralized control law that forces the system state to reach the sliding surface in a finite amount of time and stay on it thereafter.

Since $\text{rank}(B_i) = m_i$, then from [15] by the state transformation $\bar{z}_i = T_i x_i$ such that system (1) has following regular form.

$$\begin{aligned} \dot{\bar{z}}_i &= (\begin{bmatrix} A_{ii1} & A_{ii2} \\ A_{ii3} & A_{ii4} \end{bmatrix} + \begin{bmatrix} D_{ii1} \\ D_{ii2} \end{bmatrix} F_{ii} [E_{ii1} \quad E_{ii2}]) \bar{z}_i + \begin{bmatrix} 0 \\ B_{i2} \end{bmatrix} u_i + \sum_{j=1, j \neq i}^L \begin{bmatrix} A_{ij1} & A_{ij2} \\ A_{ij3} & A_{ij4} \end{bmatrix} \bar{z}_j \\ y_i &= [0 \quad C_{i2}] \bar{z}_i \end{aligned} \quad (2)$$

where $T_i A_{ii} T_i^{-1} = \begin{bmatrix} A_{ii1} & A_{ii2} \\ A_{ii3} & A_{ii4} \end{bmatrix}$, $T_i D_{ii} F_{ii} E_{ii} T_i^{-1} = \begin{bmatrix} D_{ii1} \\ D_{ii2} \end{bmatrix} F_{ii} [E_{ii1} \quad E_{ii2}]$, $T_i A_{ij} T_j^{-1} = \begin{bmatrix} A_{ij1} & A_{ij2} \\ A_{ij3} & A_{ij4} \end{bmatrix}$,

$T_i B_i = \begin{bmatrix} 0 \\ B_{i2} \end{bmatrix}$ and $C_i T_i^{-1} = [0 \quad C_{i2}]$. $B_{i2} \in R^{m_i \times m_i}$ and $C_{i2} \in R^{p_i \times p_i}$ are nonsingular.

Letting $\bar{z}_i = \begin{bmatrix} z_{i1} \\ z_{i2} \end{bmatrix}$ where $z_{i1} \in R^{n_i - m_i}$, $z_{i2} \in R^{m_i}$

$$\dot{z}_{i1} = (A_{ii1} + D_{ii1}F_{ii}E_{ii1})z_{i1} + \sum_{\substack{j=1 \\ j \neq i}}^L A_{ij1}z_{j1} + (A_{ii2} + D_{ii1}F_{ii}E_{ii2})z_{i2} + \sum_{\substack{j=1 \\ j \neq i}}^L A_{ij2}z_{j2} \quad (3)$$

$$\dot{z}_{i2} = (A_{ii3} + D_{ii2}F_{ii}E_{ii1})z_{i1} + (A_{ii4} + D_{ii2}F_{ii}E_{ii2})z_{i2} + B_{i2}u_i + \sum_{\substack{j=1 \\ j \neq i}}^L (A_{ij3}z_{j1} + A_{ij4}z_{j2}) \quad (4)$$

Obviously, system (3) represents the sliding-motion dynamic of system (2), and hence, the corresponding sliding surface can be chosen as follows:

$$\sigma_i = [0_{m_i x(p_i - m_i)} \quad K_i] C_{i2}^{-1} y_i \quad (5)$$

where matrix $K_i \in R^{m_i \times m_i}$ is nonsingular. In the sliding mode which can be further rewritten as

$$\sigma_i = [0_{m_i x(n_i - m_i)} \quad K_i] \begin{bmatrix} z_{i1} \\ z_{i2} \end{bmatrix} = K_i z_{i2} = 0 \quad (6)$$

so $z_{i2} = 0$ and

$$\dot{z}_{i1} = (A_{ii1} + D_{ii1}F_{ii}E_{ii1})z_{i1} + \sum_{\substack{j=1 \\ j \neq i}}^L A_{ij1}z_{j1} \quad (7)$$

3.1 Sliding Surface Design

Let us first consider the problem of sliding-surface design, the result of which is given in the form of LMI. The first result of designing sliding surface can be stated as follows.

Theorem 1: Suppose that the LMI (8) has solution $P_{ii} > 0$, sliding-surface is given by equation (5) and the resulting $(n_i - m_i)$ reduced - order dynamics of the closed subsystem (7) restricted to the switching surface $\sigma_i = 0$ is asymptotically stable.

$$\begin{bmatrix} A_{ii1}^T P_{ii} + P_{ii} A_{ii1} + E_{ii1}^T E_{ii1} + \sum_{\substack{j=1 \\ j \neq i}}^L A_{ji1}^T A_{ji1} & D_{ii1}^T P_{ii} & P_{ii} \\ P_{ii} D_{ii1} & -I & 0 \\ P_{ii} & 0 & -I \end{bmatrix} < 0 \quad (8)$$

Proof: To analyze the stability of the sliding motion (7), we consider the following candidate of Lyapunov function:

$$V = \sum_{i=1}^L z_{i1}^T P_{ii} z_{i1} \quad (9)$$

Then, taking the time derivative along the state trajectory of system (9), we have

$$\begin{aligned}\dot{V} = & \sum_{i=1}^L (z_{ii}^T \{(A_{ii1} + D_{ii1}E_{ii}E_{ii1})^T P_{ii} + P_{ii}(A_{ii1} + D_{ii1}E_{ii}E_{ii1})\} z_{ii}) \\ & + \sum_{i=1}^L \sum_{j=1, j \neq i}^L \{z_{ii}^T P_{ii} A_{ij1} z_j + z_j^T A_{ij1}^T P_{ii} z_{ii}\}\end{aligned}\quad (10)$$

Then, using Lemma 2 and Lemma 3 yields that

$$\begin{aligned}\dot{V} \leq & \sum_{i=1}^L (z_{ii}^T \{A_{ii1}^T P_{ii} + P_{ii} A_{ii1} + E_{ii1}^T E_{ii1} + P_{ii} D_{ii1} D_{ii1}^T P_{ii}\} z_{ii}) \\ & + \sum_{i=1}^L \sum_{j=1, j \neq i}^L \{z_{ii}^T P_{ii} P_{ii} z_{ii} + z_{ji}^T A_{ij1}^T A_{ij1} z_{ji}\} \\ = & \sum_{i=1}^L (z_{ii}^T \{A_{ii1}^T P_{ii} + P_{ii} A_{ii1} + E_{ii1}^T E_{ii1} + P_{ii} D_{ii1} D_{ii1}^T P_{ii}\} z_{ii}) \\ & + \sum_{i=1}^L \sum_{j=1, j \neq i}^L \{z_{ii}^T P_{ii} P_{ii} z_{ii} + z_{ji}^T A_{ji1}^T A_{ji1} z_{ji}\} \\ = & \sum_{i=1}^L (z_i^T \{A_{ii1}^T P_{ii} + P_{ii} A_{ii1} + E_{ii1}^T E_{ii1} + P_{ii} D_{ii1} D_{ii1}^T P_{ii} + P_{ii} P_{ii} + \sum_{j=1, j \neq i}^L A_{ji1}^T A_{ji1}\} z_i)\end{aligned}\quad (11)$$

By the Schur complement, equation (8) is equivalent to equation (12)

$$A_{ii1}^T P_{ii} + P_{ii} A_{ii1} + E_{ii1}^T E_{ii1} + P_{ii} D_{ii1} D_{ii1}^T P_{ii} + P_{ii} P_{ii} + \sum_{j=1, j \neq i}^L A_{ji1}^T A_{ji1} < 0 \quad (12)$$

so

$$\dot{V} \leq \sum_{i=1}^L (z_i^T \{A_{ii1}^T P_{ii} + P_{ii} A_{ii1} + E_{ii1}^T E_{ii1} + P_{ii} D_{ii1} D_{ii1}^T P_{ii} + P_{ii} P_{ii} + \sum_{j=1, j \neq i}^L A_{ji1}^T A_{ji1}\} z_i) < 0 \quad (13)$$

Note that (8) holds, which further implies that sliding motion is asymptotically stable.

3.2 Decentralized Output Feedback Reaching – Law Design

In order to develop a reachability condition based on decentralized output feedback control, the following condition is imposed on the system (1).

Assumption 4: there exists a constant $\eta_i > 0$ such that $\|z_{ii}\| \leq \eta_i$

Theorem 2: Suppose that the LMI (8) has solution $P_{ii} > 0$. And consider the closed loop of the uncertain subsystem (1) with the following decentralized output feedback controller (14) where linear sliding-surface is given by equation (5). Then, the linear sliding surface is not only reachable but also the $(n_i - m_i)$ reduced - order equivalent dynamics is stable and invariant with mismatched uncertainties.

$$\begin{aligned} u_i = & [(K_i B_{i2})^{-1} \{ \|K_i D_{ii2}\| \|E_{ii1}\| \|\eta_i + \|K_i A_{ii4} K_i^{-1}\| \|\sigma_i\| + \|K_i D_{ii2}\| \|E_{ii2} K_i^{-1}\| \|\sigma_i\| \}] \\ & + \|K_i A_{ii3}\| \|\eta_i + \alpha_i\| \|\sigma_i\| + \sum_{\substack{j=1 \\ j \neq i}}^L (\|K_j A_{ji3}\| \|\eta_i + \|K_j A_{ji4} K_i^{-1}\| \|\sigma_i\|) \frac{\sigma_i}{\|\sigma_i\|} \end{aligned} \quad (14)$$

Proof: Let us consider the following Lyapunov function:

$$V = \sum_{i=1}^L \|\sigma_i\| \quad (15)$$

Then, by using (4), we have

$$\begin{aligned} \dot{V} = & \sum_{i=1}^L \frac{\sigma_i^T}{\|\sigma_i\|} K_i A_{ii3} Z_{ii} + \sum_{i=1}^L \frac{\sigma_i^T}{\|\sigma_i\|} K_i D_{ii2} F_i E_{ii1} Z_{ii} + \sum_{i=1}^L \frac{\sigma_i^T}{\|\sigma_i\|} K_i A_{ii4} Z_{ii} + \sum_{i=1}^L \frac{\sigma_i^T}{\|\sigma_i\|} K_i D_{ii2} F_i E_{ii2} Z_{ii} \\ & + \sum_{i=1}^L \frac{\sigma_i^T}{\|\sigma_i\|} K_i B_{i2} u_i + \sum_{i=1}^L \sum_{\substack{j=1 \\ j \neq i}}^L \frac{1}{\|\sigma_i\|} (\sigma_i^T K_i A_{ij3} Z_{ji} + \sigma_i^T K_i A_{ij4} Z_{ji}) \\ \leq & \sum_{i=1}^L \|K_i A_{ii3}\| \|\eta_i + \sum_{i=1}^L \|K_i D_{ii2}\| \|E_{ii1}\| \|\eta_i + \sum_{i=1}^L \|K_i A_{ii4} K_i^{-1}\| \|\sigma_i\| + \sum_{i=1}^L \|K_i D_{ii2}\| \|E_{ii2} K_i^{-1}\| \|\sigma_i\| \| \\ & + \sum_{i=1}^L \sum_{\substack{j=1 \\ j \neq i}}^L (\|K_j A_{ji3}\| \|\eta_i + \|K_j A_{ji4} K_i^{-1}\| \|\sigma_i\|) + \sum_{i=1}^L \frac{\sigma_i^T}{\|\sigma_i\|} K_i B_{i2} u_i \end{aligned} \quad (16)$$

Thus, substituting equation (14) into equation (16), we obtain

$$\begin{aligned} \dot{V} \leq & \sum_{i=1}^L \|K_i A_{ii3}\| \|\eta_i + \sum_{i=1}^L \|K_i D_{ii2}\| \|E_{ii1}\| \|\eta_i + \sum_{i=1}^L \|K_i A_{ii4} K_i^{-1}\| \|\sigma_i\| + \sum_{i=1}^L \|K_i D_{ii2}\| \|E_{ii2} K_i^{-1}\| \|\sigma_i\| \| \\ & + \sum_{i=1}^L \sum_{\substack{j=1 \\ j \neq i}}^L (\|K_j A_{ji3}\| \|\eta_i + \|K_j A_{ji4} K_i^{-1}\| \|\sigma_i\|) - \sum_{i=1}^L \frac{\sigma_i^T}{\|\sigma_i\|} K_i B_{i2} [(K_i B_{i2})^{-1} \{ \|K_i A_{ii3}\| \|\eta_i + \|K_i D_{ii2}\| \|E_{ii1}\| \|\eta_i + \sum_{i=1}^L \|K_i D_{ii2}\| \|E_{ii1}\| \|\eta_i + \sum_{i=1}^L \|K_i A_{ii4} K_i^{-1}\| \|\sigma_i\| + \sum_{i=1}^L (\|K_j A_{ji3}\| \|\eta_i + \|K_j A_{ji4} K_i^{-1}\| \|\sigma_i\|) \} \frac{\sigma_i}{\|\sigma_i\|}] \\ \leq & - \sum_{i=1}^L \alpha_i \|\sigma_i\| \end{aligned} \quad (17)$$

Constant value $\alpha_i > 0$ so equation (17) implies that the state trajectory will reach the switching surface in finite time and stay on it thereafter.

Remark: we can know that the controller (8) use only the output signal indeed.

4 Numerical Examples

In this section, we present numerical examples to show the advantages of the control schemes proposed in this paper. Consider an large scale system composed of two third-order subsystems

Subsystem 1

$$A_{11} = \begin{bmatrix} -8 & 0 & 1 \\ 0 & -8 & 1 \\ 1 & 1 & 0 \end{bmatrix}, B_1 = \begin{bmatrix} 0 \\ 0 \\ 1 \end{bmatrix}, C_1 = \begin{bmatrix} 1 & 1 & 0 \\ 0 & 0 & 1 \end{bmatrix}, D_{11} = \begin{bmatrix} 1 \\ 1 \\ 0 \end{bmatrix}, E_{11} = [1 \ 0 \ 0],$$

$$A_{12} = \begin{bmatrix} 1 & 0 & 0 \\ 0 & 0 & 1 \\ 0 & 1 & 0 \end{bmatrix}, F_{11} = \xi_{11} \sin(t)$$

Subsystem 2

$$A_{22} = \begin{bmatrix} -6 & 0 & 1 \\ 0 & -6 & 1 \\ 1 & 1 & 0 \end{bmatrix}, B_2 = \begin{bmatrix} 0 \\ 0 \\ 1 \end{bmatrix}, C_2 = \begin{bmatrix} 1 & 1 & 0 \\ 0 & 0 & 1 \end{bmatrix}, D_{22} = \begin{bmatrix} 0 \\ 1 \\ 1 \end{bmatrix},$$

$$A_{21} = \begin{bmatrix} 1 & 0 & 0 \\ 0 & 1 & 0 \\ 0 & 1 & 0 \end{bmatrix}, E_{22} = [0 \ 0 \ 1], F_{22} = \xi_{22} \sin(t)$$

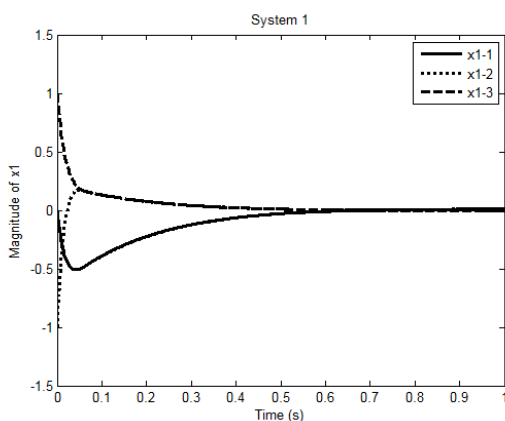


Fig. 1. The time histories of x_{1-1} , x_{1-2} , x_{1-3} of system 1

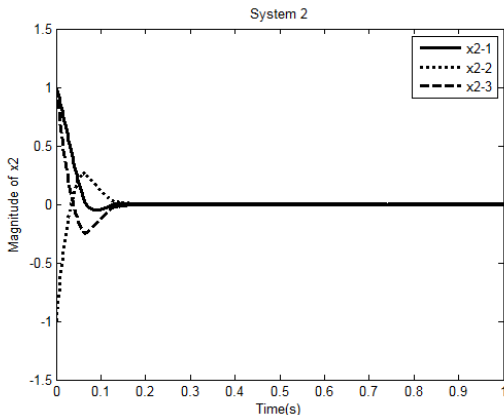


Fig. 2. The time histories of x_{2-1} , x_{2-2} , x_{2-3} of system 2

Simulation results for the first subsystem and the second subsystem are shown, respectively, in Fig. 1, Fig. 2. It can be seen that the proposed controller has a good performance and is effective in dealing with matched and mismatched uncertainties large scale system.

5 Conclusion

In this paper, we formulated and solved the decentralized output feedback design problems for large-scale linear systems with matched and mismatched uncertainties. New existence condition of linear sliding surfaces are given in terms of LMI. Our approach does not need the availability of the state variables so that our method is very useful and more realistic since it can be easily implemented in practice. Finally, a numerical example is given to prove the synthesis procedure for the proposed decentralized output feed back controllers.

Acknowledgments. The support of this work by the Ministry of Economic Affairs, Taiwan, R.O.C under the contract 102-D0624-C-C3 is gratefully acknowledged.

References

- [1] Ye, X.: Decentralized Adaptive Stabilization of Large-Scale Nonlinear Time-Delay Systems With Unknown High-Frequency-Gain Signs. *IEEE Transactions on Automatic Control* 56(6) (June 2011)
- [2] Tsai, Y.-W., Shyu, K.-K., Chang, K.-C.: Decentralized variable structure control for mismatched uncertain large-scale systems: a new approach. *Systems & Control Letters* 43, 117–125 (2001)
- [3] Zheng, D.-Z.: Decentralized output feedback stabilization of a class of nonlinear interconnected systems. *IEEE Trans. Automat. Contr.* 34, 1297–1300 (1989)

- [4] Shi, L., Singh, S.K.: Decentralized control for interconnected uncertain systems: Extensions to higher-order uncertainties. *Int. J. Contr.* 57, 1453–1468 (1993)
- [5] Gavel, D.T., Siljak, D.D.: Decentralized adaptive control: Structural conditions for stability. *IEEE Trans. Automat. Contr.* 34, 413–426 (1989)
- [6] Kalsi, K., Lian, J., Zak, S.H.: Decentralized Dynamic Output Feedback Control of Nonlinear Interconnected Systems. *IEEE Transactions on Automatic Control* 55(8) (August 2010)
- [7] Shyu, K.-K., Tsai, Y.-W., Lai, C.-K.: A dynamic output feedback controllers for mismatched uncertain variable structure systems. *Automatica* 37, 775–779 (2001)
- [8] Li, W., Wei, X., Zhang, S.: Decentralized output-feedback control for high-order stochastic non-linear systems. *ET Control Theory Appl.* 6(6), 838–846 (2012)
- [9] Khargonekar, P.P., Petersen, I.R., Zhou, K.: Robust Stabilization of Uncertain Linear Systems: Quadratic Stabilizability and H^∞ control Theory. *IEEE Transactions on Automatic Control* 35(3) (March 1990)
- [10] Li, W.Q., Jing, Y.W., Zhang, S.Y.: Adaptive state-feedback stabilization for a large class of high-order stochastic nonlinear systems. *Automatica* 47, 819–828 (2011)
- [11] Li, W.Q., Liu, X.H., Zhang, S.Y.: Further results on adaptive state feedback stabilization for stochastic high-order nonlinear systems. *Automatica* (accepted 2012)
- [12] Koo, G.B., Park, J.B., Joo, Y.H.: Decentralized fuzzy observer-based output-feedback control for nonlinear large-scale systems: an LMI approach. *IEEE Transactions on Fuzzy Systems* PP(99) (2013)
- [13] Liu, S.J., Jiang, Z.P., Zhang, J.F.: Global output-feedback stabilization for a class of stochastic non-minimum-phase nonlinear systems. *Automatica* 44, 1944–1957 (2008)
- [14] Yan, X.-G., Spurgeon, S.K., Edwards, C.: Global decentralised static output feedback sliding mode control for interconnected time-delay systems. *IET Control Theory Appl.* 6(2), 192–202 (2012)
- [15] Zhang, J., Shi, P., Xia, Y.: Robust Adaptive Sliding-Mode Control for Fuzzy Systems With Mismatched Uncertainties. *IEEE Transactions on Fuzzy Systems* 18(4) (August 2010)
- [16] Boyd, S., Ghaoui, L.E., Feron, E., Balakrishnan, V.: *Linear Matrix Inequalities in System and Control theory*. SIAM, Philadelphia (1994)

A Simulation Study of Power Management for a Series Hydraulic Hybrid Vehicle

Chih-Keng Chen, Tri-Vien Vu, and Chih-Wei Hung

Department of Mechanical and Automation Engineering, Da-yeh University,
168 University Road, Dacun, Changhua, Taiwan 515 ROC
ckchen@mail.dyu.edu.tw

Abstract. Possessing the flexibility of engine management and regenerative braking properties, series hydraulic hybrid vehicle has been an attractive candidate for a better fuel economy automobile. As in any hybrid power system, the presence of two or more different power sources caused many power management issues. These issues become more difficult for hydraulic hybrid technology when the hydraulic accumulator is a low energy density component. The main purpose of the development of the control strategies is to propose a better approach to coordinate multiple power sources. In this work, a model of the series hydraulic hybrid truck is established. Dynamic programming (DP) methodology is applied to estimate an optimal-benchmark solution. A rule-based control strategy is utilized to predict the fuel economy improvement of the SHHV system. The effectiveness of the proposed control strategies are figured out by simulation results.

Keywords: Dynamic-Programming, Hydraulic Hybrid Vehicle, Power Management, Rule-Based.

1 Introduction

Gasoline depletion risks forecasting and environmental concerns are the main reasons that motivate the development for a higher efficient transportation system nowadays. In 2009, more than 70% of U.S oil consumption was consumed by transportation sector in which light-duty vehicles accounted for 45% [1]. Hence improving the efficiency of light-duty vehicle fleet is one of the most effective approaches to reduce the dependency on oil.

In all types of hybrid vehicle, the main function of supervisory controller is to coordinate multiple power sources to satisfy the power demand of the driveline with minimum fuel consumption in the most convenient way. In general, control strategies of the hybrid propulsion systems can be classified into three categories: rule-based, semi-optimal, and global optimal. Among these, the rule-based control strategy is a real-time implementable power management. This control strategy uses several rules that would consider the vehicle load level and maintain the engine at its efficient operating range. Most papers regarding rule-based control strategy for HHV used the state-of-charge (SOC) of accumulator as the sole state variable [2]-[5].

Dynamic programming is one of methodologies to find a global optimization solution for sequential or multi-stages decision problems. The algorithm searches for optimal decision at discrete points in a time sequence with chosen cost functions. In the hybrid system, the power split between the two energy sources is selected as the control variable and the total equivalent fuel consumption over a given driving cycle is the cost function of DP technique. DP has been shown to be a powerful tool for optimal control in automotive applications. It can be used to optimize powertrain parameters, gear shifting strategy in conventional vehicles [6]-[8] and for the control variables replied on torque split or power split factors in hybrid vehicles [2] [9] [10]. DP also has been successfully applied to replace the Rule-based control strategy for hybrid electric vehicle [11] or to optimize the Rule-Based control strategy for hydraulic-electric hybrid vehicle [12].

In this work, a series hydraulic hybrid propulsion system tailored for a light-duty delivery truck has been established. The remainder of this paper is organized as follows. The analysis and modeling of the system will be discussed in the second section of this paper. Then, the fundamental formulation of DP technique will be introduced in the first part of section three. The simulation results of DP application and the improved rule-based control strategies will be present and discussed in the second part of that section. The main contributions of this work will be concluded in the last section.

2 Modeling of a SHHV

2.1 System Configuration Description

This paper proposes a configuration of SHHV for a Rear-wheel-drive 3.5 ton Light-duty class II truck. The schematic and control signal path of the system is shown in Fig. 1. The specifications of the vehicle are listed in Table 1. In this configuration, Diesel Engine E is connected to hydraulic pump $P1$; P/M unit $P2$ is connected to the rear wheels through differential DF; high-pressure accumulator Acc functions as a secondary power source of SHHV system. When the vehicle is in the traction mode, P/M $P2$ operates as a motor to propel the wheels. Hydraulic power is provided by hydraulic accumulator Acc and/or pump $P1$. When the brake event occurs, $P2$ will work as a pump to convert the vehicle kinetic energy into hydraulic power. Thus, the braking energy thus will be captured and stored by Acc . The mechanical braking system will be activated in emergency event or in case the pressure of Acc exceeding its maximum working pressure during vehicle braking mode. The required driving/braking torque is satisfied by adjusting the displacement of $P2$. Since the engine is decoupled from the wheel loads, it can be easily controlled to operate at desired location. The desired torque and speed of the engine can be achieved by control the displacement of $P1$ and the throttle position of the engine.

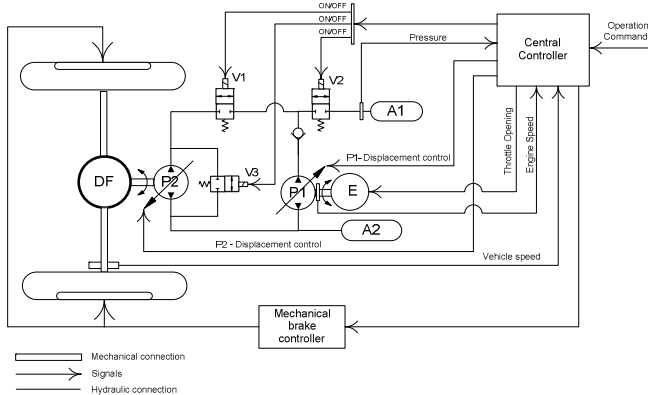


Fig. 1. Schematic and Control Signal Paths of SHHV

2.2 System Modeling and Component Sizing

In a SHHV, the overall fuel economy fundamentally depends on the efficiency of the fuel converter, the hydraulic, and the vehicle mass and losses. Since most of trucks already use highly efficient diesel engines and the truck weight is dictated by the payload, tailoring the design and control parameters of hydraulic components for the vehicle with a certain driving cycle offers high potential significant improvement of the fuel economy. The objective of this work is to modify an existed delivery truck to establish a SHH one, so the parameters of the engine and the driveline are given. Hydraulic component are selected and sized to ensure that the proposed SHHV can work under a given driving cycle and has highest potential of fuel economy improvement.

The first parameter to consider is the capacitor of the accumulator since this parameter will determine the available energy that an accumulator can absorb or delivery. The available energy amount of a bladder accumulator can be estimate approximately by below equation.

$$E_{acc} = p_0 V_0^k \left(p^{(k-1)/k} - p_0^{(k-1)/k} \right) / (k-1) \quad (1)$$

where V_0 is the capacitor, p_0 is the initial pressure, p is current pressure, and k is the specific heat ratio the accumulator. From above expression, it is obviously that with a given accumulator, the capacitor is fixed and the amount of the accumulator energy is depended on its initial and maximum working pressure. Therefore, increasing the working pressure is a solution to improve the energy density. However, the noise, the vibration, and the sealing problems of a high-pressure hydraulic system must be taken into account. Considering the safety aspect and the working pressure limitation of hydraulic pump, the maximum pressure of 330bar is selected. With a fixed highest working pressure, the optimal initial pressure of the accumulator can be estimate by solving the equation $dE_{acc}/dp_0 = 0$.

With low energy density property, the accumulator only provides a limited amount of energy to propel the vehicle. The effort to increase the size of accumulator to lengthen the time span of accumulator propelling may be inefficient when considering the added cost of system mass increase. Hence, for a predefined driving cycle, the size of accumulator in a hydraulic hybrid system is normally calculated to be large enough in order to store the maximum braking energy. This hypothesis is simply expressed by Eq.(2).

$$E_{acc} \geq E_{brk,max} \quad (2)$$

where $E_{brk,max}$ is the maximum potential energy of the vehicle. Neglected the effect of rolling resistance and air drag, the energy is estimated as below.

$$E_{brk} = 0.5mv_{max}^2 \quad (3)$$

where $m[\text{kg}]$ is the mass and v_{max} is the maximum working speed of the vehicle. From above equations, the desired capacitor of the accumulator in the SHHV working on a predefined driving cycle can be found.

The second parameter that affects the drivability of the vehicle is the volumetric displacement of the hydraulic pump/motor. Assumed the vehicle travels in a level road, the total load torque on the wheels of the vehicle is given by:

$$T_l = r \times (\delta ma + A_d v^2 + mgf_r) \quad (4)$$

where $r[\text{m}]$ is the tire radius, $\delta[-]$ is the equivalent rotation mass factor, $a[\text{m/s}^2]$ is the acceleration of the vehicle; A_d is the air-drag coefficient, f_r is the rolling friction coefficient, $g = 9.81 [\text{m/s}^2]$ is the gravity acceleration.

The maximum torque that the pump/motor can afford is:

$$T_{P2,max} = D_{2,max} \Delta p \quad (5)$$

where $D_{2,max}$ is the maximum displacement [m^3/rad] and Δp is the pressure difference across the pump/motor. From (4) and (5), the maximum displacement of the pump/motor P2 is estimated by:

$$D_{2,max} = T_{l,max} p_{min} / i_{df} \quad (6)$$

where $T_{l,max}$ is the maximum loading torque estimated from the given driving cycle, p_{min} is the minimum working pressure of the hydraulic system, and $i_{df}[-]$ is the differential gear ratio of the vehicle.

The hydraulic pump P1 is initially sized to satisfy the requirement of engine power absorption when the pressure of the hydraulic system is at the minimum state. The maximum displacement of the pump P1 is estimated by:

$$D_{1,max} = P_{e,max} / (p_{min} \omega_{e,p max}) \quad (7)$$

where $P_{e,\max}$ [W] is the maximum power, $w_{e,p\max}[\text{rad/s}]$ is the speed of the engine at its maximum power.

Based on MATLAB/SIMULINK, the system is modeled as shown in Fig. 2. The component models are used directly from the built-in SimScape/Simulink toolbox. The parameter of the system using in this simulation can be found in [16].

3 Control Strategy Development and Simulation Results

3.1 Fundamental of DP

In the SHHV system, when the system configuration, component parameters, and driving cycle are defined, the fuel economy strongly depends on the coordinating of two power sources to propel the system. The objective of DP application is to find out optimal power split factor u that will minimize the fuel consumption Δm_f of the engine. The SOC of hydraulic accumulator is selected as the model state variable. Since there is no power split device available for SHHV. The purpose of applying DP is to estimate the optimal power threshold, the throttle position of the engine, and the displacement of the hydraulic pump.

The optimization problem of minimizing the total fuel mass consumed over Japan 1015 driving cycle can be stated as the discrete-time optimal control problem as below.

$$\min_{u_k \in U_k} J(u) = \sum_{k=0}^{N-1} \Delta m_f(u_k, k) \quad (8)$$

subject to

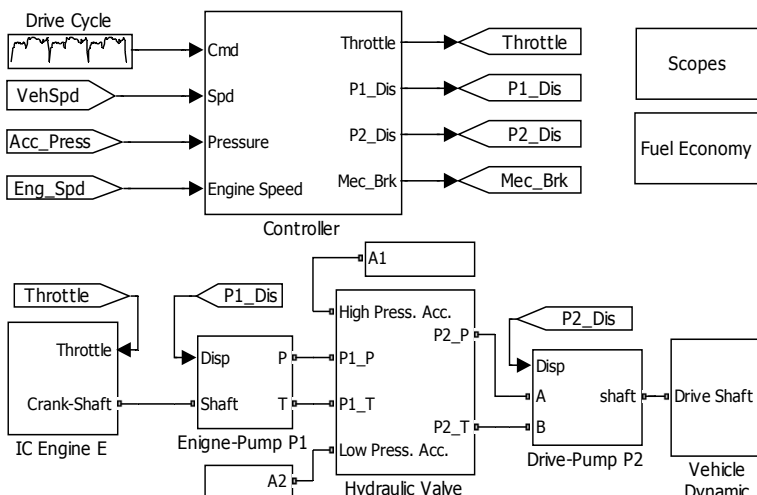


Fig. 2. Simulink Model of SHHV

$$x_{k+1} = f_k(x_k, u_k) + x_k \quad (9)$$

$$x(N) = x(0) \quad (10)$$

and

$$N = 660 / T_s + 1 \quad (11)$$

where Δm_f is the fuel mass consumption at each time step, x_k is the state variable of the system at step k , T_s is the time step.

In order to apply DP algorithm, the control variable u and the state variable x are needed to discretize. Unlike the hybrid electric vehicle system, the state variable of the HHV system can be varied from zero to one. Due to the limitation of the engine power of our current experiment platform, the lower bound of the control variable is select as zero. This prevents the engine from charging the accumulator during braking event to avoid unnecessary and inefficient energy conversion and storing the regenerative brake energy effectively. The state variable and the control variable are gridded into 50 points. The general function *dpm*, written in matlab [13] is adopted in this work.

The first simulation is to consider the effect of the end-point constraint of the SOC to the fuel economy of the proposed system. This constraint implied that there is no pre-charged energy in the accumulator during the test. The engine does not provide any unused energy stored in the accumulator. Different end-point constraint is evaluated and the results are shown in Fig. 3.

The fuel economy of the system with different end-point constraints is estimated and fitted as shown in Fig. 4. The results show that when the initial SOC is small the energy assistant from accumulator is small. In this case the engine must operate at its high rate power which apart from its optimal region. However, if the SOC is too high, the space of the accumulator reserved for braking energy is not enough, an amount of braking energy will not be recovery hence the fuel economy of the system is reduced. The best fuel economy of the system is of 21.5 Km/L if the initial and the final value of the SOC is about 90%. The behaviors of the system with DP are shown in Fig. 5. Interestingly, the SOC can go down closely to zero, it means that the stored energy can be fully used at each vehicle start and the accumulator has enough space for effective regenerative braking. Besides, the whole braking energy over the driving test schedule is captured and reused. Mechanical braking system is not involved during the test. It also can be seen that the operating power of the engine remain nearly constant even when the demand power is low or high. When the power demand is low, the exceeded power from engine is absorbed by the accumulator. When the power demand is high, extra power is assisted by the accumulator. As a result, the engine can operate at its high fuel efficiency region. In addition, avoiding transient operating of the engine and concerning its low energy density characteristic, the accumulator is only used to absorb the exceeded engine power during tracking phase but not charging directly. Hence, the power split factor is limited within zero and one.

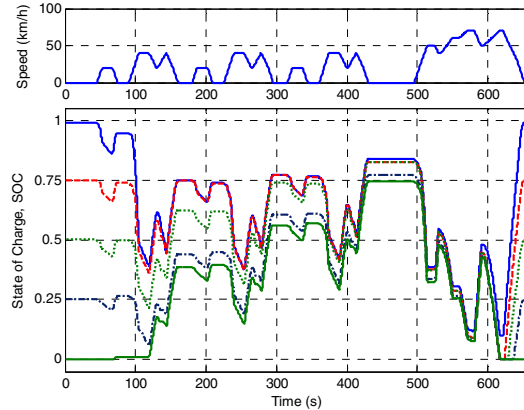


Fig. 3. Several SOC Histories with Different Final Constraint

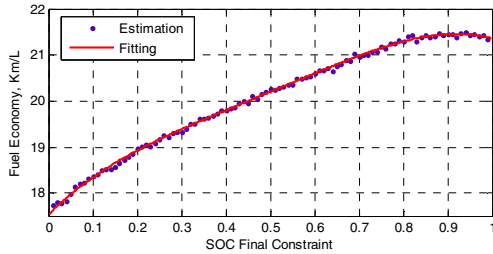


Fig. 4. The Relationship between Fuel Economy and Final Constraint on System SOC

3.2 Improved Rule-Based Control Strategy

The results of DP application indicated that the optimal SOC initial condition is about 90%, the optimal power threshold is about 20 kW, and the optimal range of accumulator pressure is from 150bar to 250bar. From above analysis, the primary rule-based control strategy is derived by extracting the optimal control trajectories from dpm results. The behaviors of the system with the improved control strategy under Japan 1015 drive cycle is shown in Fig. 13. When the high power demand occurs, the pre-charge energy in accumulator will be used to provide the exceeded power, hence the engine will not necessary to be shifted to the higher power region. In addition, the pressure of accumulator is kept at low value before each hard deceleration event.

A summary of the effects of different control strategies over the performance and the fuel economy improvement of proposed SHHV system is given in Table III. The fuel economy improvement of the system was estimated with two different criteria. In the first criterion, the fuel economy of the system working on Hydrostatic was selected as the baseline to estimate the fuel economy improvement of the system with other control strategies; in the second criterion, the fuel economy of 11.42 Km/L was selected.

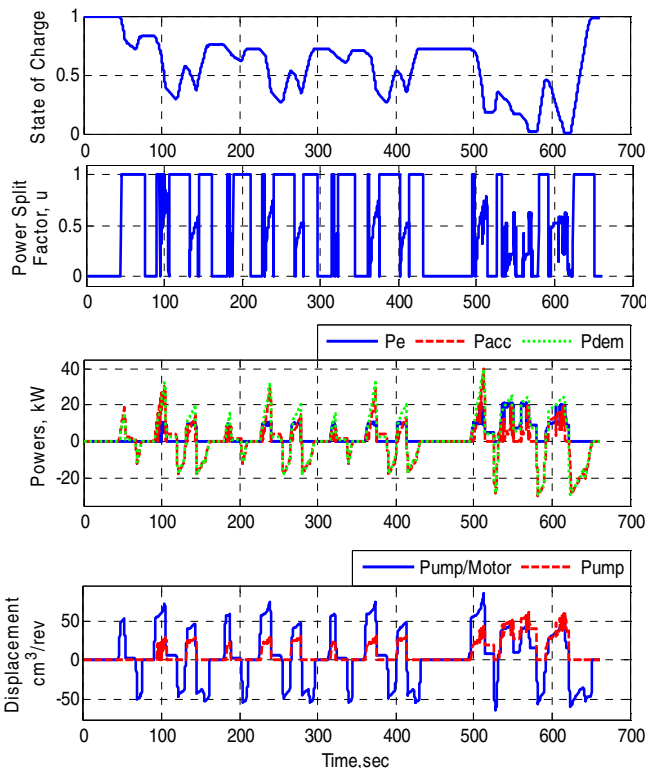


Fig. 5. SHHV DP results over Japan 1015 Driving Cycle

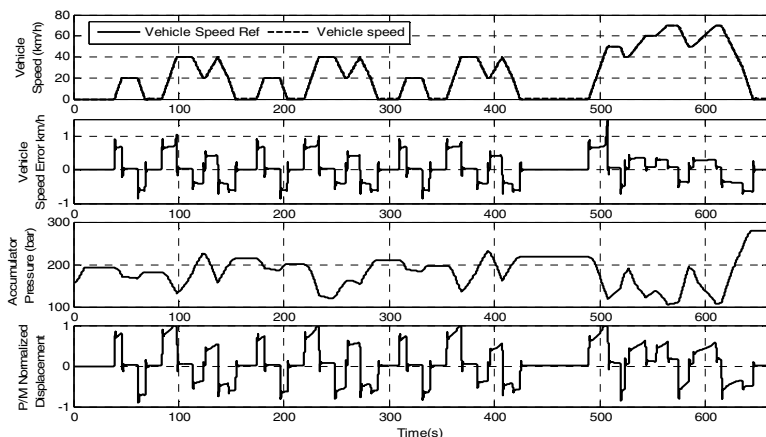


Fig. 6. System Behavior of the Optimal-Thermostatic Control Strategy

Table 1. Summary of the SHHV Predicted Performance and Fuel Economy Improvement

No.	Name	Fuel Economy	Fuel Economy
		[Km/L]	Improvement [%]
		Criterion 1	Criterion 2
1	Hydrostatic	10.15	-
2	Thermostatic	12.01	18.33
3	Optimal-Thermostatic	18.13	78.64
4	DP	21.5	112
			88

4 Conclusion

In this work, DP optimal control technique has been applied successfully for the SHHV system. The optimal trajectories has been studied and adopted to establish implementable rule-based control strategy. The control strategy has been simulated in the MATLAB/Simulink environment to predict the improvement of fuel economy of the proposed system in different modes.

Simulation results show that the fuel economy improvement of proposed system using rule-based control strategy can be up to 80% in comparing with a traditional hydrostatic control strategy and up to 60% in comparing with MYs 2012-2016 standards. With DP technique, the results can be up to 112% and 88% respectively.

In the future, since the power split device in SHHV has not been available, it is necessary to take the engine speed, engine-pump displacement and pump/motor displacement as control variables into account for more reasonable and accuracy problem.

Acknowledgments. This work is supported by the National Science Council under Grant NSC 101-3113-E-006-008 and by Taiwan Automotive Research and Testing Center.

References

- [1] Curtis, C.: President Obama Announces New Fuel Economy Standards (July 29, 2011), <http://www.whitehouse.gov/blog/2011/07/29/president-obama-announces-new-fuel-economy-standards>
- [2] Wu, B., Lin, C.C., Filipi, Z., Peng, H., Assanis, D.: Optimal Power Management for a Hydraulic Hybrid Delivery Truck. *Vehicle Syst. Dyn.* 42(1-2), 23–40 (2004)
- [3] Filipi, Z., Loucas, L., Daran, B., Lin, C.-C., Yildir, U., Wu, B., Kokkolaras, M., Assanis, D., Peng, H., Papalambros, P., Stein, J., Szkubiel, D., Chapp, R.: Combined Optimization of Design and Power Management of the Hydraulic Hybrid Propulsion System for the 6x6 Medium Truck. *Int. J. Heavy Veh. Syst.* 11, 371–401 (2004)
- [4] Kim, Y., Filipi, Z.: Series Hydraulic Hybrid Propulsion for a Light Truck - Optimizing the Thermostatic Power Management. *SAE Technical Paper 2007-24-0080* (2007)

- [5] Tavares, F., Johri, R., Salvi, A., Baseley, S.: Hydraulic Hybrid Powertrain-In-the-Loop Integration for Analyzing Real-World Fuel Economy and Emissions Improvements. SAE Technical Paper 2011-01-2275 (2011)
- [6] Kolmanovsky, I.V., Sivashankar, S.N., Sun, J.: Optimal Control-Based Powertrain Feasibility Assessment: A Software Implementation Perspective. In: ACC 2005, USA, pp. 4452–4457 (2005)
- [7] Lin, C.C., Peng, H., Grizzle, J.W.: Control System Development for an Advanced-Technology Medium-Duty Hybrid Electric Truck. SAE Technical Paper 2003-01-3369 (2003)
- [8] O'Keefe, M.P., Markel, T.: Dynamic Programming Applied to Investigate Energy Management Strategies for a Plug-in HEV. presented at the Conf. EVS-22, Yokohama, Japan (2006)
- [9] Kim, Y.A.: Integrated Modeling and Hardware-In-The-Loop Study for Systematic Evaluation of Hydraulic Hybrid Propulsion Options. PhD. dissertation, Dept. Mech. Eng., Michigan Univ., MI (2008)
- [10] Shan, M.: Modeling and Control Strategy for Series Hydraulic Hybrid Vehicles. PhD. dissertation, Col. Eng. Toledo Univ., OH (2009)
- [11] Lin, C.-C., Kang, J.-M., Grizzle, J.W., Peng, H.: Energy Management Strategy for a Parallel Hybrid Electric Truck. In: Proceedings of the American Control Conference, vol. 4, pp. 2878–2883 (2001)
- [12] Lin, X.K., Ivancic, A., Filipi, Z.: Optimization of Rule-Based Control Strategy for a Hydraulic-Electric Hybrid Light Urban Vehicle Based on Dynamic Programming
- [13] Sundström, O., Guzzella, L.: A Generic Dynamic Programming MATLAB Function. In: 2009 Proc. IEEE Control Appl. Intell. Control, pp. 1625–1630 (2009)
- [14] Elbert, P., Ebbesen, S., Guzzella, L.: Implementation of Dynamic Programming for n-Dimensional Optimal Control Problems with Final State Constraints. IEEE Transactions on Control Systems Technology PP(99) (2012)
- [15] Pourmovahed, A., Beachley, N.H., Fronczak, F.J.: Modeling of a Hydraulic Energy Regeneration System - Part I. Analytical Treatment. AEME Journal of Dynamic Systems, Measurement, and Control 114(1), 155–159 (1992)
- [16] Vu, T.V.: Simulation and Design of Hydraulic Hybrid Vehicle. M.S thesis, Dept. Mech. and Eng. Da-yeh Univ., Changhua, Taiwan (2011)

Fuzzy Model Predictive Control of DC-DC Converters

O. Hazil^{1,*}, S. Bououden¹, M. Chadli², and S. Filali¹

¹ Laboratoire d'automatique et de robotique-

Faculté des Sciences Route d'Ain El Bey, Université Constantine1, Alegria

Omar-h94@hotmail.fr

² University of Picardie Jules Verne, MIS (EA 4029)

7 rue Moulin Neuf, 80000 Amiens, France

mohammed.chadli@u-picardie.fr

Abstract. This paper presents a model predictive control (MPC) approach for buck-boost converter, a mathematical model is required to synthesis this controller, the typically used model is the averaged model, which describes the converter behavior on the operating point. Buck-boost converter has a nonlinear dynamic behavior; the Takagi-Sugeno (T-S) fuzzy model is used to represent the state-space model of nonlinear system where the consequent part of the fuzzy rule is replaced by linear systems.

Keywords: Predictive controller, non-linear systems, DC-DC power converters, averaged model, T-S fuzzy model.

1 Introduction

Power converters are used extensively in most of the power supply systems such as personal computers, laptops, aircrafts and electronic equipment. A DC-DC converter is a switching circuit, which transform a certain electrical voltage to another level of voltage, this is obtained by switches operating (open or closed) at high frequencies; the control objective of such devices is to maintain regulation of the output voltage at the desired value [1-2]. DC-DC converters are nonlinear systems in essence [3], different control techniques ranging from linear control based on linearized model [10] to passivity based control [11] and sliding mode [12] have been used in recent years in the control of switching converters. These works are usually based on a small signal model using the method of averaging of the state space; the model obtained by these methods is useful only for small variations around a specific operating point, will result in poor dynamic performance.

Recently, the approach of T-S Fuzzy Modeling reflected much interest for DC-DC converters. The fuzzy model proposed by Takagi and Sugeno [13] is described by fuzzy IF-THEN rules which represent local linear input-output relations of a nonlinear system. The main feature of T-S fuzzy model is to express the local dynamics of each

* Corresponding author.

fuzzy implication by a linear system model. The passage of the nonlinear model T-S model is not unique, and the number of sub-models increases exponentially according to the number of nonlinearities considered. The curse of the number of rules makes controller design difficult. To loosen the curse, we proposed a fuzzy model based on the so-called sector nonlinearity concept [14]. The method by transformation in nonlinear sector is based on bounded function and gives a minimum number of local models.

Recently, the approach of T-S Fuzzy Modeling reflected much interest for DC-DC converters. The fuzzy model proposed by Takagi and Sugeno [13] is described by fuzzy IF-THEN rules which represent local linear input-output relations of a nonlinear system. The main feature of T-S fuzzy model is to express the local dynamics of each fuzzy implication by a linear system model. The passage of the nonlinear model T-S model is not unique, and the number of sub-models increases exponentially according to the number of nonlinearities considered. The curse of the number of rules makes controller design difficult. To loosen the curse, we proposed a fuzzy model based on the so-called sector nonlinearity concept [14]. The method by transformation in nonlinear sector is based on bounded function and gives a minimum number of local models.

In DC-DC converters, the duty ratio is bounded in the interval [0,1]. The classical control techniques applied to power converters do not take into account neither state nor input constraints, and thus violations of component specifications regularly occur, in practice we can apply model predictive control [2].

Model predictive control (MPC) [4], also known as receding horizon control or moving horizon control is one of the most successful modern control methodologies that offer good solutions, already successfully implemented in industry, for the regulation of constrained linear or nonlinear systems. MPC has ability to handle hard constraints on states/outputs and inputs [5-6]. Its basic principle is to use a model of the system in order to predict the process output over some future horizon, to obtain the optimal control value by minimizing a cost function, when the optimal sequence of future inputs is determined, only the first input is implemented and the whole process is repeated again to determine the next optimized input [7].

The paper is organized as follows: Section 2 gives the averaged model of basic PWM Buck-Boost converter. Section 3 presents the T-S fuzzy model of the DC-DC converter. Section 4 is devoted to the controller theoretical design. Section 5 present simulation results illustrating the performance of the proposed control approach.

2 Averaged Model of Basic PWM Buck-Boost Converter

This section shows the state-space averaged models of the Buck-Boost converter, which includes the PWM (Pulse Width Modulation) and has as control input the duty ratio d . The DC-DC converter can operate in both continuous conduction mode (CCM) and discontinuous conduction mode (DCM). We assume that the converter operates in continuous conduction mode (CCM) and that the inductor current is always larger than zero.

Figure 1 shows the schematic circuit diagram of a DC-DC buck-boost converter and the relevant control signals.

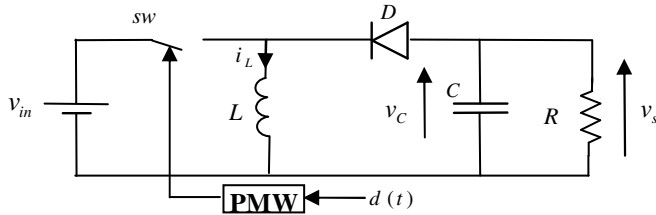


Fig. 1. Schematic of the buck-boost converter

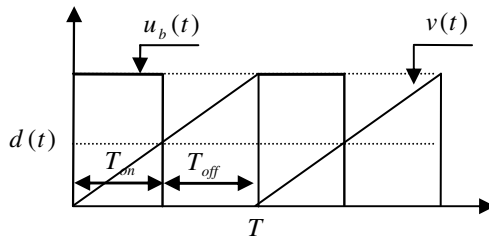


Fig. 2. Waveforms of the PWM process

In Fig. 1, v_s the output voltage and v_{in} the line voltage. The output voltage must be kept at a given constant v_{ref} value, the diode D is on inverse polarization, R models the converter load, while C and L represent, respectively, capacitor and inductor values, the switch sw was a power transistor controlled by a binary signal u_b . The binary signal that triggers on and off the switches is controlled by a fixed-frequency pulse width modulation (PWM) circuit (Fig. 2). The constant switching frequency is $1/T_s$, with T_s the switching period is given by the sum of T_{on} (when $u_b = 1$) and T_{off} (when $u_b = 0$) and the ratio $T_{on}/(T_{on}+T_{off})$ is the duty cycled $d(t)$. Duty cycle is compared with a sawtooth signal $v(t)$ of amplitude equals to 1. Consequently $0 \leq d \leq 1$

values, the switch sw was a power transistor controlled by a binary signal u_b . The binary signal that triggers on and off the switches is controlled by a fixed-frequency pulse width modulation (PWM) circuit (Fig. 2). The constant switching frequency is $1/T_s$, with T_s the switching period is given by the sum of T_{on} (when $u_b = 1$) and T_{off} (when $u_b = 0$) and the ratio $T_{on}/(T_{on}+T_{off})$ is the duty cycled $d(t)$. Duty cycle is compared with a sawtooth signal $v(t)$ of amplitude equals to 1. Consequently $0 \leq d \leq 1$

So, the studied converter has two working topologies corresponding to its switch states. The first topology (Fig. 3-(a)) corresponds to the on state of the switch ($d = 0$) during a period fraction dT_s the system can be presented by the following equations:

$$\frac{di_L}{dt} = \frac{v_{in}}{L} \quad (1)$$

$$\frac{dv_C}{dt} = -\frac{v_C}{CR} \quad (2)$$

$$v_s = v_C \quad (3)$$

The second topology, presented by the (Fig. 3-(b)) corresponds to the off state of the switch ($d = 1$) during the rest of the sampling period $(1-d)T_s$, for this case, the diode conducts, and the dynamical equations of the converter are expressed as

$$\frac{di_L}{dt} = \frac{v_C}{L} \quad (4)$$

$$\frac{dv_C}{dt} = -\frac{i_L}{C} - \frac{v_C}{CR} \quad (5)$$

$$v_s = v_C \quad (6)$$

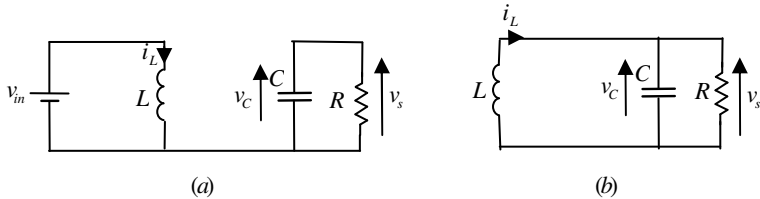


Fig. 3. Equivalent circuit of the buck-boost converter (a) switch on (b) switch off

Choosing the state vector as $x = [i_L, v_c]^T$ where v_c is the capacitor voltage; i_L is the inductor current, the general equation that governs the operation of the buck-boost converter is:

$$\begin{cases} \dot{x} = A_i x + B_i \\ y = C_i x \end{cases} \quad (7)$$

Where: $i=1$ to the first configuration described in Figure 3-(a) and: $i=2$ the second configuration shown in Figure 3-(b). Where:

$$A_1 = \begin{bmatrix} 0 & 0 \\ 0 & -1/RC \end{bmatrix}, \quad B_1 = \begin{bmatrix} v_m/L \\ 0 \end{bmatrix}, \quad C_1 = [0 \ 1] \quad A_2 = \begin{bmatrix} 0 & 1/L \\ -1/C & -1/RC \end{bmatrix}, \quad B_2 = \begin{bmatrix} 0 \\ 0 \end{bmatrix}, \quad C_2 = [0 \ 1]$$

So the combination of state-space representation of mode 1 (on mode) and mode 2 (off mode) induces the following linear state space representation:

$$\begin{cases} \dot{x} = Ax + Bu \\ y = Cx \end{cases} \quad (8)$$

With: $A = dA_1 + d'A_2$, $B = dB_1 + d'B_2$, $C = dC_1 + d'C_2$,

And: $d' = 1-d$, $u = d$

This gives:

$$A = \begin{bmatrix} 0 & (1-d)/L \\ -(1-d)/C & -1/RC \end{bmatrix}, \quad B = \begin{bmatrix} v_m/L \\ 0 \end{bmatrix}, \quad C = [0 \ 1]$$

Discrete-Time State-Space Model

The MPC is to be fed with a discrete time model which is easily obtained from the continuo model assuming that the switching period T_s is much smaller than the time constants associated with the circuit, the following discrete-time model is obtained using the forward Euler approximation, from the continuous time version (8):

$$\dot{x}(k+1) = (I + T_s)x(k) + T_s B d(k) \quad (9)$$

Using this assumption, the discrete-time state-space model of the buck-boost converter can be written as:

$$\begin{bmatrix} x_1(k+1) \\ x_2(k+1) \end{bmatrix} = \begin{bmatrix} 1 & (1-d(k))T_s/L \\ -(1-d(k))T_s/C & 1-(T_s/RC) \end{bmatrix} \begin{bmatrix} x_1(k) \\ x_2(k) \end{bmatrix} + \begin{bmatrix} T_s v_m(k)/L \\ 0 \end{bmatrix} d(k) \quad (10)$$

3 T-S Fuzzy Model of Buck-Boost Converter

The system (10) is a non-linear system because there are products of two input signals; this system can be represented by linear subsystems called Takagi-Sugeno. The main feature of T-S fuzzy model is to express nonlinear dynamics by means of a set of IF-THEN rules. The consequent parts of the rules are local linear systems obtained from specific information about the original nonlinear plant.

The i^{th} rule of fuzzy model for the nonlinear discrete-time systems has the following form:

$$R_i : \text{if } z_i(t) \text{ is about } M_{ji} \text{ and } z_q(t) \text{ is about } M_{qj} \text{ then } \begin{cases} \dot{x}(t) = A_i x(t) + B_i u(t) \\ y(t) = C_i x(t) \end{cases} \text{ for } i=1, \dots, r \quad (11)$$

in which M_{ji} is the fuzzy set of $z_i(t)$ in rule R_i , r is the number of IF-THEN fuzzy rules and $z_i(t)$ are the decision variable assumed measurable, $x \in R^n$ is the system state vector, $y \in R^p$ is the measurable output, The global dynamic system is inferred as follows:

$$\dot{x}(t) = \sum_{i=1}^r \mu_i(z(t))(A_i x(t) + B_i u(t)) \quad (12)$$

$$y(t) = \sum_{i=1}^r \mu_i(z(t))(C_i x(t)) \quad (13)$$

Where

$$\mu_i = \frac{\prod_{j=1}^q M_{ji}(z_j(t))}{\sum_{i=1}^r (\prod_{j=1}^q M_{ji}(z_j(t)))} \quad (14)$$

$M_{ji}(z_j(t))$ is the grade of membership of $z_j(t)$ in M_{ji} , The normalized activation function $\mu_i(z(t))$ in relation with the i^{th} sub model is such that

$$\sum_{i=1}^r \mu_i(z(t)) = 1 , \quad 0 \leq \mu_i(z(t)) \leq 1 \quad (15)$$

A nonlinear system may also be represented by sectors [16]. The following Lemma will be used in the sequel of the paper.

Lemma 1. Let $f(x(t)) : R \rightarrow R$ is a bounded function ($\alpha \leq f(x(t)) \leq \beta$), it always exist tow functions, $\eta_1(x(t))$ and $\eta_2(x(t))$ and two scalars α and β such that:

$$f(x(t)) = \alpha \times \eta_1(x(t)) + \beta \eta_2(x(t)) \quad (16)$$

With $\eta_1(x(t)) + \eta_2(x(t)) = 1$, $\eta_1(x(t)) \geq 0$, $\eta_2(x(t)) \geq 0$

And: $\alpha = \max(f(x(t)))$, $\beta = \min(f(x(t)))$

$$\eta_1(x(t)) = \frac{f(x(t)) - \beta}{\alpha - \beta} \quad \eta_2(x(t)) = \frac{\alpha - f(x(t))}{\alpha - \beta}$$

We can rewrite the non linear model of buck-boost converter as follows:

$$\begin{bmatrix} x_1(k+1) \\ x_2(k+1) \end{bmatrix} = \begin{bmatrix} 1 & T_s/L \\ -T_s/C & 1-(T_s/RC) \end{bmatrix} \begin{bmatrix} x_1(k) \\ x_2(k) \end{bmatrix} + \begin{bmatrix} T_s(v_{in} - v_c(k))/L \\ T_s I_L(k)/C \end{bmatrix} d(k) \quad (17)$$

The obtained T-S fuzzy model represents exactly the nonlinear system for $x \in R^n$ with 2^l locals models where l represents the number of local models.

Assuming that, $I_{\min} \leq i_L(k) \leq I_{\max}$ and $V_{\min} \leq v_c(k) \leq V_{\max}$ the system described by (17) is modeled with a four rules T-S fuzzy system as follows:

- R_1 : if $i_L(k)$ is I_{\min} and $v_c(k)$ is V_{\min} then: $x(k+1) = A_1 x(k) + B_1 d(k)$
- R_2 : if $i_L(k)$ is I_{\max} and $v_c(k)$ is V_{\min} then: $x(k+1) = A_2 x(k) + B_2 d(k)$
- R_3 : if $i_L(k)$ is I_{\min} and $v_c(k)$ is V_{\max} then: $x(k+1) = A_3 x(k) + B_3 d(k)$
- R_4 : if $i_L(k)$ is I_{\max} and $v_c(k)$ is V_{\max} then: $x(k+1) = A_4 x(k) + B_4 d(k)$

The overall model of T-S fuzzy system can be given by the following:

$$x(k+1) = Ax(k) + B_\mu d(k) \quad (18)$$

With

$$B_\mu = \sum_{i=1}^4 \mu_i(x(k)) B_i \quad (19)$$

And

$$\begin{aligned} A = A_1 = A_2 = A_3 = A_4 &= \begin{bmatrix} 1 & T_s/L \\ -T_s/C & 1-(T_s/RC) \end{bmatrix} \\ B_1 &= \begin{bmatrix} T_s(v_{in} - V_{\min})/L \\ T_s I_{\min}/C \end{bmatrix}, \quad B_2 = \begin{bmatrix} T_s(v_{in} - V_{\min})/L \\ T_s I_{\max}/C \end{bmatrix}, \\ B_3 &= \begin{bmatrix} T_s(v_{in} - V_{\max})/L \\ T_s I_{\min}/C \end{bmatrix}, \quad B_4 = \begin{bmatrix} T_s(v_{in} - V_{\max})/L \\ T_s I_{\max}/C \end{bmatrix} \end{aligned}$$

The membership function is such that:

$$\begin{aligned}\mu_1 &= \frac{-i_L(k) + I_{\max}}{I_{\max} - I_{\min}} & \mu_2 &= \frac{i_L(k) - I_{\min}}{I_{\max} - I_{\min}} \\ \mu_3 &= \frac{-v_C(k) + V_{\max}}{V_{\max} - V_{\min}} & \mu_4 &= \frac{v_C(k) - V_{\min}}{V_{\max} - V_{\min}}\end{aligned}$$

Figure 4 shows the membership functions of the fuzzy model

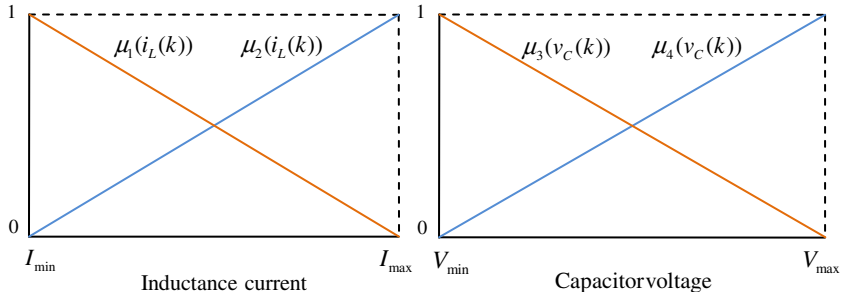


Fig. 4. Membership functions of the T-S fuzzy model

4 Model-Based Predictive Control

The basic model to calculate the predictions is discrete state model given by [9]:

$$\begin{cases} x(k+1) = Ax(k) + Bu(k) \\ y(k) = Cx(k) \end{cases} \quad \begin{array}{l} x(k) \in R^n; u(k) \in R^l \\ y(k) \in R^m \end{array} \quad (20)$$

\$J\$ the cost function to be minimized at each sampling period penalizes deviations from the predicted output \$y(k+i|k)\$ of a reference trajectory \$r(k+i|k)\$, and variations of the control vector \$\Delta u(k) = u(k) - u(k-1)\$, it is often given by the quadratic form

$$J(k) = \sum_{i=H_u}^{H_p} \|\hat{y}(k+i|k) - r(k+i|k)\|_{Q(i)}^2 + \sum_{i=0}^{H_u} \|\Delta \hat{u}(k+i|k)\|_{R(i)}^2 \quad (21)$$

Where \$H_u\$ is the control horizon, \$H_w\$ is first point of the prediction horizon, \$H_p\$ is last point of the prediction horizon, \$H_u < H_p\$, and \$\Delta u(k+i|k)=0\$ if \$i < H_u\$, \$R(i)\$ and \$Q(i)\$ are suitable weighting matrixes.

The state-space representation allows us to write the predicted output as follows:

$$\hat{y}(k+i|k) = C(A^j \hat{x}(k|k) + \sum_{i=1}^j A^{i-1} B u(k+j-i|k)) \quad (22)$$

We can rewrite the model output of local prediction for future moments in matrix form:

$$Y(k) = \Psi x(k) + \Gamma u(k-1) + \Theta \Delta u(k) \quad (23)$$

Where

$$\Psi = \begin{bmatrix} CA \\ \vdots \\ CA^{H_u} \\ \vdots \\ CA^{H_{u+1}} \\ \vdots \\ CA^{H_p} \end{bmatrix}, \quad \Gamma = \begin{bmatrix} CB \\ \vdots \\ C \sum_{i=0}^{H_u-1} A^i B \\ C \sum_{i=0}^{H_p} A^i B \\ \vdots \\ C \sum_{i=0}^{H_p-1} A^i B \end{bmatrix}, \quad \Theta = \begin{bmatrix} CB & \cdots & 0 \\ C(AB + B) & \cdots & CB \\ \vdots & \ddots & \vdots \\ C \sum_{i=0}^{H_u-1} A^i B & \cdots & CB \\ C \sum_{i=0}^{H_u} A^i B & \ddots & C(AB + B) \\ \vdots & \ddots & \vdots \\ C \sum_{i=0}^{H_p-1} A^i B & \cdots & C \sum_{i=0}^{H_p-H_u} A^i B \end{bmatrix}$$

The cost function (21) can be rewritten as:

$$J(k) = \varepsilon(k)^T Q \varepsilon(k) - \Delta u(k)^T G + \Delta u(k)^T H \Delta u(k) \quad (24)$$

Where:

$$\varepsilon(k) = r(k) - \Psi x(k) - \Gamma u(k-1) \quad (25)$$

$$G = 2\Theta^T Q \varepsilon(k) \quad (26)$$

$$H = 2\Theta^T Q \Theta + R \quad (27)$$

Therefore the control law that minimizes the local cost function (21) is given by:

$$\Delta u(k) = \frac{1}{2} H^{-1} G \quad (28)$$

5 Simulations and Results

The performances of the proposed control design are illustrated through simulations. The parameters nominal values of the Buck-boost converter are illustrated in Table 1:

Table 1. The parameters values of the buck-boost converter

Parameter	Values
L	$4.2mF$
C	$2200\mu H$
R	165Ω
v_{in}	$15V$
T_s	$0.654kms$
I_{min}	$0A$
I_{max}	$0.05A$
V_{min}	$-4.2V$
V_{max}	$0V$

Figure 5 illustrates the transient simulation of the buck-boost converter with change in the reference voltage from $-4V$ to $-3V$ at time $t = 0.5$ seconds. The waveforms depicted in the Fig.5 are the duty-cycle d capacitor voltage v_c and inductor current i_L . We can notice that the output voltage settle to their desired value without any overshoot and the settling time of the circuit as clearly seen in the graph is 0.05 seconds. The best performances are obtained for $H_p = 7$ $H_u = 3$.

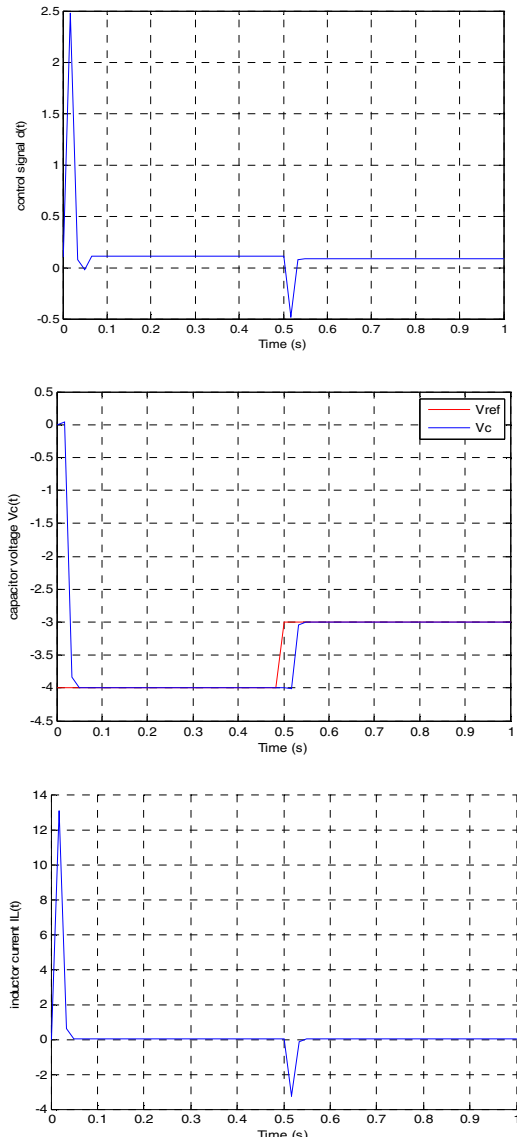


Fig. 5. The transient simulation of the buck-boost converter

6 Conclusion

In this paper, we have presented a MPC controller for the buck-boost converter operating in CCM mode. At first the non linear state-space model is generated, this nonlinear model can be exactly represented using a fuzzy model based on the sector nonlinearity concept. The fuzzy model obtained was then used to design a MPC controller that ensures the output voltage regulation with good performances.

References

1. Guldemir, H.: Modeling and Sliding Mode Control of Dc-Dc Buck-Boost Converter. In: 6th International Advanced Technologies Symposium (IATS 2011), Elazığ, Turkey, May 16-18 (2011)
2. Ahmad, A., Zhiliu, K., Kinoshita, H.: High Performance Algorithms For the Control of Buck Dc-Dc Converters. *International Journal of Engineering Science and Technology* 2(10), 5799–5812 (2010)
3. Inglés, J.V., Garcés, P., Leyva, R.: Robust LMI Control of a Buck-Boost Converter with Low Ripple Propagation. In: Preprints of the 2012 20th Mediterranean Conference on Control & Automation (MED), Barcelona, Spain, July 3-6 (2012)
4. García, C.E., Prett, D.M., Morari, M.: Model predictive control: Theory and practice, a survey. *Automatica* 25, 335–348 (1989)
5. Tatjewski, P., Nczuk, M.: Soft Computing in Model-Based Predictive Control. *Int. J. Appl. Math. Comput. Sci.* 16(1), 7–26 (2006)
6. Bououden, S., Chadli, M., Filali, S., El Hajjaji, A.: Fuzzy Model Based Multivariable Predictive Control of a Variable Speed Wind Turbine: LMI approach. *Renewable Energy* 37(1), 434–439 (2012)
7. Carneiro, G.L., Galvão, R.K.H.: Model Based Predictive Control of an Aircraft With Actuator Failure in a Terrain Following Task. In: 3rd CTA-DLR Workshop on Data Analysis & Flight Control, J. Campos, SP, Brazil, September 14-16 (2009)
8. Hichem, B., Faouzi, M.: Fast Nonlinear Model Predictive Control using Second Order Valera Models Based Multi-agent Approach. Institut Supérieur Des Etudes Technologiques de SFAX Ecole Nationale d'ingénieur de Monastir Tunisia
9. Lazar, M., Roset, B.J.P., Heemels, W.P.M.H., Nijmeijer, H., van den Bosch, P.P.J.: Input-To-State Stabilizing Sub-Optimal Nonlinear Mpc Algorithms with an Application to DC-DC Converters. In: IFAC (2006)
10. Leung, F.H.F., Tam, P.K.S., Li, C.K.: The Control of Switching DC-DC Converters—A General LQR Problem. *IEEE Transactions on Industrial Electronics* 38, 65–71 (1991)
11. Sira-Ramirez, H., Perez-Moreno, R.A., Ortega, R., Garcia-Esteban, M.: Passivity-based controllers for the stabilization of DC-to-DC power converters. *Automatica* 33, 499–513 (1997)
12. Sira-Ramirez, H.: On the Generalized PI Sliding Mode Control of DC-to-DC Power Converters: A Tutorial. *International Journal of Control* 76, 1018–1033 (2003)
13. Takagi, T., Sugeno, M.: Fuzzy identification of systems and its applications to modeling and control. *IEEE Transactions on Systems, Man, and Cybernetics* 15, 116–132 (1985)
14. Tanaka, K., Wang, H.O.: *Fuzzy Control Systems Design and Analysis: A Linear Matrix Inequality Approach*. Wiley, New York (2001)

Adaptive Network-Based Fuzzy Inference System (ANFIS) Controller for an Active Magnetic Bearing System with Unbalance Mass

Seng-Chi Chen, Dinh-Kha Le, and Van-Sum Nguyen

Department of Electrical Engineering,
Da-Yeh University,
Changhua 51591, Taiwan (R.O.C)
amt.f.csg@mail.dyu.edu.tw,
ledinhkha@yahoo.com,
nvsum@hueic.edu.vn

Abstract. Active magnetic bearing (AMB) system supports a rotating shaft, without any physical contact by using electromagnetic forces. This paper proposes an intelligent control method for displacements of the air gap between the stator and the rotor in an Active Magnetic Bearing (AMB) system, using the emerging approaches of the Fuzzy Logic Controller (FLC) and Adaptive Neuro-Fuzzy Inference System (ANFIS). The AMB systems are inherently unstable and the relationship between the current and electromagnetic force is nonlinear. In this paper, the control model uses Takagi-Sugeno fuzzy logic, in which the back-propagation algorithm processes information from neural networks to adjust suitably the parameters of the fuzzy controller. This method can be applied to improve the control performance of nonlinear systems. This controller also satisfies the requirements of real-time response and stability under disturbances of system. The ANFIS controller can be feasibly applied to AMB systems with unbalance mass disturbances.

Keywords: Adaptive neuro-fuzzy inference system (ANFIS), Active magnetic bearing (AMB), Fuzzy neural network (FNN), Fuzzy logic control (FLC).

1 Introduction

Magnetic bearings are electromechanical devices that use magnetic force to suspend the rotor in an air gap without physical contact. Each radial AMB uses two pairs of electromagnets at opposite sides of the rotor. This allows the rotor to float in the air gap, and the machine to operate without frictional losses. Additionally, the contactless operation of the AMBs eliminate the maintenance of lubrication at bearing components, allowing them to operate cleanly and longer periods of time [1],[2],[5]. The rotor displacement in this AMB system is inherently unstable and the relationship between the current and electromagnetic force is highly nonlinear. The fuzzy control for nonlinear system produces good output response when the controlled system is understood [4],[7]. The results of simulation for AMB system indicate that the system

responds with satisfactory control performance is very small overshoot and with zero steady-state error. This controller also satisfies the requirements of real-time response and stability under disturbances of the control systems.

2 Magnetic Bearing System and System Model

2.1 The Magnetic Bearing System Construction

Figure 1(a) shows the typical structure of a motor drive system is suspended with magnetic bearings. The motor is located between two radial magnetic bearings. Each radial magnetic bearing generates radial forces in two perpendicular radial axes. The radial forces are controlled so that the shaft position is regulated in the center of the stator where is the equilibrium position.

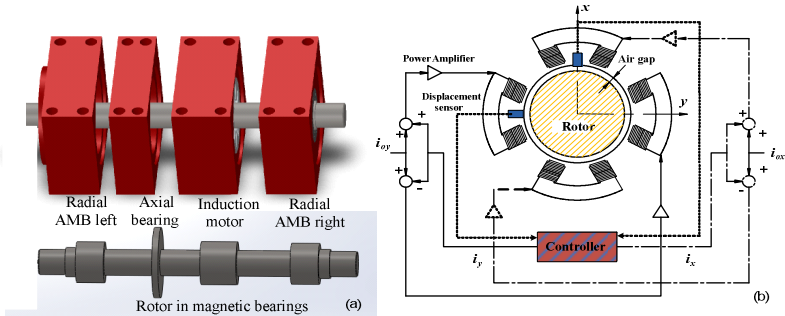


Fig. 1. (a). Horizontal shaft – AMB structure; (b). Radial AMB with current control

2.2 Magnetic Force Model

Figure 1(b) presents the technical application of the AMB. For each of two degrees of freedom, two opposing electromagnets are operated in the differential driving mode. In this configuration, the electromagnetic force can be exerted on the rotor in arbitrary directions of x axis and y axis to keep the rotor in the center position. With i_{0x} and i_{0y} are bias current; i_x and i_y are control currents along x axis and y axis, respectively. Elucidating the operational principles of an AMB, in Fig. 2(a), an electromagnet and a main geometrical characteristic of a single actuator AMB force is considered. The angle between the direction of force and the center of the cross-section A is determined by α in Fig. 2(a). For a common four-pole radial AMB, which has eight actuator teeth, α is 22.5° . The force for one actuator is given [1],[2],[3]:

$$f = k \frac{i^2}{s^2} \cos \alpha \quad \text{with} \quad k = \frac{1}{4} \mu_0 n^2 A \quad (1)$$

Here, μ_0 represents the permeability of air ($\mu_0 = 4\pi 10^{-7}$ [H/m]), n is the number of coil turns on the magnetic actuator; i is the total current in the magnet coils, and s is the air gap between the stator and the rotor, A is the cross-section of the air-gap s [1],[10].

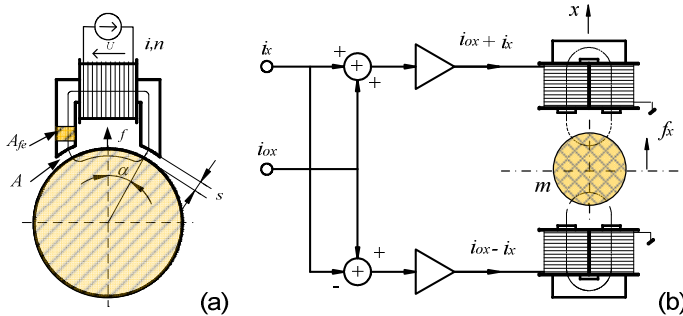


Fig. 2. (a). Magnetic force generated by an AMB; (b). A pair of electromagnets force

Radial AMB includes two pair of controlling opposite electromagnets in differential driving mode. In Fig. 2(b), the magnet at x axis is driven with the bias current i_{0x} and control current i_x . One magnet is driven with sum of bias current and control current $i_{0x} + i_x$ and the other one is driven with $i_{0x} - i_x$. The forces from one electromagnet increases while the force from the other decreases, as if two forces act on the rotor simultaneously. A simplified form of Eq. (1) is presented above. The air gaps are defined by the deviation x and the nominal air gap s_0 ; the variable s is defined for the differential driving mode as: $s_+ = s_0 - x$ and $s_- = s_0 + x$, where the subscripts “+” and “-” denote the electromagnets that receive the added and subtracted currents, respectively. Maxwell's equations yield the rotor magnetic levitation force [1],[2],[5]:

$$f_x = f_+ - f_- = k \left(\frac{(i_0 + i_x)^2}{(s_0 - x)^2} - \frac{(i_0 - i_x)^2}{(s_0 + x)^2} \right) \cos \alpha \quad (2)$$

Taylor expansion and linearization Eq.(2) [1]:

$$k_i = \frac{\partial f_x}{\partial i_x} \Big|_{x,i_x=0} = \left(\frac{4ki_0}{s_0^2} \cos \alpha \right) \text{ and } k_s = \frac{\partial f_x}{\partial x} \Big|_{x,i_x=0} = \left(\frac{4ki_0^2}{s_0^3} \cos \alpha \right) \quad (3)$$

Therefore, the magnetic force Eq. (2) can be rewritten:

$$f_x = k_i i_x + k_s x \quad (4)$$

where k_s is force-displacement factor and k_i is force-current factor.

Similar for y axis, the magnetic force: $f_y = k_i i_y + k_s y$ (5)

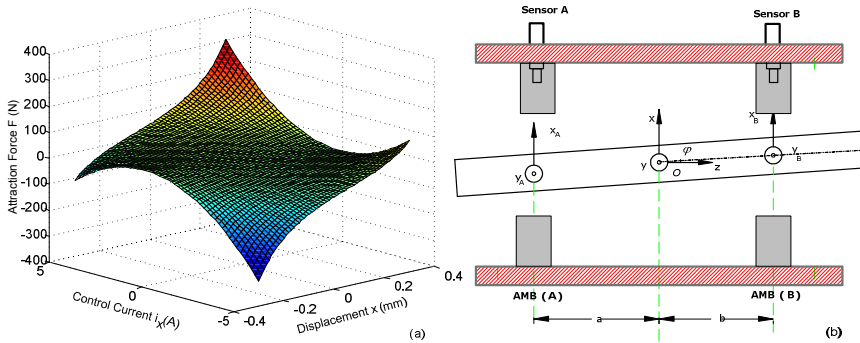


Fig. 3. (a). Characteristics of electromagnetic force, (b). Diagram of a rigid motor suspended

Figure 3(a) presents a three-dimensional plot of the magnetic force, which is nonlinearly related to the current and the rotor displacement.

2.3 Rigid Rotor – High Speed Model

Figure 3(b) shows a sketch of the AMB system. The rigid rotor is suspended by two magnetic bearing at station AMB (A) and AMB (B). The displacement sensors are collocated with the bearing. The mathematical model refers only to a rigid rotor body and the system is suspended by two identical radial active magnetic bearings. We assume that, the thrust movement is independent with x and y axes and system is balance with z axis. In Fig. 3(b), the left-hand magnetic bearing is regulated in two radial axis coordinates x_A and y_A , the right-hand radial magnetic bearing is regulated in radial axis coordinates x_B and y_B . The differential equation for a rigid rotor with its degrees of freedom transformed into bearing coordinates with displacement matrix output $\mathbf{v}_c = [x_A \ x_B \ y_A \ y_B]^T$ and the input vector $\mathbf{u}_c = [i_{xA} \ i_{xB} \ i_{yA} \ i_{yB}]^T$ is given [1]:

$$\mathbf{M}_c \ddot{\mathbf{v}}_c + \mathbf{G}_c \dot{\mathbf{v}}_c - \mathbf{K}_s \mathbf{v}_c = \mathbf{K}_i \mathbf{u}_c + \mathbf{f}_d \quad (6)$$

Where \mathbf{M}_c is mass matrix, \mathbf{G}_c is gyroscopic matrix, \mathbf{K}_s is force-displacement factors matrix, \mathbf{K}_i is force-current factors matrix; \mathbf{f}_d is mass unbalance disturbance.

Using transfer matrix \mathbf{T} from O to AMB (A) and AMB (B), the entire matrix is given [1],[5]:

$$\mathbf{T} = \frac{1}{a+b} \begin{bmatrix} b & a & 0 & 0 \\ -1 & 1 & 0 & 0 \\ 0 & 0 & b & a \\ 0 & 0 & -1 & 1 \end{bmatrix}; \mathbf{M}_c = \mathbf{T}' \mathbf{M} \mathbf{T} = \mathbf{T}' \begin{bmatrix} m & 0 & 0 & 0 \\ 0 & I_x & 0 & 0 \\ 0 & 0 & m & 0 \\ 0 & 0 & 0 & I_y \end{bmatrix} \mathbf{T} \quad (7)$$

$$\mathbf{G}_c = \mathbf{T}' \mathbf{G} \mathbf{T} = \mathbf{T}' \left(\begin{bmatrix} 0 & 0 & 0 & 0 \\ 0 & 0 & 0 & 1 \\ 0 & 0 & 0 & 0 \\ 0 & -1 & 0 & 0 \end{bmatrix} I_z \Omega \right) \mathbf{T} \quad (8)$$

$$\mathbf{K}_s = \begin{bmatrix} k_{s_xA} & 0 & 0 & 0 \\ 0 & k_{s_xB} & 0 & 0 \\ 0 & 0 & k_{s_yA} & 0 \\ 0 & 0 & 0 & k_{s_yB} \end{bmatrix}; \mathbf{K}_i = \begin{bmatrix} k_{i_xA} & 0 & 0 & 0 \\ 0 & k_{i_xB} & 0 & 0 \\ 0 & 0 & k_{i_yA} & 0 \\ 0 & 0 & 0 & k_{i_yB} \end{bmatrix} \quad (9)$$

Where m is rotor mass; I_x , I_y are radial inertia moments ; I_z is polar inertia moment; Ω is angular speed of the shaft around z -axis; a , b is the axial distance from the radial bearing to O; $k_{s_xA}, k_{s_xB}, k_{s_yA}, k_{s_yB}$ are force-displacement factors of electromagnet x_A, x_B, y_A, y_B ; and $k_{i_xA}, k_{i_xB}, k_{i_yA}, k_{i_yB}$ are force-current factors of $i_{xA}, i_{xB}, i_{yA}, i_{yB}$, respectively.

The resulting continuous time state space model is given by bearing coordinates in the form:

$$\begin{aligned} \dot{\mathbf{x}} &= \mathbf{Ax} + \mathbf{Bu} \\ \mathbf{y} &= \mathbf{Cx} \end{aligned} \quad (10)$$

With $\mathbf{x} = [\mathbf{v}_c \quad \dot{\mathbf{v}}_c]^T$ and $\mathbf{u} = [\mathbf{0} \quad \mathbf{u}_c]^T$

$$\mathbf{A} = \begin{bmatrix} \mathbf{0} & \mathbf{I} \\ -\mathbf{M}_c^{-1} \mathbf{K}_s & -\mathbf{M}_c^{-1} \mathbf{G}_c \end{bmatrix}; \mathbf{B} = \begin{bmatrix} \mathbf{0} \\ \mathbf{M}_c^{-1} \mathbf{K}_i \end{bmatrix}; \mathbf{C} = [\mathbf{I} \quad \mathbf{0}] \quad (11)$$

Where \mathbf{x} is the state vector, \mathbf{u} denotes control input signal, \mathbf{y} is output vector; \mathbf{A} is state matrix, \mathbf{B} is input matrix, \mathbf{C} is output matrix.

Figure 4(a) presents the control law for pole placement state feedback $\mathbf{u} = -\mathbf{Kx}$ with state feedback matrix \mathbf{K} , with the closed loop poles should lie at $\mu_1, \mu_2 \dots \mu_l$, where specific desired locations.

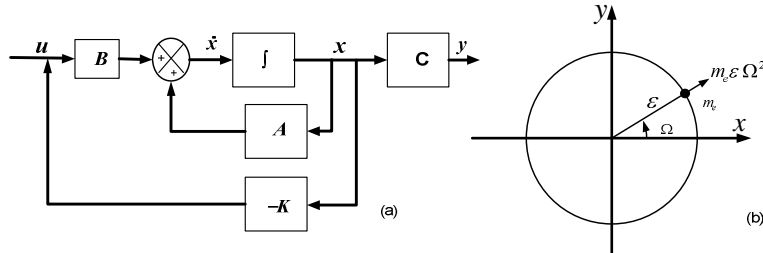


Fig. 4. (a). Pole placement state feedback; (b). Unbalance mass force

2.4 Unbalance Force Disturbance

Vibration is caused by mechanical unbalance in rotating system. Where m_e is an additional mass at a radius of ε in the direction of Ωt . In Fig. 4b, the unbalance mass force $\mathbf{f}_d = [f_{xd} \ f_{yd}]^T$ in x, y are defined by [2],[11]:

$$\begin{aligned} f_{xd} &= m_e \varepsilon \Omega^2 \cos \Omega t \\ f_{yd} &= m_e \varepsilon \Omega^2 \sin \Omega t \end{aligned} \quad (12)$$

3 Adaptive Neuro-Fuzzy Inference System Controller (ANFIS)

Recently, the Fuzzy Logic Controller (FLC) has emerged as an effective tool to stabilize a nonlinear system, such as AMB system, magnetic levitation system or other power electronic devices [4],[9],[12]. Fig. 5(a) presents the design of an FLC for stabilizing a magnetic bearing system. The error signal $e(t) = r - y$, which is the difference between the measured signal y and the reference input (r).

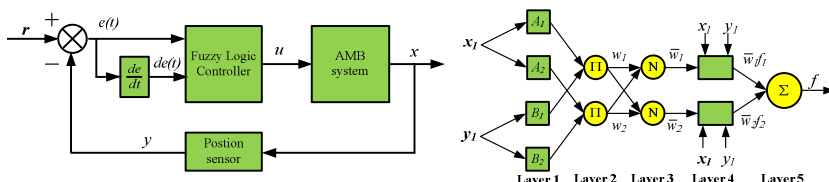


Fig. 5. (a). FLC for an AMB system; (b). ANFIS architecture

In this paper, the inputs and the outputs are normalized for the base values that are defined for the system. A Gaussian membership's function is employed as the inputs and outputs fuzzy sets of the FLC. In Fig. 5(a), the designed membership functions for $e(t)$, $de(t)$ are inputs and u is the output. The control rules of the fuzzy controllers are a set of heuristic selected fuzzy rules.

ANFIS is a simple data learning technique that uses Fuzzy Logic to transform specified inputs into a desired output through highly interconnected neural network processing elements and information connections[4],[6],[12]. An ANFIS functions by using neural network learning methods to tune the parameters of a Fuzzy Inference System (FIS). Fig. 5(b) presents the equivalent ANFIS architecture of a first-order Sugeno fuzzy model with two rules. The model is composed of five layers and every node in a given layer has a similar function. In Fig. 5(b), a circle represents a fixed node, where as a square indicates an adaptive node [7],[8].

In developing the ANFIS architecture, two fuzzy IF-THEN rules, based on a first-order Sugeno model, are considered:

Rule 1: if x_I is A_I and y_I is B_I then $f_I = p_I x_I + q_I y_I + r_I$

Rule 2: if x_I is A_2 and y_I is B_2 then $f_2 = p_2 x_I + q_2 y_I + r_2$

Here, x_I and y_I are the inputs; A_i and B_i are the fuzzy sets; f_i are the outputs within the fuzzy region that is specified by the fuzzy rule, and p_i , q_i and r_i are the design parameters which values are determined during the training process. ANFIS is composed of five-layer architecture. Each layer is explained in detail below.

In *layer 1*, all nodes are adaptive. The outputs of *layer 1* are the fuzzy membership grade of the inputs, which are given by the following equations:

$$MF_{I,i} = \mu A_i(x_I), \quad i = 1, 2 \quad \text{and} \quad MF_{I,i} = \mu B_{i-2}(y_I), \quad i = 3, 4 \quad (13)$$

Where x_I and y_I are the inputs to node i , and A_i and B_i are the linguistic labels that is associated with this node function. $\mu A_i(x_I)$ and $\mu B_{i-2}(y_I)$ can include any fuzzy membership function. For example, if the triangular membership function is employed, then $\mu A_i(x_I)$ is given by Eq. (14) or the Gaussian membership function given by Eq. (15)

$$MF_{I,i} = \max \left(\min \left(\frac{x-a_i}{b_i-a_i}, \frac{c_i-x}{c_i-b_i} \right), 0 \right); i=1,2 \quad (14)$$

$$MF_{I,i} = e^{-\frac{1}{2} \left(\frac{x-c_i}{a_i} \right)^2} \quad (15)$$

Where $MF_{I,i}$ is the output of the i^{th} node in the first layer, and a_i , b_i and c_i are the premise parameters that are used to adjust the shape of the membership function.

In *layer 2*, the nodes are fixed nodes. This layer involves fuzzy operators; it uses the AND operator to fuzzy the inputs. These inputs are labeled with π , indicating that they perform as a simple multiplier. The output of this layer can be represented as:

$$MF_{2,i} = w_i = \mu A_i(x_I) * \mu B_i(y_I), \quad i=1,2 \quad (16)$$

In *layer 3*, the outputs of *layer 3* are the normalized firing strengths. Each node is a fixed rule that is labeled N . The output of the i^{th} node is the ratio of the i^{th} rule's firing strength to the sum of all of the firing strengths of all of the rules:

$$MF_{3,i} = \bar{w}_i = \frac{w_i}{\sum_{i=1}^R w_i}, i = 1, 2 \quad (17)$$

In *layer 4*, the nodes are adaptive. The output of each node in this layer is simply the product of the normalized firing strength and the first order polynomial. The output of this layer is given by:

$$MF_{4,i} = \bar{w}_i f_i = \bar{w}_i (p_i x_1 + q_i y_1 + r_i), i = 1, 2 \quad (18)$$

Where \bar{w}_i is a normalized firing strength from layer 3, and (p_i, q_i, r_i) is the consequent parameter set of the node.

In *layer 5*, the single node in layer 5, labeled Σ , calculates the overall ANFIS output from the sum of the node inputs:

$$MF_{5,i} = O = \frac{\sum_{i=1}^R w_i f_i}{\sum_{i=1}^R w_i} \quad (19)$$

Figure 6 shows the step response of AMB model, using the ANFIS control. AMB system is a MIMO system. In this paper, we assume the AMB model with displacement output $\mathbf{v}_c = [x_A \ x_B \ y_A \ y_B]^T$, so we use 4 ANFIS controllers to control this system.

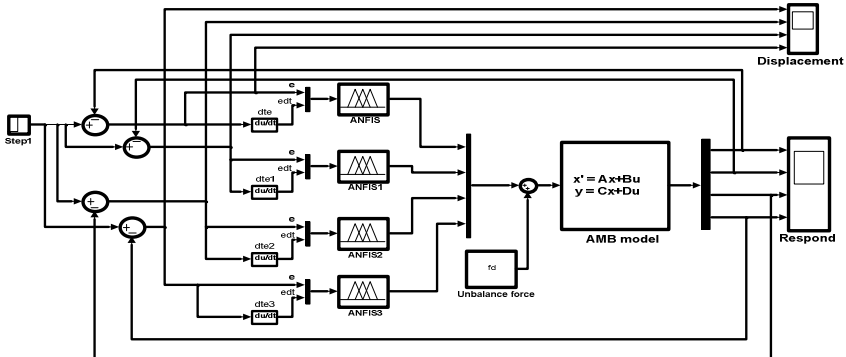


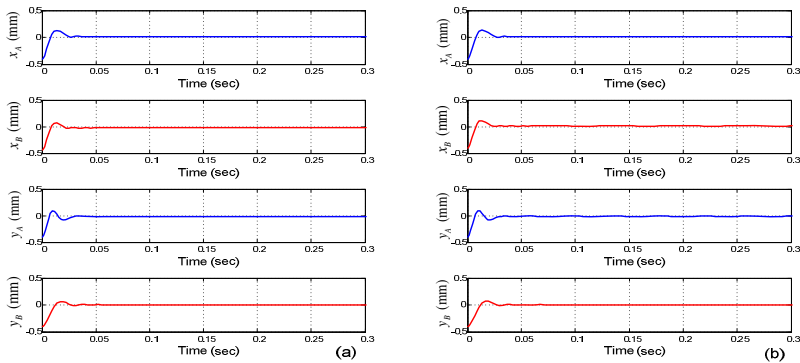
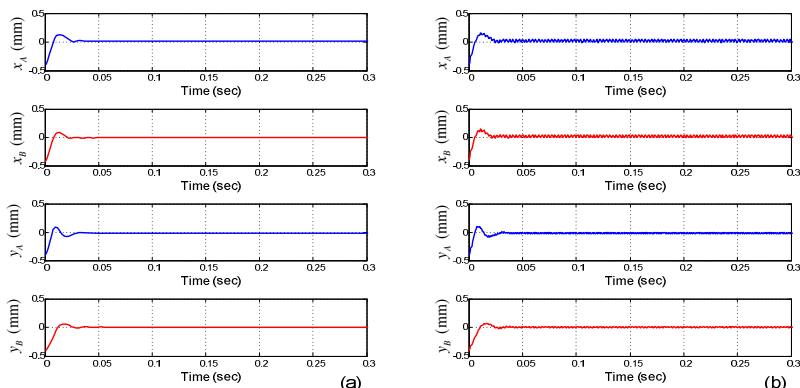
Fig. 6. ANFIS control for AMB

4 Simulation Results

The model of AMB had been implemented in Matlab/Simulink with parameter in Table 1. After the simulation model run, the performance characteristics are observed on the scopes. The displacements are observed with non-disturbance and with disturbance in Figure 7 and Figure 8.

Table 1. Parameters of an active magnetic bearing system

1	Mass of shaft, m	2.2kg	7	Bias currents to be used, i_0	1A
2	Number of coil turns, n	120	8	Pole cross-sectional area, A	180 mm ²
3	Polar moment of inertia, I_z	2.3e-3 kgm ²	9	Distant from O to AMB (A), a	0.15m
4	Radial moment of inertia : I_x, I_y	1.3e-3 kgm ²	10	Distant from O to AMB (B), b	0.17m
5	Angular speed, Ω	3000 ~ 15000rpm	11	Radius of rotor, \mathcal{E}	0.015m
6	Nominal air gap length, s_0	0.5mm	12	Mass unbalance, m_e	80e-3 kg

**Fig. 7.** Displacement with $\Omega = 3000\text{rpm}$; (a). Non-unbalance mass; (b). Unbalance mass**Fig. 8.** Displacement with $\Omega = 15000\text{rpm}$; (a). Non-unbalance mass; (b). Unbalance mass

From Fig. 7(a) and Fig. 8(a), we see that ANFIS controller manages to bring the system in steady state, with a short steady time and low overshoot. From Fig. 7(b) and Fig.8(b), we add unbalance mass in AMB system, with the same unbalance mass. When the motor rotate with low speed at $\Omega = 3000\text{rpm}$; this system is still stable. But, we increase the speed of rotor to $\Omega = 15000\text{rpm}$; the system has a slight oscillation.

5 Conclusions

The AMB systems are unstable and the relationship between the current control, air gap and electromagnetic force is nonlinear. In this paper, ANFIS controller was developed for a highly unstable AMB system through simulation with MATLAB software. ANFIS controller manages to bring the rotor displacement to steady state, with a short steady time and low over shoot. Simulation results also show the effect of unbalance mass to the AMB rotor shaft: increasing the speed of rotor, the system has a slight oscillation. So, eliminations the unbalance mass of rotor shaft are very important to produce the real AMB systems. The proposed control method is effective in AMB system and other nonlinear systems.

References

- [1] Schweitzer, G., Traxler, A., Bleuler, H.: Active Magnetic Bearing – Basics, Properties and Applications, pp. 55–71, 156-165. vdf Hochschulverlag AG, Zurich (1994)
- [2] Chiba, A., Fukao, T., Ichikawa, O., Oshima, M., Takemoto, M., Dorrell, D.G.: Magnetic bearing and bearingless drivers, pp. 61–95. Newnes (2005)
- [3] Daoud, M.I., Abdel-Khalik, A.S., Massoud, A., Ahmed, S., Abbasy, N.H.: A Design Example of An 8-pole Radial AMB for Flywheel Energy Storage. In: 2012 XXth International Conference Electrical Machines (ICEM), September 2-5, pp. 1153–1159 (2012)
- [4] Chen, S.C., Sum, N.V., Jyh, L.Y., Mao, S.M.: Novel fuzzy neural network controller for maglev system with controlled-PM electromagnets. In: First International Conference on Intelligent Technologies and Engineering Systems, Taiwan (December 2012)
- [5] Shafai, B., Beale, S., LaRocca, P., Cusson, E.: Magnetic bearing control systems and adaptive forced balancing. IEEE Control Systems 14, 4–13 (1994)
- [6] Jang, J.S.R., Sun, C.T.: Neuro-fuzzy modeling and control. Proc. IEEE 83, 378–406 (1995)
- [7] Jang, J.R.: ANFIS: Adaptive-network-based fuzzy inference system. IEEE Trans. Syst. Man Cybern. 23, 665–685 (1993)
- [8] Huann, C.K., Chu, C.T., Jhou, J.Y.: Fuzzy control with fuzzy basis function neural network in magnetic bearing system. Industrial Electronics (ISIE) 12, 846–851 (2012)
- [9] Chen, S.C., Tung, P.C.: Application of a rule self-regulating fuzzy controller for robotic deburring on unknown contours. Fuzzy Sets and Systems 110, 341–350 (2000)
- [10] Johnson, D., Brown, G.V., Adaptive, D.J.: variable bias magnetic bearing control. American Control Conference 4, 2217–2223 (1998)

- [11] Arredondo, I., Jugo, J.: Stability analysis and robust control design on an AMB system. In: 2007 46th IEEE Conference on Decision and Control, vol. 83, pp. 2199–2204 (December 2007)
- [12] Chen, S.C., Sum, N.V., Chang, G.: Application of self-tuning fuzzy PID controller on magnetic levitation system. In: The 11th Taiwan Power Electronics Conference & Exhibition. National Tsing Hua University (September 2012)

Stabilization of the Rotational Inverted Pendulum Using Mixed H_2/H_∞ PID Controller

Vo Hoang Duy, Dong Si Thien Chau, Vo Huu Hau, Phan Thai Hoa,
and Tran Trong Dao

Faculty of Electrical and Electronics Engineering,
Ton Duc Thang University, No. 19 Nguyen Huu Tho Street, Tan Phong Ward, District 7,
Ho Chi Minh City, Vietnam
[vhduy, chaudst, vohuuuhau, trantrongdao}@tdt.edu.vn](mailto:{vhduy, chaudst, vohuuuhau, trantrongdao}@tdt.edu.vn),
hoapt91@stu.tdt.edu.vn

Abstract. This paper proposes a mixed H_2/H_∞ optimal PID controller with a genetic algorithm based on the dynamic model of a Rotational Inverted Pendulum (RIP) and applies it for balancing control. In the dynamic model of the rotational inverted pendulum with perturbation, the proposed controller guarantees robust and optimal performance to the stabilization of the rotational inverted pendulum. A genetic algorithm was used to obtain parameters for the PID controller that satisfies the mixed H_2/H_∞ constraint. To implement the proposed controller, a control system based on microcontroller dsPIC30F4011 was developed. Experimental results are shown to prove the performance of the proposed controller when changing the weight and shape of pendulum.

Keywords: Inverted pendulum, PID controller, Robust control, Optimal control.

1 Introduction

Inverted pendulum is typically unstable system and it is a classical problem in control theory. Many researches applied some control algorithms to control inverted pendulum as sliding mode control [1], adaptive control [2], backstepping [3] and fuzzy logic [4]. The inverted pendulum can be controlled swing up or stabilization. However, these solutions had the disadvantage that the controller was complicated.

The other controller is simpler but can be replaced these above controller is PID controller. PID controller is one of the most popular controllers in the real process control because it is very simple and robust with noise. As a result, there have been a lot of approaches using PID controllers to control of inverted pendulum; including using genetic algorithm to find the optimal parameter of PID controller [5] [6], combining with fuzzy logic [7] or with neural network [8] or between two PID controllers [9]. However, most of them only satisfy one of two criterions: optimal performance or robust performance.

In this paper, the mixed H_2/H_∞ method is used to achieve an optimal robust PID controller which is applied to balance the rotational inverted pendulum. Experimental results are shown to prove the performance of the proposed controller when changing the weight and shape of pendulum.

2 Model of the Rotational Inverted Pendulum System

Figure 1 presents a diagram of the rotational inverted pendulum. The state-space equation of rotational inverted pendulum can be represented by using the Euler-Lagrange formulation [10].

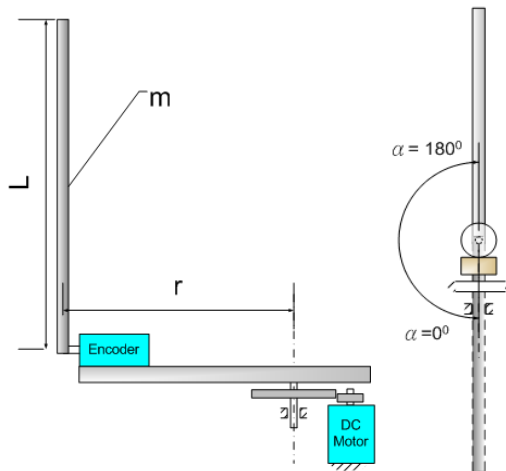


Fig. 1. Rotational inverted pendulum

$$\begin{bmatrix} \dot{\theta} \\ \dot{\alpha} \\ \ddot{\theta} \\ \ddot{\alpha} \end{bmatrix} = \begin{bmatrix} 0 & 0 & 1 & 0 \\ 0 & 0 & 0 & 1 \\ 0 & \frac{b.d}{E} & -\frac{c.G}{E} & 0 \\ 0 & \frac{a.d}{E} & \frac{b.G}{E} & 0 \end{bmatrix} \begin{bmatrix} \theta \\ \alpha \\ \dot{\theta} \\ \dot{\alpha} \end{bmatrix} + \begin{bmatrix} 0 \\ 0 \\ \frac{c.\eta_m.\eta_g.K_t.K_g}{R_m.E} \\ \frac{b.\eta_m.\eta_g.K_t.K_g}{R_m.E} \end{bmatrix} V_m \quad (1)$$

where, $a = J_{eq} + mr^2$; $b = mLr$; $c = 4mL^2/3$; $d = mgL$; $E = ac - b^2$;
 $G = \frac{\eta_m.\eta_g.K_t.K_m.K_g^2 - B_{eq}.R_m}{R_m}$

The transfer function of the rotational inverted pendulum can be obtained based on the above state-space equation.

$$G_{RIP}(s) = \frac{\alpha(s)}{U(s)} = \frac{K_6 s^2 + (K_4 K_5 - K_2 K_6)s}{s^4 - K_2 s^3 - K_3 s^2 + (K_3 K_2 - K_1 K_4)s} \quad (2)$$

here,

$$K_1 = \frac{b.d}{E}; \quad K_2 = -\frac{c.G}{E}; \quad K_3 = \frac{a.d}{E}; \quad K_4 = -\frac{b.G}{E}; \quad K_5 = \frac{c.\eta_m \eta_g .K_t .K_g}{R_m .E};$$

$$K_6 = \frac{b.\eta_m \eta_g .K_t .K_g}{R_m .E}$$

The System parameters of the rotational inverted pendulum are shown in Table 1. From Table 1, the transfer function of the rotational inverted pendulum is as follows:

$$G_{RIP}(s) = \frac{\alpha(s)}{U(s)} = \frac{146.1s^2}{s^4 + 11.46s^3 - 82.07s^2 - 137.5s} \quad (3)$$

Table 1. System parameters of the rotational inverted pendulum

Symbol	Description	Value
L	Length of the inverted pendulum	0.355 m
m	Mass of the inverted pendulum	76.83e-3 kg
r	Length from the center of rotating arm to the pendulum	0.246 m
η_m	Motor efficiency	0.69
η_g	Gearbox efficiency	0.9
K_m	Back-emf constant	0.00767 V/(rad/s)
K_t	Motor-torque constant	0.096 N.m/A
K_g	Gear ratio	5
B_{eq}	Equivalent viscous damping coefficient	0.8e-3 N.m/(rad/s)
R_m	Armature resistance	0.9 Ohm
J_{eq}	Moment of inertia of the arm and pendulum about the axis of θ	0.157e-4 Kg.m ²
g	Gravitational acceleration	9.81 m/s ²
α	The angular displacement of the inverted pendulum	-
θ	The angular displacement of the rotating arm rotated	-
u	Input voltage of the armature circuit	-

3 A Mixed H_2/H_∞ PID Controller Designer

Consider the PID control system in Fig. 2, where $r(t)$, $e(t)$, $u(t)$ and $y(t)$ are respectively the reference, error, control signal and output. The plant $G_{RIP}(s)$ to be controlled undergoes perturbation $\Delta G(s)$:

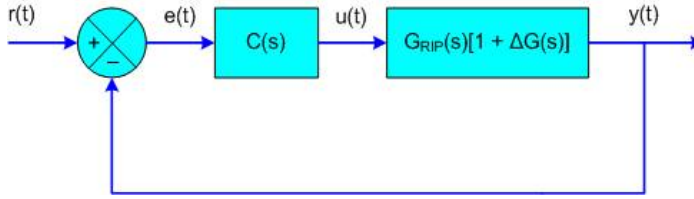


Fig. 2. PID control system with plant perturbation

where the plant $\Delta G(s)$ is assumed to be stable but uncertain, and bounded according to

$$|\Delta G(j\omega)| < |\xi(j\omega)|, \quad \forall \omega \in [0, \infty) \quad (4)$$

The mixed H_2/H_∞ design problem includes two problems as follows [11]:

3.1 The Robust Stability Constraint

If a controller $C(s)$ is chosen so that the nominal closed loop system in Fig. 2 is asymptotically stable and the following inequality holds:

$$\left\| \frac{G_{RIP}(s)C(s)\xi(s)}{1 + G_{RIP}(s)C(s)} \right\|_\infty \leq 1 \quad (5)$$

then the closed loop system in Fig. 2 is also asymptotically stable under plant perturbation $\Delta G(s)$ in (5). The above equation is equivalent to the following:

$$\begin{aligned} \left\| \frac{G_{RIP}(s)C(s)\xi(s)}{1 + G_{RIP}(s)C(s)} \right\|_\infty &= \sup_{\omega \in [0, \infty)} \sqrt{\frac{G_{RIP}(-j\omega)G_{RIP}(j\omega)C(-j\omega)C(j\omega)\xi(-j\omega)\xi(j\omega)}{(1 + G_{RIP}(-j\omega)C(-j\omega))(1 + G_{RIP}(j\omega)C(j\omega))}} \\ &= \sup_{\omega \in [0, \infty)} \sqrt{\frac{\beta(\omega)}{\alpha(\omega)}} = \sqrt{\sup_{\omega \in [0, \infty)} \frac{\beta(\omega)}{\alpha(\omega)}} \leq 1 \end{aligned} \quad (6)$$

In general, scanning ω in $[0, \infty]$ to find the peaks of $\beta(\omega)/\alpha(\omega)$ in (6) is not an easy task. The peaks of $\beta(\omega)/\alpha(\omega)$ occur at the points that must satisfy the following equation:

$$\frac{d}{d\omega} \frac{\beta(\omega)}{\alpha(\omega)} = \frac{\alpha(\omega) \frac{d\beta(\omega)}{d\omega} - \beta(\omega) \frac{d\alpha(\omega)}{d\omega}}{\alpha^2(\omega)} = 0 \quad (7)$$

therefore, only the real root λ_i of the following equation need be found:

$$\alpha(\omega) \frac{d\beta(\omega)}{d\omega} - \beta(\omega) \frac{d\alpha(\omega)}{d\omega} = \prod_{i=1}^n (\omega - \lambda_i) = 0 \quad (8)$$

with the above results, the robust stability constraint in (5) is equivalent to

$$\sqrt{\max_{\lambda_i} \frac{\beta(\lambda_i)}{\alpha(\lambda_i)}} \leq 1 \quad (9)$$

3.2 The Minimization Problem

The H₂ performance is as follows:

$$J = \min_C \int_0^{\infty} e^2(t) dt \quad (10)$$

where $e(t)$ is the tracking error in nominal case that is shown in Fig. 2 and

$$e(s) = \frac{r(s)}{1 + G_{RIP}(s)C(s)} \quad (11)$$

By Parseval's theorem, the quality index function can be obtained:

$$\begin{aligned} J &= \min_C \int_0^{\infty} e^2(t) dt \\ &= \min_{k_1, k_2, k_3} \frac{1}{2\pi j} \int_{-\infty}^{\infty} \frac{r(-s)r(s)}{(1 + G_{RIP}(-s)C(-s))(1 + G_{RIP}(s)C(s))} ds \\ &= \min_{k_1, k_2, k_3} \frac{1}{2\pi j} \int_{-\infty}^{\infty} \frac{B(s)B(-s)}{A(s)A(-s)} ds \end{aligned} \quad (12)$$

The above equation can be rewritten as follows:

$$J_m(k_p, k_i, k_d) = \frac{1}{2\pi j} \int_{-\infty}^{\infty} \frac{\left(\sum_{k=0}^{m-1} b_k s^k \right) \left(\sum_{k=0}^{m-1} b_k (-s)^k \right)}{\left(\sum_{k=0}^m a_k s^k \right) \left(\sum_{k=0}^m a_k (-s)^k \right)} ds \quad (13)$$

where

$$A(s) = \sum_{k=0}^m a_k s^k, \quad B(s) = \sum_{k=0}^{m-1} b_k s^k$$

The minimization problem in the above equation can be solved via the aid of the residue theorem. The value of $J_m(k_p, k_i, k_d)$ can be found from [12].

Then, the H₂ performance in (10) must be the following form:

$$J_m = \min_{k_p, k_i, k_d} J_m(k_p, k_i, k_d) \quad (14)$$

where J_m is a function of PID parameters (k_p, k_i, k_d) with appropriate m .

From the above analysis, the mixed H₂/H_∞ design problem becomes how to solve the minimization problem (14) under the inequality constraint (9).

The parameters (k_p , k_i , k_d) of the PID controller are decided by genetic algorithm. The procedure of a simple genetic algorithm [11] is given as follows:

- Step 1: Specify the condition of (k_p , k_i , k_d) to guarantee the stability of the nominal closed loop system via the Routh-Hurwitz criterion.
- Step 2: Specify the stability domain of (k_p , k_i , k_d).
- Step 3: Establish the parameters of genetic algorithm: crossover probability, mutation probability, population size, maximum generation and termination criterion.
- Step 4: Make the initial population and chromosome coding.
- Step 5: Compute λ_i from (8).
- Step 6: Compute the fitness function.
- Step 7: Create the next generation
- Step 8: Check the stop condition. If it is not satisfactory, repeat procedure step 5 to step 8.

The flowchart of mixed H_2/H_∞ control design procedure is shown in Fig. 3.

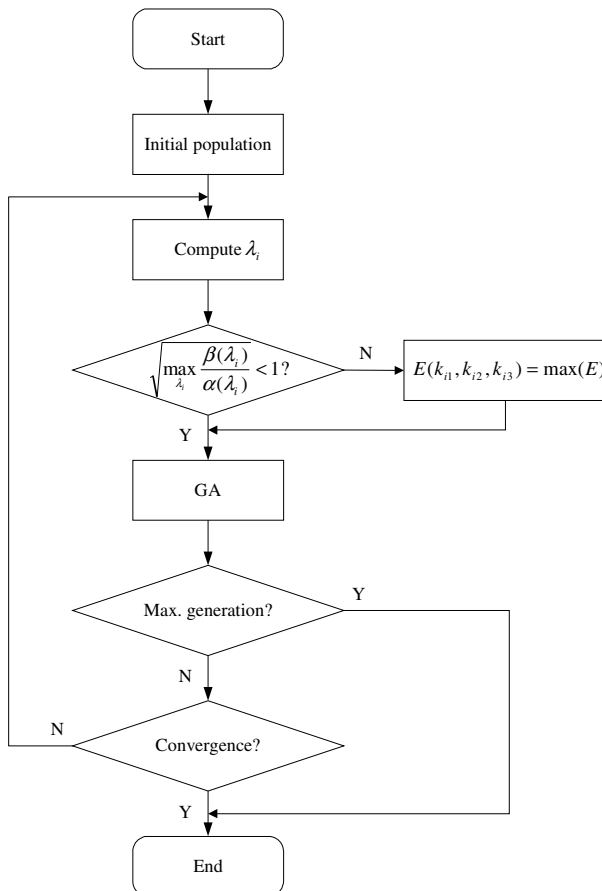


Fig. 3. The flowchart of mixed H_2/H_∞ control design procedure

where E is the cost function as follows:

$$E(k_p, k_i, k_d) = J_m(k_p, k_i, k_d) \quad (15)$$

4 Experimental Results

For the control system as shown in Fig. 2, suppose the plant perturbation is bounded as follows:

$$|\Delta G(s)| \leq \left| \frac{0.1}{s^2 + 0.1s + 10} \right| \quad (16)$$

The error transfer function $E(s)$ can be obtained as follows:

$$e(s) = \frac{s^4 + 11.5s^3 - 82.1s^2 - 237.5s}{s^5 + (146.1k_d + 11.5)s^4 + (146.1k_p - 82.1)s^3 + (146.1k_i - 237.5)s^2} \quad (17)$$

In this case, $m=5$, the quality index function is J_5 [12]. The parameters of the controller are searched into the following bounds: $k_p=[0 1000]$, $k_i=[0 1000]$, $k_d=[0 100]$.

The genetic algorithm begins by randomly generating a population of 300 chromosomes. After 25 generations, proper PID controller parameters are obtained, and the corresponding PID control parameters are $k_p=152.8745$, $k_i=524.5013$, $k_d=1.1702$.

To illustrate the effectiveness, a stabilization control scheme of rotational inverted pendulum is implemented as shown in Fig. 4. The main controller is microcontroller dsPIC30F4011 microchip and encoder as an angle feedback sensor with the resolution is 1024 pulses.

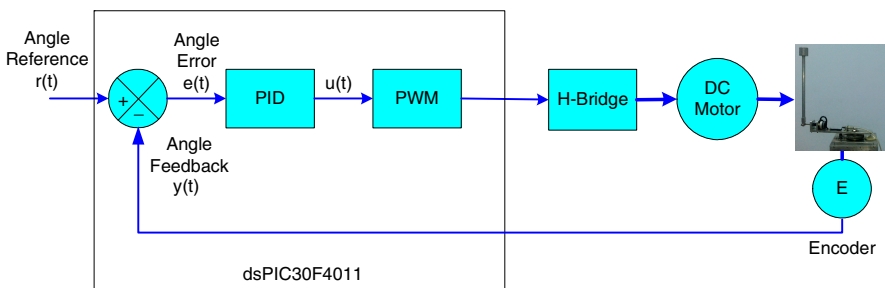


Fig. 4. Block diagram of the proposed stabilization control scheme

In order to demonstrate the effectiveness of the proposed controllers, the plant uncertainties are used in the experiment as shown in Fig. 5. Table 2 lists the parameters of the plant uncertainties.



Fig. 5. The plant uncertainties

Table 2. The parameters of the plant uncertainties

Object	Weight	Length
m	76.83 g	-
$M1$	37.27 g	-
$M2$	67.38 g	-
$M3$	119.26 g	-
$M4$	105.77 g	20.3 cm

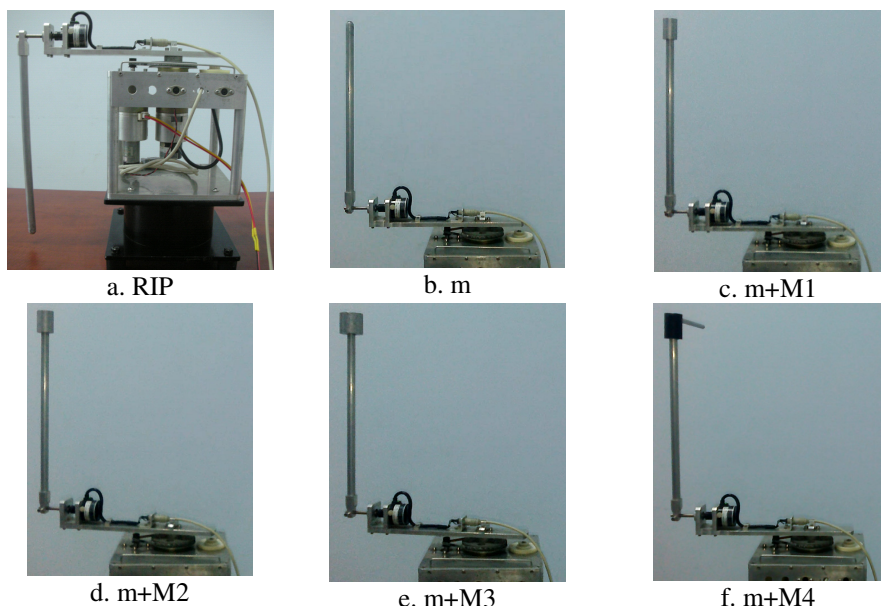


Fig. 6. Experimental results of the inverted pendulum

The experimental results are implemented in the case of the mass of the inverted pendulum is varied as shown in Fig. 6 when the mass of pendulum is increased from nominal value (76.83 g) to 196.09 g. Especially, the pendulum is attached to the bar with the length is 20.3 cm and the weight is 105.77 g in Fig. 6f. The angular displacement of the inverted pendulum is shown in Fig. 7-11.

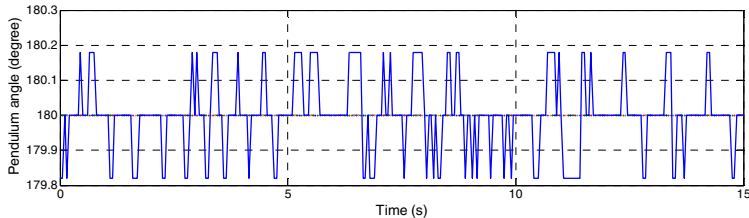


Fig. 7. The angular displacement of the inverted pendulum

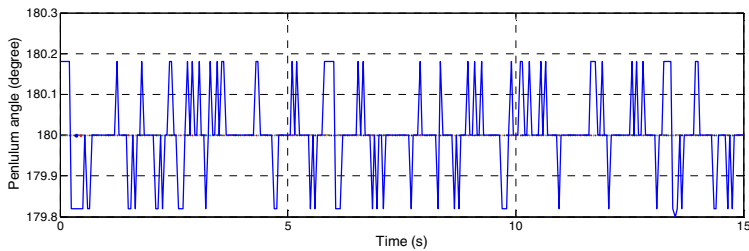


Fig. 8. The angular displacement of the inverted pendulum with load $m+M_1$

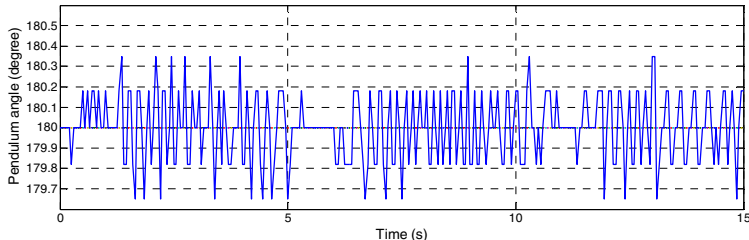


Fig. 9. The angular displacement of the inverted pendulum with load $m+M_2$

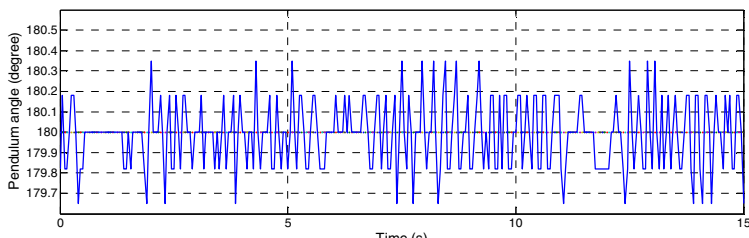


Fig. 10. The angular displacement of the inverted pendulum with load $m+M_3$

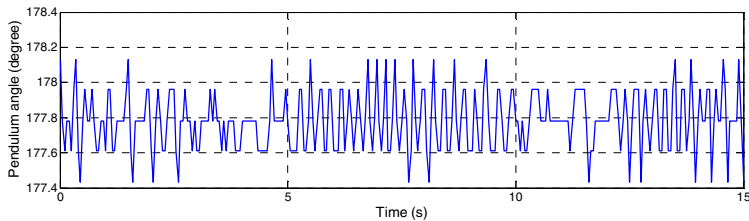


Fig. 11. The angular displacement of the inverted pendulum with load $m+M_4$

The proposed method can control the inverted pendulum on the vertical line in a stable way as shown in Fig. 6. It is seen from the Fig. 7 and 8 when the mass of pendulum increased from 76.83 g to 109.1 g, the errors are quite similar and the values are 0.1 degree. The errors are increased to 0.32 degree when the mass of pendulum is increased to 144.66 g (Fig. 9) or 196.09 g (Fig. 10). It is also seen that the pendulum is still stable when the mass of pendulum is attached to a bar as shown in Fig. 11. However, the errors are increased to 3 degrees. It means that the pendulum angle tends to tilt to the bar's position. The results show that the controller obtained by the proposed method can control the perturbed plant successfully.

5 Conclusion

In this paper, the mixed H_2/H_∞ PID has been applied and investigated to balance the rotational inverted pendulum. Performance of the optimal robust PID is analyzed. An uncertain model has been also considered to show the robustness of the PID controller. From the experimental results show that the mixed H_2/H_∞ PID adapts with the changing of weight and shape of pendulum.

References

1. Grossimon, P.G., Barbieri, E., Drakunov, S.: Sliding mode control of an inverted pendulum. In: Proceedings of the 28th Southeastern Symposium on System Theory, pp. 248–252 (1996)
2. Hirata, H., Haga, K., Ratiroch-Anant, P.: Self-Tuning Control for Rotation Type Inverted Pendulum Using Two Kinds of Adaptive Controllers. In: IEEE Conference on Robotics, Automation and Mechatronics (2006)
3. Fu, Y.-C., Lin, J.-S.: Nonlinear Backstepping Control Design of the Furuta Pendulum. In: IEEE Conference on Control Applications (August 2005)
4. Yurkovich, S., Widjaja, M.: Fuzzy Controller Synthesis for an Inverted Pendulum System. Journal of Control Engineering Practice 4(4), 455–469 (1996)
5. Omatsu, S., Deris, S.: Stabilization of inverted pendulum by the genetic algorithm. In: IEEE Conference on Emerging Technologies and Factory Automation (November 1996)
6. Chakraborty, K., Mukherjee, R.R., Mukherjee, S.: Tuning of PID Controller of Inverted Pendulum using Genetic Algorithm. International Journal of Soft Computing and Engineering (IJSCE) 3(1) (March 2013)

7. Park, G.-Y., Baeg, M.-H., Hong, S.-C., Yang, H.-W.: An implementation of a rotational inverted pendulum using adaptive fuzzy controllers. In: IEEE International Conference on Industrial Electronics (1999)
8. Omatsu, S., Yoshioka, M.: Stability of inverted pendulum by neuro-PID control with genetic algorithm. IEEE World Congress on Computational Intelligent (1998)
9. Rani, M.R., Selamat, H., Zamzuri, H., Ahmad, F.: PID controller optimization for a rotational inverted pendulum using genetic algorithm. In: IEEE International Conference on Modeling, Simulation and Applied Optimization (ICMSAO) (April 2011)
10. Akhtaruzzaman, M., Shafie, A.A.: Modeling and control of a rotary inverted pendulum using various methods, comparative assessment and result analysis. In: International Conference on Mechatronics and Automation, ICMA (2010)
11. Chen, B.S., Cheng, Y.M., Lee, C.H.: A genetic approach to mixed H_2/H_∞ optimal PID control. IEEE Control System Magazine 15, 51–60 (1995)
12. Jury, E.I., Dewey, A.G.: A general formulation of the total square integrals for continuous systems. IEEE trans. Automatic Control AC-10, 119–120 (1965)

Study on Control of Quarter Car Suspension Using Simple Force Actuator for Education Purpose

Duy Anh Nguyen¹, Hwan Seong Kim², Sang Bong Kim³, and Tan Tien Nguyen¹

¹ Faculty of Mechanical Eng., Hochiminh City University of Technology, Vietnam

² Dept. of Logistics, Korea Maritime University, Korea

³ Dept. of Mechanical and Automotive Eng., Pukyong National University, Korea

duyanhkmu@yahoo.com, hskim@hhu.ac.kr,

kimsb@pknu.ac.kr, ntien.dhbk@gmail.com

Abstract. Quarter car models is one of popular examples using in study of vibration and vibration control, especially for engineering students. Usually the experiment equipment for studying this subject are very expensive. This paper proposes a simple, low cost force actuator for studying control of active suspension system. Through this system, engineering students can achieve their hands-on learning, control challenges for a quarter-car model, as well as mass, spring and damper systems in general.

Keywords: Quarter-car suspension system, force actuator.

1 Introduction

An automotive suspension system is one of the important components in a vehicle and is one of most popular study subjects in car manufacturing. A suspension system consists of four suspensions in four-wheel vehicles. The main purposes of a vehicular suspension are[4]: (a) to isolate the vehicle body from external disturbances coming from irregular road surfaces and internal disturbances created by cornering, acceleration, or deceleration, in order to have ride comfort; (b) to carry the weight of the vehicle body; (c) to react to variations in load, which are whether generated by changes in the number of passengers and luggage, or from internal disturbances; and (d) to keep a firm contact between the road and the tires, in order to have good handling performance that means drive safety. It can be seen that safety and ride comfort characteristics of a vehicle mainly depend on the suspension system. To improve the performance of automotive suspension systems, the semi-active and active suspension system is introduced. Semi-active system based on the controlling of stiffness of damper achieved by switching the characteristics of dampers. An active suspension is one including an actuator that can supply active force, which is regulated by a control algorithm using data from sensors attached to the vehicle.

To supply the required force in active suspension system, there are some force actuators commonly used such as: hydraulic force actuators, pneumatic force actuators, electromagnetic force actuators. Hydraulic and pneumatics force actuator are applicable in real systems, however with their high costs, the experimental system

just only can be done with large support fund. Kruczak A. et al using linear motor as an actuator generating required forces for active suspension [2]. Here, the electromagnetic force can be applied directly to the payload without the intervention of a mechanical transmission, what results in high rigidity of the whole system, its higher reliability and longer lifetime. However, the cost for this force actuator is rather expensive with large size, not suitable for small scale experimental equipment.

This paper focus to study on control of a quarter-car active suspension using the simple force actuator. A dc motor and lead screw incorporating with a spring can generate the required force in suitable frequency range necessary for study the controlling of an active suspension. The organization of this paper is given as follows: first, the review of quarter-car model and its mathematical model are presented; then the proposed force actuator is introduced; next, the experimental and simulation results comparing with passive cases with different frequencies of disturbances are given to show the effectiveness of the proposed force actuator; and finally, the conclusion is given.

2 A Quarter-Car Suspension Model

There are some types of suspension models have been proposed so far: a quarter-car model, a half-car model and the full-car model. In this paper, a quarter-car model is used for illustrated the introduced force actuator.

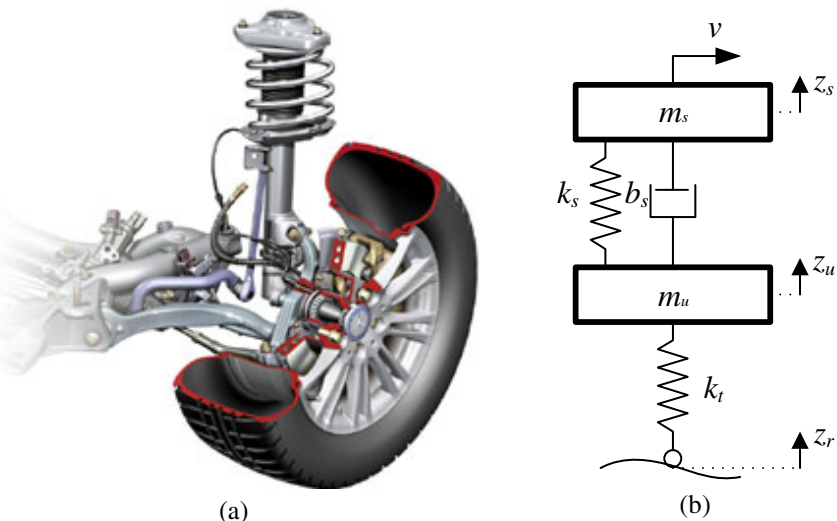
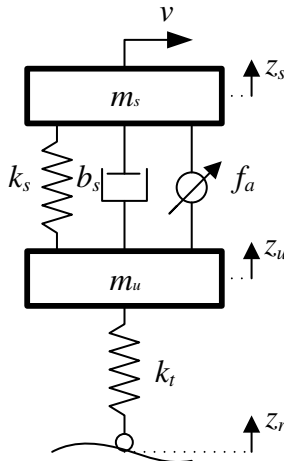


Fig. 1. (a) Passive Car Suspension System and (b) Its mathematical model

A conventional passive suspension system is composed of spring and the shock absorbing damper. They work mechanically in parallel and are fixed between the wheel supporting structure (unsprung mass, m_u) and the vehicle body (sprung mass, m_s). The damper (b_s) is a cylinder filled with hydraulic oil or compressed gas. The

passive suspension is shown in Fig.1(a) and the quarter-car model of a passive suspension are illustrated in Fig.1(b). Passive suspension systems can be found popular in vehicles due to their simplicity, small volume, low cost and high reliability. However, passive suspensions cannot achieve perfect performances due to its constant elastic characteristics and damping characteristics.

To improve the performance of suspension, the actuator force is applied between its sprung mass and unsprung mass as shown in the Fig.2.



m_s : sprung mass; m_u : unsprung mass; b_s : damping coefficient; k_s : spring stiffness coefficient; k_t : tire stiffness coefficient; v : car velocity; z_s : position of sprung mass; z_u : position of unsprung mass; z_r : position of road; f_a : active force

Fig. 2. Active suspension system with applied control force f_a

The active 1/4 car suspension model in Fig.2 has been used by many researchers to investigate both passive and active automotive suspension. The mathematical model is given as[7].

$$\dot{x} = Ax + Bu + \Gamma d \quad (1)$$

$$y = Cx \quad (2)$$

$$\text{here } x = \begin{bmatrix} x_1 \\ x_2 \\ x_3 \\ x_4 \end{bmatrix}; A = \begin{bmatrix} 0 & 1 & 0 & -1 \\ -\frac{k_s}{m_s} & -\frac{b_s}{m_s} & 0 & \frac{b_s}{m_s} \\ 0 & 0 & 0 & 1 \\ \frac{k_s}{m_u} & \frac{b_s}{m_u} & -\frac{k_t}{m_u} & -\frac{b_s}{m_u} \end{bmatrix}; B = \begin{bmatrix} 0 \\ \frac{1}{m_s} \\ 0 \\ -\frac{1}{m_u} \end{bmatrix};$$

$$C = \begin{bmatrix} 1 & 0 & 0 & 0 \\ 0 & 1 & 0 & 0 \\ 0 & 0 & 1 & 0 \\ 0 & 0 & 0 & 1 \end{bmatrix}; \Gamma = \begin{bmatrix} 0 \\ 0 \\ -1 \\ 0 \end{bmatrix}$$

with the defined state variables as the follows

$$\begin{array}{ll} x_1 = z_s - z_u : \text{suspension deflection} & x_2 = \dot{z}_s : \text{velocity of sprung mass} \\ x_3 = z_u - z_r : \text{tire deflection} & x_4 = \dot{z}_u : \text{velocity of unsprung mass} \\ u = f_a : \text{active control force} & d = \dot{z}_r : \text{road disturbance} \end{array}$$

3 The Proposed Simple Force Actuator

The Fig.3 describes the actuator based on motor-ball screw-spring.

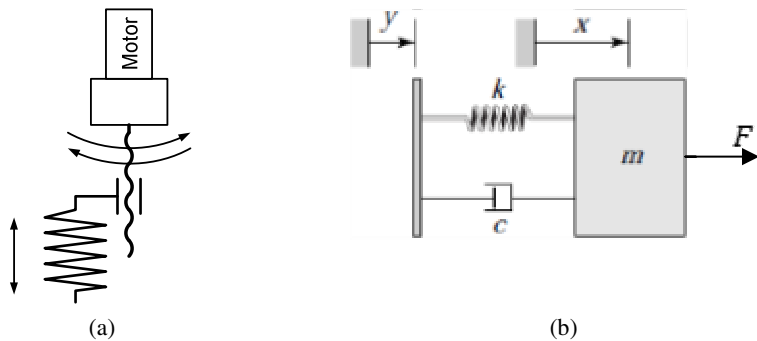


Fig. 3. Active force generated from simple force actuator

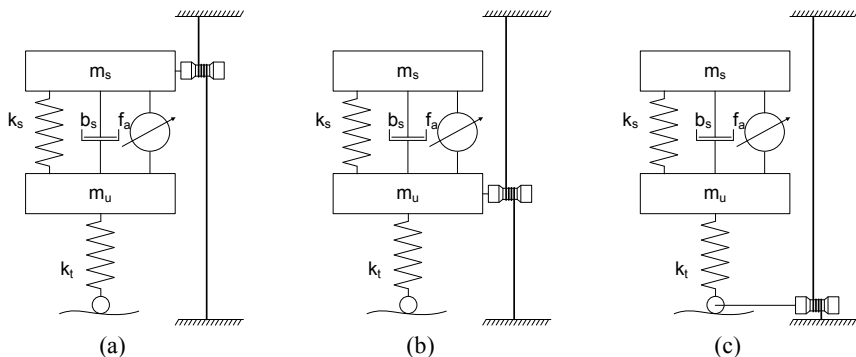


Fig. 4. Measuring vertical displacements of (a) sprung mass, (b) unsprung mass and (c) road disturbance

The actuator have includes a DC motor which drives ball screw in serial with conventional spring. Active force is generated by theory Hook's law described in this formula.

$$F = k|x - y| \quad (3)$$

In which F is the force generated, k is spring stiffness, and $|x - y|$ is spring travel. In this mechanism, spring stiffness is considered as a linear value, neglect its nonlinearity characteristic. Additionally, spring stiffness is also the proportion between force and spring travel. To determine spring travel for generating force, two potentiometers are used for measuring the positions of two sides of the spring.

The motion of equation

$$m\ddot{x} + c\dot{x} + kx = c\dot{y} + ky \quad (4)$$

The force can be derived from the above equations (3) and (4).

The active force is regulated by a control algorithm using data from sensors attached to the vehicle. In this study, three potentiometers are arranged with three positions to determine absolute displacement of the body car, unsprung mass and road profile compared with the ground as shown in the Fig.4.

4 Simulation and Experimental Results

To study the effectiveness of the proposed force actuator, an experiment is setup as shown in the Fig.5.

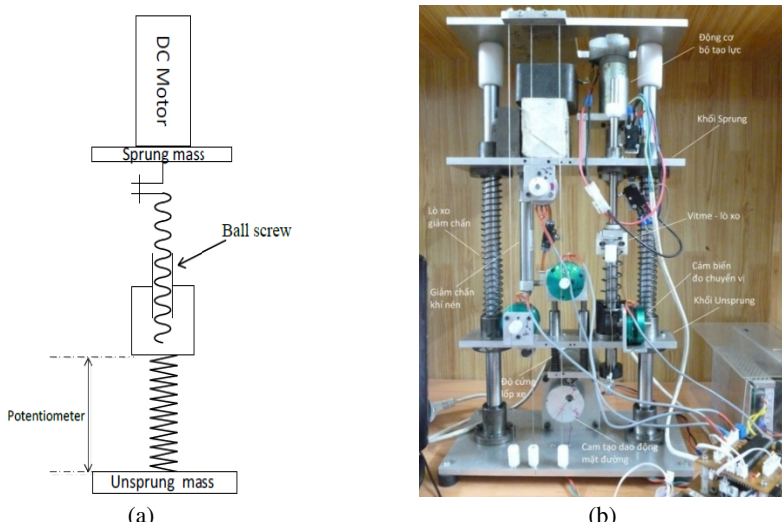


Fig. 5. Experiment system: (a) force actuator and (b) real system

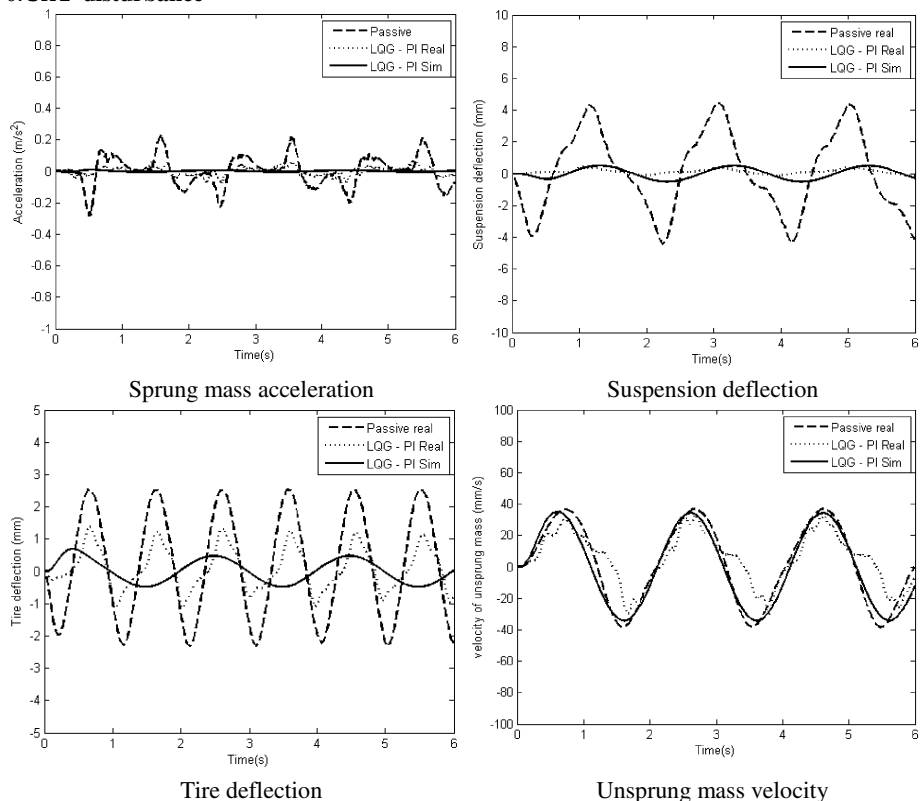
The numerical values of system parameters used in simulation and experiment are given in Table 1 and Table 2.

Table 1. Numerical values of suspension system

Parameters	Value	Unit
Sprung mass m_s	9.3	Kg
Unsprung mass m_u	1.4	Kg
Damping coefficient b_s	80	Ns/m
Spring stiffness coefficient k_s	911	N/m
Tire stiffness coefficient k_t	9217	N/m

Table 2. Numerical values of force actuator

Parameters	Value	Unit
Maximum force generated	10	N
Lead screw pitch	1	mm
Spring stiffness coefficient	1000	N/m
Maximum force frequency	1.2	Hz

0.5Hz disturbance**Fig. 6.** System response at frequency of 0.5Hz

At each frequency, we measure displacement of sprung mass and unsprung mass. The vertical change of the road is measured by vertical displacement of cam follower. Thus, the road disturbance is calculated. From the displacement of sprung mass, car body velocity and acceleration are derived. From sprung mass and unsprung mass displacement, we have suspension deflection. Tire deflection is calculated from the relative displacement of the unsprung mass and the road displacement. Such as the acceleration of car body, suspension and tire as well.

Two cases are investigated: passive system and active system with PI-Observer base LQG controller[7].

Simulation and experimental results are presented in the following Fig.s 6,7 and 8 corresponding with 0.5, 0.75 and 1Hz road disturbances.

0.75Hz disturbance

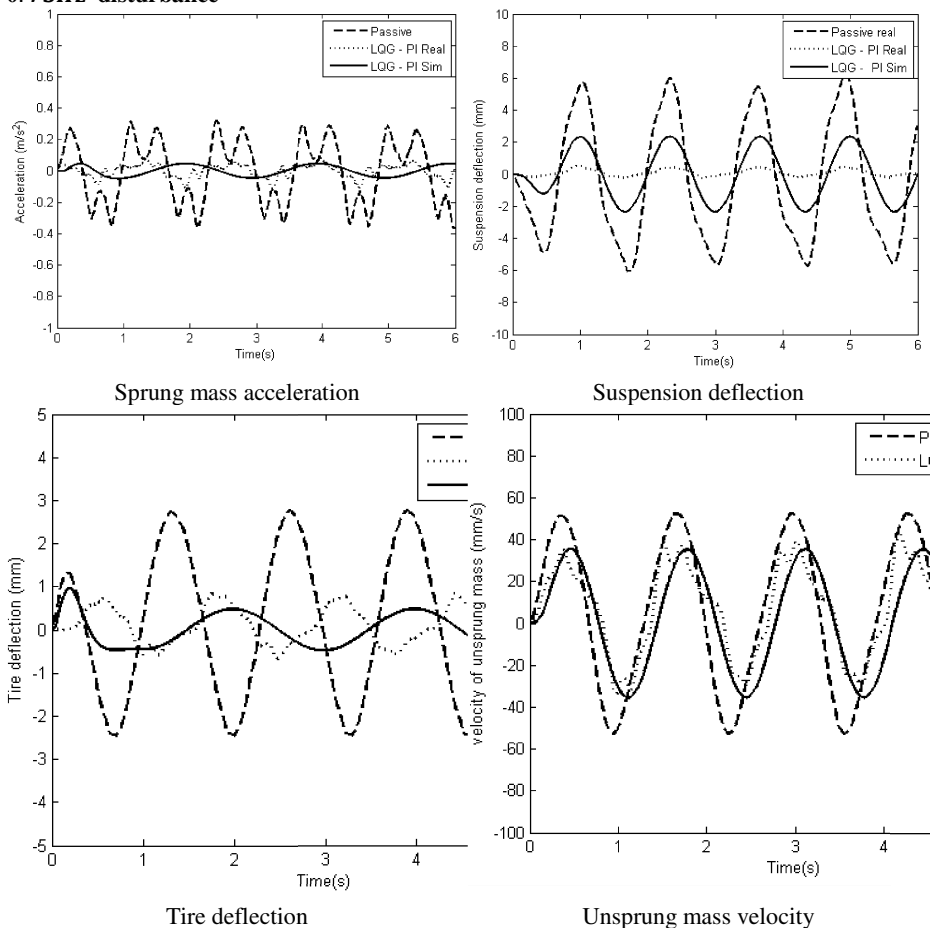
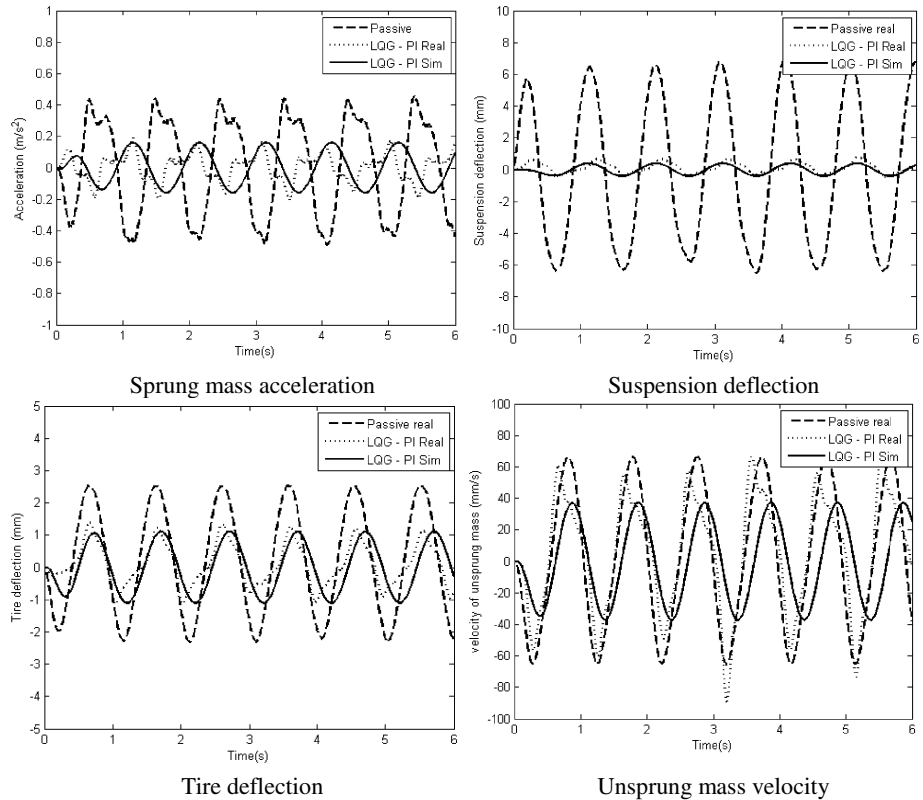


Fig. 7. System response at frequency of 0.75Hz

1Hz disturbance**Fig. 8.** System response at frequency of 0.75Hz

In the above figures, the slashed line is the result of passive suspension, the continuous line is the result of active suspension in simulation, and the other is result of active suspension in the fact. The line of passive suspension show that the body car vibration include road vibration add to natural vibration of body car. The results shown that the controlled system has better performances comparing with the passive one. Also, the experimental results are not as good as the simulation results due to the different values of real system and values using in the simulation. Off course, this differences are also due to the proposed force actuator. However, in the view of education purpose, the results of the proposed force actuator is acceptable with the its simple and low cost.

5 Conclusion

This paper proposes a simple force actuator incorporating with simple rotating potentiometers for studying of control quarter-car suspension system. The

experimental results achieved the good performance comparing to the passive one. Hopefully that, this experimental system can be used for engineering students studying hands-on learning, relevant to the automotive industry. This also teaches active control challenges for a quarter-car model, as well as mass, spring and damper systems in general.

References

1. Wakeham, K.J., Geoff Rideout, D.: Model Complexity Requirements in Design of Half Car Active Suspension Controllers. In: Proc. of ASME Dynamic Systems and Controls Conference, Arlington, VA, October 31-November 2, pp. 1–8 (2011)
2. Kruczak, A., et al.: Active Suspension - Case Study on Robust Control. World Academy of Science, Engineering and Technology 54, 411–416 (2011)
3. Ram Mohan Rao, T., et al.: Analysis of Passive and Semi Active Controlled Suspension Systems for Ride Comfort in An Omnibus Passing over Speed Bump. IJRRAS 5(1), 7–17 (2010)
4. Xue, X.D., et al.: Study of Art of Automotive Active Suspensions. In: Proc. of the 4th International Conference on Power Electronics Systems and Applications, pp. 360–366 (2011)
5. Allen, J.A.: Design of Active Suspension Control based Upon Use of Tubular Linear Motor and Quater-Car Model. MS Thesis, Texas A&M University (August 2008)
6. Bui, T.H.: Control of Active Suspension System with Full-Car Model Using H and Nonlinear Adaptive Control Methods. MS. Thesis, Pukyong National University, Pusan, Korea (February 2002)
7. Nguyen, H.S., Nguyen, T.T., Kim, J.Y., Kim, S.B.: Robust Controller Design for Active Suspension System by Using PI Observer. In: APVC 1997, pp. 262–267 (November 1997)
8. Ichikawa, K.: A Theory of Active Suspension Design. In: The 2nd Int. Conf. on Motion and Vibration Control, pp. 852–857 (1994)
9. Gillespie, T.D.: Fundamentals of Vehicle Dynamics. Society of Automotive Engineers, Inc., (1992)

Remote Mouse Control Using Fingertip Tracking Technique

Phuong Dat Le and Vinh Hao Nguyen

Faculty of Electrical and Electronic Engineering, Ho Chi Minh City University of Technology,
Ho Chi Minh City, Vietnam
lephuongdat1988@gmail.com, vinhhao@hcmut.edu.vn

Abstract. This paper proposes a real-time fingertip tracking technique using a web camera to enable users to remotely control their computer mouse by their own bare hands. The hand region is firstly extracted by background subtraction and filtered by the morphological opening operations and blob labeling. Then, convex hull and convexity defect are used to count the fingers and detect the coordinates of the fingertip. Next, the coordinates of the fingertip is mapped to the screen coordinates and smoothed by the Moving Average. Finally, the events corresponding to the detected fingers are sent to the computer system to control the mouse. Experimental results show that the proposed technique can successfully count the finger with the accuracy of 98.3% and work well in real time.

1 Introduction

Along with the development of technologies, computer systems have become vital to the world we live in. Most computer systems require more and more interaction. Thus, it is necessary to have types of interaction which are natural and easy to use.

Human computer interaction (HCI) can be described as an interaction to convey information from users to computer systems. Traditional interaction that relies on the mouse and keyboard is still the most familiar HCI. However, these devices are inconvenient and unnatural. Combining computer vision and HCI, it is possible to create an advanced input device which is an attractive alternative to these cumbersome interface devices. The use of hand gestures via computer vision is one of the most interesting parts of HCI. Using their hands as an input device can help people communicate with computers in a more intuitive and natural way.

There have been many attempts to recognize hand gestures. Most of them are based on hand segmentation because it can decrease the amount of image information. Colored gloves [1], [2] and markers [3] are used to detect user actions. However, these methods are inconvenient and too complex to use. Another popular method is using skin color [4]-[8]. Skin color detection is a very challenging task as the skin color in an image is sensitive to various factors such as light condition, background color, motion, and ethnicity. Edge in [9], [10] has been used for detection, but the limitation of this method is that the hand can easily be extracted only from uniform background images. References [11], [12] propose background subtraction for hand

segmentation. They archived quite good results; though they need the background to be unchanging and different from skin color. To overcome the limitations of the methods above, some studies use special cameras such as infrared cameras [13] or kinect [14], [15]. They can detect the hand from the input image even in complex backgrounds and under different lighting conditions, yet they are not very practical, owing to the expense of the devices.

Real time fingertip detection and tracking in a 2-D plane can be applied in computer system as a visual mouse [16]-[18]. Inspired by those systems, the main focus of the paper is finding an efficient method to detect the fingertips and control the mouse pointer, utilizing a bare hand and a simple web camera with a frame rate of approximately 30 frames per second. This paper also suggests a robust user interface which is intuitive and easy to use. In each frame, hand regions are first detected by background subtraction and filtered by the morphological opening operations and blob labeling. Next, the forearm is removed by using distance transform. Then, fingers and fingertips are detected with convex hulls and convexity defects. After that, the coordinates of the fingertip is mapped to the screen coordinates and smoothed by the Moving Average. Finally, the event which is determined by the number of fingers, and the coordinates are sent to the computer to control the mouse.

2 Hand Segmentation and Finger Detection

2.1 Hand Segmentation

Mouse movement is based on finger trajectory, as well as hand motion. Background subtraction is one of the best methods to obtain the moving areas. Therefore, it is suitable for the proposed technique. Average background is used to achieve the better segmentation. Equation (1) shows how to obtain the average background in the initial phase.

$$\overline{I_{bg}} = \frac{1}{N} \times \sum_{k=1}^N I^k \quad (1)$$

where I represents the value of color at a specific position, N is the number of frames which are used to calculate the average background.

The difference frame is obtained using the difference of the average background and the current frame. If the result is greater than a threshold (th), it is defined as the foreground.

$$I_{fg} = \begin{cases} 1, & |I^k - \overline{I_{bg}}| > th \\ 0, & \text{else} \end{cases} \quad (2)$$

The web cameras always produce a varying degree of noise. In the experiment, the noise of the web camera image can be removed by the morphological opening operation. This operation is performed by using image erosion and image dilation. Erosion trims down the difference frame, and thus the speckles are eroded to nothing while the larger regions that contain visually significant content are not affected. Dilation expands the frame pixels to get back the original shape of the content.

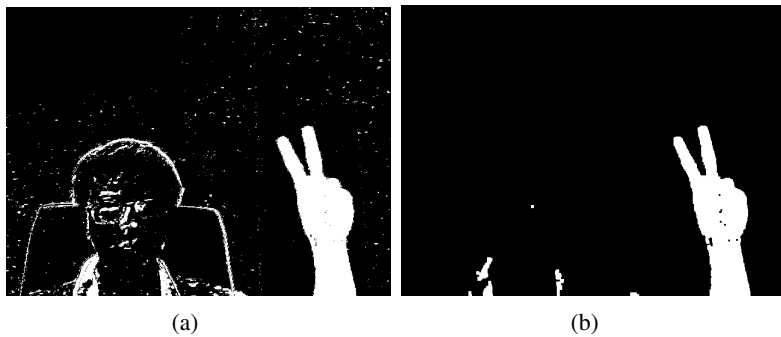


Fig. 1. Result of background subtraction. (a) Difference frame with the opening operation.

Fig. 1 shows a result of background subtraction with and without the opening operation. To detect the hand regions, blob labeling is used in [11]. This method labels each pixel in the foreground image. These pixels which get the same label are connected with each other and are considered as a blob. Information about the minimum size window surrounding separate blobs is also obtained. Limiting the size of the window and choosing the rightmost blob can help remove the unexpected movement of face and body. The rightmost blob is also extracted and it contains the hand region. Fig. 2 shows some results of the blob labeling method.

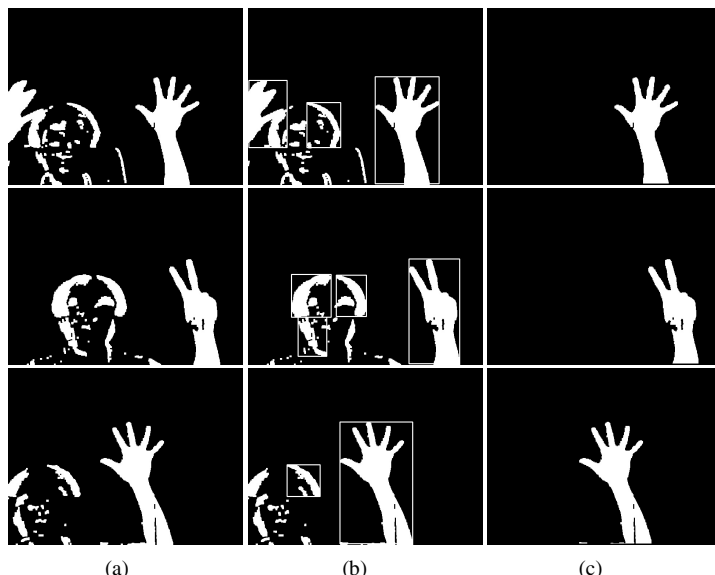


Fig. 2. Some results of blob labeling. (a) Difference frames, (b) blobs with limited size, (c) rightmost blobs.

2.2 Finger Detection

2.2.1 Forearm Filtering

In order to enhance the finger detection, the forearm should be filtered from the hand region. Using the distance transform which was introduced in [19], the research in [4], [12] proposed a very useful way to remove the forearm.

The distance transform of an image is defined as a new image in which every output pixel is set to a value equal to the distance to the nearest zero pixel in the input image. The distance transform of the hand region is computed by using the 5x5 neighborhood fast chamfer distance transform [18] that gives a good approximation to the exact Euclidean distance.

Fig. 3 illustrates the procedure of forearm filtering. The binary image which contains hand region is firstly converted to a distance transform image. The pixel with max value in distance transform image represents the palm center. Then, the offset circumference whose radius is 1.65 times the palm center value is calculated. All pixels outside this circumference and lower than the palm center are assumed to represent the forearm and are removed.

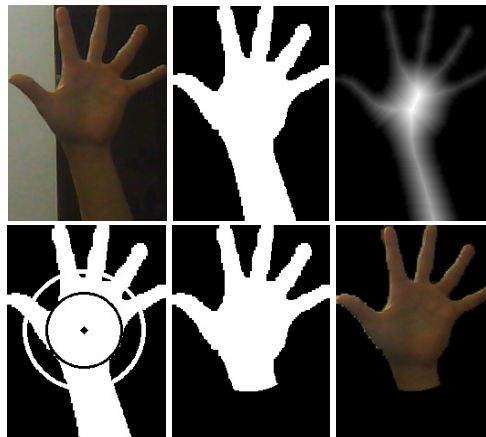


Fig. 3. Forearm filtering

2.2.2 Finger Detection

A useful way to find out the coordinates of the fingertip and the number of fingers is to compute a convex hull for palm region and then compute its convexity defect which is introduced in [20].

Using a lower limit for the depth of defect, the defects between two fingers are detected. After that, the coordinates of the fingertips are computed based on the start point and end point of these defects. The number of fingers equals the number of these defects plus 1. When the hand is closed or only 1 finger is opened, no defect is detected. In this case, the maximum distance from palm center to the points of convex hull is used to determine whether the hand is closed or not. If this value is less than a

specific value, there is a closed hand. If not, the farthest point on the convex hull is assumed to represent the fingertip of the hand. Fig. 4 shows six cases of the finger counting stage.

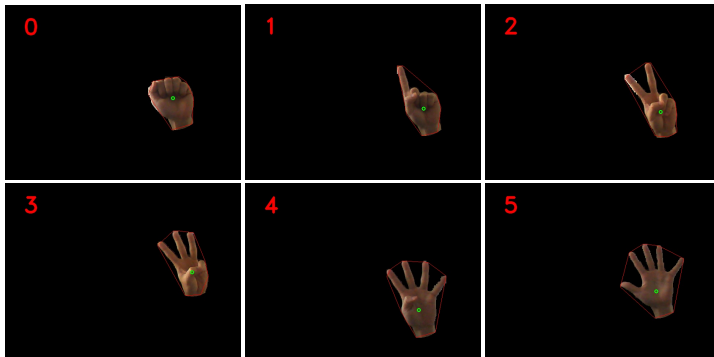


Fig. 4. Six cases of finger counting stage

3 Mouse Control

3.1 Mouse Coordinates

The experiment shows that the mouse pointer is not as smooth and natural as real mouse, even if the coordinates of the fingertip is detected correctly. This issue is caused by the following reasons. First, the coordinates of the fingertip are extracted from each frame; therefore, they are just the discontinuous coordinates of fingertip locations. If we use these coordinates directly, the mouse pointer will jump around in a very unnatural way. Second, the difference of the resolution between the camera and the screen require a coordinate conversion and this makes it difficult to position the mouse pointer accurately. To overcome these difficulties, we suggest using the Moving Average algorithm to average the displacement of the detected fingertip position and use this displacement as the coordinates of mouse pointer on the screen.

Moving Averages are the techniques that can be applied to time series data to help smooth data and filter out the noise. The two most popular types of moving averages are the Simple Moving Average (SMA) and the Exponential Moving Average (EMA). SMA as in (3), is the simplest way and can filter out a lot of noise; however, it also increases the lag and decreases the precision of the data.

$$S(k) = \frac{1}{N} \times \sum_{k=1}^N x(k) \quad (3)$$

Here x represents the value of input data, S represents the EMA output value and N is the number of time periods.

This paper proposed EMA which was first suggested in [21], to smooth the fingertip trajectory. EMA reduces the lag by applying more weight to recent data. The EMA for a series data is calculated as follows:

$$E(0) = \frac{1}{N} \times \sum_{k=1}^N x(k) \quad (4)$$

$$\alpha = 2 / (N + 1) \quad (5)$$

$$E(t) = E(t-1) + (x(t) - E(t-1)) \times \alpha \quad (6)$$

Here E is the EMA output value, α is the weighting multiplier between 0 and 1.

3.2 Mouse Events

To control the computer mouse, it is necessary to define some conditions to trigger mouse events. Reference [11] proposes a very natural and convenient way to trigger draw function by only one bare hand. In this paper, we improved and systematized those conditions. Let's assume that users only use their right hand, and the hand and the face are not overlap. The events which are determined by the number of the fingers are tied with the corresponding coordinates and sent to the computer via *SendInput* routine to control the mouse.

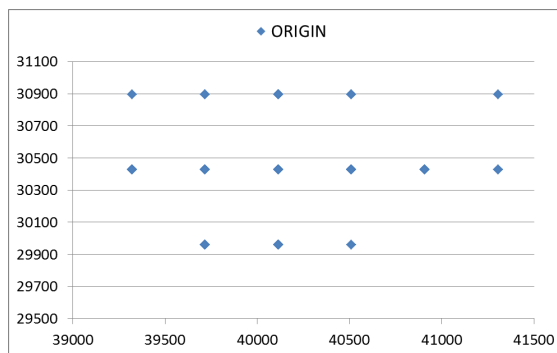
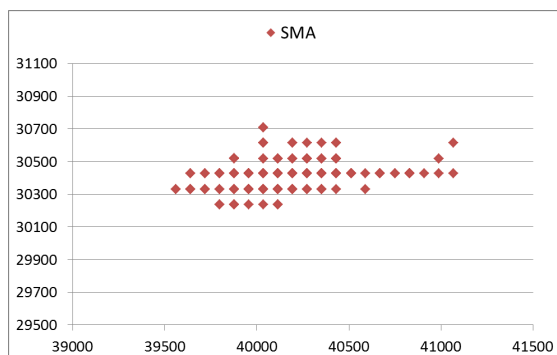
4 Experimental Results

The proposed technique was implemented in Microsoft Visual Studio 2010 with OpenCV 2.4.5 library. The input images with 24 bit-true color were captured by an embedded camera on the laptop or a common web camera (GENIUS FaceCam 1320) with a resolution of 320x240 pixels. The average processing time per frame was between 30 and 37 milliseconds. This is the same as 30 fps, suggesting that it is fast enough to be used in real time applications.

Compared to some previous studies, our proposed method can provide more precise hand regions while filtering out the forearm. It can recognize 6 cases of finger counting, while [4] and [11] can only recognize 5. The finger counting stage has also been tested with 40 different people with different hand size under varied lighting conditions. Each person was asked to show 6 gestures representing numbers from 0 to 5 in front of the camera. Table 1 shows the experimental test results of finger counting. The average rate of recognition of finger counting is 98.3%. This is a good result when comparing with other studies. The misdetections were observed when the fingers with short lengths were shown or one of them overlap with the others. After the coordinates of the fingertip is detected, it will be converted to screen coordinates to control the mouse pointer. Fig. 5, Fig. 6 and Fig. 7 show the 271 consequent coordinates before and after applying the Moving Averages when the finger was standing still.

Table 1. The test results of finger counting

Number of fingers inputted	Number of successful counting	Accuracy (%)
0	40	100
1	40	100
2	40	100
3	38	95
4	39	97.5
5	39	97.5

**Fig. 5.** The original coordinates of the mouse when the finger was standing still**Fig. 6.** The SMA coordinates of the mouse when the finger was standing still

In Fig. 5, the coordinates of the mouse jump a long distance around the real coordinates because of the noise from the sources and the conversion. This makes it very difficult to control the mouse. By using the Moving Averages with the time periods $N = 5$, Fig. 6 and Fig. 7 give much better results for controlling the mouse pointer. We reduced a lot of noise and jitter that appear in the original mouse coordinates.

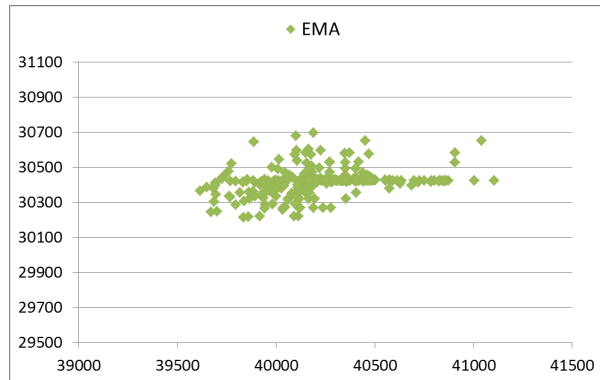


Fig. 7. The EMA coordinates of the mouse when the finger was standing still

The Moving Average also helps smooth the mouse trajectory and makes it become more natural. Fig. 8 shows the comparison of the 25 consequent coordinates when the finger is moving. The EMA coordinates give the best trajectory when reducing the noise and the lag which appear on ORIGIN and SMA trajectories. The sample video about an application of our proposed technique is stored in the following link: <https://www.youtube.com/watch?v=r78D1BBgIs0&list=P>

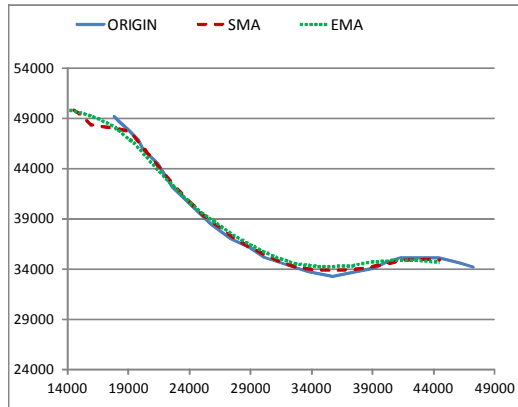


Fig. 8. The coordinates of the mouse when the finger was moving

5 Conclusion

In this paper, we have presented a background model for the real time fingertip tracking technique. Based on natural hand gestures, we have created an interface which is intuitive and easy to use for the users. We also used our proposed technique to interact with the computer such as playing game, surfing the web. Through

experiments, we are able to confirm that our model works with real time speed and high accuracy.

The main drawbacks of the proposed technique are that it only works well in an unchanging background, and it has trouble with objects at the same color as the skin. These drawbacks can be overcome by using a gradient or 3-D model. With six cases of finger counting stage and the fingertip coordinates, our model can be extended to handle more events and applied to interact with other smart environments in future works.

References

1. Wang, R.Y., Popovic, J.: Real-Time Hand-Tracking with a Color Glove. *ACM Transaction on Graphics* 28(3) (2009)
2. Geebelen, G., Maesen, S., Cuyvers, T., Bekaert, P.: Real-time hand tracking with a colored glove. In: Proc. 3D Stereo Media (December 2010)
3. Choondal, J.J., Sharavanabhavan, C.: Design and Implementation of a Natural User Interface Using Hand Gesture Recognition Method. *International Journal of Innovative Technology and Exploring Engineering* 2(4) (March 2013)
4. Lee, B., Chun, J.: Interactive Manipulation of Augmented Objects in Marker-Less AR Using Vision-Based Hand Interaction. In: 2010 Seventh International Conference on Information Technology, pp. 398–403 (2010)
5. Nagarajan, S., Subashini, T.S., Ramalingam, V.: Vision Based Real Time Finger Counter for Hand Gesture Recognition. *International Journal of Technology* 2(2) (December 2012)
6. Abdallah, M.B., Sessi, A., Kallel, M., Bouhlel, M.S.: Different Techniques of Hand Segmentation in the Real Time. *International Journal of Computer Applications & Information Technology* 2(I), 45–49 (2013)
7. Raheja, J.L., Das, K., Chaudhary, A.: An Efficient Real Time Method of Fingertip Detection. In: 7th International Conference on Trends in Industrial Measurements and Automation (TIMA 2011), Chennai, India, pp. 447–450 (January 2011)
8. Vivek Veeriah, J., Swaminathan, P.L.: Robust Hand Gesture Recognition Algorithm for Simple Mouse Control. *International Journal of Computer and Communication Engineering* 2(2), 219–221 (2013)
9. Crampton, S.C., Betke, M.: Counting Fingers in Real Time: A Webcam-Based Human-Computer Interface with Game Applications. In: Proc. Conf. Universal Access Human-Comput. Interaction, pp. 1357–1361 (2003)
10. Ravikiran, J., et al.: Finger Detection for Sign Language Recognition. In: Proc. The International MultiConference of Engineers and Computer Scientists (IMECS 2009), Hong Kong, vol. I (March 2009)
11. Park, H.-S., Jo, K.-H.: Real Time Hand Gesture Recognition for Augmented Screen using Average Background and CAMshift. In: The 19th Korea-Japan Joint Workshop on Frontiers of Computer Vision, pp. 18–21 (2013)
12. Pedro, L.M., Caurin, G.A.P., Belini, V.L., Pechoneri, R.D.: Hand Gesture Recognition for Robot Hand Teleoperation. In: ABCM Symposium Series in Mechatronics, vol. 5, pp. 1065–1074 (2012)
13. Oka, K., Sato, Y., Koike, H.: Real-time Tracking of Multiple Fingertips and Gesture Recognition for Augmented Desk Interface Systems. In: Proc. The Fifth IEEE International Conference on Automatic Face and Gesture Recognition (2002)

14. Oikonomidis, I., Kyriazis, N., Argyros, A.A.: Efficient model-based 3D tracking of hand articulations using Kinect. In: Proc. The 22nd British Machine Vision Conference (2011)
15. Raheja, J.L., Chaudhary, A., Singal, K.: Tracking of Fingertips and Centers of Palm using KINECT. In: Computational Intelligence, Modelling and Simulation, pp. 248–252 (September 2011)
16. Park, J., Yi, J.-H.: Efficient Fingertip Tracking and Mouse Pointer Control for a Human Mouse. In: Crowley, J.L., Piater, J.H., Vincze, M., Paletta, L. (eds.) ICVS 2003. LNCS, vol. 2626, pp. 88–97. Springer, Heidelberg (2003)
17. Argyros, A.A., Lourakis, M.I.A.: Vision-Based Interpretation of Hand Gestures for Remote Control of a Computer Mouse. In: Huang, T.S., Sebe, N., Lew, M., Pavlović, V., Kölsch, M., Galata, A., Kisacanin, B. (eds.) ECCV 2006 Workshop on HCI. LNCS, vol. 3979, pp. 40–51. Springer, Heidelberg (2006)
18. Vivek Veeriah, J., Swaminathan, P.L.: Robust Hand Gesture Recognition Algorithm for Simple Mouse Control. International Journal of Computer and Communication Engineering 2(2) (March 2013)

Rotor Speed Estimation Based on Extended Kalman Filter for Sensorless Vector Control of Induction Motor

Phuc Thinh Doan¹, Thanh Luan Bui¹, Hak Kyeong Kim¹, Gi Sig Byun²,
and Sang Bong Kim^{1,*}

¹ Department of Mechanical & Automotive Eng., College of Eng.,
Pukyong National University, Busan, Korea

² Department of Control and Instrumentation Eng., College of Eng.,
Pukyong National University, Busan, Korea
kimsb@pknu.ac.kr

Abstract. In this paper, a sensorless vector control method is introduced where rotor speed is estimated based on extended Kalman filter (EKF). The EKF is a recursive optimum stochastic state estimator. The proposed EKF is designed to obtain a small estimation speed error in both transient and steady state over a wide speed range. A major challenge at very low and zero speed is the lost coupling effect from the rotor to the stator, which makes the information on rotor variables unobservable on the stator side. To solve this problem, in the proposed EKF, the load torque and the rotor speed with unmeasurable information are estimated simultaneously. The rotor speed is considered via the equation of motion and the estimation of load torque, on the other hand, is performed as a constant parameter. Hardware and software for experiment of the AC induction motor drive are introduced. The experimental results are presented to show the effectiveness of the proposed system.

Keywords: Sensorless Vector Control, Rotor Speed Estimation, AC Induction Motor, Extended Kalman Filter.

1 Introduction

The Adjustable Speed Drives (ADS) are used in a wide variety of industrial applications such as pumps, fans, elevator, electrical vehicles, wind generation systems, etc. There are various types of electric motors in electric drives such as DC motors, AC motors and stepper motors. AC induction motors are the most popularly motor type used in industrial due to their simple construction, reliability, robustness and low cost.

Many attempts have been made to develop a sensorless vector control of AC induction motor. Several techniques have been proposed. Magnetic-Salience-Based methods are very promising for standstill and low-speed operation [1, 2]. Their main disadvantage is the need for high precision voltage and current measurements. Also,

* Corresponding author.

these methods require a proper machine design. Model-Reference Adaptive System (MRAS) have a good performance over a large speed range [3, 4]. Their disadvantage is the large influence of parameter deviation at low-speed and standstill operation. The current harmonic spectral estimation method estimates the rotor speed from current harmonics [6]. This method have a very good performance at low speed, but needs a complicated hardware and software setup for measuring and filtering the currents. Artificial intelligence methods [7, 8] that use artificial intelligence techniques such as fuzzy logic and neural networks are robust to parameter deviation and measurement noise. However, they need long development times and an expertise in several artificial intelligence procedures. There are also EKF applications in the literature for the sensorless control of IMs [5, 9,10]. The EKF is a recursive optimum stochastic state estimator. Therefore, model uncertainties and nonlinearities inherent in IMs are well suited to the stochastic nature of EKFs.

This paper develops a sensorless vector controlled method for AC induction motor based on EKF. The proposed EKF is designed to obtain a small estimation speed error in both transient and steady state over a wide speed range. A major challenge at very low and zero speed is the lost coupling effect from the rotor to the stator, which makes the information on rotor variables unobservable on the stator side. To solve this problem, in the proposed EKF, the load torque and the rotor speed with unmeasurable information are estimated simultaneously. The rotor speed is considered via the equation of motion and not constant parameter, which is common in most previous paper. The estimation of load torque, on the other hand, is performed as a constant parameter to account for Coulomb and viscous friction at steady state to improve the estimation performance at very low and zero speed. Hardware and software for experiment of the AC induction motor drive are introduced. The experimental results are presented to show the effectiveness of the proposed system.

2 Mathematical Model of Induction Motor

To estimation the rotor speed using EKF, it is possible to use various machine models. However, the model established in the stationary reference frame proposes more advantages as follows [12]:

- reduced computation time (reduced non-linearity);
- smaller sampling times;
- higher accuracy;
- more stable behavior.

The following state-space equation and output equation of the induction motor in the stationary reference frame are given when the stator currents $i_{s\alpha}$ and $i_{s\beta}$, rotor flux linkages $\psi_{r\alpha}$ and $\psi_{r\beta}$, motor shaft angular speed ω_m and load torque T_L are the state variables.

$$\dot{X} = AX + BU \quad (1)$$

$$Y = CX \quad (2)$$

where

$X = [i_{s\alpha} \ i_{s\beta} \ \psi_{r\alpha} \ \psi_{r\beta} \ \omega_m \ T_L]^T$ is the state vector;

$Y = [i_{s\alpha} \ i_{s\beta}]^T$ is the output vector;

$U = [u_{s\alpha} \ u_{s\beta}]^T$ is the input vector;

$$A = \begin{bmatrix} -\left(\frac{R_s}{L_\sigma} + \frac{L_m^2 R_r}{L_\sigma L_r^2}\right) & 0 & \frac{L_m R_r}{L_\sigma L_r^2} & \omega_m z_p L_m / (L_\sigma L_r) & 0 & 0 \\ 0 & -\left(\frac{R_s}{L_\sigma} + \frac{L_m^2 R_r}{L_\sigma L_r^2}\right) & -\frac{L_m}{L_\sigma L_r} z_p \omega_m & \frac{L_m R_r}{L_\sigma L_r^2} & 0 & 0 \\ L_m \frac{R_r}{L_r} & 0 & -\frac{R_r}{L_r} & -z_p \omega_m & 0 & 0 \\ 0 & L_m \frac{R_r}{L_r} & z_p \omega_m & -\frac{R_r}{L_r} & 0 & 0 \\ -\frac{3}{2} \frac{z_p}{J} \frac{L_m}{L_r} \psi_{r\beta} & \frac{3}{2} \frac{z_p}{J} \frac{L_m}{L_r} \psi_{r\alpha} & 0 & 0 & 0 & -\frac{1}{J} \\ 0 & 0 & 0 & 0 & 0 & 0 \end{bmatrix}$$

is the system matrix;

$B = [1/L_\sigma \ 0 \ 0 \ 0 \ 0]^T$ is the input matrix;

$C = [1 \ 0 \ 0 \ 0 \ 0]$ is the output matrix.

In Eqs. (1) and (2), z_p is number of pole pairs; $L_\sigma = \sigma L_s$ is stator transient inductance; σ is leakage or coupling factor; L_s and R_s are stator inductance and stator resistance, respectively; L_r and R_r are rotor inductance and rotor resistance, respectively; L_m is mutual inductance; $u_{s\alpha}$ and $u_{s\beta}$ are stator stationary axis components of stator voltages; $i_{s\alpha}$ and $i_{s\beta}$ are stator stationary axis components of stator currents; $\psi_{s\alpha}$ and $\psi_{s\beta}$ are stator stationary axis components of stator flux; $\psi_{r\alpha}$ and $\psi_{r\beta}$ are stator stationary axis components of rotor flux; J is inertia moment and T_L is load torque.

It should be noted that in Eq. (1), the rotor speed is considered via the equation of motion. The estimation of load torque, on the other hand, is performed as a constant parameter, $dT_L/dt = 0$.

For digital implementation of the EKF, the discretized equations are required and can be obtained from Eqs. (1) and (2) as follows:

$$\dot{X}(k+1) = A_d X(k) + B_d U(k) \quad (3)$$

$$Y(k) = C_d X(k) \quad (4)$$

where A_d , B_d and C_d are the discretized system matrix, input matrix and output matrix, respectively. They can be obtained from continuous system as follows: $A_d = e^{AT} \approx I + AT$; $B_d \approx BT$; $C_d = C$ where T is the sampling time, and I is 6×6 identity matrix.

The system and measurement noises are considered to be in the form of white noise. The discretized system model with the system noise and the output model with the measurement noise become:

$$\dot{X}(k+1) = A_d X(k) + B_d U(k) + v(k) \quad (5)$$

$$Y(k) = C_d X(k) + w(k) \quad (6)$$

where $v(k)$ is system noise with covariance matrix Q and $w(k)$ is measurement noise with covariance matrix R as follows:

$$Q = \begin{bmatrix} q_{11} & 0 & 0 & 0 & 0 & 0 \\ 0 & q_{22} & 0 & 0 & 0 & 0 \\ 0 & 0 & q_{33} & 0 & 0 & 0 \\ 0 & 0 & 0 & q_{44} & 0 & 0 \\ 0 & 0 & 0 & 0 & q_{55} & 0 \\ 0 & 0 & 0 & 0 & 0 & q_{66} \end{bmatrix}; R = \begin{bmatrix} r_{11} & 0 \\ 0 & r_{22} \end{bmatrix} \quad (7)$$

where Q and R are diagonal positive matrices.

3 Implementation of the Discretized EKF Algorithm

The state estimation based on EKF is obtained by the following steps:

Step 1: initialization of the state vector and covariance matrices

Initial values of the state vector $X_0 = X(t_0)$, the noise covariance matrices $Q(6 \times 6)$ and $R(2 \times 2)$ are set together with the initial value of the state covariance matrix $P_0(6 \times 6)$. The initial values of the covariance matrices reflect the degree of knowledge of the initial states.

Step 2: Prediction of the state vector

The predicted state vector $X^*(k+1)$ at the sampling instant time $(k+1)$ is obtained from the input $U(k)$ and the estimated state vector $\hat{X}(k)$ at the sampling instant time k as follows:

$$X^*(k+1) = A_d \hat{X}(k) + B_d U(k) \quad (8)$$

where, $\hat{X}(k) = \begin{bmatrix} \hat{i}_{s\alpha}(k) & \hat{i}_{s\beta}(k) & \hat{\psi}_{r\alpha}(k) & \hat{\psi}_{r\beta}(k) & \hat{\omega}_m(k) & \hat{T}_L \end{bmatrix}^T$ and $U = \begin{bmatrix} u_{s\alpha} & u_{s\beta} \end{bmatrix}^T$.

Step 3: Covariance estimation of prediction

The predicted covariance matrix is estimated as

$$P^*(k+1) = f(k+1)\hat{P}(k)f^T(k+1) + Q \quad (9)$$

where f is the gradient matrix as follows:

$$f(k+1) = \frac{\partial}{\partial X} [A_d X + B_d U]_{X=\hat{X}(k)} \quad (10)$$

$$f = \begin{bmatrix} 1 - T \left(\frac{R_s}{L_\sigma} + \frac{L_m^2 R_r}{L_\sigma L_r^2} \right) & 0 & \frac{TL_m R_r}{L_\sigma L_r^2} & \frac{TL_m}{L_\sigma L_r} z_p \omega_m & \frac{TL_m}{L_\sigma L_r} z_p \psi_{r\beta} & 0 \\ 0 & 1 - T \left(\frac{R_s}{L_\sigma} + \frac{L_m^2 R_r}{L_\sigma L_r^2} \right) & -\frac{TL_m}{L_\sigma L_r} z_p \omega_m & \frac{TL_m R_r}{L_\sigma L_r^2} & -\frac{TL_m}{L_\sigma L_r} z_p \psi_{r\alpha} & 0 \\ TL_m \frac{R_r}{L_r} & 0 & 1 - T \frac{R_r}{L_r} & -T z_p \omega_m & -T z_p \psi_{r\beta} & 0 \\ 0 & TL_m \frac{R_r}{L_r} & T z_p \omega_m & 1 - T \frac{R_r}{L_r} & T z_p \psi_{r\alpha} & 0 \\ -\frac{3}{2} \frac{z_p}{J} \frac{L_m}{L_r} T \psi_{r\beta} & \frac{3}{2} \frac{z_p}{J} \frac{L_m}{L_r} T \psi_{r\alpha} & \frac{3}{2} \frac{z_p}{J} \frac{TL_m}{L_r} i_{s\beta} & -\frac{3}{2} \frac{z_p}{J} \frac{TL_m}{L_r} i_{s\alpha} & 1 & -\frac{T}{J} \\ 0 & 0 & 0 & 0 & 0 & 1 \end{bmatrix}$$

where $\omega_m = \hat{\omega}_m(k)$, $\psi_{r\alpha} = \hat{\psi}_{r\alpha}(k)$ and $\psi_{r\beta} = \hat{\psi}_{r\beta}(k)$.

Step 4: Kalman filter gain computation

For this model, the 6×2 Kalman gain matrix can be obtained as

$$K(k+1) = P^*(k+1) h^T(k+1) [h(k+1) P^*(k+1) h^T(k+1) + R]^{-1} \quad (11)$$

where $h(k+1)$ is the gradient matrix can be obtained as

$$h(k+1) = \frac{\partial}{\partial X} [C_d X]_{X=X^*(k+1)} = \begin{bmatrix} 1 & 0 & 0 & 0 & 0 & 0 \\ 0 & 1 & 0 & 0 & 0 & 0 \end{bmatrix} \quad (12)$$

Step 5: State-vector estimation

The estimated state vector at time $(k+1)$ is performed as follows:

$$\hat{X}(k+1) = X^*(k+1) + K(k+1) [Y(k+1) - \hat{Y}(k+1)] \quad (13)$$

$$\hat{Y}(k+1) = C_d X^*(k+1) \quad (14)$$

Step 6: Covariance matrix of estimation error

The estimation error covariance matrix is obtained from

$$\hat{P}(k+1) = P^*(k+1) - K(k+1)h(k+1)P^*(k+1) \quad (15)$$

Step 7: Updating

Put $k = k + 1$, $X(k) = X(k+1)$, $P(k) = P(k+1)$ and go to step 2.

The EKF described above can be used to estimate the motor speed under both steady state and transient conditions. The proposed EKF design has been implemented in sensorless vector control as shown in Fig. 1.

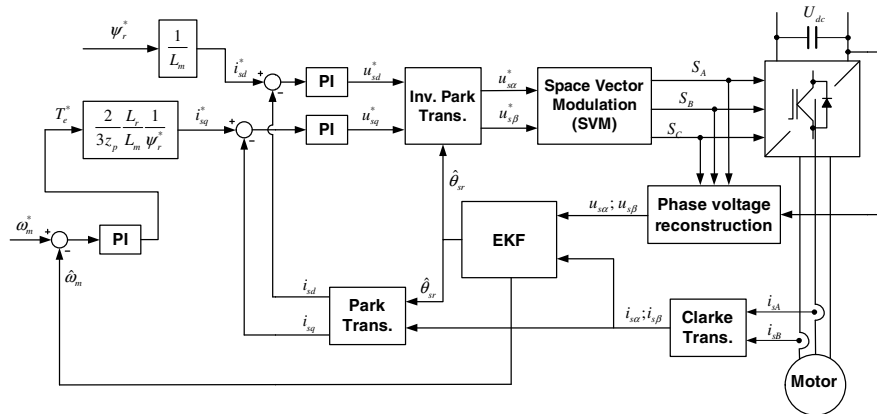


Fig. 1. Block diagram of sensorless vector control using EKF

4 Hardware Configuration

Fig. 2 shows the motor testing system used in experiment. It consists of an AC induction motor, an encoder, a torque sensor, a powder brake and two couplings.

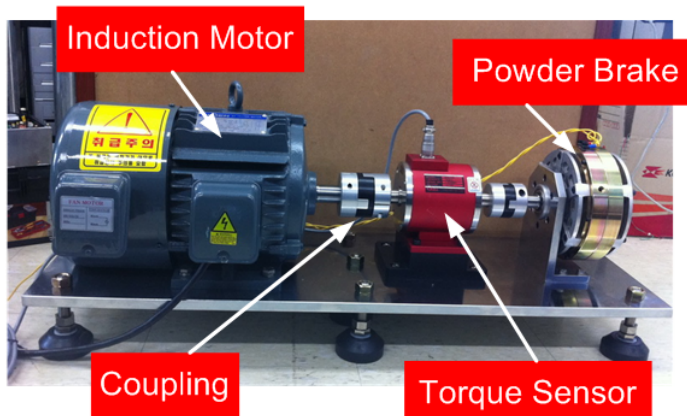


Fig. 2. Motor testing system

The induction motor under consideration has three phase, four poles and 2HP/1.5Kw with its specification and parameter values given in Table 1.

Table 1. Rated value and parameters of the IM

Rated power $P[kW]$	Rated voltage $V[V]$	Rated current $I[A]$	Rated frequency $f[Hz]$	Rated speed $N[rpm]$	Rated torque $T[Nm]$	Rated flux $\psi[Wb]$
1.5	220	6	60	1750	10	0.49
z_p	$J[kg.m^2]$	$R_s[\Omega]$	$R_r[\Omega]$	$L_s[H]$	$L_r[H]$	$L_m[H]$
2	0.089	3.285	2.715	0.387117	0.387117	0.374

Fig. 3 shows voltage source inverter based on DSP 320F28335 used in experiments. The inverter includes two parts: the controller board and the IGBT driver. The IGBT driver is designed based on smart power module FSBB30CH60.

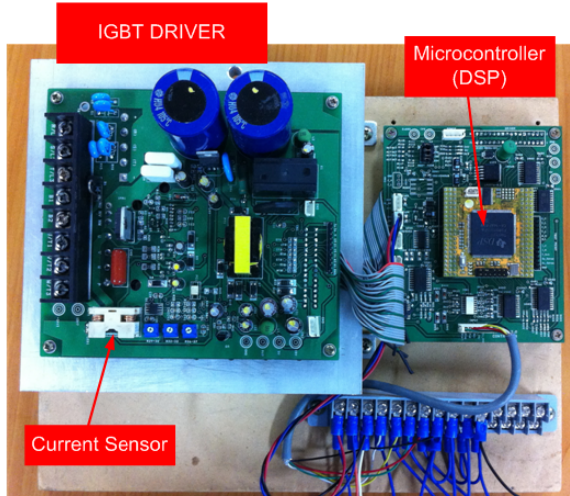


Fig. 3. Voltage source inverter

5 Experimental Results

The operation of induction motor is considered at high speed $500 rpm$ and at low speed $50 rpm$. The sampling time for two EKF models is $0.1ms$.

Fig. 4 shows the motor speed estimations using the proposed EKF design. The dash line is the real speed value and the continuous line is the estimated speed value. Fig. 5 shows the motor speed estimations error using the proposed EKF design. The estimation error is about $3.5 rpm$ at high speed and $2 rpm$ at low speed in steady state.

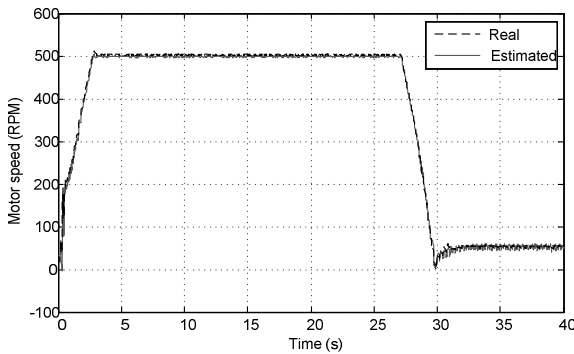
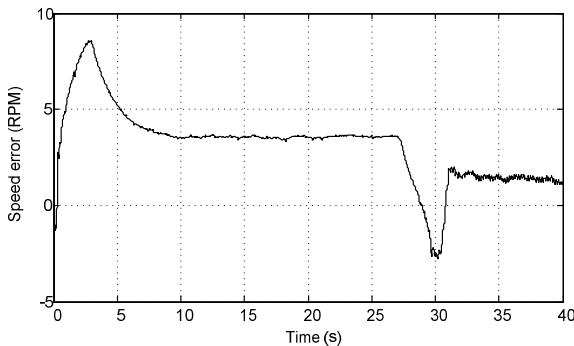
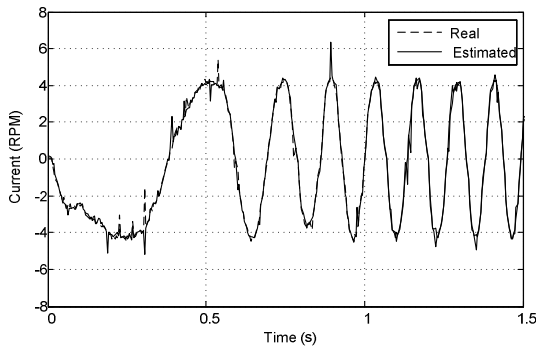
**Fig. 4.** Motor speed estimation using EKF design**Fig. 5.** Motor speed estimation error using EKF design**Fig. 6.** Phase current estimation using the EKF design

Fig. 6 shows the phase current estimation using the proposed EKF design. The magnitude of the phase current estimation using the proposed EKF design is about 4 A . Fig. 7 shows the phase current estimation error. The estimation error is bounded within $\pm 1.5\text{ A}$.

Fig. 8 shows the phase current and phase voltage to control induction motor. Fig. 8(a) shows the magnitude of phase current is about 4 A at both high speed and low speed. Fig. (8b) shows the magnitude of phase voltage is about 180V at high speed and 100V at low speed.

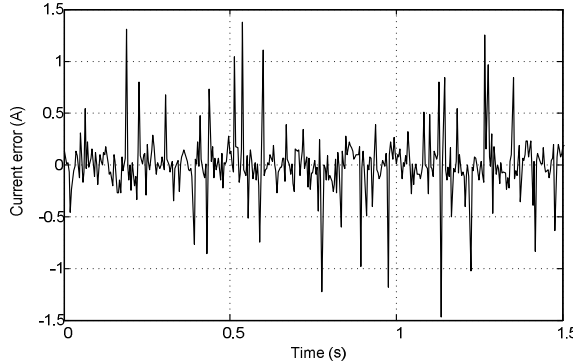


Fig. 7. Phase current estimation error using the EKF design

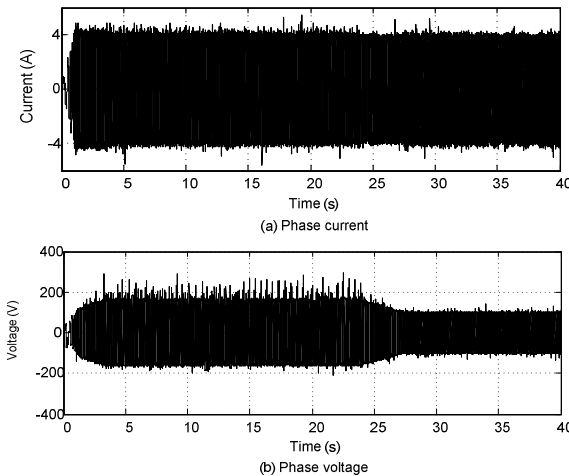


Fig. 8. Phase current and phase voltage

6 Conclusions

The rotor speed estimation based on EKF for sensorless vector control has been applied successfully. The hardware for testing system is described. The VSI is designed based on DSP 320F28335 and the smart power module IGBT. The operation of induction motor is considered at high speed 500 RPM and at low speed 50 RPM. The experimental results show that the motor speed estimation error is small enough,

about 3.5 rpm at high speed and 2 rpm at low speed. The current estimation error is small and bounded within $\pm 0.5 \text{ A}$. The EKF described above can be used to estimate the motor speed under both steady state and transient conditions.

Acknowledgement. This research was supported by a grant (11Transportation System – Logistics02) from Transportation System Efficiency Program funded by Ministry of Land, Infrastructure and Transport (MOLIT) of Korean government.

References

1. Schroedl, M.: Sensorless Control of AC Machines at Low Speed and Standstill Based on the INFORM Method. Proc. IEEE-IAS Annual Meeting 1, 270–277 (1996)
2. Jansen, P.L., Lorentz, R.D.: Transducer-less Position and Velocity Estimation in Induction and Salient AC Machines. IEEE Trans. Ind. Appl. 31(2), 240–247 (1995)
3. Dezza, F.C., Foglia, G., Iacchetti, M.F.: An MRAS Observer for Sensorless DFIM Drives with Direct Estimation of the Torque and Flux Rotor Current Components. IEEE Trans. Power Electron. 27(5), 2576–2584 (2012)
4. Maes, J., Melkebeek, J.A.: Speed Sensorless Direct Torque Control of Induction Motors using an Adaptive Flux Observer. IEEE Trans. Ind. Appl. 30(5), 1225–1233 (2000)
5. Barut, M., Bogosyan, S., Gokasan, M.: Experimental Evaluation of Braided EKF for Sensorless Control of Induction Motors. IEEE Trans. Ind. Appl. 55(2), 620–632 (2008)
6. Hurst, K.D., Habetler, T.G.: Sensorless Speed Measurement using Current Harmonic Spectral Estimation in Induction Machines Drives. IEEE Trans. Power Electron. 11(1), 66–73 (1996)
7. Vas, P.: Artificial-intelligence-based Electrical M. and Drives Appl. of Fuzzy, Neural, Fuzzy-Neural and Genetic-Algorithm Based Techniques. Oxford Univ. Press, UK (1999)
8. Gadoue, S.M., Damian, G., Finch, J.W.: MRAS Sensorless Vector Control of an Induction Motor Using New Sliding-Mode and Fuzzy-Logic Adaptation Mechanisms. IEEE Trans. on Energy Conversion 25(2), 620–632 (2010)
9. Barut, M., Bogosyan, S., Gokasan, M.: Speed-Sensorless Estimation for Induction Motors Using Extended Kalman Filters. IEEE Trans. on Ind. Elect. 54(1) (February 2007)
10. Douiri, M.R., Cherkaoui, M., Douiri, S.M.: Rotor Resistance and Speed Identification using Extended Kalman Filter and Fuzzy Logic Controller for Induction Machine Drive. In: Int. Conf. on Digital Object Identifier, pp. 1182–1187 (2012)

Application of Stepper Motors in Medical Electronics

Vaclav Sladecek¹, Petr Palacky¹, Josef Oplustil¹, Miroslav Uchoc¹,
Karel Frydrysek², Leopold Pleva³, and Lubos Zilka⁴

¹ VSB-Technical University of Ostrava, Faculty of Electrical Engineering and
Computer Science, Department of Electronics, Ostrava, Czech Republic
{miroslav.uchoc, vaclav.sladecek}@vsb.cz

² VSB-Technical University of Ostrava, Faculty of Mechanical Engineering,
Department of Mechanics of Materials, Ostrava, Czech Republic

³ Trauma Centre, University Hospital in Ostrava, Czech Republic

⁴ Medin, a.s., Nové Město na Moravě, Czech Republic

Abstract. This article reports about the new design of external fixators invented at the VŠB - Technical University of Ostrava, Trauma Centre of The University Hospital in Ostrava and MEDIN a.s. These fixators are intended for the treatment of open, unstable and complicated fractures in traumatology and orthopaedics for humans or animals. The new design is based on shape and weight optimization based on composite materials, application of smart materials, nanotechnology, low x-ray absorption, antibacterial protection, patient's comfort, reduction in the duration of the surgical treatment, and cost).

Keywords: biomechanics, traumatology, design, external fixators, stepper motors.

1 Introduction

Currently, major therapeutic methods in the treatment of open, complicated and unstable fractures in traumatology, orthopaedics and surgery (limbs, joints, the pelvis, jaws, etc.) include external fixators. This therapeutic method provides the advantage of simple application of the external fixator with perfect stabilisation of the fracture, allowing for timely rehabilitation of the patient. External fixators can also be used to extend limbs or to correct axial deformities. However, no fixator has been made until now that would provide motor control of joint movement – advisable and desired for therapy associated with rehabilitation in unconscious patients or patients with complicated joint fractures. VSB-TU Ostrava has gained practical experience in this field in cooperation with University Hospital in Ostrava; fixator prototypes which are equipped with an electric stepper motor to control joint bending in patients exist. There are currently two solution variants that can be considered for the electric actuation, in principle.

1.1 Hybrid Actuators with Stepper Motors

Hybrid actuators transfer the rotation movement of the stepper to the movement of a linear screw with the help of a special patented nut. The actuator contains a hybrid stepper motor, which utilizes both the advantages of a reluctance motor and a motor with permanent magnets. The construction is based on a reluctance motor and ensures a small step angle (up to 0.9°) and fine resolution. The use of permanent magnets on the other hand increases the turning moment and provides a stronger motor. The composition of these two technologies together with the movement nut into a single case creates an affordable compact linear drive – a hybrid stepper actuator.

Hybrid actuators represent an affordable solution for all application requiring small and exact control of a linear movement. Actuators create large forces in small spaces. The actuator contains a standard stepper motor, which may be simply controlled in the same way as stepper motors. The core of the hybrid actuator is an exact trapezoidal movement screw and nut shaped for the corresponding load. Integration of the movement screw in the motor provides a compact and precise drive unit which simplifies the construction of the resulting machine. Actuators find applications in medicine, measuring technology, handling technology and in other areas. One type of such actuators is shown in Figure 1.



Fig. 1. Haydon Kerk hybrid actuator

1.2 Stepper Motor Combined with a Linear Lead

The other possibility is offered by using a linear lead in connection with a standard (two-phase) stepper motor. The Kuroda linear lead used to convert rotational linear movement can be mentioned as an example. (www.microcon.cz).

The lead is equipped with a ball screw for positioning medium- up to heavy-weight loads. The lead converts rotational movement of the stepper motor to the linear movement of the positioned load. An optimum configuration of the linear drive is obtained by combining the stepper motor and linear lead. A possible configuration is shown in Figure 2.

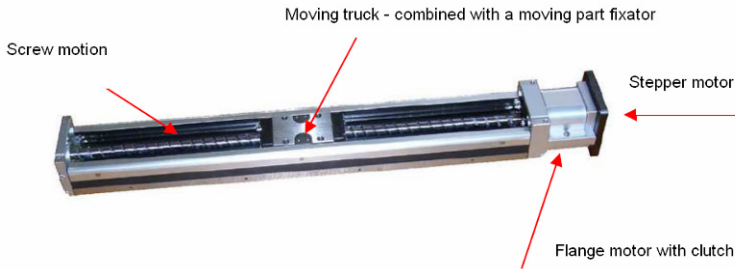


Fig. 2. Linear drive with stepper motor

The following type was specified for our application: SG3310A-600H with SX23-2727 stepper motor (www.microcon.cz).

2 Original Project Design

The project was aimed at designing, constructing, producing and clinical testing of an external fixator with electric-controlled motor actuation for the treatment of open, unstable elbow fractures. The designed fixator prototype was made through computer modelling in Autodesk Inventor.

The fixator includes 3 essential construction elements:

- Fixator body (rings, segments, sleeves, connecting elements);
- Holders of supporting elements;
- Supporting elements for osteosynthesis – nails (screws) or K-wires, respectively.

Originally, a direct-current electric motor was designed for the drive with the following parameters:

- Supply voltage 10 V
- Nominal current 5 A
- Maximum rounds 5,600/min
- Efficiency 67%

In the process of development, this drive was tested in the fixator (Figure 4) with the load of 4 kg.

The fixator was functional; however, high current load was detected in the motor at start-up. The turning moment necessary for starting the fixator was experimentally verified in the fixator; $M_k = 0.1207 \text{ Nm}$ (movement screw M4, brass nut). Given that practical application of this motor would pose considerable problems (relatively low efficiency, high current consumption and in particular, problematic evaluation of the position), this solution was soon abandoned. Based on further experiments, the Microcon SL23-0704 0.35 Nm control system stepper motor was chosen with the output shaft diameter of 6.35 mm (Figure 5). A movement screw with the ball nut was chosen from the SKP catalogue with the aim to reduce the resistance at the movement screw and the nut.

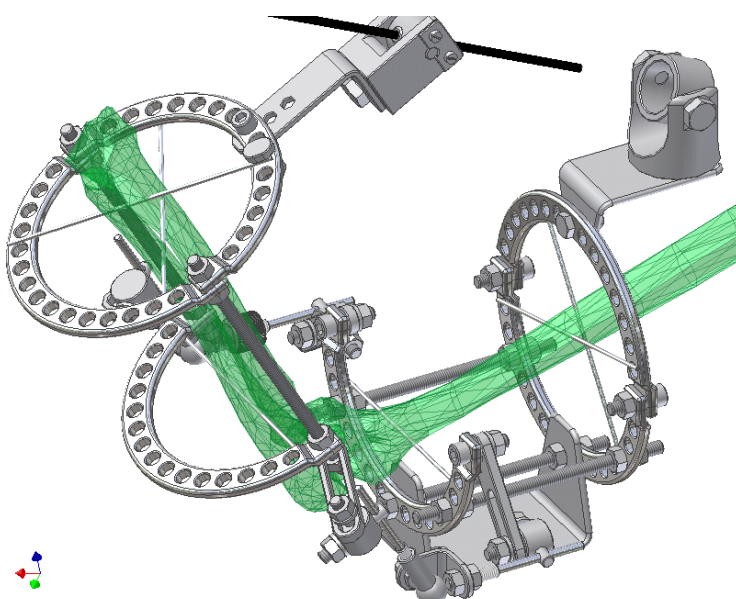


Fig. 3. Designed elbow fixator obtained through computer modelling in Auto desk Inventor

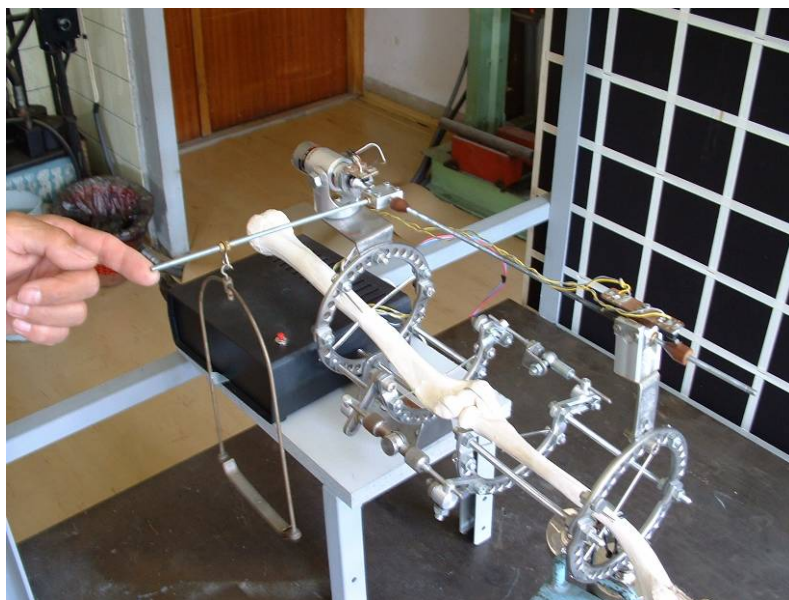


Fig. 4. Original fixator model in the measurement of the maximum produced moment



Fig. 5. Prototype of the designed external fixator with the stepper motor and movement screw

A Microcon CD30 control unit (www.microcon.cz) was used to supply the stepper motor, providing the advantage of simple program tuning in a development environment executable on any common PC computer. The choice of the movement screw with the ball nut also proved to be well justified given the high efficiency of this solution (higher than 85%).

3 Current Development Status

Since 2011, the Faculty of Mechanical Engineering and the Faculty of Electrical Engineering and Computer Science, VSB-TU Ostrava, have been engaged in the FR-TI3/818 – EXTERNAL FIXATION (2011-2013, MPO/FR) project. Other participants include the MEDIN a.s., Trauma Centre in Brno and University Hospital in Ostrava. One of the project items consists precisely in implementation of our own electric drive for variable fixator types with electronic-controlled actuation. Several variants are available for implementation of the actuation unit of the motor fixator. Considering the requirements for a relatively wide range of parameter values in the settings, a controlled drive must be used, capable of handling collision states to prevent any injury in the patient upon potential failure. In terms of potential uses, a direct- or alternating-current motor can be used in principle, with low supply voltages (for safety's sake). Given that the drive must handle positioning between 2 final points, it actually defines the angle in which the fixated limb shall move. Considering

that this angle will be required to remain constant for at least one preset time cycle or to provide an option of its changing in predefined ranges, information on the initial and terminal position of the actuating mechanism must be entered in the control system. When classical, direct- or alternating-current motors are used, this task can only be resolved using an incremental sensor and terminal position scanners. The concept of using small, alternating-current motors for low supply voltage is not very common; while direct-current motors can be used, they are usually implemented as high-speed motors or alternatively with an integrated transmission (Maxon, for example). The relatively high price of such a configuration plays a role in this respect. Actuation with a stepper motor therefore seems to be optimal, where provided that the mechanical parameters are observed (not exceeding the maximum shaft moment), the motor allows for system positioning without the need of a speed sensor; relatively low turning speed at sufficiently high torque (thus no transmission is needed); and, using the so called microstepping, virtually continuous turning movement in a very wide range of speed. Although in this case the system must also be provided with terminal switches for any emergency exceeding the determined position, the concept does seem most advantageous in terms of price – performance – utility characteristics. Given that the considered stepper motors operate under a safe supply voltage, the designed concept also provides enhanced safety.

4 Designed Concept of the Fixator Drive

Considering the possible solution variants, two concepts were finally chosen: one with the hybrid actuator for the elbow fixator and one with the linear actuator for knee joint fixator actuation. A control unit of RMS technologies (see Figure 6) was chosen for the actuators with the following parameters:

R356 unit parameters:

Supply voltage	12-40 V DC
Maximum output current	3 A
Resolution	up to 256 microsteps per unit step
Inputs	4
Outputs	2
Communication with the PC	RS 485

Control mode:

- "LinControl" basic software
- AT commands
- Logical inputs
- Optional control without a PC
- Optional control and visualisation using LabView



Fig. 6. R356 control unit

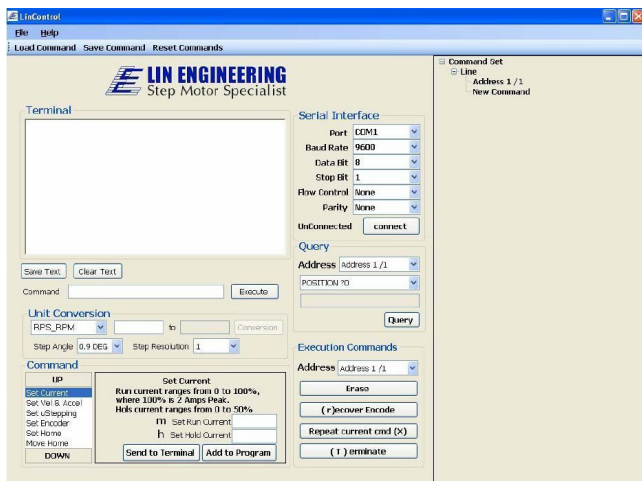


Fig. 7. Developmental environment for control unit programming

The basic connection between the stepper motor control and the R356 control unit is shown in Figure 8. Given that the concept with a permanently connected PC is unnecessarily complicated for regular operation, a variant with an AT 162 microprocessor with an LCD display has been under development with essential user variants of control by the patient.

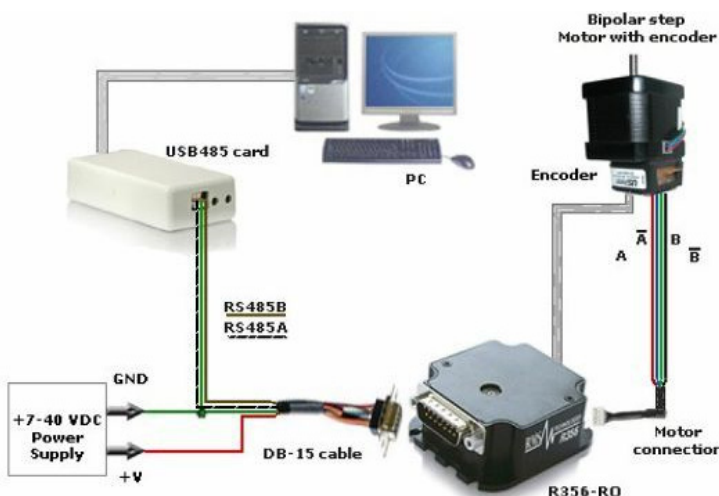


Fig. 8. Actuator control and programming using a personal computer

5 Conclusion

The paper presents the potential of the applied research (MPO project) focused on practical applications of FME and FEECS faculties in the field of medical electronics and mechanics. A fixator prototype has been designed and tests on the actuator are currently being performed, together with the final "tuning" of the control unit software.

Acknowledgments

The paper was created with the support of the projects:

MPO: FR-TI3/818

ENET: CZ.1.05/2.1.00/03.0069

References

- [1] Frydryšek, K., Pleva, L., Jořenek, J., Ječmínek, V., Klučka, R., Sivera, M.: New External Fixators for Treatment of Pelvis and Acetabulum Fractures. *International Journal of Biology and Biomedical Engineering* 7(2), 36–42 (2013)
- [2] Frydryšek, K., Pleva, L., Učeň, O., Kubín, T., Šír, M., Madeja, R., Žilka, L.: New External Fixators for Treatment of Complicated Periprosthetic Fractures. *International Journal of Biology and Biomedical Engineering* 7(2), 43–49 (2013)
- [3] Frydryšek, K.: Probabilistic Approach Applied in the Design of Machine Parts and Structures. In: *Recent Researches in Engineering and Automatic Control*, pp. 30–37. North Atlantic University Union, WSEAS Press, Puerto De La Cruz (2011) ISBN 978-1-61804-057-2

- [4] Brandstetter, P., Chlebis, P., Palacky, P., Simonik, P.: Unconventional Soft Switched Parallel Active Power Filter. In: Proceedings of the 10th International Scientific Conference Electric Power Engineering, Kouty nad Desnou, Czech Republic, pp. 347–351 (2009) ISBN 978-80-248-1947-1
- [5] Brandstetter, P., Skuta, O.: Procedure to choose alternative ANN in the control of electrical drive. In: Proceedings of Seventh International Conference on Computer Information Systems and Industrial Management Applications, pp. 38–43 (2008) ISBN 978-0-7695-3184-7, doi:10.1109/CISIM.2008.20
- [6] Brandstetter, P., Krecek, T.: Speed and Current Control of Permanent Magnet Synchronous Motor Drive Using IMC Controllers. Advances in Electrical and Computer Engineering 12(4), 3–10 (2012) ISSN 1582-7445

Optimization of Electric Energy in Three-Phase Induction Motor by Balancing of Torque and Flux Dependent Losses

Nguyen Thanh Hung¹, Nguyen Chi Thien¹, Thanh Phuong Nguyen¹,
Viet So Le², and Doan Anh Tuan³

Hochiminh City Agricultural Technical College

nguyen_hung87@yahoo.com

¹ Dept. Mechanical, Electrical & Electronic Engineering, Ho Chi Minh City University of
Technology, Ho Chi Minh, Viet Nam
phuongnt@hcmutech.edu.vn

² Dept. Electro Mechanics, Ho Chi Minh Vinatec College, Ho Chi Minh, Viet Nam
levietso@yahoo.com.vn

³ Dept. Electrical & Electronic Engineering, Da Nang University, Viet Nam

Abstract. This paper presents the solution of the energy optimal control of three-phase induction motor (IM) by balancing of torque and flux dependent losses. First, we build formula of total losses of motor (iron losses, copper losses and additional losses). Next, we will be group by i_{sd} current (flux dependent) and i_{sq} current (torque dependent). Then, we use the PI (Proportional-Integral) regulator to control so that the components two of this losses are equal. Output of PI regulator will obtain optimum rotor flux. Motor operates with this flux will make total losses of motor is the smallest. A comparative study in efficiency and tracking performances is given between the proposed optimal control and the classical Field Oriented Control that operates with constant rotor flux norm.

Keywords: induction motor, field oriented control, energy optimal control, losses minimization, energy efficient control.

1 Introduction

Currently, electricity is very large proportion of energy consumed by humans. Human use of energy are formed from other forms of energy. Along with the development of industries in the world, more and more power consumption, depleting natural resources. The new energy sources and energy converts into electrical energy which has been research and development (atomic energy, wind energy, solar energy, electricity production directly from water ...).

Alongside with the development of new energy sources, require urgent about saving power is in place. Scientists have been studying to take out the power saving

solution is best: electricity usage, the high performance devices, the device control algorithms reduces losses.

The problem of saving energy is always in place in all production systems and remains the top priority. While most of the energy consumption is to be allocated to the high capacity motor, thus saving energy issues for the motor is very important. The application of new technologies, the energy saving solution allows motor can save power about 20% of the total power consumption.

Recently the world has been much research on control algorithms losses reduce for IM offer high efficiency [1–9]. With the popularity of the extensive use of IM, combined with power saving feature promises to make new developments in the field of energy saving environmental protection, effective economical for the industry.

2 Algorithm of Optimal Energy Control

2.1 Model of Induction Motor

The state space model of three-phase IM in the dq coordinate [8]:

$$\left\{ \begin{array}{l} \frac{di_{sd}}{dt} = -\left(\frac{1}{\sigma T_s} + \frac{1-\sigma}{\sigma T_r}\right)i_{sd} + \omega_s i_{sq} + \frac{1-\sigma}{\sigma T_r L_m} \psi_{rd} + \frac{1-\sigma}{\sigma L_m} \omega \psi_{rq} + \frac{1}{\sigma L_s} u_{sd} \\ \frac{di_{sq}}{dt} = -\omega_s i_{sd} - \left(\frac{1}{\sigma T_s} + \frac{1-\sigma}{\sigma T_r}\right)i_{sq} - \frac{1-\sigma}{\sigma L_m} \omega \psi_{rd} + \frac{1-\sigma}{\sigma T_r L_m} \psi_{rq} + \frac{1}{\sigma L_s} u_{sq} \\ \frac{d\psi_{rd}}{dt} = \frac{L_m}{T_r} i_{sd} - \frac{1}{T_r} \psi_{rd} + (\omega_s - \omega) \psi_{rq} \\ \frac{d\psi_{rq}}{dt} = \frac{L_m}{T_r} i_{sq} - (\omega_s - \omega) \psi_{rd} - \frac{1}{T_r} \psi_{rq} \\ \frac{d\omega}{dt} = \frac{p}{J} (T_e - T_L) \\ T_e = \frac{3}{2} p \frac{L_m}{L_r} (\psi_{rd} i_{sq} - \psi_{rq} i_{sd}) \end{array} \right. \quad (1)$$

Where: (i_{sd}, i_{sq}) , (u_{sd}, u_{sq}) , (ψ_{rd}, ψ_{rq}) are respective the stator current , stator voltage , and rotor flux in dq coordinate; R_s , R_r are the stator and rotor resistances; L_m is the mutual inductance; L_s , L_r are the stator and rotor inductances; ω , ω_s are respective the rotor angular speed and stator angular speed; T_e , T_L are respective motor and load torque ; J is the torque of inertia; p is the number of pole pair.

$$\sigma = 1 - \frac{L_m^2}{L_s L_r} \quad (2)$$

$$T_s = \frac{L_s}{R_s}; T_r = \frac{L_r}{R_r} \quad (3)$$

Where: σ is the total leakage factor ; T_s, T_r are respective the stator and rotor time constants.

2.2 Building of Control Algorithm

The copper losses including one part for the additional losses added with the factor k_z can be separated to:

$$\Delta P_{cu} = \frac{3}{2}(1 + k_z) \left[R_s i_{sd}^2 + (R_s + (1 - \sigma)R_r) i_{sq}^2 \right] \quad (4)$$

The iron losses can be calculated approximately to:

$$\Delta P_{fe} = \frac{3}{2} \frac{(\omega_s \psi_r)^2}{R_{fe}} \quad (5)$$

Using:

$$R_{fe} \approx R_{feN} \frac{\omega_s}{\omega_{sN}} \quad (6)$$

Where: R_{fe}, R_{feN} are respective iron resistance at frequency work and rated iron resistance; ω_s, ω_{sN} are respective stator angular speed at frequency work and rated stator angular speed.

and

$$\psi_r \approx L_m i_{sd} \quad (7)$$

Replacing of the equation (6) and (7) into (5):

$$\Delta P_{fe} = \frac{3}{2} \frac{\omega_s \omega_{sN} L_m^2 i_{sd}^2}{R_{feN}} \quad (8)$$

From equation (4) and (8) can be finally written for the total losses:

$$\begin{aligned} \Delta P_T &= \Delta P_{cu} + \Delta P_{fe} \\ &= \frac{3}{2} \left[\left((1 + k_z) R_s + \frac{\omega_{sN} L_m^2}{R_{feN}} \omega_s \right) i_{sd}^2 + (1 + k_z) (R_s + (1 - \sigma) R_r) i_{sq}^2 \right] \end{aligned} \quad (9)$$

Therefore the total losses can be split into a flux (or i_{sd}) dependent part and a torque (or i_{sq}) dependent part, in which the partition is defined by the parameters of the machine, and the flux dependent part is a function of the stator frequency:

$$\Delta P_T = a(\omega_s) i_{sd}^2 + b i_{sq}^2 = \Delta P_1(i_{sd}) + \Delta P_2(i_{sq}) \quad (10)$$

Where:

$$\Delta P_1(i_{sd}) = \frac{3}{2} \left((1+k_z) R_s + \frac{\omega_{sN} L_m^2 \omega_s}{R_{feN}} \right) i_{sd}^2 \quad (11)$$

$$\Delta P_2(i_{sq}) = \frac{3}{2} (1+k_z) (R_s + (1-\sigma) R_t) i_{sq}^2 \quad (12)$$

with the side condition of a constant torque:

$$T_e \sim i_{sd} i_{sq} = \text{const} \quad (13)$$

We obtain the conditions for the total losses is smallest:

$$\Delta P_1(i_{sd}) = \Delta P_2(i_{sq}) \quad (14)$$

ie the flux dependent and the torque dependent loss components must have the same value.

The equation (14) shows the way for a direct control of the balance between the two parts losses.

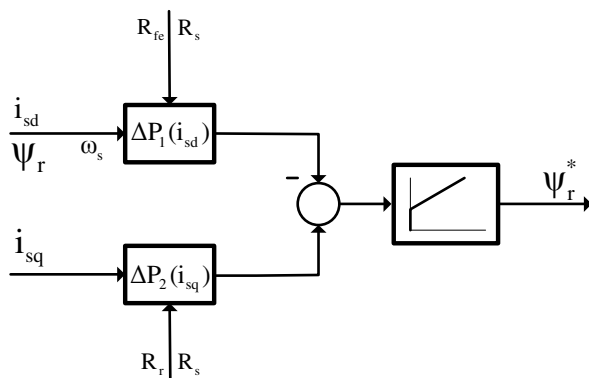


Fig. 1. Balancing of torque and flux dependent parts diagram

Where: ψ_r^* is the optimal rotor flux

2.3 Calculation of the Torque and Flux Dependent Losses

Simulation was performed with the following parameters of the IM: Rated power $P = 50$ Hp; voltage $U = 460V$; $R_s = 87m\Omega$; $R_r = 228m\Omega$; $L_{\sigma_s} = 0.8mH$; $L_{\sigma_r} = 0.8mH$, $L_m = 34.7mH$; $J = 1.662 \text{ Kg.m}^2$; $T_e = 200\text{N.m}$; rated reference rotor flux $\psi_{rN}^* = 0.96\text{Wb}$; magnetomotive force $F = 0.1\text{N.m.s}$; $p = 2$; frequency $f = 50\text{Hz}$; iron losses $\Delta P_{fe} = 862\text{W}$.

To calculating of the torque and flux dependent losses in formula (11) and (12). In addition to the existing parameters, we add calculated a number of other parameters based on the parameters of the motor.

$$L_s = L_m + L_{\sigma_s} = 35.5 \text{ mH}; L_r = L_m + L_{\sigma_r} = 35.5 \text{ mH}$$

$$\sigma = 1 - \frac{L_m^2}{L_s L_r} = 1 - \frac{34.7^2}{35.5^2} = 0.045$$

Rated stator angular speed:

$$\omega_{sN} = \frac{2\pi f}{p} = \frac{2\pi 50}{2} = 157(\text{rad/s})$$

Stator angular speed at frequency work:

(Assuming to take slip $s = 0.02$)

$$\omega_s = \frac{\omega}{1-s} = \frac{\omega}{1-0.02} = \frac{\omega}{0.98} (\text{rad/s})$$

From formula (5), we calculate:

$$R_{feN} = \frac{3}{2} \frac{(\omega_{sN} \psi_r)^2}{\Delta P_{fe}} = \frac{3}{2} \frac{(157*0.96)^2}{862} = 39(\Omega)$$

An approximate way to take $k_z = 0.3$ [8].

Replacing of the parameter calculated in (11) and (12), we get:

$$\begin{aligned} \Delta P_1(i_{sd}) &= 1.5 \left[1.3 * 0.087 + \frac{157 * 0.0347^2}{39} \frac{\omega}{0.98} \right] i_{sd}^2 \\ &= (0.17 + 7.42 * 10^{-3} \omega) i_{sd}^2 \end{aligned}$$

$$\begin{aligned} \Delta P_2(i_{sq}) &= 1.5 * 1.3 [0.087 + (1 - 0.045) * 0.228] i_{sq}^2 \\ &= 0.6 i_{sq}^2 \end{aligned}$$

3 Simulation Result and Discussion

In order to fulfill the IM energy optimization task by the proposed approaches, a numerical simulation has been carried out using Matlab/Simulink software. Motor parameters used in the simulation are shown in subsection C of section II. We setup the parameter of the simulation: constant set angular speed of rotor $\omega = 120\text{rad/s}$ and load torque change from 0 to 200N.m at $t = 2\text{s}$.

Simulation result is comparison the characteristics of motor when it operate with optimized rotor flux and rated reference rotor flux. The characteristics of the motor such as rotor speed, motor moment are used to survey tracking performances. The characteristic current or consumption power to examine the effectiveness of the energy of the proposed algorithm.

3.1 Simulation Using Matlab/Simulink

Vector Control of a Variable-Frequency Induction Motor Drive

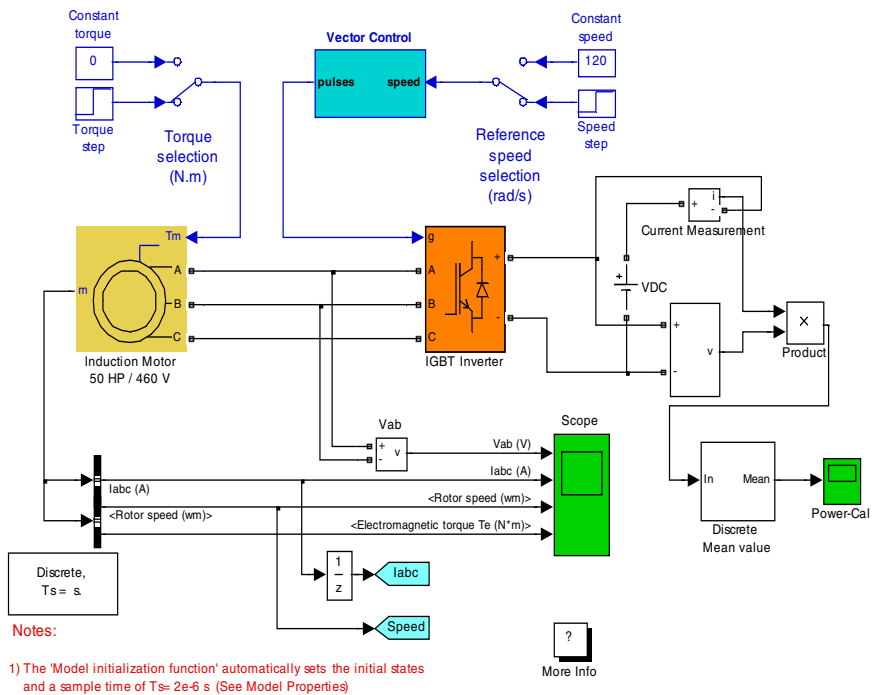


Fig. 2. Simulation diagram of motor control system

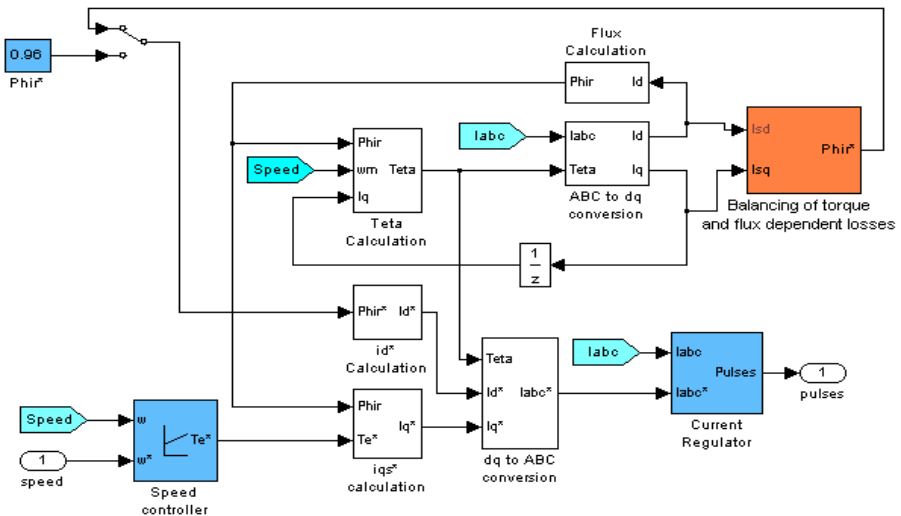


Fig. 3. Simulation diagram inside vector control block

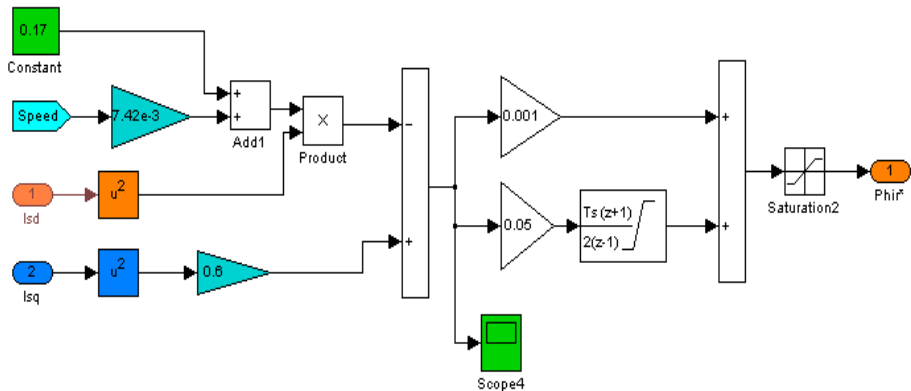


Fig. 4. Simulation diagram inside balancing torque and flux dependent losses block

3.2 Simulation Result

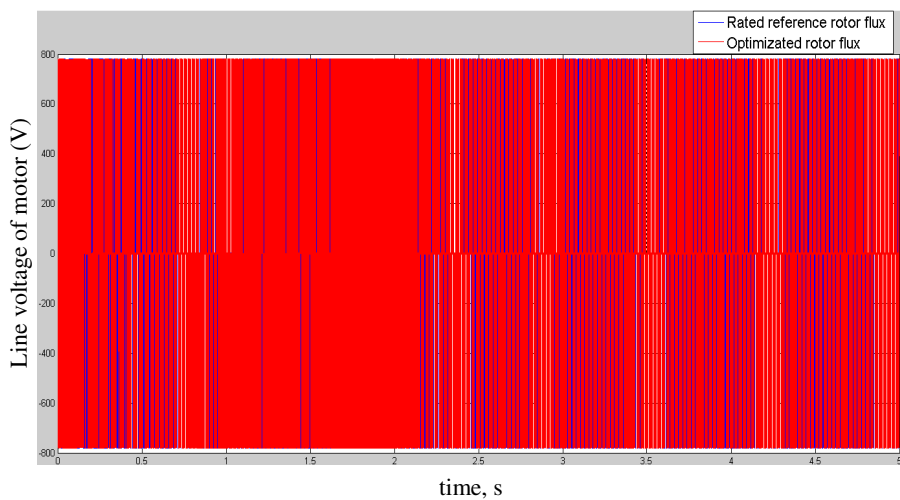


Fig. 5. Line voltage of motor

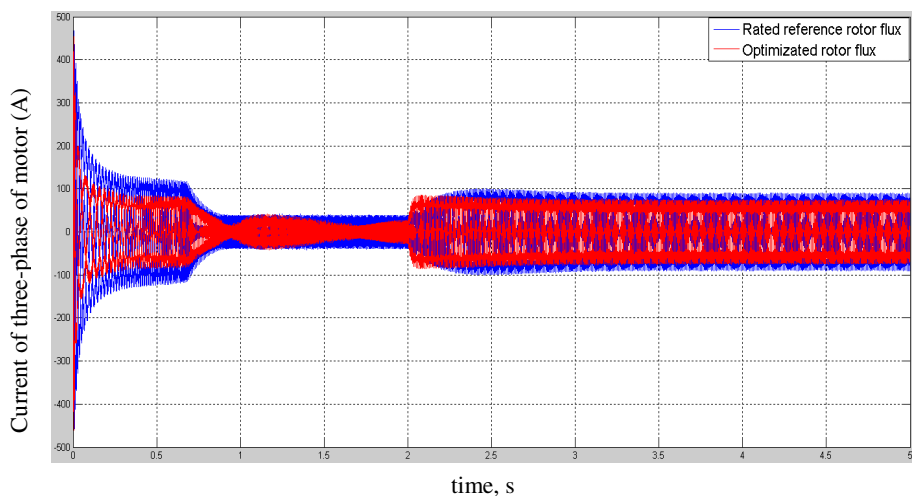


Fig. 6. Current of three-phase of motor

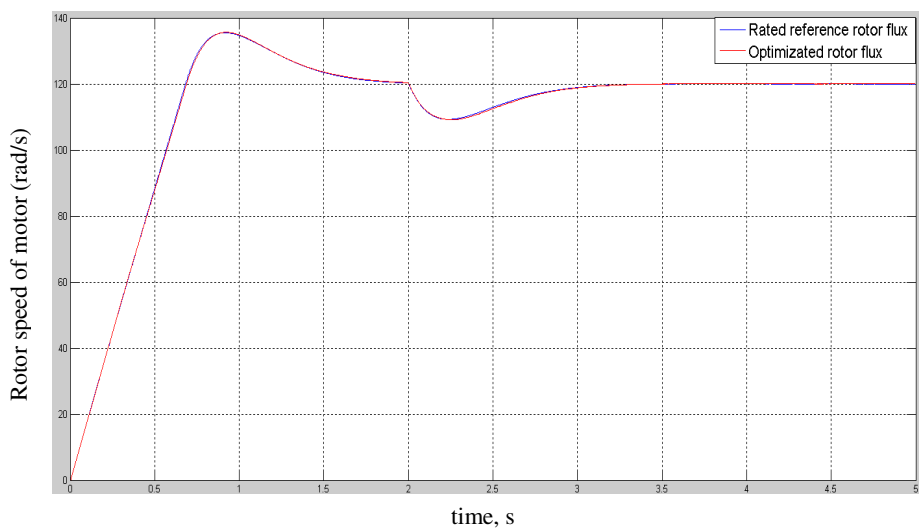


Fig. 7. Rotor speed of motor

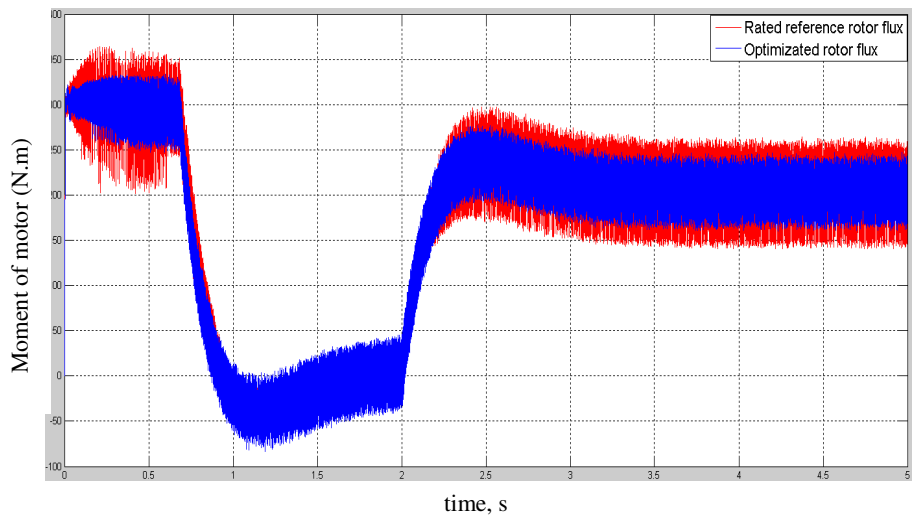


Fig. 8. Moment of motor

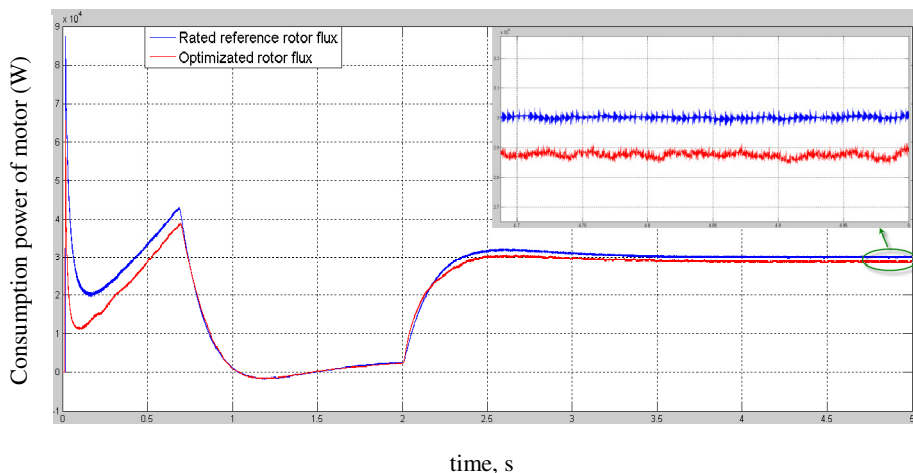


Fig. 9. Consumption power of motor

4 Conclusion

In this paper we describe a method energy optimal control of the three-phase IM. With control technique is balance torque and flux dependent losses. Simulation result shows that the control system has good performance and optimization of electric energy.

References

1. Dhaoui, M., Sbita, L.: A New Method for Losses Minimization in IFOC Induction Motor Drives. *International Journal of Systems Control* 1(2), 93–99 (2010)
2. Grouni, S., Ibtouen, R., Kidouche, M., Touhami, O.: Novel Loss Optimization in Induction Machines with Optimum Rotor Flux Control. *International Journal of Systems Control* 1(4), 163–169 (2010)
3. Uddin, M.N., Nam, S.W.: New Online Loss-Minimization-Based Control of an Induction Motor Drive. *IEEE Trans. on Power Elect.* 23(2), 926–933 (2008)
4. Aissa, K., Eddine, K.D.: Vector Control Using Series Iron Loss Model of Induction Motors and Power Loss Minimization. *World Academy of Science, Engineering and Technology* 52 (2009)
5. Lin, F.C., Yang, S.M.: On-line Tuning of an Efficiency-Optimized Vector Controlled Induction Motor Drive. *Tamkang Journal of Science and Engineering* 6(2), 103–110 (2003)
6. Mahir, R.A., Ahmed, Z.M., Amjad, J.H.: Indirect Field Orientation Control of Induction Machine with Detuning Effect. *Eng. & Tech.* 26(1), 265–277 (2008)

7. Raj, C.T., Srivastava, S.P., Agarwal, P.: Energy Efficient Control of Three-Phase Induction Motor – A Review. International Journal of Computer and Electrical Engineering 1(1), 61–70 (2009)
8. Quang, N.P., Dittrich, A.: Intelligent Electric Drive. Science and Technology Publisher (2002)
9. Abrahamsen, F.: Energy Optimal Control of Induction Drives. Aalborg University (2000)

Adaptive Motion Controller Design for an Omnidirectional AGV Based on Laser Sensor

Thanh Luan Bui¹, Phuc Thinh Doan¹, Hak Kyeong Kim¹, Van Giap Nguyen²,
and Sang Bong Kim^{1,*}

¹ Department of Mechanical and Automotive Eng., College of Eng.,
Pukyong National University, Busan, Korea

² Faculty of Mechanical Engineering, Hochiminh City University of Technology,
Hochiminh, Vietnam
kimsb@pknu.ac.kr

Abstract. Automatic Guided Vehicles (AGVs) are used in many factories. This paper proposes an adaptive tracking controller of omnidirectional AGV (OAGV) with the constant unknown mass and the uncertain bounded friction and slip force vector exerted on the driving wheels. The OAGV consists of 3 wheels with three omnidirectional wheels are equally spaced 120° from one another. The controller based on the dynamic modeling is designed based on Lyapunov stability theory to stabilize the OAGV to follow a sharp edge trajectory and OAGV doesn't change heading direction during movement. A laser sensor device NAV200 is used to detect the OAGV position in door environment in real-time. The simulation and experiment results are presented to demonstrate the effectiveness of the proposed controller.

Keywords: AGV, omnidirectional wheels, 3 wheels, NAV200, adaptive control.

1 Introduction

Nowadays, the handling of materials and parts through AGVs is of increasing importance in the automation. Many factories have adopted it into assembly line or production line such as automobile, food processing, wood working, automated delivery of medications in hospital and other factories. AGV has attracted the attention to many researchers as well as manufacturers [1]-[12]. Saha, S.K. et al. [1] introduced structural properties and classification of kinematic isotropic rolling robots with omnidirectional wheels. However, they introduced kinematic isotropy as a design criterion in the realm of mobile robots. Nagy et al. [2] proposed an innovative method generating near-optimal trajectories for an omnidirectional mobile robot in path planning. Williams, R. L. [3] derived a dynamic modeling of an omnidirectional robot with slip between the omnidirectional wheels and motion surface. Tang, J. et al. [4] have described the design of an omnidirectional holonomic mobile robot using

* Corresponding author.

three orthogonal-wheel assemblies. Xu, D. et al. [5] proposed trajectory tracking control of omnidirectional wheeled mobile manipulators with robust neural network-based sliding mode controller. However, they presented only simulation results. Kim, S. et al. [6] presented trajectory control method of three wheels omnidirectional mobile robot using fuzzy azimuth estimator. However, they proposed a PID tracking controller to follow speed command from inverse kinematic without considering the coupled nonlinear dynamics. Liu, Y. et al. [7] proposed a nonlinear controller based on trajectory linearization to improve the path flowing. Watanabe, K. et al. [9] presented the dynamic modeling of an omnidirectional mobile robot and PID control method. However their system is very simple. Kodagoda, K. R. S. et al. [10] presented fuzzy speed and steering control of an AGV. Beji, L. et al. [11] presented motion generation and adaptive control method of AGVs in road following. However, they used AGV like a car and have not yet applied to heavy industrial vehicles. The AGV usually uses conventional wheel and the structure can't move in all directions freely.

From the above discussions, this paper is about control of an industrial OAGV for tracking a reference trajectory using laser sensor NAV200. A new adaptive tracking controller for OAGV with the constant unknown mass and the uncertain bounded friction and slip force vector exerted on the driving wheels is proposed. The OAGV can move in any directions and doesn't change heading direction during movement. A kinematic modeling and dynamic modeling of the system with disturbance and friction are presented. The followings are done for this paper. The first one is system description, the second one is OAGV's modeling and the third is to design a controller for trajectory tracking of OAGV. Finally, simulation and experimental results on the OAGV with 3 omnidirectional wheels are carried out to evaluate the effectiveness of the proposed controller.

2 System Description and Modeling

2.1 System Description

Fig. 1 shows the controller system that is developed based on the integration of an industry computer. OAGV can operate in both manual mode and automatic mode.

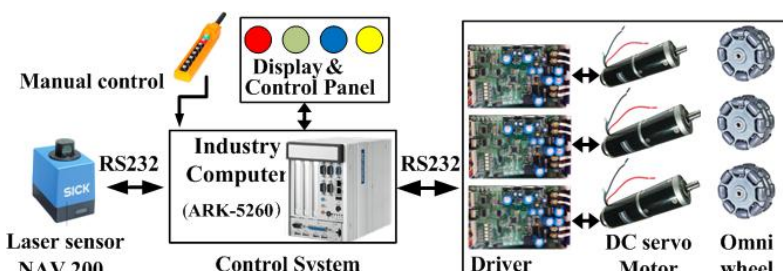


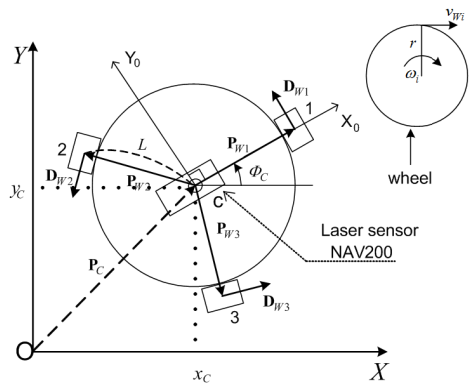
Fig. 1. Schematic of the control system developed for the OAGV

Fig. 2a shows the OAGV with three omnidirectional wheels equally spaced 120° from one another. The laser sensor NAV200 is set on the centre of the OAGV. Based on laser sensor, the postures of OAGV are measured.

An industry computer ARK-5260 is operated with the clock 1.66GHz processor. The prototype of the experimental AGV is shown in Fig. 2a.



a. Prototype of the experimental OAGV



b. Configuration for geometric model of OAGV

Fig. 2. Prototype of the experimental OAGV and configuration for geometric model of OAGV

2.2 System Modeling

Fig. 2b shows the configuration for the geometric model of the OAGV omnidirectional wheel. $\mathbf{P}_{Wi} \in \mathbb{R}^{2 \times 1}$ ($i=1, 2, 3$) is a position vector of each wheel with respect to the moving coordinate frame Cx_cy_c attached at point C on the OAGV. $\mathbf{D}_{Wi} \in \mathbb{R}^{2 \times 1}$ is the drive direction vector of each wheel with respect to the global coordinate frame OXY . The posture vector of point C in the global coordinate frame is specified by $\mathbf{q}_C = [x_C \ y_C \ \Phi_C]^T$. $\mathbf{P}_C = [x_C \ y_C]^T$ is defined as the position vector of point C with respect to the global coordinate frame. v_C is the linear velocity of the OAGV.

Kinematic Model

The kinematic equation of an OAGV [12] can be expressed as follows:

$$\mathbf{z} = \frac{1}{r} \mathbf{H}^{-1} \dot{\mathbf{q}}_C \quad (1)$$

where $\mathbf{z} = [\omega_1 \ \omega_2 \ \omega_3]^T$ is the wheel angular velocity vector, and $\mathbf{H}^{-1} \in \mathbb{R}^{3 \times 3}$ matrix is given as:

$$\mathbf{H}^{-1} = \begin{bmatrix} -\sin \Phi_C & \cos \Phi_C & L \\ -\sin(\pi/3 - \Phi_C) & -\cos(\pi/3 - \Phi_C) & L \\ \sin(\pi/3 + \Phi_C) & -\cos(\pi/3 + \Phi_C) & L \end{bmatrix} \quad (2)$$

From (1), a velocity vector of point C on the OAGV is reduced into:

$$\dot{\mathbf{q}}_C = r\mathbf{Hz} \quad (3)$$

From Fig. 2b, the velocity v_C of the OAGV can be obtained as:

$$\xi = \begin{bmatrix} v_C \\ \omega_C \end{bmatrix} = \begin{bmatrix} \cos \Phi_C & \sin \Phi_C & 0 \\ 0 & 0 & 1 \end{bmatrix} \begin{bmatrix} \dot{x}_C \\ \dot{y}_C \\ \dot{\Phi}_C \end{bmatrix} \quad (4)$$

Dynamic Model

Schematic of the OAGV with forces due to friction and slip phenomenon is shown in Fig. 3.

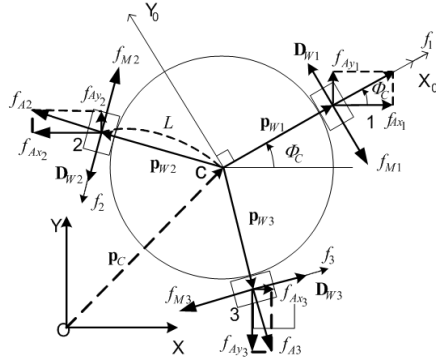


Fig. 3. Schematic of the OAGV with forces due to friction and slip

\mathbf{F}_A is a force disturbance vector due to surface friction and slip phenomena between the ground and the wheels in the wheel axial direction. f_{Mi} and f_{Ai} ($i=1,2,3$) are the magnitudes of friction forces exerted on the i^{th} wheel in the wheel motion direction and in the wheel axial direction, respectively, $\ddot{\mathbf{P}}_C \in \mathbb{R}^{2 \times 1}$ is the linear acceleration vector of the OAGV, f_i ($i=1, 2, 3$) is the magnitude of the force in the drive direction exerted on each wheel driven by the i^{th} motor, m is the mass of the OAGV and I is the moment of inertia for the OAGV about its center of gravity.

According to Newton's second law of motion, equations of linear and angular momentum balance of the OAGV including a force disturbance vector due to surface friction and slip phenomena can be written as follows:

$$\sum_{i=1}^3 (f_i - f_{Mi}) \mathbf{R}(\Phi_C) \mathbf{D}_{Wi} - \mathbf{F}_A = m \ddot{\mathbf{P}}_C \quad (5)$$

$$L \sum_{i=1}^3 (f_i - f_{Mi}) = I \ddot{\Phi}_C \quad (6)$$

$$\mathbf{F}_A = \begin{bmatrix} f_{A1} \cos \Phi_C + f_{A2} \cos\left(\frac{2\pi}{3} + \Phi_C\right) + f_{A3} \cos\left(\frac{4\pi}{3} + \Phi_C\right) \\ f_{A1} \sin \Phi_C + f_{A2} \sin\left(\frac{2\pi}{3} + \Phi_C\right) + f_{A3} \sin\left(\frac{4\pi}{3} + \Phi_C\right) \end{bmatrix} \quad (7)$$

From the dynamic characteristic of DC motor, the force generated by a wheel attached to a DC motor is described by:

$$f_i = \rho_1 u_i - \rho_2 v_{Wi} \quad (8)$$

where u_i ($i = 1, 2, 3$) is the voltage applied to the DC motors, v_{Wi} ($i = 1, 2, 3$) is the linear velocity of each wheel, ρ_1 and ρ_2 are motor characteristic coefficients depending on the parameters of DC motor that can be obtained from its catalogue or experiment [2].

From Eqs. (5) - (7), the dynamic equations of OAGV can be expressed as:

$$\begin{bmatrix} m \ddot{x}_C \\ m \ddot{y}_C \\ I \ddot{\Phi}_C \end{bmatrix} + \frac{3\rho_2}{2} \begin{bmatrix} \dot{x}_C \\ \dot{y}_C \\ 2L^2 \ddot{\Phi}_C \end{bmatrix} = \rho_1 \mathbf{H}^{-T} \mathbf{u} - \mathbf{f}_d \quad (9)$$

$\mathbf{f}_d = [f_{1d} \quad f_{2d} \quad f_{3d}]^T \in \Re^{3 \times 1}$ is a friction and slip force disturbance vector [3] as:

$$\begin{aligned} f_{1d} &= -f_{M1} \sin \Phi_C - f_{M2} \sin(\pi/3 - \Phi_C) + f_{M3} \sin(\pi/3 + \Phi_C) + f_{A1} \cos \Phi_C + \\ &\quad f_{A2} \cos(2\pi/3 + \Phi_C) + f_{A3} \cos(4\pi/3 + \Phi_C) \\ f_{2d} &= f_{M1} \cos \Phi_C - f_{M2} \cos(\pi/3 - \Phi_C) - f_{M3} \cos(\pi/3 + \Phi_C) + f_{A1} \sin \Phi_C + \\ &\quad f_{A2} \sin(2\pi/3 + \Phi_C) + f_{A3} \sin(4\pi/3 + \Phi_C) \\ f_{3d} &= L(f_{M1} + f_{M2} + f_{M3}) \end{aligned} \quad (10)$$

$$-\frac{mg}{3} \mu_{M\max} \leq f_{Mi} \leq \frac{mg}{3} \mu_{M\max}$$

$$-\frac{mg}{3} \mu_{A\max} \leq f_{Ai} \leq \frac{mg}{3} \mu_{A\max}, \quad i = 1, 2, 3$$

$\mu_{M\max}$ and $\mu_{A\max}$ are the maximum static friction coefficients in the wheel motion direction and in the wheel axial direction, respectively; g is the acceleration of gravity. The uncertain friction force vector satisfies the inequality, i.e., $\|\mathbf{f}_d\|_\infty \leq k_{\max}$, where $\|\mathbf{f}_d\|_\infty$ denotes the infinity-norm of the vector \mathbf{f}_d and k_{\max} is the least upper bound of $\|\mathbf{f}_d\|_\infty$.

By defining $\mathbf{x}_1 = \mathbf{q}_C = [x_C \ y_C \ \dot{\Phi}_C]^T$ as a posture vector of the OAGV, its velocity vector is obtained as $\mathbf{x}_2 = \dot{\mathbf{q}}_C = [\dot{x}_C \ \dot{y}_C \ \dot{\Phi}_C]^T$.

Hence, Eq. (9) can be rewritten as:

$$\begin{cases} \dot{\mathbf{x}}_1 = \mathbf{x}_2 \\ \mathbf{M}\dot{\mathbf{x}}_2 = -\mathbf{Ax}_2 + \mathbf{Bu} - \mathbf{f}_d \end{cases} \quad (11)$$

where:

$$\mathbf{M} = \begin{bmatrix} m & 0 & 0 \\ 0 & m & 0 \\ 0 & 0 & I \end{bmatrix}, \quad (11a)$$

$$\mathbf{B} = \rho_l \mathbf{H}^{-T}, \quad (11b)$$

$$\mathbf{A} = \begin{bmatrix} 1.5\rho_2 & 0 & 0 \\ 0 & 1.5\rho_2 & 0 \\ 0 & 0 & 3\rho_2 L^2 \end{bmatrix}, \quad (11c)$$

$$\mathbf{f}_d = \begin{bmatrix} f_{1d} \\ f_{2d} \\ f_{3d} \end{bmatrix}, \quad (11d)$$

3 Controller Design

In this paper, an adaptive controller is designed for the OAGV dynamic model in Eq. (11) with unknown but constant parameters m and the uncertain bounded friction and slip forces exerted on the driving wheels \mathbf{f}_d . The mass of OAGV changes by shipping and discharging of a load. Because \mathbf{f}_d may come from several factors such as the static friction between the wheel and the surface and the slip phenomena, \mathbf{f}_d is assumed to be unknown and bounded. The purpose of this controller is to control the robot to reach the destination position $R(x_r, y_r)$ without its self-rotation, $\dot{\Phi}_C = \text{constant}$ and $\ddot{\Phi}_C = 0$. Therefore, velocity vector \mathbf{x}_2 becomes: $\mathbf{x}_2 = [\dot{x}_C \ \dot{y}_C \ 0]^T$.

Then, the OAGV tracks reference trajectory as shown in Fig. 4. Because, the heading direction angle of OAGV is ignored, a tracking error vector $\mathbf{e}_p = [e_x \ e_y \ 0]^T \in \mathbb{R}^{3 \times 1}$ is defined as the difference between the tracking point C of the OAGV and the reference point R in Fig. 4. e_x, e_y are tracking errors between the reference point and the real point in x, y directions, respectively.

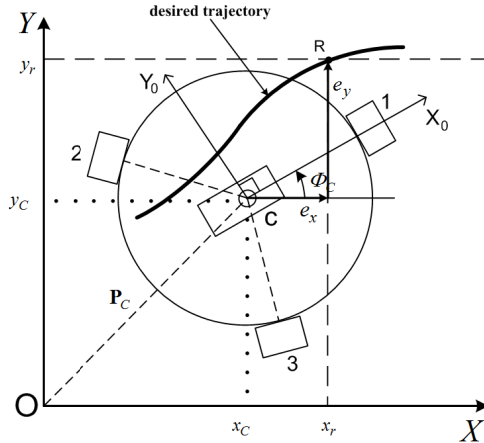


Fig. 4. Configuration of the posture tracking errors e_x, e_y

A controller and update laws are designed based on an adaptive backstepping control theory. It includes two steps: firstly, a virtual state and a stability function are introduced. Secondly, Lyapunov functions for the system are chosen and adaptive controllers that make the system stabilisable are obtained [13].

* *Step 1:* Because, the heading direction angle of OAGV is ignored, tracking error vector $\mathbf{e}_p = [e_x \ e_y \ 0]^T$ is defined as follows:

$$\mathbf{e}_p = \mathbf{x}_r - \mathbf{x}_C \quad (12)$$

where $\mathbf{x}_r = [x_r \ y_r \ 0]^T$ and $\mathbf{x}_C = [x_C \ y_C \ 0]^T$ are defined as a reference posture vector on the reference trajectory and actual posture vector of OAGV.

In applying the backstepping technique, a backstepping error vector as a velocity error vector $\mathbf{e}_b = [e_{b1} \ e_{b2} \ 0]^T$ is defined as:

$$\mathbf{e}_b = \mathbf{x}_2 - \boldsymbol{\delta} \quad (13)$$

When \mathbf{x}_2 is considered as a virtual control input and the stability function vector $\boldsymbol{\delta} = [\delta_x \ \delta_y \ 0]^T$ for \mathbf{x}_2 is designed as follows:

$$\boldsymbol{\delta} = -\mathbf{K}_p \mathbf{e}_p + \dot{\mathbf{x}}_r \quad (14)$$

where $\mathbf{K}_p = \text{diag}([k_{p1} \ k_{p2} \ k_{p3}])$ is a diagonal positive definite matrix.

From Eqs. (12)-(14), differentiating \mathbf{e}_p with respect to time yields:

$$\dot{\mathbf{e}}_p = \dot{\mathbf{x}}_l - \dot{\mathbf{x}}_r = \mathbf{x}_2 - \dot{\mathbf{x}}_r = \mathbf{e}_b + \boldsymbol{\delta} - \dot{\mathbf{x}}_r = \mathbf{e}_b - \mathbf{K}_p \mathbf{e}_p \quad (15)$$

The first Lyapunov function candidate associated with the tracking error is chosen as:

$$V_1 = \frac{1}{2} \mathbf{e}_p^T \mathbf{M} \mathbf{K}_p^2 \mathbf{e}_p \quad (16)$$

where $\mathbf{M} \mathbf{K}_p^2 = \begin{bmatrix} m k_{p1}^2 & 0 & 0 \\ 0 & m k_{p2}^2 & 0 \\ 0 & 0 & I k_{p3}^2 \end{bmatrix}$ is also a positive definite matrix because \mathbf{M} is

also a positive definite matrix from Eq. (11).

Using Eq. (15), the derivative of the Lyapunov function candidate is evaluated as:

$$\dot{V}_1 = \mathbf{e}_p^T \mathbf{M} \mathbf{K}_p^2 \dot{\mathbf{e}}_p = \mathbf{e}_p^T \mathbf{M} \mathbf{K}_p^2 (\mathbf{e}_b - \mathbf{K}_p \mathbf{e}_p) = \mathbf{e}_p^T \mathbf{M} \mathbf{K}_p^2 \mathbf{e}_b - \mathbf{e}_p^T \mathbf{M} \mathbf{K}_p^3 \mathbf{e}_p \quad (17)$$

Eq. (17) can't guarantee $\dot{V}_1 \leq 0$ when $\mathbf{e}_p \neq 0$ and $\mathbf{e}_b \neq 0$. Thus, the second Lyapunov function candidate must be considered.

* Step 2: From Eq. (13), differentiating \mathbf{e}_b with respect to time yields:

$$\dot{\mathbf{e}}_b = \dot{\mathbf{x}}_2 - \dot{\boldsymbol{\delta}} = \dot{\mathbf{x}}_2 + \mathbf{K}_p \dot{\mathbf{e}}_p - \ddot{\mathbf{x}}_r \quad (18)$$

For the control goal, to design the control law for \mathbf{u} such that $\mathbf{e}_p \rightarrow 0$ and $\mathbf{e}_b \rightarrow 0$ as $t \rightarrow \infty$, the following control law is proposed as:

$$\mathbf{u} = \mathbf{B}^{-1} \left[\mathbf{A} \mathbf{x}_2 + \hat{\mathbf{M}} \ddot{\mathbf{x}}_r - (\mathbf{K}_b + \hat{\mathbf{M}} \mathbf{K}_p) \mathbf{e}_b - \hat{k} \text{sgn}(\mathbf{e}_b) \right] \quad (19)$$

Because the OAGV doesn't spins in work place during movement, $I = \hat{I}$. $\hat{\mathbf{M}} = \text{diag}([\hat{m} \ \hat{m} \ I])$ is the estimation matrix of M ; \hat{k} is the estimation of k and positive number, and the matrix $\mathbf{K}_b = \text{diag}([k_{b1} \ k_{b2} \ k_{b3}])$ is positive-definite.

The closed-loop stability of the feedback error system and the parameter update laws for \hat{m} and \hat{k} can be simultaneously accomplished by the Lyapunov stability theory. According to step 1, the second Lyapunov function candidate is chosen as:

$$V_2 = V_1 + \frac{1}{2} \mathbf{e}_b^T \mathbf{M} \mathbf{e}_b + \frac{1}{2\lambda_m} \tilde{m}^2 + \frac{1}{2\lambda_k} \tilde{k}^2 \quad (20)$$

where $\lambda_m > 0$, $\lambda_k > 0$; $\tilde{m} = m - \hat{m}$ and $\tilde{k} = k_{max} - \hat{k}$ are real and positive numbers.

Using Eqs. (11), (15) and (17)-(19), the time derivative of the second Lyapunov function candidate is evaluated as:

$$\begin{aligned} \dot{V}_2 = & \dot{V}_1 + \mathbf{e}_b^T \mathbf{M} \dot{\mathbf{e}}_b + \frac{1}{\lambda_m} \tilde{m} \dot{\tilde{m}} + \frac{1}{\lambda_k} \tilde{k} \dot{\tilde{k}} = -\mathbf{e}_p^T \mathbf{M} \mathbf{K}_p^3 \mathbf{e}_p - \mathbf{e}_b^T \mathbf{K}_b \mathbf{e}_b - \mathbf{e}_b^T \hat{k} \operatorname{sgn}(\mathbf{e}_b) - \mathbf{e}_b^T \mathbf{f}_d \\ & + \tilde{m} \left[-\frac{1}{\lambda_m} \dot{\tilde{m}} + (k_{p1} e_{b1}^2 + k_{p2} e_{b2}^2) - (e_{b1} \ddot{x}_r + e_{b2} \ddot{y}_r) \right] + \frac{1}{\lambda_k} (-\tilde{k} \dot{\tilde{k}}) \end{aligned} \quad (21)$$

By using the inequality $\mathbf{e}_b^T \mathbf{f}_d \leq \|\mathbf{e}_b\| \|\mathbf{f}_d\| \leq \|\mathbf{e}_b\| k_{max}$ as mentioned in Eq. (10), Eq. (21) is rewritten as follows:

$$\begin{aligned} \dot{V}_2 \leq & -\mathbf{e}_p^T \mathbf{M} \mathbf{K}_p^3 \mathbf{e}_p - \mathbf{e}_b^T \mathbf{K}_b \mathbf{e}_b + \tilde{m} \left[-\frac{1}{\lambda_m} \dot{\tilde{m}} + (k_{p1} e_{b1}^2 + k_{p2} e_{b2}^2) - (e_{b1} \ddot{x}_r + e_{b2} \ddot{y}_r) \right] \\ & + \tilde{k} \left(\|\mathbf{e}_b\| - \frac{1}{\lambda_k} \dot{\tilde{k}} \right) \end{aligned} \quad (22)$$

So update laws for \hat{m} and \hat{k} are chosen as follows:

$$\dot{\hat{m}} = -\lambda_m \left[-(k_{p1} e_{b1}^2 + k_{p2} e_{b2}^2) + (e_{b1} \ddot{x}_r + e_{b2} \ddot{y}_r) \right] \quad (23)$$

$$\dot{\hat{k}} = \lambda_k \|\mathbf{e}_b\| \quad (24)$$

Substituting Eqs. (23) and (24) into Eq. (22) gives:

$$\dot{V}_2 \leq -\mathbf{e}_p^T \mathbf{M} \mathbf{K}_p^3 \mathbf{e}_p - \mathbf{e}_b^T \mathbf{K}_b \mathbf{e}_b \leq 0 \quad (25)$$

It shows that \dot{V}_2 is negative. Similarly, the use of Barbalat's lemma indicates that $\mathbf{e}_p \rightarrow 0$ and $\mathbf{e}_b \rightarrow 0$ as time goes to infinity and the estimates \hat{m} and \hat{k} are globally uniformly bounded. Hence, the globally asymptotical stability of the closed-loop error system is ensured. Before closing this step, the following theorem can be stated in the view of above controller design concept without the proof.

Theorem 1. Consider the OAGV dynamic model as in Eq. (11) with the reference differentiable path $\mathbf{x}_r = [x_r \ y_r \ \Phi_C]^T$ unknown but constant parameters m and the uncertain bounded friction and slip forces \mathbf{f}_d exerted on the driving wheels. If the control input in Eq. (19) along with the parameter adjustment rules in Eqs. (23) and (24) are applied, the OAGV can be moved to achieve trajectory tracking and stabilization in the sense of globally asymptotical stability , i.e., $\mathbf{x}_l \rightarrow \mathbf{x}_r$ and $\mathbf{x}_2 \rightarrow \dot{\mathbf{x}}_r$ as $t \rightarrow \infty$.

By using Eqs. (15), (18), (19), (23) and (24), the tracking error dynamic equations and update laws in the closed loop system are rewritten as:

$$\begin{cases} \dot{\mathbf{e}}_p = \mathbf{e}_b - \mathbf{K}_p \mathbf{e}_p \\ \dot{\mathbf{e}}_b = -\tilde{\mathbf{M}}^{-1} [\tilde{\mathbf{M}} \dot{\mathbf{x}}_2 + \mathbf{K}_b \mathbf{e}_b + (\tilde{\mathbf{M}} + \tilde{\mathbf{M}}) \mathbf{K}_p^2 \mathbf{e}_p + \hat{k} \operatorname{sgn}(\mathbf{e}_b) + \mathbf{f}_d] \end{cases} \quad (26)$$

with $\dot{\hat{k}} = \lambda_k \|\mathbf{e}_b\|$ and $\dot{\hat{m}} = -\lambda_m \left[-k_{p1} e_{b1}^2 - k_{p2} e_{b2}^2 + (e_{b1} \ddot{x}_r + e_{b2} \ddot{y}_r) \right]$

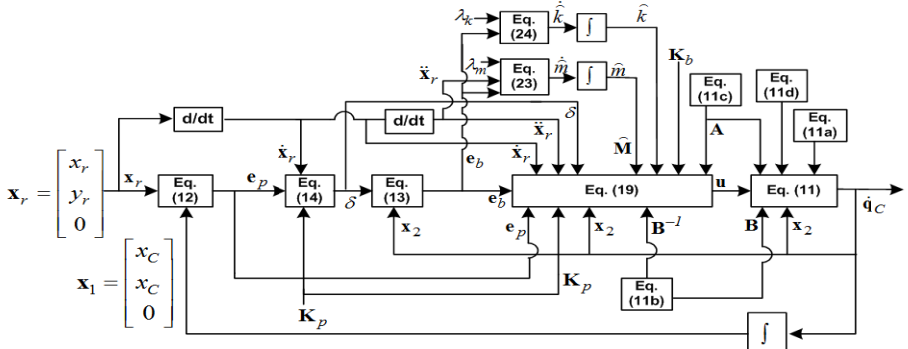


Fig. 5. Block diagram of the proposed adaptive controller of the OAGV

4 Simulation and Experimental Results

The positioning method using NAV200 is shown in Fig. 6.

The reflector positions in absolute coordinate system of the plant are saved inside the OAGV's memory. By comparing the reflector scanning result and the reflector coordinate in OAGV's memory, the absolute coordinate and orientation of OAGV are obtained. The NAV200 transfers the current position data in the form of coordinates via the RS232 data interface. On average, this system can provide up to millimeter accuracy with an update rate up to 8 Hz. The NAV200 is used in this paper and has a maximum of 320 layers, a minimum of 3 reflectors and a maximum of 32 reflectors per layer. The sensor can detect reflector marks in a 360° scanning angle. The sensor has position measurement accuracy from $\pm 4\text{mm}$ to $\pm 25\text{mm}$ depending on mean distance to reflector and range from 1.2m to 28.5m.

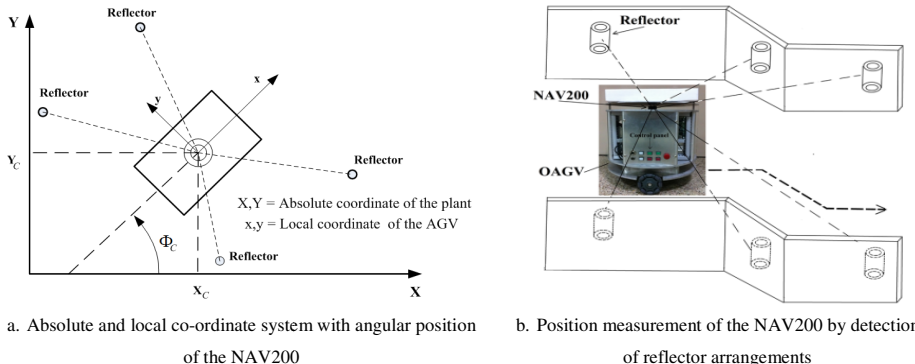


Fig. 6. Absolute and local co-ordinate system with angular position of the NAV200 and Position measurement of the NAV200 by detection of reflector arrangements

Simulation and experiment are done on OAGV system with parameter and initial values are shown in Table 1 and Table 2.

Table 1. Initial values

Parameters	x_r	y_r	x_c	y_c	Φ_c
Values	0	1	0	0.95	0
Units	[m]	[m]	[m]	[m]	[radian]

Table 2. Numerical parameter values

Parameters	L	m	K_p	K_b	ρ_1	ρ_2	λ_m	λ_k
Values	0.275	45	Diag ([22 22 0])	Diag ([40 40 0])	1.5	1.924	25.5	0.01
Units	[m]	kg						

Simulation and experimental result are shown in Fig. 7 – 11 with the sample time $T = 10\text{ ms}$. Fig. 7a shows the reference trajectory for simulation and experiment. The reference trajectory has 3 segments with 2 sharp edges. Fig. 7b shows the simulation and experimental results of tracking a reference line. It shows that the controller makes the OAGV track the reference trajectory well. Fig. 8 shows position errors e_x and e_y . The simulation error converges to zero from 0.5 seconds and the experiment error converges to zero from 5 seconds. The experimental result of the posture tracking error in X and Y directions are bounded within $\pm 1.8\text{ mm}$ and $\pm 7\text{ mm}$, respectively. The errors e_x and e_y have bigger changes in sharp edge line than in

straight line. Fig. 9 shows backstepping errors e_{b1} and e_{b2} . The simulation error converges to zero from 0.2 seconds and the experiment error converges to zero from 3 seconds. Similarly with error position, the errors e_{b1} and e_{b2} have bigger changes in sharp edge line than in straight line. Fig. 10 shows the estimation \hat{m} and \hat{k} . Fig. 10a shows simulation results of \hat{m} . The \hat{m} converges to 45kg from 22.5 seconds. In the first and the second sharp edges, the value of \hat{m} is increased rapidly. Fig. 10b shows simulation results of \hat{k} . The value of \hat{k} increases as the position error increases. The value \hat{k} is increased rapidly when OAGV goes to the sharp edges. Fig. 11 shows simulation and experiment result of control inputs. The voltage input for each motor is bounded within ± 24 v.

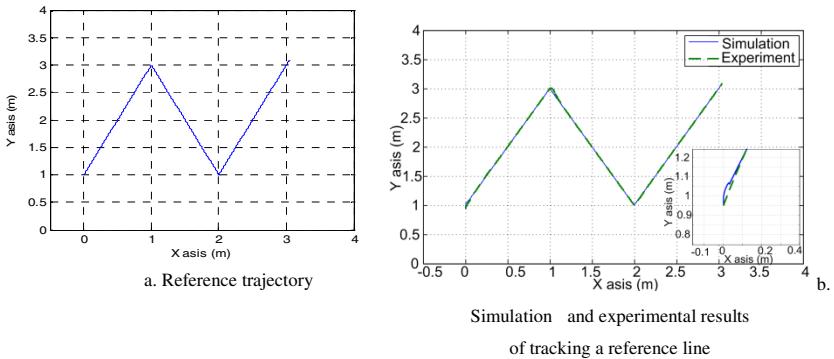


Fig. 7. Reference trajectory and simulation, experimental results of tracking a reference line

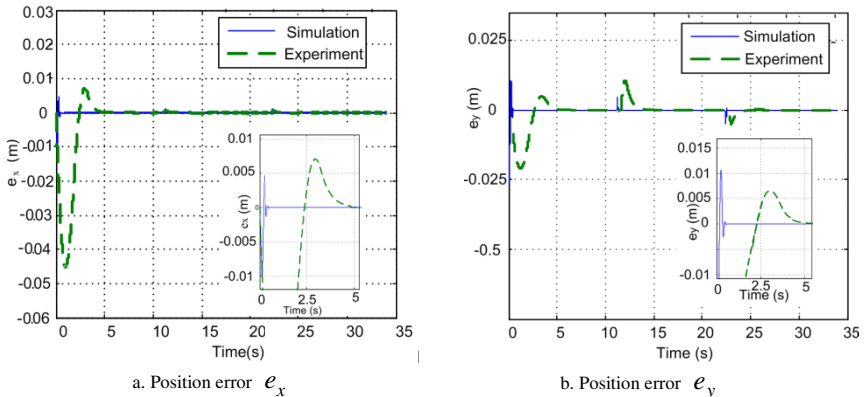
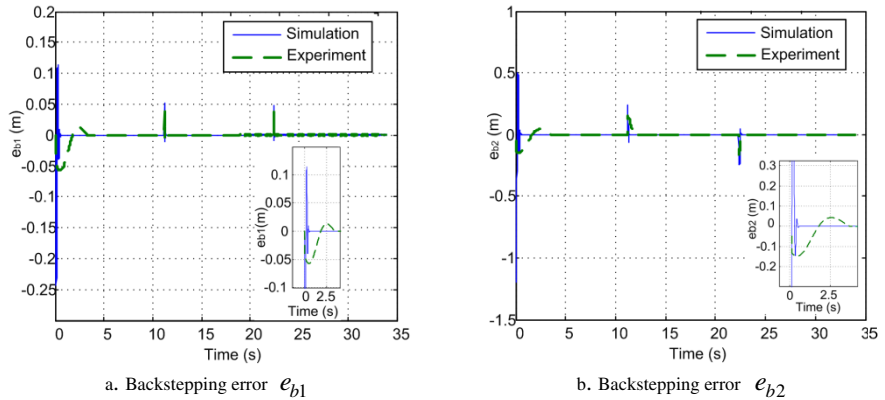
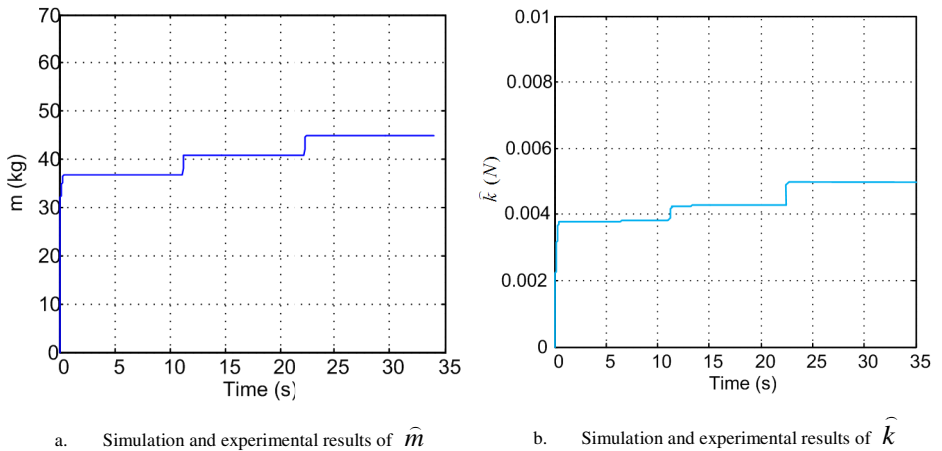
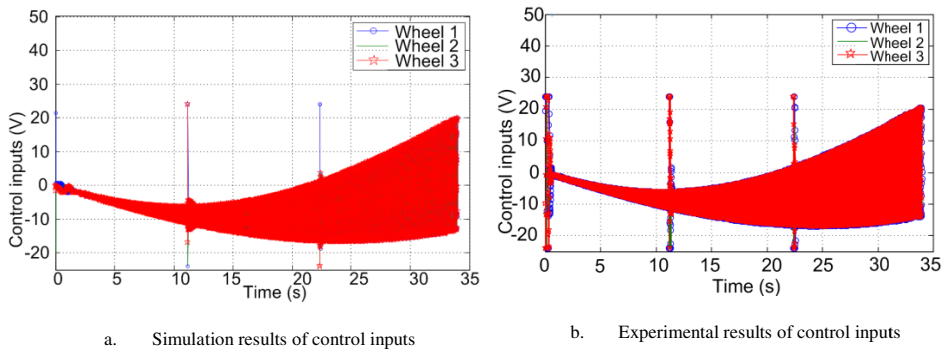


Fig. 8. Position errors e_x and e_y

**Fig. 9.** Backstepping errors e_{b1} and e_{b2} **Fig. 10.** Simulation results of \hat{m} and \hat{k} **Fig. 11.** Simulation and experimental results of control inputs

5 Conclusion

In this paper, an adaptive tracking controller of OAGV with the constant unknown mass and the uncertain bounded friction and slip force vector exerted on the driving wheels is proposed to track a reference trajectory with sharp edges. Simulation and experimental results show that the controller can follow a trajectory with sharp edges and OAGV doesn't change heading direction during movement. The simulation and experimental results show that the proposed controller is capable of making the errors converge to zero after 5 seconds. The simulation and experimental result are shown to illustrate the effectiveness of proposed controller.

Acknowledgement. This research was supported by a grant (11 Transportation System - Logistic02) from Transportation System Efficiency Program funded by Ministry of Land, Infrastructure and Transport (MOLIT) of Korea government.

References

1. Saha, S.K., Angeles, J., Darcovich, J.: The design of kinematically isotropic rolling robot with omnidirectional wheels. *Mechanism and Machine Theory* 30(8), 1127–1137 (1995)
2. Nagy, T.K., D’Andrea, R., Ganguly, P.: Near-optimal dynamic trajectory generation and control of an omnidirectional vehicle. *Robotic and Autonomous Systems* 46(1), 47–6431 (2004)
3. Williams, R.L., Carter, B.E., Gallina, P., Rosati, G.: Dynamic model with slip for wheeled omnidirectional robot. *Robotics and Automation* 18(3), 285–293 (2002)
4. Tang, J., Watanabe, K., Shiraishi, Y.: Design and traveling experiment of an omnidirectional holonomic mobile robot 1, 66–73 (1996)
5. Xu, D., Zhao, D., Yi, J., Tan, X., Chen, Z.: Trajectory tracking control of omnidirectional wheeled mobile manipulators: robust neural network-based sliding mode approach. *Robotics and Automation*, 1653–1658 (2008)
6. Kim, S., Hyun, C., Cho, Y., Kim, S.: Tracking control of 3-wheels omni-directional mobile robot using fuzzy azimuth estimator. In: 10th WSEAS Int. Conference on Robotics Control and Manufacturing Technology, pp. 47–51 (2010)
7. Ranjbar, S.B., Shabaninia, F., Nemati, A., Stan, S.: A novel robust decentralized adaptive fuzzy control for swarm formation of multigent systems. *Industrial Electronics*, 3124–3134 (2012)
8. Liu, Y., Zhu, J.J., Robert, L., Williams II, W.J.: Omni-directional mobile robot controller based on trajectory linearization. *Robotics and Autonomous Systems*, 461–479 (2008)
9. Watanabe, K., Shiraishi, Y., Spyros, G.: Feedback control of an omnidirectional autonomous platform for mobile service robots. *Intelligent and Robotic Systems*, 315–330 (1998)
10. Kodagoda, K.R.S., Wijesoma, W.S., Teoh, E.K.: Fuzzy speed and steering control of an AGV. *Control Systems Technology*, 112–120 (2002)

11. Beji, L., Bestaoui, Y.: Motion generation and adaptive control method of automated guided vehicles in road following. *Intelligent Transportation Systems*, 113–123 (2005)
12. Hung, N., Tuan, D.V., Sung, J.K., Kyeong, K.H., Bong, K.S.: Motion control of an omnidirectional mobile platform for trajectory tracking using an integral sliding mode controller. *Automation and Systems*, 1221–1231 (2010)
13. Tuan, D.V.: Control of a 2-DOF omnidirectional mobile inverted pendulum. Thesis for the Degree of Doctor of Philosophy. Pukyong National University (2012)

Position Control of a Small Scale Quadrotor Using Block Feedback Linearization Control

Van Tu Duong¹, Hak Kyeong Kim¹, Tan Tien Nguyen³,
Sea June Oh², and Sang Bong Kim^{1,*}

¹ Department of Mechanical and Automotive Eng., College of Eng.,
Pukyong National University, Busan, Korea
kimsb@pknu.ac.kr

² Division of Mechatronics Engineering, Korea Maritime University, Busan, Korea

³ Faculty of Mechanical Engineering, HCM City University of Technology, HCM, Vietnam

Abstract. This paper presents a nonlinear controller based on block control technique combined with feedback linearization to be applied to a quadrotor. A quadrotor is one type of unmanned aerial vehicles (UAV) which is equipped with four rotors. First, the quadrotor attitude balancing is kept using three PID regulators. After that, position control is achieved using block control technique which transforms a multivariable system into a SISO for the design of feedback linearization. This work deals with controlling the position of body-centered quadrotor in 3D dimensional space where the movements of quadrotor in x, y, z axes are controlled separately by the proposed controllers. To evaluate the effectiveness of the proposed controller, simulation results are shown.

Keywords: Quadrotor, block control technique, feedback linearization.

1 Introduction

In recent years, researchers in all over the world have been attracted to a quadrotor due to not only its large field application such as search and rescues, real-time forest fire monitoring, mapping and inspection in building but also its high nonlinearity. Since a quadrotor has six degree of freedoms with only four inputs, it is known as an under-actuated system. And there are two subsystems such as position and attitude in general. Derefa et al. proposed a controller based on super twisting control algorithm for tracking the attitude of quadrotor without involving position [1]. Moreover, in [2], a combination between the attitude and altitude of quadrotor was stabilized to reach the state called hovering. Similarly, Sanchez et al. [3] researched hovering flight using brushless DC motor for improving performance of a quadrotor. Joshi et al. [4] presented a method using nonlinear quaternion feedback to stabilize attitude of a quadrotor. In [5], new quaternion based on feedback control was proposed for attitude stabilization. All mentioned works strongly depend on attitude

* Corresponding author.

control without dealing with position control. In general, the position of a quadrotor is controlled by an operation through a remote control system. However, for application required for an autonomous flight, the position of a quadrotor tracks a pre-defined trajectory autonomously. Therefore, a position control is needed.

This paper proposes a controller based on feedback linearization combined with block control technique [6] for controlling position of a quadrotor. First, block control technique is used to devide the whole system into many blocks in which each block is considered as a SISO system. Then, the feedback linearization is used to linearize dynamic modeling. To validate the proposed controller, some simulations are carried on the quadrotor.

2 Quadrotor Dynamic Modeling

A quadrotor has four rotors with fixed-pitch propeller shown in Fig. 1. Each propeller i ($i=1,\dots,4$) produces a moment T_i and a thrust force $F_i = b\omega_i^2$ in which $b > 0$ is thrust factor and ω_i is an angular velocity of rotor i . To cancel the gyroscopic effect, two diagonal front and rear rotors rotate in counterclockwise, while the other two rotors in clockwise. The linear motions along to x , y , z axes and rotating motion around the z axis are accomplished by changing the speed of rotors properly.

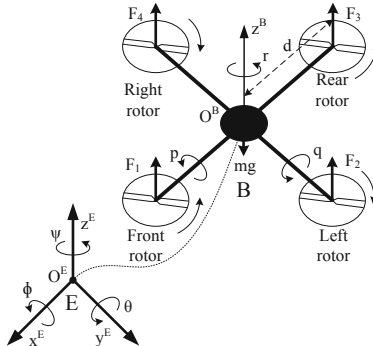


Fig. 1. Quadrotor model

Let us consider two reference frames subjected to the quadrotor: The earth fixed frame $E = (O^E, x^E, y^E, z^E)$ and the body fixed frame $B = (O^B, x^B, y^B, z^B)$. It is assumed that the body fixed frame origin and the center of gravity of the quadrotor must coincide as shown Fig. 1. To describe the behavior of the quadrotor, its absolute position vector is denoted as $X_E = \text{col}(x, y, z) \in E$ and attitudinal vector is denoted as Euler angles $\Theta = \text{col}(\phi, \theta, \psi)$. Euler angles are respectively roll angle ϕ , pitch angle θ , and yaw angle ψ with the following assumption:

$$-\frac{\pi}{2} < \phi < \frac{\pi}{2}, \quad -\frac{\pi}{2} < \theta < \frac{\pi}{2} \quad \text{and} \quad -\frac{\pi}{2} < \psi < \frac{\pi}{2} \quad (1)$$

The quadrotor is restricted by the following 6 D.O.F in 3D dimensional space according to the reference frame B: linear velocity vector $\mathbf{V} = \text{col}(u, v, w)$ and angular velocity vector $\boldsymbol{\Omega} = \text{col}(p, q, r)$ which consist of three translation velocities and three angular velocities of quadrotor frame, respectively. The relation between the velocities vector $(\dot{\mathbf{X}}_E, \dot{\boldsymbol{\Theta}})$ and $(\mathbf{V}, \boldsymbol{\Omega})$ is given by:

$$\begin{cases} \dot{\mathbf{X}}_E = R(\boldsymbol{\Theta})\mathbf{V} \\ \dot{\boldsymbol{\Theta}} = M(\boldsymbol{\Theta})^T \boldsymbol{\Omega} \end{cases} \quad (2)$$

where $R(\boldsymbol{\Theta})$ and $M(\boldsymbol{\Theta})$ are transformation velocity and rotation velocity matrices respectively from frame B to frame E as follows:

$$R(\boldsymbol{\Theta}) = \begin{bmatrix} C_\theta C_\psi & S_\phi S_\theta C_\psi - C_\phi S_\psi & C_\phi S_\theta C_\psi + S_\phi S_\psi \\ C_\theta S_\psi & S_\phi S_\theta S_\psi + C_\phi C_\psi & C_\phi S_\theta S_\psi - S_\phi C_\psi \\ -S_\theta & S_\phi C_\theta & C_\phi C_\theta \end{bmatrix}, \quad M(\boldsymbol{\Theta}) = \begin{bmatrix} -S_\theta & 0 & 1 \\ S_\phi C_\theta & C_\phi & 0 \\ C_\phi C_\theta & -S_\phi & 0 \end{bmatrix} \quad (3)$$

where $S(\bullet)$ and $C(\bullet)$ stand for Sine(\bullet) and Cosine(\bullet) functions.

The dynamic model of the quadrotor is achieved by using Newton – Euler formula expressed in the body fixed frame B as follows:

$$\begin{cases} \sum \mathbf{F}_{\text{ext}} = m \dot{\mathbf{V}} + \boldsymbol{\Omega} \times m \mathbf{V} \\ \sum \mathbf{T}_{\text{ext}} = \mathbf{J} \dot{\boldsymbol{\Omega}} + \boldsymbol{\Omega} \times \mathbf{J} \boldsymbol{\Omega} \end{cases} \quad (4)$$

where m and $\mathbf{J} = \text{diag}(J_x, J_y, J_z)$ are respectively mass and inertial moment matrix of quadrotor, the symbol \times denotes the usual vector product, $\sum \mathbf{F}_{\text{ext}}$ and $\sum \mathbf{T}_{\text{ext}}$ are total external force and moment developed in the centripetal of quadrotor as follows:

$$\begin{cases} \sum \mathbf{F}_{\text{ext}} = \mathbf{F}_{\text{prop}} - \mathbf{F}_{\text{aero}} - \mathbf{F}_{\text{grav}} \\ \sum \mathbf{T}_{\text{ext}} = \mathbf{T}_{\text{prop}} - \mathbf{T}_{\text{aero}} - \mathbf{T}_{\text{gyro}} \end{cases}, \quad \begin{cases} \mathbf{F}_{\text{aero}} = K_f (\mathbf{V} - \mathbf{V}_{\text{air}}) \\ \mathbf{T}_{\text{aero}} = K_t (\boldsymbol{\Omega} - \boldsymbol{\Omega}_{\text{air}}) \\ \mathbf{F}_{\text{grav}} = m R^T(\boldsymbol{\Theta}) \mathbf{g} \\ \mathbf{T}_{\text{gyro}} = \sum_{i=1}^4 J_R (\boldsymbol{\Omega} \times \mathbf{b}_3) (-1)^{i+1} \omega_i \end{cases} \quad (5)$$

where \mathbf{F}_{aero} and \mathbf{T}_{aero} are aerodynamic force and moment acting on the quadrotor which in general are high nonlinearity function, $(\mathbf{V}_{\text{air}}, \boldsymbol{\Omega}_{\text{air}})$ are translation and rotation velocity of air according to body frame B, (K_f, K_t) are two diagonal aerodynamic matrices, \mathbf{F}_{grav} is the force which is produced by the effect of gravity with \mathbf{g} is gravity acceleration, \mathbf{T}_{gyro} is gyroscopic moment resulting from the propeller rotating. J_R and $\mathbf{b}_3 = [0, 0, 1]^T$ are respectively the rotor inertia and unit vector with respect to B frame

and ω_i is the angular velocity of rotor i . F_{prop} and T_{prop} are respectively force and moment produced by propeller as follows:

$$F_{\text{prop}} = \begin{bmatrix} 0 \\ 0 \\ \sum_{i=1}^4 F_i \end{bmatrix}, \quad T_{\text{prop}} = \begin{bmatrix} d(F_4 - F_2) \\ d(F_3 - F_1) \\ c \sum_{i=1}^4 (-1)^i F_i \end{bmatrix} \quad (6)$$

where d is the distance from the center of mass of quadrotor to the rotor axes and c is drag factor.

Using Eq. (5), the equation dynamic model of quadrotor expressed in earth fixed frame E can be expressed as:

$$\begin{cases} \ddot{X}_E = \frac{1}{m} R \sum F_{\text{ext}} = \frac{1}{m} R [F_{\text{prop}} - F_{\text{aero}}] - g e_3 \\ \ddot{\Theta} = (JM)^{-1} \left[T_{\text{prop}} - T_{\text{aero}} - T_{\text{gyro}} - J \left(\frac{\partial M}{\partial \phi} \dot{\phi} + \frac{\partial M}{\partial \theta} \dot{\theta} \right) \dot{\Theta} - M \dot{\Theta} \times JM \dot{\Theta} \right] \end{cases} \quad (7)$$

where $e_3 = [0, 0, 1]^T$ is the unit vector with respect to E frame

3 Position Controller Design

Eq. (7) includes two subsystem which are position X_E and attitude Θ of the quadrotor. In this work, the control objective is to design a controller for the quadrotor position, whereas its attitude is assumed to be hovered by PID controller.

Let us consider the system in Eq. (7) which is expressed in the state space [7] as follows:

$$\begin{cases} \dot{x}_1 = x_2 & \dot{x}_7 = x_8 \\ \dot{x}_2 = \frac{1}{m} (C_{x_7} S_{x_9} C_{x_{11}} + S_{x_7} S_{x_{11}}) U_1 + A_x & \dot{x}_8 = x_{10} x_{12} a_1 + x_{10} a_2 \omega + A_{\dot{\phi}} + b_1 U_2 \\ \dot{x}_3 = x_4 & \dot{x}_9 = x_{10} \\ \dot{x}_4 = \frac{1}{m} (C_{x_7} S_{x_9} S_{x_{11}} - S_{x_7} C_{x_{11}}) U_1 + A_y & \dot{x}_{10} = x_8 x_{12} a_3 + x_8 a_4 \omega + A_{\dot{\theta}} + b_2 U_3 \\ \dot{x}_5 = x_6 & \dot{x}_{11} = x_{12} \\ \dot{x}_6 = \frac{1}{m} C_{x_7} C_{x_9} U_1 + A_z - g & \dot{x}_{12} = x_8 x_{10} a_5 + A_{\dot{\psi}} + b_3 U_4 \end{cases} \quad (8)$$

$$\left\{
 \begin{array}{l}
 \begin{aligned}
 &x_1 = x, \quad x_2 = \dot{x}, \quad x_3 = y, \quad x_4 = \dot{y}, \quad x_5 = z, \quad x_6 = \dot{z} \\
 &x_7 = \phi, \quad x_8 = \dot{\phi}, \quad x_9 = \theta, \quad x_{10} = \dot{\theta}, \quad x_{11} = \psi, \quad x_{12} = \dot{\psi}
 \end{aligned} \\
 U_1 = F_1 + F_2 + F_3 + F_4, \quad U_2 = F_4 - F_2, \quad U_3 = F_3 - F_1, \quad U_4 = -F_1 + F_2 - F_3 + F_4 \\
 \omega = \omega_1 + \omega_2 + \omega_3 + \omega_4
 \end{array}
 \right.$$

Where

$$\left\{
 \begin{array}{l}
 \begin{aligned}
 &[A_x, A_y, A_z]^T = \frac{1}{m} R(\Theta) F_{\text{aero}}, \quad [A_{\dot{\phi}}, A_{\dot{\theta}}, A_{\dot{\psi}}]^T = J^{-1} T_{\text{aero}} \\
 &a_1 = \frac{J_y - J_z}{J_x}, \quad a_2 = \frac{-J_R}{J_x}, \quad a_3 = \frac{J_z - J_x}{J_y}, \quad a_4 = \frac{J_R}{J_y} \\
 &a_5 = \frac{J_x - J_y}{J_z}, \quad b_1 = \frac{d}{J_x}, \quad b_2 = \frac{d}{J_y}, \quad b_3 = \frac{1}{J_z}
 \end{aligned}
 \end{array}
 \right.$$

Attitude Control

The quadrotor attitude is stabilized by three separate PID controllers with respect to three errors which are defined as follows:

$$\left\{
 \begin{array}{l}
 e_7 = \phi_r - \phi \\
 e_8 = \theta_r - \theta \\
 e_9 = \psi_r - \psi
 \end{array}
 \right. \quad (9)$$

where ϕ_r, θ_r and ψ_r are the desired roll, pitch and yaw angles, respectively.

The controllers for attitude subsystem are given by:

$$\left\{
 \begin{array}{l}
 U_2 = K_{p1}e_7 + K_{i1}\int e_7 + K_{d1}\dot{e}_7 \\
 U_3 = K_{p2}e_8 + K_{i2}\int e_8 + K_{d2}\dot{e}_8 \\
 U_4 = K_{p3}e_9 + K_{i3}\int e_9 + K_{d3}\dot{e}_9
 \end{array}
 \right. \quad (10)$$

where $K_{p\alpha}, K_{i\alpha}, K_{d\alpha}$ ($\alpha = 1 - 3$) are the gains for proportional, integral and derivative terms in PID controllers, respectively.

Position Control

Assumptions:

1. The total thrust force $U_1 = \sum_{i=1}^4 F_i = b(\omega_1^2 + \omega_2^2 + \omega_3^2 + \omega_4^2)$ obtained from Eq. (8) must be strictly positive since $\omega_i \neq 0$ is assumed for lifting up the quadrotor.
2. The term $C_{x_7} C_{x_{11}} \neq 0$ is satisfied from Eq. (1) and Eq. (8).
3. The term $C_{x_{11}} \neq 0$ is satisfied from Eq. (1) and Eq. (8).

The z position of quadrotor is known as altitude. This subsystem involves with two states x_5 and x_6 . By introducing the reference x_{5d} for the altitude variable x_5 (z position), its error is defined as follows:

$$e_5 = x_{5d} - x_5 \quad (11)$$

Taking the time derivative of Eq. (11) yields:

$$\dot{e}_5 = \dot{x}_{5d} - \dot{x}_5 \quad (12)$$

Using Block control technique (BC) [6], a desired virtual input x_{6d} for x_6 is chosen as:

$$x_{6d} = \dot{x}_{5d} + k_5 e_5 \quad \text{with } k_5 > 0 \quad (13)$$

The difference between the state x_6 and the desired virtual input x_{6d} is defined as follows:

$$e_6 = x_{6d} - x_6 \quad (14)$$

Using Eqs. (13) and (14), Eq. (12) is reduced into:

$$\dot{e}_5 = (x_{6d} - x_6) - k_5 e_5 = e_6 - k_5 e_5 \quad (15)$$

From Eqs. (8) and (13), the time derivative of the altitude velocity error e_6 is reduced into:

$$\dot{e}_6 = \dot{x}_{6d} - \dot{x}_6 = \ddot{x}_{5d} + k_5 \dot{e}_5 - A_z + g - \frac{C_{x_7} C_{x_9}}{m} U_1 \quad (16)$$

Since $C_{x_7} C_{x_9} \neq 0$ from Eq. (1) and Eq. (8), by the feedback linearization approach, a control law U_1 is chosen from Eq. (16) as:

$$U_1 = \frac{m}{C_{x_7} C_{x_9}} (\ddot{x}_{5d} + k_5 \dot{e}_5 + k_6 e_6 - A_z + g) \quad \text{with } k_5, k_6 > 0 \quad (17)$$

where ($k_5, k_6 > 0$) are proportional gains and can be adjusted to track the reference as quickly as possible.

Using Eqs. (15) – (17), the closed loop is obtained as follows:

$$\begin{cases} \dot{e}_6 = -k_6 e_6 \\ \dot{e}_5 = e_6 - k_5 e_5 \end{cases} \quad (18)$$

Eq. (18) implies that $e_6 \rightarrow 0$ and $e_5 \rightarrow 0$ as $t \rightarrow \infty$.

For x position control, by defining the difference between the state x_1 and its desired reference x_{1d} as e_1 , the time derivative of e_1 is given by:

$$\dot{e}_1 = \dot{x}_{1d} - x_2 \quad (19)$$

The virtual input x_{2d} for x_2 according to BC technique is chosen as:

$$x_{2d} = \dot{x}_{1d} + k_1 e_1 \quad \text{with } k_1 > 0 \quad (20)$$

By defining the difference between the state x_2 and its desired value x_{2d} as e_2 and using Eq. (20), Eq. (19) is reduced into:

$$\dot{e}_1 = (x_{2d} - x_2) - k_1 e_1 = e_2 - k_1 e_1 \quad (21)$$

From Eqs. (8) and (20), the time derivative of e_2 is reduced into:

$$\dot{e}_2 = \ddot{x}_{1d} + k_1 \dot{e}_1 - A_x - \frac{U_1}{m} (C_{x_7} S_{x_9} C_{x_{11}} + S_{x_7} S_{x_{11}}) \quad (22)$$

As mentioned, the motion of quadrotor along to x axis is achieved by generating the pitch angle (θ). Therefore, the control input for this subsystem is the state $x_9 = \theta$ which is considered as desired control law θ_d . To stabilize the system in Eq. (22), the desired dynamics is given into $-k_2 e_2$. By using recursive feedback linearization algorithm from Eq. (22), this following is obtained:

$$\sin \theta_d = \left[\frac{m}{U_1 C_{x_7} C_{x_{11}}} (\ddot{x}_{1d} + k_1 \dot{e}_1 + k_2 e_2 - A_x) - \frac{S_{x_7} S_{x_{11}}}{C_{x_7} C_{x_{11}}} \right] \quad (23)$$

where $k_1 > 0$, $k_2 > 0$

Eq. (23) is realizable with the assumptions 1 and 2.

Right hand term of Eq. (23) must satisfy $|\sin \theta_d| < 1$ from Eq. (1). In this case, the pitch angle θ_d as the control law is obtained as follows:

$$\theta_d = \arcsin \left[\frac{m}{U_1 C_{x_7} C_{x_{11}}} (\ddot{x}_{1d} + k_1 \dot{e}_1 + k_2 e_2 - A_x) - \frac{S_{x_7} S_{x_{11}}}{C_{x_7} C_{x_{11}}} \right] \quad \text{with } k_1, k_2 > 0 \quad (24)$$

Eq. (24) makes e_1 and e_2 be zero as $t \rightarrow \infty$ from Eqs. (21) and (22).

Similarly, the difference between the state variable x_3 and its reference x_{3d} is defined as e_3 in y position control. The desired virtual input x_{4d} for the state x_4 is chosen as by BC:

$$x_{4d} = \dot{x}_{3d} + k_3 e_3 \quad \text{with } k_3 > 0 \quad (25)$$

By defining the difference between the state x_4 and its desired value x_{4d} as e_4 , and using Eq. (25), the time derivative of e_3 is reduced into:

$$\dot{e}_3 = \ddot{x}_{3d} - \dot{x}_3 = (x_{4d} - x_4) - k_3 e_3 = e_4 - k_3 e_3 \quad (26)$$

From Eqs. (8) and (25), the time derivative of e_4 is reduced into:

$$\dot{e}_4 = \ddot{x}_{3d} - k_3 \dot{e}_3 - A_y + \frac{U_1}{m} (C_{x_7} S_{x_9} S_{x_{11}} - S_{x_7} C_{x_{11}}) \quad (27)$$

Using Eq. (27) with the assumptions 1 and 3, this following is obtained:

$$\phi_d = \arcsin \left[\frac{-m}{U_1 C_{x_{11}}} (\dot{x}_{3d} + k_3 \dot{e}_3 + k_4 e_4 - A_y) \right] \quad \text{with } k_3, k_4 > 0 \quad (28)$$

Eq. (28) makes e_3 and e_4 be zero as $t \rightarrow \infty$ from Eqs. (26) and (29).

4 Simulation Results

To validate the effectiveness and performance of proposed controller, simulation is carried on the quadrotor with the following parameters: $m = 0.4\text{kg}$, $g = 9.8 \text{ m/s}^2$, $J_x = J_y = 4.856 \times 10^{-3}$, $J_z = 8.801 \times 10^{-3}$, $J_R = 3.357 \times 10^{-5} \text{ kg m}^2$, $d = 0.225\text{m}$, $A_\phi = A_\theta = A_\psi = \sin(0.1t)$. The attitude and position of quadrotor are tested in separately. For controlling attitude, the quadrotor is assumed to be the initial condition of attitudinal angle vector $\Theta = [\pi/6, \pi/12, \pi/6]^T$ and controlled to converge to the references ($\phi_r = 0$, $\theta_r = 0$, $\psi_r = 0$). According to Fig. 2a, the roll angle converges to its reference after 1 second. The control input U_2 reaches to -6N in maximum at the initial time and converges to zero after 1 second as shown in Fig. 2b. In Fig. 3a, the pitch angle (θ) is stabilized to reach the reference in 1.5 second with small value of control input as shown in Fig. 3b. Fig. 4a shows that yaw angle goes to its reference after 1 second with the control input as shown in Fig. 4b. The response track to the reference after 1.4 second with -4N in maximum value of control input.

On the construct, the quadrotor is assumed to be the initial condition of the absolute position vector $X_E = [0, 0, 0]^T$ for controlling position. Fig. 5 shows the simulation results with respect to step input $z=1\text{m}$ and step change input $z=1.2\text{m}$ references in altitude control of quadrotor. In both cases, it is controlled to reach the desired reference after 1.5 second as shown in Fig. 5a and Fig. 5c. With respect to step input, the control input keeps about 4N after 1 second as shown Fig. 5b, whereas Fig. 5d shows control input with respect to step input change reaching to 4N after 2.5 seconds. Fig. 6a and Fig. 6b show position tracking result and pitch angle as control input in x direction with respect to step input ($x=1\text{m}$) reference, respectively. After 3.5 seconds, x position converges to the reference whereas the control input

converges to zero. The position tracking and the roll angle as control input in y direction with respect to the step input ($y=1m$) reference are shown in Fig. 7a and Fig. 7b, respectively. The response converges to the reference after 3.5 seconds. The simulation results show the good performance of the proposed controllers.

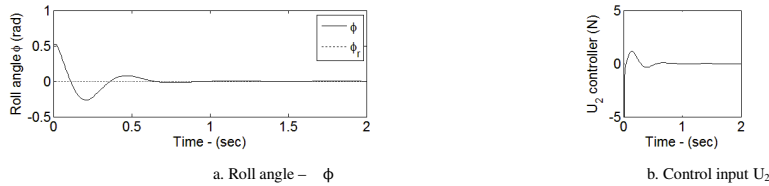


Fig. 2. PID control for stabilizing roll angle

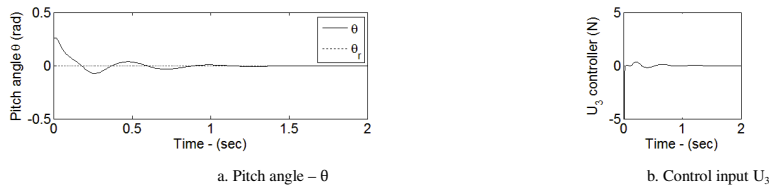


Fig. 3. PID control for stabilizing pitch angle

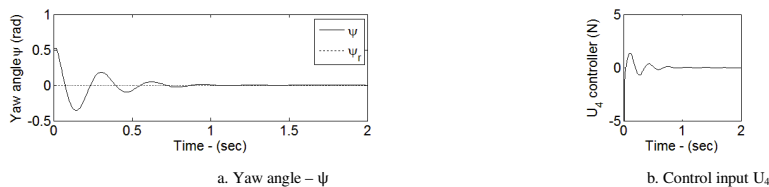


Fig. 4. PID control for stabilizing yaw angle

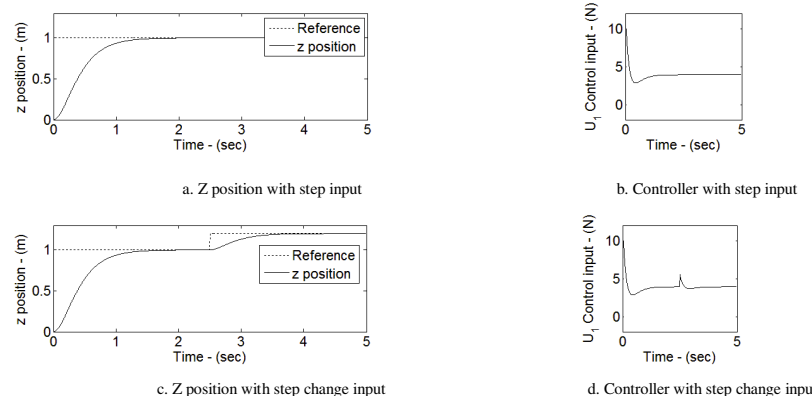
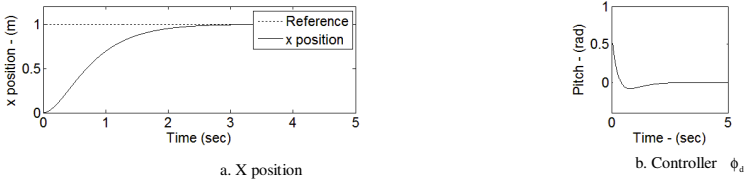
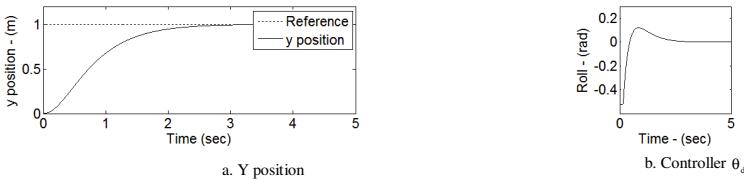


Fig. 5. Altitude control

**Fig. 6.** Position control along x direction**Fig. 7.** Position control along y direction

5 Conclusion

In this paper, the block feedback linearization and PID approach were applied successful for controlling a small scale quadrotor. The attitude of the quadrotor was controlled by PID approach. The position such as the altitude, longitudinal and latitudinal of the quadrotor was controlled by block feedback linearization method. Block control technique was used to turn out the multivariable system into a single input – single output system. The simulation results show good performance of the proposed controller in tracking position and altitude of the quadrotor.

References

1. Derefa, L., Benallegue, A., Fridman, L.: Super Twisting Control Algorithm for The Attitude Tracking of a Four Rotors UAV. *J. Franklin Institute* 349, 685–699 (2012)
2. Garcia-Carrillo, L.R., Rondon, E., Dzul, A., Sanchez, A., Lozano, R.: Hovering Quad-rotor Control: A Comparision of Nonlinear Controllers Using Visual Feedback. In: 49th IEEE Conference on Decision and Control, Atlanta, pp. 1162–1167 (2010)
3. Sanchez, A., Garcia Carrillo, L.R., Rondon, E., Lozano, R., Garcia, O.: Hovering Flight Improvement of a Quadrotor Mini UAV Using Brushless DC Motors. *J. Intell Robot Syst.* 61, 85–101 (2011)
4. Joshi, S.M., Kelkar, A.G., Wen, J.T.Y.: Robust Attitude Stabilization of Spacecraft Using Nonlinear Quaternion Feedback. *J. IEEE Transaction on Automatic Control* 40, 1800–1802 (1995)
5. Tayebi, A., McGilvray, S.: Attitude Stabilization of a VTOL Quadrotor Aircraft. *J. IEEE Transaction on Control Systems Technology* 14, 562–571 (2006)
6. Rao, S., Brandtstadter, H., Utkin, V., Buss, M.: Generalized Block Control Principle. In: IFAC, Prague (2005)
7. Luque-Vega, L., Castillo-Toledo, B., Loukianov, A.G.: Robust Block Second Order Sliding Mode Control for a Quadrotor. *J. Franklin Institute* 349, 719–739 (2012)

Trajectory Tracking Algorithm for Automatic Guided Vehicle Based on Adaptive Backstepping Control Method

Pandu Sandi Pratama¹, Bui Thanh Luan¹, Thien Phuc Tran²,
Hak Kyeong Kim¹, and Sang Bong Kim¹

¹ Department of Mechanical and Automotive Engineering,
Pukyong National University, Busan 608-739, Korea
kimsb@pknu.ac.kr

² Faculty of Mechanical Engineering, Hochiminh City University of Technology,
Hochiminh, Vietnam

Abstract. This paper proposes trajectory tracking algorithm for differential drive type of Automatic Guided Vehicle (AGV) system with the unknown wheel radii using adaptive backstepping control method. To guarantee the tracking errors go to zero, backstepping control method is proposed. By choosing appropriate Lyapunov function based on its kinematic modeling, system stability is guaranteed and a control law can be obtained. In this paper, the unknown radii of left and right wheels caused by uneven load distribution or manufacturing imperfection are considered. To solve this problem, an adaptive law is proposed to estimate the changing of wheels radii. The simulation and experimental results show that the proposed controller successfully estimates the unknown parameters and tracks the reference trajectories.

Keywords: automatic guided vehicle, trajectory tracking, adaptive, backstepping.

1 Introduction

Automatic Guided Vehicle (AGV) is a material handling system that uses independently operated, self-propelled vehicles that are guided along defined pathways in the floor [1].

In AGV application, trajectory tracking is the most important issue. Several control algorithms has been proposed to accomplish this task. Abdalla, T.Y. et al. [2] proposed optimized PID controller for trajectory tracking. Doan, P.T. et al [3] proposed fuzzy-PID using camera sensor to track the vision line. Those controllers are easy to applied to AGV system but are not robust. Parameter based controller design method has been proposed by Filipescu, A. [4] using sliding mode control theory and Bui, T.L. et al. [5] using a linear control based on Lyapunov function. In those controllers, the stability of the system is guaranteed, but to find appropriate controller law is not an easy task. Therefore, Jiang, Z.P. et al. [9] proposed backstepping control method. By choosing appropriate Lyapunov equation, the system stability is guaranteed and the control law can be obtained. Takao, T. et al. [7] proposed adaptive

tracking controller for a nonholonomic mobile robot, and Bui, T.H. et al. [8] proposed adaptive controller for partially known system. In those papers, the controllers are adaptive to the changing of wheel diameter. However, the wheels diameters are assumed to be similar.

In real application, uneven load distributions, uneven wear of the wheel or manufacturing imperfection causes the different diameter between the wheels [9]. To solve this problem, this paper proposes adaptive law to estimate the changing of wheel radii. To do this task, firstly the kinematic model of differential drive AGV is proposed. Secondly, an adaptive controller designs using backstepping method and an update law is proposed. Finally, simulation and experiment are done to verify the effectiveness and applicability of the proposed controller.

2 System Modeling

Kinematic equation of nonholonomic differential drive type of AGV system as shown in Fig. 1 can be expressed in term of its linear velocity (V_A) and angular velocity (ω_A) as:

$$\dot{\xi}_I = \begin{bmatrix} \dot{X}_A \\ \dot{Y}_A \\ \dot{\theta}_A \end{bmatrix} = \begin{bmatrix} \cos \theta_A & 0 \\ \sin \theta_A & 0 \\ 0 & 1 \end{bmatrix} \begin{bmatrix} V_A \\ \omega_A \end{bmatrix} \quad (1)$$

where (X_A, Y_A) is AGV position in global Cartesian coordinates, and angle θ_A is AGV orientation that is taken counterclockwise from the X axis.

Relation AGV's linear velocity (V_A) and angular velocities (ω_A) with left and right wheel angular velocities ($\dot{\phi}_L, \dot{\phi}_R$) can be expressed as:

$$\begin{bmatrix} \dot{\phi}_R \\ \dot{\phi}_L \end{bmatrix} = \begin{bmatrix} 1/r_R & b/r_R \\ 1/r_L & -b/r_L \end{bmatrix} \begin{bmatrix} V_A \\ \omega_A \end{bmatrix} \quad \text{or} \quad \begin{bmatrix} V_A \\ \omega_A \end{bmatrix} = \frac{1}{2} \begin{bmatrix} r_R & r_L \\ r_R/b & -r_L/b \end{bmatrix} \begin{bmatrix} \dot{\phi}_R \\ \dot{\phi}_L \end{bmatrix} \quad (2)$$

where r_R and r_L is the right and left wheel radii, and b is distance between the center of AGV and drive wheel.

By substituting Eq. (2) into Eq. (1), the kinematic modeling of AGV related with left and right wheel angular velocities ($\dot{\phi}_L, \dot{\phi}_R$) can be expressed into:

$$\dot{\xi}_I = \begin{bmatrix} \dot{X}_A \\ \dot{Y}_A \\ \dot{\theta}_A \end{bmatrix} = \begin{bmatrix} \cos \theta_A & 0 \\ \sin \theta_A & 0 \\ 0 & 1 \end{bmatrix} \frac{1}{2} \begin{bmatrix} r_R & r_L \\ r_R/b & -r_L/b \end{bmatrix} \begin{bmatrix} \dot{\phi}_R \\ \dot{\phi}_L \end{bmatrix} \quad (3)$$

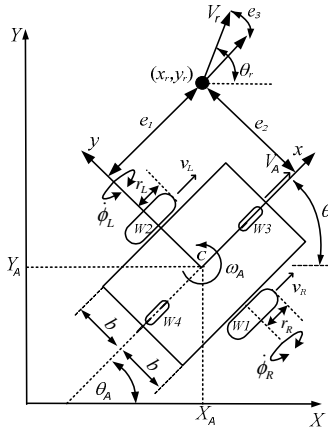


Fig. 1. Automatic Guided Vehicles (AGV) system model

3 Controller Design

The purpose of this section is to design an adaptive trajectory tracking controller for AGV to track the reference position $(x_r(t), y_r(t))$ and reference orientation $\theta_r(t)$ with reference linear velocity $V_r(t)$ and angular velocity $\omega_r(t)$ under the different wheel radii due to uneven load distributions, etc.

The tracking error vector $\mathbf{e}(t)$ with the tracking position errors (e_1 , e_2), and orientation error e_3 in AGV local coordinate as shown in Fig. 1 are defined as:

$$\mathbf{e}(t) = \begin{bmatrix} e_1 \\ e_2 \\ e_3 \end{bmatrix} = \begin{bmatrix} \cos \theta_A & \sin \theta_A & 0 \\ -\sin \theta_A & \cos \theta_A & 0 \\ 0 & 0 & 1 \end{bmatrix} \begin{bmatrix} x_r - X_A \\ y_r - Y_A \\ \theta_r - \theta_A \end{bmatrix} \quad (4)$$

By differentiating Eq. (4) and taking it into Eq. (1), the error dynamic becomes [10]

$$\begin{bmatrix} \dot{e}_1 \\ \dot{e}_2 \\ \dot{e}_3 \end{bmatrix} = \begin{bmatrix} \cos e_3 & 0 \\ \sin e_3 & 0 \\ 0 & 1 \end{bmatrix} \begin{bmatrix} V_r \\ \omega_r \end{bmatrix} + \begin{bmatrix} -1 & e_2 \\ 0 & -e_1 \\ 0 & 1 \end{bmatrix} \begin{bmatrix} V_A \\ \omega_A \end{bmatrix} \quad (5)$$

To guarantee the stability of the system, Lyapunov function is chosen as:

$$V_0 = \frac{1}{2} e_1^2 + \frac{1}{2} e_2^2 + \frac{1}{k_2} (1 - \cos e_3) \quad \text{for } k_2 > 0 \quad (6)$$

and its derivatives becomes

$$\begin{aligned} \dot{V}_0 &= e_1 \dot{e}_1 + e_2 \dot{e}_2 + \frac{1}{k_2} (\sin e_3) \dot{e}_3 \\ &= e_1 (-V_A + V_r \cos e_3) + \frac{1}{k_2} (\sin e_3) (\omega_r - \omega_A + k_2 e_2 V_r) \end{aligned} \quad (7)$$

To achieve $\dot{V}_0 \leq 0$, the control law U is chosen as follows:

$$U = \begin{bmatrix} V_A \\ \omega_A \end{bmatrix} = \begin{bmatrix} V_r \cos e_3 + k_1 e_1 \\ \omega_r + k_2 V_r e_2 + k_3 \sin e_3 \end{bmatrix} \quad (8)$$

where k_1 , k_2 and k_3 are positive constant values.

Substituting Eq. (8) into Eq. (7) yields:

$$\dot{V}_0 = -k_1 e_1^2 - \frac{k_3}{k_2} \sin^2 e_3 \leq 0 \quad (9)$$

Clearly $\dot{V}_0 \leq 0$ and tracking errors are bounded along system solution.

Let us consider the case that the wheel radii are unknown. The above control law U of Eq. (8) cannot be used as the tracking controller. Furthermore, the angular velocities of Eq. (2) and kinematic model of Eq. (3) are unavailable. To solve this problem, adaptive backstepping controller design method is used as follows:

By defining $a_1 = \frac{1}{r_R} > 0$ and $a_2 = \frac{1}{r_L} > 0$, Eq. (2) becomes

$$\begin{bmatrix} \dot{\phi}_R \\ \dot{\phi}_L \end{bmatrix} = \begin{bmatrix} a_1 & a_1 b \\ a_2 & -a_2 b \end{bmatrix} \begin{bmatrix} V_A \\ \omega_A \end{bmatrix} \quad \text{or} \quad \begin{bmatrix} V_A \\ \omega_A \end{bmatrix} = \frac{1}{2} \begin{bmatrix} \frac{1}{a_1} & \frac{1}{a_2} \\ \frac{1}{a_1 b} & -\frac{1}{a_2 b} \end{bmatrix} \begin{bmatrix} \dot{\phi}_R \\ \dot{\phi}_L \end{bmatrix} \quad (10)$$

Our control objective is as follows:

$$\begin{bmatrix} \dot{\phi}_R \\ \dot{\phi}_L \end{bmatrix} \rightarrow \begin{bmatrix} \dot{\hat{\phi}}_R \\ \dot{\hat{\phi}}_L \end{bmatrix} \quad \text{for } t \rightarrow \infty \quad \text{or} \quad \begin{bmatrix} a_1 & a_1 b \\ a_2 & -a_2 b \end{bmatrix} \begin{bmatrix} V_A \\ \omega_A \end{bmatrix} = \begin{bmatrix} \hat{a}_1 & \hat{a}_1 b \\ \hat{a}_2 & -\hat{a}_2 b \end{bmatrix} \begin{bmatrix} V_d \\ \omega_d \end{bmatrix} \quad (11)$$

where \hat{a}_1 and \hat{a}_2 are the estimation values of a_1 and a_2 . V_d and ω_d are desired linear and angular velocities. Eq. (11) means that the linear and angular velocities of V_A and ω_A follow the desire velocities of V_d and ω_d , that is, $V_A \rightarrow V_d$ and $\omega_A \rightarrow \omega_d$ for $t \rightarrow \infty$.

Eq. (11) can be rewritten as follows:

$$\begin{cases} V_d = \frac{1}{2} \left[\left(\frac{a_1}{\hat{a}_1} + \frac{a_2}{\hat{a}_2} \right) V_A + \left(\frac{a_1}{\hat{a}_1} - \frac{a_2}{\hat{a}_2} \right) b \omega_A \right] \\ \omega_d = \frac{1}{2b} \left[\left(\frac{a_1}{\hat{a}_1} - \frac{a_2}{\hat{a}_2} \right) V_A + \left(\frac{a_1}{\hat{a}_1} + \frac{a_2}{\hat{a}_2} \right) b \omega_A \right] \end{cases} \quad (12)$$

Let us define the estimation errors as $\tilde{a}_1 \equiv a_1 - \hat{a}_1$ and $\tilde{a}_2 \equiv a_2 - \hat{a}_2$. Substituting Eq. (12) into Eq. (5) yields:

$$\begin{bmatrix} \dot{e}_1 \\ \dot{e}_2 \\ \dot{e}_3 \end{bmatrix} = \begin{bmatrix} \cos e_3 & 0 \\ \sin e_3 & 0 \\ 0 & 1 \end{bmatrix} \begin{bmatrix} V_r \\ \omega_r \end{bmatrix} + \begin{bmatrix} -1 & e_2 \\ 0 & -e_1 \\ 0 & -1 \end{bmatrix} \frac{1}{2} \begin{bmatrix} 2 - \frac{\tilde{a}_1 - \tilde{a}_2}{a_1 - a_2} & b \left(-\frac{\tilde{a}_1 + \tilde{a}_2}{a_1 + a_2} \right) \\ \frac{1}{b} \left(-\frac{\tilde{a}_1 + \tilde{a}_2}{a_1 + a_2} \right) & 2 - \frac{\tilde{a}_1 - \tilde{a}_2}{a_1 - a_2} \end{bmatrix} \begin{bmatrix} V_d \\ \omega_d \end{bmatrix} \quad (13)$$

The Lyapunov function is chosen as

$$V_1 = \frac{1}{2}e_1^2 + \frac{1}{2}e_2^2 + \frac{1}{k_2}(1 - \cos e_3) + \frac{1}{2\gamma_1 a_1}\tilde{a}_1^2 + \frac{1}{2\gamma_2 a_2}\tilde{a}_2^2 \quad (14)$$

And its derivative yields

$$\begin{aligned} \dot{V}_1 &= e_1 \dot{e}_1 + e_2 \dot{e}_2 + \frac{1}{k_2}(\sin e_3) \dot{e}_3 + \frac{1}{\gamma_1 a_1} \tilde{a}_1 \dot{\tilde{a}}_1 + \frac{1}{\gamma_2 a_2} \tilde{a}_2 \dot{\tilde{a}}_2 \\ &= e_1(-V_d + V_r \cos e_3) + \frac{1}{k_2}(\sin e_3)(\omega_r - \omega_d + k_2 e_2 V_r) \\ &\quad - \frac{1}{\gamma_1 a_1} \left(\dot{\tilde{a}}_1 - \gamma_1 \frac{e_1}{2} V_d - \gamma_1 \frac{be_1}{2} \omega_d - \gamma_1 \frac{\sin e_3}{k_2} \frac{1}{2b} V_d - \gamma_1 \frac{\sin e_3}{k_2} \frac{1}{2} \omega_d \right) \\ &\quad - \frac{1}{\gamma_2 a_2} \left(\dot{\tilde{a}}_2 - \gamma_2 \frac{e_1}{2} V_d + \gamma_2 \frac{be_1}{2} \omega_d + \gamma_2 \frac{\sin e_3}{k_2} \frac{1}{2b} V_d - \gamma_2 \frac{\sin e_3}{k_2} \frac{1}{2} \omega_d \right) \end{aligned} \quad (15)$$

To achieve $\dot{V}_1 \leq 0$, the desired control law is chosen as

$$U_d = \begin{bmatrix} V_d \\ \omega_d \end{bmatrix} = \begin{bmatrix} V_r \cos e_3 + k_1 e_1 \\ \omega_r + k_2 V_r e_2 + k_3 \sin e_3 \end{bmatrix} \quad (16)$$

The two update laws for unknown parameters are chosen as

$$\begin{cases} \dot{\hat{a}}_1 = \gamma_1 \frac{e_1}{2} V_d + \gamma_1 \frac{be_1}{2} \omega_d + \gamma_1 \frac{\sin e_3}{k_2} \frac{1}{2b} V_d + \gamma_1 \frac{\sin e_3}{k_2} \frac{1}{2} \omega_d \\ \dot{\hat{a}}_2 = \gamma_2 \frac{e_1}{2} V_d - \gamma_2 \frac{be_1}{2} \omega_d - \gamma_2 \frac{\sin e_3}{k_2} \frac{1}{2b} V_d + \gamma_2 \frac{\sin e_3}{k_2} \frac{1}{2} \omega_d \end{cases} \quad (17)$$

where γ_1 , γ_2 , k_1 , k_2 and k_3 are positive constant values.

Substituting Eqs. (16-17) into Eq. (15) yields:

$$\dot{V}_0 = -k_1 e_1^2 - \frac{k_3}{k_2} \sin^2 e_3 \leq 0 \quad (18)$$

By Barbalat's lemma, e_1 and e_3 go to zero when $t \rightarrow \infty$.

Replacing ω_A in Eq. (5) by the desired control input ω_d in Eq. (16), the time derivative of error e_3 is given as:

$$\dot{e}_3 = -k_2 e_2 V_r - k_3 \sin e_3 \quad \text{or} \quad \dot{e}_3 = -k_2 e_2 V_r \quad \text{since } e_3 \rightarrow 0 \text{ as } t \rightarrow \infty \quad (19)$$

$V_r^2 e_3$ has the limit equal to zero because $e_3 \rightarrow 0$ and V_r is constant as $t \rightarrow \infty$. Therefore, from Eq. (19), the following equation can be obtain as

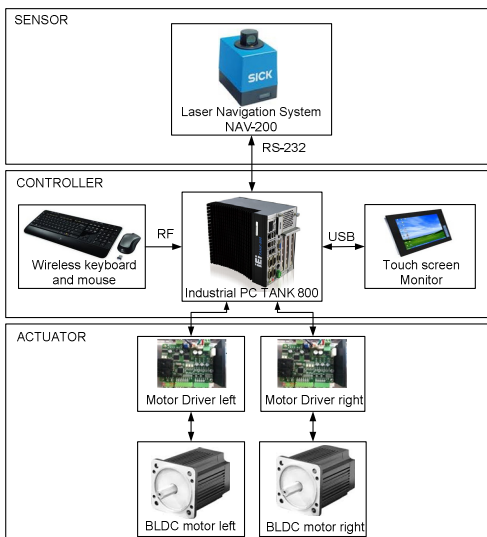
$$\frac{d}{dt} \left(V_r^2 e_3 \right) = -k_2 V_r^3 e_2 = V_r^2 \dot{e}_3 \quad (20)$$

$V_r^3 e_2$ is uniformly continuous since its time derivative is bounded. Using Barbalat's Lemma, it can be proved that $\frac{d}{dt} \left(V_r^2 e_3 \right)$ tends to zero because $e_3 \rightarrow 0$ as $t \rightarrow \infty$. Therefore, in Eq. (20), $V_r^3 e_2$ tends to zero, and thus $V_r e_2$ tends to zero. Because the velocity of V_r is constant, $e_2 \rightarrow 0$ as $t \rightarrow \infty$. Hence, the equilibrium point $\mathbf{e} = 0$ is uniformly asymptotically stable.

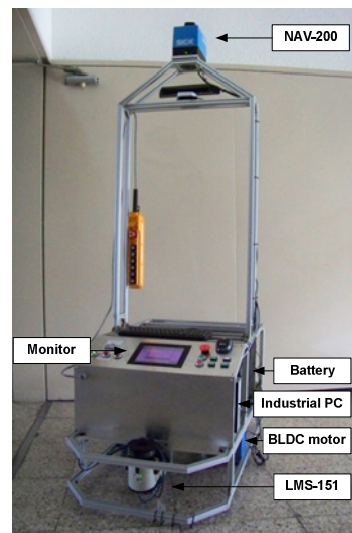
4 Simulation and Experiment

4.1 System Configuration

The design configuration of the AGV system is shown in Fig. 2. This AGV has dimension 60 cm x 100 cm x 190 cm. This system uses differential wheel drive system. Two driving wheels on the left and right sides of AGV are driven by BLDC motors. Two passive castor wheels are installed in front and back sides of AGV to support the AGV. The laser navigation system NAV-200 for positioning sensor with accuracy ± 25 mm is mounted on the top of AGV. Industrial PC TANK-800 as the main controller is placed inside the AGV platform. Touch screen monitor as the input and display is placed on back side of AGV.



a. Electrical Design



b. Mechanical

Fig. 2. Design configuration of AGV system

4.2 Simulation and Experiment Results

To verify the effectiveness of proposed controller, simulation and experiment have been done. For simulation and experiment, the reference trajectory of AGV is a circle shape with diameter 4 meter. The reference linear velocity $V_r(t)$ is 0.2 m/s and the reference angular velocity $\omega_r(t)$ is -0.1 rad/s. The numerical values and initial values for simulation and experiment are shown in Table 1.

Table 1. Numerical values and initial values

Parameter	Values	Parameter	Values	Parameter	Values
r_R	0.09 m	$\hat{r}_R(0)$	0.075 m	k_1	0.7
r_L	0.06 m	$\hat{r}_L(0)$	0.075 m	k_2	6
b	0.3 m	$X_A(0)$	-0.5 m	k_3	0.5
$V_A(0)$	0 m/s	$Y_A(0)$	1 m	γ_1	40
$\omega_A(0)$	0 rad/s	$\theta_A(0)$	0 rad	γ_2	40

The simulation and experimental results are shown in Figs. 3-9. Fig. 3 shows the trajectory from simulation and experimental results. At the beginning, the AGV adjusts its position quickly to reduce the initial error and successfully track the reference trajectory.

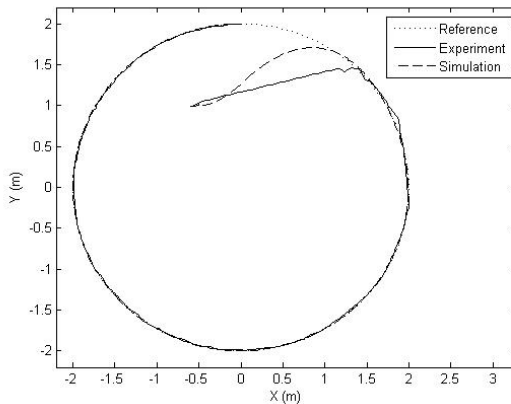


Fig. 3. Trajectory tracking

The control linear velocity V_A and angular velocity ω_A are shown in Fig. 4. The AGV move in clockwise direction, so its angular velocity is -0.1. The left and right wheel angular velocities $\dot{\phi}_R$ and $\dot{\phi}_L$ are shown in Fig. 5.

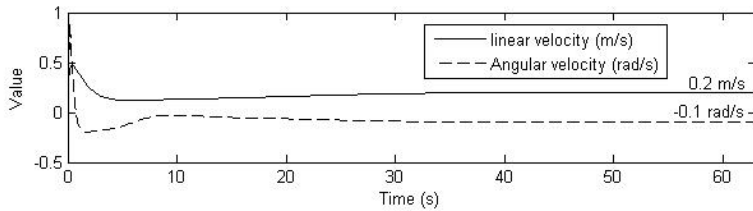


Fig. 4. Linear and angular velocity of AGV

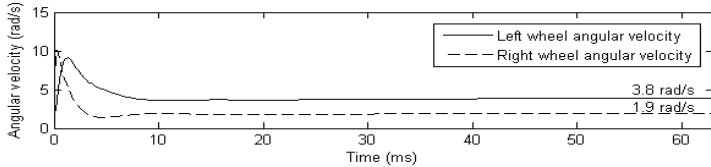


Fig. 5. Angular velocity of wheels

The position error e_1 , e_2 and orientation error e_3 from simulation and experiment result are shown in Figs. 6-8. It is shown that the experiment result are bounded around the simulation result. The error is reduce and converge to zero after 30 seconds. The estimation values of left and right wheels radii \hat{r}_R and \hat{r}_L are shown in Fig. 9. It shows that the estimation values are converging to the real value of the wheels radius after 35 seconds. The final estimation value for the right wheel radius is 0.09 m and left wheel radius is 0.06 m.

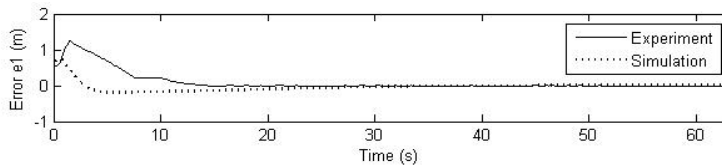


Fig. 6. Position error e_1

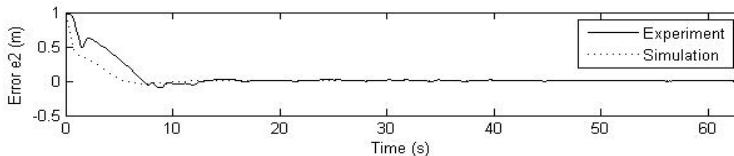


Fig. 7. Position error e_2

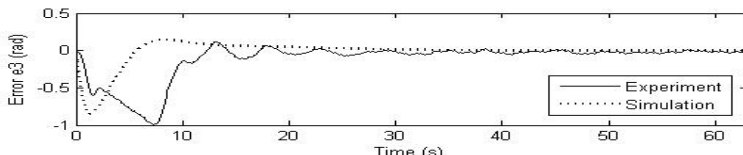


Fig. 8. Orientation error e_3

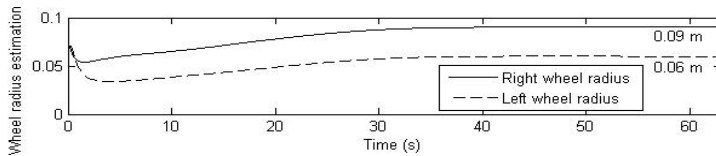


Fig. 9. Estimation of right and left wheel radii

5 Conclusion

In this paper, a trajectory tracking problem of differential drive AGV with different radii of the right and left wheels due to uneven load distributions, etc is considered. This paper proposed a nonlinear controller based on adaptive back-stepping control method to tracks the reference trajectory. The controlled system is stable in sense of Lyapunov stability and the controller is flexible with 5 adjustable parameters. The simulation and experimental results show that the proposed controller successfully tracks the reference trajectory with acceptable error. Furthermore, the wheels diameters estimation values are converge to the real values.

Acknowledgments. This research was supported by a grant (11 Transportation System- Logistics 02) from Transportation System Efficiency Program funded by Ministry of Land, Infrastructure and Transport (MOLIT) of Korean government.

References

1. Kumar, S.A.: Production and Operation Management. New Age International Ltd., New Delhi (2006)
2. Abdalla, T.Y., Abdulkarem, A.A.: PSO-based Optimum Design of PID Controller for Mobile Robot Trajectory Tracking. International Journal of Computer Applications 47(23), 30–35 (2012)
3. Doan, P.T., Nguyen, T.T., Dinh, V.T., Kim, H.K., Kim, S.B.: Path Tracking Control of Automatic Guided Vehicle using Camera Sensor. In: The 1st International Symposium on Automotive and Convergence Engineering (2011)
4. Filipescu: Trajectory-tracking and Discrete-time Sliding-mode Control of Wheeled Mobile Robots. In: IEEE International Conference on Information and Automation (ICIA), pp. 27–32 (2011)
5. Bui, T.L., Doan, P.T., Park, S.S., Kim, H.K., Kim, S.B.: AGV Trajectory Control Based on Laser Sensor Navigation. International Journal of science and Engineering 4(1), 16–20 (2013)
6. Jiang, Z.P., Nijmeijer, H.: Tracking Control of Mobile Robots: A Case Study in Backstepping. Automatica 33(7), 1393–1399 (1997)
7. Fukao, T., Nakagawa, H., Adachi, N.: Adaptive Tracking Control of a Nonholonomic Mobile Robot. IEEE Transaction on Robotics and Automation 16(5), 609–615 (2000)

8. Bui, T.H., Chung, T.L., Kim, S.B.: Adaptive Tracking Control of Two-Wheeled Welding Mobile Robot with Smooth Curved Welding Path. *KSME International Journal* 17(11), 1682–1692 (2003)
9. Feng, L., Koren, Y., Borenstein, J.: A Model-Reference Adaptive Motion Controller for a Differential-Drive Mobile Robot. In: *IEEE International Conference on Robotics and Automation*, vol. 4, pp. 3091–3096 (1994)
10. Kanayama, Y., Kimura, Y., Miyazaki, F., Noguchi, T.: A Stable Tracking Control Method for an Autonomous Mobile Robot. In: *IEEE International Conference on Robotics and Automation*, vol. 1, pp. 384–389 (1990)

A Study on Controllers Design Based on Centroid Displacements for Depth Motion of a 3-Joint Carangiform Fish Robot

Khac Anh Hoang and Tuong Quan Vo

Department of Mechatronics, Ho Chi Minh City University of Technology, Viet Nam
khacanh.hoang0605@gmail.com,
vtquan@hcmut.edu.vn

Abstract. Fish robot can move independently in the water environment, so controlling it in six degrees of freedom (6 DOFs) is a difficult problem. To simplify the problem, we can assume the motions of fish robot include two main motions: the movement of fish robot on the horizontal plane and the movement of fish robot on the vertical direction to the desired depth. This paper proposes a simple method to control a 3-joint Carangiform fish robot swim to the desired depth which is based on the centroid displacements method. The mass, which is controlled by the RC motor, is used to change the center of gravity position of the fish robot that can change the pitch angle of the robot. By controlling the rotation angles of the RC motor which is called alpha angle (α), we can control the up and the down motions of the fish robot. Fuzzy and Self-Tuning PID controllers (Fuzzy-PID) are developed to control the α angle in order to make fish robot swim to the desired depth.

Keywords: Center of gravity, centroid, fish robot, Carangiform, alpha angle, pitch angle, Fuzzy, Fuzzy-PID.

1 Introduction

Nowadays, the underwater robots as Remotely Operated Vehicles (ROVs) and Autonomous Underwater Vehicles (AUVs) have been widely used for ocean exploration and other underwater environment activities. The current demands require more advanced AUVs or ROVs. Fish robot, which is a typical biomimetic robot, is a kind of AUV moving independently in the water environment and it has high energy efficiency. Michael Sfakiotakis et al. divide fish motions into BCF (Body and/or Caudal Fin) and MPF (Median and/or Paired Fin) [1]. The BCF bases on the changing shape of body or caudal fin to create thrust force. The MPF bases on the oscillators of median and/or paired fins. Most of the researches focus much on the BCF type at present. And, there are four swimming types of BCF as: Anguilliform,

Subcarangiform, Carangiform and Thunniform. Therein, Carangiform, which moves the little oscillator body and moves the tail. So, among these types of BCF fish, most of the fish robots are developed based on the Carangiform type because of its flexibility and easiness in control.

When fish robot operates, it will make the decisions and control itself by some of the pre-defined tasks. Therefore, using the classic controllers to control fish robot in the underwater operating environment does not effective because it does not know clearly about the behavior of the harsh working environment. So, in order to help fish robot operates well in this environment we should use the concepts of intelligent controllers or advanced controllers to control fish robot.

Gi-Hun Yang et al. describe the dynamics and controlling of fish robot named "Ichthus" [2]. It has a 3-DOF serial link-mechanism and is developed by KITECH (Korea Institute of Industrial Technology). The simulation computational dynamics and speed of swimming is completed. By model-based simulation, they had made the actual model and proposed some new control parameters to minimize power consumption while operating. On the other hand, Le Zhang et al. describe the design of fish robot which is capable for 3D locomotion, and they also present their depth control methods [3]. Dynamics equation and simulation results are not presented but they make the actual model and introduce their experimental results. Jianxun Wang et al. present the dynamic model of the robot fish and the influences of hydrodynamic forces are also evaluated which is based on the estimated Lighthill theory [4]. The contributions of their paper are to introduce the drag and moment coefficients which are necessary for the motions of underwater robots. Besides, they also focus on the operations of the robot fish caused by fluctuations tail, slip, floor number and the amplitude of oscillation. And, about the Carangiform fish robot, we also have some prior researches about the optimization problems for fish robot velocity and fish robot gait as introduced in [5][6]. Besides, we also focus on the turning motion control for a 3-joint Carangiform fish robot by using Sliding Mode and Fuzzy Sliding Mode controller as discussed in [7].

In this paper, we study on the design of intelligent controllers as Fuzzy and Fuzzy-PID to control a 3-joint Carangiform fish robot type to swim to the desired depth. The method that we proposed is to change the center of gravity position of the fish robot while it is operating in order to make the fish robot change the pitch angle. Firstly, we present a new method for modeling the dynamics of this fish robot. Secondly, the design of the depth controllers will be discussed. These controllers help the fish robot swim to the desired depth and keep this depth while swimming. Then, some simulation results are introduced to prove the effectiveness and feasibility of our proposed methods.

2 System Modeling

2.1 Mechanical Design

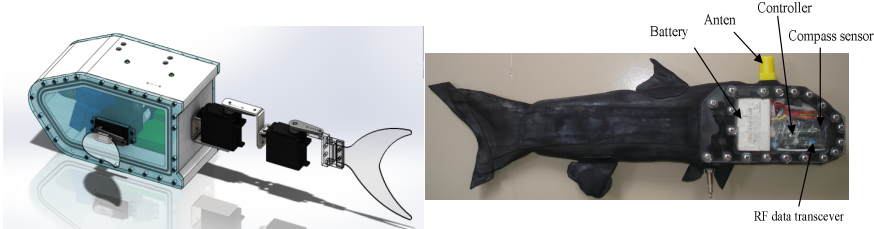


Fig. 1. Structure of 3-Joint Carangiform fish robot and real fish robot

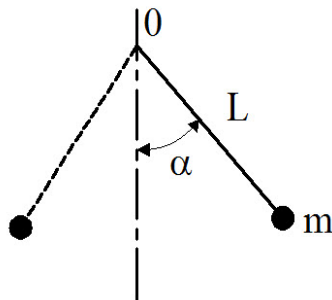


Fig. 2. The theory of centroid displacements system

With the simple design, the fish robot has 3-joint and the centroid displacements system to control the up-down motions. This system is assembled inside of the fish robot's head. The structure of our fish robot and our real fish robot are presented in Fig 1.

Centroid displacements system is a simple system which is combined the mass m and a RC motor. The mass is linked with the RC motor by a straight stick (L) as in Fig. 2. Controlling the angle α by the RC servo motor will change the centroid of fish robot in order to make the fish robot change its pitch angle. Then, with the combination between the thrust force generated by the fish robot's caudal part and the pitch angle of fish robot's head, the fish robot will be controlled to swim to the desired depth. Therefore, by changing the α angle, the fish robot will be controlled to swim to the desired depth. And, in our propose method, the propulsion force generated by fish robot's caudal part is kept as constant.

2.2 Dynamics Analysis

Based on the idea of controlling the depth motion of fish robot as discussed above, the mathematical model of fish robot is developed. The motion of the fish robot in the 3D environment is supposed to be similar to the motion of the ROVs or AUVs and it is described by Eq. (1) [8]:

$$M \cdot \dot{v} + [C(v) + D(v)] \cdot v + g(q) = T \quad (1)$$

Where:

M: Inertia matrix; C(v): Coriolis and Centripetal matrix; D(v): Damping matrix

T: Input vector; and: $v = [u \quad v \quad w \quad p \quad q \quad r]^T$

We only focus on the motion of fish robot in OXZ plane. So the Eq. (1) becomes Eq. (2):

$$\begin{bmatrix} \dot{x} \\ \dot{z} \\ \dot{\theta} \\ \dot{u} \\ \dot{w} \\ \dot{q} \end{bmatrix} = \begin{bmatrix} u \\ u \tan \theta \\ q \\ (F \cos \theta - F_{dragx}) / m \\ (m X_g q + F \sin \theta + B - W - F_{dragz}) / m \\ (m X_g w + M_H) / I_{yy} \end{bmatrix} \quad (2)$$

Where:

F: Thrust force of tail; F_{dragx} : Axial Ox drag force; F_{dragz} : Axial Oz drag force.

m: Mass of robot; W: Gravity force; B: Buoyancy force; I_{yy} : Inertial tensor.

By analyzing Eq. (2), the depth equation of fish robot is calculated by Eq. (3)

$$M_H = (Z_g W - Z_b B) \sin \theta + (X_g W - X_b B) \cos \theta \quad (3)$$

Where:

$\begin{bmatrix} X_g \\ Y_g \\ Z_g \end{bmatrix}$: position of gravity in body-fixed frame

$\begin{bmatrix} X_b \\ Y_b \\ Z_b \end{bmatrix}$: position of buoyancy in body-fixed frame

The calculation method for depth motion of fish robot is introduced in Fig. 3. W is the direction of the depth that we need to control the fish robot to reach to.

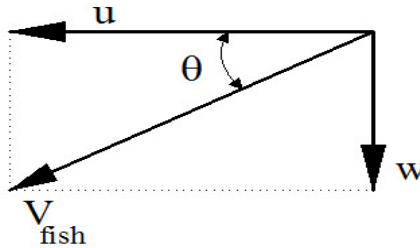


Fig. 3. The depth calculation method of fish robot

3 Controllers Design

3.1 Fuzzy Controller

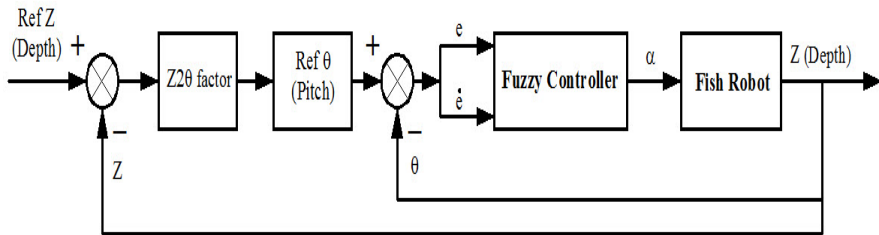


Fig. 4. The Fuzzy Controller

In our problem, the Fuzzy controller is introduced in Fig. 4 above. The Fuzzy controller has two inputs (the error (e) and the rate of the change of error (\dot{e})) and one output (α). The triangle membership function is used for input and output variables. The defuzzification method chosen is COG. The linguistic variables for e , \dot{e} and α are {NB, NM, NS, ZE, PS, PM, PB}. For the Fuzzy rule, there are total 49 rules applied to calculate the output α based on the two inputs e and \dot{e} .

3.2 Fuzzy – PID Controller

In our study, the Fuzzy logic controller is combined with conventional PID controller to make the Fuzzy-PID controller. With the unclear influences of the working environment, the Fuzzy logic controller will tune the gains of PID controller's parameters. The proposed Fuzzy-PID controller is introduced in Fig. 5 below:

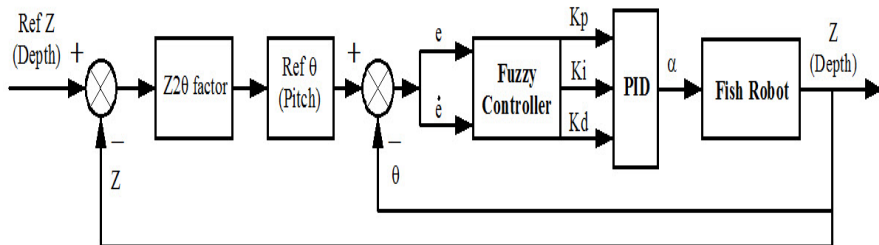


Fig. 5. The Fuzzy-PID Controller

The structure of the Fuzzy-PID controller includes four main elements: The inputs; The Fuzzy controller; PID controller; Output u (α angle).

The Fuzzy controller has two inputs (the error (e) and the rate of the change of error (\dot{e})) and three outputs (K_p , K_i , K_d). The triangle membership function is used for input and output variables. Also, the defuzzification method chosen is COG. Similar to the previous case, the linguistic variables for two inputs e , \dot{e} and three outputs K_p , K_i , K_d are {NB, NM, NS, ZE, PS, PM, PB}. For the Fuzzy-PID rule, there are also total 49 rules are applied to calculated the three outputs K_p , K_i and K_d which is based on the two inputs e and \dot{e} .

4 Simulation Results

In the simulation, the desired depth which is chosen to check our controllers is about 1 meter. In this depth, fish robot will be controlled to swim from the water surface to the desired depth which is called the down motion and it also control fish robot swim from the desired depth to the water surface which is called the up motion. The simulation results will introduce the depth respond of fish robot, the changing by time of fish robot pitch angle.

In our proposed method, about the pitch angle of fish robot, the less oscillation of fish robot's pitch angle is better and also the rapid stability of pitch angle is better. And, about the time of fish robot swim to the desire depth called 'depth reaching time', the shortest time is preferred. However, when choosing the suitable controllers for our real fish robot, we also consider two elements that are the 'less pitch angle oscillation' and the fast 'depth reaching time'.

In the simulation figures will be discussed below, the continuous line is the desired depth, the continuous curve is the respond of fish robot's depth and the dash line is the oscillation of fish robot's pitch angle.

4.1 The Down Motions

The desired depth is 1 meter and the water surface is defined is 0 meter. The fish robot will be controlled to swim from the water surface to the desired depth.

4.1.1 Fuzzy Controller

The respond of fish robot is introduced in Fig. 6 below. Base on this figure, the Fuzzy controller takes about 80 to 90 seconds to control fish robot swim to the desired

depth. And, the fish robot's pitch angle oscillates quite strong at the beginning time but it will gradually stable after about 60 seconds. When fish robot swim to the desired depth, the fish robot's pitch angle still has some small oscillations. The reason of this phenomenon is that when fish robot already reach to the desired depth, its whole body still have some light oscillations which are similar to the real fish. And, this light oscillation will keep fish robot operated in the desired depth.

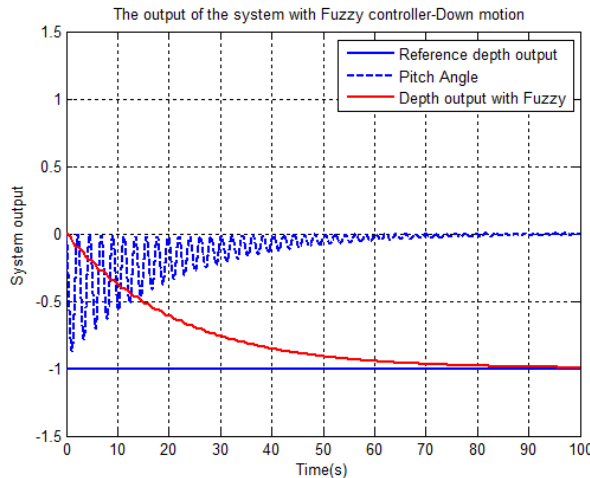


Fig. 6. The response of fish robot in down motion (Fuzzy controller)

4.1.2 Fuzzy-PID Controller

The respond of fish robot when applying Fuzzy-PID controller to control fish robot swim from the water surface to the desired depth is introduced in Fig. 7.

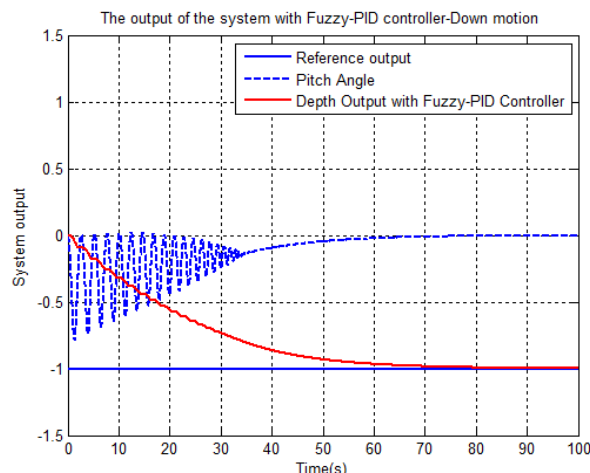


Fig. 7. The response of fish robot in down motion (Fuzzy-PID controller)

In Fig. 7, fish robot takes about 65 seconds to swim to the desired depth. This time is shorter than when we apply the Fuzzy controller as comparison to Fig. 6 above. The performance of fish robot in this case is better because of the ‘depth reaching time’ is very short. It takes about 35 seconds. And, the fish robot’s pitch angle does not oscillate as much as the Fuzzy controller.

4.2 The Up Motions

Similarity to the down motion, fish robot will also be controlled by applying Fuzzy and Fuzzy-PID controllers to make it swim from the desired depth to the water surface. In Fig. 8 and Fig. 9, the current position of fish robot is supposed to be at the desired depth and this desired depth is defined as 0 meter. And, the water surface is defined as 1 meter. The fish robot will be control to swim from the current position (0 meter) to the water surface (1 meter). This is the opposite motions of the fish robot with the cases above.

4.2.1 Fuzzy Controller

The respond of fish robot when apply Fuzzy controller to control it swim from the desired depth to the water surface is presented in Fig. 8. In this figure, fish robot takes about 80 seconds to swim from the desired depth to the water surface. And, the oscillation of pitch angle is also quite big.

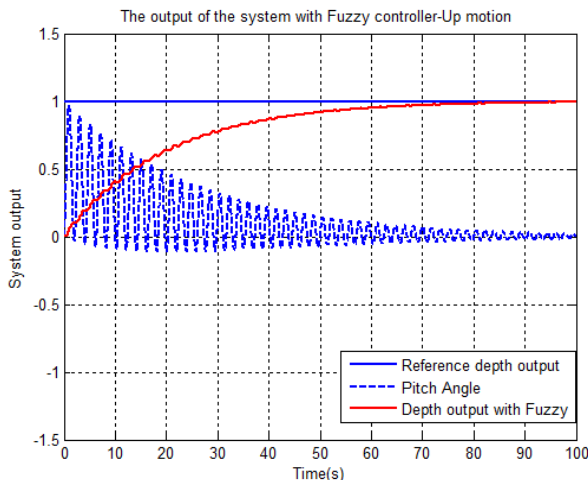


Fig. 8. The response of fish robot in up motion (Fuzzy controller)

4.2.2 Fuzzy-PID Controller

In Fig. 9 below, the fish robot will also take about nearly 60 seconds to swim from the desired depth to the water surface. However, similarity to the down motion, when we apply the Fuzzy-PID controller, the stability of the fish robot’s pitch angle takes quite short time. This is the better point of Fuzzy-PID controller in comparison to the Fuzzy controller in the depth control problem for our fish robot.

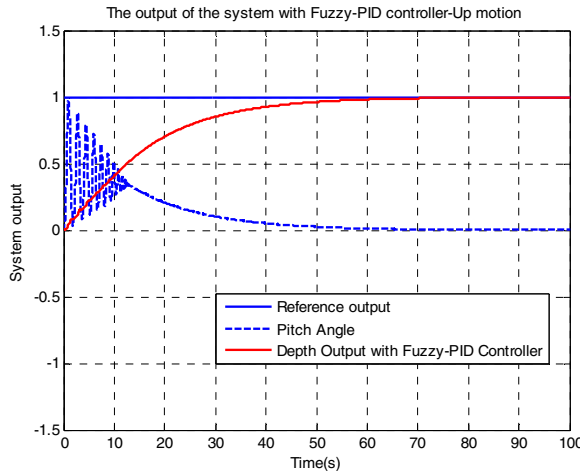


Fig. 9. The response of fish robot in up motion (Fuzzy-PID controller)

So, based on the simulation results we can get some conclusions for our fish robot in the depth control problem. The oscillations of fish robots pitch angle when applying Fuzzy-PID controller are smaller than the Fuzzy controller. And, Fuzzy-PID controller takes shorter time than Fuzzy controller to make the fish robot's pitch angle reach to the stable state. Besides, in the same depth, the down motion of the fish robot will take a little shorter time than the up motion when we apply both Fuzzy and Fuzzy-PID for our fish robot.

5 Conclusion

In this paper, we propose the method to control the depth motion for fish robot by changing the fish robot's center of gravity. And, the depth dynamic equation of a 3-joint Carangiform fish robot is introduced. Then, based on the depth dynamic equation of the fish robot, we develop two different intelligent controllers as the Fuzzy and the Fuzzy-PID controllers to control the depth problem for our fish robot. The simulation results when applying Fuzzy, Fuzzy-PID controllers to control fish robot swim from the water surface to the desired depth which is called the down motion and to control fish robot swim from the desired depth to the water surface which is called the up motion are quite good and quite stable.

In next step, we will continue to do some experiments to check the agreements between the simulation results and the experimental results for the depth control problem of our fish robot. Moreover, we also carry on some other researches about using the pectoral fins or the combination between pectoral fins and centroid displacement system to change the depth motion for our fish robot. Besides, some other controllers will be considered to control the depth problem for our fish robot such as optimal controller and robust controller.

Acknowledgement. This research is funded by Viet Nam National University Ho Chi Minh City (VNU-HCM) under Grant number B-2013-20-01.

References

- [1] Sfakiotakis, M., Lane, D.M., Bruce, J., Davies, C.: Review of Fish Swimming Modes for Aquatic Locomotion. *IEEE Journal of Oceanic Engineering* 24(2) (April 1999)
- [2] Yang, G.-H., Choi, W., Lee, S.-H., Kim, K.-S., Lee, H.-J., Choi, H.-S., Ryuh, Y.-S.: Control and Design of a 3 DOF Fish Robot ICHTUS. In: Proceedings of the 2011 IEEE International Conference on Robotics and Biomimetics, Phuket, Thailand, December 7-11 (2011)
- [3] Zhang, L., Zhao, W., Hu, Y., Zhang, D., Wang, L.: Development and Depth Control of Biomimetic Robotic Fish. In: Proceedings of the 2007 IEEE/RSJ International Conference on Intelligent Robots and Systems San Diego, CA, USA, October 29-November 2 (2007)
- [4] Wang, J.: Freddie Alequin-Ramos and Xiaobo Tan, Dynamic Modeling of Robotic Fish and Its Experimental Validation. In: 2011 IEEE/RSJ International Conference on Intelligent Robots and Systems (IROS), CA, September 25-30 (2011)
- [5] Vo, T.Q., Kim, H.S., Lee, B.R.: Propulsive Velocity Optimization of 3-Joint Fish Robot Using Genetic-Hill Climbing Algorithm. *Journal of Bionic Engineering* 6, 415–429 (2009)
- [6] Vo, T.Q., Kim, H.S., Lee, B.R.: Smooth Gait Optimization of a Fish Robot Using The Genetic-Hill Climbing Algorithm. *Robotica Journal* 30, 257–278 (2012)
- [7] Vo, T.Q., Nguyen, T.T., Tran, T.P., Lee, B.R.: Turning Motion Control of a 3-Joint Carangiform Fish Robot Using Sliding Mode and Fuzzy Sliding Controllers. In: The 11st Asia Pacific Industrial Engineering and Management Systems Conference, Melaka Malaysia, December 7-10 (2010)
- [8] Fjellstad, O.-E.: Control of Unmanned Underwater Vehicles in Six Degrees of Freedom A Quaternion Feedback Approach. Dr. Ing Thesis, Department of Engineering Cybernetics, The Norwegian Institute of Technology, University of Trondheim (November 1994)

Experimental Comparison of A* and D* Lite Path Planning Algorithms for Differential Drive Automated Guided Vehicle

Yuhanes Dedy Setiawan¹, Pandu Sandi Pratama¹, Sang Kwon Jeong²,
Vo Hoang Duy³, and Sang Bong Kim¹

¹ Department of Mechanical and Automotive Engineering, Pukyong National University,
Yongdang Campus, Nam-Gu, Busan 608-739, Korea

kimsb@pknu.ac.kr

² Han Sung WellTech Co., LTD.

#119-5, SamNak-dong, SaSang-Gu, Busan Korea

³ Department of Electrical and Electronic Engineering, Ton Duc Thang University,
Ho Chi Minh City, VietNam

Abstract. Nowadays there are some path planning algorithms for mobile robot which have been documented and explained individually in detail such as A*, LPA*, D* and D* Lite. However, there is still a lack of a comparative analysis of these algorithms. Therefore, in this paper a research of comparing A* and D* Lite algorithm for AGV's path planning is conducted by using simulation and experiment. The goal is to compare the characteristic of each algorithm when they are applied in a real differential drive AGV and give the reader a guide in choosing algorithms for their own planning domains. The emphasis of this comparison is on the computation time of generating trajectory and the distance of the generated trajectory. The simulation and experimental results show that generally D* Lite can plan the shorter path with faster computation time than A*. However, there are some cases when D* Lite is less effective than A*. It means which of the algorithms should be chosen depends on the requirement of the system.

Keywords: Autonomous Guided Vehicle, Path Planning, D* Lite, A*

1 Introduction

Automated Guided Vehicle (AGV) is a mobile robot that moves materials around manufacturing facilities or warehouse in industrial application. Thus, AGV has been used widely because it can increase efficiency and reduce cost of material handling. To be able to work autonomously, AGV needs to be able to plan a path for itself. Path planning is a very important step that AGV has to perform. Therefore, there are many researches related to this area.

Path planning is a process of robot planning a path where it should navigate with avoiding obstacles in the surroundings. Robot has to do this process continuously

until it reaches the goal position even in the presence of unknown obstacles that suddenly appear in the surroundings. There are a lot of path planning algorithms that have been researched for mobile robot, such as A* [1], LPA* (Lifelong Planning A*) [2], D* [3] and D* Lite algorithms [4].

Due to lack of comparative analysis information of path planning algorithms, choosing the best algorithm to be applied in a particular system is sometimes difficult. Hence the main contribution of this paper is to compare the characteristics of path planning algorithms such that their characteristics can be understood by users. In this research, the characteristics of A* and D* Lite algorithm will be researched and compared. D* Lite algorithm is the most widely used path planning algorithm due to its use of incremental updates and heuristics, whereas A* algorithm is a popular classical graph search algorithm in calculating the least-cost path on a weighted graphs [5].

This paper is organized as follows. In section 2 the path planning algorithms, both A* and D* Lite, are described. In section 3 the system description of experimental model AGV is presented. In section 4 simulation and experimental results are discussed. Conclusion is described in the end of the paper.

2 Path Planning Algorithm

In this section, A* and D* Lite algorithms are introduced about how their algorithms work. Firstly, A* algorithm is introduced in Fig. 1. This is a pseudocode of A* algorithm made for user to understand easier. The italic sentence denoted with symbol “//” is brief description of the code. The algorithm is illustrated in Fig. 2(a), which shows an example of simple path planning using A* algorithm. The numbers shown on the node are

```
ComputeShortestPath()
01. while ( $\arg \min_{s \in OPEN} (g(s) + h(s, s_{goal})) \neq s_{goal}$ ) //check whether  $s_{goal}$  is reached or not
02. remove state  $s$  from the front of  $OPEN$ ; //state with the smallest value (becomes path)
03. for all  $s' \in Succ(s)$ //successor of  $s$  to find the other state that has the smallest value
04.   if ( $g(s') > g(s) + c(s, s')$ )//to check whether the  $s'$  has been calculated or not
05.      $g(s') = g(s) + c(s, s');$ 
06.     insert  $s'$  into  $OPEN$  with value  $(g(s') + h(s', s_{goal}))$ ;
```

Main()

```
07. for all  $s \in S$  //initialization of  $s$  as element of  $S$  (set of states in finite state space)
08.    $g(s) = \infty$ ; //initiate the algorithm by making the  $g$  value of all  $s$  to be infinity
09.    $g(s_{start}) = 0$ ; //make the  $g$  value of  $s_{start} = 0$  to begin the path finding algorithm
10.  $OPEN = \emptyset$ ; //make the  $OPEN$  list empty
11. insert  $s_{start}$  into  $OPEN$  with value  $(g(s_{start}) + h(s_{start}, s_{goal}))$ ;
12. ComputeShortestPath();
```

Fig. 1. A* algorithm [5]

explained in Fig. 2(b). $g(s)$ is the sum of the current path cost from the start node, whereas $h(s, s_{goal})$ is heuristic estimate of current path cost to the goal node. The first and second calculations of the algorithm are shown in Fig. 2(c) and 2(d), respectively.

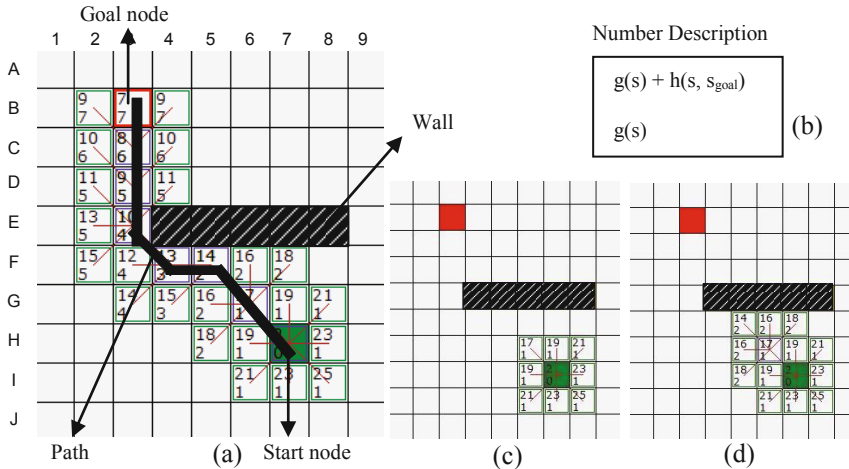


Fig. 2. Illustration of A* algorithm path planning

The algorithm begins by calculating the values of the start node as shown in Fig. 2(c). The heuristic in this case is 2 for vertical and horizontal movements and 4 for diagonal movement. Therefore, the numbers in the start node are 2 and 0 to show the heuristic that is used in this case. Then the algorithm will evaluate the neighbors' values of the start node. One of them has values of 17 and 1. Because the goal node is 8 nodes away from that node, the $h(s, s_{goal})$ is 16. Because g value of the node is 1 (calculated in line 5 in Fig. 1), the top number is 17. This node is the start node's neighbor, which has the smallest value of its neighbor values. Therefore, this node will be the path and its neighbors will be evaluated to find the other node that has the smallest value again. If this process will run until the goal node is evaluated, the path planning is finished. Detailed explanation of this algorithm can be found in references [5] for both A* algorithm and D* Lite algorithm path planning.

D* Lite algorithm has a little bit different way in planning the path. The algorithm and illustration of simple D* Lite algorithm path planning are shown in Fig. 3 and Fig. 4, respectively. Basically how D* Lite algorithm works is very similar with how A* algorithm works. Only D* Lite algorithm different from A* algorithm is in the direction of the algorithm work because the D* Lite algorithm is calculated from s_{goal} . Furthermore, there is a new parameter, i.e. rhs (right hand side) which is a one-step look-ahead cost. Similarly to A*, D* Lite algorithm utilizes a heuristic and a priority queue to perform its search and to order its cost updates efficiently. The heuristic in this algorithm is different with that in the A* algorithm. In D* Lite algorithm, the heuristic value is the distance from the state to s_{start} . So if the state is 4 nodes away

from the s_{start} , the heuristic value is also 4. Fig. 4(b) shows the number description of the node, whereas Fig. 4(c) and Fig. 4(d) show the first and second calculation of the D* Lite algorithm, respectively. According to Koenig and Likhachev, D* Lite algorithm can be two times more efficient in replanning a new path than A* algorithm because A* algorithm has to replan the path from the beginning whereas D* Lite algorithm do not replan the path because it already has information of the surroundings from the first search [7].

key(s)

01. return $\min(g(s), rhs(s)) + h(s_{start}, s); \min(g(s), rhs(s))$;

UpdateState(s)

02. if s was not visited before

03. $g(s) = \infty$;

04. if ($s \neq s_{goal}$) $rhs(s) = \min_{s' \in Succ(s)}(c(s, s') + g(s'))$;

05. if ($s \in OPEN$) remove s from $OPEN$;

06. if ($g(s) \neq rhs(s)$) insert s into $OPEN$ with key(s);

ComputeShortestPath()

07. while ($\min_{s \in OPEN}(key(s)) < key(s_{start}) \text{ OR } rhs(s_{start}) \neq g(s_{start})$)

08. remove state s with the minimum key from $OPEN$;

09. if ($g(s) > rhs(s)$)

10. $g(s) = rhs(s)$;

11. for all $s' \in \text{Pred}(s)$ UpdateState(s');

12. else

13. $g(s) = \infty$;

14. for all $s' \in \text{Pred}(s) \cup \{s\}$ UpdateState(s');

Main()

15. $g(s_{start}) = rhs(s_{start}) = \infty; g(s_{goal}) = \infty$;

16. $rhs(s_{goal}) = 0; OPEN = \emptyset$;

17. insert s_{goal} into $OPEN$ with key(s_{goal});

18. forever

19. ComputeShortestPath();

20. Wait for changes in edge costs;

21. for all directed edges (u, v) with changed edge costs

22. Update the edge costs $c(u, v)$;

23. UpdateState(u);

Fig. 3. D* Lite algorithm [5]

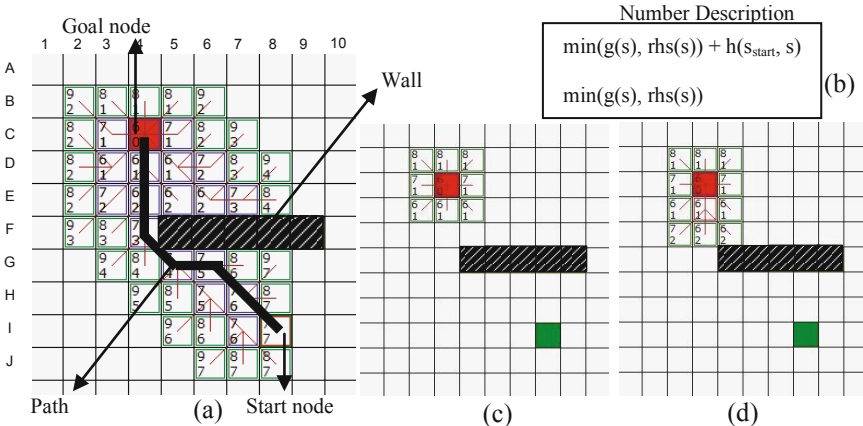


Fig. 4. Illustration of D* Lite algorithm path planning

3 System Configuration

In this experiment, a differential drive AGV is used as the experimental system. Fig. 5 shows the configuration of the AGV system. The main controller uses Tank-800 industrial computer. The connection for the industrial computer and motor driver uses half PCI MMC Board. The system has four wheels where two wheels are passive castor wheels mounted at the front and back side of AGV and the others are two driving wheels mounted at the left and right side of AGV. The driving wheels are driven by 200W/3,000 rpm BLDC motors. LCD screen used for monitoring process is mounted on the back side of the body. The AGV system is powered by 2 pieces of 12V/8AH batteries.

AGV uses NAV200 for positioning in absolute coordinate and LMS151 for obstacle detection. How the AGV works is explained as follows. First, AGV will make a map by using data from LMS151. From this map, AGV can know the surroundings of the system including the presence of obstacles. Then AGV will measure its position based on data from NAV200 sensor. After that, AGV will execute the path planning algorithm to get the path where AGV should go from current position to goal position. The next step is trajectory tracking of the path that has been built. All of these processes can be monitored from monitor. The controller will send signal to both left and right motor drivers such that they supply voltage signal to the motors to rotate according to the signal from controller. The trajectory tracking of AGV is controlled by feedback control system to make the AGV track the trajectory well.

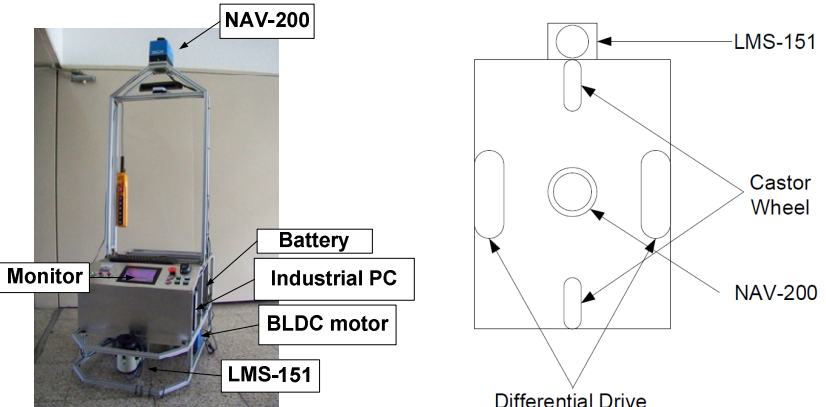


Fig. 5. Configuration of AGV System [8]

If there are unknown obstacles that suddenly appear in the surrounding, the LMS 151 will detect the object and path planning algorithm will plan a new path. This process is called path replanning and performed continuously until the AGV reaches the goal position safely.

4 Simulation and Experimental Results

The experimental comparison was conducted in two ways, i.e. simulation and experiment. In the simulation, comparison was conducted by comparing the computation time needed for generating trajectory and the distance of the generated trajectory that A* and D* Lite algorithms make. After the path is planned by both A* and D* Lite algorithm, the experimental comparison is conducted by applying the generated path to the AGV.

Fig. 6 shows the simulation results generated by A* and D* Lite path planning algorithms. The result of A* path planning algorithm is shown in Fig. 6(a), whereas the result of D* Lite algorithm in Fig. 6(b). How the path is built is explained in section 2. As it can be seen that D* Lite algorithm generates the shorter distance path from start point to goal point with faster time than A* algorithm. A* algorithm generates the path with 20 nodes in 0.0048 sec, whereas D* Lite algorithm generates the path with 17 nodes in 0.0028 sec. It can be concluded that D* Lite algorithm is able to plan a shorter path with faster time than A* algorithm.

The next comparison is conducted by experiment. Fig. 7 shows simple experimental results that make the AGV to plan a path from start node to goal node by avoiding an obstacle using A* algorithm (a) and D* Lite algorithm (b). But this experiment can show that D* Lite algorithm can also be less effective than A*

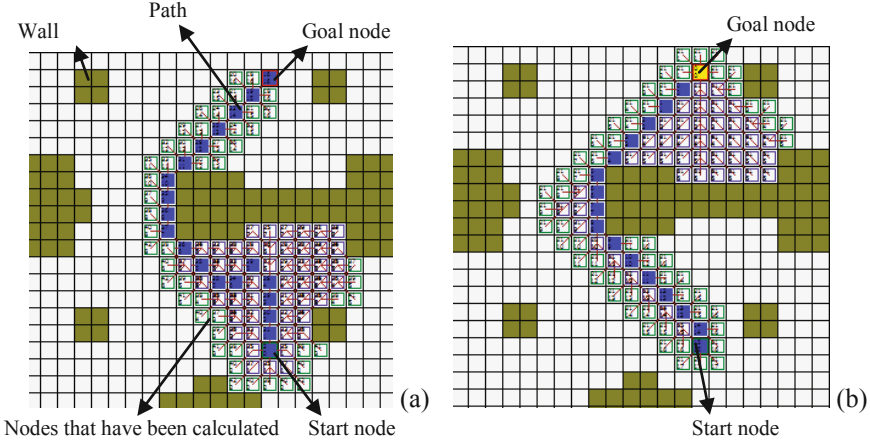


Fig. 6. Simulation results of A* algorithm (a) and D* Lite algorithm (b)

algorithm because D* Lite algorithm calculates more nodes to plan the shortest path with the purpose of replanning the path in case that unknown obstacles suddenly appear. Fig. 8(a) shows that the AGV trying to avoid obstacle, and Fig. 8(b) shows that it can successfully avoid the obstacle along the planned path in experiment.

In this case, both A* algorithm and D* Lite algorithm generate the path with 15 nodes from start point to goal point. But A* algorithm generates the path only in 0.0003 second, whereas D* Lite algorithm in 0.0052 second. However, if there is unknown obstacles in the path that make the algorithm to replan, D* Lite algorithm will be more effective because it only needs to replan with data that have been calculated before, whereas A* algorithm has to replan and calculate the path from the beginning that makes the replanning process longer than D* Lite algorithm. An example of path replanning using A* algorithm and D* Lite algorithm are shown in Fig. 9 and 10, respectively.

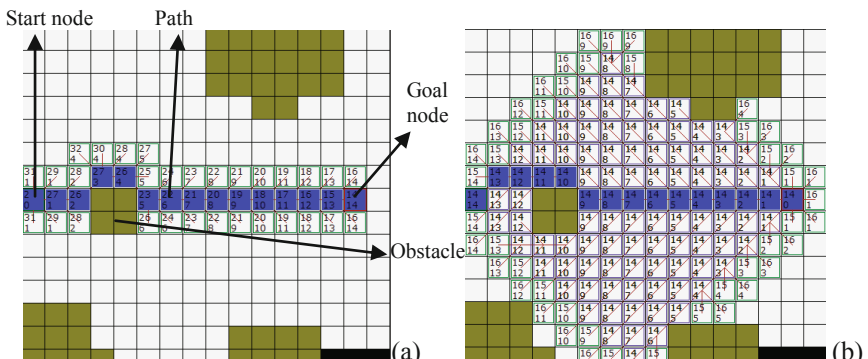


Fig. 7. Experimental results of A* algorithm (a) and D* Lite algorithm (b)

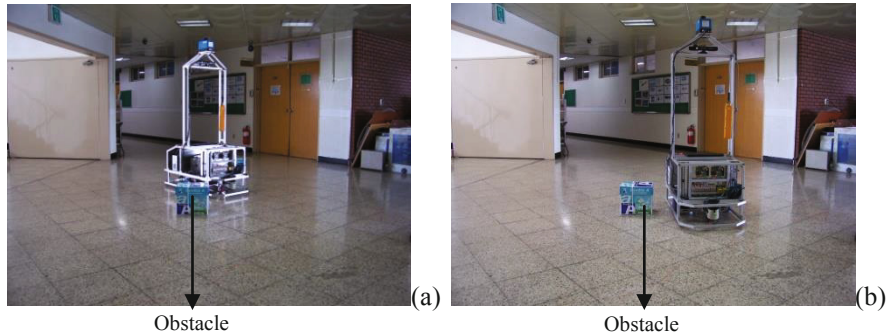


Fig. 8. Experiment results of path planning algorithm using differential drive AGV

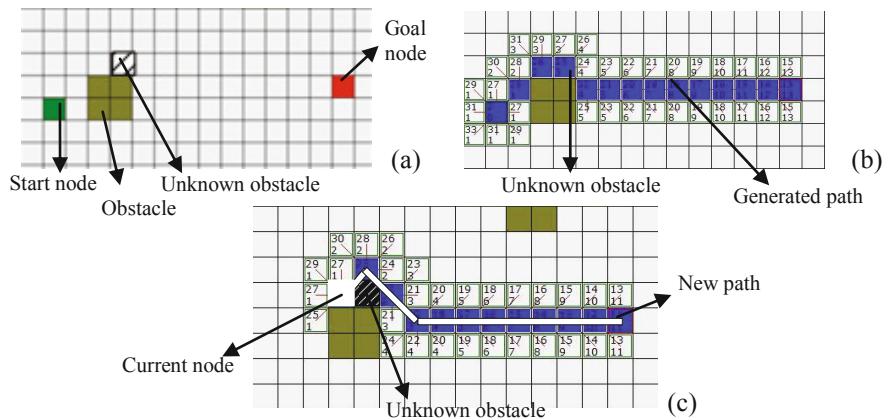


Fig. 9. Simulation results of A* path replanning algorithm

Basically, A* and D* Lite path replanning algorithms work similarly. The two replanning algorithm processes are compared in this section. Firstly, the start node of the robot is defined as shown in Fig. 9(a) for A* algorithm and Fig. 10(a) for D* Lite algorithm. Because at the start state the robot does not know that there is unknown obstacle in the surroundings, the robot plans the shortest path to the goal state that passes the unknown obstacle, which is illustrated in both Fig. 9(b) and Fig. 10(b). After the path is built, the robot tracks the generated path until the robot meets the unknown obstacle, as illustrated in Fig. 9(c) and Fig. 10(c). Because the robot cannot pass through the obstacle, it replans the path by using information data that have been obtained in the first search for D* Lite algorithm, whereas A* algorithm will replan the path from the beginning. Finally, the robot replans a path illustrated in Fig. 9(c) and Fig. 10(d) and tracks the new path to the goal state.

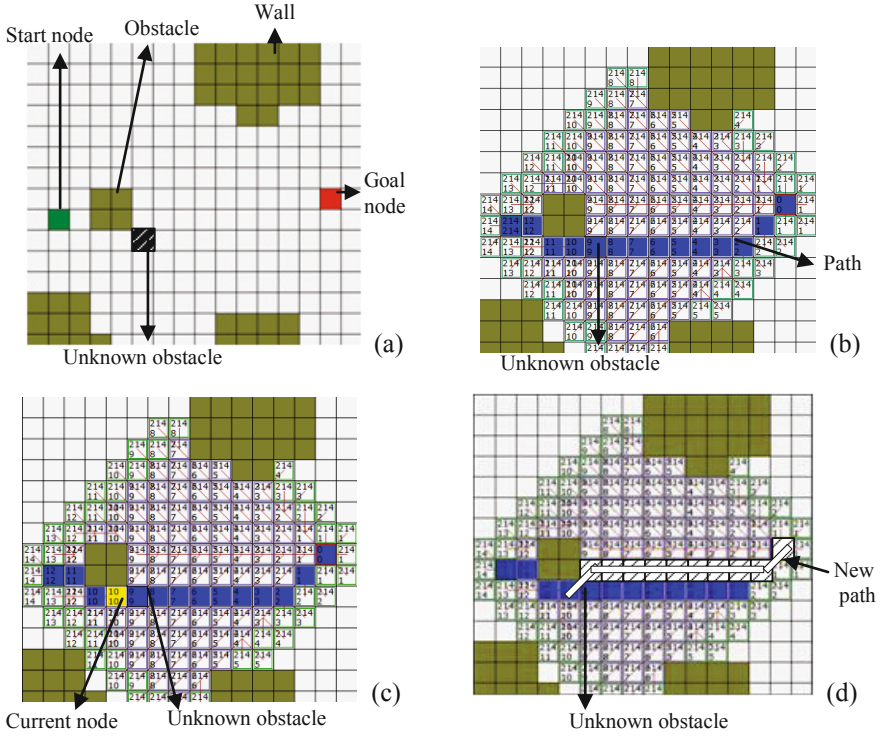


Fig. 10. Simulation results of D* Lite path replanning algorithm

In replanning case, which of algorithms is better depends on the size of the state space. If the state space has a big size, D* Lite algorithm is better than A* algorithm by giving a faster path replanning. This is because D* Lite algorithm evaluates more nodes at the first search such that replanning the path can be very fast, whereas A* algorithm has to replan it from beginning. However if the state space is small and simple like the example of replanning in Fig. 9 and 10, the A* algorithm will be more effective than D* Lite algorithm because D* Lite algorithm evaluates too many nodes. In that example, the total time is needed for A* algorithm to replan is 0.0047 second, whereas D* Lite algorithm takes 0.2988 second.

5 Conclusion

This paper presented simulation and experimental comparison results of A* algorithm and D* Lite algorithm for path planning of AGV. This research was done to give a guide for users in choosing which path planning algorithm should be used in a certain system. The simulation and experimental results show that D* Lite algorithm can plan the shorter path in a shorter time than A* algorithm because D* Lite algorithm uses heuristic to restrict the replanning process to only states that are relevant for repairing

the path. However, D* Lite algorithm can also be less effective than A* algorithm in some cases. Thus the use of these algorithms depends on the requirement of a system.

Acknowledgments. This research was supported by a grant from Construction Technology Innovation Program (CTIP) funded by Ministry of Land, Infrastructure and Transport (MOLIT) of Korean Government.

References

1. Nilsson, N.: Problem-Solving Methods in Artificial Intelligence. McGraw-Hill (1971)
2. Koenig, S., Likhachev, M.: Incremental A*. In: Proceedings of the Neutral Information Processing Systems (2001)
3. Stentz, A.: The Focused D* Algorithm for Real-Time Replanning. In: Proceedings of the International Joint Conference on Artificial Intelligence, pp. 1652–1659 (1995)
4. Koenig, S., Likhachev, M.: D* Lite. American Association for Artificial Intelligence (2002)
5. Ferguson, D., Likhachev, M., Stentz, A.: A Guide to Heuristic-based Path Planning. American Association for Artificial Intelligence (2005)
6. Koenig, S., Likhachev, M.: Fast Replanning for Navigation in Unknown Terrain. IEEE Transactions on Robotics 21(3) (2005)
7. Koenig, S., Likhachev, M.: Improved Fast Replanning for Robot Navigation in Unknown Terrain. In: Proceedings of the IEEE International Conference on Robotics and Automation-ICRA (2002)
8. Pratama, P.S., Jeong, S.K., Park, S.S., Kim, S.B.: Moving Object Tracking and Avoidance Algorithm for Differential Driving AGV Based on Laser Measurement Technology. International Journal of Science and Engineering 4(1), 11–15 (2013)

Study on Design for a New Underwater Disk Robot

Ngoc-Huy Tran, Hyeung-Sik Choi^{*}, Sang-Seob Lee, and Jeong-min Seo

Division of Mechanical and Energy Systems Engineering,
Korea Maritime University, Pusan, Korea
tran_huy1984@yahoo.com, hchoi@hhu.ac.kr

Abstract. This paper describes an analysis of the architecture and control system of a new disk-shaped underwater robot entitled an underwater disk robot (UDR) which has six degrees of freedom (DOF) motion. The UDR has three symmetrical thrusters disposed around the perimeter of a circular chassis, each facing 120 degrees apart from the others. With this disposition, the UDR has omnidirectional manoeuvrability without heading motion. Also, motion of the disk-shaped UDR can be less affected by side disturbances with a robust and swift motion along any directions. The planar motion mechanism (PMM) test and computational fluid dynamics (CFD) analysis were carried out to predict the drag force on the UDR body. Finally, the mechanical design of the UDR and the dynamics analysis including actuator mechanics were presented.

Keywords: Disk robot, autonomous underwater vehicle, Extended Kalman Filter.

1 Introduction

Unmanned undersea vehicles (UUV) have become a main tool for surveying undersea in scientific, military and commercial applications which are no risks for human [1]. Despite of considerable improvement in UUV performance, there are still many difficulties for scientists and engineers. Some of these hard tasks are how to design the shape with low hydrodynamic drag and how to dispose actuators for robust or swift motion along any directions [2] [3]. One of the solutions is the disk shape of the UUV hull. The disk-shaped profile of the vehicle hull has good performance to achieve the least side disturbance effects in the horizontal movement [4]. However, only a number of disk-shaped UUVs have been developed so far. The AQUA2 built at McGill University of Canada is flat-shaped [5]. The Shanghai Jiaotong university performed research on a dish-shaped robot [6]. Although these robots have flat shapes, the thrusters or rudder exposed outside makes its body easy to be damaged or wounded by flexible obstacles such as fish net. Moreover, a fast maneuverability is limited to a certain direction because thrusters are disposed along a certain direction [7].

To enhance performance of the UUVs mentioned above, we have developed a new six DOF UDR with disk-shaped hull and symmetrically disposed thrusters by 120

* Corresponding author.

degrees as shown in Fig.1. The horizontal thrusters are redundantly deployed so that UDR can move any directions with equal and robust thrust forces.



Fig. 1. The disk-shaped UDR

2 Vehicle Design

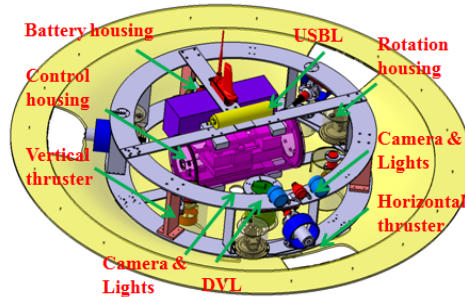


Fig. 2. The virtual and developed internal structure of the UDR

The body of the UDR is designed as disk-shaped vehicle in order to minimize the effect of water resistance from side disturbances such as currents or wave effects. However, this is a difficult problem since equipments such as thrusters, control system, sensors, camera, and lights should be included inside. In this paper, an architecture design of the UDR including all equipments is presented. The schematic design of the disk-shaped UDR is shown in Fig.2 and schematic architecture design of the system is described in table 1.

Table 1. A concept design of UDR system

Hull structure specifications	Diameter: 1.9m Height: 0.45m Max. Speed: 2 Knots
Actuators	3 vertical thrusters, 3 horizontal thrusters, 3 RC motors for rotation
Control system module	Embedded computer, Processors DSP28335, XMEGA 128A1
Navigation sensors	IMU sensor, DVL, USBL, GPS, Pressure sensor

2.1 Design of UDR Architecture

The propulsion system is composed of three vertical and three horizontal thrusters. The vertical thrusters inside the vertical channels are mounted upward on the perimeter of a circular chassis. Using the vertical thrusters, the UDR can perform heaving, rolling and pitching motion. The horizontal thrusters are mounted on the perimeter of a circular chassis. They are installed in the side direction for horizontal motion. The horizontal thrusters are disposed 120 degrees apart facing outward. The disposition of the horizontal thrusters yields a vector propulsion force along the horizontal direction. And a RC motor using a coupled belt and pulley arrangement is installed on each horizontal thruster to rotate the thrusting direction by $\delta \in \left[-\frac{\pi}{12}, \frac{\pi}{12} \right]$ as shown in Fig.3. Using the horizontal thrusters, the UDR can perform surging, swaying, and yawing motion. Hence, six DOF motion is possible with this disposition.

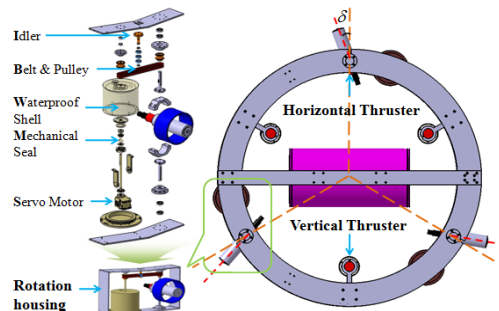


Fig. 3. The vectored propulsion scheme

2.2 Modeling of the UDR

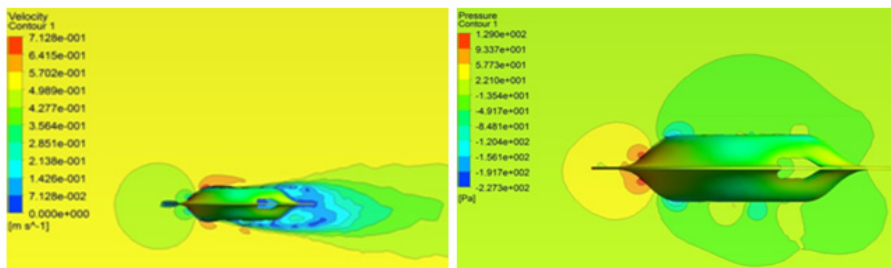


Fig. 4. Velocity and pressure distribution on the UDR body at speed 1 knot

To select appropriate thrusters to satisfy the required speed of the UDR, the drag force on the UDR body is predicted by the CFD analysis first and then compared with PMM test result.

Fig. 4 shows the pressure and velocity distribution around the UDR body. The x-directional velocity of the vehicle is 0.514 m/s (1 knot). The flow is accelerated when it reaches the stem and reduced at the stern of the UDR.

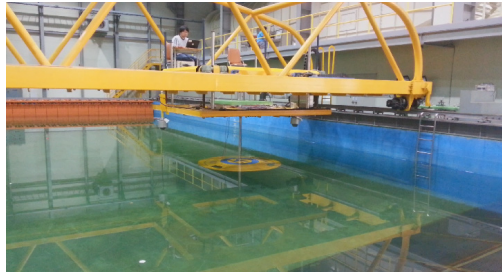


Fig. 5. Predicted drag force on the UDR body by PMM test

As shown in Fig. 5, the PMM test is carried out to predict the drag force around on the UDR body. According to maximum design velocity of the vehicle, the CFD analysis and PMM test should be performed to 2 knots. But at this velocity, derived moment values from the PMM test can make overload to sensor system. So the initial velocities of the UDR are only less than 1 knot. Hence, the drag force result of PMM test is 33.71N and CFD analysis is 28.144N at 1 knot. In general, these values are in good agreement with small different.

2.3 Design of the Control System

As shown in Fig.6, the UDR control system is composed of six parts which include a control system, navigation, power, propulsion, observation, and communication module.

The power module is composed of a lithium battery pack and DC/DC converter board contained in the battery housing. The power consumption of parts of the UDR is 2500W.

The propulsion module shown in Fig.3 is composed of three vertical 400HFS-L thrusters 400W, three horizontal thrusters 300W, and three RC motors.

The navigation module is composed of IMU, DVL, GPS, and a pressure sensor. They are used to determine the position, velocity, acceleration, path, and distance traveled of the vehicle. The UDR is equipped with an inertial navigation system (INS), which calculates the position, velocity, and attitude of the vehicles from the data given by the IMU sensor. Since INS accumulates errors due to the inherent drift of dead-reckoning velocities and integration of acceleration, an Extended Kaman Filter (EKF) algorithm is implemented, which utilizes a wide range of navigation sensors, to compensate for the accumulation in position error [8]. The DVL, NavQuest 600 with accuracy $< 0.2\% \pm 1\text{mm/s}$, is applied to slow down the position error growth in long submerged operations. The GPS, which has static accuracy of less than 1 meter, provides the position updates of the UDR when it is on the surface. In addition, the attitude and depth errors are reduced by using the pressure sensor signal and compass signal.

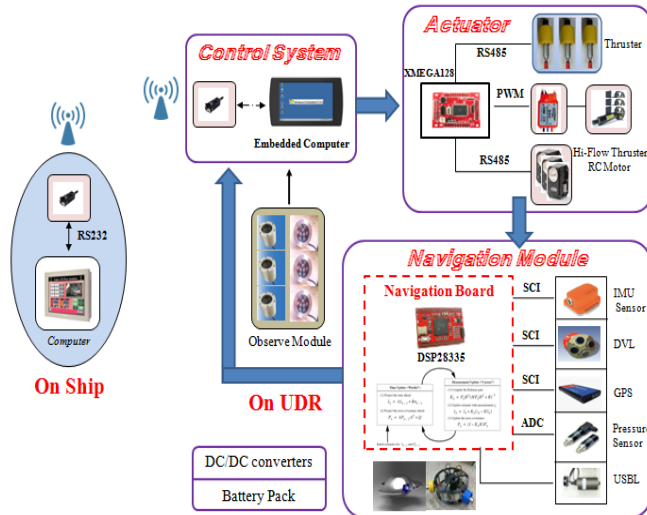


Fig. 6. Hardware architecture of UDR motion control system

The control system module contains the embedded computer IEC667 connected with two microprocessors TMS320F28335 (digital signal processors, DSP) and XMEGA128A1, which work together to perform all control tasks, as shown in Fig. 5. The TMS320F28335 processor, programmed in the navigation module, calculates the velocity, attitude and position of the UDR by using EKF, and transfers the results to the embedded computer. After receiving the data from the navigation module as well as from the observation module, automatically the IEC667 computes an optimal trajectory or path for the UDR and give commands to XMEGA128A1 for the propulsion module. Moreover, when the vehicle is on the surface, the IEC667 can receive commands directly from the control center on the ship via the RF communication module.

3 Dynamic Modeling of the Vehicle

A coordinate system fixed at the body of the vehicle, called a body-fixed coordinate system, with its origin at the center of vehicle buoyancy, is used to build a dynamics model of the UDR. The motion of the body-fixed frame is described relative to an inertial or earth-fixed reference frame, as shown in Fig. 7.

In order to simplify the dynamics of the UDR model, the following assumptions are made:

- The vehicle is a rigid body of constant mass during operation.
- The effects of the vehicle's own wake are ignored.
- The vehicle is deeply submerged in a homogeneous fluid.

3.1 Vehicle Kinematics

As shown in Fig. 7, (x, y, z) and (ϕ, θ, ψ) are the position and orientation of the vehicle with respect to the inertial reference frame, respectively. The following coordinate transform relates the translational velocities between the body-fixed and inertial coordinates:

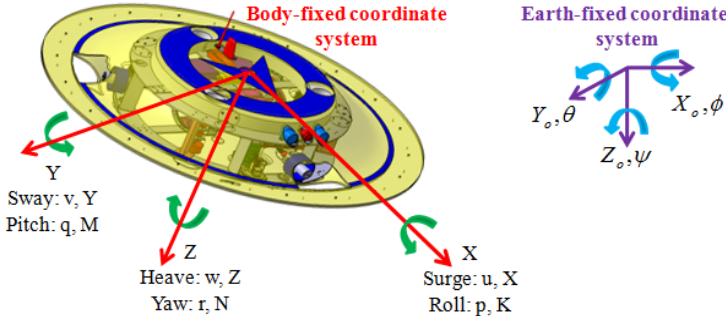


Fig. 7. Body-fixed and inertial coordinate systems

$$\begin{bmatrix} \dot{x} \\ \dot{y} \\ \dot{z} \end{bmatrix} = J_1(\eta_2) \begin{bmatrix} u \\ v \\ w \end{bmatrix} \quad (1)$$

The second coordinate transform relates the rotational velocities between the body-fixed and inertial coordinates:

$$\begin{bmatrix} \dot{\phi} \\ \dot{\theta} \\ \dot{\psi} \end{bmatrix} = J_2(\eta_2) \begin{bmatrix} p \\ q \\ r \end{bmatrix} \quad (2)$$

Note that $J_2(\eta_2)$ is not defined for pitch angle $\theta = \pm 90^\circ$ as the vehicle motion does not ordinarily approach this singularity. If it becomes necessary to model the vehicle motion through extreme pitch angles, an alternate kinematic representation such as quaternions or Rodriguez parameters can be used.

3.2 Vehicle Dynamics

In the following sections, the 6 DOF nonlinear dynamic equations of motion are conveniently expressed as:

$$M\ddot{v} + C(v)\dot{v} + D(v)v + g(\eta) = \tau \quad (3)$$

where

M : Inertia matrix (including added mass)

$C(v)$: Matrix of Coriolis and centripetal terms (including added mass)

$D(v)$: Damping matrix

$g(\eta)$: Vectors of gravitational forces and moments

τ : Vectors of control inputs

Given that the origin of the body-fixed coordinate system is located at the center of buoyancy as noted, from equation (3), the 6-DOF equations of motion for a rigid body can be expressed in terms of body-fixed coordinates [9]:

$$\begin{aligned}
 m[\dot{u} - vr + wq - x_g(q^2 + r^2) + y_g(pq - \dot{r}) + z_g(pr + \dot{q})] &= \sum X \\
 m[\dot{v} - wp + ur - y_g(r^2 + p^2) + z_g(pr - \dot{p}) + x_g(qp + \dot{r})] &= \sum Y \\
 m[\dot{w} - uq + vp - z_g(p^2 + q^2) + x_g(rp - \dot{q}) + y_g(rq + \dot{p})] &= \sum Z \\
 I_{xx}\dot{p} + (I_{zz} - I_{yy})qr - (\dot{r} + pq)I_{xz} + (r^2 - q^2)I_{yz} + (pr - \dot{q})I_{xy} \\
 + m[y_g(\dot{w} - uq + vp) - z_g(\dot{v} - wp + ur)] &= \sum K \\
 I_{yy}\dot{q} + (I_{xx} - I_{zz})rp - (\dot{p} + qr)I_{xy} + (p^2 - r^2)I_{xz} + (qp - \dot{r})I_{yz} \\
 + m[z_g(\dot{u} - vr + wq) - x_g(\dot{w} - uq + vp)] &= \sum M \\
 I_{zz}\dot{r} + (I_{yy} - I_{xx})pq - (\dot{q} + rp)I_{yz} + (q^2 - p^2)I_{xy} + (rq - \dot{p})I_{xz} \\
 + m[x_g(\dot{v} - wp + ur) - y_g(\dot{u} - vr + wq)] &= \sum N
 \end{aligned} \tag{4}$$

Where

- u, v, w : Surge, sway, heave velocities respectively.
- p, q, r : Roll, pitch, yaw rates.
- X, Y, Z : External forces.
- K, M, N : External moments.
- x_g, y_g, z_g : Center of gravity with respect to the origin at the center of buoyancy.
- I_{ab} : Moments of inertia with respect to the origin at center of buoyancy (a, b symbolize x, y, z).

3.3 Mechanics of the Propulsion System

With the 120 degrees symmetrical vector disposition of the horizontal and vertical thrusters, the UDR has six DOF and robust underwater motion under side disturbances.

The horizontal propulsion module: Each horizontal thruster is rotated by the RC motor, so it can rotate around its axis within the bound $\delta \in \left[-\frac{\pi}{12}, \frac{\pi}{12}\right]$ (rad).

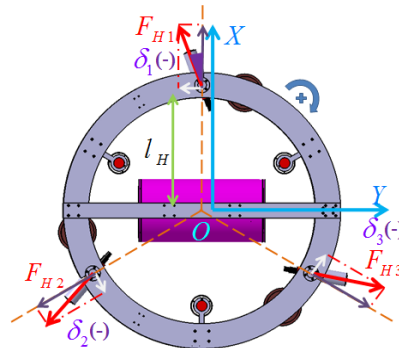


Fig. 8. The horizontal thrust forces with $\delta_1, \delta_2, \delta_3$ (rad)

In case $\delta_1 = \delta_2 = \delta_3 = 0$ (rad) shown in Fig.8, the total thrust forces along the X-axis and Y-axis:

$$\begin{bmatrix} X_T \\ Y_T \end{bmatrix} = \begin{bmatrix} 1 & -0.5 & -0.5 \\ 0 & -\frac{\sqrt{3}}{2} & \frac{\sqrt{3}}{2} \end{bmatrix} \begin{bmatrix} F_{T1} \\ F_{T2} \\ F_{T3} \end{bmatrix} \quad (5)$$

In case $\delta_1 = \delta_2 = \delta_3 \neq 0$ (rad) described in Fig.7, the thrust forces include the force along the UDR center $\overrightarrow{F_{TnP}}$, the force $\overrightarrow{F_{TnR}}$ is perpendicular to $\overrightarrow{F_{TnP}}$ for $n=1, 2, 3$. We have:

$$F_{Tn} = |\overrightarrow{F_{Tn}}| = |\overrightarrow{F_{T2}}| = |\overrightarrow{F_{T3}}| \quad (6)$$

The total force $\overrightarrow{F_T}$ in this case is zero:

$$\overrightarrow{F_T} = \overrightarrow{F_{T1}} + \overrightarrow{F_{T2}} + \overrightarrow{F_{T3}} = \vec{0} \quad (7)$$

The moment N_T makes UDR rotate around Z-axis:

$$N_T = 3F_{Tn}l_T \sin \delta \quad (8)$$

where L_T is the distance from the center to thruster side.

The vertical propulsion module: The vertical thruster is placed with a distance l_H from center. They make the vertical forces with direction along the UDR Z-axis as shown in Fig.9.

The total vertical force on the Z-axis:

$$Z_H = F_{H1} + F_{H2} + F_{H3} \quad (9)$$

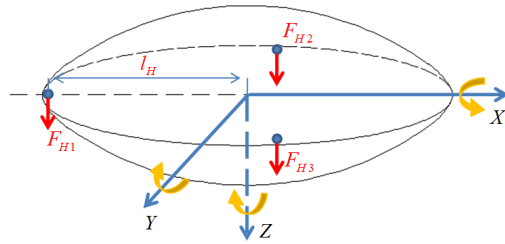


Fig. 9. The vertical forces on the UDR

The moment on the X-axis:

$$K_H = \frac{\sqrt{3}}{2} l_H (-F_{H2} + F_{H3}) \quad (10)$$

The moment on the Y-axis:

$$M_H = l_H \left(\frac{F_{H2} + F_{H3}}{2} - F_{H1} \right) \quad (11)$$

4 Conclusion

The mechanical design of the new six DOF disk-shaped UDR and the dynamics analysis on the actuator mechanics were performed and presented. The UDR has three symmetrical horizontal and three symmetric vertical thrusters disposed around the perimeter of a circular chassis. With these thruster positions, the vehicle has robust, omnidirectional manoeuvrability without heading motion. The streamline disk shape is chosen for the hull to allow the UDR to move flexibly with a low drag force in the horizontal direction. To select the appropriate thrusters to satisfy the required speed of the UDR, the drag force on the UDR body was predicted by the CFD analysis first and then compared with PMM test result. In addition, the control system of the UDR was also designed and presented.

Acknowledgements. This work was supported by the Ministry of Land, transportation and Maritime Affairs (MLTM) of Korea for the development of multi-legged walking and flying subsea robot.

References

1. Manley, J.E.: Unmanned Surface Vehicles, 15 Years of Development. In: Proceedings of Oceans 2008, Quebec City, Canada (September 2008)
2. Roman, C., Pizarro, O., Eustice, R., Singh, H.: A New Autonomous Underwater Vehicle for Imaging Research. In: Proceedings of Oceans 2000, MTS/IEEE, Providence, RI, USA (September 2000)

3. Gomes, R.M.F., Sousa, A., Fraga, S.L.: A New ROV Design: Issues on Low Drag and Mechanical Symmetry. In: Proceedings of Oceans, Europe (June 2005)
4. Wang, T., Ye, X., Wang, L., Zhang, C.: Hydrodynamic Analysis and Optimization for Dish Shaped Underwater Robot. In: Proceedings of the 2011, IEEE International Conference on Mechatronics and Automation, Beijing, China, August 7-10 (2011)
5. Dudek, G., Giguere, P., Prahacs, C.: AQUA: An Amphibious Autonomous Robot. *Proceedings of the Computer Journal* 40(1) (January 2007)
6. Zhang, H., Pan, Y.: The Resistance Performance of a Dish Shaped Underwater Vehicle. *Journal of Shanghai Jiaotong University* 40, 978–987 (2006)
7. Stokey, R.P., Roup, A., von Alt, C.: Development of the REMUS 600 autonomous underwater vehicle. In: Proceedings of Oceans 2005, MTS/IEEE, Woods Hole Oceanogr. Instn., MA, USA (June 26, 2006)
8. Tran, N.-H., Choi, H.-S., Kim, J.-Y.: Development of Rotational Motion Estimation for a UUV/USV based on TMS320F28335 Microprocessor. *International Journal of Ocean System Engineering (KSOE)*, 223–232 (2012)
9. Fossen, T.I.: Guidance and Control of Ocean Vehicles. John Wiley & Son, New York (1994)

Tracking Control of an Unmanned Surface Vehicle

Ngoc-Huy Tran, Hyeung-Sik Choi*, Se-Hoon Baek, and Hee-Young Shin

Division of Mechanical and Energy Systems Engineering,
Korea Maritime University, Pusan, Korea
tran_huy1984@yahoo.com, hchoi@hhu.ac.kr

Abstract. Nowadays, unmanned surface vehicle (USV) has been a special attention for marine research and surveying exploration in coastal area. This paper describes an analysis about architecture and control system of a USV disposed with three fixed thrusters. Therefore, hardware and software architectures of control system will be mentioned and functions of all parts are clarified. A strategy design for tracking waypoints is presented. And this algorithm will be checked by simulation and experiments.

Keywords: Unmanned Surface Vehicle, Waypoints Tracking, Dynamic Positioning, Extended Kalman Filter.

1 Introduction

Ocean is cradle of life, treasury resource and transportation artery. In the 21st century, we will face three challenges, such as the contradictions between population explosion and limited living space, between exhausted land resource and growing requirement of social production, between eco-environmental degradation and human development. Besides that, there exist sea regions with dangerous mines that should be eradicated for military affair, humanitarian reasons, and marine safety. So, it is necessary to use unmanned vehicles for ocean survey in coastal area, and support works for the underwater vehicles by aiding the communication and localization, with no risks for human as a priority, shown in Fig. 1.

Unmanned surface vessel (USV) is one of intelligent motion platforms, which can be relied on remote control or autonomous and safe navigation in the real marine environment and completely various tasks. USV has many great merits such as variegated functions, flexibility of operations, little injury and flexible network information center [1]. But it has no substantive research [2]. USV has only had 15~20 years of development and there are a number of USVs on the market or in use so far, especially compared to their Autonomous Underwater Vehicle (AUV) cousins. An Italian catamaran USV, called SESAMO, was used to support for oceanographic research [3]. The stability, payload capacity and ease for manufacturing make

* Corresponding author.

catamarans become a compelling choice for academic USVs. The ROAZ vehicles from Portugal, like SESAMO, exemplified of the general arrangements [4]. Also, there was a research on a mine disposal system using the autonomous marine surface vehicle (AMSV) [5], which has supported surveys and networked operations with AUVs. In general, USV will be highlighted for more special attention around the world in the future.



Fig. 1. The USV application

To enhance the performance of the USV, we have designed and implemented a flexible control system with three fixed thrusters and high accuracy sensors system. In this paper, some of salient technology features of our USV are introduced, and its performance is presented through a theoretic analysis and experiments.

The paper is organized as follows: section 2, vehicle dynamic and design are presented; in section 3, a design of control system; in section 4, a strategy design for waypoints tracking; respectively, simulation and experiments will be presented in section 5 and 6.

2 Vehicle Dynamic and Design

2.1 Dynamic of Vehicle

A vehicle is differentially described by six degrees of freedom (DOF) equations of motion. The position in three-dimensional space is notated by (x, y, z) that referred to surge, sway, and heave. The (ϕ, θ, ψ) , called roll, pitch, and yaw, describes the orientation of the vehicle. By assuming the vehicle is longitudinally and laterally stable with small amplitudes, we can discard the dynamics of roll and pitch. Likewise, since the vehicle is floating with $z=0$, we can discard the heave dynamics. The resulting model for a purpose of vehicle maneuvering in the horizontal plane becomes a three DOF model. The states of the vessel are then taken as $\eta = [x, y, \psi]^T$ and $v = [u, v, r]^T$ where (x, y) is the earth-fixed Cartesian position, ψ is the heading angle, (u, v) are the body-fixed linear velocities, and r is the yaw rate.

The earth-fixed velocity vector is related to the body-fixed velocity through the kinematic relationship

$$\dot{\eta} = R(\psi)v \quad (1)$$

where $R(\psi)$ is a rotation matrix

Let the origin ‘O’ of the body frame be taken as the geometric center point (CP) in the vehicle structure. Under the assumption that the vehicle is port-starboard symmetric, the center of gravity (CG) will be located a distance along the body x-axis. The three DOF nonlinear dynamic equations of motion can be expressed as [6]:

$$M\ddot{v} + C(v)\dot{v} + D(v)v = \tau + R(\psi)^T b + \omega(t) \quad (2)$$

where M is inertia matrix, $C(v)$ is the Coriolis and centripetal matrix, $D(v)$ is damping matrix, τ is actuator forces and moments, b is a slowly varying bias in the earth frame, and $\omega(t)$ is a exogeneous disturbance due to waves and wind forces.

Neglecting vertical motion and high order damping term, and selecting surging and yawing motions for simplicity, we can abbreviate the three DOF nonlinear dynamic equations (2) to linear dynamic equations as following form [7]:

$$\begin{bmatrix} m - X_{\dot{u}} & 0 & 0 \\ 0 & m - Y_{\dot{v}} & mx_g - Y_r \\ 0 & mx_g - N_{\dot{v}} & I_z - N_r \end{bmatrix} \begin{bmatrix} \dot{u} \\ \dot{v} \\ \dot{r} \end{bmatrix} + \begin{bmatrix} -X_u & 0 & 0 \\ 0 & -Y_v & -Y_r \\ 0 & -N_v & -N_r \end{bmatrix} \begin{bmatrix} u \\ v \\ r \end{bmatrix} = \begin{bmatrix} X \\ Y \\ N \end{bmatrix} \quad (3)$$

where m is vehicle mass, $X_{\dot{u}}, Y_{\dot{v}}, N_{\dot{v}}, N_r$ are added mass and moments, X_u, Y_v, N_v, N_r are hydrodynamic coefficients, x_g is distance of the center of gravity along body axis, (X, Y) are generalized external forces, N is generalized external moment.

According to the equation (3), to control surge, sway, and yaw motion, we designed three thrusters for the USV that will be described in the next section.

2.2 Mechanical Design

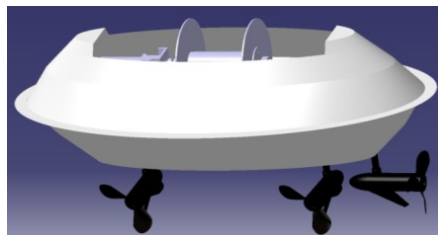


Fig. 2. The virtual design of the USV

The hull structure of USV is designed with closed-type cover so that water can't come inside. The body is made by stiffening processed from laminating FRP (Fiber Reinforced Plastic) which is high-corrosion resistant, light-weighted, and high durable. As shown in Fig. 2, the USV is designed with three thrusters. The main thruster disposed at the USV's stern is Endura50 with 50lbs (22.68kgf) thrust force, and two Endura30 lateral thrusters with 30lbs (13.61kgf) thrust force for each one. With this structure enclosed with a navigation system and control algorithm, the vehicle can flexibly move in multiple directions and automatically maintain at a desired position and heading.

3 Design of Control System

3.1 Hardware Architecture

As shown in Fig. 3, the USV control system is composed of six parts which include ground monitoring station, onboard control system, navigation, battery, actuator, and communication modules.

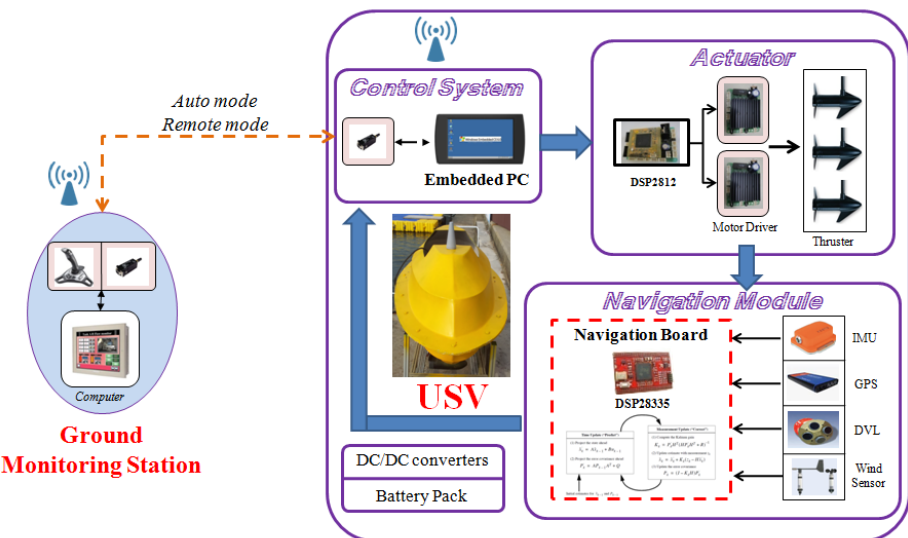


Fig. 3. Hardware architecture of the USV motion control system

The communication module is composed of a 24XStream RF one. It can transmit and receive a standard asynchronous serial data stream over-the-air between devices at 2.4 GHz operating frequency up to 10 miles with a high gain antenna. The 24XStream sends status data of the USV and receives control instructions transmitted by the other RF module on the ground.

The actuator module shown in Fig.3 is composed of one Endura50 thruster (500W) and two Endura30 thrusters (300W). Extra large windings and commutators are used to dissipate heat, resulting in cooler operation, extended battery power and longer motor life. Moreover, it can produce low rpms with high torque. So the USV will be very quiet when it operates.

The ground monitoring station is composed of computer, joystick, and wireless communication equipments. With visual multifunctional operating interface programmed by Visual Studio 2008, the USV can be controlled by two modes that are auto mode and remote mode. Furthermore, the ground monitoring station can also be built on a host ship or carried on another USV.

The navigation module is composed of IMU (Inertial Measurement Unit), compass, DVL (Doppler Velocity Logs), GPS, and wind sensor. The DVL, NavQuest 600 with accuracy $< 0.2\% \pm 1\text{mm/s}$, is applied to slow down the position error growth in long-distance operations. The GPS, which has static accuracy of less than 2 meter, provides the position updates of the USV. In addition, the attitude error, and error due to disturbance can be reduced by using compass signal, and the wind sensor signal.



Fig. 4. Appearance and components of the USV

The onboard control system module contains the embedded computer IEC667 connected with two microprocessors TMS320F28335 (Digital Signal Processors) and TMS320F2812, which cooperate together to perform all control tasks, as shown in Fig. 3. The TMS320F28335 processor, programmed in the navigation module, calculates the attitude, velocity, and position of the USV by using EKF (Extended Kalman Filter) algorithm, and transfers the calculated results to the embedded computer. After receiving the data from the navigation module as well as requirements from the ground monitoring station, automatically the IEC667 will

compute an optimal trajectory or path for the USV motion and will delivery control commands to TMS320F2812 for driving the actuator module. Moreover, at the same time, the IEC667 will inform about states of the USV and can receive commands from the control center on the ground via the RF (Radio Frequency) communication module. The completed appearance and components of the USV are shown in Fig. 4.

3.2 Software Architecture

According to the hardware architecture and mission of the unmanned vehicle, entire software of the USV includes two parts: ground monitoring system software and onboard control system software.

In the ground monitoring system, depending on different situations, the operator can select the remote control mode or the automatic control mode. The monitoring software can not only send pre-scheduled commands, and desired trajectories to the onboard control system but also transmit tuning parameters and control methods such as heading control, Dynamic Positioning (DP) control, waypoint tracking, and path tracking, etc...In addition, with question loop every 100ms, the ground monitoring system can update and log the states of the USV as well as onboard equipments and sensors during its operation.

The software architecture of the onboard control system includes some main blocks such as information processing, control task decomposition (remote control, heading control, waypoint tracking, DP control...), navigation and motion control algorithm, and sensors data processing. The information processing block is responsible for receiving commands from the ground monitoring station and sorting them according to separated missions. Then the missions will be completed by the next blocks. The state information of the USV as well as onboard equipment and sensors will be summarized to answer for question loop received from the ground monitoring station. In addition, the navigation and motion control algorithm block mainly processes the control missions (such as remote control, heading control, waypoint tracking, etc...), estimates the USV's navigation (shown detail in section 4). According to different kinds of control tasks, control instructions are calculated by the embedded computer and sent to the actuator module to operate.

4 Control Strategy for Waypoints Tracking

4.1 Navigation Algorithm for Motion Control

The USV is equipped with an Inertial Navigation System (INS), which calculates inertial position, velocity, and attitude of the vehicle from data given by the IMU sensor. Because of INS accumulative errors resulting from inherent drift of dead-reckoning velocities and integration of acceleration, an Extended Kalman Filter

(EKF) algorithm should be developed, which utilizes a wide range of navigation sensors, to compensate for the accumulation in errors (attitude, position, velocity). The error state Kalman filter is composed of four blocks that are estimate error covariance, Kalman gain computation, update error covariance, and update estimate with measurement [8]. In general, after applying EKF algorithm, we can estimate reliable attitude, position, and velocity values that used to accurately navigate the vehicle [9].

4.2 Waypoint Guidance Based on the Line of Sight (LOS)

Let the unmanned vehicle mission be given by a set of waypoint $[x_d(k), y_d(k)]$ for ($k=1\dots N$). If the desired heading angle is only changed at each waypoint, some overshoot will be observed when waypoint is changed. An alternative algorithm to generate a smooth reference trajectory is given, named LOS [6]. Hence, the desired heading angle:

$$\psi_d(t) = \tan^{-1}\left(\frac{y_d(k) - y(t)}{x_d(k) - x(t)}\right) \quad (4)$$

After the quadrant check is performed with the desired heading angle, the next waypoint can be selected on a basis of whether the vehicle lies within a circle of acceptance with radius ρ_0 around the waypoint $[x_d(k), y_d(k)]$. If the vehicle location $[x(t), y(t)]$ at the time t satisfies:

$$[x_d(k) - x(t)]^2 + [y_d(k) - y(t)]^2 \leq \rho_0^2 \quad (5)$$

the next waypoint $[x_d(k+1), y_d(k+1)]$ should be selected. A guideline could choose ρ_0 equal to two vehicle lengths.

4.3 The Fusion Control Algorithm

Fig. 5 shows the control algorithm diagram describing main functions of the USV control system influenced by environment (wave, current, wind). There are three objectives for motion control: position, heading, and speed. They are measured by using the GPS, IMU, DVL sensors, and their data are feedbacked to the filter module. An EKF algorithm was applied to filter noises out and to estimate the actual states of the USV. The PID-FUZZY controller generates force instructions for thrusters to compensate for position, yaw angle, and velocity errors of the USV. The allocation algorithm was developed to map the generalized force instructions into appropriate force instructions for the various actuators of the USV.

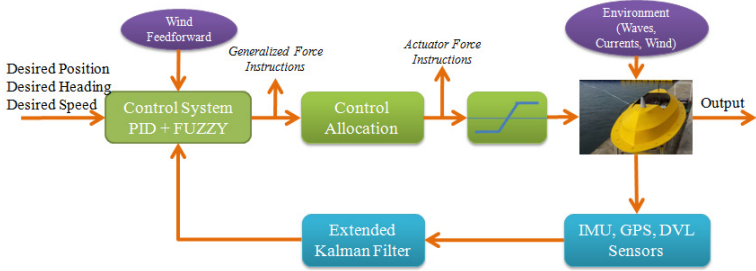


Fig. 5. The fusion control system of the USV

5 Simulation

The USV control simulation was carried out in Matlab/Simulink with designed PD controller, LOS algorithm (mentioned above), and parameters from the Cybership II [7]. In this simulation, the USV tracked four desired waypoints that were chosen as $(0, 0)$, $(40, 40)$, $(80, 0)$, $(40, -40)$ in horizontal plane. Initial conditions were selected as $x = [0, 0, 0]^T$, position at $(0, 0)$, and $\rho_0 = 1\text{ m}$.

Fig. 6 displays the simulated trajectory of the USV. The dashed red line was built by the four desired waypoints and the continuous blue line was the USV trajectory. The results demonstrated that the USV exactly moved to the desired position with stable heading.

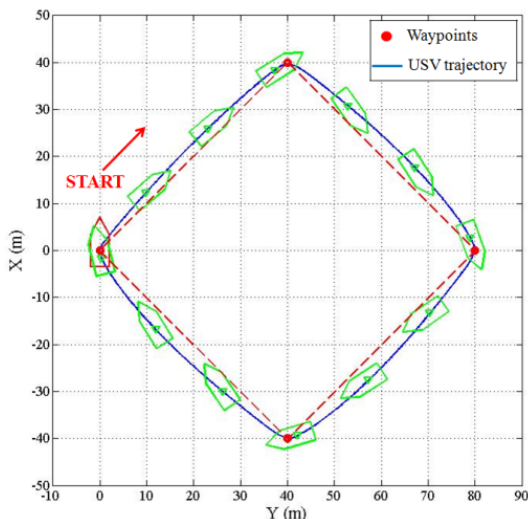


Fig. 6. The USV trajectory in horizontal plane

6 Experiments

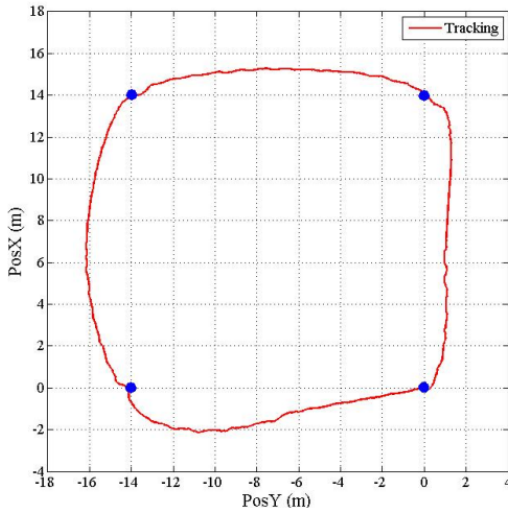


Fig. 7. Tracking the Square-type trajectory

In this test, the waypoints were given by the ground monitoring computer. Hence, we could easily select any kind of trajectories such as Square-type, S-type, Zigzag-type, etc... for tracking.

Fig. 7 shows result from a waypoints tracking experiment where the USV was programmed to track four predefined waypoints: (0, 0); (0, -14); (14, -14); (14, 0). According to the LOS algorithm (position between the vehicle and waypoints) as well as the current heading check, the USV was controlled to turn to the next waypoint and was guided to track the Square-type trajectory by passing all the waypoints.

7 Conclusion

In this paper, a design and implement about the architecture and control system of the three DOF unmanned surface vehicle was specifically presented. Besides, a strategy design for tracking waypoints was shown and simulated in horizontal plane. A waypoints tracking experiment was carried out to confirm the control performance of designed PD controller in the sea-trial. As a result, the USV could exactly move to the desired position with stable heading.

Acknowledgements. This work was supported by the Ministry of Land, transportation and Maritime Affairs (MLTM) of Korea for the development of multi-legged walking and flying subsea robot.

References

1. Roberts, G., Sutton, R.: Advances in Unmanned Marine Vehicle. Institution of Engineering and Technology (2006)
2. Manley, J.E.: Unmanned Surface Vehicles, 15 Years of Development. In: Proc. Oceans 2008 MTSIIEEE Quebec Conf. and Exhibition (Ocean 2008), pp. 1–4. IEEE Press (2008)
3. Caccia, M., Bono, R., Bruzzone, G., Bruzzone, G., Spirandelli, E., Veruggio, G., Stortini, A.M., Capodaglio, G.: Sampling sea surfaces with SESAMO. Robotics and Automation Magazine 12(3), 95–105 (2005)
4. Ferreira, H., Martins, R., Marques, E., Pinto, J., Martins, A.O., Almeida, J.M., Sousa, J.B., Silva, E.P.: Swordfish: An Autonomous Surface Vehicle for Network Centric Operations. In: Proceedings of the Oceans Europe 2007 Conference. IEEE OES, Aberdeen (2007)
5. Pereda, F.J., de Marina, H.G., Jiménez, J.F., Giron-Sierra, J.M.: A Development Project of Autonomous Marine Surface Vehicles for Sea Demining. In: Control, Automation, Robotics and Vision Conference, December 7–10. IEEE, Singapore (2010)
6. Fossen, T.I.: Guidance and Control of Ocean Vehicles. John Wiley & Sons Ltd. (1994)
7. Skjetne, R., Smogeli, Ø.N., Fossen, T.: A Nonlinear Ship Maneuvering Model: Identification and adaptive control with experiments for a model ship. Modeling, Identification and Control 25(1), 3–27
8. Titterton, D.H., Weston, J.L.: Strapdown inertial navigation technology, 2nd edn. American Institute of Aeronautics and Astronautics (2004)
9. Tran, N.H., Choi, H.S., Kim, J.Y., Lee, M.H.: Development of Rotational Motion Estimation System for a UUV/USV based on TMS320F28335 microprocessor. Int. J. of Ocean System Engineering 2(4), 223–232 (2012)

Integral Sliding Mode Control of Two-Wheeled Welding Mobile Robot for Tracking Desired Welding Path

Nguyen Hung*, Pham Hung Kim Khanh, and Than Van The

Faculty of Mechanical - Electrical - Electronic Engineering,
HCMC University of Technology, Vietnam

{n.hung, phk.khanh}@hutech.edu.vn, thanthe2012@gmail.com

Abstract. This paper proposes a new nonlinear controller that makes the combination of a kinematic controller (KC) and an integral sliding mode controller (ISMC) for a welding mobile robot (WMR) to track a desired welding path with a constant velocity. First, the kinematic controller is designed to make the position error vector go to zero asymptotically. Second, the integral sliding mode controller is designed to make velocity error vector also go to zero asymptotically. The stability of system is proved based on the Lyapunov stability theory. The simulation results are shown to illustrate effectiveness of the proposed nonlinear controller.

Keywords: kinematic controller, integral sliding mode controller, welding mobile robot.

1 Introduction

In the past years, there are many researches have been done for the welding mobile robot (WMR) using many kind of controller [1-3]. In [1], the simple nonlinear controller of WMR was applied for tracking reference welding path but considered only the kinematic model which ignored the mechanical system dynamic and external disturbances. Chung, et al. [2] proposed the sliding mode controller that integrates a kinematic controller and a dynamic controller with bounded external disturbances have been used to solve the path welding tracking problem for the WMR. Ngo, et al. [3] also proposed the adaptive sliding mode controller for the same WMR. In the above controllers, the WMR is considered in terms of dynamic model with known parameters in the presence of external disturbances. However, the linear velocity of welding point was not keep constant velocity smoothly as desired [2-4].

To solve the problem, this research proposes a new nonlinear controller that makes the integration of a kinematic controller and an integral sliding mode dynamic controller with bounded external disturbances for the WMR to track a desired welding trajectory. The system stability is proved using the Lyapunov stability theory. The

* Corresponding author.

simulation results are shown to illustrate effectiveness of the proposed nonlinear controller.

2 Modeling of Welding Mobile Robot

The configuration of the welding mobile robot for research is shown in Fig. 1. The kinematic and dynamic models of the WMR are presented with nonholonomic constraints. The WMR is modeled under the assumptions [2-4].

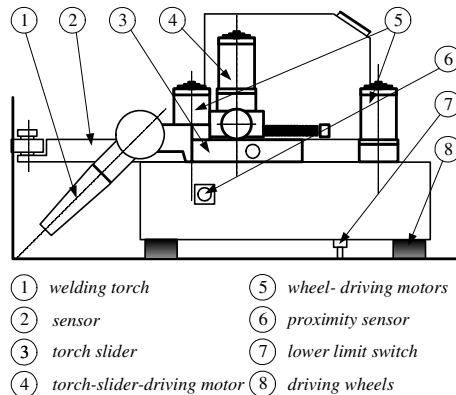


Fig. 1. Configuration of the WMR

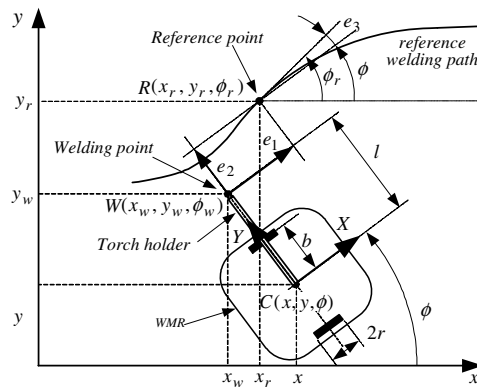


Fig. 2. Geometric configuration of the WMR

The geometric configuration of the WMR is also shown in Fig. 2 that has nomenclatures as the following:

(x, y)	: Coordinates of the WMR center [m]
ϕ	: Heading angle of the WMR [rad]
v	: Linear velocity of the WMR center [m/s]
ω	: Angular velocity of the WMR center [rad/s]
ω_{rw}, ω_{lw}	: Angular velocities of the right and the left wheels [rad/s]
(x_w, y_w)	: Coordinates of the welding point [m]
ϕ_w	: Heading angle of the welding point is equal to welding angle ϕ_r [rad]
v_w	: Linear velocity of the welding point [m/s]
ω_w	: Angular velocity of the welding point [rad/s]
x_r, y_r	: Coordinates of the reference point [m]
v_r	: Desired constant welding velocity [m/s]
ω_r	: Angular velocity of the reference point [rad/s]
b	: Distance between driving wheel and the symmetric axis [m]
r	: Radius of driving wheel [m]
l	: Torch holder length [m]

2.1 Kinematic Modeling

A reference point R moving with the constant velocity of v_r , the coordinates (x_r, y_r) , and the heading angle ϕ_r on the reference welding path satisfies the following equations:

$$\begin{cases} \dot{x}_r = v_r \cos \phi_r \\ \dot{y}_r = v_r \sin \phi_r \\ \dot{\phi}_r = \omega_r \end{cases} \quad (1)$$

Firstly, the kinematic equations for the center point of the WMR in the Cartesian space shown in to Fig. 2 are set up as the following:

$$\begin{bmatrix} \dot{x} \\ \dot{y} \\ \dot{\phi} \end{bmatrix} = \begin{bmatrix} \cos \phi & 0 \\ \sin \phi & 0 \\ 0 & 1 \end{bmatrix} \begin{bmatrix} v \\ \omega \end{bmatrix} \quad (2)$$

where $q = [x, y, \phi]^T$ is the posture vector of WMR rotating center point $C(x, y)$ in the Cartesian frame, $z = [v \ \omega]^T$ is the actual velocity vector.

The relationship between v, ω and the angular velocities of two driving wheels is given by

$$\begin{bmatrix} \omega_{rw} \\ \omega_{lw} \end{bmatrix} = \begin{bmatrix} 1/r & b/r \\ 1/r & -b/r \end{bmatrix} \begin{bmatrix} v \\ \omega \end{bmatrix} \quad (3)$$

Secondly, the kinematic equation of the welding point $W(x_w, y_w)$ which is fixed on the torch holder can be derived from the WMR's center $C(x, y)$ in Fig. 2 as follows:

$$\begin{cases} x_w = x - l \sin \phi \\ y_w = y + l \cos \phi \\ \dot{\phi}_w = \phi \end{cases} \quad (4)$$

The derivative of (4) yields

$$\begin{bmatrix} \dot{x}_w \\ \dot{y}_w \\ \dot{\phi}_w \end{bmatrix} = \begin{bmatrix} \cos \phi & -l \cos \phi \\ \sin \phi & -l \sin \phi \\ 0 & 1 \end{bmatrix} \begin{bmatrix} v \\ \omega \end{bmatrix} \quad (5)$$

2.2 Dynamic Modeling

The dynamic equations of the WMR with the external disturbances is as follows [2-4]:

$$\bar{M}(q)\dot{z} + \bar{V}(q, \dot{q})z + \tau_d = \tau \quad (6)$$

Where

$$\bar{M} = \begin{bmatrix} \frac{r^2}{4b^2}(mb^2 + I) + I_w & \frac{r^2}{4b^2}(mb^2 - I) \\ \frac{r^2}{4b^2}(mb^2 - I) & \frac{r^2}{4b^2}(mb^2 + I) + I_w \end{bmatrix}, \quad \bar{V} = \begin{bmatrix} 0 & \frac{r^2}{2b}m_c d\dot{\phi} \\ -\frac{r^2}{2b}m_c d\dot{\phi} & 0 \end{bmatrix}$$

$I = m_c d^2 + 2m_w b^2 + I_c + 2I_m$, $m = m_c + 2m_w$, $z = [v \ \ \omega]^T$, $z_d = [v_d \ \ \omega_d]^T$, $\tau = [\tau_{rw} \ \ \tau_{lw}]^T$, $f = [f_1 \ f_2]^T$, m_c is the mass of the body, m_w is the mass of each driving wheel, I_w is the moment of inertia of each driving wheel about the wheel axis, I_m is the moment of inertia of each driving wheel the wheel diameter axis, I_c is the moment of inertia of the body about a vertical axis through the intersection of the axis of symmetry with the driving wheel axis, and τ_{rw} , τ_{lw} are torques of the motors acting on the right and the left wheels, $\tau_d = \bar{M}(q)f \in R^{2x1}$ is a external disturbance torque vector, $f \in R^{2x1}$ is a external disturbance force vector, $\tau \in R^{2x1}$ is a control input vector.

First, a control vector $u \in R^{2x1}$ is defined by computed-torque method as follows:

$$\tau = \bar{M}(q)\dot{z}_d + \bar{V}(q, \dot{q})z + \bar{M}(q)u \quad (8)$$

where $z_d \in R^{2x1}$ is a control velocity vector.

From (6) and (8), the following is obtained.

$$\dot{z}_d - \dot{z} = f - u \quad (9)$$

3 Controller Design for Solving the Problem

The reference point $R(x_r, y_r, \phi_r)$ is moving on the desired trajectory with the constant velocity. In Fig. 2, the tracking error vector $e = [e_1, e_2, e_3]^T$ is defined as the difference between the welding point W and the reference point R as follows:

$$e = \begin{bmatrix} e_1 \\ e_2 \\ e_3 \end{bmatrix} = \begin{bmatrix} \cos \phi & \sin \phi & 0 \\ -\sin \phi & \cos \phi & 0 \\ 0 & 0 & 1 \end{bmatrix} \begin{bmatrix} x_r - x_W \\ y_r - y_W \\ \phi_r - \phi_W \end{bmatrix} \quad (10)$$

Our objective is to design a nonlinear controller so that the welding point W tracks to the reference point R that mean tracking error vector $e \rightarrow 0$ when $t \rightarrow \infty$.

Because of controllable torch length, the first derivative of e yields

$$\dot{e} = \begin{bmatrix} \dot{e}_1 \\ \dot{e}_2 \\ \dot{e}_3 \end{bmatrix} = \begin{bmatrix} -1 & e_2 + l \\ 0 & -e_1 \\ 0 & -1 \end{bmatrix} \begin{bmatrix} v \\ \omega \end{bmatrix} + \begin{bmatrix} v_r \cos e_3 \\ v_r \sin e_3 - l \\ \omega_r \end{bmatrix} \quad (11)$$

The Lyapunov function candidate is defined as follows:

$$V = V_1 + V_2 \geq 0 \quad (12)$$

where

$$V_1 = \frac{1}{2}(e_1^2 + e_2^2 + e_3^2) \geq 0, \quad (13)$$

$$V_2 = \frac{1}{2}S^T S \geq 0, \quad (14)$$

$S_v = [S_{v1} \ S_{v2}]^T$ is a sliding surface vector.

The kinematic controller is designed as [1]

$$z_d = \begin{bmatrix} v_d \\ \omega_d \end{bmatrix} = \begin{bmatrix} l(\omega_R + C_3 e_3) + v_R \cos e_3 + C_1 e_1 \\ \omega_R + C_3 e_3 \end{bmatrix} \quad (15)$$

and the length of torch satisfies

$$l = v_R \sin e_3 + C_2 e_2 \quad (16)$$

where C_1, C_2, C_3 is a positive values.

With the velocity control input (15), the \dot{v}_1 becomes

$$\dot{v}_1 = -C_1 e_1^2 - C_2 e_2^2 - C_3 e_3^2 \leq 0 \quad (17)$$

The sliding surface vector S_v is defined as

$$S_v = e_v + K_v \int e_v dt \quad (18)$$

where $e_v = z_d - z = [e_{v1} \ e_{v2}]^T \in \mathbb{R}^{2 \times 1}$ is a velocity error vector and K_v is a positive diagonal matrix.

The control law $u = [u_1 \ u_2]^T$ is chosen as

$$u = QS_v + P\text{sign}(S_v) + K_v e_v \quad (19)$$

where $S_v = \begin{bmatrix} S_{v1} \\ S_{v2} \end{bmatrix}$, $Q = \begin{bmatrix} Q_1 & 0 \\ 0 & Q_2 \end{bmatrix}$, $P = \begin{bmatrix} P_1 & 0 \\ 0 & P_2 \end{bmatrix}$, $f = \begin{bmatrix} f_1 \\ f_2 \end{bmatrix} \leq \begin{bmatrix} f_1^m \\ f_2^m \end{bmatrix}$, Q_i and P_i , $i = 1, 2$ are constant positive values; f_i^m , $i = 1, 2$ is the upper bounded value of f_i .

With the control law (19), (18) becomes

$$\dot{S}_v = -QS_v - P\text{sign}(S_v) + f \quad (20)$$

Substituting (20) into the first derivative of V_2 is derived

$$\dot{V}_2 = S_v^T \dot{S}_v \leq -S_v^T QS_v - |S_{v1}|(P_1 - f_1^m) - |S_{v2}|(P_2 - f_2^m) \quad (21)$$

If $Q_i \geq 0$ and $P_i \geq f_i^m$, $i = 1, 2$, $\dot{V}_2 \leq 0$. By Barbalat's lemma [6], $S_v \rightarrow 0$ as $t \rightarrow \infty$. That is, there exists the control law u stabilizing sliding surfaces go to zero.

From (12)-(14) and (17), (21), $\dot{V} \leq 0$. That mean both $e \rightarrow 0$ and $e_v \rightarrow 0$, the W point of the WMR tracks a reference point R which is moving on a desired trajectory at a constant velocity.

4 Simulation Results

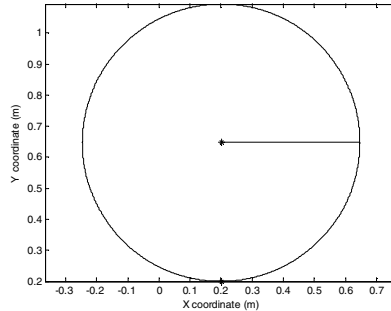


Fig. 3. The desired welding path

Fig. 3 shows the desired welding path. The designed parameters of the controller are as follows: $P_1 = 10$, $P_2 = 12$, $Q_1 = 20$, $Q_2 = 25$; and $C_1 = 15.7$, $C_2 = 1.5$ and $C_3 = 22.5$, $K_v = [0.2 \ 0; 0 \ 0.5]$, $f_{m1} = 0.7N$, $f_{m2} = 0.7N$. The numerical parameter values and the initial values for simulation are given in Table 1 and Table 2.

Table 1. The numerical parameters values for simulation

Parameters	Values	Units
b	0.105	[m]
r	0.025	[m]
l	0.145	[m]
m_c	10	[kg]
m_w	0.2	[kg]
I_c	0.2081	[kgm ²]
I_w	0.0135	[kgm ²]
I_m	4.96×10^{-4}	[kgm ²]

Table 2. The initial values for simulation

Parameters	Values	Units
x_r	0.2	[m]
y_r	0.2	[m]
ϕ_r	0°	[deg]
x_w	0.195	[m]
y_w	0.195	[m]
ϕ	7°	[deg]
v_r	7.5	[mm / s]
v	0	[mm / s]
ω_r	0	[rad / s]
ω	0	[rad / s]
l	0.145	[m]

The simulation results for tracking welding path are shown in Figs. 4~9. Figs. 4 and 5 show the movement of the WMR along the desired welding trajectory for the time beginning and full time 374.4 seconds. The simulation results for error tracking vector during 15 seconds at beginning and 374.4 seconds for full time are shown in Figs. 6 and 7. The errors go to zero from 12 seconds. The linear velocity is shown in Fig. 8. It shows that the linear velocity at the welding point w of the WMR converge to the constant velocity in the vicinity of 7.5mm / s as desired. Fig. 9 shows the torch length of WMR. It goes from 145mm at initial time to 150mm after about 3 seconds and keeps the that value for remain time. The simulation results are shown that the WMR has good welding path tracking performance.

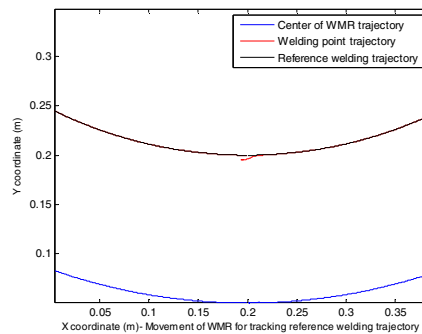


Fig. 4. Movement of the WMR at the beginning time

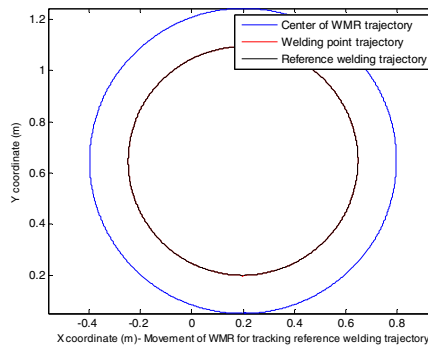


Fig. 5. Movement of the WMR for full time

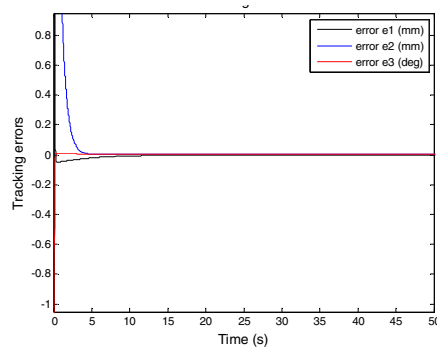


Fig. 6. Tracking errors at beginning time (12 seconds)

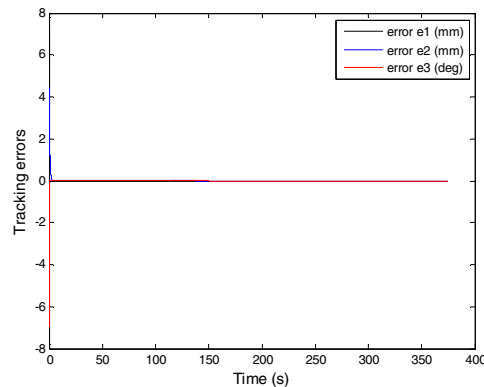


Fig. 7. Tracking errors for full time (374.4 seconds)

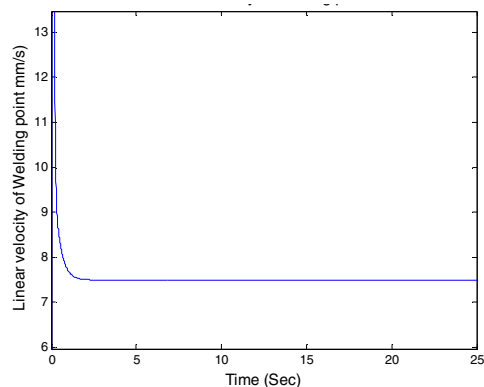


Fig. 8. Linear velocity of the welding point W

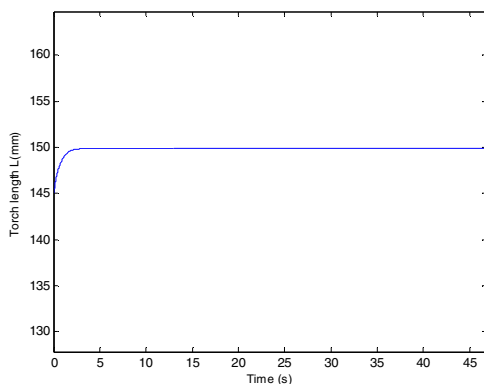


Fig. 9. Torch length l

5 Conclusion

This paper proposes a new nonlinear controller that makes the combination of a kinematic controller (KC) and an integral sliding mode dynamic controller (ISMC) for the two wheeled welding mobile robot to track a desired welding trajectory with a desired constant velocity. The system stability is guaranteed by Lyapunov theory. The simulation results show that linear velocity of the the welding point W of the WMR converge to the constant value very quickly and keep zero value more smoothly than the results in [2, 3] and the proposed controller can be applicable in the practical applications.

References

- [1] Bui, T.H., Nguyen, T.T., Chung, T.L., Kim, S.B.: A Simple Nonlinear Control of a Two-Wheeled Welding Mobile Robot. *International Journal of Control, Automation, and Systems* 1(1), 35–42 (2003)
- [2] Chung, T.L., Bui, T.H., Nguyen, T.T., Kim, S.B.: Sliding Mode Control of Two-Wheeled Welding Mobile Robot for Tracking Smooth Curved Welding Path. *KSME International Journal* 18(7), 1094–1106 (2004)
- [3] Ngo, M.D., Vo, H.D., Nguyen, T.P., Kim, S.B., Oh, M.S.: Two-Wheeled Welding Mobile Robot for Tracking Smooth Curved Welding Path Using Adaptive Sliding Mode Control Technique. *International Journal of Control, Automation, and Systems (IJCAS)* 5(3), 283–294 (2007)
- [4] Hung, N., Jeong, S.K., Im, J.S., Kim, H.K., Kim, S.B.: Design of Sliding Mode Controller for Automatic Guided Vehicle and Its Implementation. *International Journal of Control, Automation and Systems (IJCAS)* 8(-90), 81–90 (2010)
- [5] Hung, N., Tuan, D.V., Jae, S.I., Kim, H.K., Kim, S.B.: Motion Control of Omnidirectional Mobile Platform for Trajectory Tracking Using Integral Sliding Mode Controller. *International Journal of Control, Automation and Systems (IJCAS)* 8(6), 1221–1231 (2010)
- [6] Slotine, J.-J.E., Li, W.: *Applied Nonlinear Control*, pp. 122–125. Prentice-Hall International, Inc. (1991)

A Study on Locomotions of Quadruped Robot

Than Trong Khanh Dat and Tran Thien Phuc

Faculty of Mechanical Engineering, Ho Chi Minh City University of Technology, Vietnam
ttphuc.rectie@hcmut.edu.vn

Abstract. In this study, we focus on planning the gait of quadruped robot on flat terrain. Modeling and simulation of quadruped robot with three joint legs are carried out with MSC ADAMS software. The two phase discontinuous gait represents the sequential motion of the legs and robot body for the locomotion of going straight and turning. The simulation presents the values of the moment on joint of leg and the trajectory of the center of robot body. The experiment analyzes the locus of the center of gravity of the robot body in the gait: go straight; go straight and turn right, go straight and turn left, go forward and backward, and turn the corner. The results of simulation and experiment provides theoretical basis for building algorithm the quadruped robot motion control.

Keywords: Quadruped robot, kinematics simulation, dynamic modeling, MSC ADAMS simulation, trajectory planning, gait, stability.

1 Introduction

A multi-legged robot possesses a tremendous potential for maneuverability over rough terrain, particularly in comparison to conventional wheeled or tracked mobile robot. It has more flexibility and terrain adaptability at low speed. However, the requirements for coordinating between the leg motion, controlling and computing of four legs robot encountered more difficulties than other types. Kinematic and dynamic characteristics of the quadruped robot comprehensively impact the ability to meet the motion control of the robot. For robot can move according to our purpose, we must plan the gait, calculate kinematic problem and construct dynamical system with complex dynamics of the interaction between links-joints, including trunk body, and contacting the ground with feet. Therefore, the purpose of this research is to build a complete kinematic models, plan the gait, make sure the shape is moved, the stability for the robot, from which to build dynamic models, this is the basis for the construction of motion controllers, enhances the ability to move, perform the task, and the optimization of energy supply.

This paper has presented the gaits for four-legged robots and built dynamic models more accurate than current methods with the combined method of Lagrange-Euler with model simulation on ADAMS (Automatic Dynamic Analysis of Mechanical System). From there we will create the basis for the construction of the motion control for robot to interact with the model that was built on the ADAMS.

2 Problem Formulation

2.1 Quadruped Model

A simple 3D model of four-legged robot built on environment of ADAMS/View is shown on Fig. 1.

Robot has all 13 parts with 12 DC servo motors. In this model, the robot has 4 legs, each leg has three degrees of freedom, and movement of the legs make it possible to free movement of the body (6 degrees of freedom). So robot has a total of all 18 degrees of freedom ($3 \times 4 + 6 = 18\text{DOF}$).

Table 1. Physical parameters of each leg

Link parameters	Body	Link 1	Link 2	Link 3
Mass (Kg)	6	0.2	0.3	0.4
Moment of Inertia ($10^{-2} \cdot \text{kg.m}^2$)	I_x 5.4 4.927 1.687	0.294 0.247 0.247	0.498 0.493 0.108	2.320 2.316 0.189
Length (mm)	400x200x150	50	100	200

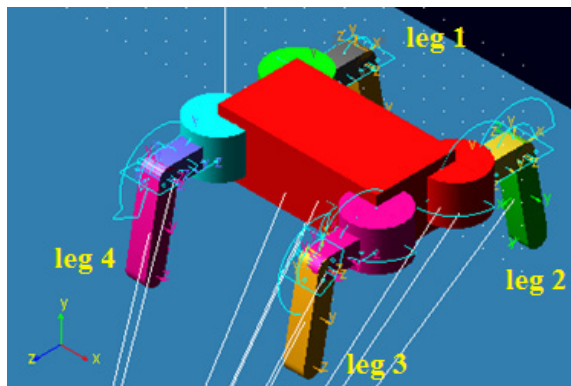


Fig. 1. Quadruped robot model in MSC.ADAMS

2.2 Planning the Gait

The gait of robot is two-phase discontinuous [1]. With models such steps, at each point of the robot body is kept in balance by three legs on ground, making it very stable when moving robot. Robot motion with gait is two-phase discontinuous. The body is propelled forward/backward with all of the feet securely placed on the ground and a leg is transferred with all other three legs and body halted. For every phase, body robot will propel forward once. The gait is shown on Fig. 2.

1. Go straight gaits

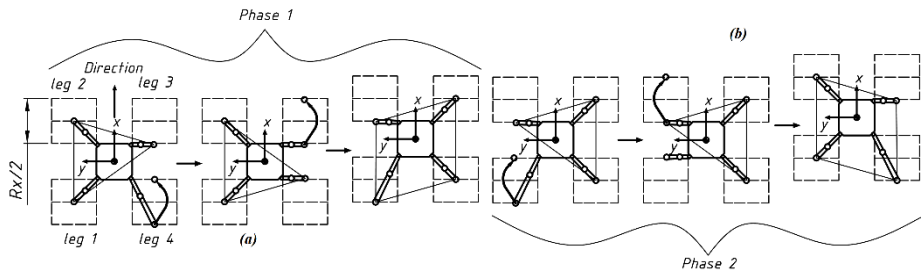


Fig. 2. Diagram of two phase discontinuous gait, (a) phase 1, (b) phase 2. With R_x is leg stroke following x axial

2. Turning gaits

Fig.3 shows the leg state at the beginning (dot line piece) and finishing (dark solid line) in the first phase. Body robot and leg space at the end of phase 1 rotate an angle $\alpha/2$. In phase 1, the sequence of transferring leg is 1-4-3-2. Similarly, in phase 2 is 2-3-4-1. With this sequence, the turning process would ensure stability.

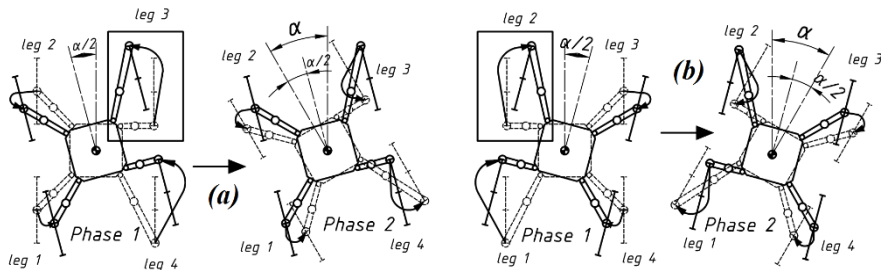


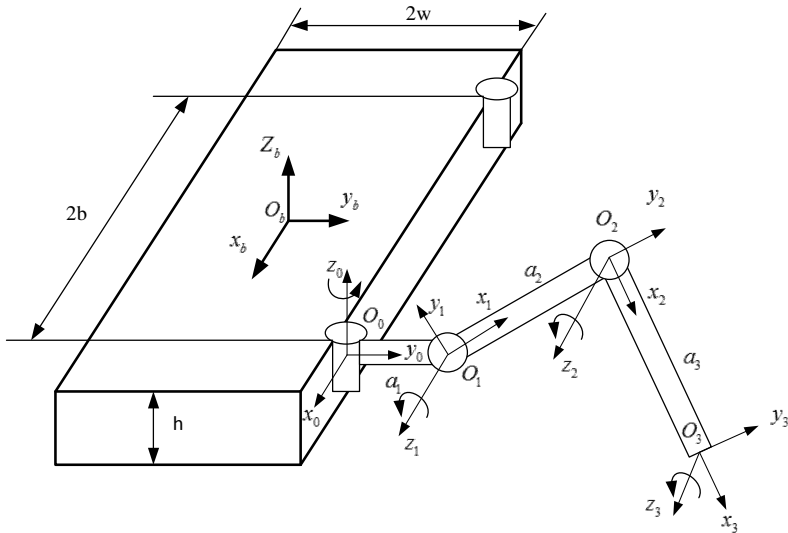
Fig. 3. Diagram of turning gait, (a) turn left, (b) turn right

2.3 Kinematic Problem

This section derives the forward kinematic model by using the Denavit - Hartenberg (D-H) convention [2]. The D-H notations have been used in kinematic modeling of each leg (refer to Fig. 4).

Table 2. D-H parameters for three joint legs

Link	a_i	α_i	d_i	θ_i
1	$a_1=33\text{mm}$	$\pi/2$	0	θ_1
2	$a_2=78\text{mm}$	0	0	θ_2
3	$a_3=130\text{mm}$	0	0	θ_3

**Fig. 4.** Four-legged walking robot model

3. Forward kinematic

To describe the relationship of the orientation and position of the coordinate system attached to two adjacent stages (link i to link $i-1$), we used the matrix ${}^{i-1}T_i$, is represented by the transformation. The foot tip reference frame $\{3\}$ can be expressed in the hip or leg reference frame $\{0\}$ as given below.

$${}^{i-1}T_i = \text{Trans}(Z_{i-1}; d_i). \text{Rot}(Z_{i-1}; \theta_i). \text{Trans}(X_{i-1}; a_i). \text{Rot}(X_{i-1}; \alpha_i) \quad (1)$$

$${}^0T = {}^0T \cdot {}^1T \cdot {}^2T \cdot {}^3T = \begin{bmatrix} C_1.C_{23} & -C_1.S_{23} & S_1 & C_1(a_3.C_{23} + a_2.C_2 + a_1) \\ S_1.C_{23} & -S_1.S_{23} & -C_1 & S_1(a_3.C_{23} + a_2.C_2 + a_1) \\ S_{23} & C_{23} & 0 & a_3.S_{23} + a_2.S_2 \\ 0 & 0 & 0 & 1 \end{bmatrix} \quad (2)$$

where $C_i = \cos \theta_i$; $S_i = \sin \theta_i$; $C_{ij} = \cos(\theta_i + \theta_j)$; $S_{ij} = \sin(\theta_i + \theta_j)$ for $i, j = 1-3$.

The x, y and z coordinates of the foot tip point with respect to leg reference frame $\{0\}$ can be determined for given the joint variables: θ_1 , θ_2 and θ_3 . The position of the foot is given by the following expressions

$$\Rightarrow \begin{cases} p_x = C_1(a_3.C_{23} + a_2.C_2 + a_1) \\ p_y = S_1(a_3.C_{23} + a_2.C_2 + a_1) \\ p_z = a_3.S_{23} + a_2.S_2 \end{cases} \quad (3)$$

4. Inverse kinematic

The inverse kinematics consists in determining the joint variables ($\theta_1, \theta_2, \theta_3$) in terms of the foot position and orientation.

By solving equations (3), the joint angles: $\theta_1, \theta_2, \theta_3$ have been determined as given below.

$$\begin{cases} \theta_1 = a \tan 2(p_y; p_x) \\ \theta_2 = -a \tan 2(B, A) + a \tan 2(D, \pm\sqrt{A^2 + B^2 - D^2}) \\ \theta_3 = a \tan 2(p_z - a_2 \cdot S_2; p_x \cdot C_1 + p_y \cdot S_1 - a_2 \cdot C_2 - a_1) - \theta_2 \end{cases} \quad (4)$$

where $\begin{cases} A = -p_z; B = a_1 - (p_x \cdot C_1 + p_y \cdot S_1) \\ D = \frac{2.a_1.(p_x \cdot C_1 + p_y \cdot S_1) + a_3^2 - a_2^2 - a_1^2 - z^2 - (p_x \cdot C_1 + p_y \cdot S_1)^2}{2.a_2} \end{cases}$ (5)

3 Simulation and Experiment

3.1 Result of Simulation

The process simulation was carried out in MSC.ADAMS/View software [7], it provides a dynamic environment like real environment to get high accuracy: contact between foot to ground, coefficient friction, coefficient damping, gravity, external force...

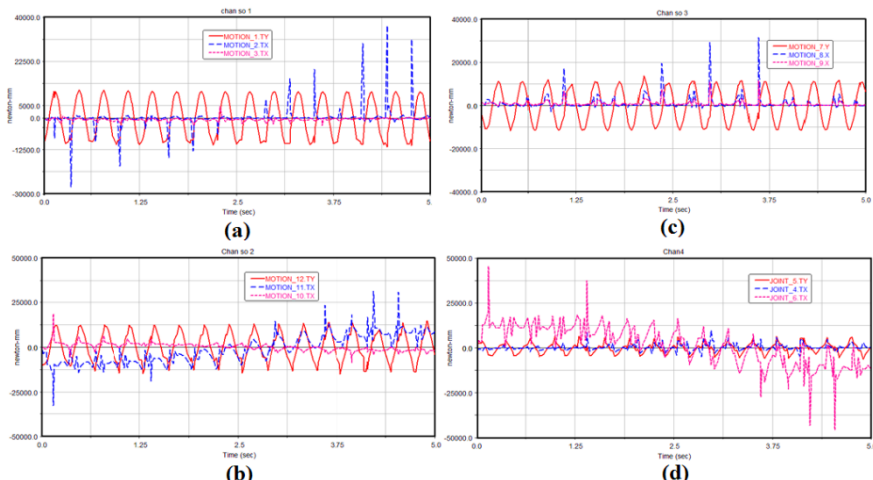


Fig. 5. (a) (b) (c) (d) joint torques of leg 1, leg 2, leg 3, leg 4

The result of simulation shows parameters of joints and trajectory center gravity of body robot. Fig. 6 shows that in the period from 0 to 4s, the trajectory of the center of the robot body coordinates x by the time estimate the road, so that robot moves in a straight line, starting from the first 4 seconds, the robot stops and rotates in a position to turn.

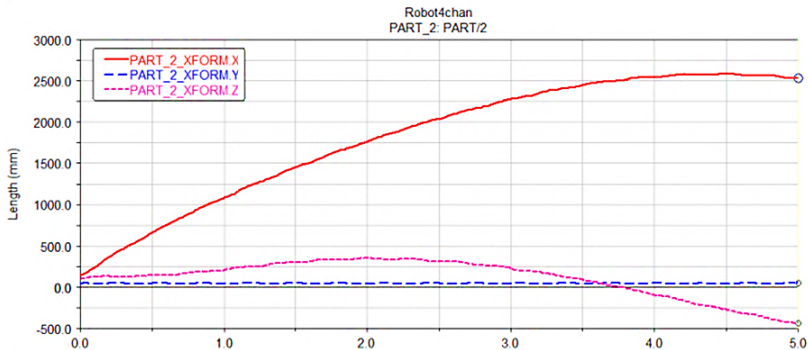


Fig. 6. Trajectory center of the body

The simulation results are moving trajectories and torque properties at the joints in each legs robot. Due to the characteristics of the problem is simulated robot motion, it is the result of the evaluation data to the system, since the construction of the robot motion controller error of trajectories so huge and unregulated. The simulation results are moving trajectories and torque properties at the joints in each legs robot. Due to the problem of robot motion simulation, this result is data to evaluate the system, since the construction of the robot motion controller, so the error of trajectories is very large, and not controlled.

3.2 Results of Experiment

3.2.1. Experiment

In going straight, gaits have four basic 1-2-3-4 states (refer Fig. 2). The process will be done straight away by following cycle (refer in Fig. 7). Fig. 8 and 9 show the gait in real model.

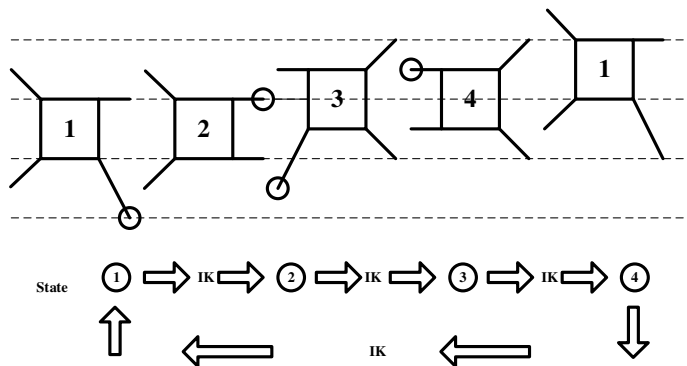


Fig. 7. The basic state of robot's legs (IK: inverse kinematic)

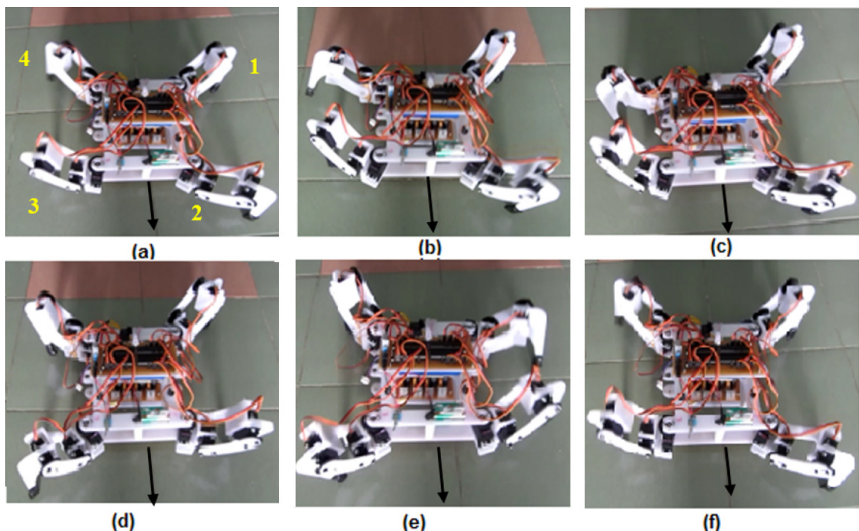


Fig. 8. Sequence of going straight forward

Fig.8 presented the sequence of going straight forward. With fig.8 (a) shows initial position, (b) step 1 of phase 1. Leg 4 lifted up and moved forward; (c) completed step 1 of phase 1; (d) step 2 of phase 1. Leg 3 lifted up and moved forward. And then body robot propelled up a segment $R_x/2$; (e) Step 1 of phase 2. Leg 1 picked up and moved forward; (f) Step 2 of phase 2. Leg 2 lifted up and moved forward. And then body robot propelled a segment $R_x/2$.

The sequence of turning right is showed in Fig.9. This sequence is followed the principle presented in Fig.3 (section 2.2.2).

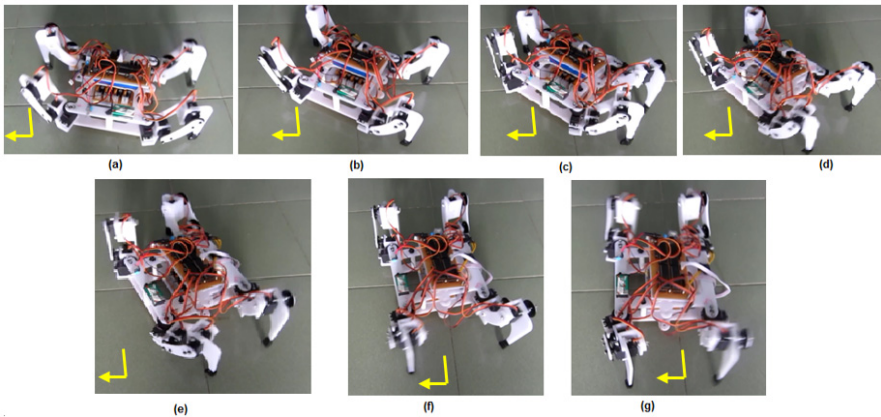


Fig. 9. (a),(b), (c), (d), (e), (f) Sequence of turning right

3.2.2. Estimation result

Experimental process has simulated the robot according to the original plan already gait. Robot has carried out the trajectory to go straight and turn 90^0 left, right, go forward and backward, turn 60^0 .

To evaluate accuracy of trajectory, the author uses image processing methods to identify the locus of center body robot. Camera was calibrated to get exact locus of the circle center on the body robot.

Distance 1 pixel on camera obtained 7.14 mm respectively with accuracy $\pm 5 \text{ mm}$.

❖ Trajectory of going straight and then turning right angle 90^0

The camera results are obtained in Fig. 10 (a), the robot go straight 128 pixels (914 mm), then proceed to turn and go a segment 84 pixels (600 mm), the deviation from turning point $(186;-125)$ to end point $(102;-132)$ according vertical is 7 pixels (50 mm). So the error of angle of turn right is 4.7^0 .

❖ Trajectory of going straight and then turning left angle 90^0

In the Fig. 10 (b), the robot go straight 125 pixels (892 mm), then proceed to turn left 90^0 and go straight 144 pixel (1028 mm), we find that deviations from turning point $(170;-125)$ to stopping point $(129;-316)$ according vertical axial is 4 pixels (28.56 mm). So the error of angle of turn left is 1.59^0 .

❖ Trajectory of going forward and backward

Robot go straight forward and backward on the length of 1 m . Fig. 10 (c) shows the robot trajectories at the end is deflected a segment horizontally 9 pixels (64 mm). In the half of path going backward, trajectory overlap, starting at half the difference between the two trajectories goes on and on.

❖ Trajectory of turning an angle 60^0

With each cycle phase is 15 degrees, robot has carried out three cycles to achieve an angle 60^0 . From Fig. 10 (d), the robot performs the trajectory goes straight forward 77 pixels (550 mm), then the robot turns right and goes straight from point $(180,-77)$ to point $(316,-15)$. The corner turn that robot achieved is 69^0 . So the error of angle of turn is 9^0 on a length of 145 pixels (1035 mm).

❖ Estimation result

At the beginning of the turn (Fig. 10 a and b) robot has sliding phenomenon, this is explained by the robot rotating in place, the force acting on the ground of foot is not controlled due without sensor underfoot. However, the results are accepted with the trajectory programming, no feedback signal, just based on the position kinematic.

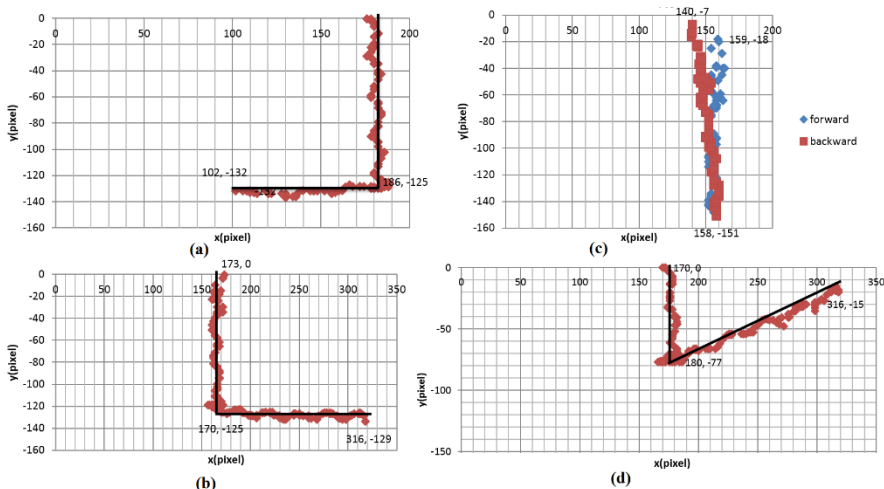


Fig. 10. The trajectory of robot (a) go straight and then turn right 90^0 , (b) go straight and then turn left 90^0 , (c) go forward and backward, (d) turn an angle 60^0 . The black dark solid line shown the desired trajectories.

The results in Figure 10 shows that, with the uncontrolled interaction force between the feet to the ground, cannot be determined coplanar between the body and the ground, this creates a different impact of the foot on the ground, so the trajectory error exists. The largest error of straight trajectory is 3 pixels (21.42 mm), turning an angle 90^0 is 4.7^0 , and turning an angle 60^0 is 9^0 , this is explained by repeated cycles of turning angle increases, this proves in every phase of the rotation exist an error, cause error accumulation. Trajectory of going forward and backward has error, the cause is the open-loop controller, and we do not control the foot position changes, so we cannot make to overlap position between going forward and backward.

To increase the accuracy of the robot move, we need to control the impact force from the legs to the ground and the reaction from ground to the legs. Therefore, robot

should have force sensor. Simultaneously, to move correctly, there must be additional compass to determine the direction, camera system for image processing, accelerometer sensor to determine the inclination of the robot body. In addition, the mechanical structure must be accurate and reliable.

4 Conclusion

The simulation results will be the basis for the motion control of the robot. Simulation conditions are still limited, excluding the case from sliding foot robot, the robot moves only on a flat surface, not simulated stability on inclined surfaces. However, experiments have achieved certain results, to facilitate further research. Future research on the topic is to develop a motion controller of the robot, the robot moves on different terrain, reduce slip, increase the accuracy of the trajectory, and optimize energy consumption with a quadruped robot model more complete.

References

- [1] de Santos, P.G., Garcia, E., Estremera, J.: An Introduction to the Control of Four-legged Robots. Springer (2006)
- [2] Jazar, R.N.: Theory of Applied Robotics. Springer (2010)
- [3] Tarokh, M., Lee, M.: Kinematics Modeling of Multi-legged Robots Walking on Rough Terrain. In: Second International Conference on Future Generation Communication and Networking Symposia, pp. 13–16 (2008)
- [4] Mahapatra, A., Roy, S.S.: Computer Aided Dynamic Simulation of Six-Legged Robot. International Journal of Recent Trends in Engineering 2(2) (November 2009)
- [5] Roy, S.S., Pratihar, D.K.: Effects of turning gait parameters on energy consumption and stability of a six-legged walking robot. Robotics and Autonomous Systems 60, 72–82 (2012)
- [6] Niwa, T., Inagaki, S., Suzuki, T.: Locomotion Control of Multi-Legged Robot based on Follow-the-Contact-Point Gait. In: ICROS-SICE International Joint Conference, pp. 2247–2253 (2009)
- [7] <http://www.mscsoftware.com/product/adams>

Adaptive Line Trajectory Identification of Industrial 5-DOF Robot Arm Using Neural MIMO NARX Model

Ho Pham Huy Anh¹ and Nguyen Thanh Nam²

¹ Ho Chi Minh City University of Technology, Viet Nam

hphanh@hcmut.edu.vn

² DCSELAB, Ho Chi Minh City University of Technology, Viet Nam

thanhnam@dcselab.edu.vn

Abstract. This paper investigates a novel forward adaptive neural MIMO NARX model which is applied for modeling and identifying the forward kinematics of the industrial 5-DOF robot arm system. The nonlinear features of the forward kinematics of the industrial 5-DOF robot arm drive are thoroughly modeled based on the adaptive identification process using experimental input-output training data. This paper proposes the novel use of a back propagation (BP) algorithm to generate the forward neural MIMO NARX (FNMN) model for the forward kinematics of the industrial 5-DOF robot arm. The results show that the proposed adaptive neural NARX model trained by Back Propagation learning algorithm yields outstanding performance and perfect accuracy.

Keywords: Forward Kinematics of Industrial 5-DOF Robot Arm, Back Propagation Learning Algorithm (BP), Adaptive Neural MIMO NARX Model, Modeling and Identification.

1 Introduction

The forward and inverse kinematics equations of the industrial manipulators are highly unpredictable as these equations are highly nonlinear and contain transcendental function. The complexity in solving these equations increases due to increase in higher DOF. In spite of the difficulties and time consuming in solving the inverse kinematics of a complex robot, researchers used traditional methods like algebraic (Craig 1989), geometric (Lee 1982), and iterative (Korein 1982) procedures. Nevertheless these methods have their own drawbacks. Consequently, nowadays, various authors had used neuro-fuzzy methods to solve the nonlinear and complex equations arised in different fields. These intelligent methods are adopted by different researchers in their work as they have high range of potential for solving the complex and nonlinear equations arising in different fields like in marketing, manufacturing industries, civil engineering, etc. (Srinivasan et al. 2008) applied neuro-fuzzy method to solve the kinematic solution of industrial robot arm.

(Alavandar S. et al. 2008) applied ANFIS based on PD plus I controller to the dynamic model of 6-DOF robot manipulator. (Hasan 2010) adopted an application of neuro-fuzzy method to the solution of the inverse kinematics problem for serial robot manipulators.

Recently, robust adaptive control approaches combining conventional methods with new learning techniques are realized. During the last decade, several adaptive neural network models and learning schemes have been applied to offline and online learning of robot arm dynamics (Velagic 2008) (Sadjadian 2006). Recently, (Ahn 2007) and (Anh 2010) have successfully optimized a NARX neural model of the kinematics of the PAM-based robot arm. The drawback of all these results is related to the inverse kinematics of the industrial robot arm being considered as an independent decoupling system and the external force variation to have negligible effect.

To overcome these drawbacks, this paper proposes the novel use of adaptive neural NARX model to generate the forward neural MIMO NARX (FNMN) model for a nonlinear forward kinematics of the 5-DOF industrial robot arm system. The Back Propagation (BP) learning algorithm is used to process the experimental input-output data that is measured from the forward kinematics of the industrial robot arm system to optimize all nonlinear and dynamic features of this system. Thus, the BP algorithm optimally generates the appropriate neural weightings to perfectly characterize the features of the forward kinematics of the industrial robot arm. Consequently, the proposed method of the industrial 5-dof robot arm forward neural MIMO NARX model identification approach has successfully modeled the nonlinear forward kinematics of the industrial robot arm system with good performance.

The rest of the paper is organized as follows. Section 2 introduces the calculation of the 5-DOF industrial robot arm forward kinematics. Section 3 presents the novel neural MIMO NARX model using for the forward kinematics model identification of the industrial 5-DOF robot arm. The results from the proposed forward kinematics identification are presented in Section 4. Finally, Section 5 contains the concluding remarks.

2 Forward Kinematics of the Industrial 5-DoF Robot Arm System

Robot control actions are executed in the joint coordinates while robot motions are specified in the Cartesian coordinates. Conversion of the position and orientation of a robot manipulator end-effector from Cartesian space to joint space is called as inverse kinematics problem, which is of fundamental importance in calculating desired joint angles for robot manipulator design and control. The Denavit-Hartenberg (DH) notation and methodology is used to derive the kinematics of the 5-DOF redundant manipulator.

Table 1. The D-H parameters of the 5-DOF redundant manipulator

Frames	θ_i (degree)	d_i (mm)	a_i (mm)	α_i (degree)
O ₀ -O ₁	θ_1	$d_1=130$	$a_1=70$	-90
O ₁ -O ₂	θ_2	0	$a_2=160$	0
O ₂ -O ₃	$-90+\theta_3$	0	0	-90
O ₃ -O ₄	θ_4	$d_4=140$	0	90
O ₄ -O ₅	θ_5	0	0	-90

The transformation matrix A_i between two neighboring frames O_{i-1} and O_i is expressed in Eq. (1) as

$$A_i = \text{Rot}(z, \theta_i) \text{Trans}(z, d_i) \text{Trans}(x, a_i) \text{Rot}(x, \alpha_i) \\ = \begin{bmatrix} \cos(\theta_i) & -\sin(\theta_i)\cos(\alpha_i) & \sin(\theta_i)\sin(\alpha_i) & a_i\cos(\theta_i) \\ \sin(\theta_i) & \cos(\theta_i)\cos(\alpha_i) & -\cos(\theta_i)\sin(\alpha_i) & a_i\sin(\theta_i) \\ 0 & \sin(\alpha_i) & \cos(\alpha_i) & d_i \\ 0 & 0 & 0 & 1 \end{bmatrix} \quad (1)$$

By substituting the D-H parameters in Table 1 into Eq. (1), it can be obtained the individual transformation matrices A₁ to A₆ and the general transformation matrix from the first joint to the last joint of the 5-DOF redundant manipulator can be derived by multiplying all the individual transformation matrices (⁰T₆).

$${}^0T_6 = A_1 A_2 A_3 A_4 A_5 A_6 = \begin{bmatrix} n_x & o_x & a_x & p_x \\ n_y & o_y & a_y & p_y \\ n_z & o_z & a_z & p_z \\ 0 & 0 & 0 & 1 \end{bmatrix} \quad (2)$$

where (p_x, p_y, p_z) are the positions and {(n_x, n_y, n_z), (o_x, o_y, o_z), (a_x, a_y, a_z)} are the orientations of the end-effector. The orientation and position of the end-effector can be calculated in terms of joint angles and the D-H parameters of the manipulator are shown in following matrix as:

$$\begin{bmatrix} c_1 s_{23} c_4 c_5 + s_1 s_4 c_5 \\ + c_1 c_{23} s_5 & -c_1 s_{23} c_4 s_5 - s_1 s_4 s_5 & -d_6 c_1 s_{23} c_4 s_5 - d_6 s_1 s_4 s_5 + d_6 c_1 c_{23} c_5 + \\ & + c_1 c_{23} c_5 & d_4 c_1 c_{23} + a_2 c_1 c_2 + a_1 c_1 \\ s_1 s_{23} c_4 c_5 - c_1 s_4 c_5 \\ + s_1 c_{23} s_5 & -s_1 s_{23} c_4 s_5 + c_1 s_4 s_5 & -d_6 s_1 s_{23} c_4 s_5 + d_6 c_1 s_4 s_5 + d_6 s_1 c_{23} c_5 + \\ & + s_1 c_{23} c_5 & d_4 s_1 c_{23} + a_2 s_1 c_2 + a_1 s_1 \\ c_{23} c_4 c_5 - s_{23} s_5 & -c_{23} s_4 & -c_{23} c_4 s_5 - s_{23} c_5 & -d_6 c_{23} c_4 s_5 - d_6 s_{23} c_5 - d_4 s_{23} - \\ & 0 & 0 & a_2 s_1 + d_1 & 1 \end{bmatrix} \quad (3)$$

with c_i = cos(θ_i), s_i = sin(θ_i), c₂₃ = cos($\theta_2 + \theta_3$) and s₂₃ = sin($\theta_2 + \theta_3$).

By equalizing the matrices in equations (2) and (3), the following equations are derived as follows:

$$p_x = -d_6 c_1 s_{23} c_4 s_5 - d_6 s_1 s_4 s_5 + d_6 c_1 c_{23} c_5 + d_4 c_1 c_{23} + a_2 c_1 c_2 + a_1 c_1 \quad (4)$$

$$p_y = -d_6 s_1 s_{23} c_4 s_5 + d_6 c_1 s_4 s_5 + d_6 s_1 c_{23} c_5 + d_4 s_1 c_{23} + a_2 s_1 c_2 + a_1 s_1 \quad (5)$$

$$p_z = -d_6 c_{23} c_4 s_5 - d_6 s_{23} c_5 - d_4 s_{23} c_5 - d_4 s_{23} - a_2 s_2 + d_1 \quad (6)$$

$$n_x = c_1 s_{23} c_4 c_5 + s_1 s_4 c_5 + c_1 c_{23} s_5 \quad (7)$$

$$n_y = s_1 s_{23} c_4 c_5 - c_1 s_4 c_5 + s_1 c_{23} s_5 \quad (8)$$

$$n_z = c_{23} c_4 c_5 - s_{23} s_5 \quad (9)$$

$$o_x = -c_1 s_{23} s_4 + s_1 c_4 \quad (10)$$

$$o_y = -s_1 s_{23} s_4 - c_1 c_4 \quad (11)$$

$$o_z = -c_{23} s_4 \quad (12)$$

$$a_x = -c_1 s_{23} c_4 s_5 - s_1 s_4 c_5 + c_1 c_{23} c_5 \quad (13)$$

$$a_y = -s_1 s_{23} c_4 s_5 + c_1 s_4 s_5 + s_1 c_{23} c_5 \quad (14)$$

$$a_z = -c_{23} c_4 s_5 - s_{23} c_5 \quad (15)$$

From Eqs. (4) - (15), the position and orientation of the 5-DOF redundant manipulator end-effector can be calculated if all the joint angles are given. This is the solution to the forward kinematics.

3 Adaptive Forward Neural MIMO NARX (FNNN) Model Identification of the Industrial 5-DoF Robot Arm System

We will design the proposed Forward Neural MIMO NARX11 (FNMN11) model (with $n_a = 1$, $n_b = 1$, $n_k = 1$) for the industrial 5-DOF robot arm with 7 inputs (including five joint-angle input value $q_1(k)$, $q_2(k)$, $q_3(k)$, $q_4(k)$ and $q_5(k)$ and two recurrent delayed values $y(k-1)$, $x(k-1)$), and 2 output values ($y_{hat}(k)$, $x_{hat}(k)$). We remember that five input values $q_1(k)$, $q_2(k)$, $q_3(k)$, $q_4(k)$ and $q_5(k)$ representing the five joint angles [deg] of the 5-DOF robot arm and the two output values $y_{hat}(k)$ and $x_{hat}(k)$ representing the Cartesian coordinates (x,y) of the 5-DOF robot arm end-effector respectively. Its structure is shown in Fig. 1,

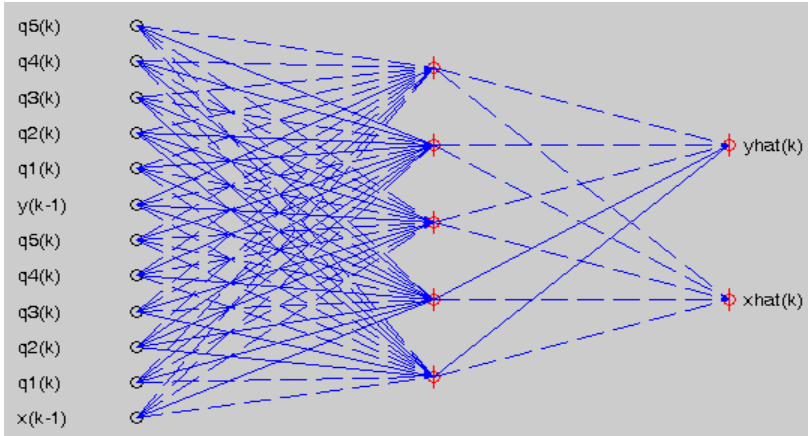


Fig. 1. Structure of the forward neural MIMO NARX11 model of the 5-DOF robot arm

By this way, the fourteen parameters $a_{11}, a_{12}, b_{11}, b_{12}, b_{11}, b_{12}, a_{21}, a_{22}, b_{21}, b_{22}, b_{31}, b_{11}, b_{12}$ of the ARX structure of joint-angle output variables $y_{hat}(t)$ and $x_{hat}(t)$, respectively, now become adaptively nonlinear and will be determined from the weighting values W_{ij} and w_{jl} of the proposed forward Neural MIMO NARX11 model. This feature makes adaptive forward Neural MIMO NARX (FNMN) model very powerful in modeling, identification and in model-based advanced control as well.

The prediction error approach, which is the strategy applied here, is based on the introduction of a measure of closeness in terms of a mean sum of square error (MSSE) criterion:

$$E_N(\theta, Z^N) = \frac{1}{2N} \sum_{i=1}^N [y(t) - \hat{y}(t|\theta)]^T [y(t) - \hat{y}(t|\theta)] \quad (16)$$

Based on the conventional error Back-Propagation (BP) training algorithm, the weighting value is calculated as follows:

$$W(k+1) = W(k) - \lambda \frac{\partial E(W(k))}{\partial W(k)} \quad (17)$$

with k is k^{th} iterative step of calculation and λ is learning rate which is often chosen as a small constant value.

Concretely, the weights W_{ij} and w_{jl} of neural model are then updated as:

$$\begin{aligned} W_{ij}(k+1) &= W_{ij}(k) + \Delta W_{ij}(k+1) \\ \Delta W_{ij}(k+1) &= \lambda \cdot \delta_i \cdot O_j \\ \delta_i &= \hat{y}_i(1 - \hat{y}_i)(y_i - \hat{y}_i) \end{aligned} \quad (18)$$

with δ_i is search direction value of i^{th} neuron of output layer ($i=[1 \rightarrow m]$); O_j is the output value of j^{th} neuron of hidden layer ($j=[1 \rightarrow q]$); y_i and \hat{y}_i are truly real output and predicted output of i^{th} neuron of output layer ($i=[1 \rightarrow m]$), and

$$\begin{aligned} w_{jl}(k+1) &= w_{jl}(k) + \Delta w_{jl}(k+1) \\ \Delta w_{jl}(k+1) &= \lambda \cdot \delta_j \cdot u_l \\ \delta_j &= O_j(1 - O_j) \sum_{i=1}^m \delta_i W_{ij} \end{aligned} \quad (19)$$

in which δ_j is search direction value of j^{th} neuron of hidden layer ($j=[1 \rightarrow q]$); O_j is the output value of j^{th} neuron of hidden layer ($j=[1 \rightarrow q]$); u_l is input of l^{th} neuron of input layer ($l=[1 \rightarrow n]$).

4 Modeling and Identification Results

In general, the procedure which must be executed in attempting to identify a dynamical system consists of four basic steps.

- *STEP 1 (Getting Training Data)*
- *STEP 2 (Select Model Structure)*
- *STEP 3 (Estimate Model)*
- *STEP 4 (Validate Model)*

In Step 1, the identification procedure is based on experimental input-output data values measured from the forward kinematics of the industrial 5-DOF robot arm system. The input signals $\theta_1, \theta_2, \theta_3, \theta_4$ and θ_5 (or $q_1(k), q_2(k), q_3(k), q_4(k), q_5(k)$ in z-domain) represented five joint-angles which are needed to be applied to the five joints of the industrial robot arm when we apply a linear trajectory represented by output signals (x,y) corresponding the Cartesian coordinates of the end-effector of the industrial 5-DOF robot arm. Therefore, the chosen output Cartesian coordinates (x,y) are to formulate a linear trajectory of the robot arm's end-effector. Fig. 2 presents the collected input-output data composes of the five input signals $\theta_1, \theta_2, \theta_3, \theta_4$ and θ_5 applied to the five joints of the industrial 5-DOF robot arm system and the responding $x(t)$ and $y(t)$ outputs of the industrial robot arm's end-effector Cartesian coordinates.

These collected input-output data is used for training and validating the proposed forward neural MIMO NARX (FNMN) model. The Cartesian coordinates (x,y) considered as reference outputs resulted from the forward kinematics of the industrial 5-DOF robot arm angles $(\theta_1, \theta_2, \theta_3, \theta_4, \theta_5)$ considered as reference inputs. Fig.2 and 3 show that the input signals $\theta_1, \theta_2, \theta_3, \theta_4$ and θ_5 (or $\theta_1(k), \theta_2(k), \theta_3(k), \theta_4(k), \theta_5(k)$ in z-domain) represented joint-angles applied to the five joints of the industrial 5-DOF robot arm and the output signals (x,y) represented the Cartesian coordinates of the end-effector of the industrial 5-DOF robot arm.

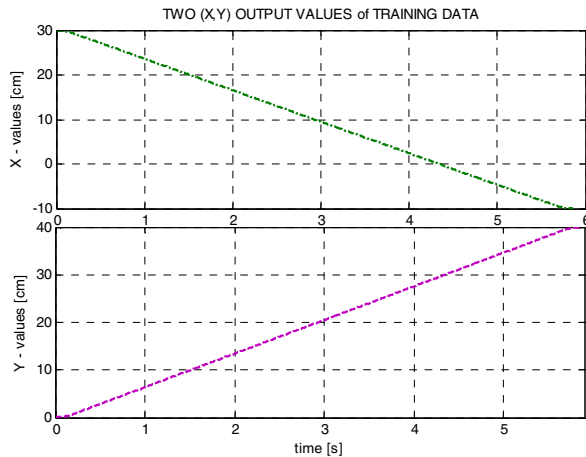


Fig. 2. Output training data for identification process, $x(t)$ and $y(t)$

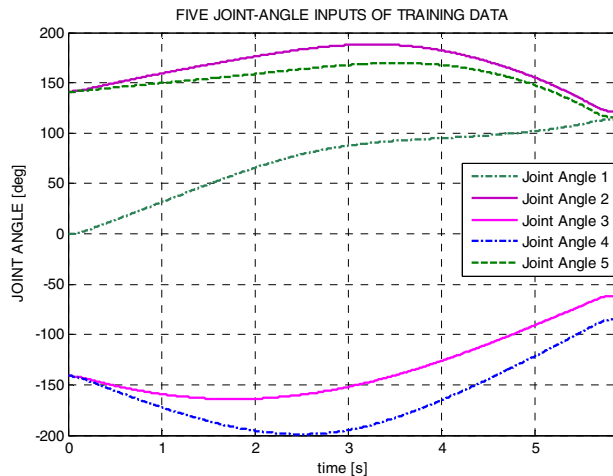


Fig. 3. Input training data used in identification process, $(\theta_1, \theta_2, \theta_3, \theta_4, \theta_5)$ [rad]

Back Propagation (BP) learning algorithm is based on the error between the (x,y) reference outputs and the responding (x_h, y_h) outputs of forward neural MIMO NARX model to update the weights of proposed forward neural MIMO NARX model. Fig.4 illustrates identification scheme of the industrial 5-DOF robot arm using proposed forward Neural MIMO NARX11 (FNMN11).

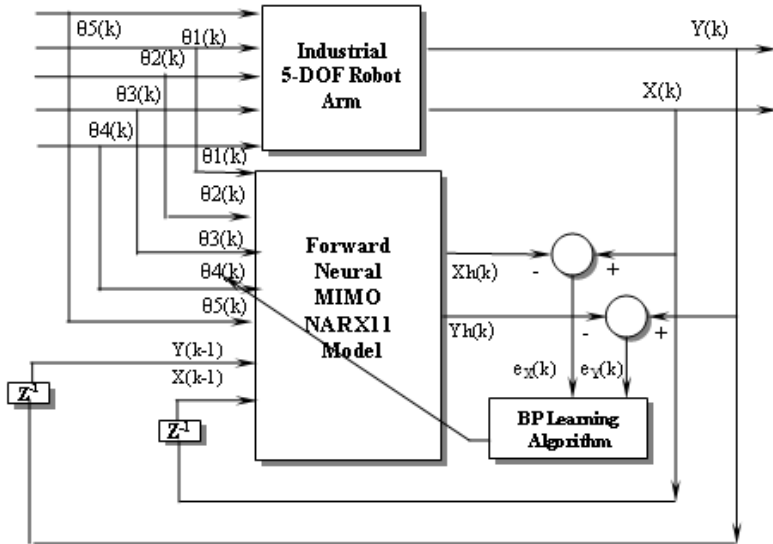


Fig. 4. Proposed identification scheme of forward kinematics of the industrial 5-DOF robot arm using forward neural MIMO NARX11 model

The second step relates to selecting the model structure. The block diagrams in Fig.4 illustrate the identification scheme of these two proposed FNMN models. The proposed forward neural MIMO NARX11 (FNMN11) model structure is attempted. Its model structure was presented in Fig. 1.

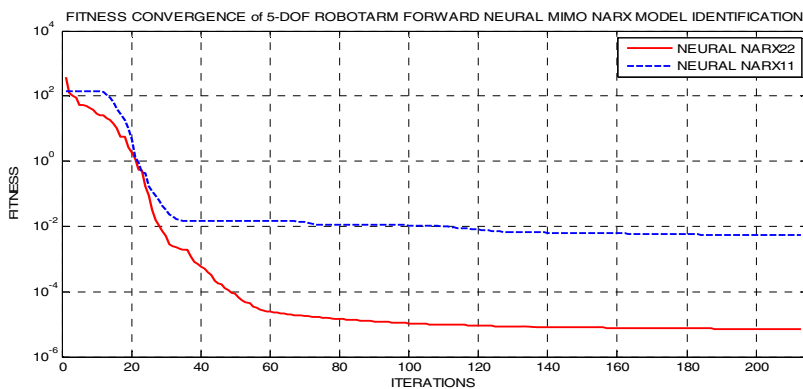


Fig. 5. Fitness convergence of forward kinematics of industrial robot arm

The third step estimates values for the trained forward Neural NARX model. The optimal fitness value to use for the BP-based optimization and identification process is calculated. The estimation result is presented in Fig. 5. This figure represents the fitness convergence values of the proposed forward kinematics of the industrial robot arm FNMN system which corresponds to two different FNMN models (forward neural NARX11 and forward neural NARX22 models) and both of them were identified and optimized with Back Propagation (BP) learning algorithm. The fitness value of the proposed forward kinematics of the 5-DOF industrial robot arm FNMN model produces an excellent global optimal value (equal to 0.000036 with FNMN11 and 0.000027 with FNMN22 model).

These good results are due to how the proposed FNMN model combines the extraordinary approximating capability of the neural system with the powerful predictive and adaptive potentiality of the nonlinear NARX structure that is implied in the FNMN model. Consequently, the BP-based forward kinematics of the industrial robot arm FNMN model addresses all of the nonlinear features of the forward kinematics of the industrial robot arm system that are implied in the responding output signals (x, y) from joint angle inputs ($\theta_1, \theta_2, \theta_3, \theta_4, \theta_5$).

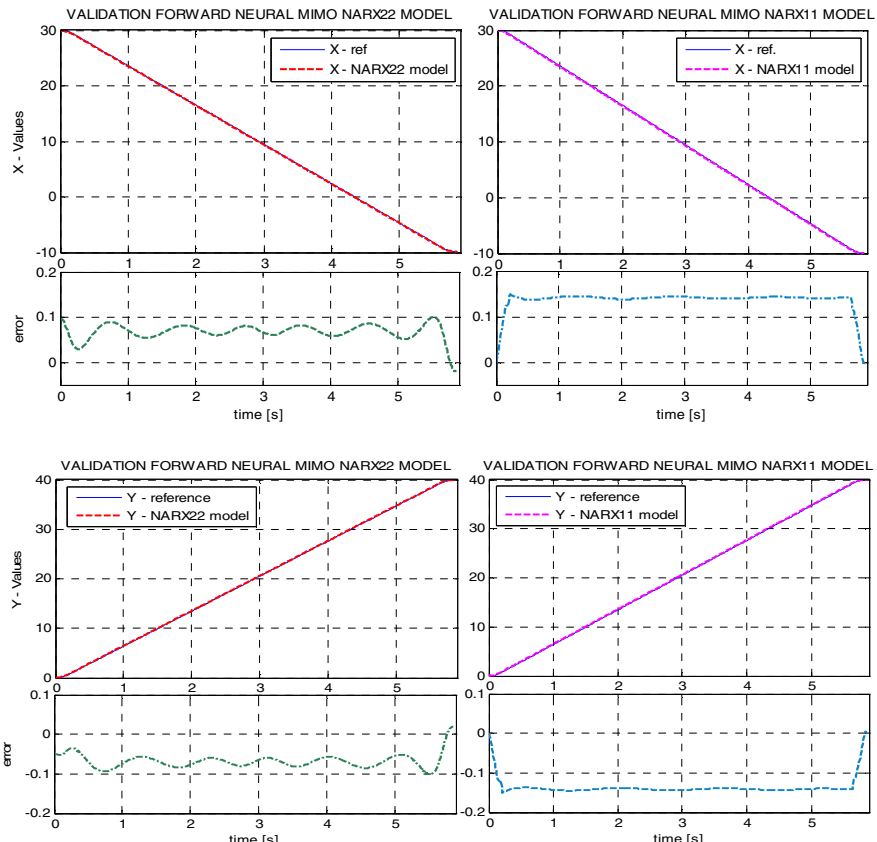


Fig. 6. Validation of circular trajectory of industrial 5-dof robot arm end-effector

The last step relates to validating the resulting nonlinear FNMN models. Applying the same training diagram in Fig. 4, a good validating result demonstrates the performance of the resulting forward Neural MIMO NARX (FNMN) model which are presented in Fig.6. The error, optimized nearly zero between the real industrial 5-DOF robot arm system responding reference output signals (x, y) and the forward Neural MIMO NARX11 and forward Neural MIMO NARX22 model responding output signals (x_{hat}, y_{hat}), asserts the very good performance of proposed FNMN model. Forwardly, the error shown in Fig.6 consolidates again the quality of forward Neural MIMO NARX22 model is similar in comparison with forward Neural MIMO NARX11 one.

Finally, Fig. 7 illustrates the auto-tuning variation of adaptive ARX parameters of proposed forward Neural MIMO NARX11 Model of the industrial 5-DOF robot arm. Concretely, the fifteen parameters $a_{11}, a_{12}, a_{13}, b_{11}, b_{12}, a_{21}, a_{22}, a_{23}, b_{21}, b_{22}$ and $a_{31}, a_{32}, a_{33}, b_{31}, b_{32}$ of the two 1st order ARX structures integrated in proposed FNMN11 model were adaptively auto-tuning as illustrated in Fig. 7. These results show that the parameters of the ARX structure integrated in proposed FNMN models now become adaptively nonlinear and will be adaptively determined from the optimized weighting values W_{ij} and w_{jl} of the forward Neural MIMO NARX model. This feature once more proves that the proposed adaptive forward Neural MIMO NARX (FNMN) model is very powerful and adaptive in identification and in model-based advanced control as well.

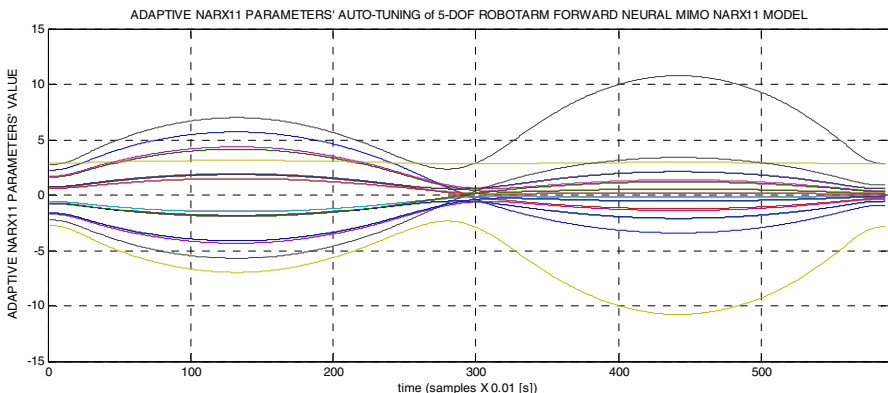


Fig. 7. Adaptive parameters of NARX structure embedded in proposed FNMN11 model

5 Conclusion

In this paper a new approach of forward neural MIMO NARX model firstly was utilized in modeling and identification of the forward kinematics of the industrial 5-dof robot arm system. Training and testing results showed that the newly proposed inverse dynamic neural MIMO NARX model presented in this paper can be used in online control with better dynamic property and strong robustness. This proposed

intelligent FNMN model is quite suitable to be applied for the modeling, identification and control of various complex plants, including linear and nonlinear processes without concerns of large change in external environments.

Acknowledgements. This research is supported by DCSELAB (VNU-HCM) and by Vietnam National Foundation for Science and Technology Development (NAFOSTED) under grant number 107.04-2012.23.

References

1. Craig, J.J.: *Introduction to Robotics: Mechanisms and Controls*. Addison-Wesley, Reading (1989)
2. Lee, G.C.S.: Dynamics and Control, Robot Arm Kinematics. *Computer* 15(12), 62–79 (1982)
3. Korein, J.U., Balder, N.I.: Techniques for generating the goal-directed motion of articulated structures. *Institute of Electrical and Electronics Engineers Computer Graphics Applications* 2(9), 71–81 (1982)
4. Srinivasan, A., Nigam, M.J.: Neuro-Fuzzy based Approach for Inverse Kinematics Solution of Industrial Robot Manipulators. *International Journal of Computers, Communications and Control*, III (3), 224–234 (2008)
5. Alavandar, S., Nigam, M.J.: Adaptive Neuro-Fuzzy Inference System based control of six DOF robot manipulator. *Journal of Engineering Science and Technology Review* 1, 106–111 (2008)
6. Hasan, A.T., Al-Assadi, H.M.: Performance Prediction Network for Serial Manipulators Inverse Kinematics solution Passing Through Singular Configurations. *International Journal of Advanced Robotic Systems* 7(4), 10–23 (2010)
7. Velagic, J., Osmic, N., Lacevic, B.: Neural Network Controller for Mobile Robot Motion Control. *International Journal of Intelligent Systems and Technologies* (2008)
8. Sadjadian, H., Taghirad, H.D., Fatehi, A.: Neural Networks Approaches for Computing the Forward Kinematics of a Redundant Parallel Manipulator. *International Journal of Computational Intelligence* (2006)
9. Ahn, K.K., Anh, H.P.H.: A new approach of modeling and identification of the PAM robot arm based on recurrent neural network. *Proceedings IMechE, Part I: Journal of Systems and Control Engineering* 221(I8), 1101–1122 (2007)
10. Anh, H.P.H., Ahn, K.K.: Inverse Double NARX Neural Model for System Identification. *IEEE/ASME Transactions on Mechatronics* 15(1), 136–148 (2010)

An Alternative Method to Approximate the Inverse Kinematics of Unknown Geometry Manipulators Using an RBFN with Regularly-Spaced Position Centres

Bach H. Dinh, Thang T. Nguyen, and Bao Q. Nguyen

Faculty of Electrical and Electronics Engineering,
Ton Duc Thang University, No. 19 Nguyen Huu Tho Street, Tan Phong Ward, District 7,
Ho Chi Minh City, Vietnam
`{dhhbach, trungthangttt, nqbao}@tdt.edu.vn`

Abstract. This paper presents a novel solution using Radial Basis Function Networks (RBFNs) to approximate the inverse kinematics of unknown geometry manipulators (e.g. a robot-vision system). This approach has two fundamental principles: centres of hidden-layer units are regularly distributed in the workspace and constrained training data is used where inputs are collected around the centre positions in the workspace. To verify the performance of the proposed approach, simulations in Matlab and practical experiment have been performed. The results of both the simulation and experiment prove that the proposed approach is effective.

Keywords: Radial Basis Function Networks, regularly-spaced position centres, constrained training data.

1 Introduction

In robot kinematics there are two important problems, forward and inverse kinematics. Forward kinematics can be regarded as a one-to-one mapping from the joint variable space to the Cartesian coordinate space (world space). From a set of joint angles, forward kinematics determines the corresponding location (position and orientation) of the end-effector. This problem can be easily solved by the 4×4 homogenous transformation matrices using the Denavit & Hartenberg representation [1]. Inverse kinematics is used to compute the corresponding joint angles from location of the end-effector in space. Obviously, inverse kinematics is a more difficult problem than forward kinematics because of its multi-mapping characteristic. There are many traditional solutions to solve the inverse kinematics problem, such as the geometric, algebraic, and numerical iterative methods [2]. In particular, some of the most popular methods are mainly based on inversion of the mapping established between the joint space and the task space using the Jacobian matrix [2]. This solution uses numerical iteration to invert the forward kinematic Jacobian matrix and does not always guarantee to produce all the possible inverse kinematic solutions and involves significant computation. However, in cases where the manipulator geometry cannot be exactly specified, the traditional methods become difficult, for example the robot-vision systems.

The artificial neural network which has significant flexibility and learning abilities has been used in many robot control problems. In fact, for the inverse kinematics problem several neural network architectures have been used, such as MLP (Multi-Layer Perceptron), Kohonen self-organizing map and RBFN [3]-[9]. However, all the previously mentioned approaches tried to produce an inverse solution of the forward kinematic transformation to build the mapping from world coordinate space to joint angle space. It means that the manipulator geometry or the forward kinematics must be known to collect the training patterns for the neural networks. Therefore, it seems that the performance of existing approaches (both MLPNs and RBFNs) described earlier is still insufficiently accurate and inefficient for practical applications (i.e., unknown forward kinematics).

In this paper, an RBFN is used to learn the inverse kinematics of a completely unknown geometry manipulator. To enhance the performance of the RBFN, a new approach is proposed

- using regularly-spaced position centres as a predefined structure of the RBFN,
- using constrained data for the training phase (this constrained training pattern is collected around centre positions with a reasonable degree of accuracy),
- using strict interpolation, or the least mean square (LMS) algorithm, to update the linear weights.

The proposed approach focus on the application in real robotic systems with unknown geometry. Thus, using a robot vision system, which the manipulator position in the workspace is represented by an image coordinate in the camera's plane instead of a world coordinate, is a typical unknown geometry manipulator. This robot-vision system has been used for many practical applications such as remotely controlled robot systems.

The paper is organized as follows. The first section has introduced the basic ideas and background of the inverse kinematics problem using neural networks. In the second section, the approach using the RBFN to approximate the manipulator inverse kinematics is presented. It describes the RBFN architecture and presents the training methods and constrained training data as well to learn the inverse kinematics function. The simulation and practical experiment are described in the next sections that verify the proposed approach. Finally, the main conclusions are outlined in the last section.

2 Training Radial Basis Function Network to Approximate the Inverse Kinematics of an Unknown Geometry Manipulator

The accuracy of a function approximation based neural networks depends on three main factors: the structure of the network, the training method and the training data. Thus, in this paper, we proposed a new idea solving these three factors by using regularly-spaced position centres for the hidden-layer, as well as using constrained

data and strict interpolation method for training phase to enhance the performance of the RBFN.

2.1 Building the Structure of an RBFN with Regularly-Spaced Position Centres

The basic architecture of an RBFN is the three layer network consisting of an input layer, a hidden layer and a linear output layer [8][9]. The unique feature of the RBFN compared to the MLP and other networks is the process performed at the hidden layer in which the corresponding output depends on the distance between its centre and input. It can be presented as:

$$\Phi_i(x) = \exp\left(-\frac{\|x - c_i\|}{\sigma^2}\right) = \exp\left(-\frac{r_i^2}{\sigma^2}\right) \quad (1)$$

$$r_i = \sqrt{\sum_{k=1}^K (x_k - c_{ki})^2} \quad (2)$$

where

Φ_i – Radial basis function (Gaussian function)

c_i – centre of the i -th hidden unit ($i = 1, 2, \dots, I$)

σ - width of the Gaussian function

r_i - distance between input and centre of the i -th hidden unit

x – input of the RBFN – image coordinates ($k = 1, 2$).

Then, the outputs of the RBFN are expressed as:

$$y_j(x) = \sum_{i=1}^M W_{ji} \Phi_i(x) \quad (3)$$

in which

W_{ji} – synaptic weight between the i -th hidden unit and the j -th output,

y_j – the j -th output of the RBFN- joint angles ($j = 1, 2$).

Because of the distinctive structure of the RBFN, its training process can be separated into two phases, building a hidden layer structure where centres and widths of the hidden units are firstly determined, and then training the linear weights based on input-output patterns [4][7]. Normally, these centres can be determined with relation to the inputs of the training data by some unsupervised methods, such as the self-organizing method, clustering techniques or randomly selected [6][7]. In this paper, we proposed a new idea in which the selection of RBFN configurations is independent of training data collected. The structure of the hidden layer should be pre-defined so that the centres of hidden units are distributed regularly in the workspace and the width of the Gaussian functions are fixed as a proportion of the centre distance. Therefore, the hidden-layer structure is persistent to make the regular generalization through the whole workspace despite the difference of training sets. This approach is very simple because these hidden-layer parameters can be adjusted

by only varying the distance of hidden layer centres. Moreover, as the centres of the hidden layer units (Gaussian functions) are regularly distributed in the workspace, these functions should have the same width (or spread). This spread value affects the smoothness of the network by varying the local-filter feature of the hidden units. It is easily adjusted in proportion to the centre's distance. As a result, using this proposed approach, the hidden-layer parameters can be simply experimented in various values before a satisfactory set is chosen for a specific application.

2.2 Collecting Constrained Traing Data

In this paper, a new concept of using constrained data whose inputs are closed to centre positions is proposed for the training process. This approach uses a data selector to refine training patterns whose inputs are picked randomly around the centres' positions. This procedure can be described as below:

- i/ At beginning, a set of chosen centres' points is loaded as criteria of data.
- ii/ When one new data point is picked, its position is sequentially compared with that of all centre points in the criterion set.
- iii/ If this data point drops in the centre's neighbor area of any centre points, it is selected and the corresponding centre point is deleted from the criterion set.
The condition to select a random point into constraint training data set is

$$\begin{aligned} \|P_x - C_x\| &\leq \text{MaxDev}, \text{and} \\ \|P_y - C_y\| &\leq \text{MaxDev} \end{aligned} \quad (4)$$

where MaxDev is the maximum deviation from the centre position and $\{C_x, C_y\}$ are the known coordinates of a centre point.

Step (ii) and (iii) of the collecting phase are continuously performed until the criterion set empty.

Using equation (4), a set of constrained training data can be easily created by first randomly collecting or scanning data from the whole workspace, then selecting only some appropriate points according to the maximum deviation. It can also be programmed to collect training data automatically. Thus, the new concept of training an RBFN by using constrained data can be implemented conveniently for a specific problem with a simply additional data processing step.

2.3 Strict Interpolation Training Method

In the training phase, a linear optimisation algorithm to determine a set of optimal weights which minimises the cost function in the least mean squares manner called the strict interpolation method [8]. The linear weights are calculated from the target outputs and the interpolation matrix from the following equation [16]:

$$\mathbf{W} = (\Phi^T \Phi)^{-1} \Phi^T \mathbf{T} \quad (5)$$

Where Φ is the NxN matrix called the interpolation matrix and can be obtained by

$$\Phi = \begin{bmatrix} \Phi_1(1) & \Phi_2(1) & \cdots & \Phi_N(1) \\ \Phi_1(2) & \Phi_2(2) & \cdots & \Phi_N(2) \\ \vdots & \vdots & \ddots & \vdots \\ \Phi_1(N) & \Phi_2(N) & \cdots & \Phi_N(N) \end{bmatrix} \quad (6)$$

$\Phi_i(j)$ is the output of a Gaussian function i under stimulating of the j th input of the data set.

This solution is an exact mapping function for all patterns presenting to the RBFN and its generalization depends on the appropriateness of the selection of the hidden layer structure (centres and width of Gaussian function). In this paper, using centres regularly distributed in the workspace can produce an appropriate approximation of the inverse kinematics function with a small number of hidden units.

3 Simulation and Practical Work

Before applying this approach to practical experiments, a variety of simulations in Matlab, in which PA10-6CE system is modelled as a two-link manipulator, have been performed. It consists of two inputs and two outputs to perform a transformation from the world space (x, y) to the joint angle space (θ_1, θ_2). Moreover, to demonstrate the proposed approach, a real unknown geometry manipulator has been developed as the followings:

- A Mitsubishi PA10-6CE manipulator, the six link multipurpose arm, connected to an industrial PC (IPC) via an ARC-Net interface.
- A standard webcam mounted on a vertical shaft that permits rotation captures the manipulator images in the two dimensional space.
- All of the main application programmes were written in C/C++ and run in the APC.

3.1 Simulation Implementation and Result

The simulation was implemented according to the following procedure:

- The structure of the hidden layer was built with pre-defined centres regularly distributed in the workspace (e.g., 10 mm x 10 mm grids). The spread was experimentally selected so that the RBFN can produce an appropriate inverse kinematics approximation.
- Training patterns $\{(x, y); (\theta_1, \theta_2)\}$ were collected as either constrained or random data in the workspace. There were three sets of training data used for this simulation. A set of constrained data whose inputs were coincident with the centres of hidden units was collected. Two others were randomly

collected around centre positions with a maximum deviation of 3 mm and 4 mm (30% and 40% of centre distances, respectively).

- The linear weights were adjusted by strict interpolation.

The RBFN performance was tested by presenting a set of new data that is different from the training data. At this stage, two independent test data sets, a trajectory inside (test trajectory 1) and a trajectory near the edge (test trajectory 2) of the workspace (Fig.1), were presented to the network.

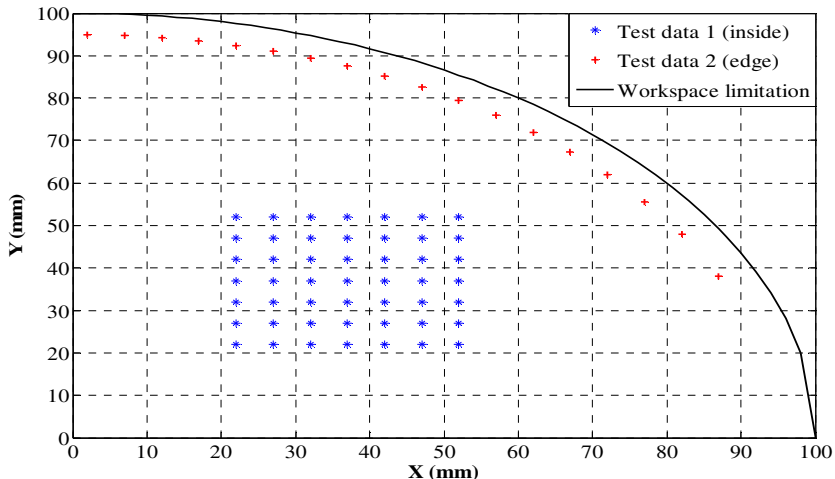


Fig. 1. Test trajectories for the two-link manipulator simulations

The simulation investigated the network's performance for three different training data sets (constrained and random with a maximum deviation of 3 mm and 4 mm) and a variety of spread values (e.g., 6 - 28 mm). To verify the network's performance, the mean absolute errors (MAEs) between desired and actual positions in X and Y directions were calculated for each condition. Fig.2 presents the network's performance using test trajectory 1 (inside the workspace) after training by the strict interpolation method for various spread values. Fig.3 presents the performance of the same network using test trajectory 2 (near the edge of the workspace).

For test trajectory 1, using the constrained data produces the best performance in which the average MAE (of MAE_X and MAE_Y) is approximately 0.1 mm for spreads between 16 and 22 mm. Using the random data with a maximum deviation of 3 mm also produces a good performance where the average MAE is approximately 0.2 mm for spreads between 16 and 22 mm. When using the random data with a maximum deviation of 4 mm, an average MAE of 0.5 mm is achieved for the same range of spread values. The performance of the RBFN is better for test trajectory inside the workspace. This is because at the edge of the workspace, the network does not have enough hidden radial basis functions to be able to create appropriate

responses. Varying the spread leads to differences in the performance. An increase in the spread value can improve the network's performance (i.e., decrease in MAEs). However, the performance will become poorer if the spread is increased significantly, especially for test trajectory 2. There is a spread value between 16 and 22 mm that can produce an optimal inverse kinematics approximation for both test trajectories when training with any of the three training data sets. Thus, the idea of using an RBFN with regularly-spaced position centres has produced an excellent approximation of the

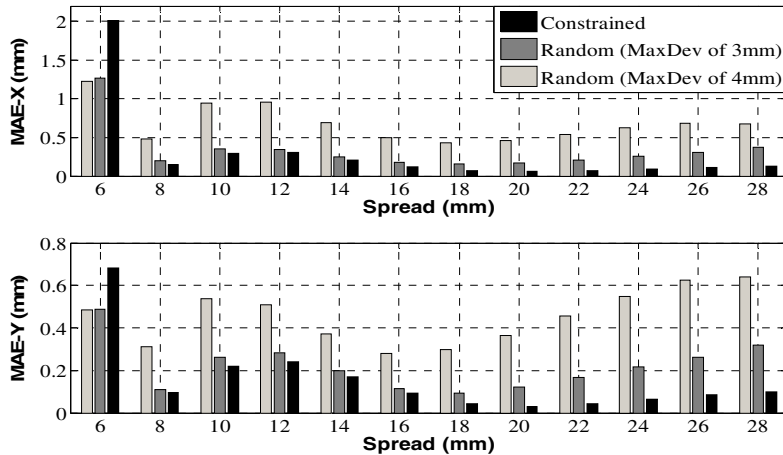


Fig. 2. Performance after training by the strict interpolation for test trajectory 1

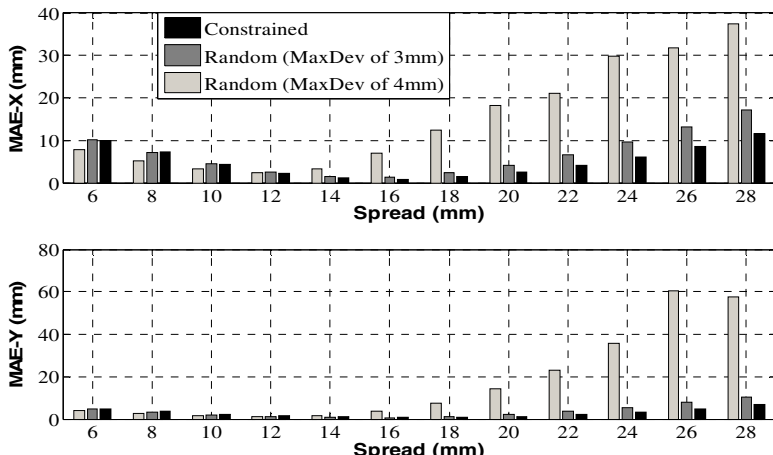


Fig. 3. Performance after training by the strict interpolation for test trajectory 2

inverse kinematics function for a two-link manipulator. These results are significantly better compared to other relevant approaches [4]-[6]. The closer the training data to the centre positions, the better the inverse kinematics approximation. The RBFN trained with a set of random data where the maximum deviation is no higher than 30% of the centre distance also produces good results.

3.2 Practical Experiment

The experiments using an RBFN to approximate the inverse kinematics transformation of a robot-vision system can be described as follows:

- The hidden layer of the RBFN was built with a set of pre-defined centres regularly distributed in the workspace (10 pixel x 10 pixel grids). These centres had to be chosen in the operational region which is constrained due to joint angle limits. The number of hidden centres was 150 points.
- Training data was collected as constrained patterns by using the joint servo-controllers and the visual measurement system. The deviation between training data and centre points was no higher than 30% of the centre distance.
- The linear weights were adjusted by the strict interpolation with collected training data. At this stage, various spread values can be investigated to select a suitable RBFN structure that produces a good approximation of the inverse kinematics transformation.

To verify the network's performance a test data set was presented as desired positions in the workspace. The error between the desired and actual position was calculated to verify how well the RBFN approximates the actual inverse kinematics function. This practical error is affected not only by the quality of the RBFN but also measurement error and joint servo-controller error.

Figs.4 and 5 present the RBFN performance with a spread of 12 pixels. Fig.4 presents the distribution of desired and actual positions in the workspace and Fig.5 shows the errors between the desired and actual positions. As shown in Fig.4, most of the actual positions were close to the desired positions with an error of 1 pixel (one pixel is approximately equivalent to 1.8 mm). However, there were some positions which deviated significantly from the actual desired positions. This happened in all experiments with different spreads because these test points were located near the edge of the workspace where the RBFN may have insufficient basis functions to produce an adequate generalisation in that region. This situation is similar to the simulation results with the test points located near the edge of the workspace. The performance is highly satisfactory because the quality of this robotic system is dependent not only on the RBFN learning ability but also the accuracy of the training data, quality of the visual measurement system, and even the precision of the servo controller.

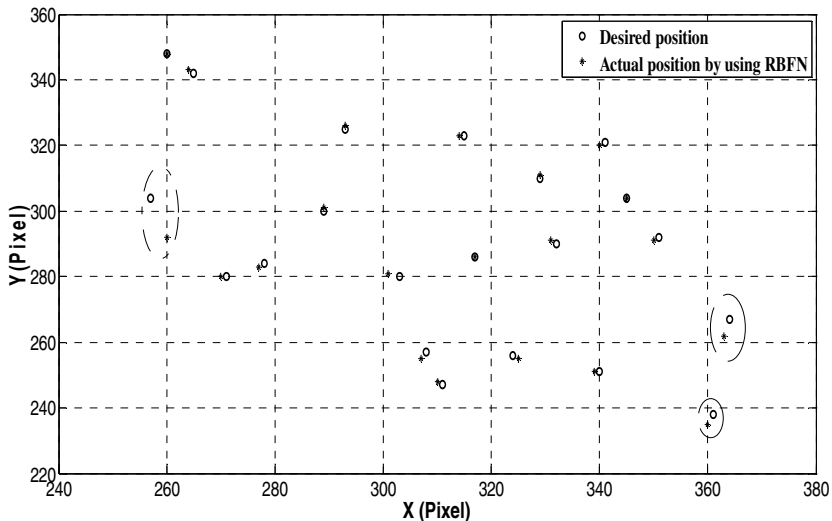


Fig. 4. RBFN performance (centre distance of 10 pixels, spread of 7 pixels)

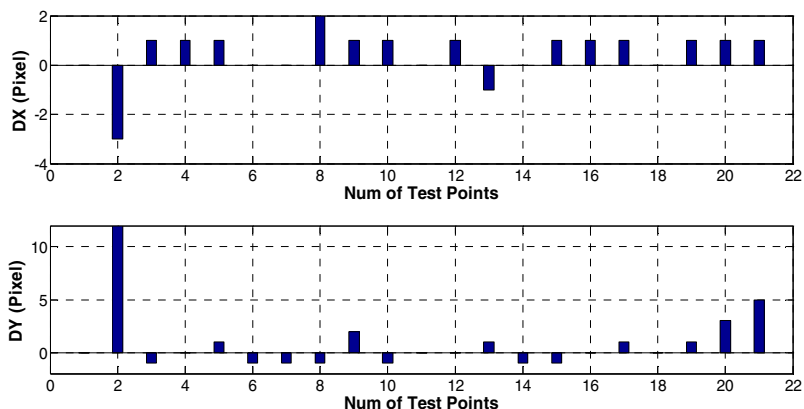


Fig. 5. Error between desired and actual positions

In this practical work, the additional errors are because of the visual measurement system and the joint servo-controllers. The visual measurement error always exists as there is at least an error of 0.5 pixels due to the discrete form of image data.

4 Conclusion

The new approach using an RBFN can produce an appropriate approximation of the inverse kinematics transformation of an unknown geometry manipulator (i.e., a robot-vision system). The selection of hidden unit centres as regularly-spaced positions in the workspace significantly improves the network's performance. The generalisation capability of the RBFN is closely related to the structure of the hidden layer (centre distance and spread). If the centre distance is fixed due to the limited number of hidden units, the spread value chosen affects the network's performance significantly, especially when using the strict interpolation method. The training process using the strict interpolation method with constrained data collected closely to the centre positions enhances the network's performance. Both the simulation and practical work verified the proposed approach.

References

- [1] Khalil, W., Dombre, E.: *Modeling, Identification, and Control of Robots*. Hermes Penton (2002)
- [2] Choi, B.B., Lawrence, C.: Inverse Kinematics Problem in Robotics Using Neural Networks. NASA Technical Memorandum 105869 (October 1992)
- [3] Morris, A.S., Mansor, A.: Finding the Inverse Kinematics of Manipulator Arm Using Artificial Neural Network with Lookup Table. *Robotica* (Cambridge University Press) 15, 617–625 (1997)
- [4] Zhang, P.-Y., Lu, T.S., Song, L.B.: RBF Networks-Based Inverse Kinematics of 6R Manipulator. *The International Journal of Advanced Manufacturing Technology* 26, 144–147 (2004)
- [5] Yang, S.S., Moghavvemi, M., Tolman, J.D.: Modelling of Robot Inverse Kinematics Using Two ANN Paradigms. In: Proceedings of TENCON2000-Intelligent System and Technologies for the New Millennium, Kuala Lumpur, Malaysia, September 24-27, vol. 3, pp. 173–177 (2000)
- [6] Hermann, G., Wira, P., Urban, J.P.: Neural Networks Organisations to Learn Complex Robotics Functions. In: Proc. of the 11th European Symposium on Artificial Neural Networks, Bruges, Belgium, pp. 33–38 (April 2003)
- [7] Song, K.T., Chang, J.M.: Experimental Study on Robot Visual Tracking Using A Neural Controller. In: Proc. of the 22nd Int. Conf. on Industrial Electronics, Control, and Instrumentation, pp. 1850–1855 (1996)
- [8] Haykin, S.: *Neural networks - A Comprehensive Foundation*. Prentice Hall, Inc. (1999)
- [9] Irwin, G.W., Warwick, K., Hunt, K.J.: *Neural Network Applications in Control*. IEE Control Engineering Series 53 (1995)
- [10] Dinh, B.H., Dunnigan, M.W., Reay, D.S.: Position Control of a Robotic Manipulator Using a Radial Basis Function Network and a Simple Vision System. In: Proc. of the IEEE Int. Symposium on Industrial Electronics (ISIE 2008), Cambridge, United Kingdom, pp. 1371–1376 (July 2008)
- [11] Dinh, B.H., Dunnigan, M.W., Reay, D.S.: A Practical Approach for Position Control Of a Robotic Manipulator Using a RBFN and a Simple Vision System. *WSEAS Transactions on System and Control* 3(4), 289–298 (2008)

Study on Plasma Nitriding Technology Imposed to Several Machine Parts Made of 40CrMo Steel

Luc Van Thuong¹, Dao Duy Trung¹, Hoang Van Chau¹, Hoang Minh Thuan²,
and Dao Quang Ke³

¹ National Research Institute of Mechanical Engineering, Hanoi, Vietnam

² Constructional and Industrial College, Quang Ninh, Vietnam

³ Hanoi University of Agriculture, Hanoi, Vietnam

{thuongweld, hvchauweld}@gmail.com, trungdd@narime.gov.vn,
hoangminhthuan@cic.edu.vn, dqke@hua.edu.vn

Abstract. Plasma nitriding has been considered as the modern technology, enabling to form the nitriding layer on the surface which owns the high wear resistance, corrosion protection and enhances the fatigue resistance of the machine parts. This article presents the researches on plasma nitriding and the effects of several technology parameters on the quality of nitriding layer. This research results have been applied on a number of specific 40CrMo steel machine parts, such as hydraulic pumping gears, GN91 tractor transmission gears...

Keywords: plasma nitriding, quality of nitriding layer, 40CrMo steel.

1 Introduction

Surface treatment technology is a synthetic scientific sector, including research and technical activities to design and manufacture products to satisfy the requirements of hardness, corrosion protection, fatigue resistance, wear resistance...

Quality and useful life of machine and equipment shall depend highly on quality of machine parts. The application of plasma nitriding technology plays an considerable part in the target of improve product quality of engineering industry in particular and in the industry in general.

Applying plasma nitriding technology instead of normal nitriding method shall contribute to improve the parts' quality and useful life, reduce environmental pollution and serving efficiently for industrial manufacturing [2, 4, 5].

2 Research Contents

2.1 Research Materials and Devices

40CrMo Steel has been commonly utilized in manufacturing machine parts which is steady load bearing, high collision and wear resistance. 40CrMo Steel's major

components include: 0.4% C; 0.97% Cr; 0.25% Mo; 0.85% Mn; 0.25% Si; 0.02% V; 0.024% P; 0.017% S [4].

The Eltropuls H045x080, a plasma nitriding device produced by ETROPUL GmbH (Germany) [7, 8] was installed at Vietnam State Key Laboratory of Welding and Surface Treatment Technology (National Research Institute of Mechanical Engineering). Devices testing the nitriding layer consist of: microscopic structure testing device, microscopic hardness measuring device; nitriding layer component analyzing device.

2.2 Theoretical Research

Nitriding is chemical and thermal treatment method. During the nitriding process, nitrogen atom shall be formed in permeable environment, adsorbed into the steel surface and diffused into steel (Fig 1) [2, 3, 4, 5, 7, 8].

Plasma nitriding is an advanced technology, it was invented as an alternative of a gas nitriding technology. Plasma nitriding is carried out in ionized environment at low temperature (about 450–600°C). This method is used to handle the disadvantage which gas and liquid nitriding methods may encounter. Some kinds of gas used during the process are usually inert and safe to people and equipments (Fig 2) [1, 7, 8].

The mechanism of the nitride layer formation during plasma nitriding process is based on Koelbel's proposal, the sample surface is considered to be bombarded by the plasma atoms, iron atoms is sputtered in combination with nitrogen, the reaction in plasma occurs even in the surrounding area with cathode surface, forming iron nitride (FeN) condensing on the sample surface (Fig 3) [1, 3, 7, 8].

FeN is formed by combining iron atoms with plasma nitride which react and condense on cathode surface. FeN is constituted at temperatures from 350 to 600°C and separates each other to form into more stable phases ($\text{Fe}_{2.3}\text{N}$, Fe_4N) and nitrogen atoms. A portion of nitrogen atoms returns into plasma flow and partly diffuses into the crystal structure of the substrate forming a diffusion areas. This process is basically due to gradients' diffusion, inelastic collisions with time and plasma flow [1, 2, 3, 7, 8].

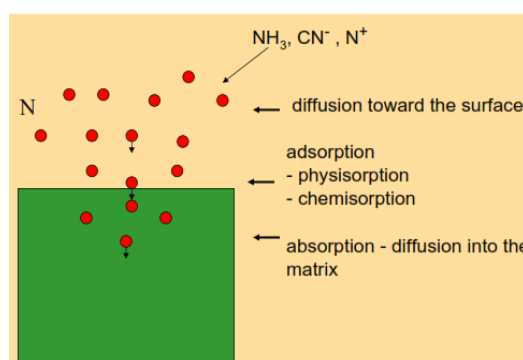


Fig. 1. Nitriding process

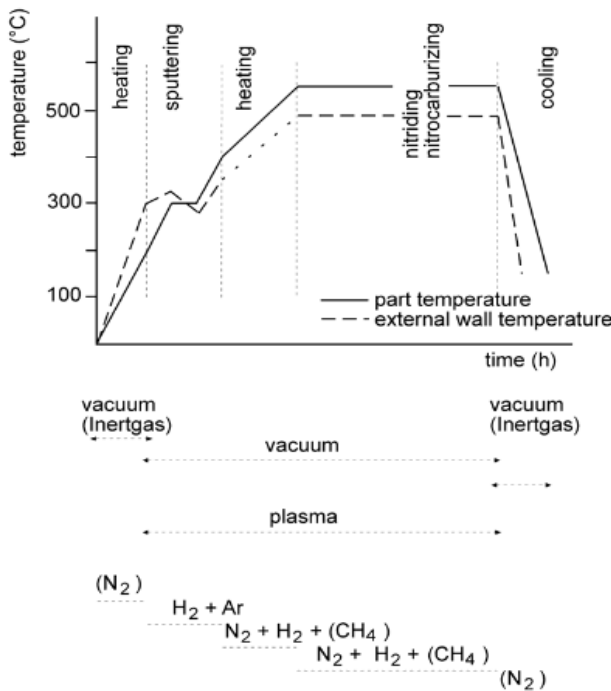


Fig. 2. Plasma nitriding process

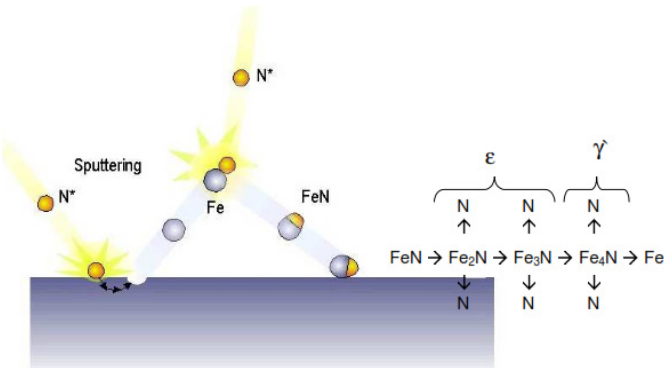


Fig. 3. The mechanism of the nitride layer formation during plasma nitriding process

2.3 Experimental Research

By experimental planning, the study determine the single relationship among surface hardness E (HV0.3), wear intensity m ($10^{-12} g/N.mm$), $\epsilon + \gamma'$ phase thickness, d_1 (μm) and α phase thickness, d_2 (μm) with technological parameters, namely temperature of nitriding T ($^{\circ}C$), the time of nitriding t (h) and the nitrogen/hydrogen gas ratio a (%);

to find out the optimal range of technological parameters in order to maximize nitriding layer's quality [4]:

Temperature of nitriding $T = 510 \div 550 (^{\circ}\text{C})$;

Time of nitriding $t = 12 \div 18 (\text{h})$;

The nitrogen/hydrogen gas ratio $a = 20 \div 40 (\%)$.

The above values used to find out optimal range in consideration of multi-factorial conditions.

Under the results of single-factor experiments, optimal range is utilized to test the effects of multiple factors on the quality of nitriding layer by experimental planning approach level 2 of Box-Wilson. Based on the variation of the technological parameters, experimental matrix and experimental results were set up, the regression coefficients were calculated and adaptability was tested, then regression was developed as follows [4]:

$$\begin{aligned} E = & -2329,572 + 10,493.T + 13,835.t + 16,818.a - 0,0234.T.t - \\ & -0,0163.T.a + 0,09.t.a - 0,0092.T^2 - 0,1252.t^2 - 0,1453.a^2 \end{aligned} \quad (1)$$

$$m = 345,463 - 1,122.T + 0,532.t - 1,497.a - 0,001.T^2 + 0,017.t^2 - 0,026.a^2 \quad (2)$$

$$\begin{aligned} d_1 = & -543,047 + 2,625.T + 3,229.t + 1,295.a - 0,004.T.t + 0,009.t.a - \\ & -0,002.T^2 - 0,044.t^2 - 0,022.a^2 \end{aligned} \quad (3)$$

$$\begin{aligned} d_2 = & -2958,426 + 11,707.T + 38,755.t - 12,786.a - 0,06.T.t + 0,074.T.a - \\ & -0,012.T^2 - 0,164.t^2 - 0,424.a^2 \end{aligned} \quad (4)$$

Thus, when replacing different technological parameters into the formula (1), (2), (3) and (4), the respective nitriding result and quality shall be obtained [4]. For experimental verification, a set of standard technological parameters are chosen as a "center" optimal parameter, using the general optimal function value method to determine optimal function $D = f(T, t, a)$.

$$\begin{aligned} D = & -25,552 + 0,088.T + 0,230.t + 0,058.a - 0,0004.T.t - \\ & -0,0001.T^2 - 0,0013.t^2 - 0,0008.a^2 \end{aligned} \quad (5)$$

Optimal value $D = 0,955$ is highly reliable and utilizable. Accordingly, values of some parameters are defined: $E = 791,950$ (HV0.3); $m = 29,653 (10^{-12} \text{g/N.mm})$; $d_1 = 16,992 (\mu\text{m})$; $d_2 = 370,227 (\mu\text{m})$ being respective to technological parameters $T = 537,4 (^{\circ}\text{C})$; $t = 16,03 (\text{h})$ và $a = 34,62 (\%)$ [4,5].

3 Outcome and Discussion

On the basis of studying plasma nitriding technology and experimental research results, the optimal technological parameters on the devices have been identified,

technological diagram (Figure 4) and plasma nitriding technological process imposed on 40CrMo steel to improve product quality after nitriding (Figure 5) have been developed .

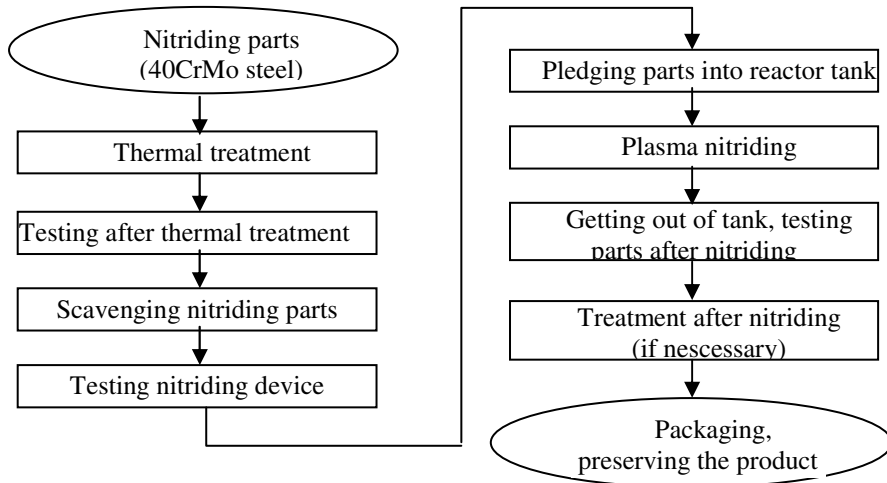


Fig. 4. Technological diagram

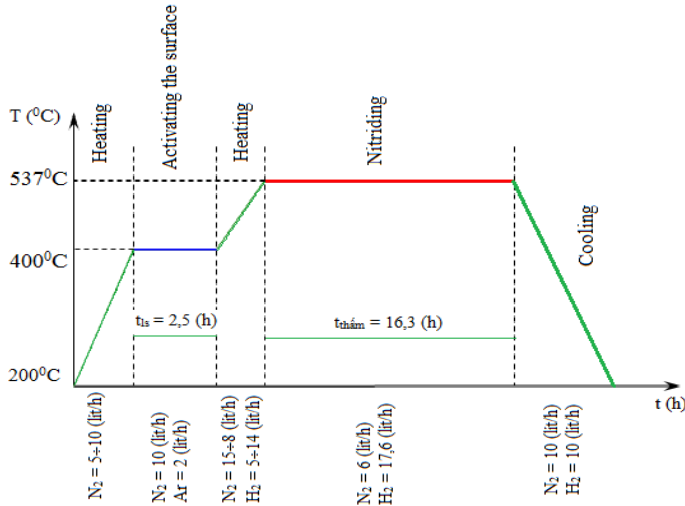


Fig. 5. Technological process

3.1 Microscopic Structure

Through microscopic structure image (Figure 6), it can be found that the sample surface corresponding to part's materials contains clear nitriding layer. The phase

ϵ and phase γ' are white layer which is perceived upon etching and being taken through microscope. Microscopic structure consists of carbide, nitride distributed in ferrite.

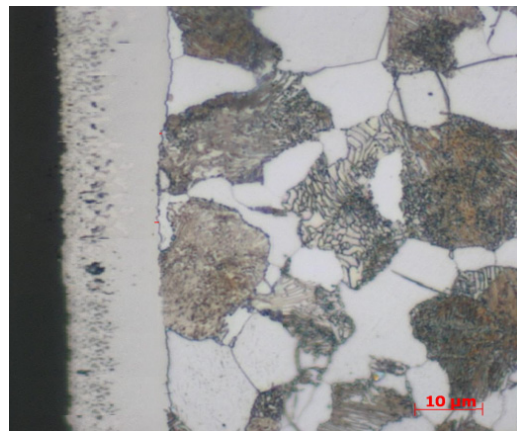


Fig. 6. Microscopic structure of plasma nitriding layer on 40CrMo Steel (500x)

3.2 Microscopic Hardness

Microscopic hardness according to nitriding layer's depth are conducted to measure on cross sections through the nitriding layer and according to the distance. High surface hardness is 795 HV0.3, the deeper the nitriding layer is, the less hardness is. The surface hardness is constant when reaching to 350 μm depth, corresponding to the base metal's hardness (340 HV0.3) (Fig 7).

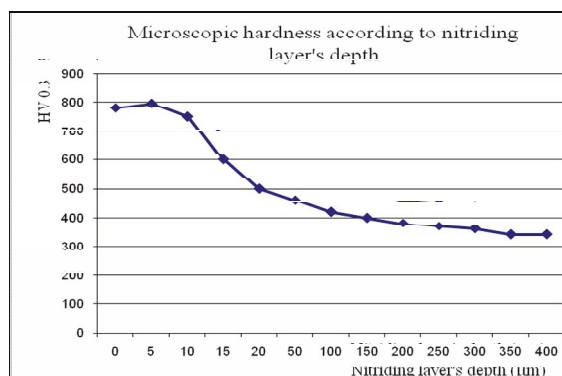


Fig. 7. Allocation of hardness according to nitriding layer's depth

3.3 Allocation of Nitrogen in Nitriding Layer

Under the %N content according to nitriding layer depth, the thickness of the phase $\epsilon + \lambda'$ and phase α can be identified.

EDX analysis results showed that level of %N on the surface is high (10.68%N), however, it is lower when the depth increase (Fig 8).

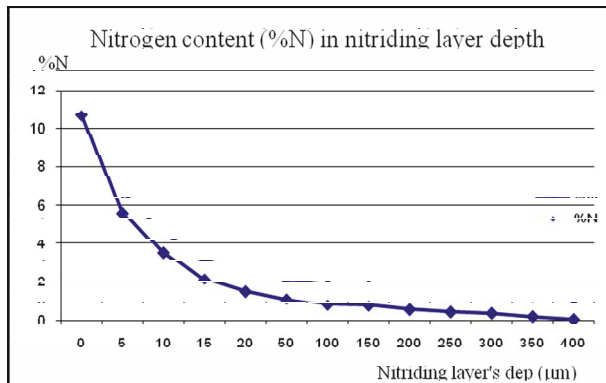


Fig. 8. Allocation of nitrogen content (%N) in nitriding layer depth

In bolt-dish grinding system (a bolt is made of 40CrMo steel including plasma nitriding and non-nitriding, a dish is made of C45 steel with hardness of 45HRC under thermal treatment), friction coefficients between the nitriding sample and non-nitriding ones are 0.51 and 0.64, respectively. Thus, the friction coefficient of nitriding sample is about 20% lower than that of non-nitriding sample. The corrosion intensity of nitriding samples were reduced 25% in comparison with the non-nitriding.

This research results have been applied on a number of specific 40CrMo steel machine parts, such as hydraulic pumping gears, GN91 tractor transmission gears... (Fig 9 and Fig 10)



Fig. 9. Hydraulic pumping gears



Fig. 10. GN91 tractor transmission gears

4 Conclusion

Research on application of plasma nitriding technology on 40CrMo steel create new approach to new technology, with high applicability. Technology process has been applied to some specific machine parts made of 40CrMo steel represents great advantages of plasma nitriding method in comparison with normal nitriding methods. The achieved results can be utilized to find out technological process for many type of steel grades under plasma nitriding so as to obtain the best effectiveness.

References

1. Balles, A.C.: Nitretação a plasma como meio alternativo ou complementar à oxidação negra na proteção à corrosão do aço de baixo teor de carbono. Pipe - Programa Interdisciplinar de pos Graduação em Engenharia, Curitiba, 5–14 (2004)
2. Baranowska, J.: Plasma Nitriding and Plasma Immersion Ion Implantation, pp. 9–25. Szczecin University of Technology (2008)
3. Greßmann, T.: Fe-C and Fe-N compound layers: Growth kinetics and microstructure, Institut für Metallkunde der Universität Stuttgart, Max-Planck-Institut für Metallforschung. Stuttgart (2007)
4. Thuan, H.M., Ke, D.Q., Van Chau, H.: Optimizing plasma nitriding regime of 40CrMo steel on Eltropuls H045x080 device. Vietnam Mechanical Engineering Magazine (6), 62–69 (2012)
5. Thuan, H.M., Ke, D.Q., Van Chau, H., Quoc, T.V., Van Đong, P.: Applying plasma nitriding technology to strengthen epicyclic gears of fresh concrete mixing - transporting truck. In: Summary Record of the Second National Science and Engineering Industry Conference, pp. 388–391 (2009)
6. Giang, H.V., Van Thuong, L., Thuan, H.M.: Applying plasma nitriding technology for machine's parts made of chromium alloy. Vietnam Mechanical Engineering Magazine (5), 15–17 (2010)
7. Huchel, U., et al.: Pulsed Plasma Nitriding of Tools, ELTRO GmbH, Baesweiler, Germany, pp. 1–4 (2005)
8. Huchel, U.: Short Description of Pulsed Plasma Nitriding, ELTRO GmbH, Knol.google.com, pp. 1–10

Characteristic of Corrosion Resistance under Different Heat Treatment Conditions of Coated Zinc Coating Steel with Cr-Free Solution

Ki-Woo Nam¹, Dae-Woong Kim², Nam-Suk Kim³, and Ki-Yong Seong⁴

¹ Department of Materials Science and Engineering, Pukyong National University, 365 Sinseonro, Namgu, Busan, Korea

² UR Interdisciplinary Program of Mechanical Engineering, Graduate School, Pukyong National University, Busan, Korea

³ Samjin Oil Pressure Co. Ltd., Busan, Korea

⁴ DM Co Ltd., Kimhae, Korea

namkw@pknu.ac.kr, dwkim@koreates.com, 64namseok@hanmail.net,
mssky1@nate.com

Abstract. This study performed a salt water spray test using zinc-coated steel sheet specimens, which are coated with S-700 solution and LR-0317. Test specimens were treated in the drying oven at 170~210 °C for 5 minutes and at 190 °C for 3 to 9 minutes. Corrosion resistance of specimen was evaluated for 72 hours by salt water spray test. The coating layer was evaluated the adhesion by the cross-cut and the stability by the dipping of acid/alkali solution. In cross-cut test of coated specimens by S-700 and LR-0317, it was no peeling, and showed excellent adhesion. EGI and HDGI specimens appeared the lowest rust at the heat treatment of 190 °C for 5 minutes, and had the most good corrosion resistance. The acid resistance is not much affected by ambient temperature. The rusts of 60 °C dipping were more than the R.T dipping regardless of the type of material. The acid resistance of EGI by the S-700 solution improved without elemental difference by the oxide formed during the heat treatment. The Si oxide by LR-0317 solution had improved the corrosion resistance regardless of EGI and HDGI. This is judged that the component of Si oxide had control the corrosion.

Keywords: Electrolytic Galvanized, Salt water spray test, Cr-free coating solution, Organic/inorganic hybrid coating, White rust.

1 Introduction

Galvanized steel with chromate treatment is widely used to suppress the white rust as way of cheap anticorrosive treatment [1, 2]. However, international organizations have been constantly tightening restrictions on use of environmental load materials such as Cr⁺⁶ for the environmental protection. This trend is expanding in the field of all the structures. In the trend of growing demand for environmental protection, numerous researches on environment-friendly rust prevention techniques, such as Cr⁺³

chromate [3-6], Cr-free [7-10] and organic/inorganic surface treatment [11-15], have been being performed.

This study performed a salt water spray test using zinc-coated steel sheet specimens, which are coated with a Cr-free polymer solution (S-700) and an organic/inorganic hybrid solution (LR-0317) containing Si, to find optimal heat treatment conditions. Corrosion resistance of specimen was evaluated by salt water spray test. The coating layer was evaluated the adhesion by the cross-cut and the stability by the dipping of acid/alkali solution.

2 Materials and Test Methods

The coating solution used in this study was S-700 (urethane 20 wt.%) and LR-0317 (Si polysilicate 10 wt.% + urethane 10 wt.%), produced by NGE Tech. The ratio of solid content of two solutions which were diluted with distilled water was 20%. Specimens were made by EGI (Electrolytic Galvanized Steel) and HDGI (Hot Dip Galvanized Steel) produced by Union Steel. In both zinc coated specimen, the amount and thickness of zinc are shown in Table 1. Specimen was washed by ultrasound for 5 minutes in isopropanol, and dried. The coating was carried out using bar-coater No.3 (wet film thickness; 6.86 μm). The two kind of heat treatment were performed; first: at 170, 180, 190, 200 and 210 $^{\circ}\text{C}$ for 5 minutes, second: at 190 $^{\circ}\text{C}$ for 3 to 9 minutes, and was immediately water cooling. The thickness of heat-treated coating layer was approximately 1.37 μm . After water cooling, specimens were treated as a taping to prevent corrosion from the edges as shown Fig. 1. The specimens were tilted about 20° in the salt water spray tester, and the neutral salt water spray tests were conducted at 35 $^{\circ}\text{C}$ for 72 hours.

Table 1. Specification of EGI and HDGI

Materials Specific character	EGI	HDGI
Deposited weight of Zn(g/m^2)	18.4	122.8
Thickness of plating layer(μm)	1.6~4.0	5.4~7.4

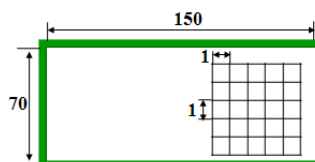


Fig. 1. Dimensions of specimen (unit: mm)

The specimen was observed at intervals of 2 hours, and was performed for 72 hours. Evaluation of corrosion resistance of test specimens were assessed by the occurrence time of initial white rust and the area of white rust by a captured photo. Fig. 2 shows a flowchart of the salt water spray test.

As shown in Fig 1, the coating adhesion was evaluated by 3M tape after a cross-cut to 1 mm intervals in the area of the 5 x 5 mm. The stability of the coating was dipped in acid (0.36% hydrochloric acid) and alkaline (3% NaOH) solutions. Each specimen was cut to size of 30 x 40 mm, and the edges were treated with the tape. Specimens, with and without heat treatment at 50°C for 4 days after coating, were used in the dipping test. Dipping time is $\frac{1}{2}$, $\frac{1}{2}$, 1, 3, 5 hours and the test specimens were half dipping in acid and alkaline solution.

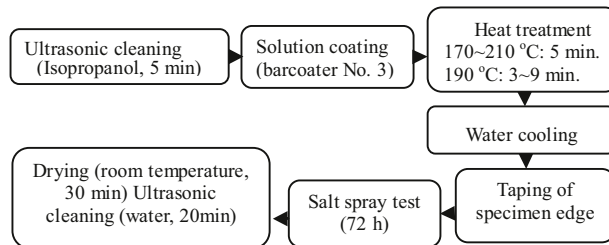


Fig. 2. Flow chart of salt water spray test

After the salt water spray test of 72 hours, the specimen was removed by washing Na as much as possible. The compositions of corroded parts were investigated by EDS (Energy Dispersive X-Ray Spectrometer; SHIMADZU EPMA-1600).

3 Results and Discussion

3.1 Coating Adhesion

Fig. 3 shows the surface of the specimens after the cross-cut test. The specimens were no peeling, and showed excellent adhesion.

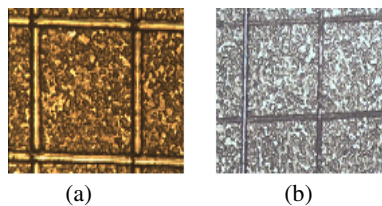


Fig. 3. Appearance after cross-cut adhesion test (x50). (a) Coated EGI specimen with S-700 solution, (b) Coated EGI specimen with LR-0317 solution

3.2 Salt Spray Test

Fig. 4 shows the relationship between the percentage of white rust and salt water spray test time according to the heat treatment temperature. Fig. 4(a), (b) is the result

of S-700 and LR-0317 coating specimen, respectively. In figure (a) and (b), EGI and HDGI specimens appeared the lowest rust at 190 °C, and had the good corrosion resistance.

Fig. 5 is the result of salt spray test to obtain the optimal heat treatment time at 190 °C for 3 to 9 minutes. It shows the relationship between the percentage of white rust and salt spray test time. Heat treated specimens at 190 °C for 5 minutes were the most good corrosion resistance.

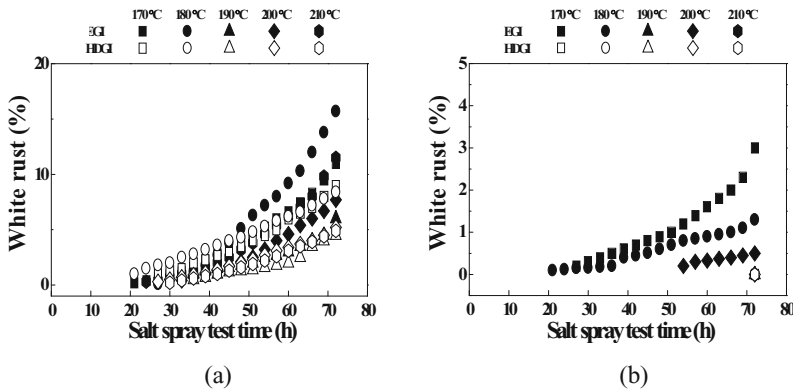


Fig. 4. Corrosion resistance according to heat treatment temperature. (a) S-700 coating, (b) LR-0317 coating

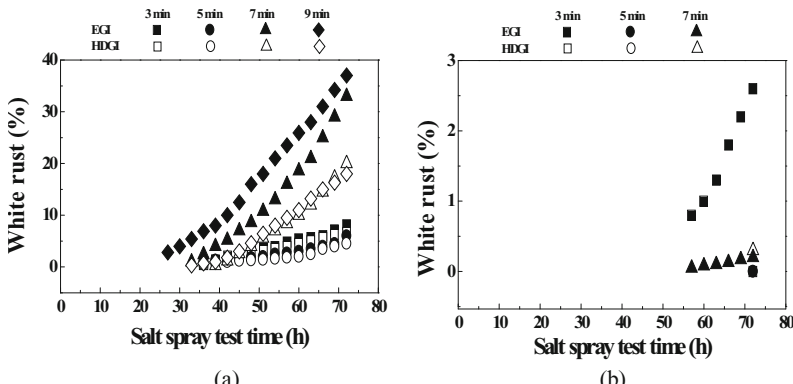


Fig. 5. Corrosion resistance according to heat treatment time. (a) S-700 coating, (b) LR-0317 coating

3.3 Coating Stability Test

At high temperature, the apparent stability of the coating layer is very important. Fig. 6 shows the results of stability test of the specimens. Fig. 6(a) is the heat treated specimen at 190 °C for 5 minutes. Fig. 6(b) is heat treated specimen at 50 °C for 4 days with the Fig. 6(a). Both specimens did not change on the surface.



Fig. 6. Stability test of S-700 and LR-0317 coating specimens. (a) Heat treated specimen for 5 minutes at 190 °C, (b) Heat treated (a) for 4 days at 50 °C

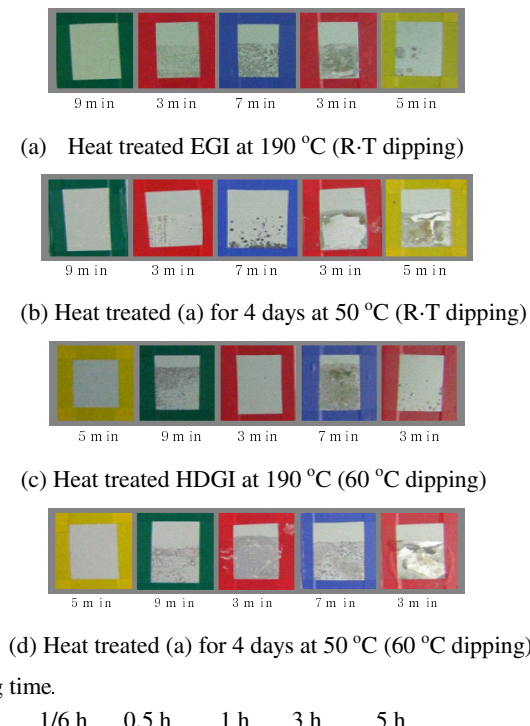


Fig. 7. Acid resistance test of R-T and 60 °C using coated EGI and HDGI specimen with S-700 solution

Figs. 7 and 8 show the results of the acid resistance test. Figs. 7 and 8 are the results of a coated EGI and HDGI specimen with S-700 and LR-0317 solution, respectively. The specimens were dipped in acid solution of room temperature and 60 °C. The acid resistance is not much affected by ambient temperature. However, the heat treated S-700 coating specimen for 4 days at 50 °C was bad regardless of the dipping condition and the type of material. The coated EGI specimen with LR-0317 solution occurred red rust after about two hours. The rust of 60 °C dipping was higher than the R.T dipping regardless of the type of material. Even though a figure did not show, the alkali resistance of the LR-0317 coating EGI specimen is better than the

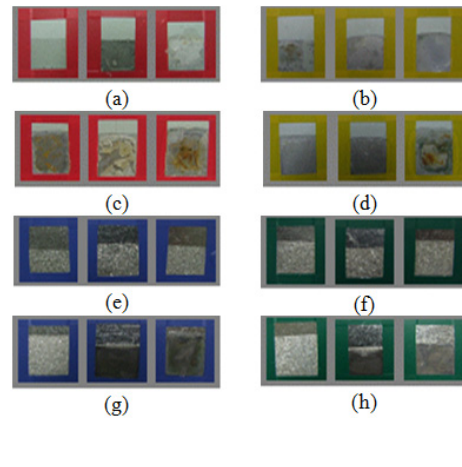


Fig. 8. Acid resistance test of R-T and 60 °C using coated EGI and HDGI specimen with LR-0317 solution. (a) Heat treated EGI at 190 °C (R-T dipping), (b) Heat treated EGI for 4 days at 50 °C (R-T dipping), (c)=(a) (60 °C dipping), (d)=(b) (60 °C dipping), (e) Heat treated HDGI at 190 °C (R-T dipping), (f) Heat treated (e) for 4 days at 50 °C (R-T dipping), (g)=(e) (60 °C dipping), (h)=(f) (60 °C dipping).

S-700 coating specimen. HDGI specimen regardless of coating solution shows a better acid and alkali resistance compared to the EGI specimen.

3.4 EDS Analysis

Surface elemental analysis was performed for the EGI and HDGI specimens. The specimens were coated with the S-700 and LR-0317 solution. The heat treatment is the two kind of condition. That is, the first condition is 7 minutes at 190 °C. The second condition is 4 days at 50 °C with first condition.

Figs. 9 and 10 show the elemental analysis of surface of S-700 and LR-0317 coating specimen, respectively. The specimen surfaces with heat treatment for 4 days had dispersed fine white oxide. In the EGI specimen of Fig. 9(a) and (b), this was given to resistance on the acid, but was not given to resistance on the alkali. Meanwhile, in Fig. 9(c) and (d), the acid/alkali resistance of HDGI specimen had not affected by the heat treatment. Table 2 is the surface element from Fig. 9. The elements of (a)/(b) and (c)/(d) are almost same in spite of the difference in heat treatment condition, respectively. The acid resistance of EGI improved without elemental difference by the oxide formed during the heat treatment.

In Fig. 10, the heat treatment made almost no difference in oxide distribution of the specimens. Table 3 is the surface element from Fig. 10. Si and O element is plenty. This is because of the reaction of Si precursor and O. The Si oxide had improved the corrosion resistance. The elements are almost no difference. But the elements of C

and Zn were detected less than the Fig. 9. This is judged that the component of Si oxide had control the corrosion.

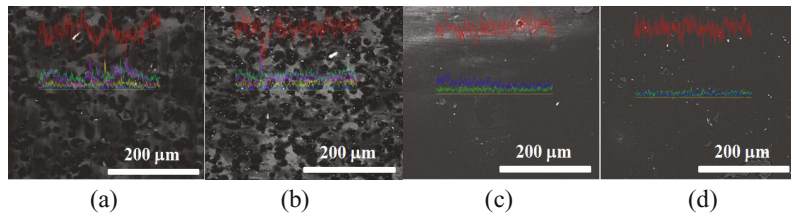


Fig. 9. Elemental analysis of S-700 coated specimen surface. (a) Heat treated EGI during 7 minutes at 190 °C, (b) Heat treated EGI for 4 days at 50 °C with (a), (c) Heat treated HDGI for 7 minutes at 190 °C, (d) Heat treated HDGI for 4 days at 50 °C with (c)

Table 2. Percentage (%) of each element of Fig. 9

	C	O	Zn	Fe	P
(a)	44 ~ 52	4 ~ 7	12 ~ 19	1 ~ 4	13 ~ 18
(b)	43 ~ 50	5 ~ 7	7 ~ 11	1 ~ 4	12 ~ 14
(c)	54 ~ 62	4 ~ 7	9 ~ 14	-	-
(d)	53 ~ 60	4 ~ 7	4 ~ 7	-	-

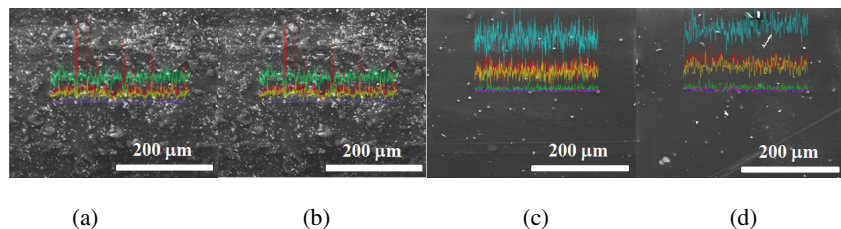


Fig. 10. Elemental analysis of LR-0317 coated specimen surface. (a) Heat treated EGI for 5 minutes at 190 °C, (b) Heat treated EGI for 4 days at 50 °C with (a), (c) Heat treated HDGI for 5 minutes at 190 °C, (d) Heat treated HDGI for 4 days at 50 °C with (c)

Table 3. Percentage (%) of each element of Fig. 10

	C	O	Zn	Fe	Si	Al
(a)	20 ~ 25	15 ~ 22	1 ~ 3	1 ~ 4	38 ~ 45	X
(b)	21 ~ 28	16 ~ 21	1 ~ 2	1 ~ 3	36 ~ 42	X
(c)	19 ~ 24	17 ~ 23	1 ~ 3	1 ~ 3	38 ~ 48	3 ~ 5
(d)	15 ~ 19	14 ~ 18	1 ~ 3	1 ~ 2	32 ~ 38	2 ~ 4

4 Conclusions

This study investigated the corrosion resistance of EGI and HDGI, which were coated with a urethane solution and an organic/inorganic hybrid solution containing Si, according to heat treatment temperature and time. The results obtained were as follows;

- 1) In cross-cut test of coated specimens by S-700 and LR-0317, it was no peeling, and showed excellent adhesion.
- 2) EGI and HDGI specimens appeared the lowest rust at the heat treatment of 190 °C for 5 minutes, and had the most good corrosion resistance.
- 3) Using the heat treated specimen at 190 oC for 5 minutes, the preserving specimens at 50 oC for 4 days did not change the surface, and coating layer was stable.
- 4) The acid resistance is not much affected by ambient temperature. The rusts of 60 oC dipping were more than the R.T dipping regardless of the type of material.
- 5) The acid resistance of EGI by the S-700 solution improved without elemental difference by the oxide formed during the heat treatment. The Si oxide by LR-0317 solution had improved the corrosion resistance regardless of EGI and HDGI. This is judged that the component of Si oxide had control the corrosion.

References

- [1] Mekhalif, Z., Forget, L., Delhalle, J.: Investigation of the protective action of chromate coatings on hot-dip galvanized steel: role of wetting agents. *Corrosion Science* 47, 547–566 (2005)
- [2] Marder, A.R.: The metallurgy of zinc-coated steel. *Progress in Materials Science* 45, 191–271 (2000)
- [3] Kim, S.W., Lee, C.T.: Environment-friendly Trivalent Chromate Treatment for Zn Electroplating. *J. Korean Ind. Eng. Chem.* 17, 433–442 (2006)
- [4] Kim, M., Lee, J.J., Kim, D.Y., Park, S.E., Kwon, S.C.: The Trend of Study of Echo-Friendly Hard Trivalent Chromium Deposition. *Korea Ins. Surf. Eng.* 37, 179–184 (2004)
- [5] Chang, Y.T., Wen, N.T., Chen, W.K., Ger, M.D., Pan, G.T., Yang, T.C.K.: The effects of immersion time on morphology and electrochemical properties of the Cr(III)-based conversion coatings on zinc coated steel surface. *Corrosion Science* 50, 3494–3499 (2008)
- [6] Bellezze, T., Roventi, G., Fratesi, R.: Electrochemical study on the corrosion resistance of Cr III-based conversion layers on zinc coatings. *Surf. Coat. Technol.* 155, 221–230 (2002)
- [7] Simka, W., Nawrat, G., Nieuzyła, L., Krzakała, A.: Stripping of copper coatings from steel in Cr(VI)-free commercial bath. *Journal of Hazardous Materials* 168, 193–196 (2009)
- [8] Duarte, R.G., Bastos, A.C., Castela, A.S., Ferreira, M.G.S.: A comparative study between Cr(VI)-containing and Cr-free films for coil coating systems. *Progress in Organic Coatings* 52, 320–327 (2005)

- [9] Mahlis, J., Abbadie, A., Kolbesen, B.O.: A comparison of the etching behaviour of the FS Cr-free SOI with that of the Secco etching solution on silicon-on-insulator substrates. *Materials Science and Engineering B*, 159–160, 309–313 (2009)
- [10] Michael, E.N., Gordon, P.B.: Mg-rich coatings: A new paradigm for Cr-free corrosion protection of Al aerospace alloys. *Journal of Coating Technology and Research* 1, 69–80 (2004)
- [11] Judeinstein, P., Sanchez, C.: Hybrid organic-inorganic materials: a land of multidisciplinarity. *J. Mater. Chem.* 6, 511–525 (1996)
- [12] Lise, T.D.J., Sander, C.G.L., Joop, G.C.W., John, A.J.: Organic-Inorganic Surface Modifications for Titanium Implant Surfaces. *Pharmaceutical Research* 25, 2357–2369 (2008)
- [13] Louis, M., Thomas, J.P.: Direct Synthesis of Hybrid Organic-Inorganic Nanoporous Silica by a Neutral Amine Assembly Route:Structure-Function Control by Stoichiometric Incorporation of Organosiloxane Molecules. *Chem. Mater.* 12, 188–196 (2000)
- [14] Deflorian, F., Rossi, S., Fedrizzi, L., Bonora, P.L.: EIS study of organic coating on zinc surface pretreated with environmentally friendly products. *Progress in Organic Coatings* 29, 89–96 (1996)
- [15] Steven, J.H., Lowe, C., Maxted, J.T., Perruchot, C., Watts, J.F.: Intercoat adhesion failure in a multilayer organic coating system: An X-ray photoelectron spectroscopy study. *Progress in Organic Coatings* 54, 20–27 (2005)

Author Index

- Adachi, Yuto 135
Anh, Ho Pham Huy 605
Anh, Quyen Huy 145
Anh Tuan, Do 29

Baek, Se-Hoon 575
Berhan, Eshetie 211
Bououden, S. 423
Bui, Quang Anh 75
Bui, Thanh Luan 477, 509
Byun, Gi Sig 477

Cahyani, Nila Gita 201
Chadli, M. 25, 423
Chamnongthai, Kosin 135
Chaq, Whilda 201
Chau, Dong Si Thien 445
Chau, Hoang Van 627
Chen, Chih-Keng 413
Chen, Seng-Chi 433
Chi Kien, Le 39
Chlebis, Petr 125
Choi, Hyeung-Sik 565, 575
Chong, Jong-Wha 241

Dang, Duc Ngoc Minh 191
Dang, Hanh Ngoc 191
Dang, Khoa L. 181
Dao, Tran Trong 445
Dat, Than Trong Khanh 595
Davendra, Donald 371
Dieu, Vo Ngoc 57
Dinh, Bach H. 617
Do, The Cuong 191
Doan, Phuc Thinh 477, 509

Dong, Bui An 329
Dung, Huynh Xuan 145
Duong, Anh-Duc 339
Duong, ThanhLong 47
Duy, Lai Nguyen 229
Duy, Vo Hoang 363, 445, 555

Filali, S. 423
Frydrysek, Karel 487
Fu, Ho-Ling 85

García-Moreno, Angel-Iván 317
Giau, Le Van Manh 159
Go, Seungryeol 241
Gonzalez-Barbosa, José-Joel 317

Hanh, Chu Dinh 29
Hau, Vo Huu 445
Hazil, O. 423
Higuchi, Kohji 135
Hoa, Phan Thai 445
Hoang, Khac Anh 545
Hong, Choong Seon 191
Hung, Chih-Wei 413
Hung, Nguyen 585
Hung, Nguyen Thanh 497
Hurtado-Ramos, Juan B. 317

Jahan, Ibrahim Salem 289
Jasek, Roman 371
Jeong, Sang Kwon 555
JianGang, Yao 47

Kalvar, Daniel 259
Ke, Dao Quang 627

- Khanh, Pham Hung Kim 585
 Kim, Dae-Woong 635
 Kim, Hak Kyeong 477, 509, 525, 535
 Kim, Hwan-Seong 391, 457
 Kim, Nam-Suk 635
 Kim, Sang Bong 457, 477, 509, 525, 535, 555
 Kim, Sang-deok 241
 Koga, Hidetsugu 247
 Kurosaki, Masayuki 247
- Le, Dinh-Kha 433
 Le, Phuong Dat 467
 Le, Tan Thanh Tung 75, 93
 Le, Tat-Hien 363
 Le, Trong Nghia 75, 93
 Le, Viet So 497
 Lee, Gueesang 307
 Lee, Sang-Seob 565
 Le Khoa, Dang 221
 Li, Ying-chun 241
 Luan, Bui Thanh 535
- Minh, Tran Hoang Quang 67
 Mochizuki, Yohei 135
- Nam, Jong-Ho 363
 Nam, Ki-Woo 635
 Nam, Nguyen Thanh 605
 Nam, Vo Xuan 159
 Nghia, Nguyen Thanh 145
 Ngo, Chi Trung 169
 Nguyen, Bao Q. 617
 Nguyen, Buu Pham Nhat Tan 103, 113
 Nguyen, Duy Anh 457
 Nguyen, Hien M. 297
 Nguyen, LeAnhTu 47
 Nguyen, Phuong H. 181
 Nguyen, Tan Tien 457, 525
 Nguyen, Thang T. 617
 Nguyen, Thanh Phuong 497
 Nguyen, Tri M. 181
 Nguyen, Tu T. 181
 Nguyen, Van Giap 509
 Nguyen, Van-Sum 433
 Nguyen, Viet D. 297
 Nguyen, Vinh Hao 467
 Nhan, Nguyen Huu Khanh 269
 Nhan, Pham Thanh 145
- Ochi, Hiroshi 247
 Oh, Hoon 169
 Oh, Sea June 525
 Oplatkova, Zuzana Kominkova 371
 Oplustil, Josef 259, 487
 Ornelas-Rodriguez, Francisco-Javier 317
- Palacky, Petr 259, 487
 Pham, Thi Minh Thuy 93
 Phu, Bui Huu 145, 229
 Phuc, Tran Thien 595
 Phuoc, Dong Tan 229
 Phuong, Nguyen Huu 221
 Phuong, Pham Nhat 363
 Platos, Jan 211
 Pleva, Leopold 487
 Pluhacek, Michal 371
 Pratama, Pandu Sandi 535, 555
 Prilepok, Michal 211, 289
- Quang, Pham Minh 229
 Quyen, Huy Anh 75, 93
- Šaloun, Petr 349
 Senkerik, Roman 371
 Seo, Jeong-min 565
 Seong, Ki-Yong 635
 Setiawan, Yuhanes Dedy 555
 Shin, Hee-Young 575
 Shyu, Kuo-Kai 403
 Skanderova, Lenka 381
 Sladecek, Vaclav 259, 487
 Snasel, Vaclav 211, 289
 Soori, Hussein 211
 Sprlak, Roman 125, 259
 Stonawski, Jakub 349
- Tan, Tran Duc 279
 Thang, Nguyen Trung 57
 Thien, Huynh Thanh 85
 Thien, Nguyen Chi 497
 Thinh, Huynh Quoc 329
 Thu, Nguyen Thi Hong 221
 Thuan, Hoang Minh 627
 Thuong, Luc Van 627
 Ting, Lee Cua 403
 Tran, Khoa Anh 307
 Tran, Minh-Triet 339
 Tran, Ngoc-Huy 565, 575
 Tran, Thanh-Do 391

- Tran, Thien Phuc 535
Tran, Xuan-Thuong 391
Trang, Tran Thanh 103, 113, 145, 159
Trinh, Chu Duc 279
Trung, Dao Duy 627
Truong, Toan-Thinh 339
Truong, Trung Hieu 103, 113
Tsai, Yao-Wen 403
Tu, Nguyen Thanh 221
Tuan, Doan Anh 497
Tu Duong, Van 525
Uchoc, Miroslav 259, 487
Van, Tan Luong 103, 113
Van Nho, Nguyen 159
Van Thang, Nguyen 279
Van The, Than 585
Van Van, Huynh 403
Vo, Tuong Quan 545
Voznak, Miroslav 1
Vu, Thai T. 297
Vu, Tri-Vien 413
Winanda, Mukti 201
Yoo, Hyung-ryeol 241
Zelinka, Ivan 15, 349, 371, 381
ZhenWei, Guo 47
Zilka, Lubos 487